Topics in Gravitational Wave Physics: Black-Hole Spectroscopy, Neutron Star Dynamical Tides, and Numerical Relativity

Thesis by
Sizheng Ma

In Partial Fulfillment of the Requirements for the
Degree of
Doctor of Philosophy

CALIFORNIA INSTITUTE OF TECHNOLOGY
Pasadena, California

2023
Defended May 24, 2023

Sizheng Ma
ORCID: 0000-0002-4645-453X

ACKNOWLEDGEMENTS

I am deeply grateful to Yanbei Chen, Mark Scheel, and Saul Teukolsky for their invaluable mentorship, insightful discussions, and invaluable advice throughout my research journey. I would like to especially thank them for their unwavering support and encouragement as I explored numerous research ideas, even when some did not yield the desired results.

My heartfelt gratitude goes to Matthew Giesler for being an exceptional mentor who patiently taught me how to use the numerical-relativity code SpEC during my first year. It was a great pleasure to reconnect with him in my final year to investigate black-hole spectroscopy. Our productive discussions, which could last for four hours on Tuesdays, were an unforgettable experience, and I will miss them dearly.

I owe a debt of thanks to Vijay Varma for introducing me to the field of numerical relativity and for his guidance on paper writing, being accountable, and being an excellent co-author.

I am grateful to Jordan Moxon for being an incredibly patient mentor in teaching me how to use another numerical-relativity code SpECTRE.

I would like to express my sincere appreciation to my SXS collaborators, including Keefe Mitman, Kyle Nelli, Nils Deppe, Leo Stein, Francois Focuart, Geoffrey Lovelace, Katerina Chatziioannou for their insightful discussions.

I am indebted to Ling Sun for sparking ideas, polishing papers, and helping me through LIGO-related matters. I also want to thank Hang Yu, Dongjun Li, Rico K.L. Lo, Maximiliano Isi, and Will Farr for their enlightening discussions.

To my friends Xiang Li, Yuxin Liu, Yiqiu Ma, Baoyi Chen, and my roommate Xiuqi Ma, I am deeply grateful for all kinds of support and assistance.

Finally, I would like to also thank Alan Weinstein and Jim Fuller for serving on my thesis committee.

ABSTRACT

In this thesis, we explore various topics in gravitational wave physics, including black hole spectroscopy, dynamical tides of neutron stars, numerical relativity, and modified theories of gravity.

In our study of black hole spectroscopy, we develop a novel framework for identifying quasinormal modes in ringdown signals. We apply this method to numerical-relativity waveforms of binary black hole systems and find second-order and retrograde quasinormal modes in the ringdown regime. We also apply this method to GW150915, resulting in new insights into the existence of the first overtone. On the other hand, we explore how the excitation of quasinormal modes encodes information about binaries' parameters. Focusing on superkick configurations, we find universal dependence of the mode amplitudes and phases on the binary's configurations.

Tidal effects have significant imprints on gravitational waves emitted during the final stage of the coalescence of binaries involving neutron stars. We examine how dynamical tides can be significant when neutron stars' characteristic oscillations become resonant with orbital motion, and we investigate their impact on measuring neutron-star parameters with gravitational waves. Specifically, we conduct systematic studies on the tidal excitation of fundamental and Rossby modes of spinning neutron stars and find that their effects may be significant and detectable in the era of third-generation gravitational-wave detectors, which in turn could lead to more stringent constraints on the properties of neutron stars.

Regarding numerical relativity, we implement a fully relativistic three-dimensional Cauchy-characteristic matching algorithm to establish a more accurate boundary condition for numerical-relativity simulations. We justify the correctness of the algorithm by nonlinearly propagating gravitational-wave pluses and find that the new boundary condition does reduce spurious numerical reflection at outer boundaries and improves the accuracy of the generated waveforms. The second part focuses on the initial data of binary black holes for numerical simulations. We extend the superposed harmonic initial data, which breaks down for high-spin black holes (dimensionless spin > 0.7), to higher spins by introducing a new spatial coordinate system: superposed modified harmonic. We find that the new initial data preserves a nice property of the superposed harmonic system: the suppression of junk radiation.

Furthermore, we find that the volume-weighted constraint violations for the new initial data converge with numerical resolution during the junk stage, which means there are fewer high-frequency components at outer spacetime regions.

Finally, we investigate the features of gravitational waves within theories beyond general relativity, focusing on two specific aspects. First, we present a numerical-relativity simulation of a black hole-neutron star merger in scalar-tensor gravity with binary parameters consistent with the gravitational wave event GW200115. We consider the Damour-Esposito-Farèse extension to Brans-Dicke theory and find that the scalar-tensor system evolves faster than its general-relativity counterpart due to dipole radiation, merging a full gravitational-wave cycle before the GR counterpart. We also compare the numerical waveforms with post-Newtonian theory and find good agreement during the inspiral. Second, we propose a new approach, based on numerical-relativity waveforms, for reconstructing the late-time near-horizon geometry of merging binary black holes and computing gravitational-wave echoes from exotic compact objects. We use a physically-motivated way to impose boundary conditions near the horizon and apply the Boltzmann reflectivity to compute the quasinormal modes of non-rotating ECOs, as well as gravitational-wave echoes. Additionally, we investigate the detectability of these echoes in current and future detectors and prospects for parameter estimation.

PUBLISHED CONTENT AND CONTRIBUTIONS

[1] Sizheng Ma, Ling Sun, and Yanbei Chen. "Black hole spectroscopy by mode cleaning." *Phys. Rev. Lett.* 130.14 (2023), p. 141401. DOI: 10.1103/PhysRevLett.130.141401. arXiv: 2301.06705 [gr-qc].
S.M. conceived the framework, did all the calculations, and wrote the manuscript.

[2] Sizheng Ma, Ling Sun, and Yanbei Chen. "Using rational filters to uncover the first ringdown overtone in GW150914." *Phys. Rev. D* 107.8 (2023), p. 084010. DOI: 10.1103/PhysRevD.107.084010. arXiv: 2301.06639 [gr-qc].
S.M. conceived the framework, did all the calculations, and wrote the manuscript.

[3] Sizheng Ma, Vijay Varma, Leo C. Stein, Francois Foucart, Matthew D. Duez, Lawrence E. Kidder, Harald P. Pfeiffer, and Mark A. Scheel. "Numerical simulations of black hole-neutron star mergers in scalar-tensor gravity." (Apr. 2023). arXiv: 2304.11836 [gr-qc].
S.M. debugged the numerical-relativity code, ran all the simulations, analyzed all the results, and wrote the manuscript.

[4] Keefe Mitman et al. "Nonlinearities in black hole ringdowns." *Phys. Rev. Lett.* 130.8 (2023), p. 081402. DOI: 10.1103/PhysRevLett.130.081402. arXiv: 2208.07380 [gr-qc].
S.M. participated in the discussions.

[5] Lorenzo Pompili et al. "Laying the foundation of the effective-one-body waveform models SEOBNRv5: Improved accuracy and efficiency for spinning non-precessing binary black holes." (Mar. 2023). arXiv: 2303.18039 [gr-qc].
S.M. ran some numerical-relativity simulations for the calibration of the EOB model.

[6] Nils Deppe et al. "Simulating magnetized neutron stars with discontinuous Galerkin methods." *Phys. Rev. D* 105.12 (2022), p. 123031. DOI: 10.1103/PhysRevD.105.123031. arXiv: 2109.12033 [gr-qc].
S.M. contributed the Cauchy-characteristic matching part of the code.

[7] Sizheng Ma et al. "Gravitational-wave echoes from numerical-relativity waveforms via spacetime construction near merging compact objects." *Phys. Rev. D* 105.10 (2022), p. 104007. DOI: 10.1103/PhysRevD.105.104007. arXiv: 2203.03174 [gr-qc].
S.M. conceived the method, did all the calculations, and wrote the manuscript.

[8] Sizheng Ma et al. "Quasinormal-mode filters: A new approach to analyze the gravitational-wave ringdown of binary black-hole mergers." *Phys. Rev.*

D 106.8 (2022), p. 084036. DOI: 10.1103/PhysRevD.106.084036. arXiv: 2207.10870 [gr-qc].
S.M. led the conception of the project, did all the calculations, and wrote the manuscript.

[9] Sizheng Ma, Hang Yu, and Yanbei Chen. "Detecting resonant tidal excitations of Rossby modes in coalescing neutron-star binaries with third-generation gravitational-wave detectors." *Phys. Rev. D* 103.6 (2021), p. 063020. DOI: 10.1103/PhysRevD.103.063020. arXiv: 2010.03066 [gr-qc].
S.M. participated in the conception of the project, did all the calculations, and wrote the manuscript.

[10] Sizheng Ma et al. "Extending superposed harmonic initial data to higher spin." *Phys. Rev. D* 103.8 (2021), p. 084029. DOI: 10.1103/PhysRevD.103.084029. arXiv: 2102.06618 [gr-qc].
S.M. conceived the method, did all the calculations, and wrote the manuscript.

[11] Sizheng Ma et al. "Universal features of gravitational waves emitted by superkick binary black hole systems." *Phys. Rev. D* 104.8 (2021), p. 084003. DOI: 10.1103/PhysRevD.104.084003. arXiv: 2107.04890 [gr-qc].
S.M. participated in the conception of the project, did all the calculations, and wrote the manuscript.

[12] Shuo Xin et al. "Gravitational-wave echoes from spinning exotic compact objects: Numerical waveforms from the Teukolsky equation." *Phys. Rev. D* 104.10 (2021), p. 104005. DOI: 10.1103/PhysRevD.104.104005. arXiv: 2105.12313 [gr-qc].
S.M. participated in the discussions.

[13] Sizheng Ma, Hang Yu, and Yanbei Chen. "Excitation of f-modes during mergers of spinning binary neutron star." *Phys. Rev. D* 101.12 (2020), p. 123020. DOI: 10.1103/PhysRevD.101.123020. arXiv: 2003.02373 [gr-qc].
S.M. participated in the conception of the project, did all the calculations, and wrote the manuscript.

[14] Hang Yu et al. "Spin and eccentricity evolution in triple systems: From the Lidov-Kozai interaction to the final merger of the inner binary." *Phys. Rev. D* 102 (2020), p. 123009. DOI: 10.1103/PhysRevD.102.123009. arXiv: 2007.12978 [gr-qc].
S.M. calculated the gravitational kicks.

[15] Davide Gerosa et al. "Multiband gravitational-wave event rates and stellar physics." *Phys. Rev. D* 99.10 (2019), p. 103004. DOI: 10.1103/PhysRevD.99.103004. arXiv: 1902.00021 [astro-ph.HE].
S.M. proposed to use the "effective time window" to estimate multiband event rates (Fig. 1).

TABLE OF CONTENTS

LIST OF ILLUSTRATIONS

Number *Page*

LIST OF TABLES

Chapter 1

INTRODUCTION

Gravitational wave (GW) astronomy has been flourishing since the groundbreaking detection of GW150914 [1, 2]. Nowadays, GWs have become a powerful tool for probing the properties of compact binaries, and the neutron stars (NSs) and black holes (BHs) they contain. Detecting GWs is a challenging task because astrophysical gravitational waves become very weak when they arrive at the vicinity of the earth. Therefore, the success of GW astrophysics requires close collaborations between different fields, including accurate modeling of the merging of compact objects with analytical and numerical tools, as well as efficient data analysis methods to extract astrophysical information from noise. This thesis, comprising ten research papers, aims to contribute to these ongoing efforts in GW measurements by discussing some of the techniques involved.

The thesis covers four aspects. Part I (Chapters 2-4) focuses on the development of a new tool for BH spectroscopy to explore the nature of BHs and their corresponding GW emissions. Part II (Chapters 5-6) investigates the dynamical tides of neutron stars (NSs) and their imprints on GWs. Part III (Chapters 7-8) delves into numerical relativity (NR). Part IV (Chapters 9-10) explores beyond-general relativity (GR) theories. In the rest of this chapter, I will provide background information on these aspects separately.

1.1 Black hole spectroscopy

The ringdown stage of a GW event emitted by a binary black hole (BBH) corresponds to the oscillation of the remnant BH, which encodes rich information about the remnant black hole, as well as the binary that produced it. At the linear order, a ringdown waveform is dominated by a superposition of a set of quasinormal modes (QNMs), with complex eigenfrequencies [3–6], labeled by two angular numbers (l, m) and one overtone index n. Within GR, the mode frequencies are fully determined by the mass, spin, and charge of the corresponding BH due to the no-hair theorem [7–10]. Thus measuring the frequency and decay rate of a single QNM from a ringdown signal can already lead to the estimates of the properties of the remnant BH [11]. If additional modes are also detected from the same event, we can then use them to test the no-hair theorem [12–14]. This method is known as *BH*

spectroscopy [15–41].

With an increasing number of GW events [42–45] observed by ground-based detectors [46–48], comprehensive studies of the ringdown signal and its rich features become crucial to understanding the geometry of extreme spacetimes and testing GR. An important theoretical foundation of BH spectroscopy is to understand which QNMs are present in the ringdown of a NR waveform [49–66] and when they start [67–69]. To address these questions, a common method is to fit the NR waveform after the merger, starting at, say, t_0, using a ringdown template that consists of a group of QNMs via linear combination, and explore when the mismatch between the NR waveform and the QNM template can be minimized by varying the QNMs and the fitting start time t_0. In particular, Giesler *et al.* [64] demonstrated that the ringdown of a GW150914-like NR waveform [70] starts as early as when the strain amplitude reaches its peak, if seven overtones are included. Motivated by this result, Isi *et al.* [28, 32] extended the initial ringdown analyses [31, 71] of GW150914 [1] and explored earlier start times for fitting. A significance of 3.6σ was found for the existence of the first overtone. However, these conclusions have been challenged. Baibhav *et al.* [72] and Nee *et al.* [73] revisited some numerical waveforms and found that the evidence for overtones was weak, implying that the conclusion by Giesler *et al.* [64] could be a result of overfitting. Cotesta *et al.* [30] also challenged the results by Isi *et al.* [32] and argued that the early (ringdown) signal of GW150914 could be noise dominated, and thus the existence of the first overtone might not be reliable.

QNMs do not form a complete or orthogonal basis, posing difficulties in decomposing a ringdown waveform. This task becomes even more challenging when overtones decay rapidly. Therefore, the current QNM fitting techniques, such as least-square fit, may not be robust enough to reveal the existence of overtones—the poor fit results presented in [72, 73] do not necessarily mean that overtones lack physical significance in the ringdown of the waveforms. In response, we propose a complementary tool to analyze a ringdown waveform in Chapters 2 and 3. Our approach defines two frequency-domain filters that can remove specific QNMs from the ringdown. By filtering out the dominant mode, we can provide new insights into the presence of a QNM in the waveform. This approach has the potential to overcome challenges associated with the least-square technique.

1.2 Dynamical tides of neutron stars

NSs are fascinating objects in our universe governed by laws of physics from multiple disciplines, ranging from macroscopic magnetohydrodynamics to microscopic Quantum Chromodynamics, from electromagnetic emissions to GWs. The study of NSs provides valuable information about the properties of dense matter in extreme gravity environments [74–76]. The detection of GW170817 and its electromagnetic counterparts [77–80] has opened a new era of multimessenger astrophysics and has allowed for more precise constraints on NS properties. Since then, subsequent events such as GW190425 [81], GW200105, and GW200115 [82] have provided additional information on tidal deformabilities [83–86], the maximum mass [84, 87–90], radii [83, 86] and f-mode frequencies [91] of NSs. With improved detector sensitivity, we expect more detections of binary neutron star (BNS) and black hole-neutron star (BHNS) mergers in the near future [92–95]. Additionally, 3G detectors like the Einstein Telescope [96, 97] and the Cosmic Explorer [98] are planned to be operational in the 2030s and may increase BHNS and BNS detection rates by 3-4 orders of magnitude [99]. This highlights the need for more accurate modeling of the imprints of NSs in corresponding GW signals [100–105].

Mass, radius, and tidal deformability are three important macroscopic observables that can be learned from the multimessenger detections [106]. They provide insights into the equation of state of a NS and serve as a critical link to understanding their internal structure and dense matter microphysics [107, 108]. Specifically, the tidal deformability measures the response of the NS to the tidal gravitational field induced by its binary companion during orbital motion [109–111]: The tidal gravitational field causes deformation in the NS and induces multipole moments. The coupling between these moments and the tidal field alters the binding energy of the binary system and increases the rate of energy dissipation [110, 112], which in turn hastens the evolution of the binary.

In general, tidal effects can be divided into two categories. In the early inspiral stage [110], the NS is in a quasi-equilibrium state, and the tidal response can be approximated using a quasi-equilibrium approach, known as the *adiabatic tide* [109, 110, 112–119]. As the evolution progresses towards the final few minutes, the tidal driving frequency from the companion may approach a normal mode frequency of the NS. This can lead to resonant excitation of stellar internal fluid motion, causing energy and angular momentum exchanges with the orbital motion. This phenomenon is known as the *dynamical tide* [120–126].

In contrast to a BH's QNM spectra, which are fully characterized by two angular indices (l, m) and an overtone index n, a NS's characteristic oscillation exhibits much richer structures [127]. The $f-$mode, which is driven by pressure, represents the lowest-order, fundamental, zero-radial-node oscillation of the NS. Its overtones are called $p-$modes, which have more radial nodes and higher frequencies. The $g-$modes are another branch, and their restoring force is mainly determined by buoyancy resulting from thermal or compositional gradients. Typically, their frequencies are lower than that of the $f-$mode. As the $f-$mode, $g-$modes, and $p-$modes possess even parity, they are collectively referred to as polar modes. On the other hand, axial modes emerge when the NS rotates, such as $r-$modes and $i-$modes. These modes are mainly sustained by the Coriolis force [128–130] and have odd parity.

If some of the characteristic modes of the NS are excited during the inspiral stage, the imprints in the corresponding GW emissions could provide new channels to probe the stellar inner structure in addition to the adiabatic tide. Below in Chapters 5 and 6, we will focus on the excitability of the $f-$mode and $r-$modes and investigate how these two new channels can be used to put tighter constraints on the properties of NSs.

1.3 Numerical relativity

NR is to use computer simulations to perform numerical experiments for GR and beyond-GR theories. To date, NR still remains the only *ab initio* method to simulate highly dynamic gravitational processes, such as the coalescence of BBH systems. Generally speaking, the formulations of NR can be classified into two groups: Cauchy [131, 132] and characteristic [133–140] formalisms, depending on how spacetime is foliated.

The Cauchy approach to NR involves decomposing 4-dimensional spacetime into 3-dimensional space and 1-dimensional time, and splitting Einstein's equations into constraint and evolution parts. This method converts Einstein's equations into an initial-boundary value problem, which is also known as the *Cauchy problem*. To begin a simulation, initial data are constructed by solving the constraint equations on the first space-like hypersurface. These data are then propagated using the evolution equations. A drawback of the Cauchy method is that it cannot be used to simulate the entire unbounded spacetime due to the limit of computational resources. As a result, the spatial domain is typically truncated at a finite distance from the source to create a finite computational domain. Suitable boundary conditions need to be

specified at the artificial boundary, and proper waveform extraction methods [139–142] must be used to compute GWs at future null infinity, where GW detectors are approximately located.

In contrast, the characteristic formalism is a different formulation of GR and is capable of overcoming some of Cauchy method's limitations. With this approach, spacetime is sliced into a sequence of null hypersurfaces that extend to future null infinity. Einstein's equations are formulated in terms of the unambiguous geometric treatment of gravitational radiation in curved spacetimes due to Bondi *et al.* [143] Sachs [144] and Penrose [145]. Meanwhile, future null infinity is rigorously encompassed on the characteristic grid via a compactified coordinate system and treated as a perfect absorbing outer boundary. In this way, the characteristic formalism offers the most natural and correct way to extract faithful GWs at future null infinity without any ambiguity [141, 142, 146–148]. However, the characteristic method cannot evolve the near-field region of BBHs when caustics of null rays are present. Therefore, the Cauchy and characteristic systems can be used jointly in practice to simulate both near-zone and wave-zone. This procedure is known as *Cauchy-characteristic evolution* [133–140, 149].

The initial data and boundary conditions are crucial components of a Cauchy simulation as they provide all the necessary information about the physical system under investigation. To ensure a high-accuracy NR simulation, it is imperative that the initial data and boundary conditions capture the correct and precise information about the system. Failure to achieve this can lead to systematic errors, which can significantly affect the quality of the produced results. For instance, when simulating a BBH system, the initial data should correspond to a quasi-equilibrium state of the inspiral that started at an infinite time in the past. If the initial data fails to recover the full tidal distortion of a BH or the gravitational radiation that is already present, the system will relax into a quasi-equilibrium state once the evolution begins, resulting in junk radiation during the evolution. This junk transient can contaminate the quality of the produced gravitational waveforms, and affect the accuracy of the adaptive mesh refinement algorithm [150] to control numerical errors. Similarly, perfect boundary conditions should make the artificial boundary as transparent as possible so that the numerical solution is identical to one that would be evolved on an infinite domain. In particular, outgoing GW radiation at arbitrarily far distances can backscatter off the spacetime curvature due to the nonlinear feature of GR. Ideal boundary conditions should include this nonlinear backscattering. If poor boundary

conditions are prescribed, not only will the effect of backscattering be incorrectly implemented, but spurious reflections can also be introduced at the boundary and contaminate the whole simulation.

Below we will analyze the boundary-value and initial-data problems individually. Chapter 7 will focus on the boundary-value problem, where we will explore how the characteristic system can be employed to create more precise boundary conditions for the Cauchy system. In Chapter 8, we will discuss the initial-data problem and introduce a new gauge that can generate weaker junk radiation, which will assist in establishing Cauchy's initial data.

1.4 Beyond general relativity

Einstein's famous quote, "I would feel sorry for the good Lord. The theory is correct," succinctly summarizes the elegant foundations of GR. To date, GR has successfully passed many tests [151, 152] and remains the best description of gravity. However, it is not renormalizable and is ultraviolet-incomplete, which suggests that it may not be correct at all scales. Therefore, non-negligible corrections to GR might arise in extreme conditions; probing these environments can help us search for such deviations, which can place stringent constraints on both GR and beyond-GR theories.

The collision of two BHs creates one of the most curved spacetime environments in the universe, making their GW emissions a crucial tool for this purpose [75, 151–171]. To rigorously test GR, accurate predictions of GWs are necessary for both GR and modified theories of gravity. To date, numerous extensions to GR have been proposed [152], and their resulting GW emissions exhibit diverse features. In this thesis, we mainly focus on two specific aspects: scalar-tensor (ST) theory, which modifies Einstein's Equations; and GW echoes, which arise from direct modifications of the geometries of spacetime near the horizons of BHs.

1.4.1 Scalar-tensor theory

ST theory [172–175] is the simplest alternative theory of gravity, where the strength of gravity is modulated by scalar field(s). An important feature of ST theory is scalar radiation, an extra energy dissipation channel in addition to the usual tensor radiation in GR. The leading scalar radiation is dipolar, and thus more important at low frequencies than the quadrupolar waves that control a GR inspiral [154, 176–190]. Under this effect, the evolution of some strong-gravity systems can deviate from the prediction of GR and leave imprints on observables. For instance,

binary-pulsar systems have been shown to be a good laboratory [167, 176, 184, 190–209] since the celebrated Hulse-Taylor PSR B1913+16 [210]. By measuring the orbital decay rate of the systems, one can examine and constrain ST theory via the parametrized post-Keplerian formalism [203–205, 211].

The deviation could be even more amplified if the system is a BH-NS binary, and the NS undergoes *spontaneous scalarization* [212–221]. As pointed out by Damour and Esposito-Farèse [205, 222], for certain variants of the ST theory, the equilibrium solutions for a NS's structure bifurcates into several branches at some critical central density, and the GR branch becomes unstable [223, 224]. The most stable solution corresponds to a scalarized NS with a much larger scalar charge [185, 195, 222, 225]. Therefore, the dipole radiation and consequential deviations from GR are significantly amplified in such a scalarized BHNS system, which makes it, if exists, an ideal environment for studying ST theory.

In Chapter 9 we will use NR to simulate a BHNS merger in ST theory, with a particular focus on how GW emission is impacted by spontaneous scalarization.

1.4.2 GW echoes

GW echoes are the repeating and delayed pulses that follow the primary GWs emitted by binary mergers [226–229]. These echoes could be indicative of several phenomena, including deviations from the laws of gravity described by GR [230, 231], the presence of near-horizon quantum structures surrounding BHs [232–241], or the existence of horizonless Exotic Compact Objects (ECOs) [242–246]. Regardless of the underlying cause, all of these scenarios share the common characteristic that the remnant object resulting from the merger has the same geometry as a BH described by GR, except in a small region near the horizon (i.e., with size $\ll M$, where M is the BH mass) [247–249]. This non-GR zone acts as a reflective surface, forming a cavity with the light ring, which consequently traps GWs and causes them to bounce back and forth within it. During this process, portions of the trapped GWs escape to infinity, resulting in the echoes observed by observers at future null infinity. Therefore, the detection of GW echoes, if they exist, could provide compelling evidence of Planck-scale structures near horizons and ECOs. In Chapter 10, we will discuss how to build an approximate GW echo model using NR simulations.

1.5 Organization of the thesis

Here is a list of brief summaries of Chapters 2 to 10 of this thesis.

1.5.1 Chapter 2: Quasinormal-mode filters: A new approach for black-hole spec- troscopy

We propose two frequency-domain filters to analyze ringdown signals of BBH mergers. The first rational filter is constructed based on a set of (arbitrary) QNMs of the remnant BHs, whereas the second full filter comes from the transmissivity of the remnant BHs. The two filters can remove corresponding QNMs from original time-domain ringdowns, while changing early inspiral signals in a trivial way—merely a time and phase shift. After filtering out dominant QNMs, we can visualize the existence of various subdominant effects. For example, by applying our filters to a GW150914-like NR waveform, we find second-order effects in the $(l = 4, m = 4)$, $(l = 5, m = 4)$ and $(l = 5, m = 5)$ harmonics; the spherical-spheroidal mixing mode in the $(l = 2, m = 2)$ harmonic; and a mixing mode in the $(l = 2, m = 1)$ harmonic due to a gravitational recoil. In another NR simulation where two component spins are anti-aligned with the orbital angular momentum, we also find retrograde modes. Furthermore, we investigate the stability of the full filter. Its connection to the instability of QNM spectra is discussed.

1.5.2 Chapter 3: Black hole spectroscopy by mode cleaning

We formulate a Bayesian framework to analyze ringdown GWs from colliding BBHs and test the no-hair theorem. The idea hinges on mode cleaning—revealing subdominant oscillation modes by removing dominant ones using newly proposed *rational filters*. By incorporating the filter into Bayesian inference, we construct a likelihood function that depends only on the mass and spin of the remnant BH (no dependence on mode amplitudes and phases) and implement an efficient pipeline to constrain the remnant mass and spin without Markov chain Monte Carlo (MCMC). We test ringdown models by cleaning combinations of different modes and evaluating the consistency between the residual data and pure noise. The model evidence and Bayes factor are used to demonstrate the presence of a particular mode and to infer the mode starting time. In addition, we design a hybrid approach to estimate the remnant BH properties exclusively from a single mode using MCMC after mode cleaning. We apply the framework to GW150914 and demonstrate more definitive evidence of the first overtone by cleaning the fundamental mode.

1.5.3 Chapter 4: Universal features of gravitational waves emitted by superkick binary black hole systems

We use NR to study the merger and ringdown stages of "superkick" BBH systems (those with equal mass and anti-parallel spins). We find a universal way to describe the mass and current quadrupole GWs emitted by these systems during the merger and ringdown stage: (i) The time evolutions of these waves are insensitive to the progenitor's parameters (spins) after being normalized by their own peak values. (ii) The peak values, which encode all the spin information of the progenitor, can be consistently fitted to formulas inspired by post-Newtonian theory. We find that the universal evolution of the mass quadrupole wave can be accurately modeled by the so-called Backwards One-Body (BOB) model. However, the BOB model, in its present form, leads to a lower waveform match and a significant parameter-estimation bias for the current quadrupole wave. We also decompose the ringdown signal into seven overtones, and study the dependence of mode amplitudes on the progenitor's parameters. Such dependence is found to be insensitive to the overtone index (up to a scaling factor). Finally, we use the Fisher matrix technique to investigate how the ringdown waveform can be at least as important for parameter estimation as the inspiral stage. Assuming the Cosmic Explorer, we find the contribution of the ringdown portion dominates as the total mass exceeds $\sim 250\,M_\odot$. For massive BBH systems, the accuracy of parameter measurement is improved by incorporating the information of ringdown—the ringdown sector gives rise to a different parameter correlation from the inspiral stage, hence the overall parameter correlation is reduced in the full signal.

1.5.4 Chapter 5: Excitation of f-modes during mergers of spinning binary neutron star

We use semi-analytic methods to carry out a systematic study on the tidal excitation of f-modes of spinning NSs in coalescing binaries, focusing on the case when the NS spin is anti-aligned with the orbital angular momentum – where the tidal resonance is most likely to take place. We first expand NS oscillations into stellar eigenmodes, and then obtain a Hamiltonian that governs the tidally coupled orbit-mode evolution. We then find a new approximation that can lead to analytic expressions of tidal excitations to high accuracy, and are valid in all regimes of the binary evolution: adiabatic, resonant, and post-resonance. Using the method of osculating orbits, we obtain semi-analytic approximations of the orbital evolution and GW emission; their agreements with numerical results give us confidence in our understanding of

the system's dynamics. In particular, we recover both the averaged post-resonance evolution, which differs from the pre-resonance point-particle orbit by shifts in orbital energy and angular momentum, as well as instantaneous perturbations driven by the tidal motion. Finally, we use the Fisher matrix technique to study the effect of dynamical tides on parameter estimation.

1.5.5 Chapter 6: Detecting resonant tidal excitations of Rossby modes in coalescing neutron-star binaries with third-generation gravitational-wave detectors

We study NSs' r-mode excitation by the gravitomagnetic forces in coalescing binary systems, and explore its impact on measuring NS parameters in the era of 3G detectors. We incorporate two universal relations among NS properties predicted by different equations of state: (i) the well-known I-Love relation between momentum of inertia and (f-mode) tidal Love number, and (ii) a relation between the r-mode overlap and tidal Love number, which is newly explored in this paper. We find that r-mode dynamical tide will provide rich information about slowly rotating NSs with frequency $10-100$ Hz and spin inclination angle $18^\circ-110^\circ$. For a BNS system (with a signal-to-noise ratio ~ 1500 in the Cosmic Explorer), the spin frequency of each individual NS can be constrained to 6% (fractional error) in the best-case scenario. The degeneracy between the Love numbers of individual NSs is dramatically reduced: each individual Love number can be constrained to around 20% in the best case, while the fractional error for both symmetric and anti-symmetric Love numbers are reduced by factors of around 300. Furthermore, the dynamical tide also allows us to measure the spin inclination angles of the NSs, to 0.09 rad in the best case, and thus place constraints on NS natal kicks and supernova explosion models.

1.5.6 Chapter 7: Fully relativistic 3D Cauchy-characteristic matching

We implement a fully relativistic 3D Cauchy-characteristic matching (CCM) algorithm in a NR code SpECTRE. The stability of the algorithm is demonstrated by propagating a GW pulse on a flat background nonlinearly. We consider two physical systems (a) the (ingoing) pulse is put on the characteristic grid initially (b) the (outgoing) pulse is put on the Cauchy grid initially. The former case verifies that our CCM algorithm can send the pulse from the exterior characteristic grid to the interior Cauchy grid accurately. It is also shown that the interface between two grids is transparent to the GW since spurious reflection is reduced. In the second case, we

illustrate that the matching algorithm leads to better boundary conditions for the inner Cauchy evolution by precisely modeling the back-scattering of GWs. Compared with a run without the matching, the CCM system exhibits better agreement with a reference simulation whose outer boundary is put far away to ensure it is causally disconnected from the system.

1.5.7 Chapter 8: Extending superposed harmonic initial data to higher spin

Numerical simulations of BBHs are accompanied by an initial spurious burst of gravitational radiation (called 'junk radiation') caused by a failure of the initial data to describe a snapshot of an inspiral that started at an infinite time in the past. A previous study showed that the superposed harmonic (SH) initial data gives rise to significantly smaller junk radiation. However, it is difficult to construct SH initial data for black holes with dimensionless spin $\chi \gtrsim 0.7$. We here provide a class of spatial coordinate transformations that extend SH to higher spin. The new spatial coordinate system, which we refer to as superposed modified harmonic (SMH), is characterized by a continuous parameter — Kerr-Schild and harmonic spatial coordinates are only two special cases of this new gauge. We compare SMH with the superposed Kerr-Schild (SKS) initial data by evolving several BBH systems with $\chi = 0.8$ and 0.9. We find that the new initial data still leads to less junk radiation and only small changes in BH parameters (e.g., mass and spin). We also find that the volume-weighted constraint violations for the new initial data converge with resolution during the junk stage ($t \lesssim 700M$), which means there are fewer high-frequency components in waveforms at outer regions.

1.5.8 Chapter 9: Numerical simulations of black hole–neutron star mergers in scalar-tensor gravity

We present a numerical-relativity simulation of a BHNS merger in ST gravity with binary parameters consistent with the GW event GW200115. In this exploratory simulation, we consider the Damour-Esposito-Farèse extension to Brans-Dicke theory, and maximize the effect of spontaneous scalarization by choosing a soft equation of state and ST theory parameters at the edge of known constraints. We extrapolate the GWs, including tensor and scalar (breathing) modes, to future null-infinity. The numerical waveforms undergo ~ 22 wave cycles before the merger, and are in good agreement with predictions from post-Newtonian theory during the inspiral. We find the ST system evolves faster than its GR counterpart due to dipole radiation, merging a full GW cycle before the GR counterpart. This enables easy differen-

tiation between the ST waveforms and GR in the context of parameter estimation. However, we find that dipole radiation's effect may be partially degenerate with the NS tidal deformability during the late inspiral stage, and a full Bayesian analysis is necessary to fully understand the degeneracies between ST and binary parameters in GR.

1.5.9 Chapter 10: Gravitational-wave echoes from numerical-relativity waveforms via space-time construction near merging compact objects

We propose a new approach toward reconstructing the late-time near-horizon geometry of merging BBHs, and toward computing GW echoes from ECOs. A BBH merger spacetime can be divided by a time-like hypersurface into a Black-Hole Perturbation (BHP) region, in which the space-time geometry can be approximated by homogeneous linear perturbations of the final Kerr BH, and a nonlinear region. At late times, the boundary between the two regions is an infalling shell. The BHP region contains late-time GWs emitted toward the future horizon, as well as those emitted toward future null infinity. In this region, by imposing no-ingoing wave conditions at past null infinity, and matching out-going waves at future null infinity with waveforms computed from NR, we can obtain waves that travel toward the future horizon. In particular, the Newman-Penrose ψ_0 associated with the in-going wave on the horizon is related to tidal deformations measured by fiducial observers floating above the horizon. We further determine the boundary of the BHP region on the future horizon by imposing that ψ_0 inside the BHP region can be faithfully represented by QNMs. Using a physically-motivated way to impose boundary conditions near the horizon, and applying the so-called Boltzmann reflectivity, we compute the QNMs of non-rotating ECOs, as well as GW echoes. We also investigate the detectability of these echoes in current and future detectors, and prospects for parameter estimation.

References

[1] Benjamin P. Abbott et al. "Observation of gravitational waves from a binary black hole merger." *Phys. Rev. Lett.* 116.6 (2016), p. 061102. DOI: 10.1103/PhysRevLett.116.061102. arXiv: 1602.03837 [gr-qc].

[2] Benjamin P. Abbott et al. "Properties of the binary black hole merger GW150914." *Phys. Rev. Lett.* 116.24 (2016), p. 241102. DOI: 10.1103/PhysRevLett.116.241102. arXiv: 1602.03840 [gr-qc].

[3] Kostas D. Kokkotas and Bernd G. Schmidt. "Quasinormal modes of stars and black holes." *Living Rev. Rel.* 2 (1999), p. 2. DOI: 10.12942/lrr-1999-2. arXiv: gr-qc/9909058.

[4] Hans-Peter Nollert. "Quasinormal modes: the characteristic 'sound' of black holes and neutron stars." *Classical and Quantum Gravity* 16.12 (Nov. 1999), R159–R216. DOI: 10.1088/0264-9381/16/12/201. URL: https://doi.org/10.1088/0264-9381/16/12/201.

[5] Vitor Cardoso and Leonardo Gualtieri. "Testing the black hole 'no-hair' hypothesis." *Class. Quant. Grav.* 33.17 (2016), p. 174001. DOI: 10.1088/0264-9381/33/17/174001. arXiv: 1607.03133 [gr-qc].

[6] Emanuele Berti, Vitor Cardoso, and Andrei O. Starinets. "Quasinormal modes of black holes and black branes." *Class. Quant. Grav.* 26 (2009), p. 163001. DOI: 10.1088/0264-9381/26/16/163001. arXiv: 0905.2975 [gr-qc].

[7] Roger Penrose. ""Golden Oldie": Gravitational collapse: The role of general relativity." *General relativity and Gravitation* 34.7 (2002), pp. 1141–1165.

[8] Piotr T. Chrusciel, Joao Lopes Costa, and Markus Heusler. "Stationary black holes: uniqueness and beyond." *Living Rev. Rel.* 15 (2012), p. 7. DOI: 10.12942/lrr-2012-7. arXiv: 1205.6112 [gr-qc].

[9] Brandon Carter. "Axisymmetric black hole has only two degrees of freedom." *Phys. Rev. Lett.* 26 (6 Feb. 1971), pp. 331–333. DOI: 10.1103/PhysRevLett.26.331. URL: https://link.aps.org/doi/10.1103/PhysRevLett.26.331.

[10] Werner Israel. "Event horizons in static vacuum space-times." *Phys. Rev.* 164 (5 Dec. 1967), pp. 1776–1779. DOI: 10.1103/PhysRev.164.1776. URL: https://link.aps.org/doi/10.1103/PhysRev.164.1776.

[11] Fernando Echeverria. "Gravitational-wave measurements of the mass and angular momentum of a black hole." *Phys. Rev. D* 40 (10 Nov. 1989), pp. 3194–3203. DOI: 10.1103/PhysRevD.40.3194. URL: https://link.aps.org/doi/10.1103/PhysRevD.40.3194.

[12] Olaf Dreyer et al. "Black hole spectroscopy: Testing general relativity through gravitational wave observations." *Class. Quant. Grav.* 21 (2004), pp. 787–804. DOI: 10.1088/0264-9381/21/4/003. arXiv: gr-qc/0309007 [gr-qc].

[13] Emanuele Berti, Vitor Cardoso, and Clifford M. Will. "On gravitational-wave spectroscopy of massive black holes with the space interferometer LISA." *Phys. Rev.* D73 (2006), p. 064030. DOI: 10.1103/PhysRevD.73.064030. arXiv: gr-qc/0512160 [gr-qc].

[14] Emanuele Berti et al. “Matched-filtering and parameter estimation of ringdown waveforms.” *Phys. Rev. D* 76 (2007), p. 104044. DOI: 10.1103/PhysRevD.76.104044. arXiv: 0707.1202 [gr-qc].

[15] Sarah Gossan, John Veitch, and Bangalore S. Sathyaprakash. “Bayesian model selection for testing the no-hair theorem with black hole ringdowns.” *Phys. Rev.* D85 (2012), p. 124056. DOI: 10.1103/PhysRevD.85.124056. arXiv: 1111.5819 [gr-qc].

[16] Vishal Baibhav and Emanuele Berti. “Multimode black hole spectroscopy.” *Phys. Rev. D* 99.2 (2019), p. 024005. DOI: 10.1103/PhysRevD.99.024005. arXiv: 1809.03500 [gr-qc].

[17] Gregorio Carullo et al. “Empirical tests of the black hole no-hair conjecture using gravitational-wave observations.” *Phys. Rev. D* 98.10 (2018), p. 104020. DOI: 10.1103/PhysRevD.98.104020. arXiv: 1805.04760 [gr-qc].

[18] Richard Brito, Alessandra Buonanno, and Vivien Raymond. “Black-hole spectroscopy by making full use of gravitational-wave modeling.” *Phys. Rev. D* 98.8 (2018), p. 084038. DOI: 10.1103/PhysRevD.98.084038. arXiv: 1805.00293 [gr-qc].

[19] Hiroyuki Nakano et al. “Comparison of various methods to extract ringdown frequency from gravitational wave data.” *Phys. Rev. D* 99.12 (2019), p. 124032. DOI: 10.1103/PhysRevD.99.124032. arXiv: 1811.06443 [gr-qc].

[20] Miriam Cabero et al. “Black hole spectroscopy in the next decade.” *Phys. Rev. D* 101.6 (2020), p. 064044. DOI: 10.1103/PhysRevD.101.064044. arXiv: 1911.01361 [gr-qc].

[21] Swetha Bhagwat et al. “Detectability of the subdominant mode in a binary black hole ringdown.” *Phys. Rev. D* 102.2 (2020), p. 024023. DOI: 10.1103/PhysRevD.102.024023. arXiv: 1910.13203 [gr-qc].

[22] Iara Ota and Cecilia Chirenti. “Overtones or higher harmonics? Prospects for testing the no-hair theorem with gravitational wave detections.” *Phys. Rev. D* 101.10 (2020), p. 104005. DOI: 10.1103/PhysRevD.101.104005. arXiv: 1911.00440 [gr-qc].

[23] Juan Calderón Bustillo, Paul D. Lasky, and Eric Thrane. “Black-hole spectroscopy, the no-hair theorem, and GW150914: Kerr versus Occam.” *Phys. Rev. D* 103.2 (2021), p. 024041. DOI: 10.1103/PhysRevD.103.024041. arXiv: 2010.01857 [gr-qc].

[24] Xisco Jiménez Forteza et al. “Spectroscopy of binary black hole ringdown using overtones and angular modes.” *Phys. Rev. D* 102.4 (2020), p. 044053. DOI: 10.1103/PhysRevD.102.044053. arXiv: 2005.03260 [gr-qc].

[25] Maximiliano Isi and Will M. Farr. "Analyzing black-hole ringdowns." (July 2021). arXiv: 2107.05609 [gr-qc].

[26] Sarah Caudill et al. "Reduced basis representations of multi-mode black hole ringdown gravitational waves." *Class. Quant. Grav.* 29 (2012), p. 095016. DOI: 10.1088/0264-9381/29/9/095016. arXiv: 1109.5642 [gr-qc].

[27] Eliot Finch and Christopher J. Moore. "Frequency-domain analysis of black-hole ringdowns." *Phys. Rev. D* 104.12 (2021), p. 123034. DOI: 10.1103/PhysRevD.104.123034. arXiv: 2108.09344 [gr-qc].

[28] Maximiliano Isi and Will M. Farr. "Revisiting the ringdown of GW150914." (Feb. 2022). arXiv: 2202.02941 [gr-qc].

[29] Eliot Finch and Christopher J. Moore. "Searching for a ringdown overtone in GW150914." *Phys. Rev. D* 106.4 (2022), p. 043005. DOI: 10.1103/PhysRevD.106.043005. arXiv: 2205.07809 [gr-qc].

[30] Roberto Cotesta et al. "On the detection of ringdown overtones in GW150914." (Jan. 2022). arXiv: 2201.00822 [gr-qc].

[31] Benjamin P. Abbott et al. "Tests of general relativity with GW150914." *Phys. Rev. Lett.* 116.22 (2016). [Erratum: Phys. Rev. Lett.121,no.12,129902(2018)], p. 221101. DOI: 10.1103/PhysRevLett.116.221101. arXiv: 1602.03841 [gr-qc].

[32] Maximiliano Isi et al. "Testing the no-hair theorem with GW150914." *Phys. Rev. Lett.* 123.11 (2019), p. 111102. DOI: 10.1103/PhysRevLett.123.111102. arXiv: 1905.00869 [gr-qc].

[33] Collin D. Capano et al. "Observation of a multimode quasi-normal spectrum from a perturbed black hole." (May 2021). arXiv: 2105.05238 [gr-qc].

[34] Collin D. Capano et al. "Statistical validation of the detection of a sub-dominant quasi-normal mode in GW190521." (Sept. 2022). arXiv: 2209.00640 [gr-qc].

[35] Jeroen Meidam et al. "Testing the no-hair theorem with black hole ringdowns using TIGER." *Phys. Rev. D* 90.6 (2014), p. 064009. DOI: 10.1103/PhysRevD.90.064009. arXiv: 1406.3201 [gr-qc].

[36] Swetha Bhagwat, Duncan A. Brown, and Stefan W. Ballmer. "Spectroscopic analysis of stellar mass black-hole mergers in our local universe with ground-based gravitational wave detectors." *Phys. Rev. D* 94.8 (2016). [Erratum: Phys.Rev.D 95, 069906 (2017)], p. 084024. DOI: 10.1103/PhysRevD.94.084024. arXiv: 1607.07845 [gr-qc].

[37] Emanuele Berti et al. "Spectroscopy of Kerr black holes with Earth- and space-based interferometers." *Phys. Rev. Lett.* 117.10 (2016), p. 101102. DOI: 10.1103/PhysRevLett.117.101102. arXiv: 1605.09286 [gr-qc].

[38] Vishal Baibhav et al. "Black hole spectroscopy: systematic errors and ringdown energy estimates." *Phys. Rev. D* 97.4 (2018), p. 044048. DOI: 10.1103/PhysRevD.97.044048. arXiv: 1710.02156 [gr-qc].

[39] Andrea Maselli, Kostas Kokkotas, and Pablo Laguna. "Observing binary black hole ringdowns by advanced gravitational wave detectors." *Phys. Rev. D* 95.10 (2017), p. 104026. DOI: 10.1103/PhysRevD.95.104026. arXiv: 1702.01110 [gr-qc].

[40] Huan Yang et al. "Black hole spectroscopy with coherent mode stacking." *Phys. Rev. Lett.* 118.16 (2017), p. 161101. DOI: 10.1103/PhysRevLett.118.161101. arXiv: 1701.05808 [gr-qc].

[41] Carlos Filipe Da Silva Costa et al. "Detection of (2,2) quasinormal mode from a population of black holes with a constructive summation method." *Phys. Rev. D* 98.2 (2018), p. 024052. DOI: 10.1103/PhysRevD.98.024052. arXiv: 1711.00551 [gr-qc].

[42] Benjamin P. Abbott et al. "Binary black hole mergers in the first advanced LIGO observing run." *Phys. Rev. X* 6.4 (2016). [Erratum: Phys.Rev.X 8, 039903 (2018)], p. 041015. DOI: 10.1103/PhysRevX.6.041015. arXiv: 1606.04856 [gr-qc].

[43] Benjamin P. Abbott et al. "GWTC-1: A gravitational-wave transient catalog of compact binary mergers observed by LIGO and Virgo during the first and second observing runs." *Phys. Rev. X* 9.3 (2019), p. 031040. DOI: 10.1103/PhysRevX.9.031040. arXiv: 1811.12907 [astro-ph.HE].

[44] Richard Abbott et al. "GWTC-2: Compact binary coalescences observed by LIGO and Virgo during the first half of the third observing run." *Phys. Rev. X* 11 (2021), p. 021053. DOI: 10.1103/PhysRevX.11.021053. arXiv: 2010.14527 [gr-qc].

[45] Richard Abbott et al. "GWTC-3: Compact binary coalescences observed by LIGO and Virgo during the second part of the third observing run." (Nov. 2021). arXiv: 2111.03606 [gr-qc].

[46] J. Aasi et al. "Advanced LIGO." *Classical and Quantum Gravity* 32 (2015), p. 074001. DOI: 10.1088/0264-9381/32/7/074001.

[47] Fausto Acernese et al. "Advanced Virgo: A second-generation interferometric gravitational wave detector." *Classical and Quantum Gravity* 32.2 (2015), p. 024001. DOI: 10.1088/0264-9381/32/2/024001.

[48] Yoichi Aso et al. "Interferometer design of the KAGRA gravitational wave detector." *Phys. Rev. D* 88 (4 Aug. 2013), p. 043007. DOI: 10.1103/PhysRevD.88.043007. URL: https://link.aps.org/doi/10.1103/PhysRevD.88.043007.

[49] Alessandra Buonanno, Gregory B. Cook, and Frans Pretorius. "Inspiral, merger and ring-down of equal-mass black-hole binaries." *Phys. Rev.* D75 (2007), p. 124018. DOI: 10.1103/PhysRevD.75.124018. arXiv: gr-qc/0610122 [gr-qc].

[50] Arnab Dhani and Bangalore S. Sathyaprakash. "Overtones, mirror modes, and mode-mixing in binary black hole mergers." (July 2021). arXiv: 2107.14195 [gr-qc].

[51] Xisco Jiménez Forteza and Pierre Mourier. "High-overtone fits to numerical relativity ringdowns: Beyond the dismissed n=8 special tone." *Phys. Rev. D* 104.12 (2021), p. 124072. DOI: 10.1103/PhysRevD.104.124072. arXiv: 2107.11829 [gr-qc].

[52] Eliot Finch and Christopher J. Moore. "Modelling the ringdown from precessing black hole binaries." (Feb. 2021). arXiv: 2102.07794 [gr-qc].

[53] Xiang Li et al. "Angular emission patterns of remnant black holes." *Phys. Rev. D* 105.2 (2022), p. 024016. DOI: 10.1103/PhysRevD.105.024016. arXiv: 2110.03116 [gr-qc].

[54] Lorena Magaña Zertuche et al. "High precision ringdown modeling: Multimode fits and BMS frames." *Phys. Rev. D* 105 (2022), p. 104015. DOI: 10.1103/PhysRevD.105.104015. arXiv: 2110.15922 [gr-qc].

[55] Sizheng Ma et al. "Universal features of gravitational waves emitted by superkick binary black hole systems." *Phys. Rev. D* 104.8 (2021), p. 084003. DOI: 10.1103/PhysRevD.104.084003. arXiv: 2107.04890 [gr-qc].

[56] Keefe Mitman et al. "Nonlinearities in black hole ringdowns." *Phys. Rev. Lett.* 130.8 (2023), p. 081402. DOI: 10.1103/PhysRevLett.130.081402. arXiv: 2208.07380 [gr-qc].

[57] Mark Ho-Yeuk Cheung et al. "Nonlinear effects in black hole ringdown." (Aug. 2022). arXiv: 2208.07374 [gr-qc].

[58] Macarena Lagos and Lam Hui. "Generation and propagation of nonlinear quasi-normal modes of a Schwarzschild black hole." (Aug. 2022). arXiv: 2208.07379 [gr-qc].

[59] Emanuele Berti et al. "Inspiral, merger and ringdown of unequal mass black hole binaries: A multipolar analysis." *Phys. Rev. D* 76 (2007), p. 064034. DOI: 10.1103/PhysRevD.76.064034. arXiv: gr-qc/0703053.

[60] Emanuele Berti et al. "Mining information from binary black hole mergers: A Comparison of estimation methods for complex exponentials in noise." *Phys. Rev. D* 75 (2007), p. 124017. DOI: 10.1103/PhysRevD.75.124017. arXiv: gr-qc/0701086.

[61] Ioannis Kamaretsos et al. "Black-hole hair loss: Learning about binary progenitors from ringdown signals." *Phys. Rev. D* 85 (2012), p. 024018. DOI: 10.1103/PhysRevD.85.024018. arXiv: 1107.0854 [gr-qc].

[62] Lionel London, Deirdre Shoemaker, and James Healy. "Modeling ringdown: Beyond the fundamental quasinormal modes." *Phys. Rev. D* 90.12 (2014). [Erratum: Phys.Rev.D 94, 069902 (2016)], p. 124032. DOI: 10.1103/PhysRevD.90.124032. arXiv: 1404.3197 [gr-qc].

[63] Eric Thrane, Paul D. Lasky, and Yuri Levin. "Challenges testing the no-hair theorem with gravitational waves." *Phys. Rev. D* 96.10 (2017), p. 102004. DOI: 10.1103/PhysRevD.96.102004. arXiv: 1706.05152 [gr-qc].

[64] Matthew Giesler et al. "Black hole ringdown: The importance of overtones." *Phys. Rev.* X9.4 (2019), p. 041060. DOI: 10.1103/PhysRevX.9.041060. arXiv: 1903.08284 [gr-qc].

[65] Gregory B. Cook. "Aspects of multimode Kerr ringdown fitting." *Phys. Rev. D* 102.2 (2020), p. 024027. DOI: 10.1103/PhysRevD.102.024027. arXiv: 2004.08347 [gr-qc].

[66] Arnab Dhani. "Importance of mirror modes in binary black hole ringdown waveform." *Phys. Rev. D* 103.10 (2021), p. 104048. DOI: 10.1103/PhysRevD.103.104048. arXiv: 2010.08602 [gr-qc].

[67] Swetha Bhagwat et al. "On choosing the start time of binary black hole ringdowns." *Phys. Rev. D* 97.10 (2018), p. 104065. DOI: 10.1103/PhysRevD.97.104065. arXiv: 1711.00926 [gr-qc].

[68] Swetha Bhagwat et al. "Ringdown overtones, black hole spectroscopy, and no-hair theorem tests." *Phys. Rev. D* 101.4 (2020), p. 044033. DOI: 10.1103/PhysRevD.101.044033. arXiv: 1910.08708 [gr-qc].

[69] Maria Okounkova. "Revisiting non-linearity in binary black hole mergers." (Apr. 2020). arXiv: 2004.00671 [gr-qc].

[70] Geoffrey Lovelace et al. "Modeling the source of GW150914 with targeted numerical-relativity simulations." *Class. Quant. Grav.* 33.24 (2016), p. 244002. DOI: 10.1088/0264-9381/33/24/244002. arXiv: 1607.05377 [gr-qc].

[71] Gregorio Carullo, Walter Del Pozzo, and John Veitch. "Observational black hole spectroscopy: A time-domain multimode analysis of GW150914." *Phys. Rev.* D99.12 (2019). [Erratum: Phys. Rev.D100,no.8,089903(2019)], p. 123029. DOI: 10.1103/PhysRevD.99.123029,10.1103/PhysRevD.100.089903. arXiv: 1902.07527 [gr-qc].

[72] Vishal Baibhav et al. "Agnostic black hole spectroscopy: quasinormal mode content of numerical relativity waveforms and limits of validity of linear perturbation theory." (Feb. 2023). arXiv: 2302.03050 [gr-qc].

[73] Peter James Nee, Sebastian H. Völkel, and Harald P. Pfeiffer. "To ring or not to ring, the tale of black hole quasi-normal modes." (Feb. 2023). arXiv: 2302.06634 [gr-qc].

[74] Benjamin P. Abbott et al. "Properties of the binary neutron star merger GW170817." *Phys. Rev. X* 9.1 (2019), p. 011001. DOI: 10.1103/PhysRevX.9.011001. arXiv: 1805.11579 [gr-qc].

[75] Laura Sampson et al. "Projected Constraints on scalarization with gravitational waves from Neutron star Binaries." *Phys. Rev. D* 90.12 (2014), p. 124091. DOI: 10.1103/PhysRevD.90.124091. arXiv: 1407.7038 [gr-qc].

[76] Elias R. Most et al. "New constraints on radii and tidal deformabilities of neutron stars from GW170817." *Phys. Rev. Lett.* 120.26 (2018), p. 261103. DOI: 10.1103/PhysRevLett.120.261103. arXiv: 1803.00549 [gr-qc].

[77] Benjamin P. Abbott et al. "GW170817: Observation of gravitational waves from a binary neutron star Inspiral." *Phys. Rev. Lett.* 119.16 (2017), p. 161101. DOI: 10.1103/PhysRevLett.119.161101. arXiv: 1710.05832 [gr-qc].

[78] Benjamin P. Abbott et al. "Gravitational waves and Gamma-rays from a binary neutron star merger: GW170817 and GRB 170817A." *Astrophys. J.* 848.2 (2017), p. L13. DOI: 10.3847/2041-8213/aa920c. arXiv: 1710.05834 [astro-ph.HE].

[79] Adam Goldstein et al. "An ordinary short gamma-ray burst with extraordinary implications: Fermi-GBM detection of GRB 170817A." *Astrophys. J.* 848.2 (2017), p. L14. DOI: 10.3847/2041-8213/aa8f41. arXiv: 1710.05446 [astro-ph.HE].

[80] Volodymyr Savchenko et al. "INTEGRAL detection of the first prompt gamma-ray signal coincident with the gravitational-wave event GW170817." *Astrophys. J.* 848.2 (2017), p. L15. DOI: 10.3847/2041-8213/aa8f94. arXiv: 1710.05449 [astro-ph.HE].

[81] Benjamin P. Abbott et al. "GW190425: Observation of a compact binary coalescence with total mass $\sim 3.4 M_{\odot}$." *Astrophys. J. Lett.* 892.1 (2020), p. L3. DOI: 10.3847/2041-8213/ab75f5. arXiv: 2001.01761 [astro-ph.HE].

[82] Richard Abbott et al. "Observation of gravitational waves from two neutron star–black hole coalescences." *Astrophys. J. Lett.* 915.1 (2021), p. L5. DOI: 10.3847/2041-8213/ac082e. arXiv: 2106.15163 [astro-ph.HE].

[83] Benjamin P. Abbott et al. "GW170817: Measurements of neutron star radii and equation of state." *Phys. Rev. Lett.* 121.16 (2018), p. 161101. DOI: 10.1103/PhysRevLett.121.161101. arXiv: 1805.11581 [gr-qc].

[84] Benjamin P Abbott et al. "Model comparison from LIGO-Virgo data on GW170817's binary components and consequences for the merger remnant." *Class. Quant. Grav.* 37.4 (2020), p. 045006. DOI: 10.1088/1361-6382/ab5f7c. arXiv: 1908.01012 [gr-qc].

[85] Eemeli Annala et al. "Gravitational-wave constraints on the neutron-star-matter equation of state." *Phys. Rev. Lett.* 120.17 (2018), p. 172703. DOI: 10.1103/PhysRevLett.120.172703. arXiv: 1711.02644 [astro-ph.HE].

[86] Elias R. Most et al. "New constraints on radii and tidal deformabilities of neutron stars from GW170817." *Phys. Rev. Lett.* 120.26 (2018), p. 261103. DOI: 10.1103/PhysRevLett.120.261103. arXiv: 1803.00549 [gr-qc].

[87] Ben Margalit and Brian D. Metzger. "Constraining the maximum mass of neutron stars From multi-messenger observations of GW170817." *Astrophys. J.* 850.2 (2017), p. L19. DOI: 10.3847/2041-8213/aa991c. arXiv: 1710.05938 [astro-ph.HE].

[88] Luciano Rezzolla, Elias R. Most, and Lukas R. Weih. "Using gravitational-wave observations and quasi-universal relations to constrain the maximum mass of neutron stars." *Astrophys. J.* 852.2 (2018). [Astrophys. J. Lett.852,L25(2018)], p. L25. DOI: 10.3847/2041-8213/aaa401. arXiv: 1711.00314 [astro-ph.HE].

[89] Milton Ruiz, Stuart L. Shapiro, and Antonios Tsokaros. "GW170817, General relativistic magnetohydrodynamic simulations, and the neutron star maximum mass." *Phys. Rev.* D97.2 (2018), p. 021501. DOI: 10.1103/PhysRevD.97.021501. arXiv: 1711.00473 [astro-ph.HE].

[90] Masaru Shibata et al. "Modeling GW170817 based on numerical relativity and its implications." *Phys. Rev.* D96.12 (2017), p. 123012. DOI: 10.1103/PhysRevD.96.123012. arXiv: 1710.07579 [astro-ph.HE].

[91] Geraint Pratten, Patricia Schmidt, and Tanja Hinderer. "Gravitational-wave asteroseismology with fundamental modes from compact binary inspirals." (2019). arXiv: 1905.00817 [gr-qc].

[92] Jacques Abadie et al. "Predictions for the rates of compact binary coalescences observable by ground-based gravitational-wave detectors." *Class. Quant. Grav.* 27 (2010), p. 173001. DOI: 10.1088/0264-9381/27/17/173001. arXiv: 1003.2480 [astro-ph.HE].

[93] Vassiliki Kalogera et al. "The cosmic coalescence rates for double neutron star binaries." *Astrophys. J.* 601 (2004). [Erratum: Astrophys. J.614,L137(2004)], pp. L179–L182. DOI: 10.1086/425868. arXiv: astro-ph/0312101 [astro-ph].

[94] Chunglee Kim, Vicky Kalogera, and Duncan R. Lorimer. "The effect of PSR J0737-3039 on the DNS merger rate and implications for gravity-wave detection." *New Astron. Rev.* 54 (2010), pp. 148–151. DOI: 10.1016/j.newar.2010.09.010. arXiv: astro-ph/0608280 [astro-ph].

[95] Richard O'Shaughnessy et al. "Constraining population synthesis models via empirical binary compact object merger and supernova rates." *The Astrophysical Journal* 672.1 (2008), p. 479.

[96] Stefan Hild et al. "A xylophone configuration for a third generation gravitational wave detector." *Class. Quant. Grav.* 27 (2010), p. 015003. DOI: 10.1088/0264-9381/27/1/015003. arXiv: 0906.2655 [gr-qc].

[97] Bangalore Sathyaprakash et al. "Scientific objectives of Einstein Telescope." *Class. Quant. Grav.* 29 (2012). [Erratum: Class. Quant. Grav.30,079501(2013)], p. 124013. DOI: 10.1088/0264-9381/29/12/124013,10.1088/0264-9381/30/7/079501. arXiv: 1206.0331 [gr-qc].

[98] Benjamin P Abbott et al. "Exploring the sensitivity of next generation gravitational wave detectors." *Class. Quant. Grav.* 34.4 (2017), p. 044001. DOI: 10.1088/1361-6382/aa51f4. arXiv: 1607.08697 [astro-ph.IM].

[99] Vishal Baibhav et al. "Gravitational-wave detection rates for compact binaries formed in isolation: LIGO/Virgo O3 and beyond." *Phys. Rev.* D100.6 (2019), p. 064060. DOI: 10.1103/PhysRevD.100.064060. arXiv: 1906.04197 [gr-qc].

[100] Tanja Hinderer et al. "Effects of neutron-star dynamic tides on gravitational waveforms within the effective-one-body approach." *Phys. Rev. Lett.* 116.18 (2016), p. 181101. DOI: 10.1103/PhysRevLett.116.181101. arXiv: 1602.00599 [gr-qc].

[101] Tim Dietrich, Sebastiano Bernuzzi, and Wolfgang Tichy. "Closed-form tidal approximants for binary neutron star gravitational waveforms constructed from high-resolution numerical relativity simulations." *Phys. Rev. D* 96.12 (2017), p. 121501. DOI: 10.1103/PhysRevD.96.121501. arXiv: 1706.02969 [gr-qc].

[102] Sarp Akcay et al. "Effective-one-body multipolar waveform for tidally interacting binary neutron stars up to merger." *Phys. Rev. D* 99.4 (2019), p. 044051. DOI: 10.1103/PhysRevD.99.044051. arXiv: 1812.02744 [gr-qc].

[103] Alessandro Nagar et al. "Time-domain effective-one-body gravitational waveforms for coalescing compact binaries with nonprecessing spins, tides and self-spin effects." *Phys. Rev. D* 98.10 (2018), p. 104052. DOI: 10.1103/PhysRevD.98.104052. arXiv: 1806.01772 [gr-qc].

[104] Kevin Barkett et al. "Gravitational waveforms of binary neutron star inspirals using post-Newtonian tidal splicing." *Phys. Rev. D* 102.2 (2020), p. 024031. DOI: 10.1103/PhysRevD.102.024031. arXiv: 1911.10440 [gr-qc].

[105] Francesco Messina et al. "Quasi-5.5PN TaylorF2 approximant for compact binaries: point-mass phasing and impact on the tidal polarizability inference." *Phys. Rev. D* 99.12 (2019), p. 124051. DOI: 10.1103/PhysRevD.99.124051. arXiv: 1904.09558 [gr-qc].

[106] Mohammad Al-Mamun et al. "Combining electromagnetic and gravitational-wave Constraints on neutron-Star Masses and Radii." *Phys. Rev. Lett.* 126.6 (2021), p. 061101. DOI: 10.1103/PhysRevLett.126.061101. arXiv: 2008.12817 [astro-ph.HE].

[107] Joshua A. Faber et al. "Measuring neutron star radii with gravitational wave detectors." *Phys. Rev. Lett.* 89 (2002), p. 231102. DOI: 10.1103/PhysRevLett.89.231102. arXiv: astro-ph/0204397 [astro-ph].

[108] Michal Bejger et al. "Impact of the nuclear equation of state on the last orbits of binary neutron stars." *Astron. Astrophys.* 431 (2005), p. 297. DOI: 10.1051/0004-6361:20041441. arXiv: astro-ph/0406234 [astro-ph].

[109] Tanja Hinderer. "Tidal love numbers of neutron stars." *Astrophys. J.* 677 (2008), pp. 1216–1220. DOI: 10.1086/533487. arXiv: 0711.2420 [astro-ph].

[110] Eanna E. Flanagan and Tanja Hinderer. "Constraining neutron star tidal Love numbers with gravitational wave detectors." *Phys. Rev.* D77 (2008), p. 021502. DOI: 10.1103/PhysRevD.77.021502. arXiv: 0709.1915 [astro-ph].

[111] Katerina Chatziioannou. "Neutron star tidal deformability and equation of state constraints." *Gen. Rel. Grav.* 52.11 (2020), p. 109. DOI: 10.1007/s10714-020-02754-3. arXiv: 2006.03168 [gr-qc].

[112] Justin E. Vines and Eanna E. Flanagan. "Post-1-Newtonian quadrupole tidal interactions in binary systems." *Phys. Rev.* D88 (2013), p. 024046. DOI: 10.1103/PhysRevD.88.024046. arXiv: 1009.4919 [gr-qc].

[113] Tiziano Abdelsalhin, Leonardo Gualtieri, and Paolo Pani. "Post-Newtonian spin-tidal couplings for compact binaries." *Phys. Rev.* D98.10 (2018), p. 104046. DOI: 10.1103/PhysRevD.98.104046. arXiv: 1805.01487 [gr-qc].

[114] Tanja Hinderer et al. "Tidal deformability of neutron stars with realistic equations of state and their gravitational wave signatures in binary inspiral." *Phys. Rev.* D81 (2010), p. 123016. DOI: 10.1103/PhysRevD.81.123016. arXiv: 0911.3535 [astro-ph.HE].

[115] Thibault Damour, Michael Soffel, and Chong-ming Xu. "General relativistic celestial mechanics. 1. Method and definition of reference systems." *Phys. Rev.* D43 (1991), pp. 3273–3307. DOI: 10.1103/PhysRevD.43.3273.

[116] Thibault Damour, Michael Soffel, and Chongming Xu. "General-relativistic celestial mechanics II. Translational equations of motion." *Phys. Rev. D* 45 (4 Feb. 1992), pp. 1017–1044. DOI: 10.1103/PhysRevD.45.1017. URL: https://link.aps.org/doi/10.1103/PhysRevD.45.1017.

[117] Thibault Damour, Michael Soffel, and Chong-ming Xu. "General relativistic celestial mechanics. 3. Rotational equations of motion." *Phys. Rev.* D47 (1993), pp. 3124–3135. DOI: 10.1103/PhysRevD.47.3124.

[118] Thibault Damour, Michael Soffel, and Chong-ming Xu. "General relativistic celestial mechanics. 4: Theory of satellite motion." *Phys. Rev.* D49 (1994), pp. 618–635. DOI: 10.1103/PhysRevD.49.618.

[119] Etienne Racine and Eanna E. Flanagan. "Post-1-Newtonian equations of motion for systems of arbitrarily structured bodies." *Phys. Rev.* D71 (2005). [Erratum: Phys. Rev.D88,no.8,089903(2013)], p. 044010. DOI: 10.1103/PhysRevD.71.044010,10.1103/PhysRevD.88.089903. arXiv: gr-qc/0404101 [gr-qc].

[120] Dong Lai. "Resonant oscillations and tidal heating in coalescing binary neutron stars." *Mon. Not. Roy. Astron. Soc.* 270 (1994), p. 611. DOI: 10.1093/mnras/270.3.611. arXiv: astro-ph/9404062 [astro-ph].

[121] Andreas Reisenegger and Peter Goldreich. "Excitation of neutron star normal modes during binary inspiral." *Astrophys. J.* 426 (May 1994), pp. 688–691. DOI: 10.1086/174105.

[122] Kostas D. Kokkotas and Gerhard Schaefer. "Tidal and tidal resonant effects in coalescing binaries." *Mon. Not. Roy. Astron. Soc.* 275 (1995), p. 301. DOI: 10.1093/mnras/275.2.301. arXiv: gr-qc/9502034.

[123] Dong Lai. "Dynamical tides in rotating binary stars." *Astrophys. J.* 490 (1997), p. 847. DOI: 10.1086/304899. arXiv: astro-ph/9704132 [astro-ph].

[124] Wynn C. G. Ho and Dong Lai. "Resonant tidal excitations of rotating neutron stars in coalescing binaries." *Mon. Not. Roy. Astron. Soc.* 308 (1999), p. 153. DOI: 10.1046/j.1365-8711.1999.02703.x. arXiv: astro-ph/9812116 [astro-ph].

[125] Jan Steinhoff et al. "Dynamical tides in general relativity: Effective action and effective-one-body hamiltonian." *Phys. Rev.* D94.10 (2016), p. 104028. DOI: 10.1103/PhysRevD.94.104028. arXiv: 1608.01907 [gr-qc].

[126] Tanja Hinderer et al. "Effects of neutron-star dynamic tides on gravitational waveforms within the effective-one-body approach." *Phys. Rev. Lett.* 116.18 (2016), p. 181101. DOI: 10.1103/PhysRevLett.116.181101. arXiv: 1602.00599 [gr-qc].

[127] John P Cox. *Theory of stellar pulsation.(PSA-2), Volume 2*. Vol. 31. Princeton University Press, 2017.

[128] Lee Lindblom and James R. Ipser. "Generalized r modes of the Maclaurin spheroids." *Phys. Rev.* D59 (1999), p. 044009. DOI: 10.1103/PhysRevD.59.044009. arXiv: gr-qc/9807049 [gr-qc].

[129] Keith H. Lockitch and John L. Friedman. "Where are the r modes of isentropic stars?" *Astrophys. J.* 521 (1999), p. 764. DOI: 10.1086/307580. arXiv: gr-qc/9812019 [gr-qc].

[130] Shijun Yoshida and Umin Lee. "Inertial modes of slowly rotating isentropic stars." *Astrophys. J.* 529 (2000), p. 997. DOI: 10.1086/308312. arXiv: astro-ph/9908197 [astro-ph].

[131] Thomas W. Baumgarte and Stuart L. Shapiro. *Numerical relativity: Solving Einstein's equations on the Computer*. Cambridge University Press, 2010. DOI: 10.1017/CBO9781139193344.

[132] SXS Collaboration. *The SXS collaboration catalog of gravitational waveforms*. http://www.black-holes.org/waveforms..

[133] Jeffrey Winicour. "Characteristic evolution and matching." *Living Reviews in Relativity* 15.1 (2012), pp. 1–99. DOI: 10.12942/lrr-2012-2.

[134] Nigel T. Bishop. "Some aspects of the characteristic initial value problem in numerical relativity." *Approaches to Numerical relativity*. Ed. by Ray D'Inverno. Jan. 1992, pp. 20–33.

[135] Nigel T. Bishop et al. "Cauchy-characteristic extraction in numerical relativity." *Phys. Rev.* D54 (1996), pp. 6153–6165. DOI: 10.1103/PhysRevD.54.6153. arXiv: gr-qc/9705033 [gr-qc].

[136] Nigel T. Bishop et al. "High powered gravitational news." *Phys. Rev. D* 56 (1997), pp. 6298–6309. DOI: 10.1103/PhysRevD.56.6298. arXiv: gr-qc/9708065.

[137] Nigel T. Bishop et al. "Cauchy characteristic matching." *Black holes, Gravitational radiation and the Universe: Essays in Honor of C.V. Vishveshwara*. Ed. by Bala R. Iyer and Biblap Bhawal. Jan. 1998, pp. 383–408. DOI: 10.1007/978-94-017-0934-7_24. arXiv: gr-qc/9801070.

[138] Kevin Barkett et al. "Spectral Cauchy-characteristic extraction of the gravitational wave news function." *Phys. Rev. D* 102.2 (2020), p. 024004. DOI: 10.1103/PhysRevD.102.024004. arXiv: 1910.09677 [gr-qc].

[139] Jordan Moxon, Mark A. Scheel, and Saul A. Teukolsky. "Improved Cauchy-characteristic evolution system for high-precision numerical relativity waveforms." *Phys. Rev. D* 102.4 (2020), p. 044052. DOI: 10.1103/PhysRevD.102.044052. arXiv: 2007.01339 [gr-qc].

[140] Jordan Moxon et al. "The SpECTRE Cauchy-characteristic evolution system for rapid, precise waveform extraction." (Oct. 2021). arXiv: 2110.08635 [gr-qc].

[141] Michael Boyle and Abdul H. Mroue. "Extrapolating gravitational-wave data from numerical simulations." *Phys. Rev.* D80 (2009), p. 124045. DOI: 10.1103/PhysRevD.80.124045. arXiv: 0905.3177 [gr-qc].

[142] Dante A. B. Iozzo et al. "Extending gravitational wave extraction using Weyl characteristic fields." *Phys. Rev. D* 103.2 (2021), p. 024039. DOI: 10.1103/PhysRevD.103.024039. arXiv: 2010.15200 [gr-qc].

[143] Hermann Bondi, M. G. Julian van der Burg, and A. W. Kenneth Metzner. "Gravitational waves in general relativity. VII. Waves from axi-symmetric isolated systems." *Proceedings of the Royal Society of London Series A* 269.1336 (Aug. 1962), pp. 21–52. DOI: 10.1098/rspa.1962.0161.

[144] Rainer K. Sachs. "Gravitational waves in general relativity. 8. Waves in asymptotically flat space-times." *Proc. Roy. Soc. Lond. A* 270 (1962), pp. 103–126. DOI: 10.1098/rspa.1962.0206.

[145] Roger Penrose. "Asymptotic properties of fields and space-times." *Phys. Rev. Lett.* 10 (2 Jan. 1963), pp. 66–68. DOI: 10.1103/PhysRevLett.10.66. URL: https://link.aps.org/doi/10.1103/PhysRevLett.10.66.

[146] Maria Babiuc et al. "Gravitational wave extraction based on Cauchy-characteristic extraction and characteristic evolution." *Class. Quant. Grav.* 22 (2005), pp. 5089–5108. DOI: 10.1088/0264-9381/22/23/011. arXiv: gr-qc/0501008.

[147] Tony Chu et al. "On the accuracy and precision of numerical waveforms: Effect of waveform extraction methodology." *Class. Quant. Grav.* 33.16 (2016), p. 165001. DOI: 10.1088/0264-9381/33/16/165001. arXiv: 1512.06800 [gr-qc].

[148] Nicholas W. Taylor et al. "Comparing gravitational waveform extrapolation to Cauchy-characteristic extraction in binary black hole simulations." *Phys. Rev.* D88.12 (2013), p. 124010. DOI: 10.1103/PhysRevD.88.124010. arXiv: 1309.3605 [gr-qc].

[149] Bela Szilagyi. "Cauchy characteristic matching in general relativity." Other thesis. June 2000. arXiv: gr-qc/0006091.

[150] Béla Szilágyi. "Key elements of robustness in binary black hole evolutions using spectral methods." *Int. J. Mod. Phys.* D23.7 (2014), p. 1430014. DOI: 10.1142/S0218271814300146. arXiv: 1405.3693 [gr-qc].

[151] Nicolás Yunes and Xavier Siemens. "Gravitational-wave tests of general relativity with ground-based detectors and pulsar timing-arrays." *Living Rev. Rel.* 16 (2013), p. 9. DOI: 10.12942/lrr-2013-9. arXiv: 1304.3473 [gr-qc].

[152] Emanuele Berti et al. "Testing general relativity with present and future astrophysical observations." *Class. Quant. Grav.* 32 (2015), p. 243001. DOI: 10.1088/0264-9381/32/24/243001. arXiv: 1501.07274 [gr-qc].

[153] Benjamin P. Abbott et al. "Binary black hole mergers in the first advanced LIGO observing run." *Phys. Rev.* X6.4 (2016). [erratum: Phys. Rev.X8,no.3,039903(2018)], p. 041015. DOI: 10.1103/PhysRevX.6.041015,10.1103/PhysRevX.8.039903. arXiv: 1606.04856 [gr-qc].

[154] Sizheng Ma and Nicolas Yunes. "Improved Constraints on Modified Gravity with Eccentric gravitational waves." *Phys. Rev. D* 100.12 (2019), p. 124032. DOI: 10.1103/PhysRevD.100.124032. arXiv: 1908.07089 [gr-qc].

[155] Zack Carson, Brian C. Seymour, and Kent Yagi. "Future prospects for probing scalar–tensor theories with gravitational waves from mixed binaries." *Class. Quant. Grav.* 37.6 (2020), p. 065008. DOI: 10.1088/1361-6382/ab6a1f. arXiv: 1907.03897 [gr-qc].

[156] Paul D. Scharre and Clifford M. Will. "Testing scalar tensor gravity using space gravitational wave interferometers." *Phys. Rev. D* 65 (2002), p. 042002. DOI: 10.1103/PhysRevD.65.042002. arXiv: gr-qc/0109044.

[157] Clifford M. Will and Nicolas Yunes. "Testing alternative theories of gravity using LISA." *Class. Quant. Grav.* 21 (2004), p. 4367. DOI: 10.1088/0264-9381/21/18/006. arXiv: gr-qc/0403100.

[158] Emanuele Berti, Alessandra Buonanno, and Clifford M. Will. "Testing general relativity and probing the merger history of massive black holes with LISA." *Class. Quant. Grav.* 22 (2005). Ed. by B. Mours and F. Marion, S943–S954. DOI: 10.1088/0264-9381/22/18/S08. arXiv: gr-qc/0504017.

[159] Emanuele Berti, Alessandra Buonanno, and Clifford M. Will. "Estimating spinning binary parameters and testing alternative theories of gravity with LISA." *Phys. Rev. D* 71 (2005), p. 084025. DOI: 10.1103/PhysRevD.71.084025. arXiv: gr-qc/0411129.

[160] Kent Yagi and Takahiro Tanaka. "Constraining alternative theories of gravity by gravitational waves from precessing eccentric compact binaries with LISA." *Phys. Rev. D* 81 (2010). [Erratum: Phys.Rev.D 81, 109902 (2010)], p. 064008. DOI: 10.1103/PhysRevD.81.109902. arXiv: 0906.4269 [gr-qc].

[161] Kodanad G. Arun. "Generic bounds on dipolar gravitational radiation from inspiralling compact binaries." *Class. Quant. Grav.* 29 (2012), p. 075011. DOI: 10.1088/0264-9381/29/7/075011. arXiv: 1202.5911 [gr-qc].

[162] Vitor Cardoso et al. "Floating and sinking: The Imprint of massive scalars around rotating black holes." *Phys. Rev. Lett.* 107 (2011), p. 241101. DOI: 10.1103/PhysRevLett.107.241101. arXiv: 1109.6021 [gr-qc].

[163] Benjamin P. Abbott et al. "Tests of general relativity with GW150914." *Phys. Rev. Lett.* 116.22 (2016). [Erratum: Phys.Rev.Lett. 121, 129902 (2018)], p. 221101. DOI: 10.1103/PhysRevLett.116.221101. arXiv: 1602.03841 [gr-qc].

[164] Nicolas Yunes, Paolo Pani, and Vitor Cardoso. "Gravitational waves from Quasicircular extreme mass-ratio inspirals as Probes of scalar-tensor theories." *Phys. Rev. D* 85 (2012), p. 102003. DOI: 10.1103/PhysRevD.85.102003. arXiv: 1112.3351 [gr-qc].

[165] Emanuele Berti et al. "Light scalar field constraints from gravitational-wave observations of compact binaries." *Phys. Rev. D* 85 (2012), p. 122005. DOI: 10.1103/PhysRevD.85.122005. arXiv: 1204.4340 [gr-qc].

[166] Semih Tuna, Kivanç İ. Ünlütürk, and Fethi M. Ramazanoğlu. "Constraining scalar-tensor theories using neutron star mass and radius measurements." *Phys. Rev. D* 105.12 (2022), p. 124070. DOI: 10.1103/PhysRevD.105.124070. arXiv: 2204.02138 [gr-qc].

[167] Clifford M. Will. "The Confrontation between General relativity and Experiment." *Living Rev. Rel.* 17 (2014), p. 4. DOI: 10.12942/lrr-2014-4. arXiv: 1403.7377 [gr-qc].

[168] Nicolas Yunes, Kent Yagi, and Frans Pretorius. "Theoretical physics implications of the binary black-hole mergers GW150914 and GW151226." *Phys. Rev. D* 94.8 (2016), p. 084002. DOI: 10.1103/PhysRevD.94.084002. arXiv: 1603.08955 [gr-qc].

[169] Benjamin P. Abbott et al. "Tests of general relativity with GW170817." *Phys. Rev. Lett.* 123.1 (2019), p. 011102. DOI: 10.1103/PhysRevLett.123.011102. arXiv: 1811.00364 [gr-qc].

[170] Andrzej Krolak, Kostas D. Kokkotas, and Gerhard Schaefer. "On estimation of the postNewtonian parameters in the gravitational wave emission of a coalescing binary." *Phys. Rev. D* 52 (1995), pp. 2089–2111. DOI: 10.1103/PhysRevD.52.2089. arXiv: gr-qc/9503013.

[171] Kent Yagi and Takahiro Tanaka. "DECIGO/BBO as a probe to constrain alternative theories of gravity." *Prog. Theor. Phys.* 123 (2010), pp. 1069–1078. DOI: 10.1143/PTP.123.1069. arXiv: 0908.3283 [gr-qc].

[172] Pascual Jordan. "Schwerkraft und Weltall: Grundlagen der theoretischen Kosmologie." *Die Wissenschaft* (1955).

[173] Markus Fierz. "On the physical interpretation of P. Jordan's extended theory of gravitation." *Helv. Phys. Acta* 29 (1956), pp. 128–134.

[174] Carl Brans and Robert H. Dicke. "Mach's principle and a relativistic theory of gravitation." *Phys. Rev.* 124 (3 Nov. 1961), pp. 925–935. DOI: 10.1103/PhysRev.124.925. URL: https://link.aps.org/doi/10.1103/PhysRev.124.925.

[175] Carl H. Brans. "Scalar-tensor theories of gravity: Some personal history." *Gravitation and Cosmology*. Ed. by Alfredo Herrera-Aguilar et al. Vol. 1083. American Institute of Physics Conference Series. Dec. 2008, pp. 34–46. DOI: 10.1063/1.3058577.

[176] Clifford M. Will and Helmut W. Zaglauer. "Gravitational radiation, close binary systems, and the Brans-Dicke theory of gravity." *Astrophys. J.* 346 (Nov. 1989), p. 366. DOI: 10.1086/168016.

[177] Maura Brunetti et al. "Gravitational wave radiation from compact binary systems in the Jordan-Brans-Dicke theory." *Phys. Rev. D* 59 (1999), p. 044027. DOI: 10.1103/PhysRevD.59.044027. arXiv: gr-qc/9805056.

[178] Clifford M. Will. "Testing scalar - tensor gravity with gravitational wave observations of inspiraling compact binaries." *Phys. Rev. D* 50 (1994), pp. 6058–6067. DOI: 10.1103/PhysRevD.50.6058. arXiv: gr-qc/9406022.

[179] Ryan N. Lang. "Compact binary systems in scalar-tensor gravity. II. Tensor gravitational waves to second post-Newtonian order." *Phys. Rev. D* 89.8 (2014), p. 084014. DOI: 10.1103/PhysRevD.89.084014. arXiv: 1310.3320 [gr-qc].

[180] Noah Sennett, Sylvain Marsat, and Alessandra Buonanno. "Gravitational waveforms in scalar-tensor gravity at 2PN relative order." *Phys. Rev. D* 94.8 (2016), p. 084003. DOI: 10.1103/PhysRevD.94.084003. arXiv: 1607.01420 [gr-qc].

[181] Ryan N. Lang. "Compact binary systems in scalar-tensor gravity. III. Scalar waves and energy flux." *Phys. Rev. D* 91.8 (2015), p. 084027. DOI: 10.1103/PhysRevD.91.084027. arXiv: 1411.3073 [gr-qc].

[182] Laura Bernard, Luc Blanchet, and David Trestini. "Gravitational waves in scalar-tensor theory to one-and-a-half post-Newtonian order." *JCAP* 08.08 (2022), p. 008. DOI: 10.1088/1475-7516/2022/08/008. arXiv: 2201.10924 [gr-qc].

[183] Motoyuki Saijo, Hisa-aki Shinkai, and Kei-ichi Maeda. "Gravitational waves in Brans-Dicke theory : Analysis by test particles around a Kerr black hole." *Phys. Rev. D* 56 (1997), pp. 785–797. DOI: 10.1103/PhysRevD.56.785. arXiv: gr-qc/9701001.

[184] Douglas M. Eardley. "Observable effects of a scalar gravitational field in a binary pulsar." *Astrophys. J. Lett.* 196 (Mar. 1975), pp. L59–L62. DOI: 10.1086/181744.

[185] Thibault Damour and Gilles Esposito-Farese. "Tensor multiscalar theories of gravitation." *Class. Quant. Grav.* 9 (1992), pp. 2093–2176. DOI: 10.1088/0264-9381/9/9/015.

[186] Thibault Damour and Gilles Esposito-Farese. "Testing gravity to second postNewtonian order: A field theory approach." *Phys. Rev. D* 53 (1996), pp. 5541–5578. DOI: 10.1103/PhysRevD.53.5541. arXiv: gr-qc/9506063.

[187] Saeed Mirshekari and Clifford M. Will. "Compact binary systems in scalar-tensor gravity: Equations of motion to 2.5 post-Newtonian order." *Phys. Rev. D* 87.8 (2013), p. 084070. DOI: 10.1103/PhysRevD.87.084070. arXiv: 1301.4680 [gr-qc].

[188] Laura Bernard. "Dynamics of compact binary systems in scalar-tensor theories: Equations of motion to the third post-Newtonian order." *Phys. Rev. D* 98.4 (2018), p. 044004. DOI: 10.1103/PhysRevD.98.044004. arXiv: 1802.10201 [gr-qc].

[189] Laura Bernard. "Dynamics of compact binary systems in scalar-tensor theories: II. Center-of-mass and conserved quantities to 3PN order." *Phys. Rev. D* 99.4 (2019), p. 044047. DOI: 10.1103/PhysRevD.99.044047. arXiv: 1812.04169 [gr-qc].

[190] Clifford M. Will. "Gravitational radiation from binary systems in alternative metric theories of gravity: dipole radiation and the binary pulsar." *Astrophys. J.* 214 (June 1977), pp. 826–839. DOI: 10.1086/155313.

[191] Lijing Shao et al. "Constraining nonperturbative strong-field effects in scalar-tensor gravity by combining pulsar timing and laser-interferometer gravitational-wave detectors." *Phys. Rev. X* 7.4 (2017), p. 041025. DOI: 10.1103/PhysRevX.7.041025. arXiv: 1704.07561 [gr-qc].

[192] David Anderson, Paulo Freire, and Nicolás Yunes. "Binary pulsar constraints on massless scalar–tensor theories using Bayesian statistics." *Class. Quant. Grav.* 36.22 (2019), p. 225009. DOI: 10.1088/1361-6382/ab3a1c. arXiv: 1901.00938 [gr-qc].

[193] Anne M. Archibald et al. "Universality of free fall from the orbital motion of a pulsar in a stellar triple system." *Nature* 559.7712 (2018), pp. 73–76. DOI: 10.1038/s41586-018-0265-1. arXiv: 1807.02059 [astro-ph.HE].

[194] John Antoniadis et al. "A massive pulsar in a compact relativistic binary." *Science* 340 (2013), p. 6131. DOI: 10.1126/science.1233232. arXiv: 1304.6875 [astro-ph.HE].

[195] Junjie Zhao et al. "Reduced-order surrogate models for scalar-tensor gravity in the strong field regime and applications to binary pulsars and GW170817." *Phys. Rev. D* 100.6 (2019), p. 064034. DOI: 10.1103/PhysRevD.100.064034. arXiv: 1907.00780 [gr-qc].

[196] Junjie Zhao et al. "Closing a spontaneous-scalarization window with binary pulsars." *Class. Quant. Grav.* 39.11 (2022), 11LT01. DOI: 10.1088/1361-6382/ac69a3. arXiv: 2201.03771 [astro-ph.HE].

[197] Ingrid H. Stairs. "Testing general relativity with pulsar timing." *Living Rev. Rel.* 6 (2003), p. 5. DOI: 10.12942/lrr-2003-5. arXiv: astro-ph/0307536.

[198] Lijing Shao and Norbert Wex. "Tests of gravitational symmetries with radio pulsars." *Sci. China Phys. Mech. Astron.* 59.9 (2016), p. 699501. DOI: 10.1007/s11433-016-0087-6. arXiv: 1604.03662 [gr-qc].

[199] Michael Kramer. "Pulsars as probes of gravity and fundamental physics." *Int. J. Mod. Phys. D* 25.14 (2016), p. 1630029. DOI: 10.1142/S0218271816300299. arXiv: 1606.03843 [astro-ph.HE].

[200] Norbert Wex. "Testing relativistic gravity with radio pulsars." (Feb. 2014). arXiv: 1402.5594 [gr-qc].

[201] Gilles Esposito-Farese. "Binary pulsar tests of strong field gravity and gravitational radiation damping." *10th Marcel Grossmann Meeting on Recent Developments in Theoretical and Experimental General relativity, Gravitation and relativistic Field Theories (MG X MMIII)*. Feb. 2004, pp. 647–666. DOI: 10.1142/9789812704030_0039. arXiv: gr-qc/0402007.

[202] Michael Kramer and Norbert Wex. "The double pulsar system: A unique laboratory for gravity." *Class. Quant. Grav.* 26 (2009), p. 073001. DOI: 10.1088/0264-9381/26/7/073001.

[203] Thibault Damour. "Binary systems as test-beds of gravity theories." *6th SIGRAV Graduate School in Contemporary Relativity and Gravitational Physics: A Century from Einstein Relativity: Probing Gravity Theories in binary Systems*. Apr. 2007. arXiv: 0704.0749 [gr-qc].

[204] Thibault Damour and J. H. Taylor. "Strong-field tests of relativistic gravity and binary pulsars." *Phys. Rev. D* 45 (6 Mar. 1992), pp. 1840–1868. DOI: 10.1103/PhysRevD.45.1840. URL: https://link.aps.org/doi/10.1103/PhysRevD.45.1840.

[205] Thibault Damour and Gilles Esposito-Farese. "Tensor - scalar gravity and binary pulsar experiments." *Phys. Rev. D* 54 (1996), pp. 1474–1491. DOI: 10.1103/PhysRevD.54.1474. arXiv: gr-qc/9602056.

[206] Thibault Damour and Gilles Esposito-Farese. "Gravitational wave versus binary - pulsar tests of strong field gravity." *Phys. Rev. D* 58 (1998), p. 042001. DOI: 10.1103/PhysRevD.58.042001. arXiv: gr-qc/9803031.

[207] Joseph H. Taylor et al. "Experimental constraints on strong field relativistic gravity." *Nature* (Oct. 1991). DOI: 10.1038/355132a0.

[208] Dimitrios Psaltis. "Constraining Brans-Dicke gravity with millisecond pulsars in ultracompact binaries." (Jan. 2005). arXiv: astro-ph/0501234.

[209] Paulo C. C. Freire et al. "The relativistic pulsar-white dwarf binary PSR J1738+0333 II. The most stringent test of scalar-tensor gravity." *Mon. Not. Roy. Astron. Soc.* 423 (2012), p. 3328. DOI: 10.1111/j.1365-2966.2012.21253.x. arXiv: 1205.1450 [astro-ph.GA].

[210] Russell Alan Hulse and Joseph Hooton Taylor. "Discovery of a pulsar in a binary system." *Astrophys. J. Lett.* 195 (Jan. 1975), pp. L51–L53. DOI: 10.1086/181708.

[211] Michael W. Horbatsch and Cliff P. Burgess. "Model-independent comparisons of pulsar timings to scalar-tensor gravity." *Class. Quant. Grav.* 29 (2012), p. 245004. DOI: 10.1088/0264-9381/29/24/245004. arXiv: 1107.3585 [gr-qc].

[212] Hajime Sotani. "Slowly rotating relativistic stars in scalar-tensor gravity." *Phys. Rev. D* 86 (2012), p. 124036. DOI: 10.1103/PhysRevD.86.124036. arXiv: 1211.6986 [astro-ph.HE].

[213] Daniela D. Doneva et al. "Scalarization." (Nov. 2022). arXiv: 2211.01766 [gr-qc].

[214] Fethi M. Ramazanoğlu and Frans Pretorius. "Spontaneous scalarization with massive fields." *Phys. Rev. D* 93.6 (2016), p. 064005. DOI: 10.1103/PhysRevD.93.064005. arXiv: 1601.07475 [gr-qc].

[215] Roxana Rosca-Mead et al. "Core collapse in massive scalar-tensor gravity." *Phys. Rev. D* 102.4 (2020), p. 044010. DOI: 10.1103/PhysRevD.102.044010. arXiv: 2005.09728 [gr-qc].

[216] Enrico Barausse et al. "Neutron-star mergers in scalar-tensor theories of gravity." *Phys. Rev. D* 87 (2013), p. 081506. DOI: 10.1103/PhysRevD.87.081506. arXiv: 1212.5053 [gr-qc].

[217] Masaru Shibata et al. "Coalescence of binary neutron stars in a scalar-tensor theory of gravity." *Phys. Rev. D* 89.8 (2014), p. 084005. DOI: 10.1103/PhysRevD.89.084005. arXiv: 1310.0627 [gr-qc].

[218] Keisuke Taniguchi, Masaru Shibata, and Alessandra Buonanno. "Quasiequilibrium sequences of binary neutron stars undergoing dynamical scalarization." *Phys. Rev. D* 91.2 (2015), p. 024033. DOI: 10.1103/PhysRevD.91.024033. arXiv: 1410.0738 [gr-qc].

[219] Carlos Palenzuela et al. "Dynamical scalarization of neutron stars in scalar-tensor gravity theories." *Phys. Rev. D* 89.4 (2014), p. 044024. DOI: 10.1103/PhysRevD.89.044024. arXiv: 1310.4481 [gr-qc].

[220] Noah Sennett and Alessandra Buonanno. "Modeling dynamical scalarization with a resummed post-Newtonian expansion." *Phys. Rev. D* 93.12 (2016), p. 124004. DOI: 10.1103/PhysRevD.93.124004. arXiv: 1603.03300 [gr-qc].

[221] Noah Sennett, Lijing Shao, and Jan Steinhoff. "Effective action model of dynamically scalarizing binary neutron stars." *Phys. Rev. D* 96.8 (2017), p. 084019. DOI: 10.1103/PhysRevD.96.084019. arXiv: 1708.08285 [gr-qc].

[222] Thibault Damour and Gilles Esposito-Farese. "Nonperturbative strong field effects in tensor - scalar theories of gravitation." *Phys. Rev. Lett.* 70 (1993), pp. 2220–2223. DOI: 10.1103/PhysRevLett.70.2220.

[223] Tomohiro Harada. "Stability analysis of spherically symmetric star in scalar - tensor theories of gravity." *Prog. Theor. Phys.* 98 (1997), pp. 359–379. DOI: 10.1143/PTP.98.359. arXiv: gr-qc/9706014.

[224] Tomohiro Harada. "Neutron stars in scalar tensor theories of gravity and catastrophe theory." *Phys. Rev. D* 57 (1998), pp. 4802–4811. DOI: 10.1103/PhysRevD.57.4802. arXiv: gr-qc/9801049.

[225] David Anderson and Nicolás Yunes. "Scalar charges and scaling relations in massless scalar–tensor theories." *Class. Quant. Grav.* 36.16 (2019), p. 165003. DOI: 10.1088/1361-6382/ab2eda. arXiv: 1901.00937 [gr-qc].

[226] Vitor Cardoso, Edgardo Franzin, and Paolo Pani. "Is the gravitational-wave ringdown a probe of the event horizon?" *Phys. Rev. Lett.* 116.17 (2016). [Erratum: Phys.Rev.Lett. 117, 089902 (2016)], p. 171101. DOI: 10.1103/PhysRevLett.116.171101. arXiv: 1602.07309 [gr-qc].

[227] Vitor Cardoso et al. "Gravitational-wave signatures of exotic compact objects and of quantum corrections at the horizon scale." *Phys. Rev. D* 94.8 (2016), p. 084031. DOI: 10.1103/PhysRevD.94.084031. arXiv: 1608.08637 [gr-qc].

[228] Vitor Cardoso and Paolo Pani. "Tests for the existence of black holes through gravitational wave echoes." *Nature Astron.* 1.9 (2017), pp. 586–591. DOI: 10.1038/s41550-017-0225-y. arXiv: 1709.01525 [gr-qc].

[229] Jahed Abedi et al. "Quantum black holes in the sky." *Universe* 6.3 (2020), p. 43. DOI: 10.3390/universe6030043. arXiv: 2001.09553 [gr-qc].

[230] Jun Zhang and Shuang-Yong Zhou. "Can the graviton have a large mass near black holes?" *Phys. Rev. D* 97.8 (2018), p. 081501. DOI: 10.1103/PhysRevD.97.081501. arXiv: 1709.07503 [gr-qc].

[231] Ruifeng Dong and Dejan Stojkovic. "Gravitational wave echoes from black holes in massive gravity." *Phys. Rev. D* 103.2 (2021), p. 024058. DOI: 10.1103/PhysRevD.103.024058. arXiv: 2011.04032 [gr-qc].

[232] Ahmed Almheiri et al. "Black holes: Complementarity or firewalls?" *JHEP* 02 (2013), p. 062. DOI: 10.1007/JHEP02(2013)062. arXiv: 1207.3123 [hep-th].

[233] Kabir Chakravarti, Rajes Ghosh, and Sudipta Sarkar. "Signature of nonuniform area quantization on black hole echoes." *Phys. Rev. D* 105.4 (2022), p. 044046. DOI: 10.1103/PhysRevD.105.044046. arXiv: 2112.10109 [gr-qc].

[234] Steven B. Giddings. "Gravitational wave tests of quantum modifications to black hole structure – with post-GW150914 update." *Class. Quant. Grav.* 33.23 (2016), p. 235010. DOI: 10.1088/0264-9381/33/23/235010. arXiv: 1602.03622 [gr-qc].

[235] Naritaka Oshita and Niayesh Afshordi. "Probing microstructure of black hole spacetimes with gravitational wave echoes." *Phys. Rev. D* 99.4 (2019), p. 044002. DOI: 10.1103/PhysRevD.99.044002. arXiv: 1807.10287 [gr-qc].

[236] Vitor Cardoso, Valentino F. Foit, and Matthew Kleban. "Gravitational wave echoes from black hole area quantization." *JCAP* 08 (2019), p. 006. DOI: 10.1088/1475-7516/2019/08/006. arXiv: 1902.10164 [hep-th].

[237] Qingwen Wang, Naritaka Oshita, and Niayesh Afshordi. "Echoes from quantum black holes." *Phys. Rev. D* 101.2 (2020), p. 024031. DOI: 10.1103/PhysRevD.101.024031. arXiv: 1905.00446 [gr-qc].

[238] Naritaka Oshita, Qingwen Wang, and Niayesh Afshordi. "On reflectivity of quantum black hole horizons." *JCAP* 04 (2020), p. 016. DOI: 10.1088/1475-7516/2020/04/016. arXiv: 1905.00464 [hep-th].

[239] Jahed Abedi, Luis Felipe Longo Micchi, and Niayesh Afshordi. "GW190521: First measurement of stimulated Hawking radiation from black holes." (Dec. 2021). arXiv: 2201.00047 [gr-qc].

[240] Sumanta Chakraborty et al. "Implications of the quantum nature of the black hole horizon on the gravitational-wave ringdown." (Feb. 2022). arXiv: 2202.09111 [gr-qc].

[241] Kabir Chakravarti, Rajes Ghosh, and Sudipta Sarkar. "Signature of nonuniform area quantization on gravitational waves." *Phys. Rev. D* 104.8 (2021), p. 084049. DOI: 10.1103/PhysRevD.104.084049. arXiv: 2108.02444 [gr-qc].

[242] Pawel O. Mazur and Emil Mottola. "Gravitational vacuum condensate stars." *Proc. Nat. Acad. Sci.* 101 (2004), pp. 9545–9550. DOI: 10.1073/pnas.0402717101. arXiv: gr-qc/0407075.

[243] Matt Visser and David L. Wiltshire. "Stable gravastars: An alternative to black holes?" *Class. Quant. Grav.* 21 (2004), pp. 1135–1152. DOI: 10.1088/0264-9381/21/4/027. arXiv: gr-qc/0310107.

[244] Thibault Damour and Sergey N. Solodukhin. "Wormholes as black hole foils." *Phys. Rev. D* 76 (2007), p. 024016. DOI: 10.1103/PhysRevD.76.024016. arXiv: 0704.2667 [gr-qc].

[245] Bob Holdom and Jing Ren. "Not quite a black hole." *Phys. Rev. D* 95.8 (2017), p. 084034. DOI: 10.1103/PhysRevD.95.084034. arXiv: 1612.04889 [gr-qc].

[246] Samir D. Mathur. "The fuzzball proposal for black holes: An elementary review." *Fortsch. Phys.* 53 (2005). Ed. by E. Kiritsis, pp. 793–827. DOI: 10.1002/prop.200410203. arXiv: hep-th/0502050.

[247] Qingwen Wang and Niayesh Afshordi. "Black hole echology: The observer's manual." *Phys. Rev. D* 97.12 (2018), p. 124044. DOI: 10.1103/PhysRevD.97.124044. arXiv: 1803.02845 [gr-qc].

[248] Mehdi Saravani, Niayesh Afshordi, and Robert B. Mann. "Empty black holes, firewalls, and the origin of Bekenstein–Hawking entropy." *Int. J. Mod. Phys. D* 23.13 (2015), p. 1443007. DOI: 10.1142/S021827181443007X. arXiv: 1212.4176 [hep-th].

[249] Randy S. Conklin, Bob Holdom, and Jing Ren. "Gravitational wave echoes through new windows." *Phys. Rev. D* 98.4 (2018), p. 044021. DOI: 10.1103/PhysRevD.98.044021. arXiv: 1712.06517 [gr-qc].

Part I

Black hole spectroscopy

Chapter 2

QUASINORMAL-MODE FILTERS: A NEW APPROACH FOR BLACK-HOLE SPECTROSCOPY

[1] Sizheng Ma et al. "Quasinormal-mode filters: A new approach to analyze the gravitational-wave ringdown of binary black-hole mergers." *Phys. Rev. D* 106.8 (2022), p. 084036. DOI: 10.1103/PhysRevD.106.084036. arXiv: 2207.10870 [gr-qc].

2.1 Introduction

Ringdown is the final stage of a gravitational wave (GW) signal emitted by a binary black hole (BBH) coalescence. It is associated with the oscillations of the remnant black hole (BH), and contains rich information of the system. With an increasing number of GW events [1–4] observed by ground-based detectors [5–7], comprehensive studies of the ringdown signal and its rich features become crucial to understanding the geometry of extreme spacetimes and testing General Relativity (GR).

A standard description of the ringdown comes from the BH perturbation (BHP) theory. The perturbation of a single BH has been an important topic for decades [8–11]. GWs emitted by the BH during ringdown are characterized by a set of quasinormal modes (QNMs) [1], which are complex and dissipative by their nature. As a consequence, the time-domain evolution of each QNM is a damped sinusoid. Due to the no-hair theorem [14–17], QNMs predicted by GR are completely determined by the mass and spin of the BH. Therefore, measuring the frequency and decay rate of a QNM from a ringdown signal would allow people to infer the mass and spin of the BH, as pointed out by Echeverria [18]. This method is dubbed *BH spectroscopy*. The idea was then generalized by Dreyer *et al.* [19] and Berti *et al.* [20, 21], and they showed that one could test the no-hair theorem if multiple modes are observed at the same time. Later on, a lot of effort has been made to investigate BH spectroscopy under different scenarios [22–41]. In particular, the studies by Cardoso *et al.* [10, 42, 43], Foit *et al.* [44] and Laghi *et al.* [45] implied that QNMs could reflect the quantum nature of BHs or other exotic compact objects (ECOs);

[1] Except for the late gravitational tail [12, 13].

hence one can use this fact to test GR and constrain modified gravity [46–49]. Since the detection of GW150914 [50], BH spectroscopy with real observational data has become available. Carullo *et al.* [51] studied the late-time portion of the ringdown of GW150914 and found no evidence for the presence of more than one QNM. Then Isi *et al.* [52] extended the analysis to the peak of the strain and showed evidence of at least one overtone, with 3.6σ confidence. This led to a test of the no-hair theorem at the $\sim 20\%$ level. Recently, Cotesta *et al.* [53] raised an opposing viewpoint that the search for the first overtone in the ringdown of GW150914 might be impacted by noises, therefore the conclusion still remains controversial [54, 55]. On the other hand, Capano *et al.* [56] studied the QNM spectrum of GW190521 [57] and found the $l = m = 3$ harmonic. More GW events were used to perform BH spectroscopy in Refs. [58–60].

The inspiral-merger-ringdown (IMR) consistency test is another important extension of BH spectroscopy. One can infer the properties of binaries separately from the inspiral waves and the ringdown waves, and check whether they are consistent with the predictions of GR. The idea was proposed originally by Hughes *et al.* [61], and more careful analyses were carried out later [62–65]. So far, no deviation from GR has been found in observational data [66–69]. In addition, Refs. [70, 71] used this method to test Hawking's area law [72].

An essential ingredient for BH spectroscopy is to understand how QNMs are excited at merger [73–86] and when the ringdown starts [87–89]. An accurate investigation for a BBH system during a highly nonlinear regime was not available until the numerical relativity (NR) breakthrough was made in 2005 by Pretorius [90]. Since then, a usual method to study the ringdown of a numerical waveform has been fitting it to the prediction of BHP theory. For example, Buonanno *et al.* [91] decomposed the ringdown signal into a sum of the fundamental mode and several overtones. Berti *et al.* [92, 93] and Kamaretsos *et al.* [84] fit the ringdown of unequal-mass, nonspinning systems with only the fundamental mode. London *et al.* [94] carried out a more systematic study for various nonspinning BBHs and identified overtones within the NR waveforms. On the other hand, the fitting was also an important step to calibrate the effective one-body model [95–99]. Later, given the motivation of BH spectroscopy with real observational data, Thrane *et al.* [100] fit the ringdown of a GW150914-like NR simulation without any overtone, and they found some inconsistency between the QNM model (with fundamental modes only) and NR waveform. This puzzle was resolved by Giesler *et al.* [101], where the authors found

that the inclusion of overtones could extend the linear regime to the peak strain amplitude. This work sparked another wave for ringdown modeling, including the study for multimode ringdown fitting [102], and the impacts of other effects on ringdown signals, such as retrograde modes [2] [103], more overtones [104], precessing systems [105], angular emission patterns [106], and the Bondi-van der Burg-Metzner-Sachs freedom [107].

It is surprising to see that the linear BHP theory is good enough to explain the waveform beyond the peak of the strain, given that the dynamics at the merger are believed to still be violent. Okounkova [89] provided a possible explanation based on previous Kerrness tests [87]: most of the near-zone nonlinearities [3] are absorbed by the event horizon and barely escape to infinity. Nonetheless, it still seems elusive to draw an incontrovertible conclusion, since recent studies [110, 111] showed that multipole moments of dynamical horizon are also compatible with the superposition of linear QNMs soon after the formation of the common horizon. Furthermore, it was shown that applying second-order BHP theory to the close-limit approximation could improve the agreement between the ringdown model and the full numerical waveform—the improvement was not only limited to the regime near the peak, but also extended to the late portion of the ringdown signal [112]. Then it is natural to ask: *where are the second-order effects?* In the past, the second-order perturbation of a Schwarzschild BH was used by Tomita *et al.* [113, 114] in the process of a gravitational collapse to investigate the stability of the horizon. Cunningham *et al.* [115] treated the spin as a small perturbation during the Oppenheimer-Snyder collapse and studied its second-order effect. Later on, second-order perturbation theory was motivated by the close-limit approximation [116], including the metric perturbation of a Schwarzschild BH [112, 117–122] and the perturbation of a Kerr BH within the Newman-Penrose formalism [123]. Recently, more comprehensive treatments were used to deal with the perturbation of a Kerr BH and its metric reconstruction [124–126]. An important feature of second-order BHP theory is that the master equation has the same potential as the first-order theory, while the source term is quadratic in terms of the first-order perturbations. Accordingly, the time evolution of the second-order perturbations can be influenced by the second-order QNMs, known as "sum tones" and "difference tones" [127–131]. For instance, Nakano *et al.* [129] found the existence of a component twice the $(l = 2, m = 2)$

[2] The author of Ref. [103] used the name "mirror mode" instead. In this work we will always use "retrograde mode."

[3] Here we do not consider the wave-zone nonlinearities, say the memory effect, which has been obtained from NR [108, 109].

QNM in the $(l = 4, m = 4)$ harmonic by looking at a perturbed Schwarzschild BH. So far, very few studies have been done on the second-order effects within the ringdown of a BBH waveform. London *et al.* [94] investigated 68 NR waveforms and presented the evidence of the second-order mode $(l_1, m_1, n_1)\times(l_2, m_2, n_2) = (2, 2, 0)\times(2, 2, 0)$ in the $(l = 4, m = 4)$ harmonic via time-domain fitting. Beyond the second-order effect, Sberna *et al.* [132] showed that the growth of BH mass due to the absorption of the linear QNMs can induce a third-order secular effect.

The time-domain fitting proves to be powerful to extract the physics from ringdown signals. However, one always has to be careful of overfitting—more QNMs included (e.g., overtones or retrograde modes) may act as additional basis functions to misinterpret other effects. Taking this caveat into consideration, in this chapter we propose a complementary tool to analyze a ringdown waveform—we define two frequency-domain filters that are able to remove any particular QNM from the ringdown. After the dominant mode is filtered out, we can visualize the existence of subdominant effects, including mode mixing, second-order modes, and retrograde modes.

This chapter is organized as follows. In Sec. 2.2, we introduce two types of filters and show their properties. Then in Sec. 2.3, we apply the two filters to NR waveforms and discuss the results. Section 2.4 focuses on the stability of the filter under perturbations. Next, in Sec. 2.5, we discuss how the filter depends on the remnant BH's mass and spin. We also investigate the possibility to use the filter for parameter estimation. Finally, we summarize the results in Sec. 2.6.

Throughout this chapter, we use the geometric units with $G = c = 1$. We always use the notation ω_{lmn} to refer to the (l, m, n) QNM.

2.2 QNM filters

In this section, we introduce two types of filters for QNMs. In Sec. 2.2.1 we first review briefly the QNM decomposition model of a ringdown signal. Then in Sec. 2.2.2 we describe a rational filter, which can remove any particular QNM from a ringdown signal. Two toy models are used to explore the effect of this filter. After understanding the effects of the rational filter, in Sec. 2.2.3 we argue that the inverse of the remnant BH's transmissivity can also serve as a filter. Remarkably, we find that the waveform filtered by this filter has a physical meaning.

2.2.1 Decomposing late waveforms into QNMs

It has been widely accepted that the late part of the GW emitted by binary black-hole mergers can be described as a linear combination of QNMs and a power-law tail, which arise from different features of the retarded gravitational Green's function G_{lm}: the QNMs correspond to poles of G_{lm}, while the power-law tail arises from integrating along a branch-cut G_{lm} [133].

In the special case of a high-mass-ratio merger, which can be modeled as an orbiting and then plunging particle, QNM excitations at late times have been computed [82, 83, 85] and further analyzed in terms of multipole and overtone excitations [74, 76, 77, 134]. As an example, in linear perturbation theory, the gravitational waveform at infinity sourced by the particle can be described by

$$h(t, r_*) = \sum_{lm} \int \frac{d\omega}{2\pi} e^{-i\omega t} \int dy G_{lm}(r_*, y, \omega) S_{lm}(y, \omega), \tag{2.1}$$

where $S_{lm}(y, \omega)$ is the source term, and it has the general form of

$$S_{lm}(y, \omega) = e^{i\omega T(y)} P(\omega, y) \tag{2.2}$$

where $(T(y), y)$ parametrizes the radial trajectory of the particle, and $P(\omega, y)$ is a rational function of ω. For each y, as long at $t > T(y)$ one can close the ω-contour from the lower-half complex plane, hence only collect the poles of the Green's function G_{lm} and a branch-cut contribution which corresponds to power-law tails. Even though the particle's $T(y)$ becomes infinity for $y \to -\infty$, the source term $P(\omega, y)$ exponentially decays to zero, soon after y becomes negative, i.e., when the particle plunges across the light ring and approaches the horizon.

Gravitational waveforms from collapsing stars and merging *comparable-mass* BHs were argued to have similar late-stage properties [18, 115, 135–139]. The regime of QNM decomposition is often referred to as the "linear regime," although the decomposition requires both linearity and homogeneity (i.e., the QNMs are homogeneous solutions to the linearized Einstein's equations).

Now assuming that a ringdown signal $h(\theta, \phi, t)$ is a linear combination of QNMs, starting from t_0, namely

$$\begin{aligned} h(\theta, \phi, t) &= (h_+ - i h_\times)(\theta, \phi, t) \\ &= \sum_{kmn} \Big[A_{kmn} e^{-i\omega_{kmn}(t-t_0)} {}_{-2}S_{kmn}(a\omega_{kmn}, \theta, \phi) \\ &+ A'_{kmn} e^{i\omega^*_{kmn}(t-t_0)} {}_{-2}S^*_{kmn}(a\omega_{kmn}, \pi - \theta, \phi) \Big], \end{aligned} \tag{2.3}$$

where $\times, +$ refer two polarization states of the GW, a is the dimensional spin of the BH, ω_{kmn} are the frequencies of QNMs, ${}_{-2}S_{kmn}(a\omega_{kmn}, \theta, \phi)$ are the spin-weighted spheroidal harmonics [140], and (A_{kmn}, A'_{kmn}) are the mode amplitudes. It is usually more convenient to decompose the waveform in terms of spin-weighted spherical harmonics ${}_{-2}Y_{lm}(\theta, \phi)$

$$h(\theta, \phi, t) = \sum_{lm} h_{lm}(t) {}_{-2}Y_{lm}(\theta, \phi) \tag{2.4}$$

with h_{lm} being the (l, m) spherical multipole harmonic. The mode mixing between the two bases: ${}_{-2}S_{kmn}(a\omega_{lmn}, \theta, \phi)$ and ${}_{-2}Y_{lm}(\theta, \phi)$, is given by [141, 142]

$${}_{-2}S_{kmn}(a\omega_{lmn}, \theta, \phi) = \sum_{l} \mu^{*}_{mlkn}(a\omega_{lmn}) {}_{-2}Y_{lm}(\theta, \phi). \tag{2.5}$$

By combining Eqs. (2.3), (2.4) and (2.5), we obtain the QNM decomposition model for h_{lm}:

$$h_{lm} = \sum_{k,n} \left[C_{mlkn} e^{-i\omega_{kmn}(t-t_0)} + C'_{mlkn} e^{i\omega^{*}_{k-mn}(t-t_0)} \right]. \tag{2.6}$$

Explicit relations between C_{mlkn} and A_{kmn} [Eq. (2.3)] can be found in Ref. [77]. Note that the second term in Eq. (2.6) corresponds to the retrograde modes, which are also dubbed "mirror modes" in Refs. [103, 143].

2.2.2 The rational filter and two toy models

For simplicity's sake we consider a single QNM signal in the time domain:

$$h(t) = e^{-i\omega_{lmn}(t-t_0)} \Theta(t - t_0), \tag{2.7}$$

where ω_{lmn} is the complex frequency of a specific QNM, $\Theta(t - t_0)$ is the Heaviside step function, and t_0 refers to the start time of the mode. If we are interested in the regime of $t > t_0$ and want to annihilate the mode content ω_{lmn} therein, a natural choice is to use a time-domain operator

$$\left(\frac{d}{dt} + i\omega_{lmn} \right) h(t) = \delta(t - t_0), \tag{2.8}$$

with $\delta(t-t_0)$ being the Dirac function. However, this operation can lead to additional numerical noises. Instead, we first transform the signal $h(t)$ in Eq. (2.7) to the frequency domain

$$\tilde{h}(\omega) = \frac{1}{\sqrt{2\pi}} \int h(t) e^{i\omega t} dt, \tag{2.9}$$

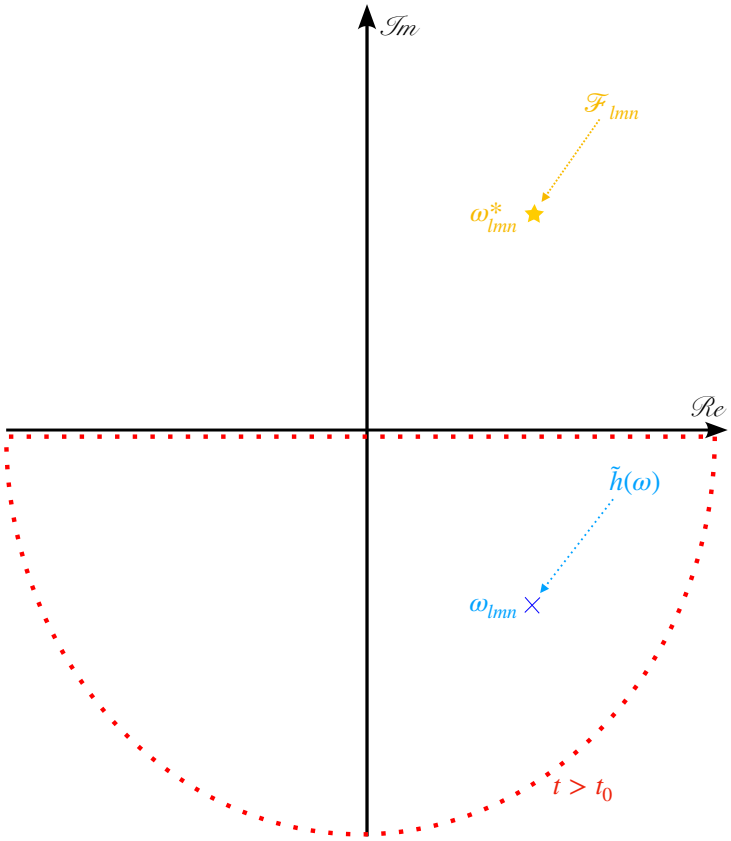

Figure 2.1: The pole of the original waveform $\tilde{h}(\omega)$ (in blue) and the filtered one $\tilde{h}^{\rm filter}(\omega)$ (in orange). The contour is closed from the upper (lower) plane when $t < t_0$ ($t > t_0$).

and obtain

$$\tilde{h}(\omega) = \frac{i}{\sqrt{2\pi}} \frac{e^{i\omega t_0}}{\omega - \omega_{lmn}}. \tag{2.10}$$

Then we define a frequency-domain filter $\mathcal{F}_{lmn}$:

$$\mathcal{F}_{lmn} = \frac{\omega - \omega_{lmn}}{\omega - \omega^*_{lmn}}, \tag{2.11}$$

where $*$ represents the complex conjugate. We remark that the numerator of $\mathcal{F}_{lmn}$ corresponds to the annihilation operator [Eq. (2.8)] in the frequency domain, while the denominator is introduced to make $|\mathcal{F}_{lmn}| = 1$ (when ω is real-valued) and therefore ensure that the filter does not diverge at high frequency. Finally, we impose the filter via

$$\tilde{h}^{\rm filter}(\omega) = \mathcal{F}_{lmn}\tilde{h}(\omega), \tag{2.12}$$

and transform the filtered signal to the time domain again

$$h^{\rm filter}(t) = \frac{1}{\sqrt{2\pi}} \int \tilde{h}^{\rm filter}(\omega) e^{-i\omega t} d\omega, \tag{2.13}$$

which yields

$$h^{\rm filter}(t) = -e^{-i\omega^*_{lmn}(t-t_0)} \Theta(t_0 - t). \tag{2.14}$$

Notice that the sign of the argument in the Heaviside step function Θ has changed. This can be understood in terms of the impact of the filter on the pole of the waveform, as shown in Fig. 2.1. The pole of the original waveform $\tilde{h}(\omega)$ (in blue) lies in the lower half plane, implying its excitation after t_0. After imposing the rational filter $\mathcal{F}_{lmn}$, the pole is lifted to the upper panel (in orange). Therefore, the filtered waveform becomes a ring-up signal prior to t_0, whereas the original ringdown is removed after that moment.

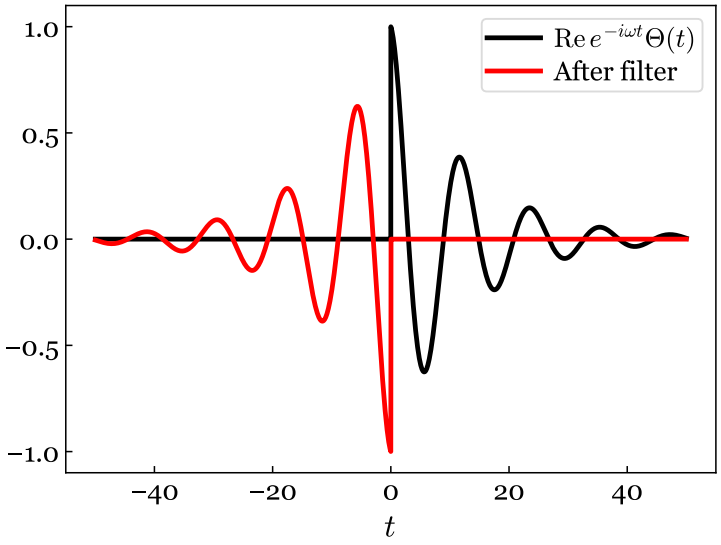

Figure 2.2: The effect of the frequency-domain filter in Eq. (2.11) on a single QNM signal. The mode is chosen to be the fundamental $(l = 2, m = 2)$ QNM of a Kerr BH with dimensionless spin 0.69. The signal starts at $t = 0$, and it is padded with 0 for $t < 0$. After applying the filter, the original signal (its real part is shown as the black curve) is removed from the regime of interest $(t > 0)$, whereas an undesired "flipped ringdown" is introduced for $t < 0$ (red curve). This "flipped ringdown" resembles the original signal, but decays backward in time.

To be specific, we consider a toy model in Fig. 2.2 to illustrate the effect of the filter. We pick the fundamental $(l = 2, m = 2)$ QNM of a Kerr BH with dimensionless spin $\chi = 0.69$. The QNM frequencies are obtained from the PYTHON package

qnm [144]. The start time t_0 is set to 0. Indeed, we can see that within our interested regime $t > t_0$, the filter is able to remove the mode content ω_{lmn} completely. Meanwhile, the ring-up signal ("flipped ringdown") is introduced before t_0. As we will see, this feature can contaminate GWs at merger, but it will not affect our analysis as long as we focus on the regime $t > t_0$. As for an early, low-frequency inspiral signal, since its frequency ω is small compared to ω_{lmn}, we can perform a Taylor expansion around $\omega = 0$

$$\mathcal{F}_{lmn} = \exp[-i\phi_{lmn} - i\omega t_{lmn} + \mathcal{O}(\omega^2)], \tag{2.15}$$

where the two real constants t_{lmn} and ϕ_{lmn} are given by

$$\phi_{lmn} = -2\tan^{-1}\frac{\omega^{\rm i}_{lmn}}{\omega^{\rm r}_{lmn}}, \qquad t_{lmn} = -\frac{2\omega^{\rm i}_{lmn}}{|\omega_{lmn}|^2}, \tag{2.16}$$

with $\omega^{\rm r}_{lmn}$ and $\omega^{\rm i}_{lmn}$ being the real and imaginary part of $\omega_{lmn} = \omega^{\rm r}_{lmn} + i\omega^{\rm i}_{lmn}$, respectively. Consequently, imposing the filter $\mathcal{F}_{lmn}$ to the low-frequency inspiral signal is equivalent to shifting the original signal in phase and backward in time[4]. For a Kerr BH with $\chi = 0.69$, the $(l = 2, m = 2)$ fundamental mode leads to $t_{lmn} \sim 0.57M_f$, which can be neglected for most of ringdown analyses. However, if we want to remove a series of QNMs, we need to apply:

$$\mathcal{F}_{\rm tot} = \prod_{lmn} \mathcal{F}_{lmn}, \tag{2.17}$$

where n stands for the overtone index. Then the time shift t_{lmn} may not be negligible anymore.

We then switch our attention to a more realistic case: a Schwarzschild BH perturbed by an even-parity Gaussian pulse. The Zerilli equation [145] is solved numerically. Figure 2.3 shows the waveform h_{22} at future null infinity. We see h_{22} (the black curve) consists of the excitation, ringdown, and tail regime. After applying the filter $\mathcal{F}_{220}$ (the red curve), the ringdown oscillations are completely removed from the tail beyond a certain time around the merger, yet a few wiggles appear prior to that time. This is due to the nonphysical "flipped ringdown" (see the red curve in Fig. 2.2). The difference between the original h_{22} and the filtered waveform, as shown in the lower panel of Fig. 2.3, corresponds to the combination of the "flipped ringdown" and the real ringdown (namely the combination of the black and red curves in Fig. 2.2).

[4]Strictly speaking, Eq. (2.16) is for zero frequency components. An accurate estimation for other low frequencies is not needed in this chapter.

Note that here we have undone the time shift induced by the filter by aligning two waveforms in the early regime. The peak of the difference (the vertical green dashed line) represents the start time of the ringdown t_0 [see Eq. (2.7)]. In addition, we see a generic feature: a new damped sinusoid that decays backward in time shows up before the onset of the original signal. For a BBH waveform, it appears before the entire inspiral regime, thus it does not impact our analysis.

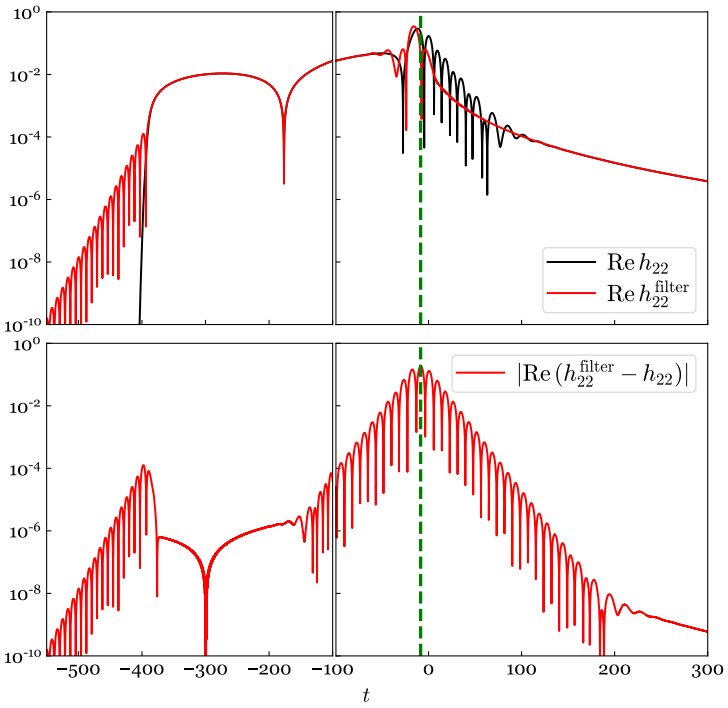

Figure 2.3: The impact of the filter $\mathcal{F}_{220}$ on the GW emitted by a single, perturbed Schwarzschild BH. In the upper panel, the real part of the filtered waveform (red curve) is compared with the original h_{22} (black curve). Note that here we have undone the time shift induced by the filter by aligning two waveforms in the early regime. In the lower panel, the difference between the two waveforms corresponds to the combination of the "flipped ringdown" and the real ringdown (see the black and red curves in Fig. 2.2). Its peak (the vertical dashed line) represents the start time of the ringdown.

2.2.3 The full filter: The inverse of BH transmissivity

Following Teukolsky's approach for the linear perturbation of a Kerr BH with dimensional spin a [146, 147], we first write

$$\Psi = \rho^{-4}\psi_4 = R_{lm}(r,\omega)\,{}_{-2}S_{lm}(a\omega,\theta,\phi)e^{i\omega t}, \tag{2.18}$$

where $\rho = -(r - ia\cos\theta)^{-1}$, (t, r, θ, ϕ) is the Boyer-Lindquist coordinate system, and ψ_4 is the Weyl scalar. The radial function $R_{lm}(r,\omega)$ satisfies the radial Teukolsky

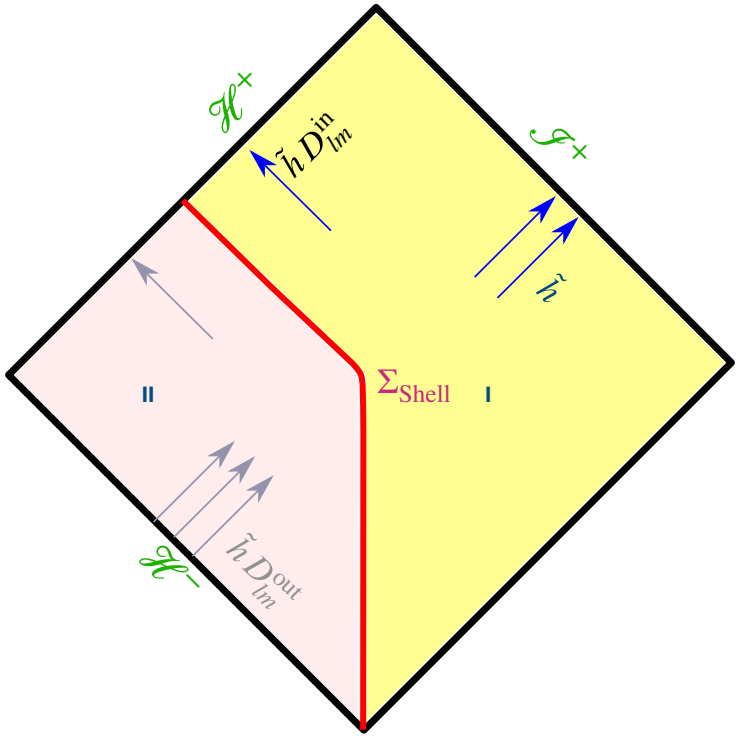

Figure 2.4: The physical meaning of $\mathcal{F}^D_{lm}$ based on the hybrid approach. The spacetime is split by a time-like world tube $\Sigma_{\rm Shell}$ (red line) into an inner PN regime II and an outer BHP regime I. During the spacetime reconstruction, we take a waveform from NR at null infinity $\mathscr{I}^+$, and evolve it backward into the bulk using BHP theory as if $\Sigma_{\rm Shell}$ were not there. The result is proportional to the up-mode solution to the homogeneous Teukolsky equation. In particular, an image wave $\tilde{h}D^{\rm out}_{lm}$ needs to appear at the past horizon $\mathscr{H}^-$, and it is proportional to the filtered waveform. The image wave is spurious since the entire $\mathscr{H}^-$ lies inside the PN regime II, where the BHP theory does not apply. It exists there as a source to drive the wave in regime I. During the ringdown phase of $\tilde{h}$, the linear QNMs are free ringing of the remnant BH and hence can be annihilated by $D^{\rm out}_{lm}$, whereas nonlinear pieces are driven by some sources and thus cannot be removed.

equation [146, 147]. The *up*-mode solution $R^{\rm up}_{lm}$ to the homogeneous Teukolsky equation is of particular interest to us. Its asymptotic behavior near future null infinity and the horizon is given by [148]

$$R^{\rm up}_{lm} \sim \begin{cases} r^3 e^{i\omega r_*}, & r_* \to +\infty, \\ D^{\rm out}_{lm} e^{i\omega r_*} + \Delta^2 D^{\rm in}_{lm} e^{-i\omega r_*}, & r_* \to -\infty, \end{cases} \tag{2.19}$$

with $\Delta = r^2 - 2r + a^2$ and r_* being the tortoise radius. Fig. 2.4 exhibits the physical meaning of the up-mode—a wave is emitted from the past horizon $\mathscr{H}^-$ and it gets

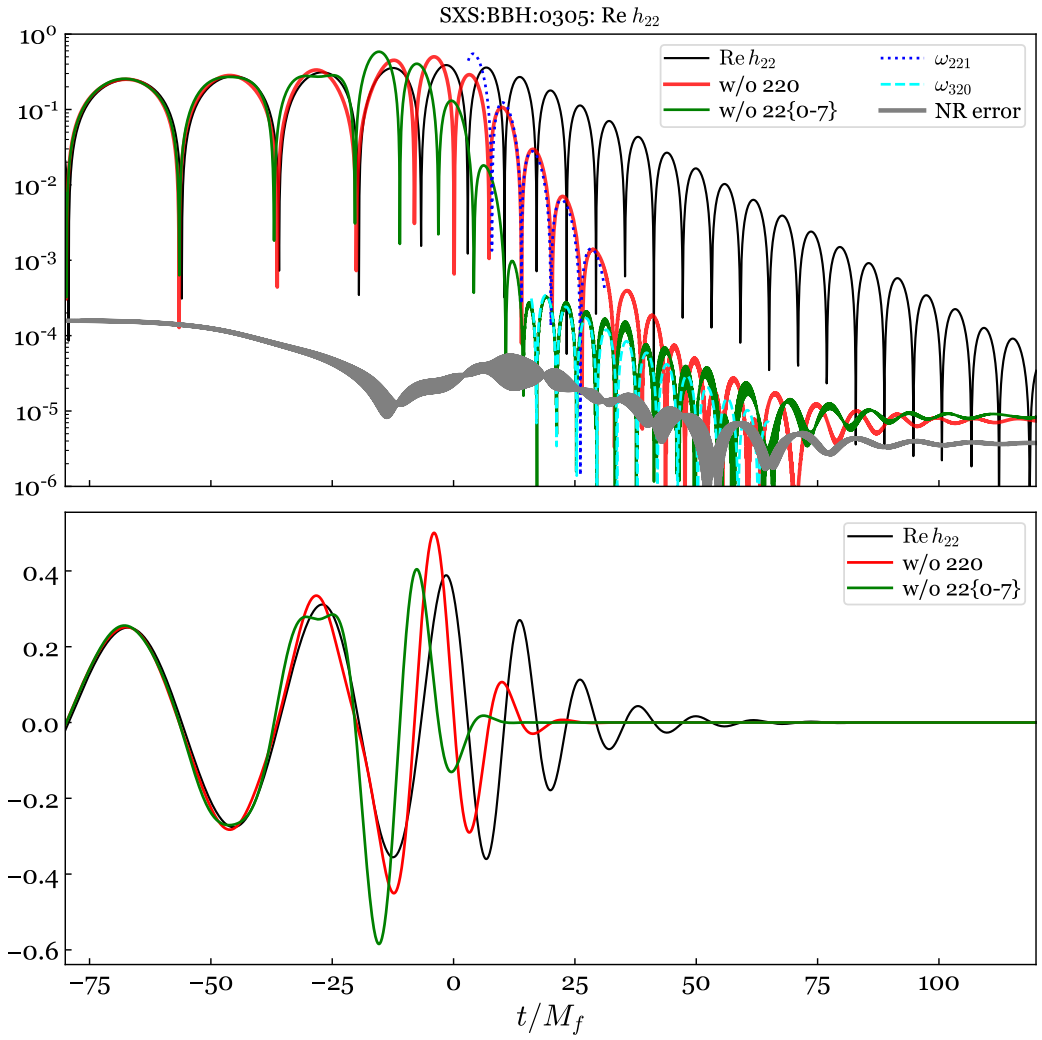

Figure 2.5: The effect of the filter $\mathcal{F}_{lmn}$ on h_{22} of SXS:BBH:0207. Here we have aligned the early inspiral portion between the original signal h_{22} (black) and the filtered waveforms. After removing ω_{220} from the original waveform, the oscillation in the ringdown of the filtered waveform (red) is consistent with the QNM ω_{221} (blue). If we further remove $\omega_{22,n=1\ldots7}$, the residual shows the existence of the QNM ω_{320} (cyan), which is caused by the spherical-spheroidal mixing. For comparison, we evaluate the numerical error of this waveform (gray) by taking the difference between two adjacent numerical resolutions.

reflected and transmitted by the BH potential. The transmissivity and reflectivity are given by $1/D^{\rm out}_{lm}$ and $D^{\rm in}_{lm}/D^{\rm out}_{lm}$, respectively. As for a QNM of the BH, its mode frequency ω_{lmn} satisfies

$$D^{\rm out}_{lm}(\omega_{lmn}) = 0. \tag{2.20}$$

Therefore, we can write

$$D^{\rm out}_{lm} \sim \prod_n (\omega - \omega_{lmn}). \tag{2.21}$$

Comparing Eq. (2.21) with the filter in Eq. (2.17) [also Eq. (2.11)], we see $D^{\rm out}_{lm}$ serves the same role as $\mathcal{F}_{\rm tot}$: it can remove all ω_{lmn}'s that are associated with the indices (l, m) at once. In practice, since $D^{\rm out}_{lm}$ diverges as $\omega \to 0$ [149], we instead define a filter

$$\mathcal{F}^D_{lm} = \frac{D^{\rm out}_{lm}}{D^{\rm out*}_{lm}}, \tag{2.22}$$

which is a direct analogue of Eq. (2.11) to ensure $|\mathcal{F}^D_{lm}| = 1$ when ω is real-valued. Below we will call $\mathcal{F}^D_{lm}$ the full filter.

Interestingly, unlike the filter in Eq. (2.11) that was introduced purely phenomenologically, the current filtered waveform $\tilde{h}\, D^{\rm out}_{lm}$ bears a physical meaning. To be concrete, in Ref. [150], some use the *hybrid approach* [137, 138] to reconstruct the spacetime near merging compact objects based on NR waveforms at future null infinity $\mathscr{I}^+$. Below we give a brief introduction and refer the interested readers to Refs. [137, 138, 150] for more details. The hybrid method is an approximated, *ab initio* waveform mode. For a BBH merger spacetime in Fig. 2.4, the spacetime is split by a time-like world tube $\Sigma_{\rm Shell}$ into an inner strong-gravity region II and an outer weak-gravity region I, where the strong-gravity metric in II is given by the post-Newtonian (PN) theory while the one in I is provided by BHP theory. The hybrid method evolves two metrics jointly and they communicate via boundary conditions on the world tube $\Sigma_{\rm Shell}$. Note that close to the merger, the PN theory may break down, but the errors stay within the BH potential as long as the shell $\Sigma_{\rm Shell}$ falls rapidly enough into the future horizon $\mathscr{H}^+$. As a result, the hybrid method was able to predict a reasonable inspiral-merger-ringdown waveform for a BBH system [137, 138].

In Ref. [150], on the other hand, we reversed the process—we started with a NR waveform at $\mathscr{I}^+$ and evolved it backward into the bulk (the region I) using BHP theory. This process allows us to construct the entire spacetime as if the worldtube were not there. It turns out that the solution is proportional to the up-mode solution in Eq. (2.19), and the coefficient is determined by the NR waveform $\tilde{h}$ at $\mathscr{I}^+$. As shown in Fig. 2.4, the process leads to an outgoing wave $\tilde{h}\, D^{\rm out}_{lm}$ at the past horizon $\mathscr{H}^-$, although it is not real because the entire $\mathscr{H}^-$ lies inside the strong-gravity region, where BHP theory does not apply. Nevertheless, we can think of

the filtered waveform $\tilde{h}\, D^{\rm out}_{lm}$ as an *image wave*, which is akin to the image charge in electrodynamics. The image wave exists there to drive the signal in region I—acting as a source—by providing a desired boundary condition on $\Sigma_{\rm Shell}$. In particular, during the ringdown phase of $\tilde{h}$, a linear QNM corresponds to the free ringing of the BH, and thus there is no corresponding source term. Consequently, it can be annihilated by $D^{\rm out}_{lm}$, which is consistent with our phenomenological construction in Sec. 2.2.2. In contrast, second-order effects (during the ringdown phase) [117, 125, 126] are driven by sources, and hence cannot be removed by $D^{\rm out}_{lm}$. The filtered waveform $\tilde{h}\, D^{\rm out}_{lm}$ represents the image wave (an effective source) for the second-order effects.

Table 2.1: A list of NR simulations (nonprecessing) used in this chapter. The first column is the SXS identifier [151]. The second column is the mass ratio $q > 1$. The third column gives the number of quasicirular orbits that the systems undergo before the merger. The fourth and fifth columns correspond to the initial spin components along the direction of the orbital angular momentum (the $z-$axis). The remnant mass (M_f), as a fraction of the total system mass $M_{\rm tot}$, and spin (χ_f) are in the final two columns. The waveform SXS:BBH:0207 is a GW150914-like system.

ID SXS:BBH:	q	$N_{\rm cycle}$	χ_1^z	χ_2^z	$\frac{M_f}{M_{\rm tot}}$	χ_f
0305	1.2	15.2	0.33	−0.44	0.952	0.692
1107	10.0	30.4	$\sim 10^{-6}$	$\sim 10^{-8}$	0.992	0.261
1936	4.0	16.5	−0.8	−0.8	0.985	0.022

2.3 Applications of the filters

In this section, we use three NR simulations, SXS:BBH:0305, 1107 and 1936, in the Simulating eXtreme Spacetimes (SXS) catalog [151] as examples to demonstrate the applications of the filters. As summarized in Table 2.1, these three waveforms are for nonprecessing systems: the initial individual spins $\chi^z_{1,2}$ are (anti-)aligned with the orbital angular momentum (along the z-axis), and the mass ratio between the primary BH and the secondary BH is denoted by q, i.e., $q > 1$. The systems undergo $N_{\rm cycle}$ quasicircular orbits before the merger. The remnants are Kerr BHs with mass M_f and spin χ_f. In particular, SXS:BBH:0207 is a GW150914-like system [50]. We want to emphasize again that our rational filter leads to a time shift backwards in time. For the sake of comparison, in this section we always undo the time shift by aligning the early portions of waveforms (i.e., minimizing their mismatch).

2.3.1 The GW150914-like system: SXS:BBH:0207

In this subsection, we investigate several (l, m) harmonics of SXS:BBH:0305. We first focus on h_{22}, where we show that the ω_{320} QNM mixes into h_{22} due to the spherical-spheroidal mixing [141, 143, 152]. Then we investigate second-order effects in h_{44}, h_{54} and h_{55} contributed by the quadratic couplings h_{22}^2 and $h_{22}h_{33}$, respectively. Finally, we study the leakage of the ω_{220} mode into the harmonic h_{21} due to the gravitational recoil [152, 153].

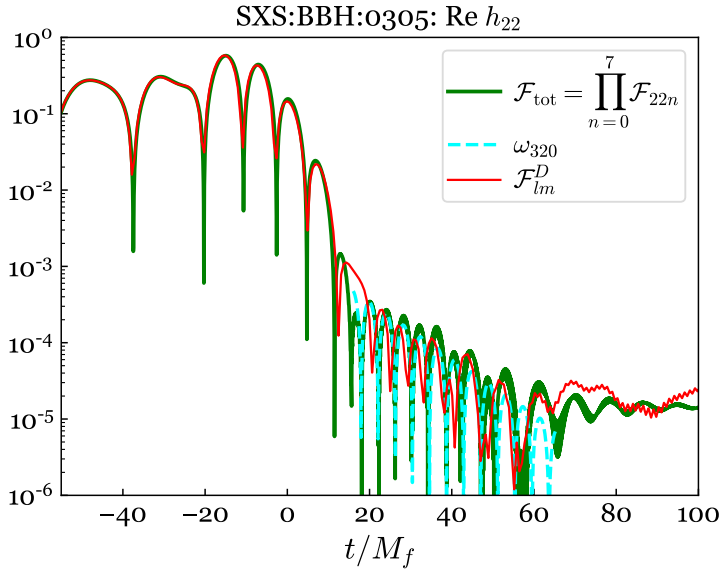

Figure 2.6: A comparison between the full filter $\mathcal{F}^{D}_{lm}$ [Eq. (2.22)] and the rational filter $\mathcal{F}_{\rm tot}$ [Eq. (2.17)] associated with $\omega_{22,n=0...7}$. The latter one is more accurate to reveal the existence of the QNM ω_{320} in h_{22} of SXS:BBH:0207. We attribute the inaccuracy of the full filter to the numerical noise when we interpolate the value of $D^{\rm out}_{lm}$ from the Black Hole Perturbation Toolkit.

2.3.1.1 h_{22}: *the spherical-spheroidal mixing*

It was found that the harmonic h_{22} of SXS:BBH:0207 can be modeled as a superposition of $\omega_{22,n=0...7}$ up to the peak strain amplitude [101]. To compare our analysis results using the new method with theirs, we first apply a filter $\mathcal{F}_{l=2,m=2,n=0}$ [Eq. (2.11)] to h_{22}. As shown in Fig. 2.5, the filtered waveform (the red curve) has a smaller amplitude than h_{22} in the late ringdown regime, and we see that the main residual oscillation is consistent with the frequency and the decay rate of the first overtone ω_{221} (blue). Here the blue dashed curve is obtained by fitting the filtered waveform within the window of $[12, 28]\, M_f$; and the mode amplitude and phase of the first overtone are 0.08 and -0.57 rad at $t = 12\, M_f$. We note that the amplitude

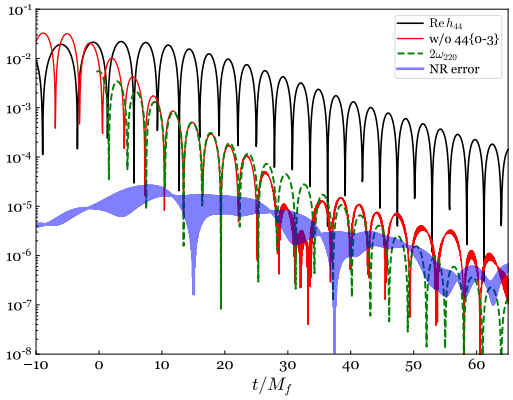

(a) SXS:BBH:0305: Re h_{44}

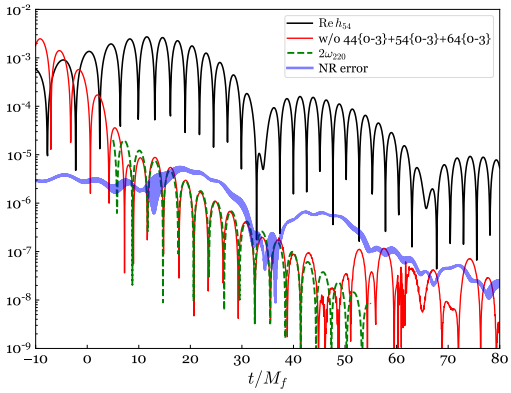

(b) SXS:BBH:0305: Re h_{54}

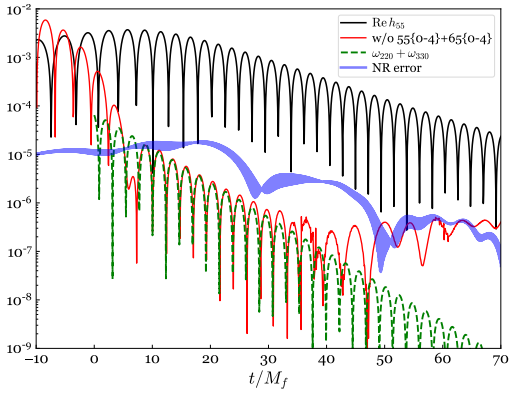

(c) SXS:BBH:0305: Re h_{55}

Figure 2.7: Second-order modes in h_{44} (top), h_{54} (bottom left), h_{55} (bottom right) of SXS:BBH:0207. After removing linear QNMs and relevant spherical-spheroidal mixing modes from original waveforms (black curves), filtered waveforms (red curves) contain oscillations that are consistent with the sum tone of $2\omega_{220}$ or $\omega_{220}+\omega_{330}$ (green dashed curves). As for the harmonics h_{55} and h_{54}, the comparison is done in the superrest frame to avoid other mixing modes.

of the first overtone is reduced by $\mathcal{F}_{220}$ [154, 155]. One needs to take the reduction factor into account while comparing with the original amplitude, and we leave this comparison for future work. On the other hand, the result serves as strong evidence to support that $\mathcal{F}_{lmn}$ is indeed able to annihilate the corresponding (l,m,n) QNM.

Next we continue to remove $\omega_{22,n=1\ldots7}$ based on the conclusion in Ref. [101], and obtain the green curve in Fig. 2.5. We can see that the oscillation is consistent with ω_{320} (cyan) in the window of $[16,65]\,M_f$, whose amplitude and phase are $\sim 4.4\times10^{-4}$ and -0.79 rad at $t=16\,M_f$ after the filters. To ensure the oscillation is physical rather than numerical artifacts, we compute the numerical (truncation) error of this NR simulation by taking the difference between two adjacent numerical

resolutions. We see that the residual in the filtered waveform is still above the numerical noise floor. Therefore, this piece of the dominant residual signal corresponds to the spherical-spheroidal mixing in the remnant Kerr spacetime[5] [141, 143, 152]. Meanwhile, we find the filter shifts the waveform backward in time by $\sim 14.1 M_f$, close to the prediction given by Eq. (2.16)

$$\sum_{n=0}^{n=7} t_{l=2,m=2,n} \sim 12.9\, M_f. \tag{2.23}$$

In Fig. 2.5 we have aligned the early inspiral portion between the original signal h_{22} (the black curve) and the filtered waveforms for comparisons.

Then in Fig. 2.6 we investigate the effect of the full filter $\mathcal{F}^D_{lm}$ [Eq. (2.22)], where the value of $D^{\rm out}_{lm}$ is obtained from the Black Hole Perturbation Toolkit [158]. The result is almost identical to that of the rational filter $\mathcal{F}_{\rm tot}$ up to $t \sim 10 M_f$, but it is less accurate to reveal the spherical-spheroidal mixing. We attribute the inaccuracy to the numerical noise when we interpolate the value of $D^{\rm out}_{lm}$ from the Black Hole Perturbation Toolkit, and we leave a more precise calculation of $D^{\rm out}_{lm}$ for future studies. In addition, we find a nice property of the full filter $\mathcal{F}^D_{lm}$: it does not give rise to any time shift, as opposed to the rational filter. One could benefit from this feature in real data analyses.

2.3.1.2 h_{44}, h_{55}, h_{54}: *the second-order QNMs*

London *et al.* [94] found evidence for the second-order mode in the h_{44} harmonic, contributed by a quadratic coupling $\sim h^2_{22}$. Therefore, it is expected to see the sum tone $2\omega_{220}$ in the ringdown of h_{44}. In the upper panel of Fig. 2.7, we first remove the linear QNMs $\omega_{44,n=0\ldots3}$ from h_{44}, and then fit the filtered waveform with $2\omega_{220}$ in the window of $[12, 30]\, M_f$. We can see a decent agreement. The corresponding mode amplitude and phase are 7.9×10^{-4} and 3.1 rad at $t = 12\, M_f$ after the filters. In addition, the signal is larger than the numerical (truncation) error, which is evaluated by computing the difference between two adjacent numerical resolutions. This result shows that the second-order mode does exist in the ringdown regime. Furthermore, we find evidence for the presence of $\omega_{220} + \omega_{221}$ and $2\omega_{221}$ in the ringdown of h_{44} as well, and we leave more discussions in our follow-up work [159]. On the other

[5] The supertranslation can also make h_{32} leak into h_{22}, e.g., Eq. (8) of Ref. [152]. We have checked that the presence of the mode ω_{320} is due to the spherical-spheroidal mixing by transforming the waveform to the superrest frame using the technique presented in Ref. [156]. For more on this, see Ref. [107, 156, 157].

hand, while we are preparing our manuscript, we notice that Ref. [160] also carries out comprehensive studies on the second-order modes with a different approach, so we refer the interested reader to Ref. [160] for more details.

In addition, it is also expected that h_{55}, h_{54} can be sourced by $h_{22}h_{33}$ and h_{22}^2, respectively. In this case, we find that one has to map the waveforms to the superrest frame [107, 157] to reveal these second-order effects. We do this using the technique presented in Ref. [156], based on the SpECTRE code [161, 162]. In the bottom left panel of Fig. 2.7, after removing the linear QNMs $\omega_{54,n=0...3}$, as well as $\omega_{44,n=0...3}$ and $\omega_{64,n=0...3}$ caused by the spherical-spheroidal mixing, we find the residual signal of h_{54} is consistent with the sum tone $2\omega_{220}$ in the window of $[10, 40]\, M_f$, with an amplitude of 1.2×10^{-5} and a phase of -2.9 rad at $t = 10\, M_f$. As for h_{55}, the bottom right panel of Fig. 2.7 shows the existence of $\omega_{220} + \omega_{330}$ in $[8, 28]\, M_f$, whose amplitude and phase are 1.9×10^{-5} and -1.96 rad at $t = 8\, M_f$. Nevertheless, we see the amplitudes of these two second-order effects are on the same order of the numerical noise, therefore their existence is not conclusive.

Finally, we want to remark again that the amplitudes of the second-order effects are reduced by the filters. In consequence, the amplitudes obtained from our approach are smaller than their original values.

2.3.1.3 h_{21}: *the mode mixing due to a gravitational recoil*

We repeat our process for the harmonic h_{21} of SXS:BBH:0207. As shown in Fig. 2.8, after removing the linear QNMs $\omega_{21,n=0...2}$ and the spherical-spheroidal mixing modes $\omega_{31,n=0,1}$, we find the remaining oscillation is consistent with the mode ω_{220} (the red and yellow dashed curves). We then use ω_{220} to fit the filtered waveform in the window of $[55, 92]\, M_f$. The result is shown as the yellow dashed curves. The corresponding mode amplitude and phase are 9.5×10^{-6} and -0.62 rad at $t = 55\, M_f$. This leakage is caused by a boost in the orbital plane, and this phenomenon has been discussed by Kelly *et al.* [152] and Boyle [153]. To verify this, we transform the waveform to the superrest frame (the blue curve) [107, 157], where the remnant BH is in the center-of-mass frame. After applying the same filter, we can see the mixing is completely removed (the green curve), while the other portion of the waveform remains unchanged.

We note that the leakage of ω_{220} into h_{21} is a common phenomenon, especially for high mass-ratio events whose kick velocities are relatively large. Failing to take

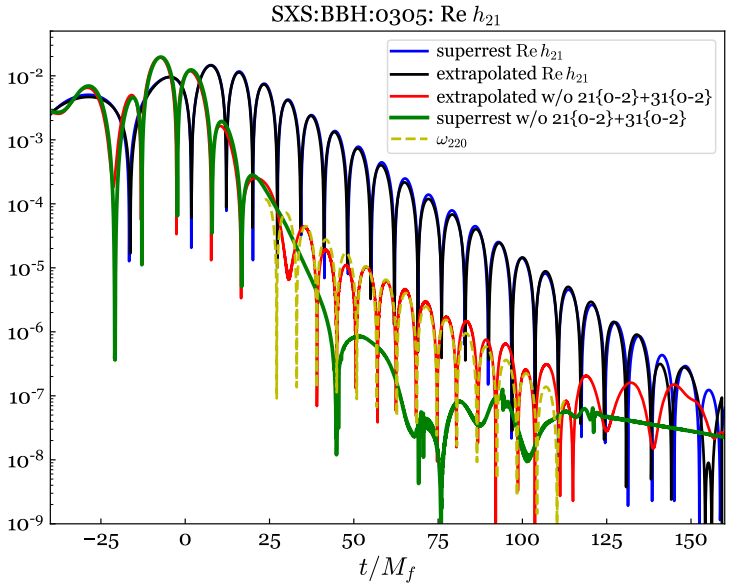

Figure 2.8: Leakage of the ω_{220} mode into the h_{21} harmonic due to the gravitational recoil. After removing $\omega_{21,n=0...2}$ and $\omega_{31,n=0,1}$ from the original h_{21} waveform (black curve), the red curve exhibits the presence of the ω_{220} mode (yellow dashed curve). If we transform the waveform to the superrest frame (blue curve) and repeat our filtering process, the mixing mode ω_{220} will be completely removed (green curve).

this effect into account may misinterpret the mixing mode ω_{220} as retrograde modes [103, 143]. We will explain more details in Sec. 2.3.2.

2.3.2 The retrograde modes

It was found that taking into account the retrograde modes [e.g., the second term of Eq. (2.6)] would expand the linear perturbation regime. To partially address the debate on overfitting, we use our rational filter as a complementary tool to visualize the presence of the retrograde modes.

We first take SXS:BBH:1936 with non-negligible retrograde modes (see Sec. 10.8). In the top panel of Fig. 2.9, we remove the prograde modes $\omega_{22,n=0...3}$ and the spherical-spheroidal mixing mode ω_{320} from the original harmonic h_{22} (the black curve), then the red curve shows the existence of $-\omega^*_{2-20}$ in the residual. In the plot, the green dashed curve is obtained by fitting the filtered waveform with $-\omega^*_{2-20}$ in the window of $[28, 60]\ M_f$. Its mode amplitude and phase are 3.9×10^{-4} and 2.6 rad at $t = 28\ M_f$. To further support our result, we investigate the phase evolution of the waveforms. For a prograde mode, its phase should decrease monotonically over time due to the term $e^{-i\omega_{lmn}t}$ [see the first term of Eq. (2.6)], whereas a retrograde mode's

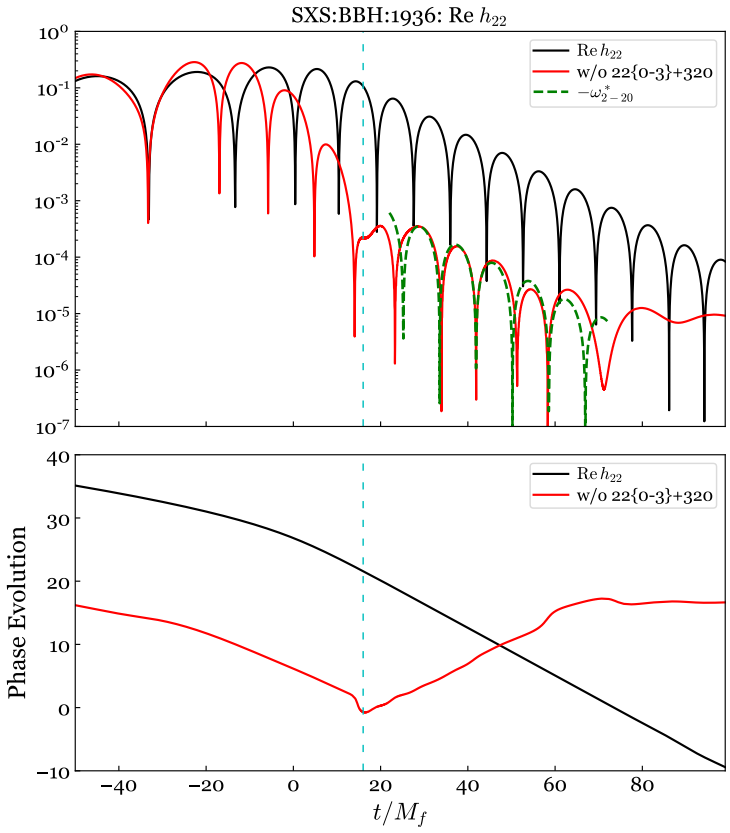

Figure 2.9: Retrograde mode $-\omega^*_{2-20}$ in the ringdown of SXS:BBH:1936. Top panel: after removing the $\omega_{22,n=0...3}$ modes and the spherical-spheroidal mixing mode ω_{320} from the original harmonic h_{22} (black curve), we reveal the presence of $-\omega^*_{2-20}$ (green dashed curve) in the residual waveform (red curve). Bottom panel: the phase evolution of the original waveform (black curve) and the filtered waveform (the red curve). The phase of the original waveform decreases monotonically, indicating that the prograde modes are dominant. However, the phase of the filtered waveform starts to grow at the same time as the residual oscillations in the top panel appear, which demonstrates that the residual oscillations are retrograde modes.

phase should increase due to the term $e^{i\omega^*_{l-mn}t}$ [see the second term in Eq. (2.6)]. In the bottom panel of Fig. 2.9, we see the phase of the original waveform (the black curve) decreases with time, indicating that the progrades are more dominant. After applying the filter, the decreasing trend terminates at $\sim 16M_f$ after the peak and the phase starts to grow at the same time that the residual oscillations in the top panel appear. This observation confirms the physical origin of the residual oscillations.

Then we look into the case of SXS:BBH:1107 investigated by Dhani [103]. As shown in Fig. 2.10, there are a few cycles in the filtered residual waveform h_{22} (the red curve) that are consistent with the retrograde mode $-\omega^*_{2-20}$. Meanwhile,

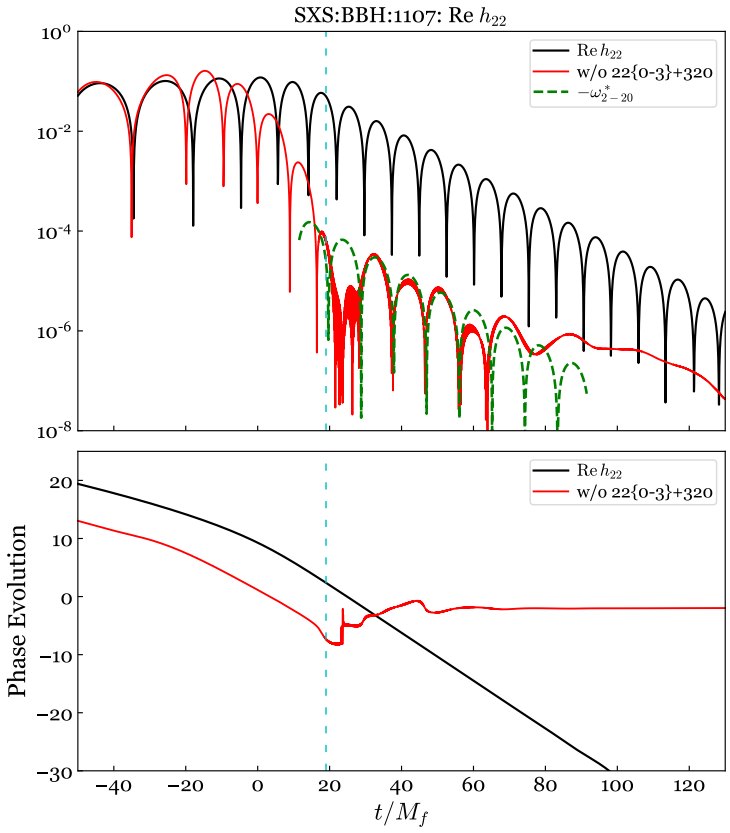

Figure 2.10: Same as Fig. 2.9, the retrograde mode $-\omega^*_{2-20}$ in the h_{22} of SXS:BBH:1107.

the phase of the filtered waveform also grows within that regime, which serves as more evidence. Nevertheless, the retrograde mode in this case is weaker and noisier than that of SXS:BBH:1936. Furthermore, we find applying retrograde filters (not only the fundamental mode but also overtones) has little impact on the early portion ($t \lesssim 0$) of the red curve in Fig. 2.10, meaning there is no strong evidence for the existence of retrograde modes within that regime. As for the harmonic h_{21}, we find it has a mixing component from the mode ω_{220} due to the gravitational recoil. This effect was not taken into consideration by Dhani [103], so we speculate that this could be the cause for the crests and troughs in the mismatch of h_{21}, e.g., Fig. 3 of Ref. [103].

Finally, we want to note that the vertical dashed lines in Figs. 2.9 and 2.10 do not necessarily correspond to the start time of the retrograde mode $-\omega^*_{2-20}$ in the original waveforms (the black curves), because of the time shift induced by our rational filter. To undo the time shift, here we simply align the early inspiral portion of the filtered waveforms with the original ones.

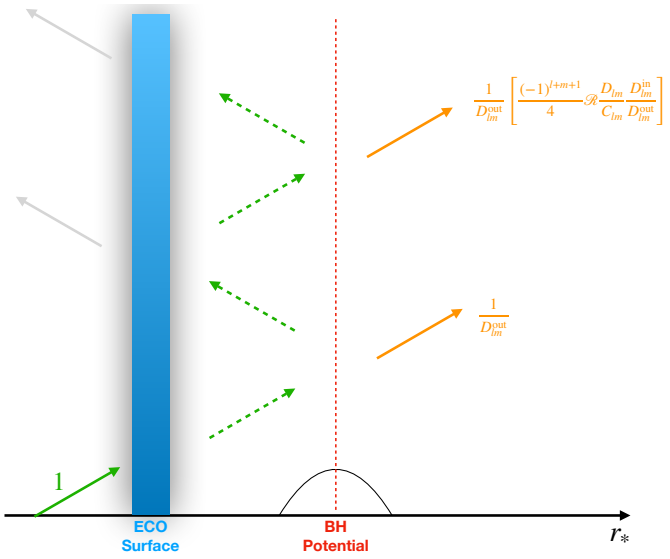

Figure 2.11: The up-mode solution of an ECO. We assume that a GW emerges from the horizon ($r_* = -\infty$) and its amplitude is unity. It bounces back and forth within the cavity formed by the ECO surface and the BH potential. The GW seen by an observer at infinity consists of the main transmissive wave $1/D^{\rm out}_{lm}$ and a series of echoes.

2.4 The stability of the full filter $\mathcal{F}^D_{lm}$

The QNM spectra of BHs have been found to be unstable [163–167]. In particular, Cheung *et al.* [167] classified the instability into two categories: "migration instability" and "overtaking instability." For migration instability, the fundamental QNM drifts drastically from its unperturbed value when the perturbation is distant from the BH. This kind of instability is related to the asymptotic behavior of the eigenfunction near the horizon ($e^{-i\omega_{lmn}r_*}$) and infinity ($e^{i\omega_{lmn}r_*}$). Recalling that Im $\omega_{lmn} < 0$, the eigenfunction of the QNM increases exponentially as $|r_*| \to \infty$. Any small perturbation of the BH potential at a large $|r_*|$ will lead to a significant change of ω_{lmn}. For overtaking instability, a family of new modes appears near a bumpy BH, trapped between two potential barriers [6]. One of the new modes might have a smaller decay rate than the unperturbed fundamental mode when the perturbation is at a large distance. Consequently, this new mode overtakes the original fundamental mode.

The spectral instability, however, may have a limited effect on observational results (e.g., time-domain responses of a BH), as discussed in Refs. [43, 163–165, 168, 169]. Nollert [163] and Barausse *et al.* [164, 165] showed that the prompt time-

[6] They are called "matter-driven" modes by Barausse *et al.* [164, 165].

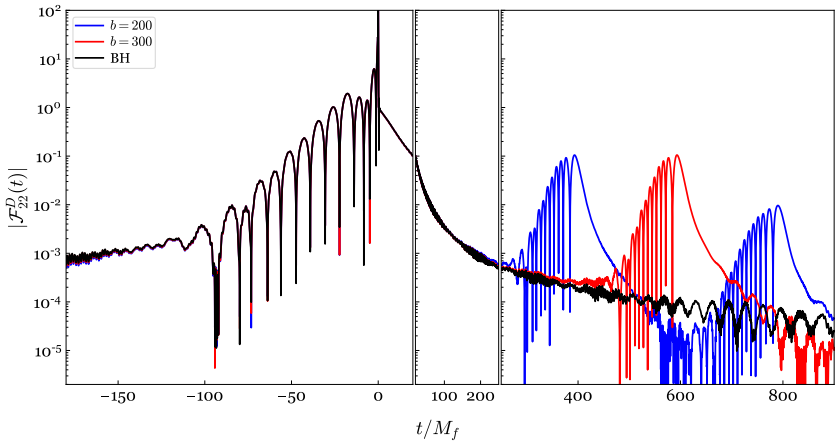

(a) $\epsilon = 10^{-1}$

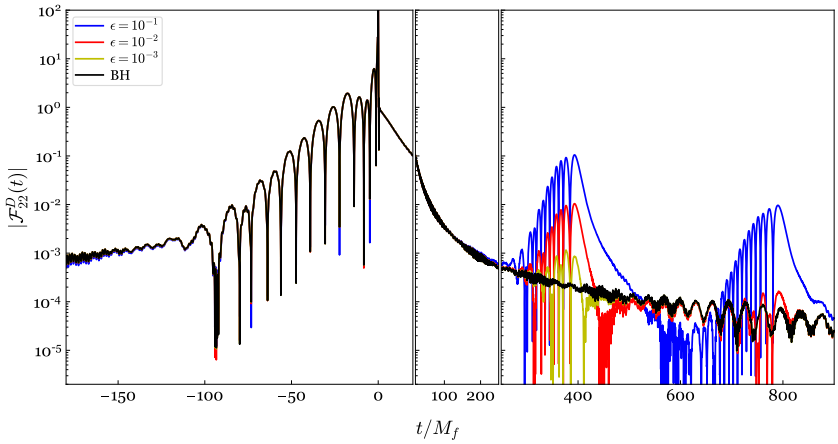

(b) $b = 200M_f$

Figure 2.12: The filter $\mathcal{F}^{D\ \mathrm{ECO}}_{lm}$ of a nonspinning ECO in the time domain. In the top panel, we set b to $200M_f$ (blue) and $300M_f$ (red), while fixing the value of ϵ to 10^{-1}. They are compared with that of a Schwarzschild BH (black). In the bottom panel, we choose $\epsilon = 10^{-1}, 10^{-2}, 10^{-3}$ (blue, red and yellow) and set b to $200M_f$. In both cases, the original signal (around $t \sim 0$) remains unchanged. The perturbation appears as periodic echoes with the time interval $2b$. The amplitude of the nth echo is proportional to ϵ^n.

domain response is independent of perturbations when the perturbations are far from the system, even though the QNMs of the perturbed system are completely different from the ones of an isolated BH. Cardoso *et al.* [43] drew a similar conclusion while considering near-horizon perturbations. In fact, as pointed out by Hui *et al.* [170] and Berti *et al.* [168], despite the nonlocality of QNMs, one needs to appreciate the causal structure of the system while considering the time-domain signals—a time response reflects the nature of each single potential bump that is causally connected

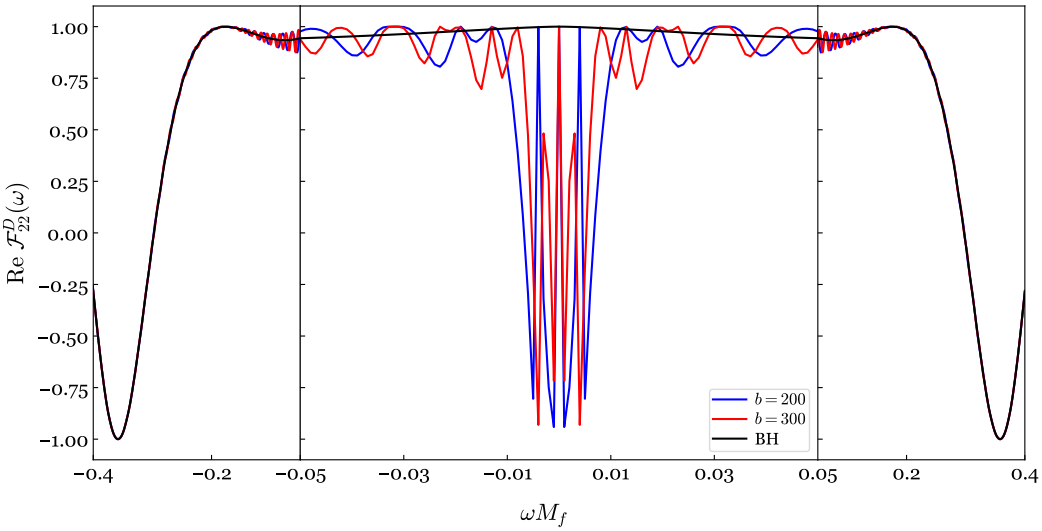

(a) $\epsilon = 10^{-1}$

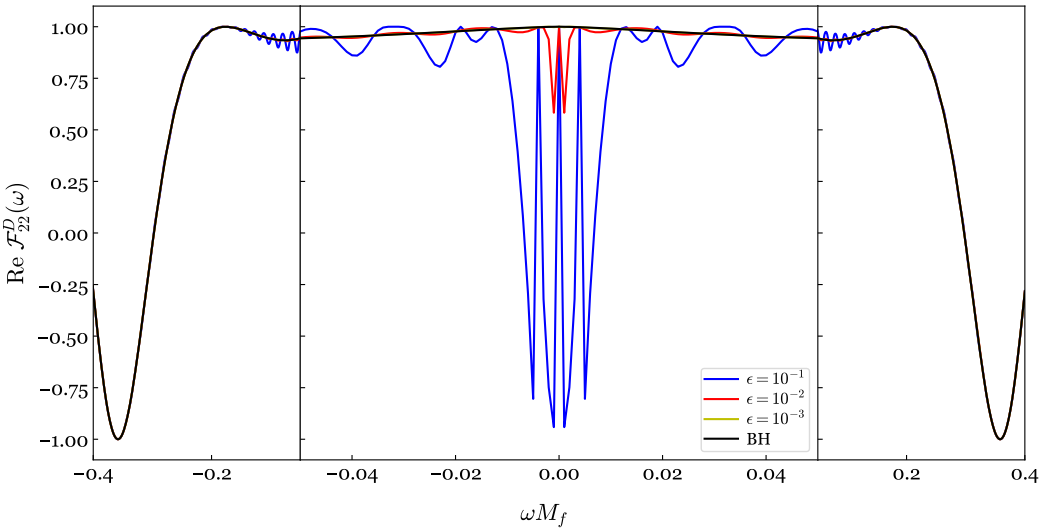

(b) $b = 200M_f$

Figure 2.13: Same as Fig. 2.12. The real part of $\mathcal{F}^D_{22}$ in the frequency domain.

to the observer, e.g., the prompt ringdown of a regular BH. The QNMs of the perturbed system do not show up until very late times as "echoes" [171] when the initial Cauchy data travels and experiences the entire potential[7]. Therefore, the time-domain signal is stable in the sense that the original waveform remains unchanged, whereas the additional perturbation appears only as echoes that are well separated

[7]We note that QNMs can become complete under some conditions [172–174] (see also Refs. [163, 175] for relevant discussions). In particular, Beyer [172] showed the completeness of QNMs of the Poeschl-Teller potential at a late time—a regime where solutions can be expanded with respect to its QNMs.

from the original signal in time.

The instability of the QNM spectra implies that QNMs may not be the most natural basis for ringdowns. One might need to rearrange QNMs into new subsets and sum each subset to form a new basis, in either time or frequency domain. In fact, the Backwards One-Body (BOB) model [176] is an inspiring example, where the contributions of overtones associated with the same (l, m) harmonic are rearranged and summed into a single time-domain function $\sim \mathrm{sech}\gamma t$, where γ is a constant. One may further postulate that the time-domain function could be treated as the leading term of a new set of basis and the term $\sim \mathrm{sech}\gamma t$ provided by the BOB model contains most power of the ringdown. Another relevant time-domain basis was discussed by some of us for superkick systems [177]: it was found that the time-domain basis can even be extended to the inspiral regime for the superkick systems. A direct consequence is the *collective excitation* of QNMs—the amplitudes of different QNMs are correlated as a result of the time-domain basis being projected to the QNM basis. In fact, such a correlation (universality) has been found in not only the superkick systems [177], but also extreme mass-ratio inspirals [74–77, 134].

Based on the above discussions, we want to ask: Do the filters reflect the nature of the system? Can we distinguish a BH from other objects (e.g., a bumpy BH or an exotic compact object) using our filters? In particular, since the full filter $\mathcal{F}^D_{lm}$ contains a collection of the corresponding QNMs ω_{lmn}'s as a result of Eq. (2.21), is the filter stable or not under perturbations in the BH potential, given the spectral instability? In fact, a similar topic has been investigated recently by Kyutoku *et al.* [169]. The "phase shift" introduced by the authors is essentially the phase of our full filter in Eq. (2.22), and they showed that the phase shift of a Schwarzschild BH is stable when it is perturbed by a small Pöschl-Teller bump. In this work, we continue their studies and adopt another simple model to provide a qualitative answer. More sophisticated discussions are left for future work.

In Fig. 2.11, we consider an exotic compact object (ECO) whose surface is close to the would-be horizon. The surface can partially reflect GWs and the reflectivity $\mathcal{R}$ is given by

$$\mathcal{R} = \epsilon e^{-2ib}, \tag{2.24}$$

where ϵ is a constant, and $r_* = -b$ is the location of the ECO surface with the factor of two representing the round trip between the ECO surface and the BH potential.

By imposing a physical boundary condition based on the membrane paradigm at the ECO surface [178], we obtain the up-mode solution [in parallel with Eq. (2.19)]:

$$R_{lm}^{\text{up ECO}} \sim \begin{cases} r^3 e^{i\omega r_*}, & r_* \to +\infty, \\ \tilde{D}_{lm}^{\text{out}} e^{i\omega r_*} + \Delta^2 \tilde{D}_{lm}^{\text{in}} e^{-i\omega r_*}, & r_* \to -\infty, \end{cases} \tag{2.25}$$

with

$$\tilde{D}_{lm}^{\text{out}} = D_{lm}^{\text{out}} \left[1 - (-1)^{l+m+1} \mathcal{R} \frac{D_{lm}}{4C_{lm}} \frac{D_{lm}^{\text{in}}}{D_{lm}^{\text{out}}} \right], \tag{2.26}$$

where the factor D_{lm}/C_{lm} comes from the Teukolsky-Starobinsky (TS) relation [148, 179]. We refer interested readers to Sec. 2.9 for derivation. Note that Eq. (2.26) takes a similar form to the Wronskian in Eq. (5.2) of Ref. [170].

We then define the filter $\mathcal{F}_{lm}^{D\ \text{ECO}}$ for the ECO system:

$$\mathcal{F}_{lm}^{D\ \text{ECO}} = \frac{\tilde{D}_{lm}^{\text{out}}}{\tilde{D}_{lm}^{\text{out}\,*}}. \tag{2.27}$$

To transform the filter to the time domain, we first need to apply the Planck-taper filter $\mathcal{F}(\omega)$ [180] to remove the high-frequency contribution:

$$\mathcal{F}(\omega; \omega_1, \omega_1) = \begin{cases} 0, & \omega < \omega_1, \\ \dfrac{1}{e^z + 1}, & \omega_1 < \omega < \omega_2, \\ 1, & \omega > \omega_2, \end{cases} \tag{2.28}$$

with

$$z = \frac{\omega_2 - \omega_1}{\omega - \omega_2} + \frac{\omega_2 - \omega_1}{\omega - \omega_1}. \tag{2.29}$$

Figure 2.12 shows a nonspinning ECO case. The filters for a spinning ECO have the same qualitative feature so we refer readers to Sec. 2.7 for results. In the absence of perturbations, we see that the black curve assembles the Dirac function $\delta(t)$ near $t = 0$ because of the fact that $|\mathcal{F}_{22}^{D\ \text{ECO}}(\omega)| = 1$. Most of the signals (i.e., the damped sinusoids) lie on the left side of the Dirac function ($t < 0$), and the reason is exactly the same as the flipped ringdown in Fig. 2.2. We also see the tail-like feature at an earlier time.

Next, we turn on the perturbation. Since Cheung *et al.* [167] found the spectral instability with b varied, in Fig. 2.12a, we first compute the filter with two choices

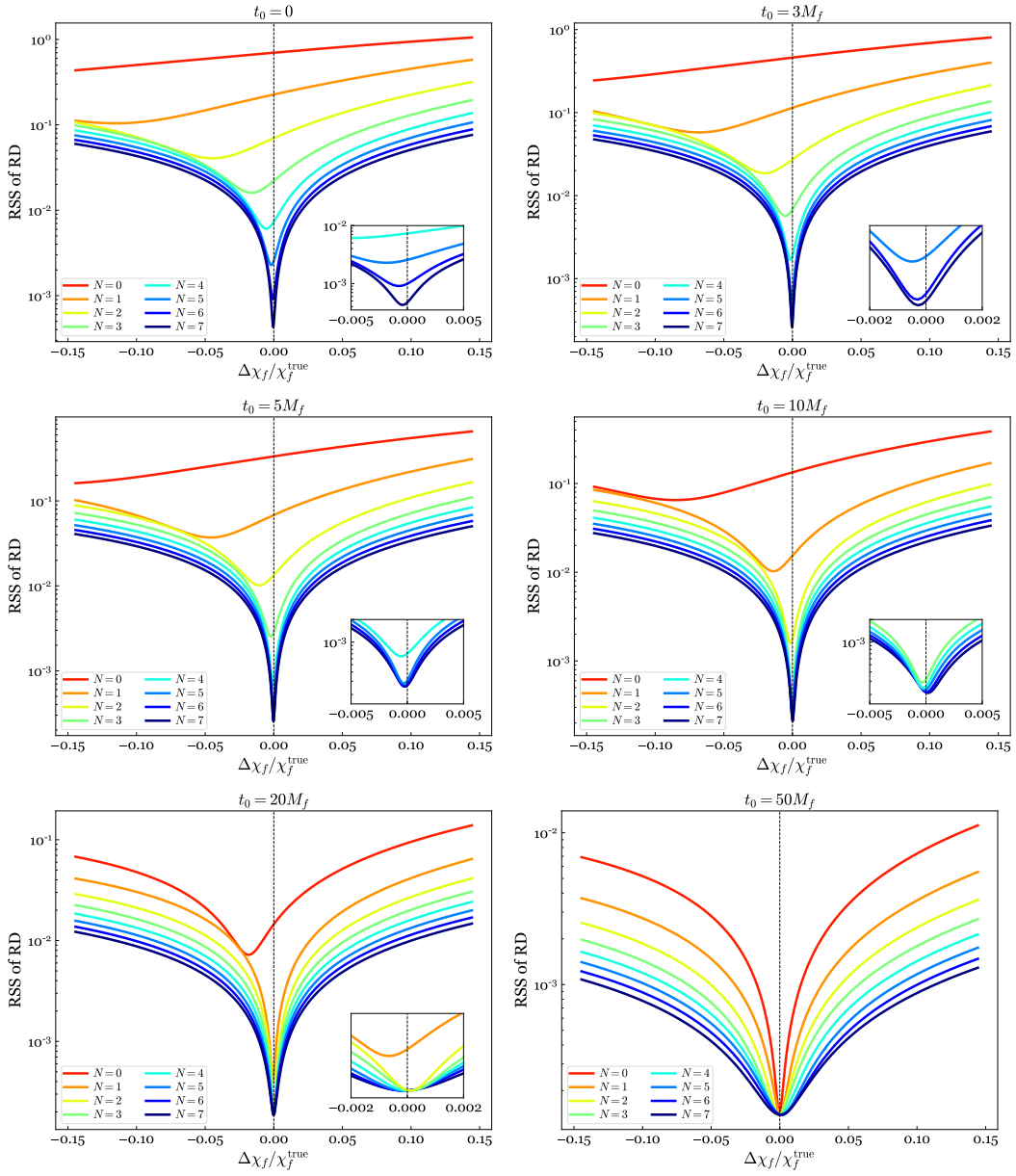

Figure 2.14: The ringdown RSS of the filtered waveform as a function of χ_f. The SXS:BBH:0207 waveform is used. The six panels correspond to different choices of the start time, i.e., t_0 in Eq. (2.30). In each panel, different colors indicate the results from removing different numbers of overtones. When t_0 is large ($\sim 50M_f$), the true value of the spin $\chi_f^{\rm true} = 0.692$ leads to the smallest RSS no matter how many overtones are removed. However, if we push t_0 to an early time, enough overtones need to be removed to obtain the true value. On the other hand, the RSS depends strongly on χ_f: a 2% change in χ_f can result in around two orders of magnitude change in the RSS, when t_0 and N are fixed to their true values.

of b, while fixing $\epsilon = 0.1$. We find the modification to the original signal is negligible. The major change is a series of echoes with an interval of $\Delta t \sim 2b$—well

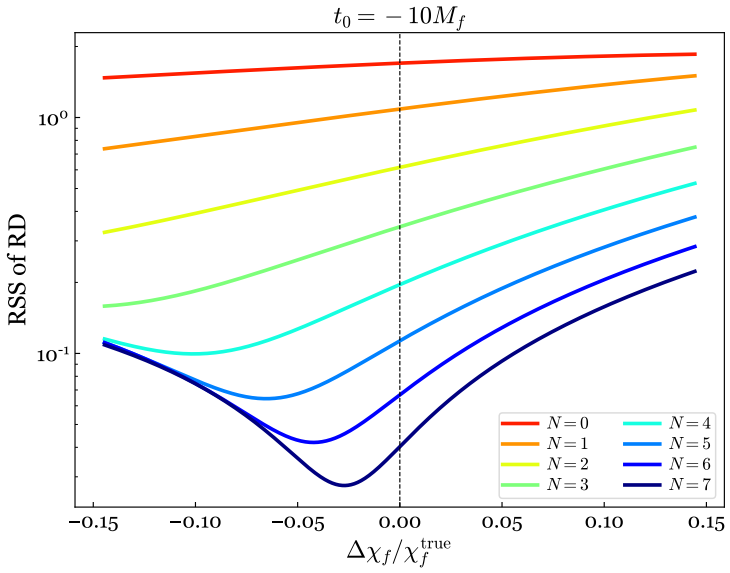

Figure 2.15: Continuation of Fig. 2.14, except that the onset of the ringdown window t_0 is set to $-10M_f$.

separated from the original signal (in the plot we only show the first one or two echoes). Meanwhile the amplitude of the echo is independent of b. We remark that the δ-function is removed from echoes since the TS coefficient $|D_{lm}/C_{lm}| \to 0$ as $\omega \to \infty$. Then in Fig. 2.12b, we fix the value of b to $200M_f$ but vary ϵ. Again, the perturbation has little impact on the original signal, and the amplitude of the echo scales linearly with ϵ. Compared to the recent work by Berti *et al.* [168], our studies include not only the fundamental mode, as Berti *et al.* [168] did, but also more overtones. Nevertheless, the qualitative features in our results are the same as theirs. Finally, Figure 2.13 shows the real part of $\mathcal{F}_{22}^{D\ \rm ECO}(\omega)$ in the frequency domain for completeness.

2.5 Inferring remnant properties from the rational filter

We have shown that our rational filter $\mathcal{F}_{lmn}$ is able to remove a specific QNM ω_{lmn} from the ringdown regime and reduce the root sum square (RSS) of the ringdown. In particular, the ringdown signal can be almost completely removed if we apply a filter with a series of corresponding modes. Since the mode frequencies ω_{lmn} are determined by the mass M_f and spin χ_f of the remnant BH, in this section, we investigate how the ringdown RSS decreases depending on the choices of M_f and χ_f.

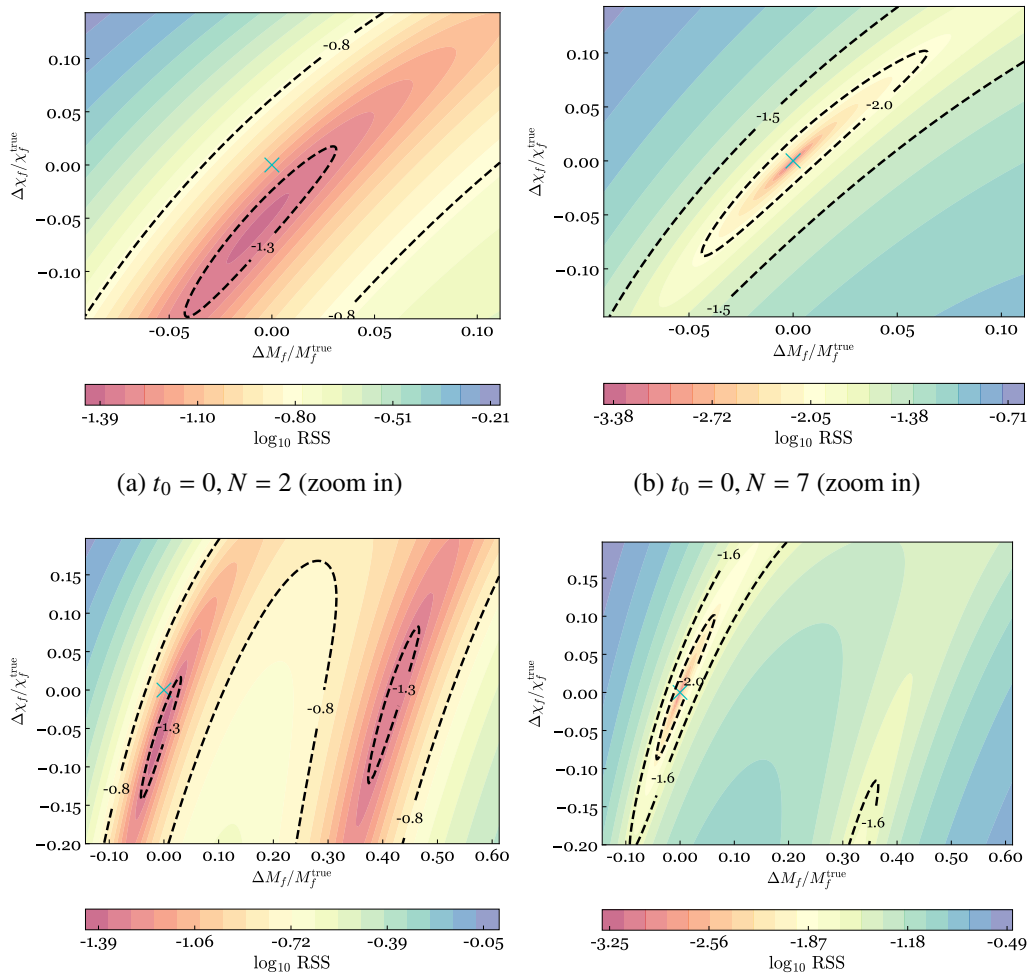

(a) $t_0 = 0, N = 2$ (zoom in)

(b) $t_0 = 0, N = 7$ (zoom in)

(c) $t_0 = 0, N = 2$ (zoom out)

(d) $t_0 = 0, N = 7$ (zoom out)

Figure 2.16: Contours of RSS with varying M_f and χ_f. To avoid redundancy, we set t_0 to 0 and choose $N = 2$ (left panels) and $N = 7$ (right panels). In the top row, we explore the parameter space near the true remnant properties, whereas in the bottom row we investigate a larger area. The true remnant mass and spin are marked with a cross. The effects of M_f and χ_f are degenerate—their difference is more constrained than their sum. In addition, we find there is a second local minimum in Fig. 2.16c.

We define the RSS of a filtered harmonic $h^f_{lm}(t)$ within a time interval $[t_0, t_1]$ to be

$$\text{RSS} = \sqrt{\int_{t_0}^{t_1} |h^f_{lm}(t)|^2 dt}. \tag{2.30}$$

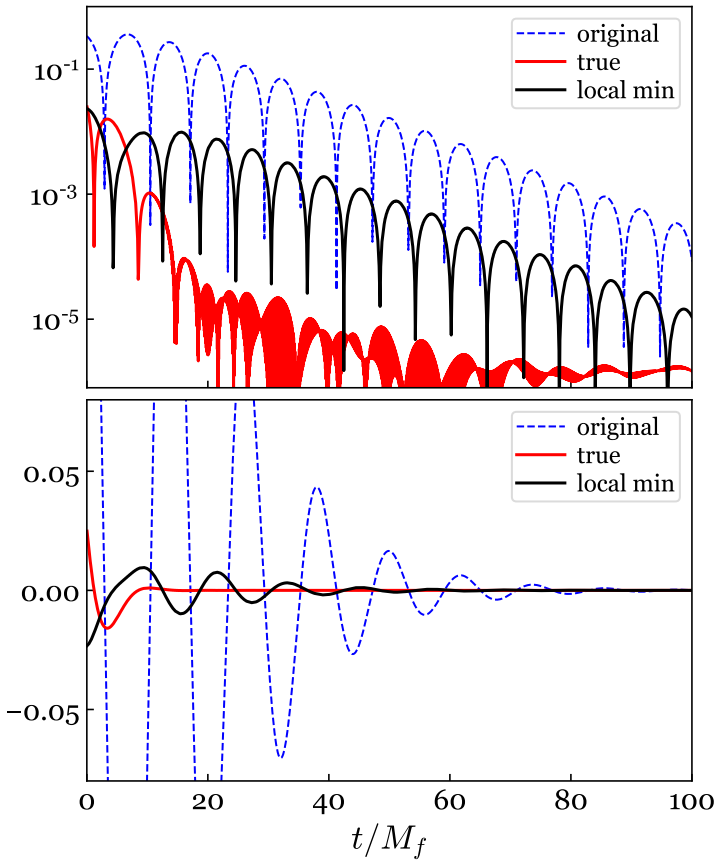

Figure 2.17: An explanation for the second local minimum in Fig. 2.16c. The blue dashed line corresponds to the original harmonic h_{22} of SXS:BBH:0207. Using the true remnant properties, the corresponding QNMs are removed (red curve). However, it has a larger amplitude at around 0. This is because adjacent overtones contribute destructively to the original waveform. Fewer QNMs reduce this cancellation and lead to a larger amplitude. On the contrary, using the remnant properties at the second local minimum (black curve), the amplitude of the original waveform diminishes even though the corresponding QNMs are not filtered away. As a result, two systems lead to similar RSS.

We still take the GW150914-like waveform SXS:BBH:0207 as an example. We fix t_1 to $100M_f$ and let t_0 vary. Then we apply a filter:

$$\mathcal{F}_N(M_f, \chi_f) = \mathcal{F}_{320}(M_f, \chi_f) \prod_{n=0}^{N} \mathcal{F}_{22n}(M_f, \chi_f), \tag{2.31}$$

to the harmonic h_{22}. The filter $\mathcal{F}_N$ is a function of remnant mass M_f and spin χ_f. It also depends on how many $(l = 2, m = 2)$ overtones we want to remove. We want to emphasize that our rational filter leads to a time shift, and in Sec. 2.3 we undid it by aligning early inspiral waveforms. However, in this case we find the alignment can pull some non-ringdown signals into the regime that we are interested in $(t > t_0)$ and make our analyses fail. To avoid this, here we do not perform this alignment. A caveat of this compromise is that the time shift itself can reduce the RSS, even though it is a subdominant effect. In this chapter, we ignore the contribution due to this time shift, and leave more self-contained studies for future work.

In Fig. 2.14, we vary the value of χ_f with different choices of N and t_0 while keeping M_f fixed at the true value. When t_0 is large ($\sim 50M_f$), we see the true value $\chi_f^{\rm true} = 0.692$ leads to the smallest RSS (namely the ringdown is mostly removed) regardless of the value of N. This is because in the regime of $t \gtrsim 50M_f$, the signal is dominated by the fundamental mode ω_{220}, and removing ω_{220} alone is enough to reduce the RSS down to roughly the numerical noise level. However, if we push t_0 to an early time, failing to filter out enough modes will result in incorrect values of χ_f when RSS achieves its local minimum—the value χ_f is degenerate with the choice of t_0. Especially, in the first panel of Fig. 2.14, we see that the ringdown RSS depends monotonically on χ_f when $t_0 = 0$ and $N = 0$; but the local minimum of the RSS does converge to the true value of χ_f after we include enough overtones. If we continue to go to an earlier regime, such as $t_0 = -10M_f$ in Fig. 2.15, we can see that the inferred spin is biased even when enough overtones are included, because of the presence of non-ringdown signals (e.g., late inspiral and merger). On the other hand, we also investigate the effect of M_f. We find that varying the value of M_f (with χ_f fixed to the true value) leads to a similar impact on the ringdown RSS, and the results are summarized in Appendix 2.8.

Our results shown in Figs. 2.14 and 2.21 are closely related to Fig. 7 of Ref. [88], in which the authors show how the mismatch varies with deviations from GR and the start time of analyses. Similarly, our results indicate that the residual RSS depends strongly on the choice of (M_f, χ_f). In our case, a 2% change in χ_f can result in

around two orders of magnitude change in the RSS, when t_0 and N are fixed to their "true" values.

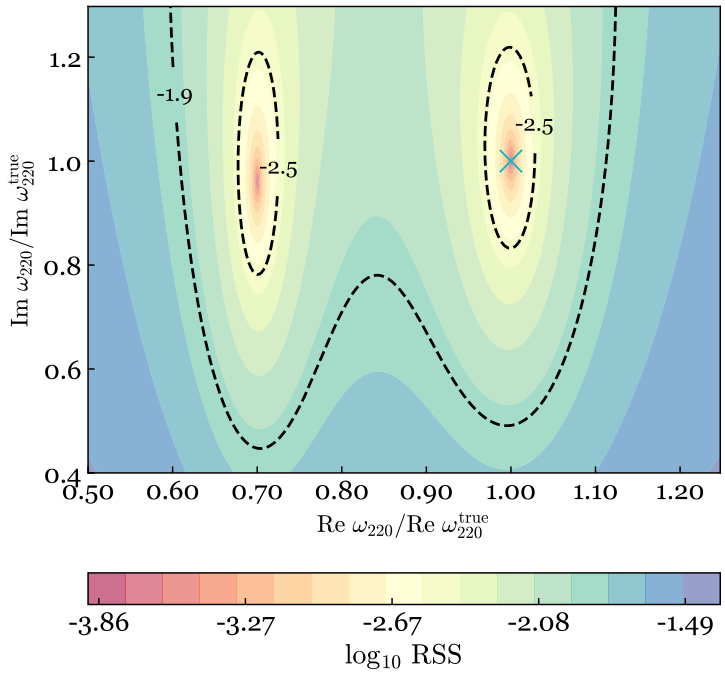

(a) $t_0 = 50M_f, N = 0$

Figure 2.18: Same as Fig. 2.16, except that the real and imaginary parts of the fundamental mode are used as two independent variables. The start time t_0 is set to $50M_f$. Similar to Fig. 2.16c, there is a second local minimum.

After studying the effects of M_f and χ_f separately, in Fig. 2.16 we provide contours of RSS with varying them together. To avoid redundancy, we set t_0 to 0 and focus on two cases: $N = 2$ and $N = 7$, respectively. If we restrict ourselves to the region near the true remnant properties (Figs. 2.16a and 2.16b), the $N = 2$ one leads to biases in extracting M_f and χ_f, whereas the latter one can recover the remnant properties (marked with a cross) accurately. In addition, we notice that the effects of M_f and χ_f are partially degenerated—their difference $\sim M_f - \chi_f$ is more constrained than their sum $\sim M_f + \chi_f$. This is consistent with Figs. 10 and 11 of Ref. [101]. On the other hand, if we explore a larger parameter space (zoom out), we find there is a second local minimum in Fig. 2.16c. To explore the reason, in Fig. 2.17 we compare two filtered waveforms with χ_f and M_f chosen at their true values (red curve) and at the second local minimum (black curve), respectively. Recall that the amplitudes of adjacent overtones are out of phase, e.g., Refs. [101] and [177], they contribute destructively to the final ringdown waveform. Removing some overtones can increase the value of the filtered waveform at an early stage. On the contrary,

when χ_f and M_f are at the second local minimum, even though the corresponding QNMs are not removed, the amplitude of the filtered waveform is reduced by around one order of magnitude. As a result, both cases lead to comparable RSS.

So far, we take (M_f, χ_f) as two independent variables. The QNM frequencies are obtained by assuming Kerr BHs with GR gravity. In Fig. 2.18, we relax this assumption and use the real and imaginary parts of a QNM as two independent variables. Here we restrict ourselves to the fundamental mode alone for simplicity, and take $t_0 = 50M_f$. We find the qualitative feature remains the same—there is a second local minimum, and the reason is exactly the same as that of Fig. 2.16c.

Our discussions indicate that the filter could serve as a new tool to infer the remnant properties from actual detection data, and we refer the interested reader to our follow-up work in Chapter 3 for more discussions.

2.6 Conclusion

We have proposed two types of frequency-domain filters that are able to remove QNM(s) from ringdown signals. Our new method serves as a complementary tool to previous studies where the ringdown was analyzed in terms of time-domain fitting (e.g., Ref. [101])—it allows visualizing the existence of subdominant modes without the risk of overfitting. By applying our filter to the waveform of SXS:BBH:0207, we find the spherical-spheroidal mixing mode ω_{320} in harmonic h_{22}, the presence of ω_{220} in h_{21} due to the gravitational recoil, and second-order effects in h_{44}, h_{54} and h_{55} due to the quadratic coupling h_{22}^2 and $h_{22}h_{33}$. We also find the existence of retrograde modes in waveform SXS:BBH:1936. Our filter leads to an unphysical flipped ringdown prior to the start time of the real ringdown. Consequently, the late-inspiral and merger signals are contaminated.

Although the rational filter in Eq. (2.17) is constructed purely empirically, the full filter $\mathcal{F}_{lm}^D$ in Eq. (2.22) reflects the nature of the BH, and the filtered waveform corresponds to the image wave on the past horizon (Fig. 2.4). Furthermore, in spite of the unstable nature of QNM spectra [166, 167], we find that the filter $\mathcal{F}_{lm}^D$ is stable in the time domain under the perturbations of the BH potential, in the sense that the original response remains unmodified, while the major correction appears as periodic echoes well-separated from the original BH response. The time interval and amplitude of the echoes depend linearly on the parameters of the perturbation.

Additionally, the rational filter takes the mass and spin of the remnant BH as free parameters. The residual ringdown RSS depends strongly on the choice of these

two parameters. The true remnant properties could be recovered accurately from the ringdown of h_{22} as long as one consider a proper number of overtones and the start time of the analysis.

In this chapter, we demonstrate that this new approach is powerful in ringdown analyses and outline a few applications. Future studies could be focused on:

(i) Nonlinearity due to the quadratic couplings. We focused exclusively on a few harmonics of SXS:BBH:0207, and exhibited the existence of second-order effects only qualitatively. A more systematic study [159] is needed to investigate quadratic couplings in other BBH systems. We also refer the interested reader to Ref. [160] for relevant discussions.

(ii) Second-order effects in the multipole moments of dynamical horizons. Although Refs. [110, 111] have shown that the multipole moments might be consistent with the superposition of linear QNMs soon after the formation of the common horizon, it is expected that a majority of nonlinearities are swallowed by horizons [89], which in turn should leave imprints on dynamical horizons. It is interesting to study these cases by applying our filters.

(iii) The stability of the two filters. In this work, we considered the stability of the full filter under a simple scenario: the perturbation arising only through a reflective boundary condition at the ECO surface that is very close to the would-be horizon. More sophisticated perturbations, e.g., the ones in Ref. [166, 167], could be investigated. In addition, it might also be interesting to study the (in)stability of the rational filter. This requires high-precision calculations of QNMs of the new system. The goal of this trend is to answer: How to distinguish a BH from its mimicker via our filters? And how do the filters reflect the nature of the system?

(iv) Inferring remnant properties from real observational data. Here we restricted ourselves to a particular harmonic h_{22} and found that the remnant properties could be recovered accurately. A possible avenue for future work is to investigate the impact of our filters on the strain that is emitted toward a single angular direction. More importantly, one could apply our filter to real BBH events [154, 155] and see whether we could place a tighter constraint on the remnant mass, spin, and also the no-hair theorem [52].

(v) Other filters. In this work, we have studied two related filters. One undesired feature of the rational filter is that it leads to a backward time-shift, which makes it

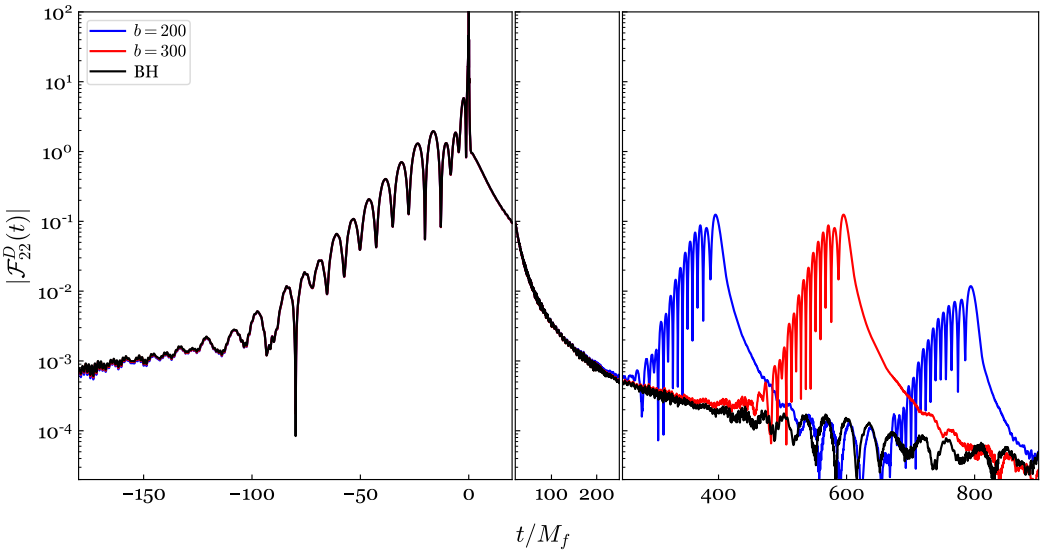

(a) $\epsilon = 10^{-1}$

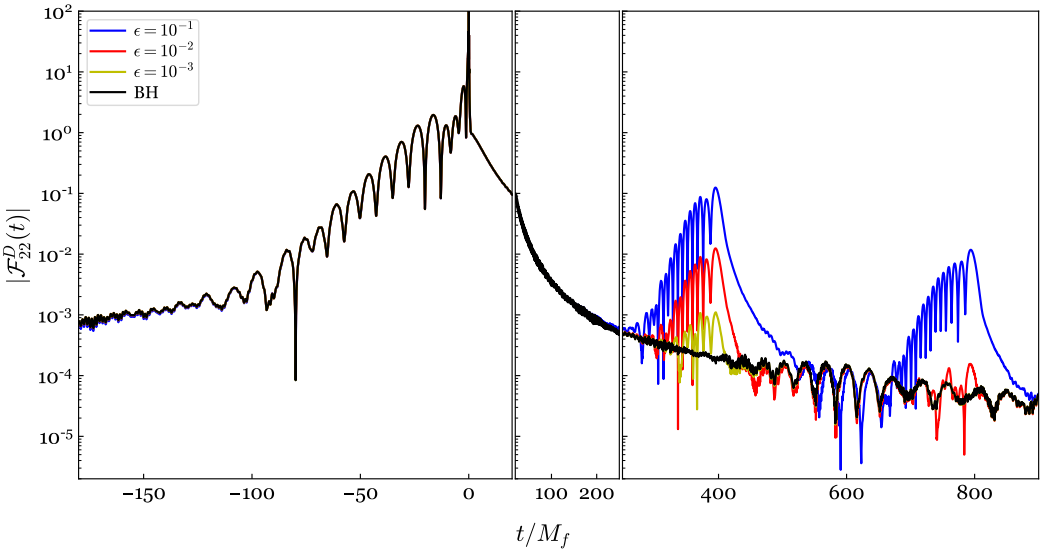

(b) $b = 200M_f$

Figure 2.19: Same as Fig. 2.12, but for a spinning ECO with $\chi_f = 0.692$.

difficult to define the start time of the ringdown in the filtered waveform[8]. The full filter does not have this problem but is more computationally expensive to obtain. Therefore it might be interesting to look for other new filters with better properties.

2.7 Appendix: $\mathcal{F}^{D\ \mathrm{ECO}}_{22}$ for a spinning ECO

Figures 2.19 and 2.20 show the filter $\mathcal{F}^{D\ \mathrm{ECO}}_{22}$ in the time and frequency domain. The spin of the ECO is $\chi_f = 0.692$. It has the same qualitative features as that of

[8]We show that the choice of the start time has a large impact on inferring remnant properties.

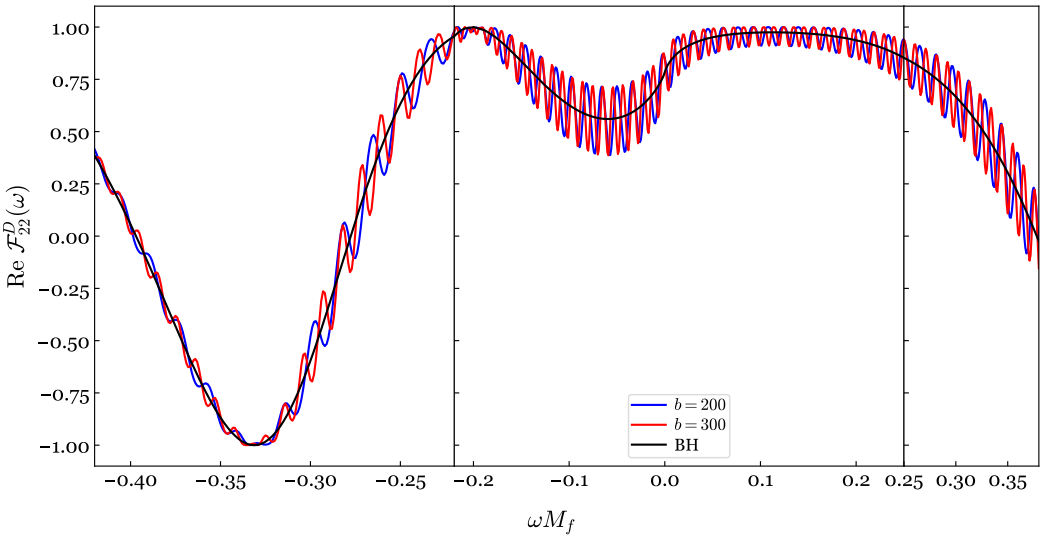

(a) $\epsilon = 10^{-1}$

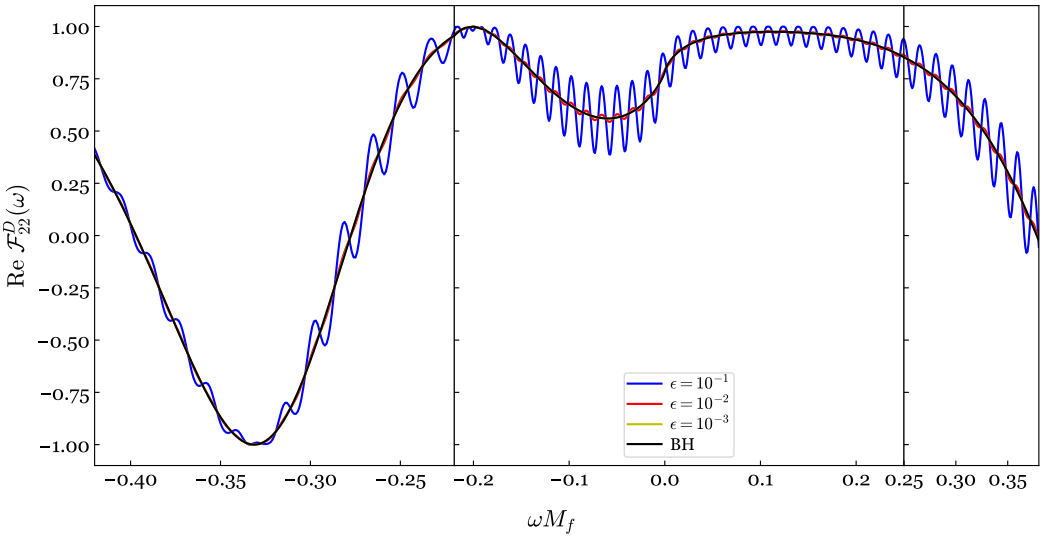

(b) $b = 200M_f$

Figure 2.20: Same as Fig. 2.13, but for a spinning ECO with $\chi_f = 0.692$.

the nonspinning ECO (Fig. 2.12).

2.8 Appendix: M_f and RSS

In Fig. 2.21, we plot the ringdown RSS of the filtered waveform as a function of the remnant mass M_f, using waveform SXS:BBH:0207.

2.9 Appendix: The up-mode solution of an ECO

Near the ECO surface, Chen *et al.* [178] proposed a physical boundary condition via a family of zero-angular-momentum fiducial observers (FIDOs). The tidal tensor

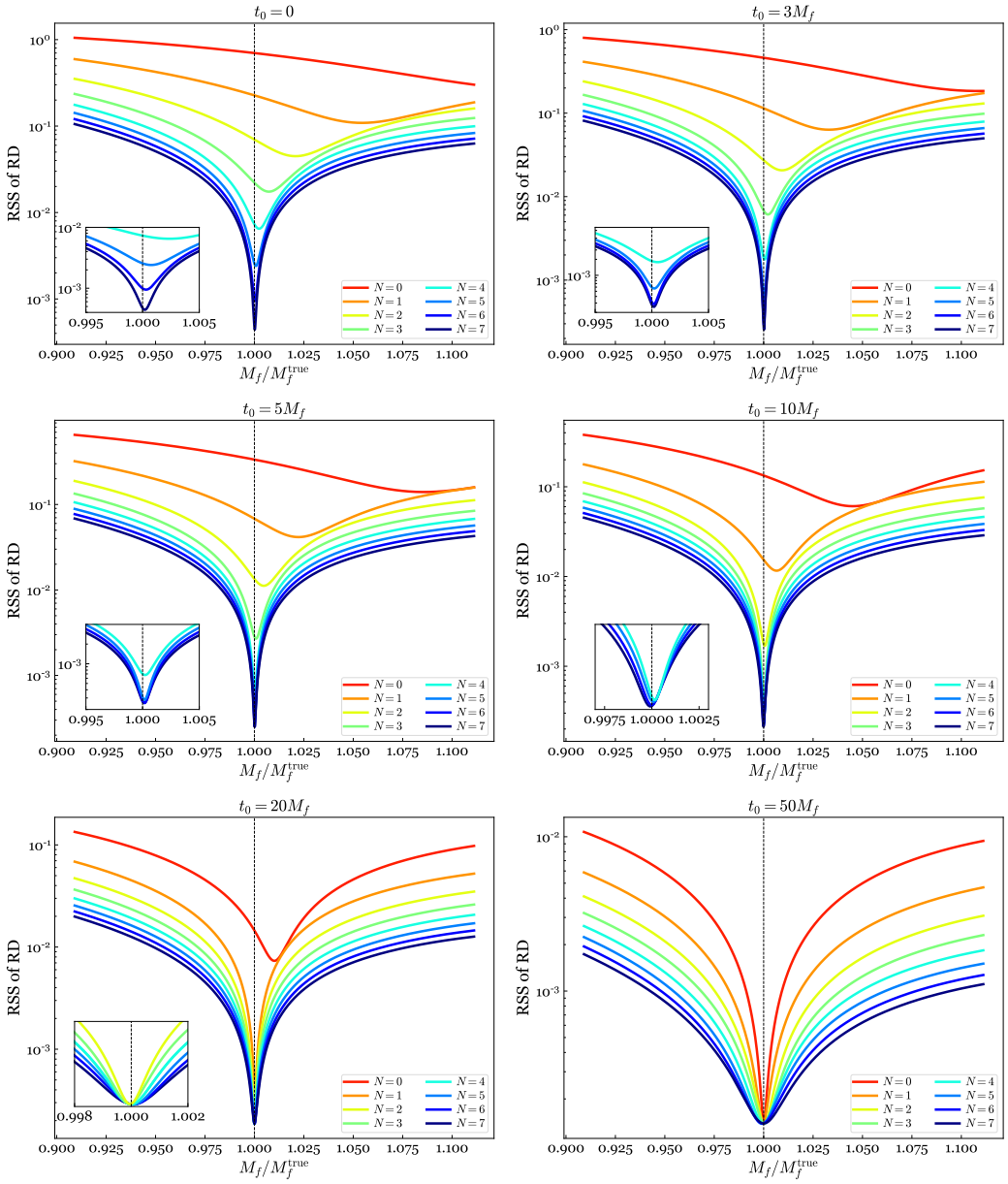

Figure 2.21: Same as Fig. 2.14, but with varying M_f and fixed χ_f.

field within the rest frame of the FIDOs is given by [181]

$$\mathcal{E}_{ij} = h_i^a h_j^c C_{abcd} U^b U^d, \tag{2.32a}$$

where C_{abcd} is the Weyl tensor, U^b is the four-velocity of the FIDOs, and $h_i^a = \delta_i^a + U^a U_i$ is the projection operator. Chen *et al.* argues that the tidal response of the ECO, namely the reflection of incident GWs, is proportional to the transverse component of the tidal field:

$$\mathcal{E}_{\rm transverse} \sim -\frac{\Delta}{4r^2}\psi_0 - \frac{r^2}{\Delta}\psi_4^*, \tag{2.32b}$$

where ψ_0 and ψ_4 are the Weyl scalars. The coefficient depends on the nature of the ECO, such as the reflectivity $\mathcal{R}$ in Eq. (2.24). By adopting this type of boundary condition, Xin *et al.* [182] shows that the ratio between the reflective wave and the incident wave reads [9] [Eq. (56) of [182]]:

$$\frac{\text{Reflective wave}}{\text{Incident wave}} = \frac{(-1)^{l+m+1}}{4}\mathcal{R}\frac{D_{lm}}{C_{lm}}, \tag{2.32c}$$

with

$$D_{lm} = 64(2r_+)^4 ik(k^2+4\epsilon^2)\left(-ik+\frac{\sqrt{1-\chi^2}}{r_+}\right), \tag{2.32d}$$

$$|C_{lm}|^2 = (Q^2+4\chi\omega m-4\chi^2\omega^2)[(Q-2)^2+36\chi\omega m-36\chi^2\omega^2]+144\omega^2(1-\chi^2)$$
$$+(2Q-1)(96\chi^2\omega^2-48\chi\omega m), \tag{2.32e}$$

$$\text{Im}\, C_{lm} = 12\omega, \tag{2.32f}$$

$$Q = \lambda + s(s+1) = \lambda + 2, \tag{2.32g}$$

$$\epsilon = \frac{\sqrt{1-\chi^2}}{4r_+}, \tag{2.32h}$$

$$k = \omega - m\Omega_+, \tag{2.32i}$$

where λ is the eigenvalue of spin-weighted spheroidal harmonics and $\Omega_+ = \chi/(2r_+)$ is the horizon frequency.

As shown in Fig. 2.11, if we consider a GW emerging from the horizon with a unity amplitude (ignoring any r_* dependent coefficient), it will bounce back and forth within the cavity formed by the ECO surface and the BH potential. In particular, the observer at infinity will see a main transmissive wave with amplitude $1/D^{\text{out}}_{lm}$, followed by a series of echoes. Using the boundary condition in Eq. (2.32c), it is straightforward to obtain the amplitude of the nth echo:

$$\frac{1}{D^{\text{out}}_{lm}}\left[\frac{(-1)^{l+m+1}}{4}\mathcal{R}\frac{D_{lm}}{C_{lm}}\frac{D^{\text{in}}_{lm}}{D^{\text{out}}_{lm}}\right]^n. \tag{2.33}$$

By summing them together, we obtain the total transmissive amplitude:

$$\sum_n \frac{1}{D^{\text{out}}_{lm}}\left[\frac{(-1)^{l+m+1}}{4}\mathcal{R}\frac{D_{lm}}{C_{lm}}\frac{D^{\text{in}}_{lm}}{D^{\text{out}}_{lm}}\right]^n$$
$$= \frac{1}{D^{\text{out}}_{lm}}\frac{1}{1-\frac{(-1)^{l+m+1}}{4}\mathcal{R}\frac{D_{lm}}{C_{lm}}\frac{D^{\text{in}}_{lm}}{D^{\text{out}}_{lm}}}. \tag{2.34}$$

The inverse of the total amplitude corresponds to $\tilde{D}^{\text{out}}_{lm}$ in Eq. (2.25).

[9] The additional factor $(-1)^l$ is due to the assumption that the system is invariant under reflection across the x-y plane [183].

References

[1] Benjamin P. Abbott et al. "Binary black hole mergers in the first advanced LIGO observing run." *Phys. Rev. X* 6.4 (2016). [Erratum: Phys.Rev.X 8, 039903 (2018)], p. 041015. DOI: 10.1103/PhysRevX.6.041015. arXiv: 1606.04856 [gr-qc].

[2] Benjamin P. Abbott et al. "GWTC-1: A gravitational-wave transient catalog of compact binary mergers observed by LIGO and Virgo during the first and second observing runs." *Phys. Rev. X* 9.3 (2019), p. 031040. DOI: 10.1103/PhysRevX.9.031040. arXiv: 1811.12907 [astro-ph.HE].

[3] Richard Abbott et al. "GWTC-2: Compact binary coalescences observed by LIGO and Virgo during the first half of the third observing run." *Phys. Rev. X* 11 (2021), p. 021053. DOI: 10.1103/PhysRevX.11.021053. arXiv: 2010.14527 [gr-qc].

[4] Richard Abbott et al. "GWTC-3: Compact binary coalescences observed by LIGO and Virgo during the second part of the third observing run." (Nov. 2021). arXiv: 2111.03606 [gr-qc].

[5] J. Aasi et al. "Advanced LIGO." *Classical and Quantum Gravity* 32 (2015), p. 074001. DOI: 10.1088/0264-9381/32/7/074001.

[6] Fausto Acernese et al. "Advanced Virgo: A second-generation interferometric gravitational wave detector." *Classical and Quantum Gravity* 32.2 (2015), p. 024001. DOI: 10.1088/0264-9381/32/2/024001.

[7] Yoichi Aso et al. "Interferometer design of the KAGRA gravitational wave detector." *Phys. Rev. D* 88 (4 Aug. 2013), p. 043007. DOI: 10.1103/PhysRevD.88.043007. URL: https://link.aps.org/doi/10.1103/PhysRevD.88.043007.

[8] Kostas D. Kokkotas and Bernd G. Schmidt. "Quasinormal modes of stars and black holes." *Living Rev. Rel.* 2 (1999), p. 2. DOI: 10.12942/lrr-1999-2. arXiv: gr-qc/9909058.

[9] Hans-Peter Nollert. "Quasinormal modes: the characteristic 'sound' of black holes and neutron stars." *Classical and Quantum Gravity* 16.12 (Nov. 1999), R159–R216. DOI: 10.1088/0264-9381/16/12/201. URL: https://doi.org/10.1088/0264-9381/16/12/201.

[10] Vitor Cardoso and Leonardo Gualtieri. "Testing the black hole 'no-hair' hypothesis." *Class. Quant. Grav.* 33.17 (2016), p. 174001. DOI: 10.1088/0264-9381/33/17/174001. arXiv: 1607.03133 [gr-qc].

[11] Emanuele Berti, Vitor Cardoso, and Andrei O. Starinets. "Quasinormal modes of black holes and black branes." *Class. Quant. Grav.* 26 (2009), p. 163001. DOI: 10.1088/0264-9381/26/16/163001. arXiv: 0905.2975 [gr-qc].

[12] Richard H. Price. "Nonspherical perturbations of relativistic gravitational collapse. I. Scalar and Gravitational perturbations." *Phys. Rev. D* 5 (10 May 1972), pp. 2419–2438. DOI: 10.1103/PhysRevD.5.2419. URL: https://link.aps.org/doi/10.1103/PhysRevD.5.2419.

[13] Richard H. Price. "Nonspherical perturbations of relativistic gravitational collapse. II. Integer-Spin, Zero-Rest-Mass fields." *Phys. Rev. D* 5 (10 May 1972), pp. 2439–2454. DOI: 10.1103/PhysRevD.5.2439. URL: https://link.aps.org/doi/10.1103/PhysRevD.5.2439.

[14] Roger Penrose. ""Golden Oldie": Gravitational collapse: The role of general relativity." *General relativity and Gravitation* 34.7 (2002), pp. 1141–1165.

[15] Piotr T. Chrusciel, Joao Lopes Costa, and Markus Heusler. "Stationary black holes: uniqueness and beyond." *Living Rev. Rel.* 15 (2012), p. 7. DOI: 10.12942/lrr-2012-7. arXiv: 1205.6112 [gr-qc].

[16] Brandon Carter. "Axisymmetric black hole has only two degrees of freedom." *Phys. Rev. Lett.* 26 (6 Feb. 1971), pp. 331–333. DOI: 10.1103/PhysRevLett.26.331. URL: https://link.aps.org/doi/10.1103/PhysRevLett.26.331.

[17] Werner Israel. "Event horizons in static vacuum space-times." *Phys. Rev.* 164 (5 Dec. 1967), pp. 1776–1779. DOI: 10.1103/PhysRev.164.1776. URL: https://link.aps.org/doi/10.1103/PhysRev.164.1776.

[18] Fernando Echeverria. "Gravitational-wave measurements of the mass and angular momentum of a black hole." *Phys. Rev. D* 40 (10 Nov. 1989), pp. 3194–3203. DOI: 10.1103/PhysRevD.40.3194. URL: https://link.aps.org/doi/10.1103/PhysRevD.40.3194.

[19] Olaf Dreyer et al. "Black hole spectroscopy: Testing general relativity through gravitational wave observations." *Class. Quant. Grav.* 21 (2004), pp. 787–804. DOI: 10.1088/0264-9381/21/4/003. arXiv: gr-qc/0309007 [gr-qc].

[20] Emanuele Berti, Vitor Cardoso, and Clifford M. Will. "On gravitational-wave spectroscopy of massive black holes with the space interferometer LISA." *Phys. Rev.* D73 (2006), p. 064030. DOI: 10.1103/PhysRevD.73.064030. arXiv: gr-qc/0512160 [gr-qc].

[21] Emanuele Berti et al. "Matched-filtering and parameter estimation of ringdown waveforms." *Phys. Rev. D* 76 (2007), p. 104044. DOI: 10.1103/PhysRevD.76.104044. arXiv: 0707.1202 [gr-qc].

[22] Sarah Gossan, John Veitch, and Bangalore S. Sathyaprakash. "Bayesian model selection for testing the no-hair theorem with black hole ringdowns." *Phys. Rev.* D85 (2012), p. 124056. DOI: 10.1103/PhysRevD.85.124056. arXiv: 1111.5819 [gr-qc].

[23] Vishal Baibhav and Emanuele Berti. "Multimode black hole spectroscopy." *Phys. Rev. D* 99.2 (2019), p. 024005. DOI: 10.1103/PhysRevD.99.024005. arXiv: 1809.03500 [gr-qc].

[24] Gregorio Carullo et al. "Empirical tests of the black hole no-hair conjecture using gravitational-wave observations." *Phys. Rev. D* 98.10 (2018), p. 104020. DOI: 10.1103/PhysRevD.98.104020. arXiv: 1805.04760 [gr-qc].

[25] Richard Brito, Alessandra Buonanno, and Vivien Raymond. "Black-hole spectroscopy by making full use of gravitational-wave modeling." *Phys. Rev. D* 98.8 (2018), p. 084038. DOI: 10.1103/PhysRevD.98.084038. arXiv: 1805.00293 [gr-qc].

[26] Hiroyuki Nakano et al. "Comparison of various methods to extract ringdown frequency from gravitational wave data." *Phys. Rev. D* 99.12 (2019), p. 124032. DOI: 10.1103/PhysRevD.99.124032. arXiv: 1811.06443 [gr-qc].

[27] Miriam Cabero et al. "Black hole spectroscopy in the next decade." *Phys. Rev. D* 101.6 (2020), p. 064044. DOI: 10.1103/PhysRevD.101.064044. arXiv: 1911.01361 [gr-qc].

[28] Swetha Bhagwat et al. "Detectability of the subdominant mode in a binary black hole ringdown." *Phys. Rev. D* 102.2 (2020), p. 024023. DOI: 10.1103/PhysRevD.102.024023. arXiv: 1910.13203 [gr-qc].

[29] Iara Ota and Cecilia Chirenti. "Overtones or higher harmonics? Prospects for testing the no-hair theorem with gravitational wave detections." *Phys. Rev. D* 101.10 (2020), p. 104005. DOI: 10.1103/PhysRevD.101.104005. arXiv: 1911.00440 [gr-qc].

[30] Juan Calderón Bustillo, Paul D. Lasky, and Eric Thrane. "Black-hole spectroscopy, the no-hair theorem, and GW150914: Kerr versus Occam." *Phys. Rev. D* 103.2 (2021), p. 024041. DOI: 10.1103/PhysRevD.103.024041. arXiv: 2010.01857 [gr-qc].

[31] Xisco Jiménez Forteza et al. "Spectroscopy of binary black hole ringdown using overtones and angular modes." *Phys. Rev. D* 102.4 (2020), p. 044053. DOI: 10.1103/PhysRevD.102.044053. arXiv: 2005.03260 [gr-qc].

[32] Maximiliano Isi and Will M. Farr. "Analyzing black-hole ringdowns." (July 2021). arXiv: 2107.05609 [gr-qc].

[33] Sarah Caudill et al. "Reduced basis representations of multi-mode black hole ringdown gravitational waves." *Class. Quant. Grav.* 29 (2012), p. 095016. DOI: 10.1088/0264-9381/29/9/095016. arXiv: 1109.5642 [gr-qc].

[34] Eliot Finch and Christopher J. Moore. "Frequency-domain analysis of black-hole ringdowns." *Phys. Rev. D* 104.12 (2021), p. 123034. DOI: 10.1103/PhysRevD.104.123034. arXiv: 2108.09344 [gr-qc].

[35] Jeroen Meidam et al. "Testing the no-hair theorem with black hole ringdowns using TIGER." *Phys. Rev. D* 90.6 (2014), p. 064009. DOI: 10.1103/PhysRevD.90.064009. arXiv: 1406.3201 [gr-qc].

[36] Swetha Bhagwat, Duncan A. Brown, and Stefan W. Ballmer. "Spectroscopic analysis of stellar mass black-hole mergers in our local universe with ground-based gravitational wave detectors." *Phys. Rev. D* 94.8 (2016). [Erratum: Phys.Rev.D 95, 069906 (2017)], p. 084024. DOI: 10.1103/PhysRevD.94.084024. arXiv: 1607.07845 [gr-qc].

[37] Emanuele Berti et al. "Spectroscopy of Kerr black holes with Earth- and space-based interferometers." *Phys. Rev. Lett.* 117.10 (2016), p. 101102. DOI: 10.1103/PhysRevLett.117.101102. arXiv: 1605.09286 [gr-qc].

[38] Vishal Baibhav et al. "Black hole spectroscopy: systematic errors and ringdown energy estimates." *Phys. Rev. D* 97.4 (2018), p. 044048. DOI: 10.1103/PhysRevD.97.044048. arXiv: 1710.02156 [gr-qc].

[39] Andrea Maselli, Kostas Kokkotas, and Pablo Laguna. "Observing binary black hole ringdowns by advanced gravitational wave detectors." *Phys. Rev. D* 95.10 (2017), p. 104026. DOI: 10.1103/PhysRevD.95.104026. arXiv: 1702.01110 [gr-qc].

[40] Huan Yang et al. "Black hole spectroscopy with coherent mode stacking." *Phys. Rev. Lett.* 118.16 (2017), p. 161101. DOI: 10.1103/PhysRevLett.118.161101. arXiv: 1701.05808 [gr-qc].

[41] Carlos Filipe Da Silva Costa et al. "Detection of (2,2) quasinormal mode from a population of black holes with a constructive summation method." *Phys. Rev. D* 98.2 (2018), p. 024052. DOI: 10.1103/PhysRevD.98.024052. arXiv: 1711.00551 [gr-qc].

[42] Vitor Cardoso and Paolo Pani. "Tests for the existence of black holes through gravitational wave echoes." *Nature Astronomy* 1.9 (Sept. 2017), pp. 586–591. ISSN: 2397-3366. DOI: 10.1038/s41550-017-0225-y. URL: https://doi.org/10.1038/s41550-017-0225-y.

[43] Vitor Cardoso, Edgardo Franzin, and Paolo Pani. "Is the gravitational-wave ringdown a probe of the event horizon?" *Phys. Rev. Lett.* 116.17 (2016). [Erratum: Phys.Rev.Lett. 117, 089902 (2016)], p. 171101. DOI: 10.1103/PhysRevLett.116.171101. arXiv: 1602.07309 [gr-qc].

[44] Valentino F. Foit and Matthew Kleban. "Testing quantum black holes with gravitational waves." *Class. Quant. Grav.* 36.3 (2019), p. 035006. DOI: 10.1088/1361-6382/aafcba. arXiv: 1611.07009 [hep-th].

[45] Danny Laghi et al. "Quantum black hole spectroscopy: probing the quantum nature of the black hole area using LIGO–Virgo ringdown detections." *Class. Quant. Grav.* 38.9 (2021), p. 095005. DOI: 10.1088/1361-6382/abde19. arXiv: 2011.03816 [gr-qc].

[46] Jose Luis Blázquez-Salcedo et al. "Perturbed black holes in Einstein-dilaton-Gauss-Bonnet gravity: Stability, ringdown, and gravitational-wave emission." *Phys. Rev. D* 94.10 (2016), p. 104024. DOI: 10.1103/PhysRevD.94.104024. arXiv: 1609.01286 [gr-qc].

[47] Kostas Glampedakis et al. "Post-Kerr black hole spectroscopy." *Phys. Rev. D* 96.6 (2017), p. 064054. DOI: 10.1103/PhysRevD.96.064054. arXiv: 1706.07658 [gr-qc].

[48] Hector O. Silva, Abhirup Ghosh, and Alessandra Buonanno. "Black-hole ringdown as a probe of higher-curvature gravity theories." (May 2022). arXiv: 2205.05132 [gr-qc].

[49] Andrea Maselli et al. "Parametrized ringdown spin expansion coefficients: A data-analysis framework for black-hole spectroscopy with multiple events." *Phys. Rev. D* 101.2 (2020), p. 024043. DOI: 10.1103/PhysRevD.101.024043. arXiv: 1910.12893 [gr-qc].

[50] Benjamin P. Abbott et al. "Observation of gravitational waves from a binary black hole merger." *Phys. Rev. Lett.* 116.6 (2016), p. 061102. DOI: 10.1103/PhysRevLett.116.061102. arXiv: 1602.03837 [gr-qc].

[51] Gregorio Carullo, Walter Del Pozzo, and John Veitch. "Observational black hole spectroscopy: A time-domain multimode analysis of GW150914." *Phys. Rev.* D99.12 (2019). [Erratum: Phys. Rev.D100,no.8,089903(2019)], p. 123029. DOI: 10.1103/PhysRevD.99.123029, 10.1103/PhysRevD.100.089903. arXiv: 1902.07527 [gr-qc].

[52] Maximiliano Isi et al. "Testing the no-hair theorem with GW150914." *Phys. Rev. Lett.* 123.11 (2019), p. 111102. DOI: 10.1103/PhysRevLett.123.111102. arXiv: 1905.00869 [gr-qc].

[53] Roberto Cotesta et al. "On the detection of ringdown overtones in GW150914." (Jan. 2022). arXiv: 2201.00822 [gr-qc].

[54] Maximiliano Isi and Will M. Farr. "Revisiting the ringdown of GW150914." (Feb. 2022). arXiv: 2202.02941 [gr-qc].

[55] Eliot Finch and Christopher J. Moore. "Searching for a ringdown overtone in GW150914." *Phys. Rev. D* 106.4 (2022), p. 043005. DOI: 10.1103/PhysRevD.106.043005. arXiv: 2205.07809 [gr-qc].

[56] Collin D. Capano et al. "Observation of a multimode quasi-normal spectrum from a perturbed black hole." (May 2021). arXiv: 2105.05238 [gr-qc].

[57] Richard Abbott et al. "GW190521: A binary black hole merger with a total mass of $150M_{\odot}$." *Phys. Rev. Lett.* 125.10 (2020), p. 101102. DOI: 10.1103/PhysRevLett.125.101102. arXiv: 2009.01075 [gr-qc].

[58] Richard Abbott et al. "Tests of general relativity with binary black holes from the second LIGO-Virgo gravitational-wave transient catalog." *Phys. Rev. D* 103.12 (2021), p. 122002. DOI: 10.1103/PhysRevD.103.122002. arXiv: 2010.14529 [gr-qc].

[59] Richard Abbott et al. "Tests of general relativity with GWTC-3." (Dec. 2021). arXiv: 2112.06861 [gr-qc].

[60] Abhirup Ghosh, Richard Brito, and Alessandra Buonanno. "Constraints on quasinormal-mode frequencies with LIGO-Virgo binary–black-hole observations." *Phys. Rev. D* 103.12 (2021), p. 124041. DOI: 10.1103/PhysRevD.103.124041. arXiv: 2104.01906 [gr-qc].

[61] Scott A. Hughes and Kristen Menou. "Golden binaries for LISA: Robust probes of strong-field gravity." *Astrophys. J.* 623 (2005), pp. 689–699. DOI: 10.1086/428826. arXiv: astro-ph/0410148.

[62] Manuel Luna and Alicia M. Sintes. "Parameter estimation of compact binaries using the inspiral and ringdown waveforms." *Class. Quant. Grav.* 23 (2006), pp. 3763–3782. DOI: 10.1088/0264-9381/23/11/006. arXiv: gr-qc/0601072.

[63] Hiroyuki Nakano, Takahiro Tanaka, and Takashi Nakamura. "Possible golden events for ringdown gravitational waves." *Phys. Rev. D* 92.6 (2015), p. 064003. DOI: 10.1103/PhysRevD.92.064003. arXiv: 1506.00560 [astro-ph.HE].

[64] Abhirup Ghosh et al. "Testing general relativity using gravitational wave signals from the inspiral, merger and ringdown of binary black holes." *Class. Quant. Grav.* 35.1 (2018), p. 014002. DOI: 10.1088/1361-6382/aa972e. arXiv: 1704.06784 [gr-qc].

[65] Abhirup Ghosh et al. "Testing general relativity using golden black-hole binaries." *Phys. Rev. D* 94.2 (2016), p. 021101. DOI: 10.1103/PhysRevD.94.021101. arXiv: 1602.02453 [gr-qc].

[66] Benjamin P. Abbott et al. "Tests of general relativity with GW150914." *Phys. Rev. Lett.* 116.22 (2016). [Erratum: Phys.Rev.Lett. 121, 129902 (2018)], p. 221101. DOI: 10.1103/PhysRevLett.116.221101. arXiv: 1602.03841 [gr-qc].

[67] Benjamin P. Abbott et al. "GW170104: Observation of a 50-Solar-Mass binary black hole Coalescence at Redshift 0.2." *Phys. Rev. Lett.* 118.22 (2017). [Erratum: Phys.Rev.Lett. 121, 129901 (2018)], p. 221101. DOI: 10.1103/PhysRevLett.118.221101. arXiv: 1706.01812 [gr-qc].

[68] Benjamin P. Abbott et al. "Tests of general relativity with the binary black hole signals from the LIGO-Virgo Catalog GWTC-1." *Phys. Rev.* D100.10 (2019), p. 104036. DOI: 10.1103/PhysRevD.100.104036. arXiv: 1903.04467 [gr-qc].

[69] Matteo Breschi et al. “IMR consistency tests with higher modes on gravitational signals from the second observing run of LIGO and Virgo.” *Class. Quant. Grav.* 36.24 (2019), p. 245019. DOI: 10.1088/1361-6382/ab5629. arXiv: 1903.05982 [gr-qc].

[70] Miriam Cabero et al. “Observational tests of the black hole area increase law.” *Phys. Rev. D* 97.12 (2018), p. 124069. DOI: 10.1103/PhysRevD.97.124069. arXiv: 1711.09073 [gr-qc].

[71] Maximiliano Isi et al. “Testing the black-hole area law with GW150914.” *Phys. Rev. Lett.* 127.1 (2021), p. 011103. DOI: 10.1103/PhysRevLett.127.011103. arXiv: 2012.04486 [gr-qc].

[72] S. W. Hawking. “Gravitational radiation from colliding black holes.” *Phys. Rev. Lett.* 26 (21 May 1971), pp. 1344–1346. DOI: 10.1103/PhysRevLett.26.1344. URL: https://link.aps.org/doi/10.1103/PhysRevLett.26.1344.

[73] Yonghe Sun and Richard H. Price. “Excitation of quasinormal ringing of a Schwarzschild black hole”. *Phys. Rev. D* 38 (4 Aug. 1988), pp. 1040–1052. DOI: 10.1103/PhysRevD.38.1040. URL: https://link.aps.org/doi/10.1103/PhysRevD.38.1040.

[74] Scott A. Hughes et al. “Learning about black hole binaries from their ringdown spectra.” *Phys. Rev. Lett.* 123.16 (2019), p. 161101. DOI: 10.1103/PhysRevLett.123.161101. arXiv: 1901.05900 [gr-qc].

[75] Anuj Apte and Scott A. Hughes. “Exciting black hole modes via misaligned coalescences: I. Inspiral, transition, and plunge trajectories using a generalized Ori-Thorne procedure.” *Phys. Rev. D* 100.8 (2019), p. 084031. DOI: 10.1103/PhysRevD.100.084031. arXiv: 1901.05901 [gr-qc].

[76] Halston Lim, Gaurav Khanna, and Scott A. Hughes. “Measuring quasinormal mode amplitudes with misaligned binary black hole ringdowns.” *Phys. Rev. D* 105.12 (2022), p. 124030. DOI: 10.1103/PhysRevD.105.124030. arXiv: 2204.06007 [gr-qc].

[77] Halston Lim et al. “Exciting black hole modes via misaligned coalescences: II. The mode content of late-time coalescence waveforms.” *Phys. Rev. D* 100.8 (2019), p. 084032. DOI: 10.1103/PhysRevD.100.084032. arXiv: 1901.05902 [gr-qc].

[78] Pablo A. Cano et al. “Gravitational ringing of rotating black holes in higher-derivative gravity.” *Phys. Rev. D* 105.2 (2022), p. 024064. DOI: 10.1103/PhysRevD.105.024064. arXiv: 2110.11378 [gr-qc].

[79] Yonghe Sun and Richard H. Price. “Excitation of Schwarzschild quasinormal modes by collapse”. *Phys. Rev. D* 41 (8 Apr. 1990), pp. 2492–2506. DOI: 10.1103/PhysRevD.41.2492. URL: https://link.aps.org/doi/10.1103/PhysRevD.41.2492.

[80] Ernst Nils Dorband et al. "A numerical study of the quasinormal mode excitation of Kerr black holes." *Phys. Rev. D* 74 (2006), p. 084028. DOI: 10.1103/PhysRevD.74.084028. arXiv: gr-qc/0608091.

[81] Emanuele Berti and Vitor Cardoso. "Quasinormal ringing of Kerr black holes. I. The Excitation factors." *Phys. Rev. D* 74 (2006), p. 104020. DOI: 10.1103/PhysRevD.74.104020. arXiv: gr-qc/0605118.

[82] Shahar Hadar et al. "Comparing numerical and analytical calculations of post-ISCO ringdown amplitudes." *Phys. Rev. D* 84 (2011), p. 047501. DOI: 10.1103/PhysRevD.84.047501. arXiv: 1105.3861 [gr-qc].

[83] Shahar Hadar and Barak Kol. "Post-ISCO ringdown amplitudes in extreme mass ratio inspiral." *Phys. Rev. D* 84 (2011), p. 044019. DOI: 10.1103/PhysRevD.84.044019. arXiv: 0911.3899 [gr-qc].

[84] Ioannis Kamaretsos et al. "Black-hole hair loss: Learning about binary progenitors from ringdown signals." *Phys. Rev. D* 85 (2012), p. 024018. DOI: 10.1103/PhysRevD.85.024018. arXiv: 1107.0854 [gr-qc].

[85] Zhongyang Zhang, Emanuele Berti, and Vitor Cardoso. "Quasinormal ringing of Kerr black holes. II. Excitation by particles falling radially with arbitrary energy." *Phys. Rev. D* 88 (2013), p. 044018. DOI: 10.1103/PhysRevD.88.044018. arXiv: 1305.4306 [gr-qc].

[86] Lionel T. London. "Modeling ringdown. II. Aligned-spin binary black holes, implications for data analysis and fundamental theory." *Phys. Rev. D* 102.8 (2020), p. 084052. DOI: 10.1103/PhysRevD.102.084052. arXiv: 1801.08208 [gr-qc].

[87] Swetha Bhagwat et al. "On choosing the start time of binary black hole ringdowns." *Phys. Rev. D* 97.10 (2018), p. 104065. DOI: 10.1103/PhysRevD.97.104065. arXiv: 1711.00926 [gr-qc].

[88] Swetha Bhagwat et al. "Ringdown overtones, black hole spectroscopy, and no-hair theorem tests." *Phys. Rev. D* 101.4 (2020), p. 044033. DOI: 10.1103/PhysRevD.101.044033. arXiv: 1910.08708 [gr-qc].

[89] Maria Okounkova. "Revisiting non-linearity in binary black hole mergers." (Apr. 2020). arXiv: 2004.00671 [gr-qc].

[90] Frans Pretorius. "Evolution of binary black hole spacetimes." *Phys. Rev. Lett.* 95 (2005), p. 121101. DOI: 10.1103/PhysRevLett.95.121101. arXiv: gr-qc/0507014 [gr-qc].

[91] Alessandra Buonanno, Gregory B. Cook, and Frans Pretorius. "Inspiral, merger and ring-down of equal-mass black-hole binaries." *Phys. Rev.* D75 (2007), p. 124018. DOI: 10.1103/PhysRevD.75.124018. arXiv: gr-qc/0610122 [gr-qc].

[92] Emanuele Berti et al. "Inspiral, merger and ringdown of unequal mass black hole binaries: A multipolar analysis." *Phys. Rev. D* 76 (2007), p. 064034. DOI: 10.1103/PhysRevD.76.064034. arXiv: gr-qc/0703053.

[93] Emanuele Berti et al. "Mining information from binary black hole mergers: A Comparison of estimation methods for complex exponentials in noise." *Phys. Rev. D* 75 (2007), p. 124017. DOI: 10.1103/PhysRevD.75.124017. arXiv: gr-qc/0701086.

[94] Lionel London, Deirdre Shoemaker, and James Healy. "Modeling ringdown: Beyond the fundamental quasinormal modes." *Phys. Rev. D* 90.12 (2014). [Erratum: Phys.Rev.D 94, 069902 (2016)], p. 124032. DOI: 10.1103/PhysRevD.90.124032. arXiv: 1404.3197 [gr-qc].

[95] Andrea Taracchini et al. "Prototype effective-one-body model for non-precessing spinning inspiral-merger-ringdown waveforms." *Phys. Rev. D* 86 (2012), p. 024011. DOI: 10.1103/PhysRevD.86.024011. arXiv: 1202.0790 [gr-qc].

[96] Yi Pan et al. "Inspiral-merger-ringdown multipolar waveforms of nonspinning black-hole binaries using the effective-one-body formalism." *Phys. Rev.* D84 (2011), p. 124052. DOI: 10.1103/PhysRevD.84.124052. arXiv: 1106.1021 [gr-qc].

[97] Andrea Taracchini et al. "Effective-one-body model for black-hole binaries with generic mass ratios and spins." *Phys. Rev.* D89.6 (2014), p. 061502. DOI: 10.1103/PhysRevD.89.061502. arXiv: 1311.2544 [gr-qc].

[98] Thibault Damour and Alessandro Nagar. "A new analytic representation of the ringdown waveform of coalescing spinning black hole binaries." *Phys. Rev. D* 90.2 (2014), p. 024054. DOI: 10.1103/PhysRevD.90.024054. arXiv: 1406.0401 [gr-qc].

[99] Andrea Taracchini et al. "Small mass plunging into a Kerr black hole: Anatomy of the inspiral-merger-ringdown waveforms." *Phys. Rev. D* 90.8 (2014), p. 084025. DOI: 10.1103/PhysRevD.90.084025. arXiv: 1404.1819 [gr-qc].

[100] Eric Thrane, Paul D. Lasky, and Yuri Levin. "Challenges testing the no-hair theorem with gravitational waves." *Phys. Rev. D* 96.10 (2017), p. 102004. DOI: 10.1103/PhysRevD.96.102004. arXiv: 1706.05152 [gr-qc].

[101] Matthew Giesler et al. "Black hole ringdown: The importance of overtones." *Phys. Rev.* X9.4 (2019), p. 041060. DOI: 10.1103/PhysRevX.9.041060. arXiv: 1903.08284 [gr-qc].

[102] Gregory B. Cook. "Aspects of multimode Kerr ringdown fitting." *Phys. Rev. D* 102.2 (2020), p. 024027. DOI: 10.1103/PhysRevD.102.024027. arXiv: 2004.08347 [gr-qc].

[103] Arnab Dhani. "Importance of mirror modes in binary black hole ringdown waveform." *Phys. Rev. D* 103.10 (2021), p. 104048. DOI: 10.1103/PhysRevD.103.104048. arXiv: 2010.08602 [gr-qc].

[104] Xisco Jiménez Forteza and Pierre Mourier. "High-overtone fits to numerical relativity ringdowns: Beyond the dismissed n=8 special tone." *Phys. Rev. D* 104.12 (2021), p. 124072. DOI: 10.1103/PhysRevD.104.124072. arXiv: 2107.11829 [gr-qc].

[105] Eliot Finch and Christopher J. Moore. "Modelling the ringdown from precessing black hole binaries." (Feb. 2021). arXiv: 2102.07794 [gr-qc].

[106] Xiang Li et al. "Angular emission patterns of remnant black holes." *Phys. Rev. D* 105.2 (2022), p. 024016. DOI: 10.1103/PhysRevD.105.024016. arXiv: 2110.03116 [gr-qc].

[107] Lorena Magaña Zertuche et al. "High precision ringdown modeling: Multimode fits and BMS frames." *Phys. Rev. D* 105 (2022), p. 104015. DOI: 10.1103/PhysRevD.105.104015. arXiv: 2110.15922 [gr-qc].

[108] Keefe Mitman et al. "Computation of displacement and spin gravitational memory in numerical relativity." *Phys. Rev. D* 102.10 (2020), p. 104007. DOI: 10.1103/PhysRevD.102.104007. arXiv: 2007.11562 [gr-qc].

[109] Keefe Mitman et al. "Adding gravitational memory to waveform catalogs using BMS balance laws." *Phys. Rev. D* 103.2 (2021), p. 024031. DOI: 10.1103/PhysRevD.103.024031. arXiv: 2011.01309 [gr-qc].

[110] Daniel Pook-Kolb et al. "Horizons in a binary black hole merger II: Fluxes, multipole moments and stability." (June 2020). arXiv: 2006.03940 [gr-qc].

[111] Pierre Mourier et al. "Quasinormal modes and their overtones at the common horizon in a binary black hole merger." *Phys. Rev. D* 103.4 (2021), p. 044054. DOI: 10.1103/PhysRevD.103.044054. arXiv: 2010.15186 [gr-qc].

[112] Reinaldo J. Gleiser et al. "Colliding black holes: How far can the close approximation go?" *Phys. Rev. Lett.* 77 (1996), pp. 4483–4486. DOI: 10.1103/PhysRevLett.77.4483. arXiv: gr-qc/9609022.

[113] Kenji Tomita and Nobuki Tajima. "Nonlinear behavior of nonspherical perturbations of the Schwarzschild metric". *Progress of Theoretical Physics* 56.2 (1976), pp. 551–560.

[114] Kenji Tomita. "On the non-linear behavior of nonspherical perturbations in relativistic gravitational collapse". *Progress of Theoretical Physics* 52.4 (1974), pp. 1188–1204.

[115] Christopher T. Cunningham, Richard H. Price, and Vincent Moncrief. "Radiation from collapsing relativistic stars. III - Second order perturbations of collapse with rotation." *Astrophys. J.* 236 (Mar. 1980), pp. 674–692. DOI: 10.1086/157787.

[116] Richard H. Price and Jorge Pullin. "Colliding black holes: The close limit." *Phys. Rev. Lett.* 72 (1994), pp. 3297–3300. DOI: 10.1103/PhysRevLett.72.3297. arXiv: gr-qc/9402039.

[117] Reinaldo J. Gleiser et al. "Second order perturbations of a Schwarzschild black hole." *Class. Quant. Grav.* 13 (1996), pp. L117–L124. DOI: 10.1088/0264-9381/13/10/001. arXiv: gr-qc/9510049.

[118] Reinaldo J. Gleiser et al. "Gravitational radiation from Schwarzschild black holes: The second order perturbation formalism." *Phys. Rept.* 325 (2000), pp. 41–81. DOI: 10.1016/S0370-1573(99)00048-4. arXiv: gr-qc/9807077.

[119] Carlos O. Nicasio, Reinaldo Gleiser, and Jorge Pullin. "Second order perturbations of a Schwarzschild black hole: Inclusion of odd parity perturbations." *Gen. Rel. Grav.* 32 (2000), p. 2021. DOI: 10.1023/A:1001994318436. arXiv: gr-qc/0001021.

[120] David Brizuela, Jose M. Martin-Garcia, and Guillermo A. Mena Marugan. "Second and higher-order perturbations of a spherical spacetime." *Phys. Rev. D* 74 (2006), p. 044039. DOI: 10.1103/PhysRevD.74.044039. arXiv: gr-qc/0607025.

[121] David Brizuela, Jose M. Martin-Garcia, and Guillermo A. Mena Marugan. "High-order gauge-invariant perturbations of a spherical spacetime." *Phys. Rev. D* 76 (2007), p. 024004. DOI: 10.1103/PhysRevD.76.024004. arXiv: gr-qc/0703069.

[122] David Brizuela, Jose M. Martin-Garcia, and Manuel Tiglio. "A complete gauge-invariant formalism for arbitrary second-order perturbations of a Schwarzschild black hole." *Phys. Rev. D* 80 (2009), p. 024021. DOI: 10.1103/PhysRevD.80.024021. arXiv: 0903.1134 [gr-qc].

[123] Manuela Campanelli and Carlos O. Lousto. "Second order gauge invariant gravitational perturbations of a Kerr black hole." *Phys. Rev. D* 59 (1999), p. 124022. DOI: 10.1103/PhysRevD.59.124022. arXiv: gr-qc/9811019.

[124] Stephen R. Green, Stefan Hollands, and Peter Zimmerman. "Teukolsky formalism for nonlinear Kerr perturbations." *Class. Quant. Grav.* 37.7 (2020), p. 075001. DOI: 10.1088/1361-6382/ab7075. arXiv: 1908.09095 [gr-qc].

[125] Nicholas Loutrel et al. "Second order perturbations of Kerr black holes: Reconstruction of the metric." *Phys. Rev. D* 103.10 (2021), p. 104017. DOI: 10.1103/PhysRevD.103.104017. arXiv: 2008.11770 [gr-qc].

[126] Justin L. Ripley et al. "Numerical computation of second order vacuum perturbations of Kerr black holes." *Phys. Rev. D* 103 (2021), p. 104018. DOI: 10.1103/PhysRevD.103.104018. arXiv: 2010.00162 [gr-qc].

[127] Yosef Zlochower et al. "Mode coupling in the nonlinear response of black holes." *Phys. Rev. D* 68 (2003), p. 084014. DOI: 10.1103/PhysRevD.68.084014. arXiv: gr-qc/0306098.

[128] Kunihito Ioka and Hiroyuki Nakano. "Second and higher-order quasi-normal modes in binary black hole mergers." *Phys. Rev. D* 76 (2007), p. 061503. DOI: 10.1103/PhysRevD.76.061503. arXiv: 0704.3467 [astro-ph].

[129] Hiroyuki Nakano and Kunihito Ioka. "Second order quasi-normal mode of the Schwarzschild black hole." *Phys. Rev. D* 76 (2007), p. 084007. DOI: 10.1103/PhysRevD.76.084007. arXiv: 0708.0450 [gr-qc].

[130] Satoshi Okuzumi, Kunihito Ioka, and Masa-aki Sakagami. "Possible discovery of nonlinear tail and quasinormal modes in black hole ringdown." *Phys. Rev. D* 77 (2008), p. 124018. DOI: 10.1103/PhysRevD.77.124018. arXiv: 0803.0501 [gr-qc].

[131] Enrique Pazos et al. "Mode coupling of Schwarzschild perturbations: Ringdown frequencies." *Phys. Rev. D* 82 (2010), p. 104028. DOI: 10.1103/PhysRevD.82.104028. arXiv: 1009.4665 [gr-qc].

[132] Laura Sberna et al. "Nonlinear effects in the black hole ringdown: Absorption-induced mode excitation." *Phys. Rev. D* 105.6 (2022), p. 064046. DOI: 10.1103/PhysRevD.105.064046. arXiv: 2112.11168 [gr-qc].

[133] Edward W. Leaver. "Spectral decomposition of the perturbation response of the Schwarzschild geometry". *Phys. Rev. D* 34 (2 July 1986), pp. 384–408. DOI: 10.1103/PhysRevD.34.384. URL: https://link.aps.org/doi/10.1103/PhysRevD.34.384.

[134] Naritaka Oshita. "Ease of excitation of black hole ringing: Quantifying the importance of overtones by the excitation factors." *Phys. Rev. D* 104.12 (2021), p. 124032. DOI: 10.1103/PhysRevD.104.124032. arXiv: 2109.09757 [gr-qc].

[135] Christopher T. Cunningham, Richard H. Price, and Vincent Moncrief. "Radiation from collapsing relativistic stars. I. Linearized odd-parity radiation." *Astrophys. J.* 224 (Sept. 1978), pp. 643–667. DOI: 10.1086/156413.

[136] Christopher T. Cunningham, Richard H. Price, and Vincent Moncrief. "Radiation from collapsing relativistic stars. II. Linearized even-parity radiation." *Astrophys. J.* 230 (June 1979), pp. 870–892. DOI: 10.1086/157147.

[137] David A. Nichols and Yanbei Chen. "A hybrid method for understanding black-hole mergers: Head-on case." *Phys. Rev. D* 82 (2010), p. 104020. DOI: 10.1103/PhysRevD.82.104020. arXiv: 1007.2024 [gr-qc].

[138] David A. Nichols and Yanbei Chen. "Hybrid method for understanding black-hole mergers: Inspiralling case." *Phys. Rev. D* 85 (2012), p. 044035. DOI: 10.1103/PhysRevD.85.044035. arXiv: 1109.0081 [gr-qc].

[139] Éanna É Flanagan and Scott A Hughes. "Measuring gravitational waves from binary black hole coalescences. I. Signal to noise for inspiral, merger, and ringdown". *Physical Review D* 57.8 (1998), p. 4535.

[140] Emanuele Berti, Vitor Cardoso, and Marc Casals. "Eigenvalues and eigenfunctions of spin-weighted spheroidal harmonics in four and higher dimensions." *Phys. Rev. D* 73 (2006). [Erratum: Phys.Rev.D 73, 109902 (2006)], p. 024013. DOI: 10.1103/PhysRevD.73.109902. arXiv: gr-qc/0511111.

[141] Emanuele Berti and Antoine Klein. "Mixing of spherical and spheroidal modes in perturbed Kerr black holes." *Phys. Rev. D* 90.6 (2014), p. 064012. DOI: 10.1103/PhysRevD.90.064012. arXiv: 1408.1860 [gr-qc].

[142] Lionel London and Edward Fauchon-Jones. "On modeling for Kerr black holes: Basis learning, QNM frequencies, and spherical-spheroidal mixing coefficients." *Class. Quant. Grav.* 36.23 (2019), p. 235015. DOI: 10.1088/1361-6382/ab2f11. arXiv: 1810.03550 [gr-qc].

[143] Arnab Dhani and Bangalore S. Sathyaprakash. "Overtones, mirror modes, and mode-mixing in binary black hole mergers." (July 2021). arXiv: 2107.14195 [gr-qc].

[144] Leo C. Stein. "qnm: A Python package for calculating Kerr quasinormal modes, separation constants, and spherical-spheroidal mixing coefficients." *J. Open Source Softw.* 4.42 (2019), p. 1683. DOI: 10.21105/joss.01683. arXiv: 1908.10377 [gr-qc].

[145] Frank J. Zerilli. "The gravitational field of a particle Falling in a Schwarzschild geometry analyzed in tensor harmonics." PhD thesis. PRINCETON UNIVERSITY., Jan. 1969.

[146] Saul A. Teukolsky. "Rotating black holes - separable wave equations for gravitational and electromagnetic perturbations." *Phys. Rev. Lett.* 29 (1972), pp. 1114–1118. DOI: 10.1103/PhysRevLett.29.1114.

[147] Saul A. Teukolsky. "Perturbations of a rotating black hole. I. Fundamental equations for gravitational, electromagnetic, and neutrino-field perturbations." *Astrophysical Journal* 185 (Oct. 1973), pp. 635–648. DOI: 10.1086/152444.

[148] Saul A. Teukolsky and William H. Press. "Perturbations of a rotating black hole. III - Interaction of the hole with gravitational and electromagnetic radiation." *Astrophys. J.* 193 (1974), pp. 443–461. DOI: 10.1086/153180.

[149] Shuhei Mano, Hisao Suzuki, and Eiichi Takasugi. "Analytic solutions of the Teukolsky equation and their low frequency expansions." *Prog. Theor. Phys.* 95 (1996), pp. 1079–1096. DOI: 10.1143/PTP.95.1079. arXiv: gr-qc/9603020.

[150] Sizheng Ma et al. "Gravitational-wave echoes from numerical-relativity waveforms via spacetime construction near merging compact objects." *Phys. Rev. D* 105.10 (2022), p. 104007. DOI: 10.1103/PhysRevD.105.104007. arXiv: 2203.03174 [gr-qc].

[151] Michael Boyle et al. "The SXS collaboration catalog of binary black hole simulations." *Class. Quant. Grav.* 36.19 (2019), p. 195006. DOI: 10.1088/1361-6382/ab34e2. arXiv: 1904.04831 [gr-qc].

[152] Bernard J. Kelly and John G. Baker. "Decoding mode mixing in black-hole merger ringdown." *Phys. Rev. D* 87.8 (2013), p. 084004. DOI: 10.1103/PhysRevD.87.084004. arXiv: 1212.5553 [gr-qc].

[153] Michael Boyle. "Transformations of asymptotic gravitational-wave data." *Phys. Rev.* D93.8 (2016), p. 084031. DOI: 10.1103/PhysRevD.93.084031. arXiv: 1509.00862 [gr-qc].

[154] Sizheng Ma, Ling Sun, and Yanbei Chen. "Using rational filters to uncover the first ringdown overtone in GW150914." (Jan. 2023). arXiv: 2301.06639 [gr-qc].

[155] Sizheng Ma, Ling Sun, and Yanbei Chen. "Black hole spectroscopy by mode cleaning." (Jan. 2023). arXiv: 2301.06705 [gr-qc].

[156] Keefe Mitman et al. "Fixing the BMS frame of numerical relativity Waveforms with BMS Charges." (Aug. 2022). arXiv: 2208.04356 [gr-qc].

[157] Keefe Mitman et al. "Fixing the BMS frame of numerical relativity waveforms." *Phys. Rev. D* 104.2 (2021), p. 024051. DOI: 10.1103/PhysRevD.104.024051. arXiv: 2105.02300 [gr-qc].

[158] *Black hole Perturbation Toolkit*. (bhptoolkit.org).

[159] Keefe Mitman et al. "Nonlinearities in black hole Ringdowns." *Phys. Rev. Lett.* 130.8 (2023), p. 081402. DOI: 10.1103/PhysRevLett.130.081402. arXiv: 2208.07380 [gr-qc].

[160] Mark Ho-Yeuk Cheung et al. "Nonlinear effects in black hole ringdown." *Phys. Rev. Lett.* 130.8 (2023), p. 081401. DOI: 10.1103/PhysRevLett.130.081401. arXiv: 2208.07374 [gr-qc].

[161] Lawrence E. Kidder et al. "SpECTRE: A task-based discontinuous Galerkin code for relativistic astrophysics." *J. Comput. Phys.* 335 (2017), pp. 84–114. DOI: 10.1016/j.jcp.2016.12.059. arXiv: 1609.00098 [astro-ph.HE].

[162] Nils Deppe et al. *SpECTRE v2022.06.14*. 10.5281/zenodo.6643787. Version 2022.06.14. June 2022. DOI: 10.5281/zenodo.6643787. URL: https://spectre-code.org.

[163] Hans-Peter Nollert. "About the significance of quasinormal modes of black holes." *Phys. Rev. D* 53 (1996), pp. 4397–4402. DOI: 10.1103/PhysRevD.53.4397. arXiv: gr-qc/9602032.

[164] Enrico Barausse, Vitor Cardoso, and Paolo Pani. "Environmental effects for gravitational-wave astrophysics." *J. Phys. Conf. Ser.* 610.1 (2015). Ed. by Giacomo Ciani, John W. Conklin, and Guido Mueller, p. 012044. DOI: 10.1088/1742-6596/610/1/012044. arXiv: 1404.7140 [astro-ph.CO].

[165] Enrico Barausse, Vitor Cardoso, and Paolo Pani. "Can environmental effects spoil precision gravitational-wave astrophysics?" *Phys. Rev. D* 89.10 (2014), p. 104059. DOI: 10.1103/PhysRevD.89.104059. arXiv: 1404.7149 [gr-qc].

[166] José Luis Jaramillo, Rodrigo Panosso Macedo, and Lamis Al Sheikh. "Pseudospectrum and black hole quasinormal mode instability." *Phys. Rev. X* 11.3 (2021), p. 031003. DOI: 10.1103/PhysRevX.11.031003. arXiv: 2004.06434 [gr-qc].

[167] Mark Ho-Yeuk Cheung et al. "The elephant and the flea: Destabilizing the fundamental mode of black holes." (Nov. 2021). arXiv: 2111.05415 [gr-qc].

[168] Emanuele Berti et al. "Stability of the fundamental quasinormal mode in Time-Domain Observations: The Elephant and the Flea Redux." (May 2022). arXiv: 2205.08547 [gr-qc].

[169] Koutarou Kyutoku, Hayato Motohashi, and Takahiro Tanaka. "Quasinormal modes of Schwarzschild black holes on the real axis." (June 2022). arXiv: 2206.00671 [gr-qc].

[170] Lam Hui, Daniel Kabat, and Sam S. C. Wong. "Quasinormal modes, echoes and the causal structure of the Green's function." *JCAP* 12 (2019), p. 020. DOI: 10.1088/1475-7516/2019/12/020. arXiv: 1909.10382 [gr-qc].

[171] Vitor Cardoso et al. "Gravitational-wave signatures of exotic compact objects and of quantum corrections at the horizon scale." *Phys. Rev. D* 94.8 (2016), p. 084031. DOI: 10.1103/PhysRevD.94.084031. arXiv: 1608.08637 [gr-qc].

[172] Horst R. Beyer. "On the completeness of the quasinormal modes of the Poschl-Teller potential." *Commun. Math. Phys.* 204 (1999), pp. 397–423. DOI: 10.1007/s002200050651. arXiv: gr-qc/9803034.

[173] Nikodem Szpak. "Quasinormal mode expansion and the exact solution of the Cauchy problem for wave equations." (Nov. 2004). arXiv: gr-qc/0411050.

[174] Hans-Peter Nollert and Richard H. Price. "Quantifying excitations of quasinormal mode systems." *J. Math. Phys.* 40 (1999), pp. 980–1010. DOI: 10.1063/1.532698. arXiv: gr-qc/9810074.

[175] Emily S. C. Ching et al. "Quasinormal mode expansion for linearized waves in gravitational system." *Phys. Rev. Lett.* 74 (1995), pp. 4588–4591. DOI: 10.1103/PhysRevLett.74.4588. arXiv: gr-qc/9408043.

[176] Sean T. McWilliams. "Analytical black-hole binary merger waveforms." *Phys. Rev. Lett.* 122.19 (2019), p. 191102. DOI: 10.1103/PhysRevLett.122.191102. arXiv: 1810.00040 [gr-qc].

[177] Sizheng Ma et al. "Universal features of gravitational waves emitted by superkick binary black hole systems." *Phys. Rev. D* 104.8 (2021), p. 084003. DOI: 10.1103/PhysRevD.104.084003. arXiv: 2107.04890 [gr-qc].

[178] Baoyi Chen, Qingwen Wang, and Yanbei Chen. "Tidal response and near-horizon boundary conditions for spinning exotic compact objects." *Phys. Rev. D* 103.10 (2021), p. 104054. DOI: 10.1103/PhysRevD.103.104054. arXiv: 2012.10842 [gr-qc].

[179] Alexei A. Starobinsky. "Amplification of waves reflected from a rotating "black hole."" *Sov. Phys. JETP* 37.1 (1973), pp. 28–32.

[180] David J. A. McKechan, Craig Robinson, and Bangalore S. Sathyaprakash. "A tapering window for time-domain templates and simulated signals in the detection of gravitational waves from coalescing compact binaries." *Class. Quant. Grav.* 27 (2010), p. 084020. DOI: 10.1088/0264-9381/27/8/084020. arXiv: 1003.2939 [gr-qc].

[181] Fan Zhang et al. "Visualizing spacetime curvature via frame-drag vortexes and tidal tendexes II. Stationary black holes." *Phys. Rev. D* 86 (2012), p. 084049. DOI: 10.1103/PhysRevD.86.084049. arXiv: 1208.3034 [gr-qc].

[182] Shuo Xin et al. "Gravitational-wave echoes from spinning exotic compact objects: Numerical waveforms from the Teukolsky equation." *Phys. Rev. D* 104.10 (2021), p. 104005. DOI: 10.1103/PhysRevD.104.104005. arXiv: 2105.12313 [gr-qc].

[183] Michael Boyle et al. "Gravitational-wave modes from precessing black-hole binaries." (Sept. 2014). arXiv: 1409.4431 [gr-qc].

Chapter 3

BLACK HOLE SPECTROSCOPY BY MODE CLEANING

[1] Sizheng Ma, Ling Sun, and Yanbei Chen. "Black hole spectroscopy by mode cleaning." *Phys. Rev. Lett.* 130.14 (2023), p. 141401. DOI: 10.1103/PhysRevLett.130.141401. arXiv: 2301.06705 [gr-qc].

[2] Sizheng Ma, Ling Sun, and Yanbei Chen. "Using rational filters to uncover the first ringdown overtone in GW150914." *Phys. Rev. D* 107.8 (2023), p. 084010. DOI: 10.1103/PhysRevD.107.084010. arXiv: 2301.06639 [gr-qc].

3.1 Introduction

The ringdown stage of a gravitational wave (GW) emitted by a binary black hole (BBH) corresponds to the oscillation of the remnant BH, which encodes rich information about the system. At the linear order, a ringdown waveform is given by a superposition of a set of complex-valued quasinormal modes (QNMs) [1–4], labeled by two angular numbers (l, m) and one overtone index n. Within the general theory of relativity, they are fully determined by the mass and spin of the corresponding BH due to the no-hair theorem [5–8]. Thus measuring the frequency and decay rate of a QNM from a ringdown signal can lead to the estimates of the mass and spin of the remnant BH [9]. Alternatively, if multiple modes are detected at the same time, we can use them to test the no-hair theorem [10–12]. This method is known as *BH spectroscopy* [13–39].

An important topic of BH spectroscopy is to understand which QNMs are present in the ringdown of a numerical relativity (NR) waveform [40–57] and when they start [58–60]. To address these questions, a common method is to fit the waveform after the merger using a ringdown template that consists of a group of QNMs, and explore when the mismatch between the two can be minimized by varying the QNMs and the fitting start time. In particular, Giesler *et al.* [55] demonstrated that the ringdown of a GW150914-like NR waveform [61] starts as early as when the strain amplitude reaches its peak, if seven overtones are included. Motivated by this result, Isi *et al.* [30] (and also [26]) extended the initial ringdown analyses [29, 62] of GW150914 [63] and explored earlier start times for fitting. A significance of 3.6σ was found for the existence of the first overtone. However, the conclusion was later challenged

by Cotesta *et al.* [28], who argued that the early (ringdown) signal could be noise dominated, and thus the existence of the first overtone might not be reliable. The claim by Cotesta *et al.* [28] was then disputed by a subsequent response by Isi *et al.* [26] who found the impact of noise was not reproducible; Finch and Moore [27] also showed that the noise fluctuations might be overestimated. On the other hand, Bustillo *et al.* [21] and Finch *et al.* [27] tackled the problem via different approaches; tentative evidence was found.

The lack of a definitive conclusion over the ringdown modes of GW150914 leaves unresolved issues for BH spectroscopy, posting questions for the ringdown analysis in the upcoming LIGO-Virgo-KAGRA fourth observing run (O4). Here we propose a new framework for BH spectroscopy and revisit the issues from a different perspective. Recently, we proposed a new methodology, the so-called "QNM filters" [64]. The method includes the use of two filter classes: a rational filter and a full filter. The rational filter is constructed via a QNM frequency, whereas the full filter is constructed from the BH transmissivity, based on the *hybrid approach* [65–67]. They were originally designed to remove QNM(s) from the ringdown when studying NR waveforms. After filtering out some dominant modes, we were able to show the existence of subdominant effects confidently, such as the mixing of modes, retrograde modes, and also the second-order QNMs [47–49]. In our recent paper [68], a novel framework for BH spectroscopy is outlined: by incorporating the rational filter into Bayesian inference, a new scheme is developed to analyze the ringdown of real GW events, independent of the usual Markov chain Monte Carlo (MCMC) method. In this chapter, we extend the discussions therein and provide full details to demonstrate the efficacy and efficiency of this framework. In particular, we demonstrate the existence of the first overtone in the ringdown of GW150914 with detailed evidence.

This chapter is organized as follows. In Sec. 3.2, we introduce the properties of the rational filter. In Sec. 3.3, we use the filter to construct a two-dimensional (2D) ringdown likelihood function in the time domain that depends only on the mass and spin of the remnant BH (independent of mode amplitudes and phases). Based on the likelihood function, we define a new method to compute model evidence and Bayes factor for QNM(s). Detailed case studies of a simulated signal using a NR waveform and the real event GW150914 are also given in the same section. Next, in Sec. 3.4, we carry out a mixed BH spectroscopy analysis by combining our new approach with the usual MCMC treatment. Again, the NR simulation (Sec. 3.4.1) and GW150914

(Sec. 3.4.2) are discussed as detailed examples. Finally, we summarize the results in Sec. 3.5.

Throughout this chapter, we use geometric units with $G = c = 1$. We always use the notation $\omega_{lmn} = 2\pi f_{lmn} - i/\tau_{lmn}$ to refer to the (l, m, n) QNM, with $2\pi f_{lmn}$ and $-1/\tau_{lmn}$ being its real and imaginary parts. All of our analyses are in the detector frame.

3.2 Rational filter and real GW data

To start with, let us consider two complex GW harmonics $h_{l,\pm m}(t)$. Below, we always assume $m > 0$; thus $h_{l,m}$ ($h_{l,-m}$) represents the harmonic component that is emitted towards the north (south) with respect to the system. Within the ringdown regime, their time evolution reads

$$h_{lm}(t) = \sum_n A_{lmn} e^{-i\omega_{lmn}(t-t_0)+i\phi_{lmn}}, \tag{3.1a}$$

$$h_{l,-m}(t) = \sum_n A'_{lmn} e^{i\omega^*_{lmn}(t-t_0)+i\phi'_{lmn}}, \tag{3.1b}$$

where n stands for the overtone index, and A_{lmn}'s and ϕ_{lmn}'s are the amplitudes and phases of the QNMs, respectively. Note that ω_{lmn} on the right-hand side of Eq. (3.1) refers to prograde modes, and we always neglect the contribution of retrograde modes in the rest of this chapter.

As discussed in Ref. [64], to clean a mode ω_{lmn} from $h_{lm}(t)$, we can apply a rational filter:

$$\frac{\omega - \omega_{lmn}}{\omega - \omega^*_{lmn}}.$$

Similarly, we need to apply another filter:

$$\frac{\omega + \omega^*_{lmn}}{\omega + \omega_{lmn}},$$

to eliminate the same mode ω_{lmn} from $h_{l,-m}(t)$. For an actual GW event, its time-domain real strain h_t consists of both the complex harmonics $h_{l,\pm m}(t)$. In consequence, the final form of the filter $\mathcal{F}_{lmn}$ that is associated with the QNM ω_{lmn} is given by

$$\begin{aligned}\mathcal{F}_{lmn}(f; M_f, \chi_f) &= \frac{\omega - \omega_{lmn}}{\omega - \omega^*_{lmn}} \frac{\omega + \omega^*_{lmn}}{\omega + \omega_{lmn}} \\ &= \frac{f - f_{lmn} + \frac{i}{2\pi\tau_{lmn}}}{f - f_{lmn} - \frac{i}{2\pi\tau_{lmn}}} \times \frac{f + f_{lmn} + \frac{i}{2\pi\tau_{lmn}}}{f + f_{lmn} - \frac{i}{2\pi\tau_{lmn}}},\end{aligned} \tag{3.2}$$

where $\omega = 2\pi f$; f_{lmn} and τ_{lmn} corresponds to the real and imaginary parts of ω_{lmn}:

$$\omega_{lmn} = 2\pi f_{lmn} - \frac{i}{\tau_{lmn}}. \tag{3.3}$$

According to the no-hair theorem [5–8], f_{lmn} and τ_{lmn} are fully determined by the mass M_f and spin χ_f of the remnant BH. We obtain f_{lmn} and τ_{lmn} using the Python package `qnm` [69]. To apply the filter $\mathcal{F}_{lmn}$ to real GW data, we first transform the time-domain data d_t to the frequency domain via fast Fourier transform (FFT)

$$\tilde{d}_f = \int d_t e^{2\pi i f t} dt. \tag{3.4}$$

Note that the length of d_t needs to be at least comparable to the entire inspiral-merger-ringdown (IMR) signal to avoid spectral leakage. Then the filtered data read

$$d_t^F = \int df \tilde{d}_f \mathcal{F}_{lmn}(f) e^{-i2\pi f t}. \tag{3.5}$$

In practice, multiple filters could be applied simultaneously via a total filter

$$\mathcal{F}_{\rm tot} = \prod_{lmn} \mathcal{F}_{lmn}. \tag{3.6}$$

Since each filter $\mathcal{F}_{lmn}(f)$ satisfies

$$\mathcal{F}_{lmn}(-f) = [\mathcal{F}_{lmn}(f)]^*, \tag{3.7}$$

the filtered data d_t^F is still real-valued.

Because we apply the filter to the entire IMR signal, different portions of the signal have distinct responses. As discussed in Ref. [64], the early low-frequency inspiral signal is shifted backward in time by the filter, which does not impact the ringdown analysis. Here we continue the discussion therein and investigate the impact of the filter on two other aspects. In Sec. 3.2.1, we study the effect of $\mathcal{F}_{lmn}$ on a different QNM $\omega_{l'm'n'}$, namely ($l \neq l'$ or $m \neq m'$ or $n \neq n'$). Then in Sec. 3.2.2, the impact of the filter on detector noise is discussed.

3.2.1 Impact on a different QNM

To investigate the impact of $\mathcal{F}_{lmn}$ on $\omega_{l'm'n'}$, let us consider a toy model for the excitation of $\omega_{l'm'n'}$

$$h_t = e^{-(t-t_0)/\tau_{l'm'n'}}$$

$$\times \cos\left[2\pi f_{l'm'n'}(t-t_0)+\phi_{l'm'n'}\right]\Theta(t-t_0), \tag{3.8}$$

where $\Theta(t-t_0)$ is the Heaviside step function, meaning that the QNM is excited at t_0. The Fourier transformation of h_t reads

$$\begin{aligned}\tilde{h}_f =& \frac{i}{2}e^{i\omega t_0}\left[\frac{e^{i\phi_{l'm'n'}}}{2\pi f-2\pi f_{l'm'n'}+i/\tau_{l'm'n'}}\right.\\ &\left.+\frac{e^{-i\phi_{l'm'n'}}}{2\pi f+2\pi f_{l'm'n'}+i/\tau_{l'm'n'}}\right].\end{aligned} \tag{3.9}$$

The two poles $f=\pm f_{l'm'n'}-i/(2\pi\tau_{l'm'n'})$ of $\tilde{h}_f$ are plotted in Fig. 2.1. Both of them lie in the lower half of the complex plane, indicating the fact that there is no $\omega_{l'm'n'}$ signal before $t=t_0$. After applying the filter $\mathcal{F}_{lmn}$, two new poles $f=\pm f_{lmn}+i/(2\pi\tau_{lmn})$ appear in the upper half of the plane. This implies that the ω_{lmn} component of the filtered waveform exists before t_0. On the other hand, the two original poles in the lower plane remain unchanged, and the start time of the $\omega_{l'm'n'}$ component remains at t_0. This is different from the situation where the early inspiral signal is shifted to an earlier time [64]. However, the amplitude and phase of the $\omega_{l'm'n'}$ component in the filtered waveform are changed. We can calculate the changes quantitatively by computing the following integral

$$h_t^F=\int df\tilde{h}_f\mathcal{F}_{lmn}(f)e^{-i2\pi ft}, \tag{3.10}$$

and obtain

$$\begin{aligned}h_t^F =& B_{lmn}^{l'm'n'}e^{-(t-t_0)/\tau_{l'm'n'}}\\ &\times\cos\left[2\pi f_{l'm'n'}(t-t_0)+\phi_{l'm'n'}+\varphi_{lmn}^{l'm'n'}\right],\quad t>t_0,\end{aligned} \tag{3.11}$$

where

$$B_{lmn}^{l'm'n'}e^{i\varphi_{lmn}^{l'm'n'}}\equiv\mathcal{F}_{lmn}(\omega_{l'm'n'}). \tag{3.12}$$

It is straightforward to show that

$$B_{lmn}^{l'm'n'}=B_{l'm'n'}^{lmn}. \tag{3.13}$$

Eq. (3.11) shows that the amplitude of the $\omega_{l'm'n'}$ mode is reduced by a factor of $B_{lmn}^{l'm'n'}$. As for a Kerr BH with $\chi_f=0.692$, we have $B_{220}^{221}=0.487$, meaning that the amplitude of the first overtone (fundamental mode) is reduced by a factor of two after applying the filter that cleans the fundamental mode (first overtone). For completeness, we also provide the expression of h_t^F when $t<t_0$,

$$h_t^F=\frac{1}{\pi f_{lmn}\tau_{lmn}}e^{(t-t_0)/\tau_{lmn}}\Phi_{lmn}^{l'm'n'}(t),\quad t<t_0, \tag{3.14}$$

with

$$\Phi_{lmn}^{l'm'n'}(t) = -\mathrm{Im}\ e^{2\pi i f_{lmn}(t-t_0)} \times \left(\frac{e^{i\phi_{l'm'n'}}}{1+\omega_{l'm'n'}/\omega_{lmn}} + \frac{e^{-i\phi_{l'm'n'}}}{1-\omega^*_{l'm'n'}/\omega_{lmn}} \right). \tag{3.15}$$

The term $e^{(t-t_0)/\tau_{lmn}}$ in Eq. (3.14) shows that h_t^F is a "ring-up" component at $t < t_0$.

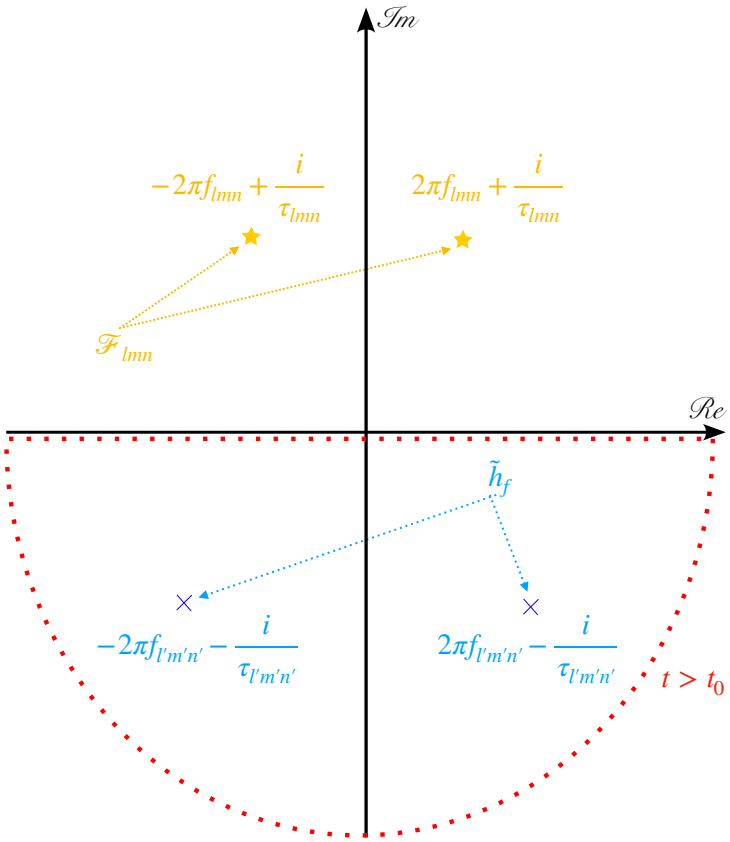

Figure 3.1: Poles of the filtered waveform [Eq. (3.10)] on the complex plane. Two poles are in the lower half-plane (blue crosses), contributed by the original waveform in Eq. (3.9). The other two (yellow stars) are in the upper half-plane, coming from the filter $\mathcal{F}_{lmn}$. The red dashed curve corresponds to the time regime of $t > t_0$. Before t_0, the time-domain signal is contributed by the two ring-up modes $f = \pm f_{lmn} + i/(2\pi\tau_{lmn})$ outside the closed region. After t_0, the two ringdown modes $f = \pm f_{l'm'n'} - i/(2\pi\tau_{l'm'n'})$ contribute.

3.2.2 Impact on detector noise

For a noise series n_t, its covariance matrix is given by

$$C_{t,t+\tau} = E[n_t n_{t+\tau}] - E[n_t]E[n_{t+\tau}], \tag{3.16}$$

where E denotes expectation. By assuming stationarity and $E[n_t] = 0$, $C_{t,t+\tau}$ takes a simple form

$$C_{t,t+\tau} = \rho(\tau), \tag{3.17}$$

where $\rho(\tau)$ is the autocovariance function (ACF). In the frequency domain, Eq. (3.17) becomes (known as the Wiener–Khinchin theorem)

$$E[\tilde{n}_f \tilde{n}^*_{f'}] = \frac{1}{2}\delta(f - f')S(f), \tag{3.18}$$

with $S(f)$ being the one-sided noise power spectral density (PSD)

$$S(f) = 2\int e^{2\pi i f\tau}\rho(\tau)d\tau. \tag{3.19}$$

Then we apply the rational filter $\mathcal{F}_{lmn}$ to $\tilde{n}_f$. Since the modulus of $\mathcal{F}_{lmn}$ is unity, we can write

$$\mathcal{F}_{lmn}(f) = e^{i\delta_{lmn}(f)}, \tag{3.20}$$

and the filtered noise writes

$$\tilde{n}^F_f = e^{i\delta_{lmn}(f)}\tilde{n}_f, \tag{3.21}$$

which still remains stationary. In addition, after plugging Eq. (3.21) into Eq. (3.18), we find that the one-sided PSD is not impacted by the filter.

To support our conclusion, we generate two noise series with a sampling rate of 8192 Hz and a total length of 4 s. One is band-limited white noise $\sim \mathcal{N}(0, 1)$ and the other is simulated Hanford noise, generated by the Bilby library [70, 71]. Next we use the Python package ringdown [23, 72] to estimate their one-sided PSDs with the Welch method [73]. On the other hand, we apply a rational filter $\mathcal{F}_{220}$ to both noise series and obtain the time-domain filtered data. Then we repeat the Welch method and obtain the PSDs of the filtered data. The results are plotted in Figs. 3.2a and 3.2b for comparison. We find the filtered PSDs are always identical to the unfiltered PSDs (the black curves completely overlap the red ones), no matter what the values of M_f and χ_f are used to generate $\mathcal{F}_{220}$.

We then move on to two more realistic cases: LIGO Hanford and Livingston data [74–77] around GW150914 [78–80]. We estimate the corresponding PSDs of 32-s raw time-series data with a sampling rate of 16384 Hz. Again, we apply the rational filter $\mathcal{F}_{220}$ to the frequency-domain data, convert them back to time series,

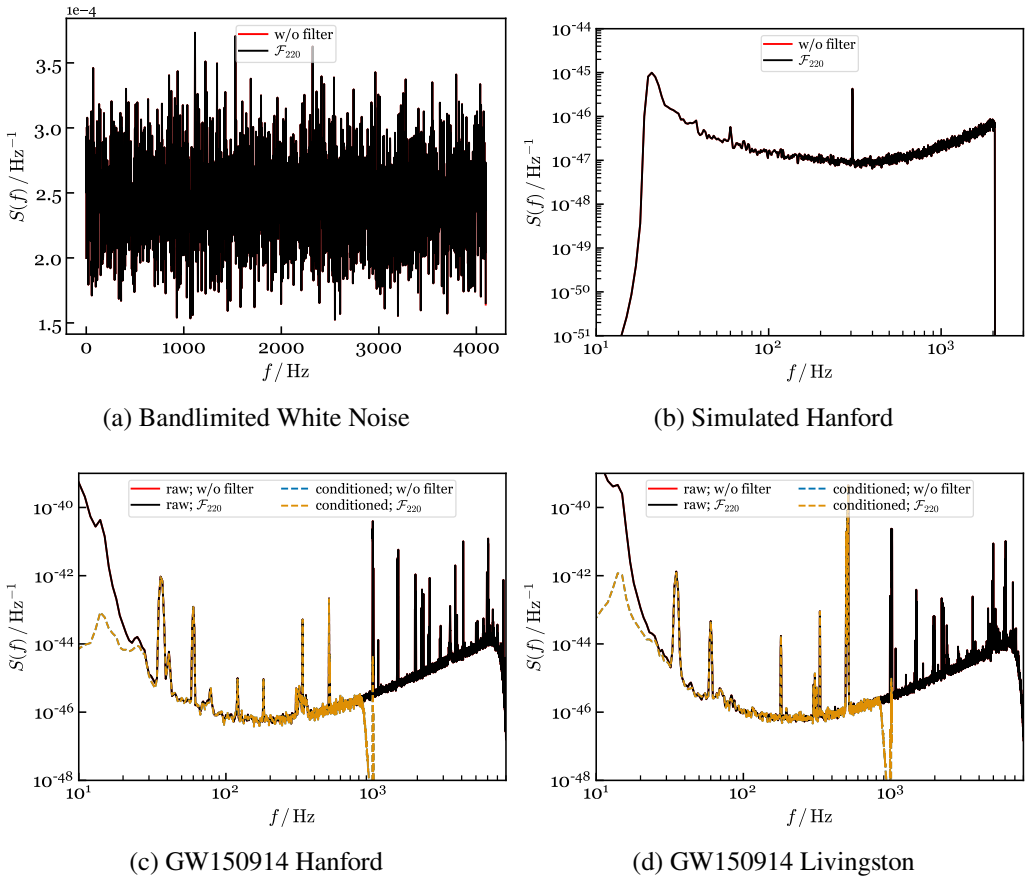

(a) Bandlimited White Noise

(b) Simulated Hanford

(c) GW150914 Hanford

(d) GW150914 Livingston

Figure 3.2: Comparison of the one-sided PSDs of the filtered and unfiltered noise. The top panels show results in (a) band-limited white noise $\sim \mathcal{N}(0, 1)$ and (b) simulated Hanford noise. The filtered and unfiltered PSDs of the raw data are shown in black and red, respectively. The bottom panels show results in (c) LIGO Hanford and (d) LIGO Livingston data around the event time of GW150914. The filtered (black) and unfiltered (red) PSDs are in perfect agreement. After conditioning the raw data, the filtered (dashed orange) and unfiltered (dashed blue) PSDs also overlap.

and compute the filtered PSDs. The PSDs of the filtered and unfiltered data are shown as black and red curves in Figs. 3.2c and 3.2d, which fully agree with each other. Furthermore, we condition both the Hanford and Livingston raw data by (a) removing frequency components that are below 20 Hz using a high-pass filter and (b) downsampling the data to 2048 Hz. The filtered and unfiltered PSDs of the conditioned data are plotted as dashed orange and blue curves, respectively, in Figs. 3.2c and 3.2d. We see that they are also in perfect agreement.

3.3 A new likelihood function

Suppose we have a BBH GW signal in observational time-series data d_t. After applying rational filters with enough QNMs to d_t[1] to remove all the QNMs, we expect that the filtered data d_t^F should be consistent with pure noise in the ringdown regime, with a likelihood function given by

$$\ln P\left(d_t|M_f,\chi_f,t_0,\mathcal{F}_{\rm tot}\right) = -\frac{1}{2}\sum_{i,j>I_0} d_i^F C_{ij}^{-1} d_j^F, \tag{3.22}$$

where $d_i^F \equiv d_{t_i}^F$ are the samples of the filtered data after the ringdown starts ($t_i > t_0$), I_0 is the index associated with t_0, and C_{ij} is the covariance matrix. Note that here we compute the likelihood in the time domain, closely following [23]. Let us then recall what the formula of $\ln P$ looks like in Ref. [23]:

$$\begin{aligned}&\ln P\left(d_t|A_{lmn},\phi_{lmn},M_f,\chi_f,t_0\right)\\ &= -\frac{1}{2}\sum_{i,j>I_0}(d_i-h_i)C_{ij}^{-1}(d_j-h_j),\end{aligned} \tag{3.23}$$

where h_t is a multiple-QNM ringdown waveform template

$$h_t = \sum_{lmn} A_{lmn} e^{-(t-t_0)/\tau_{lmn}} \cos\left[2\pi f_{lmn}(t-t_0)+\phi_{lmn}\right], \tag{3.24}$$

with A_{lmn}'s and ϕ_{lmn}'s being the amplitudes and phases of the QNMs, respectively. We can see that Eq. (3.22) is similar to Eq. (3.23) in the aspect of computing the likelihood of the data being pure noise after removing the GW signals. However, the underlying approaches of the two are quite different. In the usual unfiltered approach, one needs to build a ringdown template in terms of a set of QNMs, based on the amplitude A_{lmn} and phase ϕ_{lmn} of each mode, and then subtract the template h_t from the data d_t. On the contrary, our approach does not need A_{lmn}'s and ϕ_{lmn}'s—the rational filters can completely remove the relevant complex-frequency component corresponding to each QNM from the ringdown no matter what the amplitude and phase are. A direct analogy is that a constant can be eliminated by a derivative no matter what its value is. In the Supplemental Material of our recent paper [68], we explicitly show that the rational filter eliminates the dependency on mode amplitudes and phases through a new maximum likelihood estimator and relates to the usual time-domain approach [23] via an approximate marginalization. As a result, the new likelihood function implicitly depends on M_f and χ_f only, given that the rational filter is built using a given set of M_f and χ_f [see Eq. (3.2)].

[1] Again, d_t needs to be long enough to avoid spectral leakage.

In this chapter, we treat M_f and χ_f as the parameters of the filtered data, whereas the ringdown start time t_0 and the choice of the set of QNMs included in the filter $\mathcal{F}_{\rm tot}$ as hyperparameters. Therefore, we can convert the likelihood to the joint posterior of M_f and χ_f via

$$\begin{aligned}\ln P\left(M_f, \chi_f | d_t, t_0, \mathcal{F}_{\rm tot}\right) &= \ln P\left(d_t | M_f, \chi_f, t_0, \mathcal{F}_{\rm tot}\right) \\ &+ \ln \Pi\left(M_f, \chi_f\right) + \text{constant},\end{aligned} \tag{3.25}$$

where $\ln \Pi\left(M_f, \chi_f\right)$ is the prior. In our following discussions for the injection study and GW150914, we always place uniform priors on the final mass and spin in the ranges of $M_f \in [35M_\odot, 140M_\odot]$ and $\chi_f \in [0, 0.99]$. In addition, $P\left(M_f, \chi_f | d_t, t_0, \mathcal{F}_{\rm tot}\right)$ can be marginalized by integrating over one dimension (1D) to obtain the distribution of the other dimension:

$$P\left(\chi_f | d_t, t_0, \mathcal{F}_{\rm tot}\right) = \int P\left(M_f, \chi_f | d_t, t_0, \mathcal{F}_{\rm tot}\right) dM_f, \tag{3.26a}$$

$$P\left(M_f | d_t, t_0, \mathcal{F}_{\rm tot}\right) = \int P\left(M_f, \chi_f | d_t, t_0, \mathcal{F}_{\rm tot}\right) d\chi_f. \tag{3.26b}$$

Since this new $\ln P$ is simply a two-dimensional function, it is computationally cheap enough to directly compute the distribution of M_f and χ_f without using techniques like MCMC.

3.3.1 NR waveform injection

We first take the GW150914-like NR waveform [61] from the SXS catalog [81, 82] and build a complex strain h from the (l, m) harmonics h_{lm} in the NR waveform, given by

$$h = h_+ - i h_\times = \sum_{lm} {}_{-2}Y_{lm}\left(\iota, \beta\right) h_{lm}, \tag{3.27}$$

where ${}_{-2}Y_{lm}\left(\iota, \beta\right)$ denotes the spin-weighted spherical harmonics, and angles (ι, β) stand for the angular coordinates of an observer within the source frame. Here we choose $(\iota = \pi, \beta = 0)$ to simulate the orientation of GW150914 (face-off) [30]. For simplicity, we include only the two most dominant modes $h_{2,\pm 2}$ in Eq. (3.27) and inject the "+" polarization state to band-limited white noise. To mimic GW150914, we set the total initial mass of the system (detector frame) to $72\,M_\odot$ so that the mass of the remnant BH $M_f = 68.5\,M_\odot$ agrees with that inferred from the full IMR waveform [30]. The length of the full NR waveform is 1.38 s. We pad zeros on both ends of the waveform to prolong the length to 4 s.[2] The data $d_i \equiv d_{t_i}$ (including

[2] Since we can control the simulated noise in this case, a relatively short signal is chosen for efficiency.

white noise and simulated signal) are sampled at 16384 Hz. We also adjust the relative amplitude of the NR waveform so that the ringdown matched filter SNR is ~ 15, as measured after the peak of the strain. We then condition d_i to remove contents that are below 20 Hz and downsample the data to 4096 Hz.

To calculate $\ln P$ in Eq. (3.22), we need to estimate the covariance matrix C_{ij} first, which has an exact expression for the given band-limited white noise. We further verify this by estimating the PSD $S(f)$ from 4 s of the off-source white noise the Welch method, as described in Sec. 3.2.2. We then inverse Eq. (3.19) to obtain the value of ACF $\rho(\tau)$

$$\rho_k \equiv \rho(t_k) = \frac{1}{2T}\sum_{j=0}^{N-1} S_j e^{2\pi i j k/N}, \tag{3.28}$$

where $S_j \equiv S(f_j)$ is the PSD value at $f = f_j$, N is the total number of frequency bins in $S(f)$, and $T = 4\,\mathrm{s}$ is the total length of the noise. Finally, we get the covariance matrix C_{ij} via

$$C_{ij} = \rho(|i-j|). \tag{3.29}$$

On the other hand, to apply the rational filter to the data d_i, we transform the full length of d_i into the frequency domain via FFT

$$\tilde{d}_j = \Delta t \sum_{k=0}^{N-1} d_k e^{-2\pi i j k/N}, \tag{3.30}$$

with $\Delta t = t_{k+1} - t_k$. Then the filtered data read [see Eq. (3.6) for $\mathcal{F}_{\rm tot}$]

$$\tilde{d}^F_j = \mathcal{F}_{\rm tot}(f_j)\tilde{d}_j, \tag{3.31}$$

and the corresponding time-domain data are given by

$$d^F_k = \frac{1}{T}\sum_{j=0}^{N-1} \tilde{d}^F_j e^{-2\pi i j k/N}. \tag{3.32}$$

Next, we select the filtered time-series data d^F_k that lie within the time interval of $[t_0, t_0 + w]$, which we refer to as a ringdown window with window width w. Here we fix $w = 0.08$ s while letting t_0 be a free parameter. We discuss the impact of t_0 later in this section. Finally, we substitute the value of C_{ij} [Eq. (3.29)] and d^F_k [Eq. (3.32)] within the ringdown window into Eq. (3.22) to compute the likelihood.

For a given start time t_0, we build $\mathcal{F}_{\rm tot}$ by choosing a set of remnant black hole parameters, M_f and χ_f [Eq. (3.2)], and a set of QNMs [Eq. (3.6)]. We can calculate the posterior distribution of M_f and χ_f using Eq. (3.25) for a given set of QNMs and infer which QNMs are more likely to be present in the signal. On the other hand, for a fixed filter $\mathcal{F}_{\rm tot}$ (built with a given choice of M_f, χ_f and QNMs), we can slide the ringdown window $[t_0, t_0+w]$ by varying t_0. The t_0 value corresponding to the maximum posterior probability indicates the start time of the QNM(s) included in $\mathcal{F}_{\rm tot}$. In this example, it is found that the $l = m = 2$ harmonic can be modeled with multiple overtones ω_{22n}'s right after the time when the strain reaches its peak amplitude [55], denoted by $t_{\rm peak}$. Therefore, we set the form of the total filter to

$$\mathcal{F}_{\rm tot} = \prod_{n=0}^{X} \mathcal{F}_{22n}, \tag{3.33}$$

where X is the highest overtone included, and focus on the regime of $\Delta t_0 = t_0 - t_{\rm peak} \gtrsim 0$.

Figs. 3.3, 3.4, and 3.5 show the joint posterior of M_f and χ_f evaluated at different start times (parameterized by Δt_0), for the injected signal. Here we display a 2D grid of $M_f \in [35M_\odot, 100M_\odot]$ and $\chi_f \in [0, 0.95]$ for better readability. Other regions of the parameter space do not provide extra features. The left and right columns correspond to having $X = 0$ ("one QNM," 220) and $X = 1$ ("two QNMs," 220 and 221), respectively, in $\mathcal{F}_{\rm tot}$. Adding more overtones does not further improve the likelihoods, given the ringdown SNR level at the current stage. The true values of the remnant mass $M_f = 68.5\,M_\odot$ and spin $\chi_f = 0.692085$ are marked by white plus signs. We compute the 90% credible region by integrating the joint posterior evaluated with our filter [Eq. (3.25)] over the $M_f - \chi_f$ parameter space. The results are shown as red-dashed contours. In the meantime, the marginalized posterior distributions of M_f and χ_f are plotted as 1D histograms (red curves) in the side panels, calculated by Eq. (3.26). For comparison purposes, we also use the Python package ringdown [23, 72] to perform a conventional time-domain full-ringdown Bayesian analysis via MCMC (hereafter "full-RD MCMC"), in which the likelihoods are evaluated by Eq. (3.23). To build the ringdown template h_t in Eq. (3.24), we include the same QNM(s) as the one(s) used in the filter $\mathcal{F}_{\rm tot}$. The 90% credible interval joint posteriors evaluated by MCMC are shown as the regions enclosed by white dashed contours. Similarly, we plot the 1D histograms for M_f and χ_f, obtained via MCMC, as gray-shaded regions. For reference, we compute the matched-filter

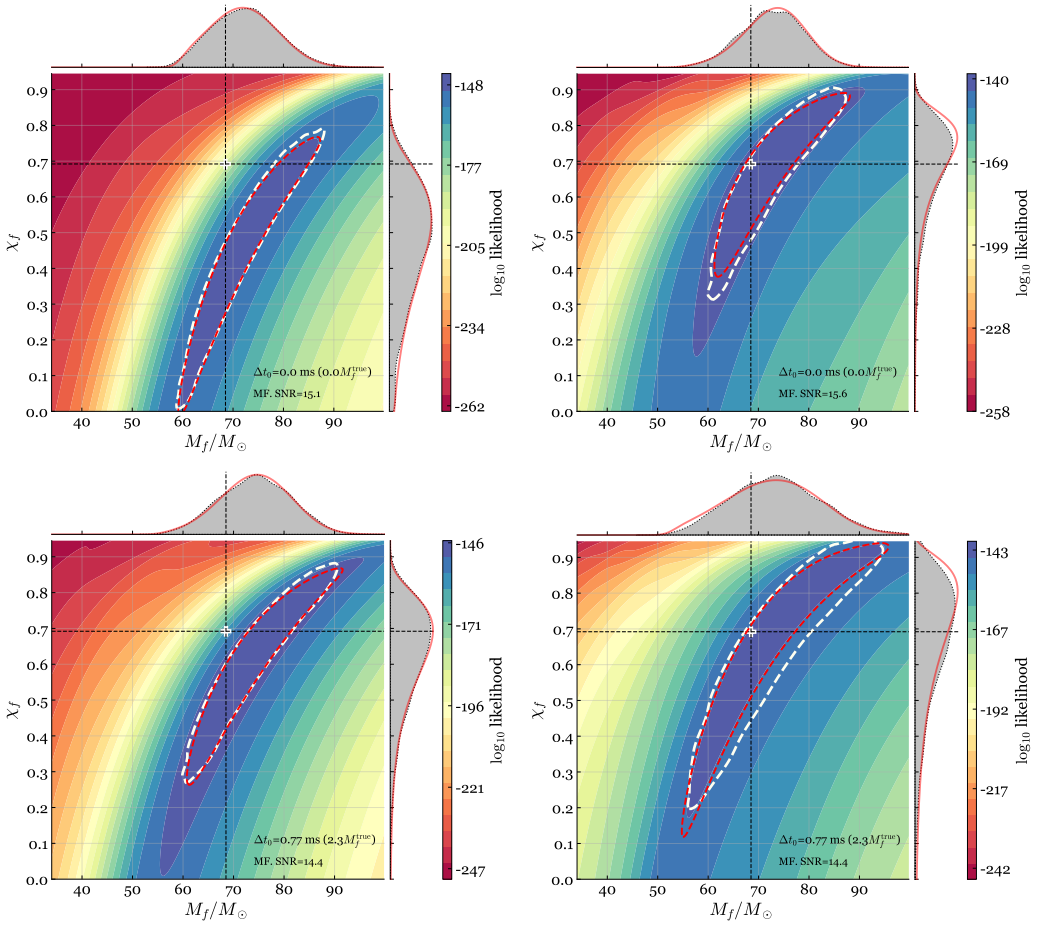

Figure 3.3: Joint posterior distributions of M_f and χ_f evaluated with Eq. (3.25). The GW150914-like NR waveform is injected into band-limited white noise. The top and bottom panels represent $\Delta t_0 = 0$ and 0.77 ms, respectively. The left and right panels show results from applying the filter for the fundamental mode only, $\mathcal{F}_{220}$, and the filter $\mathcal{F}_{221}\mathcal{F}_{220}$, respectively. The red-dashed contours display the 90% credible region by integrating our new joint posterior in Eq. (3.25); and the joint distribution is projected to the individual 1D space of χ_f and M_f (red curves in side panels) using Eq. (3.26). The white plus signs stand for the true value of M_f and χ_f obtained from NR. The white dashed contours show the 90% credible region from the full-RD MCMC approach. The MCMC results are marginalized to the 1D distributions of M_f and χ_f, shown as the gray-shaded regions in side panels. The value of the matched filter (MF) SNR is also provided.

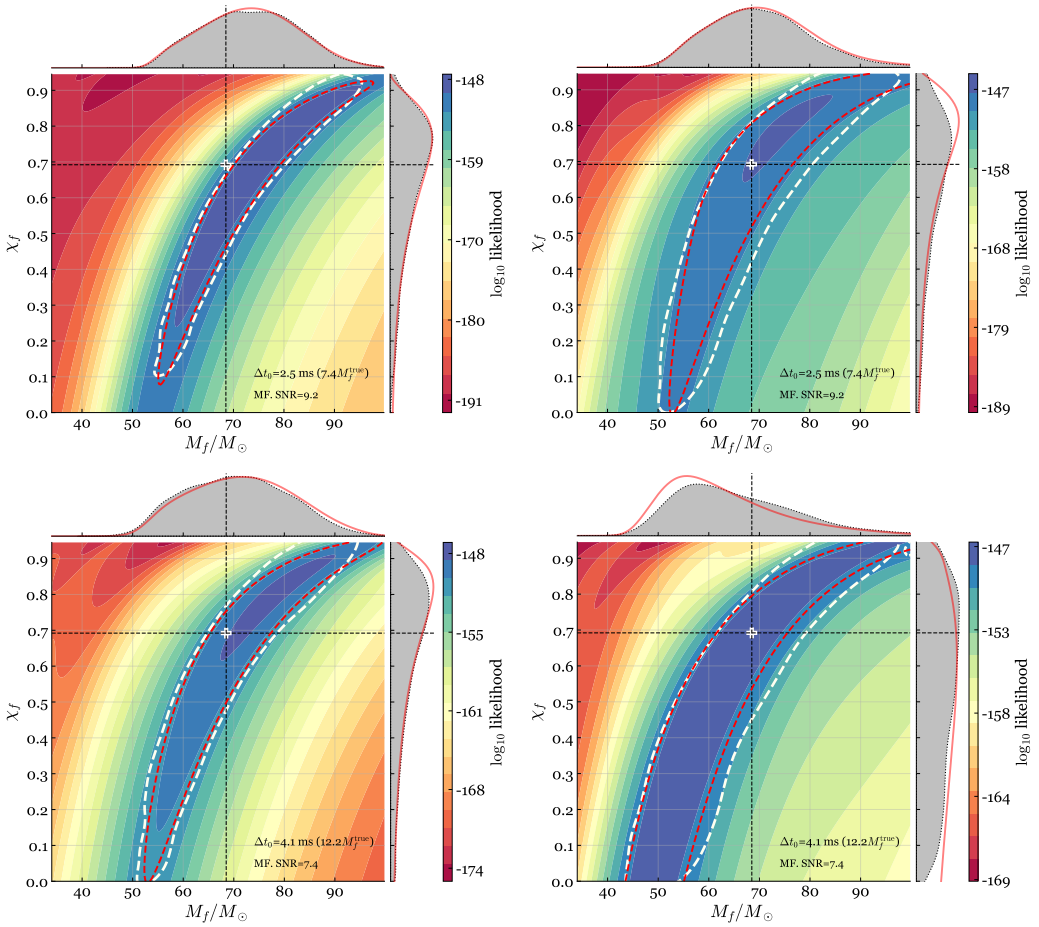

Figure 3.4: Joint posterior distributions of M_f and χ_f. Fig. 3.3 continued; more values of Δt_0 are tested.

SNRs ($\mathrm{SNR_{MF}}$) from the posterior samples via

$$\mathrm{SNR_{MF}} = \frac{\langle h_t|d_t\rangle}{\sqrt{\langle h_t|h_t\rangle}}, \tag{3.34}$$

with

$$\langle h_t|d_t\rangle = \sum_{i,j>I_0} h_i C_{ij}^{-1} d_j. \tag{3.35}$$

Now let us look at the first row of Fig. 3.3, with $\Delta t_0 = 0\,\mathrm{ms}$. In both the left and right panels, the contours obtained from our filters largely agree with the full-RD MCMC results. The true remnant properties lie within the 90% credible region when we include both the fundamental mode and the first overtone in the filter. On the contrary, there is a strong bias when the first overtone is excluded. Next, in the second row of Fig. 3.4, namely $\Delta t_0 = 4.1\,\mathrm{ms} = 12.2M_f^{\rm true}$, the true remnant mass

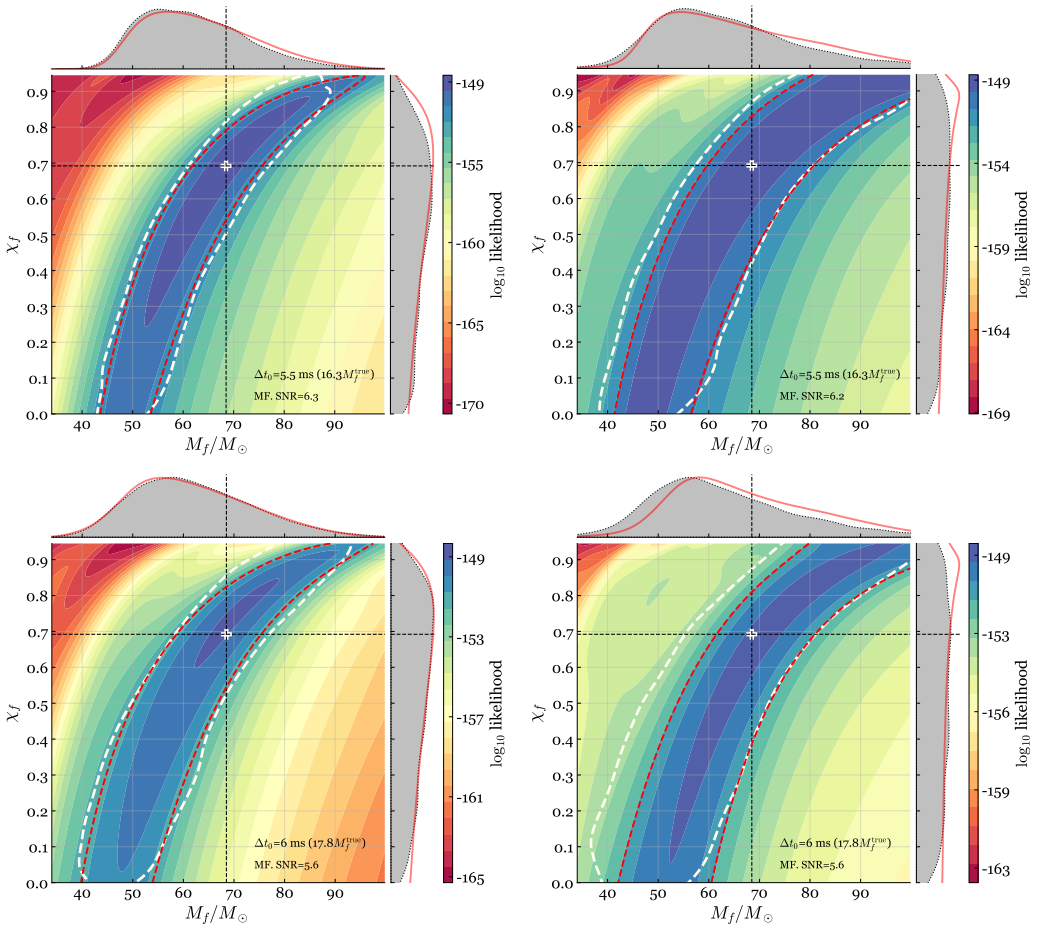

Figure 3.5: Joint posterior distributions of M_f and χ_f. Fig. 3.3 continued; more values of Δt_0 are tested.

and spin can be recovered with the fundamental mode alone, whereas the constraints of M_f and χ_f get worse after adding the filter of the first overtone $\mathcal{F}_{221}$. The reason is as follows: since the first overtone has decayed to a small value at $\Delta t_0 = 4.1$ ms, the major impact of the rational filter $\mathcal{F}_{221}$ on the signal is to reduce the amplitude of the fundamental mode by a factor of $B^{221}_{220} = 2.053$ [Eq. (3.11)], making it harder to infer the remnant properties from the filtered data.

After qualitatively discussing the posteriors obtained using Eq. (3.22), we propose some more quantitative quantities to evaluate the significance of the first overtone. First, given the hyperparameter Δt_0 and the filter model $\mathcal{F}_{\rm tot}$, we can compute model evidence (marginal likelihood) via

$$P(d_t|\Delta t_0, \mathcal{F}_{\rm tot}) = \iint P\left(d_t|M_f, \chi_f, \Delta t_0, \mathcal{F}_{\rm tot}\right)\Pi(M_f, \chi_f) dM_f d\chi_f. \tag{3.36}$$

where $\Pi(M_f, \chi_f)$ is the prior distribution of M_f and χ_f. Here we simply assume a

flat prior in $M_f \in [35M_\odot, 140M_\odot]$ and $\chi_f \in [0, 0.99]$. By comparing the evidence across different choices of $\mathcal{F}_{\rm tot}$, one could figure out which QNMs are more likely to be present in the signal. In the top panel of Fig. 3.6, we plot $P(d_t|\mathcal{F}_{220}, \Delta t_0)$ and $P(d_t|\mathcal{F}_{22\{0,1\}}, \Delta t_0)$ as functions of Δt_0, for the same simulation data set with the injected signal. As a comparison, we also show the results obtained from the off-source noise (green and black curves). The boundary between the yellow and cyan regions stands for the time when the strain reaches its peak, i.e., $\Delta t_0 = 0$. We can see both the red and blue curves surge rapidly within the regime of $[-5, 0]$ ms, implying the onset of the ringdown stage. The evidence of the QNMs starts to grow even before the peak time $\Delta t_0 = 0$ because the width of our window $w = 0.08\,\mathrm{s} = 237 M_f^{\rm true}$ is longer than the ringdown duration—the full ringdown signal already falls in the window when $\Delta t_0 \in [-5, 0]$ ms. Consequently, the QNM model evidence continues to increase as the inspiral-merger part of the signal slides out of the window. Additionally, the evidence of the "two-QNM" model ($\mathcal{F}_{22\{0,1\}}$) is greater than the "one-QNM" one ($\mathcal{F}_{220}$) near the peak time ($\Delta t_0 \sim 0$), indicating that the "two-QNM" filter is preferred in the early stage of ringdown. To provide a more quantitative evaluation, we compute the Bayes factor by taking the ratio between the marginal likelihoods of a QNM model with and without the first overtone:

$$K_{221}(\Delta t_0) = \frac{P(d_t|\mathcal{F}_{22\{0,1\}}, \Delta t_0)}{P(d_t|\mathcal{F}_{220}, \Delta t_0)}. \tag{3.37}$$

The middle panel of Fig. 3.6 shows K_{221} as a function of Δt_0. We also show the off-source results (green dash-dot curve). As expected, K_{221} drops sharply near the peak time $\Delta t_0 \sim 0$ and gradually converges to the off-source result at later times. In the absence of the GW signal, the Bayes factor simply oscillates around unity across the entire time tested, which is also expected.

On the other hand, to characterize how well we can recover the remnant properties by applying our filters, we look for the maximum a posteriori (MAP) estimates of (M_f, χ_f). Following Ref. [55], we define a dimensionless quantity ϵ to describe the distance of the MAP values $(M_f^{\rm MAP}, \chi_f^{\rm MAP})$ to the true values $(M_f^{\rm true}, \chi_f^{\rm true})$, given by

$$\epsilon(\Delta t_0) = \sqrt{\left(\chi_f^{\rm MAP}(\Delta t_0) - \chi_f^{\rm true}\right)^2 + \left(\frac{M_f^{\rm MAP}(\Delta t_0) - M_f^{\rm true}}{M_f^{\rm true}}\right)^2}. \tag{3.38}$$

The bottom panel of Fig. 3.6 shows the resulting $\epsilon(\Delta t_0)$. For both QNM models, ϵ starts to decrease before the peak time $\Delta t_0 = 0$, for the same reason that the analysis

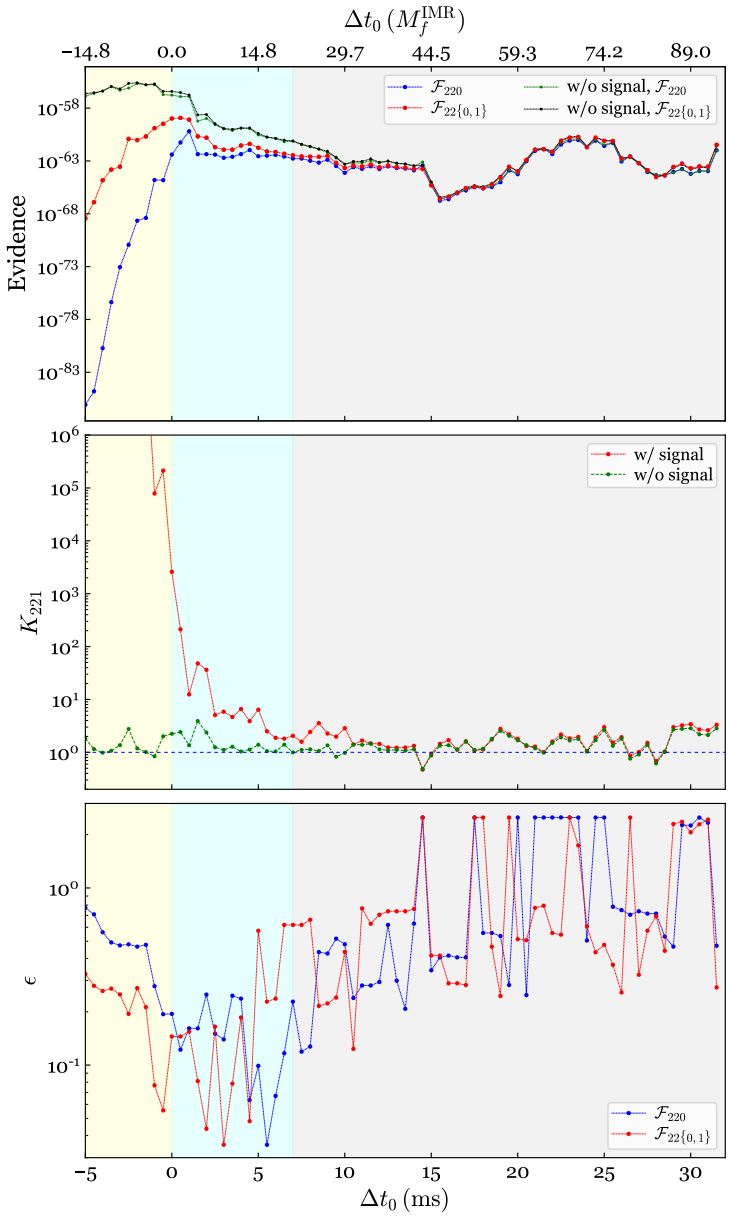

Figure 3.6: Model comparison at different Δt_0 for a GW150914-like NR waveform injected in band-limited white noise. Top: Model evidence as a function of Δt_0, evaluated by Eq. (3.36). The blue and red curves indicate the results after applying $\mathcal{F}_{220}$ (clean the fundamental mode only) and $\mathcal{F}_{22\{0,1\}}$ (clean the fundamental mode and the first overtone), respectively. The corresponding results computed with off-source noise are shown in green and black (almost indistinguishable). Middle: Bayes factor (K_{221}) of the existence of the first overtone over fundamental mode only (red curve), calculated by Eq. (3.37). As a comparison, the green curve shows the Bayes factor evaluated with the off-source noise. We take $K_{221} = 1$ as a benchmark, indicated by the horizontal dashed line. Bottom: Distance (ϵ) of the MAP values of M_f and χ_f to the true values, calculated by Eq. (3.38).

window we use is wider than the span of the ringdown signal. At $\Delta t_0 = 0$ and right after, ϵ obtained by using the filter $\mathcal{F}_{22,\{1,2\}}$ is smaller than that using $\mathcal{F}_{220}$, indicating the existence of the first overtone. After ~ 5 ms, ϵ from the filter $\mathcal{F}_{22,\{1,2\}}$ starts to increase as the first overtone decays away. By contrast, the fundamental mode still shows significance at $\Delta t_0 \sim 5.5\,\text{ms} = 16.3 M_f^{\text{true}}$, which leads to a much smaller ϵ. Beyond $\Delta t_0 = 7\,\text{ms} = 20.8 M_f^{\text{true}}$, no precise parameter information can be extracted from the fundamental mode anymore. Therefore we plot a boundary between the cyan and gray regions in the figure at $\Delta t_0 = 7\,\text{ms} = 20.8 M_f^{\text{true}}$ to indicate the time around which the whole ringdown signal fades away.

3.3.2 GW150914

After studying the injected signal, we now apply our method to analyzing GW150914 using the data collected in the first observing run of the two Advanced LIGO detectors (Hanford and Livingston) [78–80]. We adopt the same procedure described in Sec. 3.2.2 to condition the data, and the PSDs are evaluated with 32 s of the conditioned data (see Figs. 3.2c and 3.2d). Then, the PSDs are converted to the covariance matrix C_{ij} via Eqs. (3.28) and (3.29). Following [23, 30, 72], we take the inferred GPS time when the signal strain reaches its peak at geocenter, $t_{\text{start}} = 1126259462.4083$, and parameterize the analysis start time via $\Delta t_0 = t_0 - t_{\text{start}}$. The information on antenna patterns, polarization, and inclination angles are not needed within our framework, but we do need to time-shift the data to align the signals at the two detectors, based on the sky location of the event, right ascension $\alpha = 1.95$ rad and declination $\delta = -1.27$ rad [30]. To compute the joint posteriors of (M_f, χ_f) in Eq. (3.25), we fix the width of the ringdown window to $w = 0.2$ s, and we consider two types of the rational filter: $\mathcal{F}_{221}\mathcal{F}_{220}$ and $\mathcal{F}_{220}$.

The posterior distributions of M_f and χ_f at various Δt_0 are shown in Figs. 3.7, 3.8 and 3.9. The parameter estimation results obtained from the whole IMR signal, $M_f^{\text{IMR}} = 68.5\,M_\odot$ and $\chi_f^{\text{IMR}} = 0.69$ [30], are marked by the white plus signs. Again, the red-dashed contours show the 90% credible region evaluated by integrating Eq. (3.25), and the marginalized posterior distributions of M_f and χ_f are shown as 1D histograms (red curves in side panels). The results are qualitatively similar to the previous injection study. At the early stage of ringdown, the "two-QNM" results are more consistent with those from the whole IMR analysis, demonstrating the existence of the first overtone. At $\Delta t_0 = 0.77$ ms, the constraints obtained with $X = 1$ [Eq. (3.33)] start to degrade because of the first overtone decays. Meanwhile, there still exists a bias in the estimates of (M_f, χ_f) in the case of $X = 0$. This

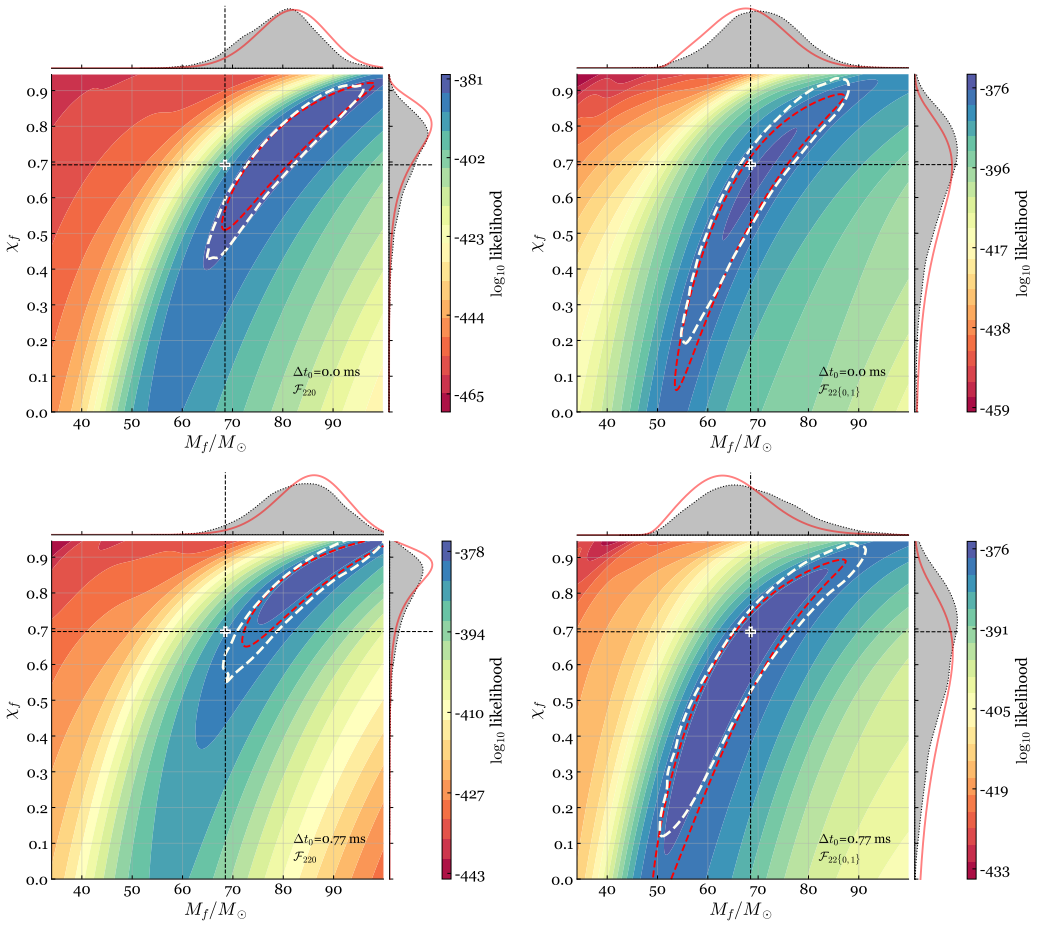

Figure 3.7: Joint posterior distributions of M_f and χ_f for GW150914 (data collected by the two Advanced LIGO detectors are used). Similar to Fig. 3.3. The top and bottom panels represent $\Delta t_0 = 0$ and 0.77 ms, respectively. The left and right panels show results from applying the filter for the fundamental mode only, $\mathcal{F}_{220}$, and the filter $\mathcal{F}_{221}\mathcal{F}_{220}$, respectively. The red-dashed contours display the 90% credible region by integrating our new joint posterior in Eq. (3.25); and the joint distribution is projected to the individual 1D space of χ_f and M_f (red curves in side panels), using Eq. (3.26). The white plus signs stand for the parameters estimated from the whole IMR waveform. The white dashed contours show the 90% credible region from the full-RD MCMC approach. The MCMC results are marginalized to the 1D distributions of M_f and χ_f, shown as the gray-shaded regions in side panels.

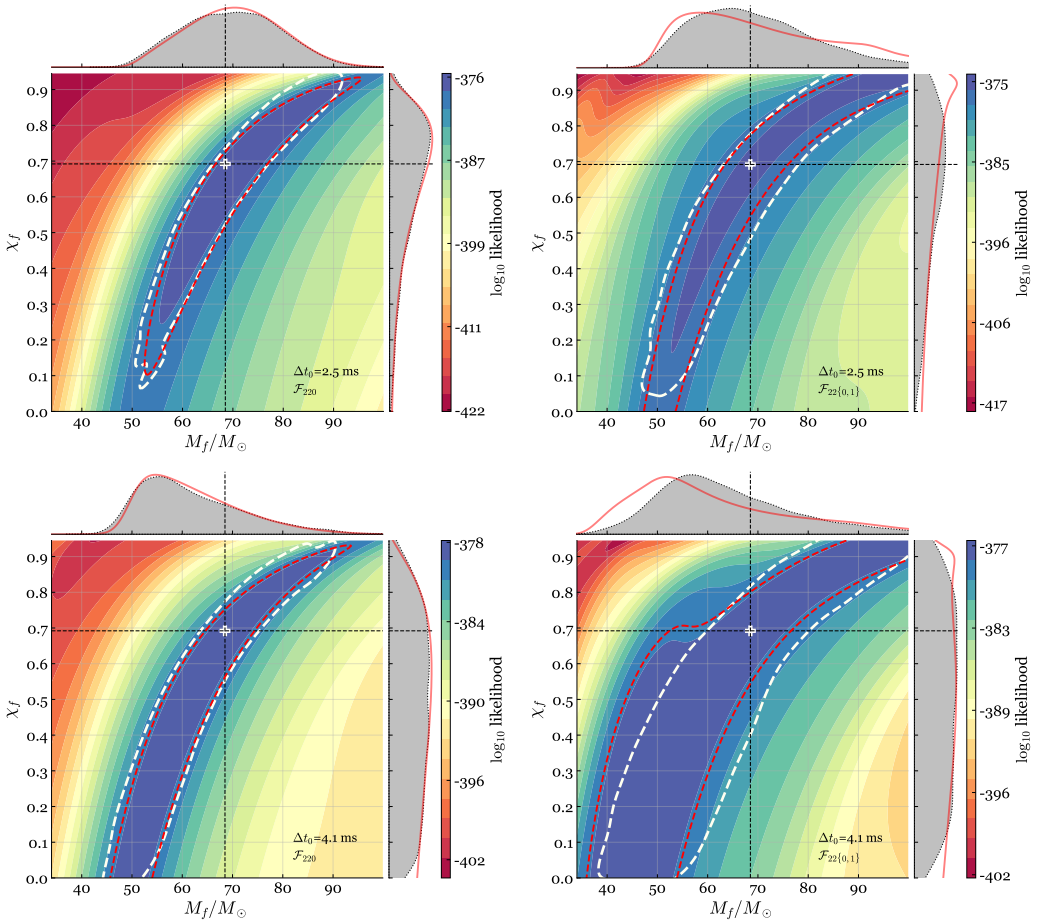

Figure 3.8: Joint posterior distributions of M_f and χ_f for GW150914. Fig. 3.7 continued; more values of Δt_0 are tested.

discrepancy between $X = 1$ and $X = 0$ becomes less significant as we move to $\Delta t_0 = 2.5\,\mathrm{ms}$, indicating that the contribution from the first overtone becomes negligible. From this time onward, the constraints of (M_f, χ_f) are worse when we apply $\mathcal{F}_{221}$ in addition to $\mathcal{F}_{220}$, since there is nearly none first overtone contribution and the extra filter of $\mathcal{F}_{221}$ reduces the amplitude of the fundamental mode. We can see the constraints keep degrading as the ringdown signal decays away.

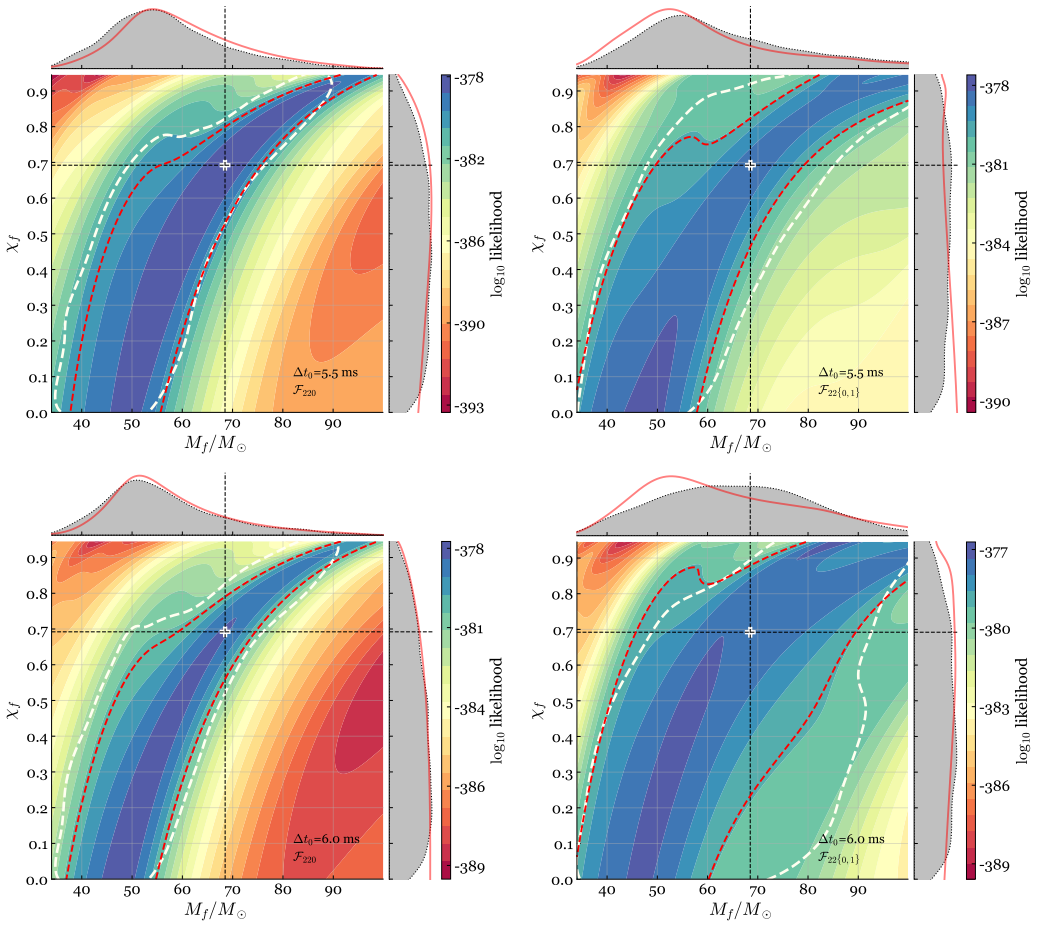

Figure 3.9: Joint posterior distributions of M_f and χ_f for GW150914. Fig. 3.7 continued; more values of Δt_0 are tested.

On the other hand, we also use MCMC to repeat the Bayesian analyses presented in [30], in which we assume the system is face-off [30], namely $\iota = \pi$. The 90% credible interval joint posterior distributions are enclosed by the white dashed contours. The corresponding 1D histograms for M_f and χ_f are represented by the gray-shaded regions. Similar to the previous injection study, the MCMC results are consistent with what we obtain from the rational filter.

For more quantitative conclusions, we use Eq. (3.36) to compute the model evidence $P(d_t|\mathcal{F}_{220}, \Delta t_0)$ and $P(d_t|\mathcal{F}_{22\{0,1\}}, \Delta t_0)$ as functions of Δt_0 and show results in the top panel of Fig. 3.10. Similar to the injection study, the two evidence curves surge quickly before the time when the signal strain reaches the peak, $\Delta t_0 = 0$, indicating the onset of the ringdown. The ratio K_{221} [Eq. (3.37)], shown in the middle panel of Fig. 3.10, reveals the relative importance of the first overtone. At the peak time $\Delta t_0 = 0$, the Bayes factor K_{221} is as high as 600. Then its value drops steeply within the first 2 ms. In the case of analyzing this real event, we take the window of $\Delta t_0 \in [15, 100]$ ms, a duration when the whole ringdown signal should have decayed, for background estimation. The mean value (~ 4.5) and the mean plus one standard deviation (~ 13.8) of K_{221} computed in the noise-only window are plotted as dashed and dash-dotted horizontal green lines, respectively, in the middle panel of Fig. 3.10. The curve of K_{221} intersects with the "mean $+1\sigma$" and "mean" lines at $\Delta t_0 = 1.9$ ms and 2.3 ms, respectively. Therefore we can conclude that the first overtone has become negligible around $\Delta t_0 \sim 2$ ms. Indeed, in the first row of Fig. 3.8, we see the remnant properties inferred from the fundamental mode alone are consistent with the IMR results at $\Delta t_0 = 2.5$ ms, a time when the first overtone is deemed vanishing.

Finally, we use Eq. (3.38) to evaluate the MAP estimations of (M_f, χ_f) and the distance to the IMR results ($M_f^{\rm IMR} = 68.5, \chi_f^{\rm IMR} = 0.69$). As shown in the bottom panel of Fig. 3.10, the results from the "two-QNM" filter are better than those from the fundamental-mode-only filter by one order of magnitude right after the peak time $\Delta t_0 \sim 0$. Beyond the time when the first overtone mostly decays ($\Delta t_0 \sim 2$ ms), the accuracy of parameter estimation using the $\mathcal{F}_{22\{0,1\}}$ filter significantly degrades. Regarding the results from using the "one-QNM" filter $\mathcal{F}_{220}$, ϵ surges after $\Delta t_0 \sim 6$ ms, indicating the time when the fundamental mode also disappears.

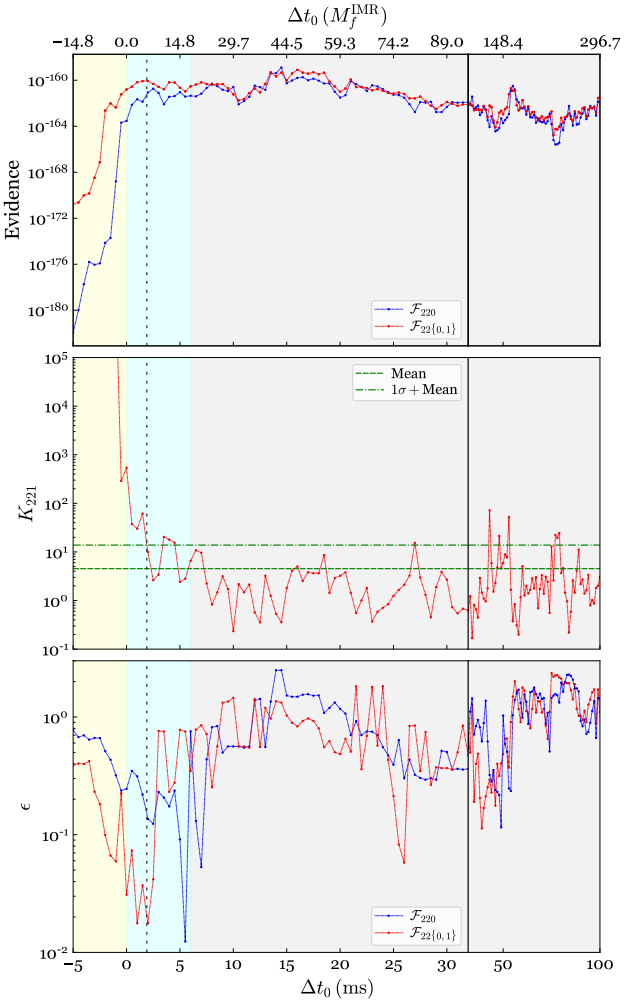

Figure 3.10: Model comparison at different Δt_0 for GW150914. Similar to Fig. 3.6. Top: Model evidence as a function of Δt_0. The blue and red curves indicate the results for applying $\mathcal{F}_{220}$ (clean the fundamental mode only) and $\mathcal{F}_{22\{0,1\}}$ (clean the fundamental mode and the first overtone), respectively. Middle: Bayes factor (K_{221}) of the existence of the first overtone over fundamental mode only (red curve). The horizontal dashed and dash-dotted green lines indicate the mean value and the standard deviation within the regime of $\Delta t_0 \in [15, 100]$ ms, respectively. The red Bayes factor curve intersects the "1σ+mean" line at a time of $\Delta t_0 = 1.9$ ms, indicating the time when the first overtone becomes negligible (vertical dashed line). Bottom: Distance (ϵ) of the MAP values of M_f and χ_f to the values estimated from the whole IMR signal.

3.4 A mixed approach to black-hole spectroscopy

We have demonstrated that the rational filter provides a powerful tool for black-hole spectroscopy by cleaning any given QNMs from the data and evaluating a simple and efficient likelihood function for remnant mass and spin [Eq. (3.22)]. One limitation

of this new method is that we do not obtain information of mode amplitudes and phases in the analysis. By combining our filters with the conventional MCMC method, we could take advantage of both and build another mixed approach for BH spectroscopy: after removing a subset of the QNMs using the rational filters, we analyze the filtered data with a ringdown model that consists of the uncleaned QNMs, using the MCMC approach. The advantage of this hybrid approach is as follows. The conventional full-RD MCMC analysis (without filter) for subdominant QNMs is likely to be biased when the strongest mode is present, especially at low-SNR regime. The mixed approach allows us to clean the most dominant mode and thus eliminate potential impacts from it when carrying out parameter estimations using the MCMC method. In addition, we can carry out a consistency check by comparing the mode amplitudes and remnant properties inferred from the subdominant QNMs (after the strongest mode is cleaned by the filter) to those obtained from the unfiltered data (when the strongest mode is present). When we observe events with high ringdown SNRs, we can even clean a set of stronger modes and study the remaining weak ones. In this way, we are able to test the no-hair theorem from a new perspective.

Below, we detail the analysis procedure and results using this mixed approach. In Sec. 3.4.1, we study the NR signal injected into Gaussian noise. In Sec. 3.4.2, we analyze GW150914.

3.4.1 NR waveform injection

We first analyze the injection of the NR waveform, focusing on the estimates of mode amplitudes and the remnant properties. Further discussion about the features seen in the mixed approach is provided afterwards.

3.4.1.1 *Estimate mode amplitudes*

With the NR signal injected into Gaussian noise, we first choose a start time for the analysis, $\Delta t_0 = 1.5\,\mathrm{ms} = 4.2 M_f$, and use the conventional full-RD MCMC method to fit the unfiltered simulation data with a two-QNM (ω_{220} and ω_{221}) ringdown template. The analysis is performed with the Python package ringdown [23, 72]. The posterior distributions of the amplitudes of the fundamental mode, A_0, and the first overtone, A_1, are plotted as the blue shaded regions in Figs. 3.11a and 3.11b. Meanwhile, we compute what the values of A_0 and A_1 should be in the injected signal by decomposing the NR waveform (the $l = m = 2$ harmonic) into a superposition of the fundamental mode and the first overtone with a least-square

fit. Here we include up to the first overtone for the least-square fit, to be consistent with the templates used in the MCMC analysis, even though Giesler *et al.* [55] points out more overtones are needed to model ringdown at such an early stage ($\Delta t_0 = 1.5\,\mathrm{ms} = 4.2M_f$). The lack of higher overtones in the least-square fit leads to a bias in the estimates of the mode amplitudes. Nevertheless, it is a fair comparison between the MCMC results and the "should-be" values (vertical dash-dotted lines in Figs. 3.11a and 3.11b) obtained from the least-square fit. We find the MCMC posteriors are consistent with the values indicated by the vertical lines, $A_0 = 148$ and $A_1 = 143$. In fact, the same feature has been pointed out by Finch and Moore (see Fig. 7 and discussions in Sec. III B in [27]).

Table 3.1: Combinations of filters and fitting templates for the mixed approach. We have two choices of the filter: $\mathcal{F}_{220}$ and $\mathcal{F}_{221}$, and two choices of the fitting template: two-QNM (ω_{220}&ω_{221}) template, ignorant of mode cleaning, and one-QNM template for the remaining mode.

Filter \ Template	two-QNM	one-QNM
$\mathcal{F}_{220}$	ω_{220} & ω_{221}	ω_{221}
$\mathcal{F}_{221}$	ω_{220} & ω_{221}	ω_{220}

We then use the mixed approach. There are four options from the combinations of the two choices of the filters and two choices of the fitting templates (see Table 3.1). We can choose to clean the fundamental mode (the first overtone) by applying the filter $\mathcal{F}_{220}$ ($\mathcal{F}_{221}$). After the filtering, we also have two choices of the ringdown template to fit the data and run MCMC: we can (a) continue to use the two-QNM model, assuming both modes exist in the data and we have no knowledge of the mode cleaning (b) use a single-mode template for the remaining QNM. We first apply the filter $\mathcal{F}_{220}$, built from the true remnant mass and spin, to remove the fundamental mode. Then we use the two-QNM template to run MCMC against the filtered data. The posteriors of A_0 and A_1 are plotted as the green dashed curves in Figs. 3.11a and 3.11b, respectively. After applying $\mathcal{F}_{220}$, it is expected that there is no ω_{220} component left in the filtered data. Indeed, we see the distribution of A_0 is pushed close to 0, demonstrating that the fundamental mode no longer exists in the data. By contrast, the posterior distribution of A_1 is only slightly impacted by the filtering (compare the green dashed curve to the blue-shaded region in Fig. 3.11b). We emphasize that, as discussed in Sec. 3.2.1, the amplitude of the first overtone is reduced by the filter $\mathcal{F}_{220}$ by a factor of $B^{221}_{220} = 2.053$ [Eq. (3.11)]. In Fig. 3.11b,

the green dashed curve is obtained by multiplying the original A_1 distribution from MCMC by a factor of $B^{220}_{221} = 2.053$, so that we can make a fair comparison to the blue distribution. On the other hand, we also fit the filtered data (ω_{220} component is cleaned) with the single-QNM model, composed of the first overtone alone, which gives the distribution shown in yellow in Fig. 3.11b. The estimate is more constrained than that from the two-QNM model, and the MAP value is closer to the "injected," although biased, mode amplitude (the vertical dash-dotted line).

Similarly, we apply $\mathcal{F}_{221}$ to the original simulation data to clean the first overtone. Fitting with the two-QNM template, the posteriors of A_0 and A_1 are plotted as black dashed curves in Figs. 3.11a and 3.11b. This time, A_1 is consistent with 0, as expected; whereas the MAP value of A_0 is mildly impacted [again, after multiplying the reduction factor $B^{221}_{220} = 2.053$ to the original distribution output by MCMC; see Eq. (3.11)]. If we use the one-QNM template of the fundamental mode, the estimated A_0 (the red shaded region in Fig. 3.11a) is more constrained, and the MAP value is closer to the injected mode amplitude (the vertical dash-dotted line).

3.4.1.2 *Estimate remnant properties*

We now estimate the remnant properties (M_f and χ_f) after a certain mode is cleaned. Here we use the one-QNM template to fit the filtered data and show the parameter estimation results obtained from MCMC in Fig. 3.11c (at $\Delta t_0 = 1.5\,\mathrm{ms} = 4.2M_f$, to be consistent with Figs. 3.11a and 3.11b), i.e., we fit for the first overtone after applying $\mathcal{F}_{220}$ (yellow) and fit for the fundamental mode after applying $\mathcal{F}_{221}$ (red). The two contours for each case correspond to the 90% and 10% credible intervals. For comparison, the estimates obtained by the full-RD MCMC method without applying the filters are plotted as blue dashed contours. The green plus sign stands for the true values. The posterior distributions obtained solely from the first overtone (yellow) are still informative, consistent with the results from the fundamental mode (red) and the full-RD MCMC approach (blue), albeit less constrained.

As we show previously, there is inevitably a bias in the estimates of the mode amplitudes at an early time of ringdown ($\Delta t_0 = 1.5\,\mathrm{ms} = 4.2M_f$) due to the lack of higher overtones in the model. In Fig. 3.11c, however, we see the remnant mass and spin inferred from the fundamental mode (red), the first overtone (yellow), and both modes (blue) are all consistent with the true NR values, indicating that the constraints of M_f and χ_f are less impacted by the residuals contributed by higher overtones and even the merger signal (if there is any). On the other hand, as shown

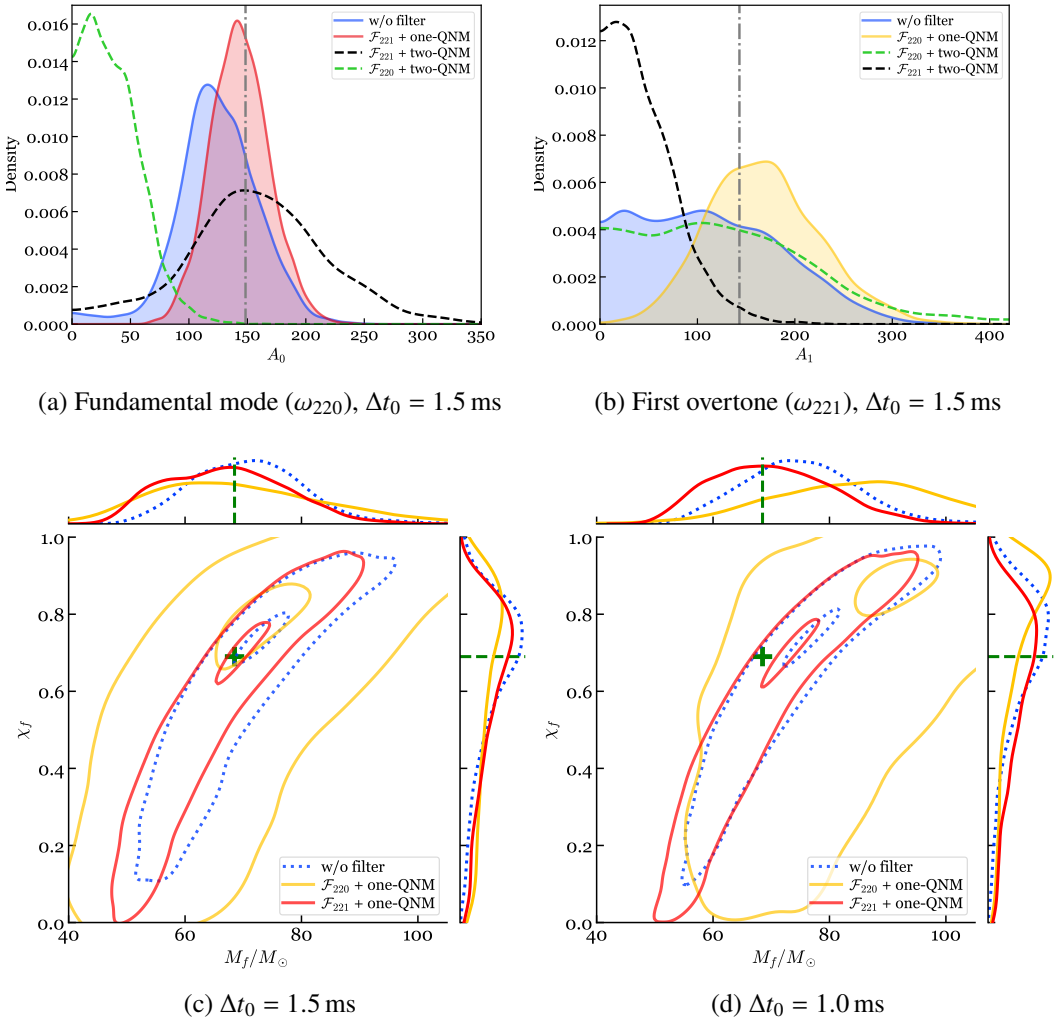

(a) Fundamental mode (ω_{220}), $\Delta t_0 = 1.5$ ms

(b) First overtone (ω_{221}), $\Delta t_0 = 1.5$ ms

(c) $\Delta t_0 = 1.5$ ms

(d) $\Delta t_0 = 1.0$ ms

Figure 3.11: Estimates of the mode amplitudes and BH properties for the injected signal using the mixed approach. The top panels display the posterior distributions of (a) the fundamental mode amplitude A_0, and (b) the first overtone amplitude A_1, evaluated at $\Delta t_0 = 1.5$ ms under various filtering conditions. The blue-shaded distributions are obtained via the full-RD MCMC method (without applying the filter). The green dashed curves correspond to removing the ω_{220} mode using $\mathcal{F}_{220}$ first and fitting the data with a two-QNM (ω_{220} and ω_{221}) signal template. The same $\mathcal{F}_{220}$-filtered data are also fitted with the one-QNM (ω_{221}) signal template, resulting in the A_1 distribution shown in yellow in (b). Similarly, the black dashed curves correspond to removing the ω_{221} mode using $\mathcal{F}_{221}$ first and fitting the data with a two-QNM (ω_{220} and ω_{221}) signal template. The $\mathcal{F}_{221}$ filtered data are then fitted with the one-QNM (ω_{220}) signal template, resulting in the A_0 distribution shown in red in (a). The two vertical lines indicate the true values of $A_0 = 148$ and $A_1 = 143$, computed from the NR waveform. The bottom panels show the posterior distributions of M_f and χ_f estimated at (c) $\Delta t_0 = 1.5$ ms, and (d) $\Delta t_0 = 1.0$ ms. The yellow curves indicate the results obtained by fitting the ω_{220}-cleaned data with a ω_{221}-only template. The red curves are the results obtained by fitting the ω_{221}-cleaned data with a ω_{220}-only template. The blue dashed curves are the results from the full-RD MCMC analysis without applying any filter. The two contours in each color correspond to the 90% and 10% credible intervals.

in Fig. 3.11d, we do see the remnant properties are less consistent with the true value at an earlier time $\Delta t_0 = 1.0\,\mathrm{ms} = 2.8M_f$. In particular, the constraints from the first overtone (yellow) deviate more significantly from the true value than the other two estimates.

Finally, we note that in terms of estimating the remnant properties (M_f and χ_f) using the filtered waveform when certain modes are cleaned, e.g., Figs. 3.11c and 3.11d, the results can also be obtained by purely using the filters, instead of running the MCMC analysis. We provide the details in Appendices 3.7 and 3.8.

3.4.1.3 *Further discussions*

We have demonstrated the statistical significance of the first overtone in the injected ringdown signal. Given that our two-QNM fitting is carried out at an early time ($\Delta t_0 = 1.5\,\mathrm{ms} = 4.2M_f$), criticisms might be raised since we do not include higher overtones at such an early time close to the signal strain peak [55]. How do we know the results are not biased by other residual effects? We discuss this from two aspects: (a) estimates of the remnant properties, and (b) estimates of the mode amplitudes.

First, the measurement of a mode frequency (or equivalently, the estimates of M_f and χ_f) needs sufficient mode cycles (duration) to accumulate a high-enough SNR. A missing mode does not bias the measurement when its cumulative SNR is small. To quantify the impact of the residual, we carry out a least-square fit to the $l = m = 2$ harmonic of the GW150914-like NR waveform using a two-QNM model ($\omega_{220} + \omega_{221}$). At an early starting time, the fitting residual comes from the modes that are not included in the template (higher overtones). We compute the cumulative SNRs of the constructed first overtone and the fitting residual via

$$\mathrm{SNR}\,(\Delta t_0) = \sqrt{\int_{\Delta t_0}^{90M_f} |h(t)|^2 dt}. \tag{3.39}$$

The ratio between the SNR of the first overtone and that of the residual as a function of Δt_0 is shown in Fig. 3.12. We see the cumulative SNR of the first overtone is ~ 5 times larger than that of the residual even starting from the peak of the waveform ($\Delta t_0 = 0$). The ratio continues to grow when $\Delta t_0 < 17M_f$, because the residual modes decay faster and the waveform becomes more consistent with the two-QNM model. After $17M_f$, the residual hits the error floor of the NR simulation and remains at that level. Thus, starting from $17M_f$, the ratio decreases exponentially as the first overtone decays away. Note that the maximum at $\Delta t_0 = 17M_f$ is close

to the starting time of the two-QNM regime at $\Delta t_0 = 19M_f$ estimated by Giesler *et al.* (see the second row of Table I in [55]). Here we convert the mass unit from the total binary mass $M_{\rm tot}$ in [55] to the remnant mass M_f using $M_f = 0.95M_{\rm tot}$.

In Bayesian analysis, the fact that the cumulative SNR of the first overtone is a few factors stronger than the residual modes allows us to perform a two-QNM MCMC analysis and infer the remnant properties from the first overtone right after the signal peak, when the full ringdown waveform has a low SNR and the systematic error caused by the residual modes is smaller than the uncertainties of the inferred parameters. In such a low-SNR regime, we might want to push our analysis as early as possible to increase the cumulative SNR of the first overtone, as long as the SNR contribution from the residual modes stays low, e.g., Fig. 3.11c ($\Delta t_0 = 1.5\,{\rm ms} = 4.2M_f$). However, as Fig. 3.12 suggests, the residual modes play a stronger role at earlier times, and thus we should be careful and avoid conducting the analysis too close to the signal peak, otherwise the residual modes can lead to systematic bias, such as the results shown in Fig. 3.11d. On the other hand, if we detect a high-SNR ringdown signal, the contribution of the residual modes becomes more significant, and leads to a bias non-negligible compared to the parameter uncertainty range. In that case, following Fig. 3.12, the analysis should be moved to later times (although still earlier than what the pure NR waveform suggests) to reduce the systematic bias caused by the residual modes. In an extreme case, when the ringdown signal becomes strong enough, the analysis reduces to the least-square fitting of the NR waveform. Then we can choose the maximum point in Fig. 3.12 as the starting time to perform the two-QNM fit, just as what Giesler *et al.* [55] did. In summary, the starting time of the analysis using a two-QNM model should be chosen based on the signal SNR; the higher the SNR, the later the starting time (in the range from $\Delta t_0 = 0$ to the maximum point in Fig. 3.12).

That said, in Figs. 3.11a and 3.11b, the mode amplitudes inferred from the Bayesian analysis are still biased, as mentioned by Finch and Moore [27]. This is because the measurement of a mode amplitude depends more heavily on the first mode cycle than the whole cumulative SNR. Therefore, the estimate of the mode amplitude is more sensitive to the existence of the residual modes at an early stage. Nevertheless, the consistency among the "$\mathcal{F}_{220}$ + one-QNM" test, the conventional full-RD analysis, and the NR least-square fit (Figs. 3.11b) implies that after cleaning the fundamental mode, the remaining signal is stably consistent with the first overtone[3]. In other

[3]This is not to be confused with the noise fluctuations raised by Cotesta *et al.* [28].

words, at a relatively early time, e.g., $\Delta t_0 = 1.5\,\mathrm{ms} = 4.2 M_f$ in Fig. 3.11b, the data-driven analysis leads to a measurement of an effective first overtone, with a correct mode frequency and decay rate albeit a biased mode amplitude [27].

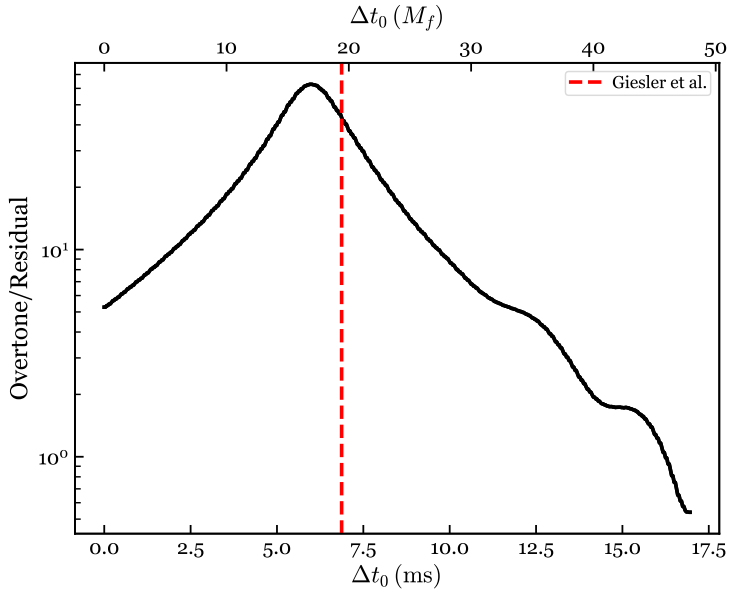

Figure 3.12: Ratio between the cumulative SNRs of the first overtone and the fitting residual as a function of Δt_0. The $l = m = 2$ harmonic of the GW150914-like NR waveform is fitted with a two-QNM model $(\omega_{220} + \omega_{221})$ at different starting times. The residual is the difference between the $l = m = 2$ harmonic in the NR waveform and the fitted two-QNM model template. At early times, the residual corresponds to the systematic bias due to the missing higher overtones in the model template. The cumulative SNRs are computed via Eq. (3.39).

3.4.2 GW150914

We now apply the mixed approach to GW150914. Similar to the NR simulation, the full-RD MCMC fitting and the four filtering scenarios listed in Table 3.1 are tested; the results are shown in Fig. 3.13. For mode cleaning, we use the BH properties estimated from the IMR signal [30], $M_f^{\mathrm{IMR}} = 68.5$, $\chi_f^{\mathrm{IMR}} = 0.69$, to build the filter. The MCMC fitting is conducted at a start time of $\Delta t_0 = 0.77\,\mathrm{ms}$ and the window length of $w = 0.2\,\mathrm{s}$. In Figs. 3.13a and 3.13b, the estimates of A_0 and A_1 under all scenarios qualitatively agree with the injection study in Sec. 3.4.1 (Fig. 3.11). These results demonstrate: (1) the fundamental mode or the first overtone can be successfully cleaned from the ringdown of GW150914 by the filters, and (2) the M_f and χ_f values obtained from the IMR signal are consistent with the evolution of the QNMs in ringdown (so that the modes can be correctly cleaned).

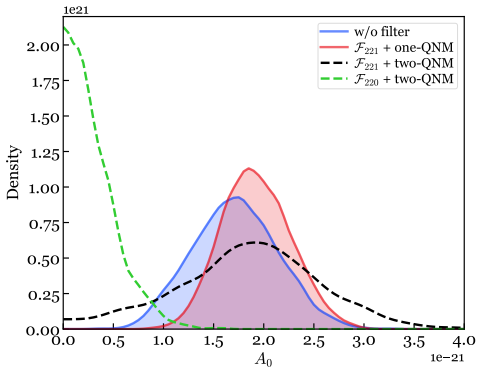

(a) Fundamental mode (ω_{220}), $\Delta t_0 = 0.77$ ms

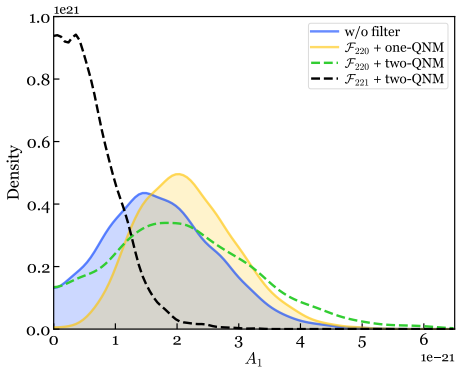

(b) First overtone (ω_{221}), $\Delta t_0 = 0.77$ ms

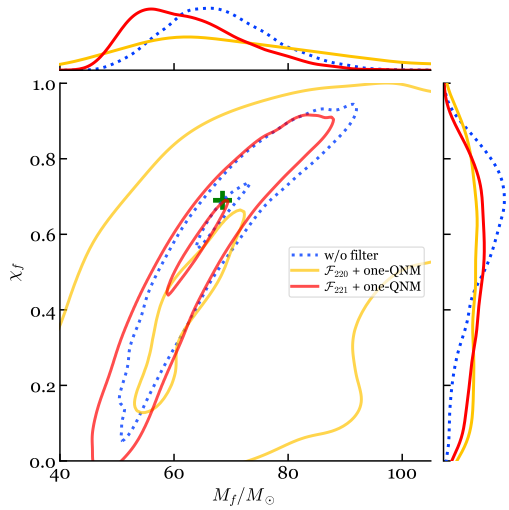

(c) $\Delta t_0 = 0.77$ ms

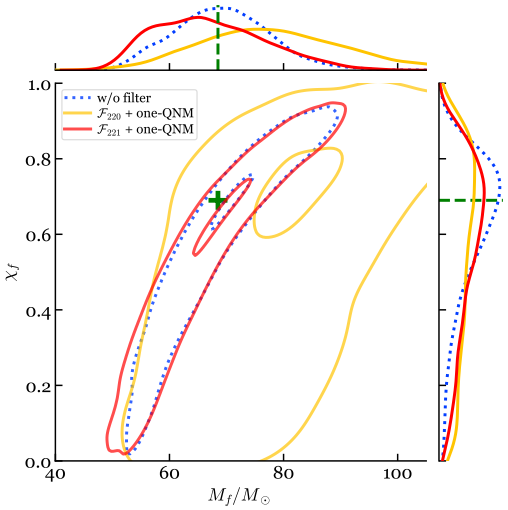

(d) $\Delta t_0 = 0.1$ ms

Figure 3.13: Estimates of the mode amplitudes and BH properties for GW150914 using the mixed approach. Similar to Fig. 3.11. See Fig. 3.11 caption for detailed descriptions. Note that different start times are used here: $\Delta t_0 = 0.77$ ms in Fig. 3.13a, 3.13b and 3.13c, and $\Delta t_0 = 0.1$ ms in Fig. 3.13d.

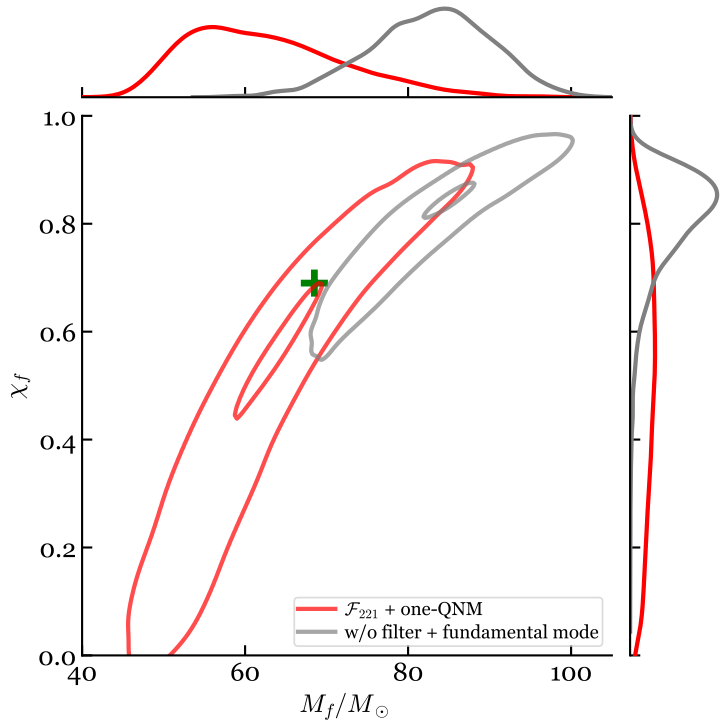

Figure 3.14: Posterior distributions of M_f and χ_f for GW150914 estimated at $\Delta t_0 = 0.77$ ms. The gray contours are obtained from the conventional full-RD MCMC analysis, where the unfiltered data (without mode cleaning) are fitted with the fundamental-mode-only template. The red contours are the same as the ones in Fig. 3.13c, where we first apply the filter $\mathcal{F}_{221}$ to remove the first overtone, and then fit the filtered data with the template of the fundamental mode.

In Fig. 3.13c, we show the estimates of M_f and χ_f at the start time $\Delta t_0 = 0.77$ ms under the three scenarios, similar to the injection case shown in Fig. 3.11c. The constraints obtained from the unfiltered and the filtered data generally agree, and are consistent with the estimates obtained from the IMR signal. In particular, we note that for the chosen start time, one needs to include both modes ω_{220} and ω_{221} to perform the usual full-RD MCMC analysis (blue-dashed contours), fitting with only the fundamental mode ω_{220} leads to a strong bias in the inferred M_f and χ_f. The gray contours in Fig. 3.14 display the corresponding joint posterior of M_f and χ_f when the first overtone is omitted from the MCMC analysis (also see Fig. 3 of Ref. [30]). But the discrepancy with the IMR results is reduced if we first apply the filter $\mathcal{F}_{221}$ to clean the first overtone ω_{221} (red contours in Fig. 3.14).

On the other hand, the yellow contours in Fig. 3.13c represent the posterior inferred from the first overtone alone. We see the estimates are still informative, although less constrained than the "$\mathcal{F}_{221}$+one-QNM" case. If we start the analysis at an

earlier time, e.g., $\Delta t_0 = 0.1$ ms (Fig. 3.13d), the constraints obtained from the first overtone alone deviate more from the IMR results, despite the fact that the contour of the 90% credible intervals is still consistent with the IMR result. Presumably, the shift is caused by the existence of other signal features in addition to the first overtone (e.g., higher overtones, similar to Fig. 3.11d), although no evidence for the existence of higher overtones is found in the ringdown of GW150914. For more choices of Δt_0, we focus on the marginalized posteriors of M_f and χ_f obtained from the "$\mathcal{F}_{220}$+one-QNM" scenario. As shown in Fig. 3.15, the posterior distribution of M_f gradually shifts toward smaller values and moves closer to the IMR result (the vertical dashed line) when $\Delta t_0 \in [0, 1]$ ms. For later times ($\Delta t_0 \gtrsim 1$ ms), the distribution widens and becomes less informative. On the other hand, the posterior distribution of χ_f flattens quickly as Δt_0 increases and becomes consistent with the prior.

3.5 Conclusion

In this chapter, we incorporate the novel rational filter [64] into a Bayesian framework (outlined in our companion paper [68]), and obtain several pieces of evidence for the existence of the first overtone in the ringdown of GW150914. We first demonstrate that the rational filter has no impact on the statistical properties of the noise (Gaussianity, stationarity, and PSDs). We then construct a 2D likelihood function that depends only on the mass and spin of the remnant BH and implement an efficient algorithm to obtain the posteriors of mass and spin without running MCMC. We use an NR injection and the GW150914 event to demonstrate that the posteriors obtained using our method are consistent with those from the full-RD MCMC approach. By applying our method to the data of GW150914 near the peak of the strain, we confirm the conclusion of Ref. [30]: The inferred remnant BH properties are more consistent with the IMR results when the first overtone is included; the contribution from the first overtone gradually fades away at later times.

Next, we compute the model evidence for filters built with different sets of QNM(s) by integrating the new likelihood function over the 2D parameter space. The evidence depends on the fitting start time, showing a sharp rise around the onset of a ringdown signal, which in turn agnostically reflects the starting time of the corresponding QNM(s). The ratio between two evidence values from two filters with different sets of QNM(s) indicates the Bayes factor for a QNM model. For GW150914, we find a Bayes factor of 600 for the model with the first overtone over the fundamental-mode-only model at the inferred strain peak. This Bayes factor

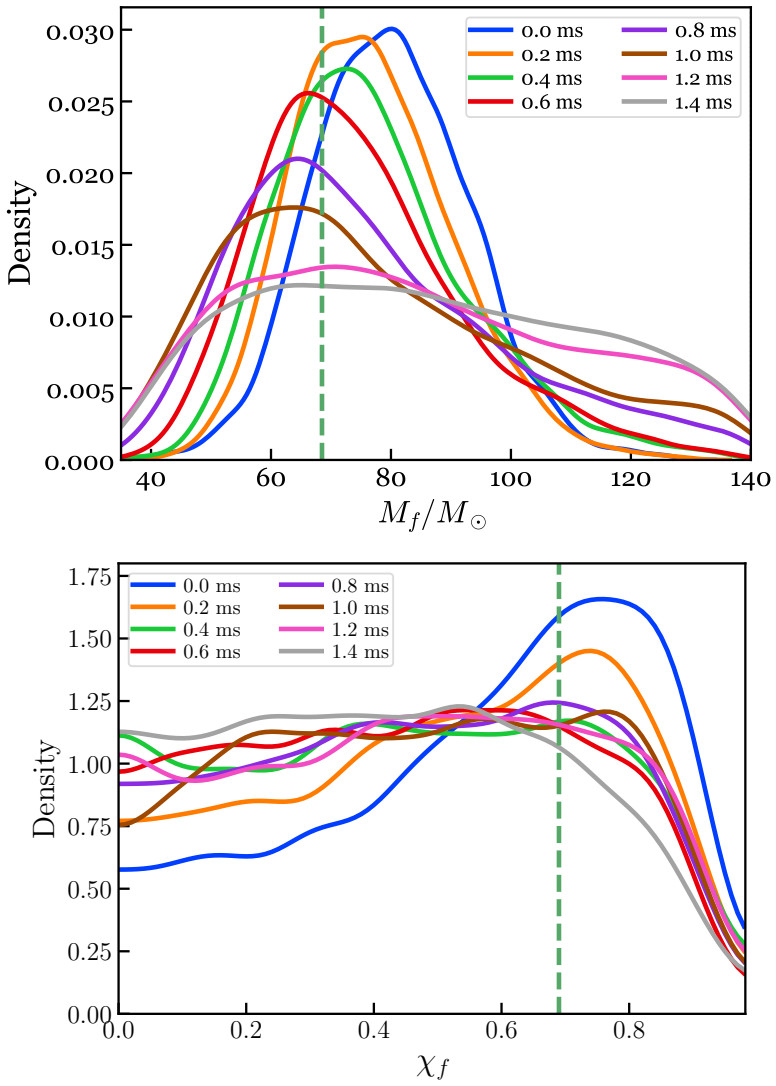

Figure 3.15: Posterior distributions of M_f (top) and χ_f (bottom) solely inferred from the first overtone in the ringdown of GW150914, at different Δt_0 times. We first apply the filter $\mathcal{F}_{220}$ to remove the fundamental mode, and then fit the filtered data with the template of the first overtone. We set uniform priors in the ranges of $M_f \in [35M_\odot, 140M_\odot]$ and $\chi_f \in [0, 0.99]$ (as shown in the horizontal axes in the plot). The vertical dashed lines indicate the estimates obtained from the full IMR signal.

decreases and levels off at later times.

Finally, we combine the mode-cleaning procedure using the rational filter with the usual MCMC method to build a mixed approach for BH spectroscopy. After cleaning the fundamental mode in the GW150914 data and fitting the filtered data using MCMC, we find the posterior of the fundamental mode amplitude gets close to zero, confirming the successful subtraction of the fundamental mode. On the other

hand, the amplitude of the first overtone is barely impacted. We also use the mixed approach to infer the remnant BH mass and spin from only the fundamental mode and only the first overtone. The results from the first overtone alone are still informative, showing consistent constraints on M_f with the full-IMR and fundamental-mode-only analyses. The recovery of the remnant BH properties (mass and mode amplitudes) from the first overtone alone serves as a more direct piece of evidence supporting the existence of the first overtone, in addition to other indicators (e.g., the Bayes factor).

This novel framework is not only powerful at revealing subdominant QNMs; it also has superior computational efficiency compared to the existing MCMC approach. In the GW150914 analysis, it takes $\sim$ 8 seconds on a general laptop to produce a low-resolution 2D M_f–χ_f posterior distribution for the remnant BH that is good enough to reveal the key features (the evaluation of the likelihood function in Eq. (3.22) for each pair of M_f and χ_f takes milliseconds). For a production run with a high resolution, e.g., a panel in Fig. 3.7, it takes $\sim$ 3 minutes on a cluster (a single node with 24 cores). The performance can be further improved by fully parallelizing the calculation, since the likelihood evaluation for each pair of mass and spin is completely independent. In addition, the code's efficiency is not impacted by including more QNMs, given that multiple filters can be applied simultaneously [Eq. (3.6)]. On the contrary, including more QNMs significantly increases the computing cost of the full-RD MCMC calculation, because the dimension of the parameter space is largely increased.

With this framework, the ringdown analysis can be easily extended to investigate more subdominant modes in addition to overtones. Future work is being planned to investigate another controversial event, GW190521 [31, 32], and new detections in the upcoming O4 run. In addition, here we combine and align the data at two LIGO detectors based on the constraint of the event sky location. It is worth studying whether we could analyze the data from each detector individually and use the common features in the results, e.g., the time when the evidence rises sharply (see Fig. 3.10), to help constrain the sky position of an event.

3.6 Appendix: Comparison between the new and conventional full-RD MCMC likelihoods in a high-SNR limit

In this section, we discuss the relationship between our new and full-RD MCMC likelihoods. For simplicity, we assume there is only one complex-valued QNM

component in time-series data

$$d = n + h_0, \tag{3.40}$$

with n being additive noise. The ringdown signal h_0 is given by

$$h_0 = A_0 e^{-i\omega_0 t}\Theta(t), \tag{3.41}$$

where ω_0 is a QNM frequency, A_0 is a complex-valued amplitude, and $\Theta(t)$ is the Heaviside step function. Then we use a QNM template,

$$h_x = A_x e^{-i\omega_x t}, \tag{3.42}$$

to fit the data. After inserting Eqs. (3.40) and (3.42) into Eq. (3.23), the full-RD MCMC likelihood reads

$$\begin{aligned}\ln P^{\mathrm{Trad}}(d|A_x,\omega_x) &= -\frac{1}{2}\langle d-h_x|d-h_x\rangle \\ &= -\frac{1}{2}\langle n+h_0-h_x|n+h_0-h_x\rangle.\end{aligned} \tag{3.43}$$

On the other hand, we apply the filter

$$\mathcal{F}_{lmn}(\omega;\omega_x) = \frac{\omega-\omega_x}{\omega-\omega_x^*}, \tag{3.44}$$

to construct the new likelihood. Based on our discussions in Sec. 3.2, the filtered ringdown signal h_0 reads

$$h_0^F = B_x^0 h_0, \quad \text{when} \quad t > 0 \tag{3.45}$$

with

$$B_x^0 = \frac{\omega_0-\omega_x}{\omega_0-\omega_x^*}. \tag{3.46}$$

In consequence, our new likelihood in Eq. (3.22) becomes

$$\ln P^F(d|\omega_x) = -\frac{1}{2}\langle n^F + h_0^F|n^F + h_0^F\rangle. \tag{3.47}$$

3.6.1 Expectation values

In a high-SNR limit, the leading order corresponds to the expectation values of the two likelihoods. For the full-RD MCMC likelihood in Eq. (3.43), we obtain

$$\ln P^{\mathrm{Trad}}(d|A_x,\omega_x) = -\frac{1}{2}\langle h_0-h_x|h_0-h_x\rangle. \tag{3.48}$$

To evaluate the inner product $\langle\cdot|\cdot\rangle$, we set the autocovariance C_{ij} to δ_{ij} for simplicity, which leads to

$$\begin{aligned}&\ln P^{\rm Trad}\left(d|A_x,\omega_x\right)\\&=\left[\frac{|A_0|^2}{4{\rm Im}\,\omega_0}+\frac{|A_x|^2}{4{\rm Im}\,\omega_x}-{\rm Im}\frac{A_0A_x^*}{\omega_x^*-\omega_0}\right].\end{aligned}\tag{3.49}$$

Marginalizing $P^{\rm Trad}$ over A_x

$$P_m^{\rm Trad}=\int P^{\rm Trad}d{\rm Re}\,A_x d{\rm Im}\,A_x,\tag{3.50}$$

yields

$$\ln P_m^{\rm Trad}\left(d|\omega_x\right)=\frac{|A_0|^2}{4{\rm Im}\,\omega_0}\left(1-\frac{4{\rm Im}\omega_0{\rm Im}\omega_x}{|\omega_0-\omega_x^*|^2}\right).\tag{3.51}$$

On the other hand, the leading order of the filtered likelihood is given by [Eq. (3.47)]

$$\begin{aligned}\ln P^F\left(d|\omega_x\right)&=-\frac{1}{2}\langle h_0^F|h_0^F\rangle=\frac{|A_0|^2}{4{\rm Im}\,\omega_0}|B_x^0|^2\\&=\frac{|A_0|^2}{4{\rm Im}\,\omega_0}\left|\frac{\omega_0-\omega_x}{\omega_0-\omega_x^*}\right|^2.\end{aligned}\tag{3.52}$$

The equivalence between $\ln P_m^{\rm Trad}\left(d|\omega_x\right)$ and $\ln P^F\left(d|\omega_x\right)$ can be established via an identity

$$1-\frac{4{\rm Im}\omega_0{\rm Im}\omega_x}{|\omega_0-\omega_x^*|^2}\equiv\left|\frac{\omega_0-\omega_x}{\omega_0-\omega_x^*}\right|^2.\tag{3.53}$$

3.6.2 Cramér–Rao bound

We now estimate the Cramér–Rao bound in terms of the Fisher matrix. For a complex template h_x, the Fisher matrix of the full-RD MCMC approach is given by

$$M_{ij}={\rm Re}\langle\partial_i h_x|\partial_j h_x\rangle|_{x=0},\tag{3.54}$$

with $i\in[{\rm Re}\,A_x,{\rm Im}\,A_x,{\rm Re}\,\omega_x,{\rm Im}\,\omega_x]$. More explicitly, we write

$$\boldsymbol{M}=\begin{pmatrix}\mathbf{B}&\mathbf{C}\\\mathbf{C}^T&\mathbf{D}\end{pmatrix},\tag{3.55}$$

where the block matrices **B**, **C**, and **D** read

$$\mathbf{C}=\begin{pmatrix}-{\rm Im}A_0&-{\rm Re}A_0\\{\rm Re}A_0&-{\rm Im}A_0\end{pmatrix}\tag{3.56}$$

$$\mathbf{B} = -\frac{1}{2\mathrm{Im}\,\omega_0}\mathbb{I}, \quad \mathbf{D} = -\frac{1}{4(\mathrm{Im}\,\omega_0)^3}\mathbb{I}. \tag{3.57}$$

Here $\mathbb{I}$ is a 2×2 identity matrix. We then marginalize $\boldsymbol{M}$ over the subspace of $[\mathrm{Re}A_x, \mathrm{Im}A_x]$, which yields[4]

$$\boldsymbol{M}_m = \mathbf{D} - \mathbf{C}^T\mathbf{B}^{-1}\mathbf{C} = -\frac{|A_0|^2}{8(\mathrm{Im}\omega_0)^3}\mathbb{I}, \tag{3.58}$$

or equivalently, $\boldsymbol{M}_m = \rho^2/(2\mathrm{Im}\,\omega_0)^2 \times \mathbb{I}$ with ρ being SNR of the original ringdown signal.

On the other hand, the Fisher matrix of our new approach is given by

$$\begin{aligned} M^F_{ij} &= \mathrm{Re}\langle h_0\partial_i B^0_x | h_0\partial_j B^0_x\rangle|_{x=0} \\ &= -\frac{|A_0|^2}{2\mathrm{Im}\,\omega_0}\mathrm{Re}\left(\partial_i B^0_x \partial_j B^0_x\right), \end{aligned} \tag{3.59}$$

with $i, j \in [\mathrm{Re}\,\omega_x, \mathrm{Im}\,\omega_x]$. After inserting Eq. (3.46), we obtain

$$\boldsymbol{M}^F = -\frac{|A_0|^2}{8(\mathrm{Im}\omega_0)^3}\mathbb{I}. \tag{3.60}$$

By comparing Eqs. (3.58) and (3.60), we see the two approaches lead to the same Cramér–Rao bound.

3.7 Appendix: Reproducing posteriors of M_f and χ_f in Sec. 3.4 via a varying filter

In Sec. 3.4, we discussed a mixed approach for BH spectroscopy, namely fitting the filtered data with MCMC. We have demonstrated that this hybrid method yields more information than either the full-RD MCMC or the pure filter method: Compared to the full-RD MCMC approach, the filter allows us to study subdominant QNMs by excluding the impact from dominant modes; compared to the pure filter method, we can still obtain the information about mode amplitudes.

With this mixed approach, we can infer the remnant properties (M_f and χ_f) exclusively from every single mode, e.g., Figs. 3.11c, 3.11d, 3.13c and 3.13d. According to our discussions in Sec. 3.3 and the Supplemental Material of our recent paper [68], the posteriors of M_f and χ_f obtained via MCMC can be reproduced by purely using the rational filter. To demonstrate the equivalence between MCMC and pure filtering, here we use a fixed filter (built with the true values of M_f and χ_f) to

[4] E.g., see Eq. (35) of [83]

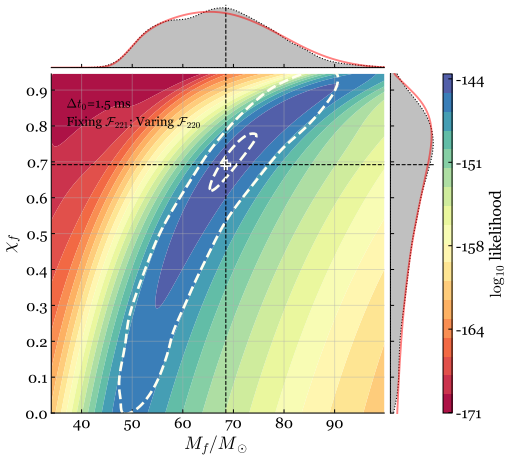

(a) Reproduce the red contours in Fig. 3.11c.

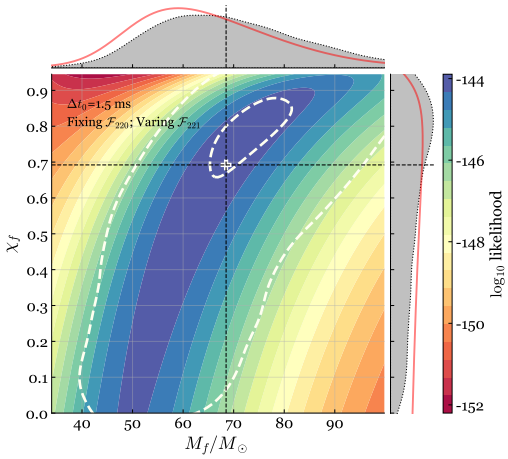

(b) Reproduce the yellow contours in Fig. 3.11c.

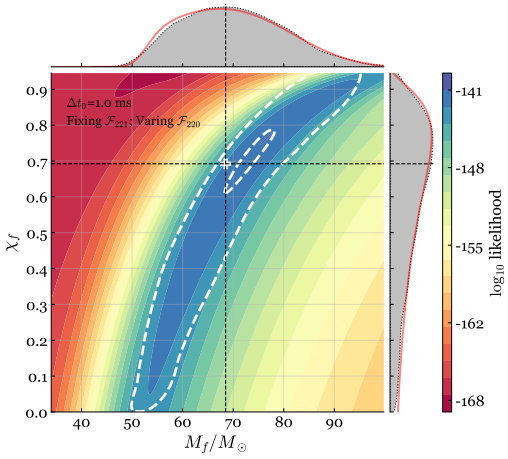

(c) Reproduce the red contours in Fig. 3.11d.

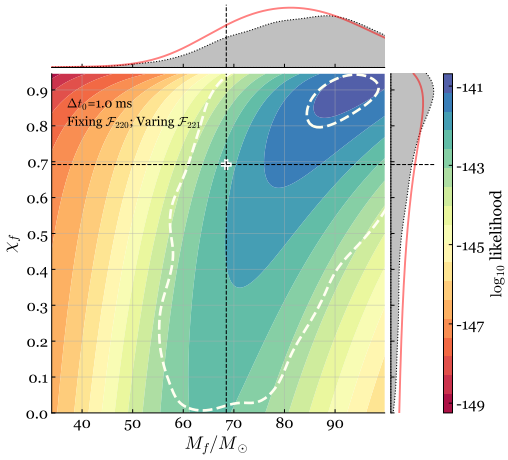

(d) Reproduce the yellow contours in Fig. 3.11d.

Figure 3.16: Reproduce the estimates of M_f and χ_f in Figs. 3.11c and 3.11d, using the filters. The top and bottom panels are for $\Delta t_0 = 1.5$ ms (cf. Fig. 3.11c) and 1.0 ms (cf. Fig. 3.11d), respectively. The left and right columns correspond to analyzing the fundamental mode only (cf. red contours in Fig. 3.11) and analyzing the first overtone only (cf. yellow contours in Fig. 3.11), respectively. The filters used to clean either the first overtone in the left panels or the fundamental mode in the right panels are built with the true values of M_f and χ_f for the injected system. The red and yellow contours in Figs. 3.11c and 3.11d are shown as white dashed contours in this figure.

remove one mode while varying (M_f, χ_f) in the other filter to find the best fit for the remaining mode—this is different from the study in Sec. 3.3, where all the filters are built from the same set of (M_f, χ_f). For example, in Figs. 3.16a and 3.16c we reproduce the "$\mathcal{F}_{221}$+one-QNM" results in Figs. 3.11c and 3.11d (red contours), where we vary $\mathcal{F}_{220}$ while fixing $\mathcal{F}_{221}$ to the injected true value. We can see the

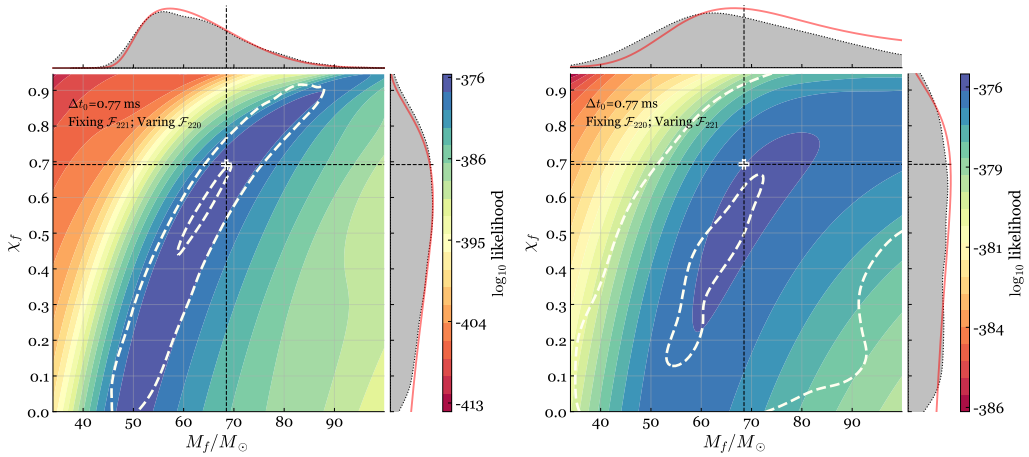

(a) Reproduce the red contours in Fig. 3.13c. (b) Reproduce the yellow contours in Fig. 3.13c.

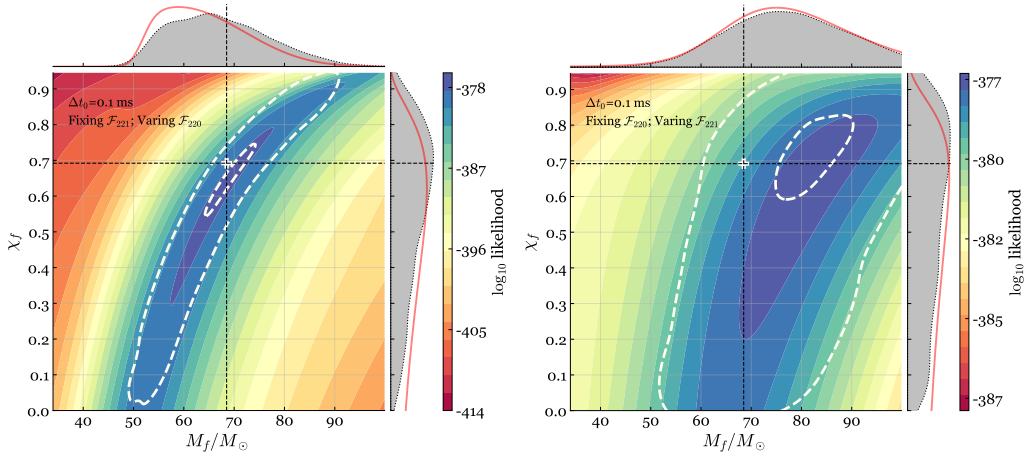

(c) Reproduce the red contours in Fig. 3.13d. (d) Reproduce the yellow contours in Fig. 3.13d.

Figure 3.17: Reproduce the estimates of M_f and χ_f in Figs. 3.13c and 3.13d, using the filters, for GW150914. Similar to Fig. 3.16. See Fig. 3.16 caption for detailed descriptions. The top and bottom panels are for $\Delta t_0 = 0.77$ ms and 0.1 ms, respectively. The filters used to remove either the first overtone in the left panels or the fundamental mode in the right panels are built with the estimated M_f and χ_f from the IMR signal.

colored contours obtained by varying the filter are in agreement with the MCMC one (white dashed contours). Similarly, we vary $\mathcal{F}_{221}$ but fix $\mathcal{F}_{220}$ to reproduce the "$\mathcal{F}_{220}$+one-QNM" results (yellow contours in Figs. 3.11c and 3.11d) in Figs. 3.16b and 3.16d. The comparisons for GW150914 are similar and the results can be found in Fig. 3.17.

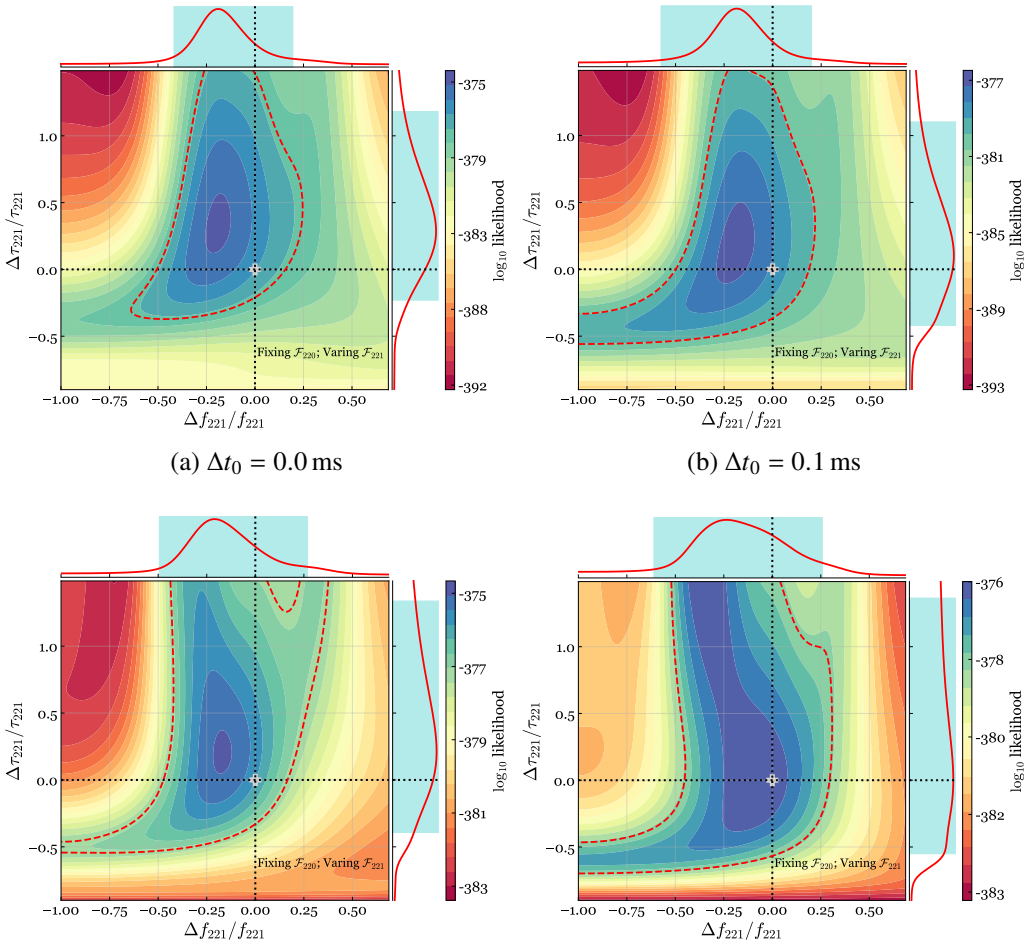

(a) $\Delta t_0 = 0.0$ ms

(b) $\Delta t_0 = 0.1$ ms

(c) $\Delta t_0 = 0.4$ ms

(d) $\Delta t_0 = 0.77$ ms

Figure 3.18: Contours of likelihoods as a function of fractional deviations in the frequency ($\Delta f_{221}/f_{221}$) and decay rate ($\Delta\tau_{221}/\tau_{221}$) of the first overtone after the fundamental mode is removed from GW150914 [different Δt_0 times from (a) to (d)]. The $\mathcal{F}_{220}$ filter used to clean the fundamental mode is built using the IMR-estimated M_f and χ_f. The fiducial values to evaluate the fractional deviations are set to the IMR results. The red-dashed contours enclose the 2D 90% credible region. The cyan-shaded regions on the side stand for the 1D 90%-credible ranges of $\Delta f_{221}/f_{221}$ and $\Delta\tau_{221}/\tau_{221}$.

Table 3.2: The measurements of $\Delta f_{221}/f_{221}$ and $\Delta\tau_{221}/\tau_{221}$ (68% credible intervals) with different choices of Δt_0, based on the "$\mathcal{F}_{220}$+one-QNM" scheme and the results in Fig. 3.18. The fiducial values are set to the IMR results.

Δt_0 (ms)	0.0	0.1	0.4	0.77
$\Delta f_{221}/f_{221}$	$-0.17^{+0.17}_{-0.13}$	$-0.18^{+0.18}_{-0.17}$	$-0.17^{+0.22}_{-0.17}$	$-0.18^{+0.25}_{-0.22}$
$\Delta\tau_{221}/\tau_{221}$	$0.38^{+0.48}_{-0.39}$	$0.20^{+0.52}_{-0.42}$	$0.40^{+0.64}_{-0.53}$	$0.33^{+0.76}_{-0.64}$

3.8 Appendix: Deviation from the Kerr assumption

The "$\mathcal{F}_{220}$+one-QNM" study in Appendix 3.7 (Figs. 3.17b and 3.17d) is closely related to the beyond-Kerr fit discussed in Refs. [27, 30], where the frequency and decay rate of the first overtone are allowed to differ from the no-hair values. Here we could do a similar thing by replacing the parameters, M_f and χ_f, with fractional deviations, $\Delta f_{221}/f_{221}$ and $\Delta\tau_{221}/\tau_{221}$, while varying $\mathcal{F}_{221}$. We still build a fixed filter $\mathcal{F}_{220}$ using the IMR-estimated M_f and χ_f, and use these IMR results as the fiducial values. The resulting posterior distributions are shown in Fig. 3.18, evaluated at different Δt_0 times. The measurements of $\Delta f_{221}/f_{221}$ and $\Delta\tau_{221}/\tau_{221}$ are summarized in Table 3.2, with 68% credibility.

References

[1] Kostas D. Kokkotas and Bernd G. Schmidt. "Quasinormal modes of stars and black holes." *Living Rev. Rel.* 2 (1999), p. 2. DOI: 10.12942/lrr-1999-2. arXiv: gr-qc/9909058.

[2] Hans-Peter Nollert. "Quasinormal modes: the characteristic 'sound' of black holes and neutron stars." *Classical and Quantum Gravity* 16.12 (Nov. 1999), R159–R216. DOI: 10.1088/0264-9381/16/12/201. URL: https://doi.org/10.1088/0264-9381/16/12/201.

[3] Vitor Cardoso and Leonardo Gualtieri. "Testing the black hole 'no-hair' hypothesis." *Class. Quant. Grav.* 33.17 (2016), p. 174001. DOI: 10.1088/0264-9381/33/17/174001. arXiv: 1607.03133 [gr-qc].

[4] Emanuele Berti, Vitor Cardoso, and Andrei O. Starinets. "Quasinormal modes of black holes and black branes." *Class. Quant. Grav.* 26 (2009), p. 163001. DOI: 10.1088/0264-9381/26/16/163001. arXiv: 0905.2975 [gr-qc].

[5] Roger Penrose. ""Golden Oldie": Gravitational collapse: The role of general relativity." *General relativity and Gravitation* 34.7 (2002), pp. 1141–1165.

[6] Piotr T. Chrusciel, Joao Lopes Costa, and Markus Heusler. "Stationary black holes: uniqueness and beyond." *Living Rev. Rel.* 15 (2012), p. 7. DOI: 10.12942/lrr-2012-7. arXiv: 1205.6112 [gr-qc].

[7] Brandon Carter. "Axisymmetric black hole has only two degrees of freedom." *Phys. Rev. Lett.* 26 (6 Feb. 1971), pp. 331–333. DOI: 10.1103/PhysRevLett.26.331. URL: https://link.aps.org/doi/10.1103/PhysRevLett.26.331.

[8] Werner Israel. "Event horizons in static vacuum space-times." *Phys. Rev.* 164 (5 Dec. 1967), pp. 1776–1779. DOI: 10.1103/PhysRev.164.1776. URL: https://link.aps.org/doi/10.1103/PhysRev.164.1776.

[9] Fernando Echeverria. "Gravitational-wave measurements of the mass and angular momentum of a black hole." *Phys. Rev. D* 40 (10 Nov. 1989), pp. 3194–3203. DOI: 10.1103/PhysRevD.40.3194. URL: https://link.aps.org/doi/10.1103/PhysRevD.40.3194.

[10] Olaf Dreyer et al. "Black hole spectroscopy: Testing general relativity through gravitational wave observations." *Class. Quant. Grav.* 21 (2004), pp. 787–804. DOI: 10.1088/0264-9381/21/4/003. arXiv: gr-qc/0309007 [gr-qc].

[11] Emanuele Berti, Vitor Cardoso, and Clifford M. Will. "On gravitational-wave spectroscopy of massive black holes with the space interferometer LISA." *Phys. Rev.* D73 (2006), p. 064030. DOI: 10.1103/PhysRevD.73.064030. arXiv: gr-qc/0512160 [gr-qc].

[12] Emanuele Berti et al. "Matched-filtering and parameter estimation of ringdown waveforms." *Phys. Rev. D* 76 (2007), p. 104044. DOI: 10.1103/PhysRevD.76.104044. arXiv: 0707.1202 [gr-qc].

[13] Sarah Gossan, John Veitch, and Bangalore S. Sathyaprakash. "Bayesian model selection for testing the no-hair theorem with black hole ringdowns." *Phys. Rev.* D85 (2012), p. 124056. DOI: 10.1103/PhysRevD.85.124056. arXiv: 1111.5819 [gr-qc].

[14] Vishal Baibhav and Emanuele Berti. "Multimode black hole spectroscopy." *Phys. Rev. D* 99.2 (2019), p. 024005. DOI: 10.1103/PhysRevD.99.024005. arXiv: 1809.03500 [gr-qc].

[15] Gregorio Carullo et al. "Empirical tests of the black hole no-hair conjecture using gravitational-wave observations." *Phys. Rev. D* 98.10 (2018), p. 104020. DOI: 10.1103/PhysRevD.98.104020. arXiv: 1805.04760 [gr-qc].

[16] Richard Brito, Alessandra Buonanno, and Vivien Raymond. "Black-hole spectroscopy by making full use of gravitational-wave modeling." *Phys. Rev. D* 98.8 (2018), p. 084038. DOI: 10.1103/PhysRevD.98.084038. arXiv: 1805.00293 [gr-qc].

[17] Hiroyuki Nakano et al. "Comparison of various methods to extract ringdown frequency from gravitational wave data." *Phys. Rev. D* 99.12 (2019), p. 124032. DOI: 10.1103/PhysRevD.99.124032. arXiv: 1811.06443 [gr-qc].

[18] Miriam Cabero et al. "Black hole spectroscopy in the next decade." *Phys. Rev. D* 101.6 (2020), p. 064044. DOI: 10.1103/PhysRevD.101.064044. arXiv: 1911.01361 [gr-qc].

[19] Swetha Bhagwat et al. "Detectability of the subdominant mode in a binary black hole ringdown." *Phys. Rev. D* 102.2 (2020), p. 024023. DOI: 10.1103/PhysRevD.102.024023. arXiv: 1910.13203 [gr-qc].

[20] Iara Ota and Cecilia Chirenti. "Overtones or higher harmonics? Prospects for testing the no-hair theorem with gravitational wave detections." *Phys. Rev. D* 101.10 (2020), p. 104005. DOI: 10.1103/PhysRevD.101.104005. arXiv: 1911.00440 [gr-qc].

[21] Juan Calderón Bustillo, Paul D. Lasky, and Eric Thrane. "Black-hole spectroscopy, the no-hair theorem, and GW150914: Kerr versus Occam." *Phys. Rev. D* 103.2 (2021), p. 024041. DOI: 10.1103/PhysRevD.103.024041. arXiv: 2010.01857 [gr-qc].

[22] Xisco Jiménez Forteza et al. "Spectroscopy of binary black hole ringdown using overtones and angular modes." *Phys. Rev. D* 102.4 (2020), p. 044053. DOI: 10.1103/PhysRevD.102.044053. arXiv: 2005.03260 [gr-qc].

[23] Maximiliano Isi and Will M. Farr. "Analyzing black-hole ringdowns." (July 2021). arXiv: 2107.05609 [gr-qc].

[24] Sarah Caudill et al. "Reduced basis representations of multi-mode black hole ringdown gravitational waves." *Class. Quant. Grav.* 29 (2012), p. 095016. DOI: 10.1088/0264-9381/29/9/095016. arXiv: 1109.5642 [gr-qc].

[25] Eliot Finch and Christopher J. Moore. "Frequency-domain analysis of black-hole ringdowns." *Phys. Rev. D* 104.12 (2021), p. 123034. DOI: 10.1103/PhysRevD.104.123034. arXiv: 2108.09344 [gr-qc].

[26] Maximiliano Isi and Will M. Farr. "Revisiting the ringdown of GW150914." (Feb. 2022). arXiv: 2202.02941 [gr-qc].

[27] Eliot Finch and Christopher J. Moore. "Searching for a ringdown overtone in GW150914." *Phys. Rev. D* 106.4 (2022), p. 043005. DOI: 10.1103/PhysRevD.106.043005. arXiv: 2205.07809 [gr-qc].

[28] Roberto Cotesta et al. "On the detection of ringdown overtones in GW150914." (Jan. 2022). arXiv: 2201.00822 [gr-qc].

[29] Benjamin P. Abbott et al. "Tests of general relativity with GW150914." *Phys. Rev. Lett.* 116.22 (2016). [Erratum: Phys. Rev. Lett.121,no.12,129902(2018)], p. 221101. DOI: 10.1103/PhysRevLett.116.221101. arXiv: 1602.03841 [gr-qc].

[30] Maximiliano Isi et al. "Testing the no-hair theorem with GW150914." *Phys. Rev. Lett.* 123.11 (2019), p. 111102. DOI: 10.1103/PhysRevLett.123.111102. arXiv: 1905.00869 [gr-qc].

[31] Collin D. Capano et al. "Observation of a multimode quasi-normal spectrum from a perturbed black hole." (May 2021). arXiv: 2105.05238 [gr-qc].

[32] Collin D. Capano et al. "Statistical validation of the detection of a subdominant quasi-normal mode in GW190521." (Sept. 2022). arXiv: 2209.00640 [gr-qc].

[33] Jeroen Meidam et al. "Testing the no-hair theorem with black hole ringdowns using TIGER." *Phys. Rev. D* 90.6 (2014), p. 064009. DOI: 10.1103/PhysRevD.90.064009. arXiv: 1406.3201 [gr-qc].

[34] Swetha Bhagwat, Duncan A. Brown, and Stefan W. Ballmer. "Spectroscopic analysis of stellar mass black-hole mergers in our local universe with ground-based gravitational wave detectors." *Phys. Rev. D* 94.8 (2016). [Erratum: Phys.Rev.D 95, 069906 (2017)], p. 084024. DOI: 10.1103/PhysRevD.94.084024. arXiv: 1607.07845 [gr-qc].

[35] Emanuele Berti et al. "Spectroscopy of Kerr black holes with Earth- and space-based interferometers." *Phys. Rev. Lett.* 117.10 (2016), p. 101102. DOI: 10.1103/PhysRevLett.117.101102. arXiv: 1605.09286 [gr-qc].

[36] Vishal Baibhav et al. "Black hole spectroscopy: systematic errors and ringdown energy estimates." *Phys. Rev. D* 97.4 (2018), p. 044048. DOI: 10.1103/PhysRevD.97.044048. arXiv: 1710.02156 [gr-qc].

[37] Andrea Maselli, Kostas Kokkotas, and Pablo Laguna. "Observing binary black hole ringdowns by advanced gravitational wave detectors." *Phys. Rev. D* 95.10 (2017), p. 104026. DOI: 10.1103/PhysRevD.95.104026. arXiv: 1702.01110 [gr-qc].

[38] Huan Yang et al. "Black hole spectroscopy with coherent mode stacking." *Phys. Rev. Lett.* 118.16 (2017), p. 161101. DOI: 10.1103/PhysRevLett.118.161101. arXiv: 1701.05808 [gr-qc].

[39] Carlos Filipe Da Silva Costa et al. "Detection of (2,2) quasinormal mode from a population of black holes with a constructive summation method." *Phys. Rev. D* 98.2 (2018), p. 024052. DOI: 10.1103/PhysRevD.98.024052. arXiv: 1711.00551 [gr-qc].

[40] Alessandra Buonanno, Gregory B. Cook, and Frans Pretorius. "Inspiral, merger and ring-down of equal-mass black-hole binaries." *Phys. Rev.* D75 (2007), p. 124018. DOI: 10.1103/PhysRevD.75.124018. arXiv: gr-qc/0610122 [gr-qc].

[41] Arnab Dhani and Bangalore S. Sathyaprakash. "Overtones, mirror modes, and mode-mixing in binary black hole mergers." (July 2021). arXiv: 2107.14195 [gr-qc].

[42] Xisco Jiménez Forteza and Pierre Mourier. "High-overtone fits to numerical relativity ringdowns: Beyond the dismissed n=8 special tone." *Phys. Rev. D* 104.12 (2021), p. 124072. DOI: 10.1103/PhysRevD.104.124072. arXiv: 2107.11829 [gr-qc].

[43] Eliot Finch and Christopher J. Moore. "Modelling the ringdown from precessing black hole binaries." (Feb. 2021). arXiv: 2102.07794 [gr-qc].

[44] Xiang Li et al. "Angular emission patterns of remnant black holes." *Phys. Rev. D* 105.2 (2022), p. 024016. DOI: 10.1103/PhysRevD.105.024016. arXiv: 2110.03116 [gr-qc].

[45] Lorena Magaña Zertuche et al. "High precision ringdown modeling: Multimode fits and BMS frames." *Phys. Rev. D* 105 (2022), p. 104015. DOI: 10.1103/PhysRevD.105.104015. arXiv: 2110.15922 [gr-qc].

[46] Sizheng Ma et al. "Universal features of gravitational waves emitted by superkick binary black hole systems." *Phys. Rev. D* 104.8 (2021), p. 084003. DOI: 10.1103/PhysRevD.104.084003. arXiv: 2107.04890 [gr-qc].

[47] Keefe Mitman et al. "Nonlinearities in black hole ringdowns." *Phys. Rev. Lett.* 130.8 (2023), p. 081402. DOI: 10.1103/PhysRevLett.130.081402. arXiv: 2208.07380 [gr-qc].

[48] Mark Ho-Yeuk Cheung et al. "Nonlinear effects in black hole ringdown." (Aug. 2022). arXiv: 2208.07374 [gr-qc].

[49] Macarena Lagos and Lam Hui. "Generation and propagation of nonlinear quasi-normal modes of a Schwarzschild black hole." (Aug. 2022). arXiv: 2208.07379 [gr-qc].

[50] Emanuele Berti et al. "Inspiral, merger and ringdown of unequal mass black hole binaries: A multipolar analysis." *Phys. Rev. D* 76 (2007), p. 064034. DOI: 10.1103/PhysRevD.76.064034. arXiv: gr-qc/0703053.

[51] Emanuele Berti et al. "Mining information from binary black hole mergers: A Comparison of estimation methods for complex exponentials in noise." *Phys. Rev. D* 75 (2007), p. 124017. DOI: 10.1103/PhysRevD.75.124017. arXiv: gr-qc/0701086.

[52] Ioannis Kamaretsos et al. "Black-hole hair loss: Learning about binary progenitors from ringdown signals." *Phys. Rev. D* 85 (2012), p. 024018. DOI: 10.1103/PhysRevD.85.024018. arXiv: 1107.0854 [gr-qc].

[53] Lionel London, Deirdre Shoemaker, and James Healy. "Modeling ringdown: Beyond the fundamental quasinormal modes." *Phys. Rev. D* 90.12 (2014). [Erratum: Phys.Rev.D 94, 069902 (2016)], p. 124032. DOI: 10.1103/PhysRevD.90.124032. arXiv: 1404.3197 [gr-qc].

[54] Eric Thrane, Paul D. Lasky, and Yuri Levin. "Challenges testing the no-hair theorem with gravitational waves." *Phys. Rev. D* 96.10 (2017), p. 102004. DOI: 10.1103/PhysRevD.96.102004. arXiv: 1706.05152 [gr-qc].

[55] Matthew Giesler et al. "Black hole ringdown: The importance of overtones." *Phys. Rev.* X9.4 (2019), p. 041060. DOI: 10.1103/PhysRevX.9.041060. arXiv: 1903.08284 [gr-qc].

[56] Gregory B. Cook. "Aspects of multimode Kerr ringdown fitting." *Phys. Rev. D* 102.2 (2020), p. 024027. DOI: 10.1103/PhysRevD.102.024027. arXiv: 2004.08347 [gr-qc].

[57] Arnab Dhani. "Importance of mirror modes in binary black hole ringdown waveform." *Phys. Rev. D* 103.10 (2021), p. 104048. DOI: 10.1103/PhysRevD.103.104048. arXiv: 2010.08602 [gr-qc].

[58] Swetha Bhagwat et al. "On choosing the start time of binary black hole ringdowns." *Phys. Rev. D* 97.10 (2018), p. 104065. DOI: 10.1103/PhysRevD.97.104065. arXiv: 1711.00926 [gr-qc].

[59] Swetha Bhagwat et al. "Ringdown overtones, black hole spectroscopy, and no-hair theorem tests." *Phys. Rev. D* 101.4 (2020), p. 044033. DOI: 10.1103/PhysRevD.101.044033. arXiv: 1910.08708 [gr-qc].

[60] Maria Okounkova. "Revisiting non-linearity in binary black hole mergers." (Apr. 2020). arXiv: 2004.00671 [gr-qc].

[61] Geoffrey Lovelace et al. "Modeling the source of GW150914 with targeted numerical-relativity simulations." *Class. Quant. Grav.* 33.24 (2016), p. 244002. DOI: 10.1088/0264-9381/33/24/244002. arXiv: 1607.05377 [gr-qc].

[62] Gregorio Carullo, Walter Del Pozzo, and John Veitch. "Observational black hole spectroscopy: A time-domain multimode analysis of GW150914." *Phys. Rev.* D99.12 (2019). [Erratum: Phys. Rev.D100,no.8,089903(2019)], p. 123029. DOI: 10.1103/PhysRevD.99.123029,10.1103/PhysRevD.100.089903. arXiv: 1902.07527 [gr-qc].

[63] Benjamin P. Abbott et al. "Observation of gravitational waves from a binary black hole merger." *Phys. Rev. Lett.* 116.6 (2016), p. 061102. DOI: 10.1103/PhysRevLett.116.061102. arXiv: 1602.03837 [gr-qc].

[64] Sizheng Ma et al. "Quasinormal-mode filters: A new approach to analyze the gravitational-wave ringdown of binary black-hole mergers." *Phys. Rev. D* 106.8 (2022), p. 084036. DOI: 10.1103/PhysRevD.106.084036. arXiv: 2207.10870 [gr-qc].

[65] David A. Nichols and Yanbei Chen. "A hybrid method for understanding black-hole mergers: Head-on case." *Phys. Rev. D* 82 (2010), p. 104020. DOI: 10.1103/PhysRevD.82.104020. arXiv: 1007.2024 [gr-qc].

[66] David A. Nichols and Yanbei Chen. "Hybrid method for understanding black-hole mergers: Inspiralling case." *Phys. Rev. D* 85 (2012), p. 044035. DOI: 10.1103/PhysRevD.85.044035. arXiv: 1109.0081 [gr-qc].

[67] Sizheng Ma et al. "Gravitational-wave echoes from numerical-relativity waveforms via spacetime construction near merging compact objects." *Phys. Rev. D* 105.10 (2022), p. 104007. DOI: 10.1103/PhysRevD.105.104007. arXiv: 2203.03174 [gr-qc].

[68] Sizheng Ma, Ling Sun, and Yanbei Chen. "Black hole spectroscopy by mode cleaning." (Jan. 2023). arXiv: 2301.06705 [gr-qc].

[69] Leo C. Stein. "qnm: A Python package for calculating Kerr quasinormal modes, separation constants, and spherical-spheroidal mixing coefficients." *J. Open Source Softw.* 4.42 (2019), p. 1683. DOI: 10.21105/joss.01683. arXiv: 1908.10377 [gr-qc].

[70] Gregory Ashton et al. "BILBY: A user-friendly Bayesian inference library for gravitational-wave astronomy." *Astrophys. J. Suppl.* 241.2 (2019), p. 27. DOI: 10.3847/1538-4365/ab06fc. arXiv: 1811.02042 [astro-ph.IM].

[71] Isobel M. Romero-Shaw et al. "Bayesian inference for compact binary coalescences with bilby: validation and application to the first LIGO–Virgo gravitational-wave transient catalogue." *Mon. Not. Roy. Astron. Soc.* 499.3 (2020), pp. 3295–3319. DOI: 10.1093/mnras/staa2850. arXiv: 2006.00714 [astro-ph.IM].

[72] Maximiliano Isi and Will Meierjurgen Farr. *maxisi/ringdown: Initial ringdown release*. Version v0.1. July 2021. DOI: 10.5281/zenodo.5094068. URL: https://doi.org/10.5281/zenodo.5094068.

[73] Peter Welch. "The use of fast Fourier transform for the estimation of power spectra: A method based on time averaging over short, modified periodograms." *IEEE Transactions on Audio and Electroacoustics* 15.2 (1967), pp. 70–73. DOI: 10.1109/TAU.1967.1161901.

[74] J. Aasi et al. "Advanced LIGO." *Class. Quant. Grav.* 32 (2015), p. 074001. DOI: 10.1088/0264-9381/32/7/074001. arXiv: 1411.4547 [gr-qc].

[75] Benjamin P. Abbott et al. "Sensitivity of the advanced LIGO detectors at the beginning of gravitational wave astronomy." *Phys. Rev. D* 93.11 (2016). [Addendum: Phys.Rev.D 97, 059901 (2018)], p. 112004. DOI: 10.1103/PhysRevD.93.112004. arXiv: 1604.00439 [astro-ph.IM].

[76] Benjamin P. Abbott et al. "GW150914: The advanced LIGO detectors in the era of first discoveries." *Phys. Rev. Lett.* 116.13 (2016), p. 131103. DOI: 10.1103/PhysRevLett.116.131103. arXiv: 1602.03838 [gr-qc].

[77] Gregory M. Harry. "Advanced LIGO: The next generation of gravitational wave detectors." *Class. Quant. Grav.* 27 (2010). Ed. by Zsuzsa Marka and Szabolcs Marka, p. 084006. DOI: 10.1088/0264-9381/27/8/084006.

[78] Benjamin P. Abbott et al. "Observation of gravitational waves from a binary black hole merger." *Phys. Rev. Lett.* 116.6 (2016), p. 061102. DOI: 10.1103/PhysRevLett.116.061102. arXiv: 1602.03837 [gr-qc].

[79] Benjamin P. Abbott et al. "GWTC-1: A gravitational-wave transient catalog of compact binary mergers observed by LIGO and Virgo during the first and second observing runs." *Phys. Rev. X* 9.3 (2019), p. 031040. DOI: 10.1103/PhysRevX.9.031040. arXiv: 1811.12907 [astro-ph.HE].

[80] LIGO Scientific Collaboration and Virgo Collaboration. "Gravitational wave open science center." (). https://www.gw-openscience.org.

[81] Michael Boyle et al. "The SXS collaboration catalog of binary black hole simulations." *Class. Quant. Grav.* 36.19 (2019), p. 195006. DOI: 10.1088/1361-6382/ab34e2. arXiv: 1904.04831 [gr-qc].

[82] SXS Collaboration. *The SXS collaboration catalog of gravitational waveforms*. http://www.black-holes.org/waveforms..

[83] Linqing Wen and Yanbei Chen. "Geometrical expression for the angular resolution of a network of gravitational-wave detectors." *Phys. Rev. D* 81 (2010), p. 082001. DOI: 10.1103/PhysRevD.81.082001. arXiv: 1003.2504 [astro-ph.CO].

Chapter 4

UNIVERSAL FEATURES OF GRAVITATIONAL WAVES EMITTED BY SUPERKICK BINARY BLACK HOLE SYSTEMS

[1] Sizheng Ma et al. "Universal features of gravitational waves emitted by superkick binary black hole systems." *Phys. Rev. D* 104.8 (2021), p. 084003. DOI: 10.1103/PhysRevD.104.084003. arXiv: 2107.04890 [gr-qc].

4.1 Introduction

The recently detected gravitational wave (GW) signal, GW190521, is consistent with the merger of two black holes (BHs) with masses of $85M_\odot$ and $66M_\odot$ [1, 2]. The detection of this event, together with its candidate optical counterpart ZTF19abanrhr [3], indicates the potential existence of BHs in the mass gap predicted by (pulsational) pair-instability supernova theory [2, 4, 5]. A few studies also suggest that this system could admit a extremely eccentric [2, 6], hyperbolic [7], or a head-on [2, 8] merger interpretation, placing possible constraints on the binary's formation channel [6, 7, 9]. For such an event, most of the GW detected by the Advanced LIGO [10], VIRGO [11] and KAGRA [12, 13] network is dominated by the merger and ringdown portions. This demonstrates the importance of understanding ringdowns for detecting more GW190521-like cases in the near future [14].

The ringdown signal can be treated as a superposition of damped sinusoids, corresponding to the quasi-normal modes (QNMs) of the final BH [15]. Due to the no-hair theorem [16], the QNM frequencies and damping time for a spinning BH in general relativity (GR) are fully determined by its mass and angular momentum. Therefore, measuring a QNM from a GW event can allow us to determine the properties of the final BH. Alternatively, if multiple modes are observed at the same time, we can use them to test the no-hair theorem and general relativity [17–36], and also constrain modified gravity [24, 25, 37–39].

In addition to measuring QNM frequencies, extensive studies have also been carried out to explore the relationship between progenitor's parameters and additional ringdown signatures. For instance, the spin (magnitude and direction) and mass of the remnant BH were fitted to progenitor's spins ($\boldsymbol{\chi}_{1,2}$) and mass ratio ($q = m_{\rm heavy}/m_{\rm light} > 1$) [40–55], as well as the peak amplitude of GW strain [56],

using numerical relativity (NR) [29], the effective-one-body (EOB) approach [57], and also a hybrid way that involves multi-timescale post-Newtonian integrations and numerical-relativity surrogate models [58]. The gravitational wave frequency at peak amplitude [45, 59] and the peak GW luminosity [42, 45, 60] were both found to have a clean dependence on the progenitor's parameters. The above facts clearly imply that the initial conditions (e.g., at merger) for the progenitor are encoded in the ringdown portion of GW, including QNM frequencies and amplitudes. Therefore it's not surprising that the ringdown can be used to learn about the component properties.

Apart from conveying the importance of ringdown studies, the detection of the candidate optical counterpart of GW190521 has also provided us with a new scheme to measure the gravitational recoil [3]. General relativity predicts that a system is kicked after merger due to the linear momentum carried away by GW [61–63]. By applying various methods, including NR, post-Newtonian (PN) theory [64–66], EOB [67], and the close-limit approximation [68], several studies showed that the kick velocity is a result of the asymmetry between different GW modes [69], or alternatively, the beating between the mass and current quadrupole waves [70, 71], caused by the unequal mass [72–76] and spins [75–83]. In particular, the superkick (SK) [78, 80, 84–86] configurations lead to relatively large kick velocities. In this work, we adopt two types of SK configurations: SKu and SKd, whose sketches are shown in Fig. 4.1. Both systems have equal mass, spin magnitude, and tilt angles. As for SKd, two individual spins are anti-parallel, whereas for SKu, only the spin components in the orbital plane are opposite. SKu and SKd are fully characterized by $(\chi_{\rm init}, \phi_{\rm init}, \theta_{\rm init})$, where the subscript refers to a reference time in the inspiral regime: $\chi_{\rm init}$ is the magnitude of the dimensionless spin; $\theta_{\rm init}$ is the polar angle of one of the holes (relative to the orbital angular momentum $\vec{L}$); $\phi_{\rm init}$ is the azimuthal angle between the in-(orbital)plane spin and the separation vector pointing from the lighter to the heavier BH.

During the evolution, the effect of frame-dragging from two anti-parallel in-plane spins move the center of mass up and down in the inertial frame [87]. This process is halted as the common horizon forms [88–90], and the kick is imparted. In addition, the SKu system usually emits more energy and linear angular momentum than SKd because of the orbital hang-up effect, which arises due to the need to radiate way additional angular momentum before the binary can merge [84], and leads to a larger kick. Recently simulations showed that the kick for the SKu system could be as

large as 5000 km/s (if extrapolated to the maximal spin) [85, 86]. Such a large kick will lead to important astrophysical consequences [91–94], as well as Doppler shifts in GWs [95], which could be detected by current and future detectors [96, 97]. Numerous studies have been implemented to fit kick velocities to progenitor's spins and mass ratio [40–42, 45, 79, 80, 98]. In particular, the development of numerical relativity surrogate model [46, 47, 99–102] has allowed a systematic study to explore much larger parameter space [103].

Interestingly, GW190521 was found to be consistent with a large in-plane spin configuration. Its kick posterior is much broader and is consistent with $0 - 3500$ km/s [2]. Meanwhile, its potential optical counterpart was predicted to have a kick velocity of ~ 200 km/s [3]. In the future, it is still likely to detect GW events with non-negligible gravitational recoils, and even SK-like binaries [104]. Accordingly, in this chapter, we aim to explore the features of ringdown for SKd binaries carefully and relate them to the phenomenon of gravitational recoil. Specifically, we shall focus on the amplitudes of QNMs [105–107], as well as mass and current quadrupole waves [70], and study how those features depend on the progenitor's parameters. Comparing to a generic BBH system, a SKd system has several advantages that can ease the difficulty of analysis. (i) The parameter space for a SKd binary is 3D, i.e., $(\chi_{\rm init}, \phi_{\rm init}, \theta_{\rm init})$, instead of generally 7D. (ii) SKd configurations have a high level of symmetry. Subsequently, the orbital angular momentum is non-precessing, and the spin direction of the remnant BH is fixed during the merger. This allows us to conveniently choose coordinates in which only the $(2, 2)$ and $(2, -2)$ modes dominate. (iii) The mass and spin of the remnant BH are not impacted by varying $(\chi_{\rm init}, \phi_{\rm init}, \theta_{\rm init})$, nor are the QNM frequencies. Hence we can study the mode excitation (complex) amplitudes exclusively while avoiding changes in the mode frequencies.

In our study, we use waveforms generated by the Spectral Einstein Code (SpEC) [108], and two NR surrogate models, also based on SpEC: NRSur7dq4, NRSur7dq4Remnant [46, 47]. In particular, NRSur7dq4 is a waveform model valid for mass ratio < 4 and dimensionless spin magnitudes < 0.8, while NRSur7dq4Remnant is a model that predicts the mass, spin, and kick velocity of the remnant BH from the parameter of individual merging BHs. Meanwhile, we have in total 35 NR simulations where systems are either in the SKd (Table 4.1) or the SKu (Table 4.5) configuration. The dimensionless spin of BH ranges from 0.4 to 0.95. Those runs will be available in the Simulating eXtreme Spacetimes (SXS) Collaboration cat-

alog [109, 110]. We have checked that our NR runs agree with the predictions of NRSur7dq4, with mismatches $\sim 10^{-5} - 10^{-4}$. For each simulation, we evolve with three numerical resolutions. Among those cases, the largest kick is $\sim$ 4050 km/s (Table 4.5).

This chapter is organized as follows. In Sec. 4.2, we decompose ringdown into QNMs (7 overtones) and explore the dependence of mode amplitudes on the progenitor's parameters. In Sec. 4.3, we study the phenomenon of radiative mass and current quadrupole waves and relate them to kick velocity. Then in Sec. 4.4, we apply the backward-one-body (BOB) model, conceived recently by McWilliams [111], to SK binaries. Sec. 4.5 focuses on parameter estimation, where we use the Fisher information matrix formalism to discuss the parameter correlations in the ringdown signal. Finally, in Sec. 4.6 we summarize our results.

Throughout this chapter we use the geometric units with $G = c = 1$. We use M to refer to the initial total mass of the binary system. All GW waveforms are aligned in the time domain such that $t = 0M$ corresponds to the time of the peak of the total amplitude $\sqrt{\sum_{l,m} |h_{lm}|^2}$.

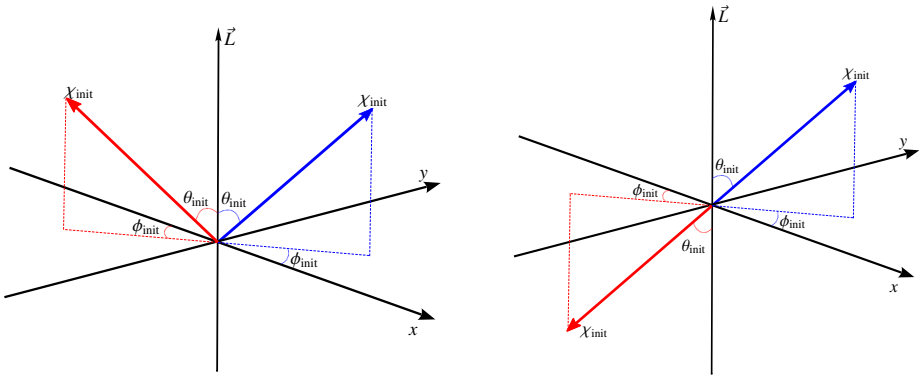

(a) SKu (b) SKd

Figure 4.1: Sketches for a SKu (a) and a SKd (b) system. Two arrows (in different colors) represent two individual spins. The letter "u" and "d" refer to the up- and down-state for the red arrow. Both SKu and SKd systems have equal mass BHs with the same dimensionless spin magnitude $\chi_{\rm init}$. For SKd, two individual spins are anti-parallel, whereas for SKu, only the orbital-plane components are opposite. SKd and SKu are fully characterized by three parameters: $(\chi_{\rm init}, \theta_{\rm init}, \phi_{\rm init})$, where $\theta_{\rm init}$ stands for the polar angle of one of the holes (relative to the orbital angular momentum), and $\phi_{\rm init}$ the azimuthal angle of the in-plane spin measured from the line of two BHs. Three parameters are specified at a reference time in the inspiral regime (labeled by the subscript 'init').

Table 4.1: A summary of 12 of our NR simulations with SpEC. All systems are in the SKd configuration, with the individual dimensionless spin $\chi_{\rm init} = 0.4$, $\theta_{\rm init} = \pi/2$, and $\phi_{\rm init} \in [-\pi, \pi]$. The reference (initial) orbital frequency is chosen to be 0.0175 (in the unit of total mass). The first and second columns are the name of runs used in this chapter, while the third column corresponds to the name in the Simulating eXtreme Spacetimes Collaboration catalog. The fourth column gives $\phi_{\rm init}$. The last three columns correspond to the mass, kick velocity, and spin of the final BH. A summary of SKu configurations is in Table 4.5.

	Run label					
	This chapter	SXS:BBH	$\phi_{\rm init}$ (rad)	m_f/M	v_f^z ($\times 10^{-3}$)	χ_f
SKd4	'01'	2451	2.25	0.952	2.36	0.686
	'02'	2452	-3.04	0.951	−4.73	0.684
	'03'	2453	-1.70	0.951	1.71	0.685
	'04'	2454	0.66	0.951	−4.45	0.683
	'05'	2455	1.30	0.951	−1.68	0.685
	'06'	2456	2.88	0.951	4.75	0.684
	'07'	2457	-2.58	0.951	4.47	0.683
	'08'	2458	-1.07	0.952	−2.11	0.686
	'09'	2459	-2.93	0.951	4.94	0.683
	'10'	2460	-1.78	0.951	1.24	0.686
	'11'	2461	-1.36	0.952	−1.41	0.686
	'12'	2462	0.21	0.951	−4.93	0.683

4.2 Multipole decomposition of the waveform and quasi-normal mode excitations

In this section, we decompose the ringdown signal into QNMs and study how each mode is excited.

4.2.1 Multipole decomposition of the waveform

In a spherical polar coordinate system, with an observer located at the (ι, β) direction, following the widely used convention for defining the + and × polarizations of the gravitational wave [112], one can define a complex strain

$$h(t, \iota, \beta) = h_+(t, \iota, \beta) - i h_\times(t, \iota, \beta), \tag{4.1}$$

and further decompose it into a sum over a set of spin-weighted spherical harmonics ${}_{-2}Y_{\ell m}(\iota, \beta)$:

$$\begin{aligned} h(t, \iota, \beta) &= h_+(t, \iota, \beta) - i h_\times(t, \iota, \beta) \\ &= \sum_{\ell=2}^{\infty} \sum_{m=-\ell}^{\ell} \frac{1}{D} h_{\ell m}(t) {}_{-2}Y_{\ell m}(\iota, \beta), \end{aligned} \tag{4.2}$$

where D is the distance between the source and the observer. Meanwhile, it is also natural to group $h_{\ell,m}$ and $h_{\ell,-m}$ into mass and current quadrupole waves [71], writing

$$I_{\ell m} = \frac{1}{\sqrt{2}}[h_{\ell m} + (-1)^m h^*_{\ell,-m}], \tag{4.3a}$$

$$S_{\ell m} = \frac{i}{\sqrt{2}}[h_{\ell m} - (-1)^m h^*_{\ell,-m}]. \tag{4.3b}$$

Here $I_{\ell m}$ ($S_{\ell m}$) is the mass (current) quadrupole wave, proportional to the ℓ-th order time derivative of the mass (current) ℓ-pole moment. For the SKd configuration, $h_{2,\pm2}$ always dominate over other modes, hence we shall primarily focus on these two modes.

4.2.2 QNM excitation in multipolar modes

As discussed in Ref. [22], the ringdown portion of $h_{2,\pm2}$ of a non-precessing system can be modeled as a sum of QNMs, as early as $t = 0M$, which is defined as the moment of time at which $\sqrt{\sum_{l,m}|h_{lm}|^2}$ peaks. The expansion reads:

$$\begin{aligned} h_{22} &= \sum_{n=0}^{N} \mathcal{A}_{22n} e^{i\psi_{22n}} e^{-i\omega_{22n}t}, \\ h_{2,-2} &= \sum_{n=0}^{N} \mathcal{A}_{2,-2n} e^{i\psi_{2,-2n}} e^{i\omega^*_{22n}t}, \end{aligned} \qquad t \geq 0M, \tag{4.4}$$

where $\mathcal{A}_{22n}e^{i\psi_{22n}}$ and $\mathcal{A}_{2,-2n}e^{i\psi_{2,-2n}}$ are the complex amplitudes of the n-th overtone, while ω_{22n} and $-\omega^*_{22n}$ are the mode frequencies. Note that ω_{22n} and $-\omega^*_{22n}$ have opposite real parts and equal imaginary parts; both correspond to the prograde $\ell = 2$ quasi-normal mode. In Eq. (4.4) we have adopted the approximation that the angular wavefunction of the $(2, 2)$ mode is given by the spin-weighted spherical harmonics instead of the spin-weighted spheroidal harmonics—the spheroidal-spherical mixing [113, 114] can be ignored because of the moderate spin of final BHs (~ 0.68) studied in this chapter. In this way, both the prograde, ω_{22}, and the retrograde, $\omega_{2,-2}$, modes share the same angular wavefunction. Meanwhile, the retrograde modes $\omega_{2,-2n}$ and $-\omega^*_{2,-2n}$ [see Eq.(3.6) of Ref. [107]], are negligible in our case.

Inserting Eqs. (4.4) to Eqs. (4.3) we have

$$\begin{aligned} I_{22} &= \sum_{n=0}^{N} \mathcal{A}^{(I)}_n e^{i\varphi^{(I)}_n} e^{-i\omega_{22n}t}, \\ S_{22} &= \sum_{n=0}^{N} \mathcal{A}^{(S)}_n e^{i\varphi^{(S)}_n} e^{-i\omega_{22n}t}, \end{aligned} \qquad t \geq 0M, \tag{4.5}$$

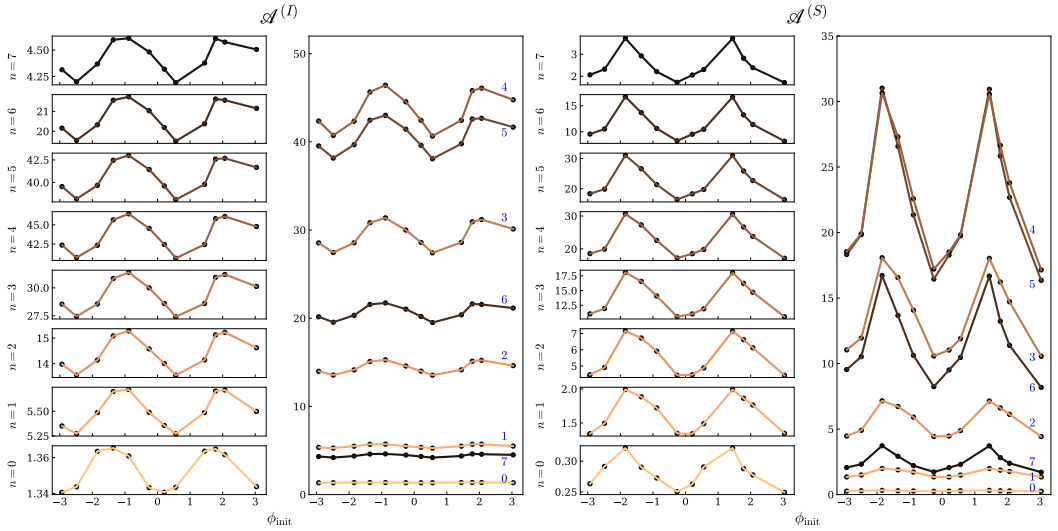

(a) mass quadrupole wave (b) current quadrupole wave

Figure 4.2: QNM magnitudes versus $\phi_{\rm init}$ for mass ($\mathscr{A}^{(I)}$) and current ($\mathscr{A}^{(S)}$) quadrupole waves. Data are from 12 of our NR simulations listed in Table 4.1. All BBH systems are in the SKd configuration. Fig. 4.2 (a) corresponds to $\mathscr{A}^{(I)}$, where the left eight panels are the zoom-in plot for each overtone. The overtone index n is in descending order. Similarly, Fig. 4.2 (b) corresponds to $\mathscr{A}^{(S)}$. The spectra peak at $n = 4$ (because the n=4 amplitude is largest), and patterns are roughly periodic with a period 2π. Examining the zoomed in plots, it can be seen that approximately, the patterns are the same for all n (up to a scaling factor).

with

$$\mathscr{A}_n^{(I)} e^{i\varphi_n^{(I)}} = \frac{1}{\sqrt{2}}(\mathcal{A}_{22n} e^{i\psi_{22n}} + \mathcal{A}_{2,-2n} e^{-i\psi_{2,-2n}}), \tag{4.6a}$$

$$\mathscr{A}_n^{(S)} e^{i\varphi_n^{(S)}} = \frac{i}{\sqrt{2}}(\mathcal{A}_{22n} e^{i\psi_{22n}} - \mathcal{A}_{2,-2n} e^{-i\psi_{2,-2n}}). \tag{4.6b}$$

To give an example, we fit the ringdown portion of SKd4 set of NR simulations (Table 4.1) with 7 overtones, following the procedure of Ref. [22]. We use unweighted linear least squares to fit the mode amplitudes and use nonlinear least squares to fit the final spin and mass. The mode frequency ω_{22n} is obtained from a Python package qnm [115].

First focusing on I_{22} and S_{22}, we plot $\mathscr{A}_n^{(I)}$ (mass) and $\mathscr{A}_n^{(S)}$ (current) as functions of $\phi_{\rm init}$ in Fig. 4.2. We can see $\mathscr{A}_n^{(I)} > \mathscr{A}_n^{(S)}$ for any n, and both of them peak at $n = 4$. Patterns have a rough period π. An interesting feature is that the dependence on $\phi_{\rm init}$ is similar for all overtones (up to a scaling factor). The analogous universal feature for EMRI was explored by Lim *et al.* [107]. After a proper normalization

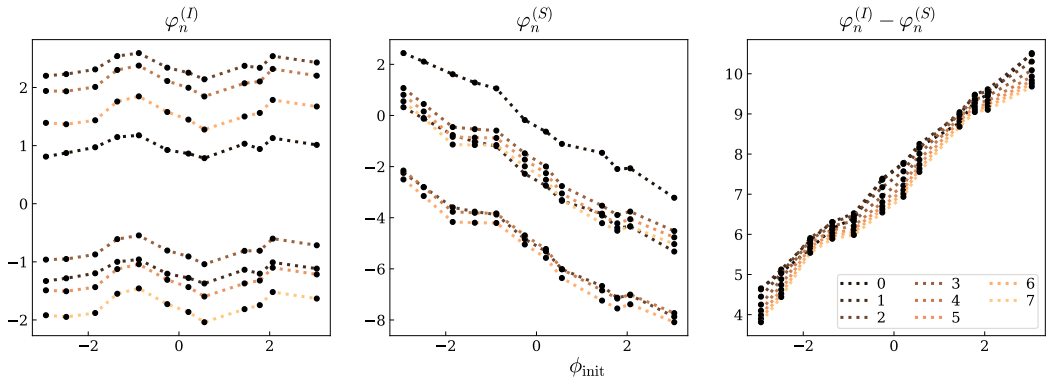

Figure 4.3: The dependence of $\varphi_n^{(I)}$, $\varphi_n^{(S)}$, as well as their difference, on $\phi_{\rm init}$. It turns out that $\varphi_n^{(I)}$ is roughly insensitive to $\phi_{\rm init}$, whereas $\varphi_n^{(S)}$ is approximately linear in $\phi_{\rm init}$.

[see their Eq. (5.1)], the angular dependence of mode amplitudes is insensitive to the mode indices [see their Fig. 12]. Similarly, for the phase of mode amplitude $\varphi_n^{(I)}$ and $\varphi_n^{(S)}$, as shown in Fig. 4.3, their dependence on $\phi_{\rm init}$ is also insensitive to the overtone index n.

The features of $\mathscr{A}_n$ and φ_n allow us to conclude that the dependence of QNM amplitudes for I_{22} and S_{22} on $\phi_{\rm init}$ can be factored out from the temporal sector, i.e.,

$$I_{22}(\phi_{\rm init}, t) \sim I_{22}^m(\phi_{\rm init}) T_I(t), \tag{4.7a}$$

$$S_{22}(\phi_{\rm init}, t) \sim S_{22}^m(\phi_{\rm init}) e^{-i\phi_{\rm init}} T_S(t), \tag{4.7b}$$

where $T_I(t)$ and $T_S(t)$ are two complex functions, corresponding to the temporal evolution of the mass and current quadrupole waves, respectively. Since $T_I(t)$ and $T_S(t)$ do not depend on $\phi_{\rm init}$, they represent the common features of all SKd binaries. We will explore the features of $T_I(t)$ and $T_S(t)$ in Sec. 4.4.

On the other hand, the progenitor configuration, at least $\phi_{\rm init}$, is encoded mainly in two functions $I_{22}^m(\phi_{\rm init})$ and $S_{22}^m(\phi_{\rm init})$. Figure 4.3 exhibits that to the leading order, $\varphi_n^{(I)}$ is insensitive to $\phi_{\rm init}$, while $\varphi_n^{(S)} \propto -\phi_{\rm init}$. As a result, $I_{22}^m(\phi_{\rm init})$ and $S_{22}^m(\phi_{\rm init})$ can be regarded approximately as two real functions. Thus the phase difference between I_{22} and S_{22}, $\Delta\Phi_{\rm IS}$, is roughly linear in $\phi_{\rm init}$. We will explore Eq. (4.7) more carefully later in Sec. 4.3, as well as extending to the full $(\chi_{init}, \theta_{\rm init}, \phi_{\rm init})$ parameter space.

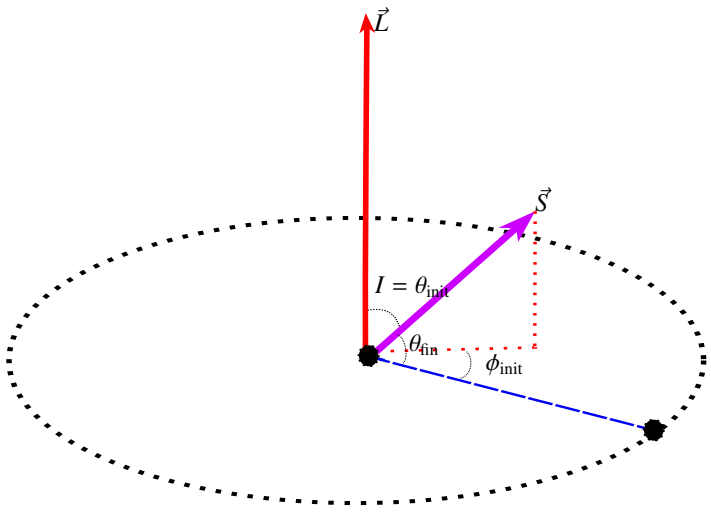

Figure 4.4: An illustration for the EMRI-parameterization $(I, \theta_{\rm fin})$ and the SKd-parameterization $(\theta_{\rm init}, \phi_{\rm init})$. The origin is chosen to be one of the BHs. Following the discussion of Hughes *et al.* [105–107], I is defined to be the angle between $\boldsymbol{L}$ (the red arrow) and $\boldsymbol{S}$ (the purple arrow), while $\theta_{\rm fin}$ is the angle between the $\boldsymbol{S}$ (the purple arrow) and the orbital separation vector (the blue dashed line). For the SKd-parameterization, $\phi_{\rm init}$ is the angle between the in-plane spin (the red dashed horizontal line) and the orbital separation vector (the blue dashed line), whereas $\theta_{\rm init}$ is the angle between $\boldsymbol{L}$ (the red arrow) and $\boldsymbol{S}$ (the purple arrow). The connection between two parameterizations is given by Eq. (4.8).

4.2.3 Full $(\theta_{\rm init}, \phi_{\rm init})$ dependence and correspondence with the extreme mass-ratio case

In the case of EMRI, Hughes *et al.* [105–107] investigated the ringdown spectra of $h_{2,\pm2}$ modes rather than I_{22} and S_{22}. In order to make a connection to their studies, we now turn our attention to $h_{2,\pm2}$.

4.2.3.1 *Mapping between SKd and EMRI system parameters*

Hughes *et al.* [105–107] parameterized EMRIs with two geometric quantities $\theta_{\rm fin}$ and I [see Fig. 1 of Ref. [105]], where $I \in [0, \pi]$ is the angle between the spin of the primary BH and the orbital angular momentum, while $\theta_{\rm fin}$ is the angle between the spin of primary BH and the orbital separation vector (at the moment of plunge), satisfying $|\cos\theta_{\rm fin}| \leq \sin I$. For SKd systems, we can find the counterparts of $(I, \theta_{\rm fin})$ if we treat one of the BHs as the "primary" object. Below we still use the same notation, namely $(I, \theta_{\rm fin})$, to refer to these two angles. As shown in Fig. 4.4, we pick the primary BH to be the center of the coordinates. I is still defined to be the angle between $\boldsymbol{L}$ (the red arrow) and $\boldsymbol{S}$ (the purple arrow), while $\theta_{\rm fin}$ remains to

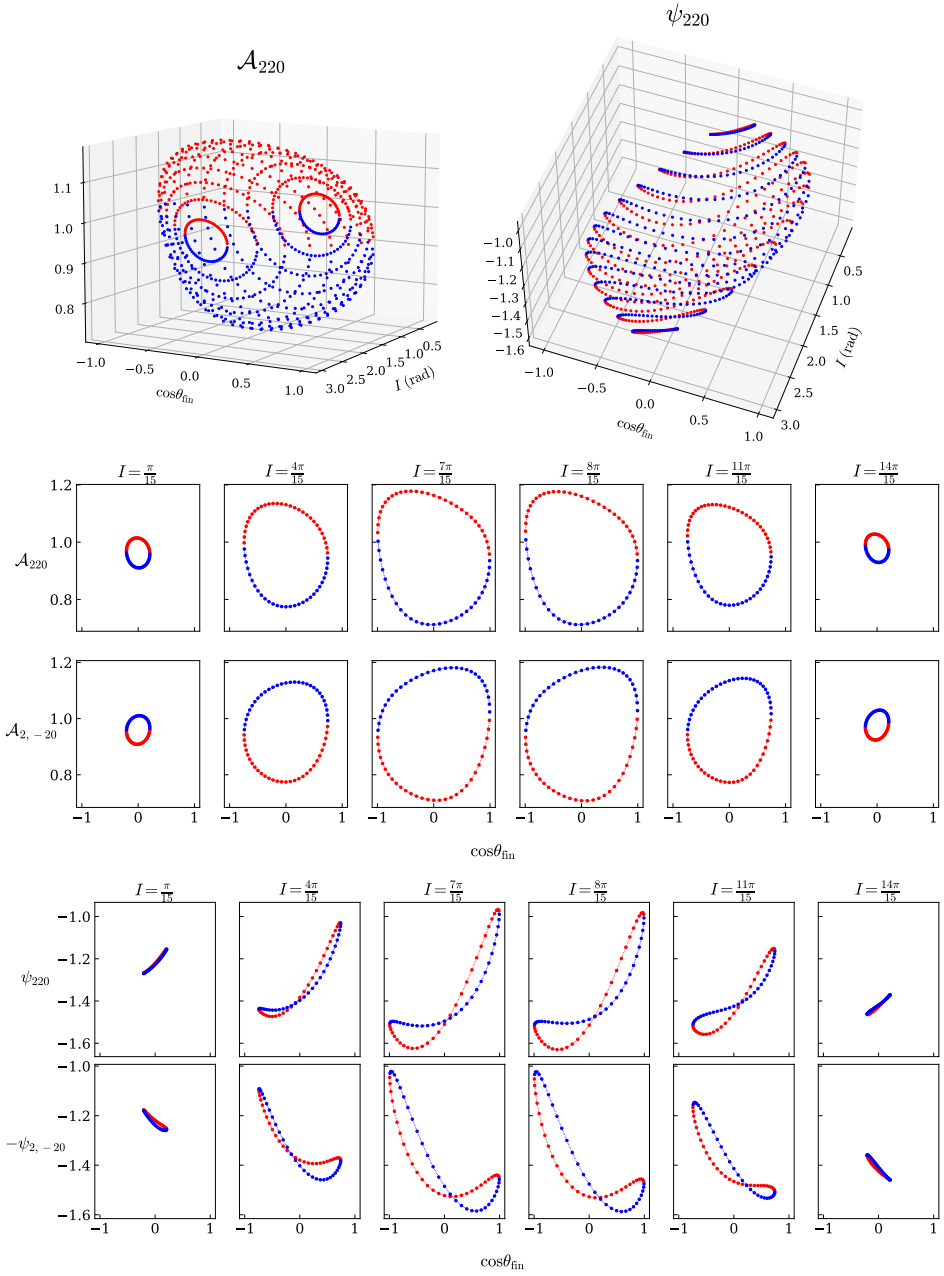

Figure 4.5: The fundamental mode amplitude and phase versus initial spin configuration $(I, \cos\theta_{\rm fin})$. Those two independent variables are chosen since they coincide with the variables used in Ref. [105] [see Eq. (4.8)]. Data are obtained from NRSur7dq4. All BBH systems are in the SKd configuration with $\chi_{\rm init} = 0.4$. Points are drawn with two colors, where blue stands for $\sin\phi_{\rm init} < 0$ while red for $\sin\phi_{\rm init} > 0$. The second and fourth rows are results of $h_{2,2}$ for some $I-$slices, while the third and fifth rows correspond to $h_{2,-2}$.

be the angle between the $\boldsymbol{S}$ (the purple arrow) and the orbital separation vector (the blue dashed line). The relations between $(I, \theta_{\rm fin})$ and our parameterization (namely

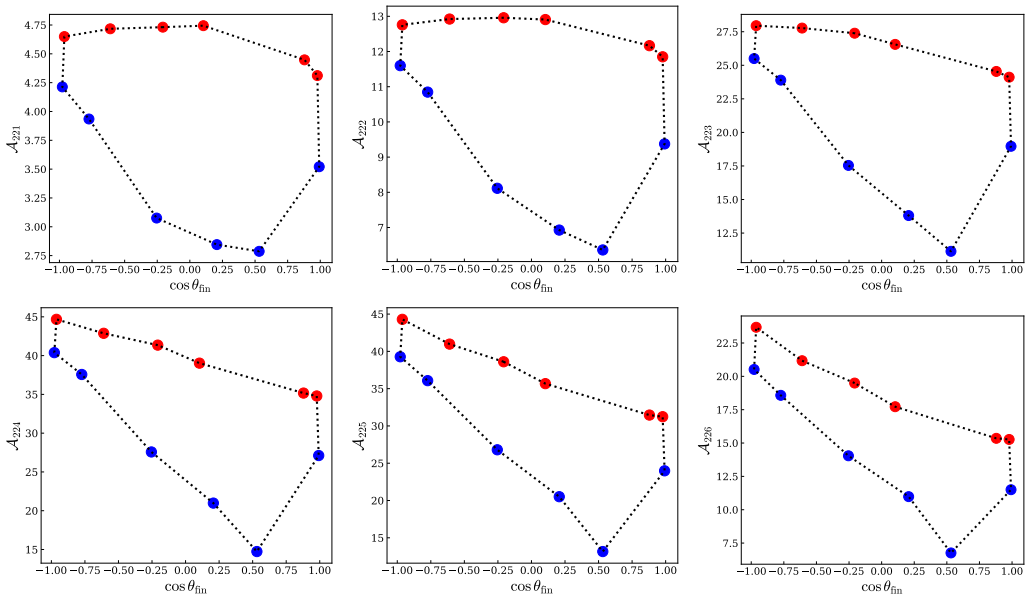

Figure 4.6: The overtone mode amplitudes $\mathcal{A}_{2,+2n}$ $(n = 1 - 6)$ versus $\cos\theta_{\rm fin}$, with the same convention as Fig. 4.5. The data are from our SKd4 runs listed in Table 4.1, which corresponds to $I = \pi/2$.

$\theta_{\rm init}$ and $\phi_{\rm init}$, see Fig. 4.1) read

$$I = \theta_{\rm init}, \qquad \cos\theta_{\rm fin} = \sin\theta_{\rm init}\cos\phi_{\rm init}. \tag{4.8}$$

We want to emphasize there are two major differences in the parameterization of EMRIs and SKds. First, the parameters for EMRIs are defined at the moment of plunge, whereas in our case, it becomes difficult to find well-defined quantities at the merger, thus we use the initial geometry instead (at a reference time during the inspiral stage). Second, for EMRIs, $\pi > I > \pi/2$ represents the retrograde motion of the small body, and hence the retrograde QNMs dominate in the ringdown signal. By contrast, only the prograde QNMs are excited for SKd systems [see Eq. (4.4)].

With the purpose of exploring the full parameter space of I and $\theta_{\rm fin}$, we now use the surrogate model NRSur7dq4. Comparing against NR ringdowns, even though NRSur7dq4 has mismatches of order $\sim 3\times10^{-4}$, we find that it is not accurate enough to reproduce the correct final mass and spin, in agreement with Ref. [116]. Mismatches of order 10^{-6} in the ringdown may be necessary to achieve this. Therefore we fix the values of the final mass and spin to the NR values (coming from NRSur7dq4Remnant) while fitting the mode amplitudes to NRSur7dq4. In addition, we consider only the fundamental mode ($n = 0$).

The results for $\mathcal{A}_{220}$ and ψ_{220} are shown in the first row of Fig. 4.5. Similar to

Refs. [105, 107], we use two colors to stand for the sign of $\dot{\theta}_{\rm fin}$, which was used in the EMRI case to represent the moving direction at the plunge ($\dot{\theta}_{\rm fin} > 0$ means that the small particle moves toward the south pole of the Kerr BH, and vice versa). In our case, $\dot{\theta}_{\rm fin}$ is determined by the sign of $\sin\phi_{\rm init}$. Comparing to Fig. 3 of Ref. [105], we can see the dependence is similar, although the absolute value of $\mathcal{A}_{220}$ differs.

In the second and third rows of Fig. 4.5, we present how mode amplitudes depend on $\cos\theta_{\rm fin}$ for several I slices [Eq. (4.8)]. Those are direct analogs Fig. 4 of Ref. [107]. It is interesting to note that $\mathcal{A}_{2,+20}$ and $\mathcal{A}_{2,-20}$ are symmetric about the axis of $\cos\theta_{\rm fin} = 0$, so are the patterns for $\psi_{2,+20}$ and $-\psi_{2,-20}$. The other intriguing feature is that the patterns for I and $\pi - I$ are similar.

For overtones $\mathcal{A}_{2,+2n}$ ($n > 0$), NRSur7dq4 is not accurate enough to provide any prediction, so we use our SKd4 runs instead (see Table 4.1), which corresponds to the $I = \pi/2$ slice. We translate our previous results in Fig. 4.2 and 4.3 to the cases of $h_{2,\pm2}$ based on Eq. (4.6). Results are shown in Fig. 4.6. We can see the patterns for high-n are more distorted.

4.2.3.2 *Understanding the QNM excitation of $h_{2,\pm2}$ in terms of (I_{22}, S_{22})*

It turns out that the features in the amplitudes $\mathcal{A}_{2,\pm2,0}$ that we discussed previously can be understood based on what we have learned about (I_{22}, S_{22}). In order to translate our previous results about (I_{22}, S_{22}) to $h_{2,\pm2}$, we use the inverse of Eq. (4.6)

$$\mathcal{A}_{2,\pm2n} e^{\pm i\psi_{2,\pm2n}} = \frac{1}{\sqrt{2}}\left[\mathscr{A}_n^{(I)} e^{i\varphi_n^{(I)}} \mp i\mathscr{A}_n^{(S)} e^{i\varphi_n^{(S)}}\right], \tag{4.9}$$

and hence

$$\mathcal{A}^2_{2,\pm2n} = \frac{1}{2}\left[\mathscr{A}_n^{(I)2} + \mathscr{A}_n^{(S)2} \mp 2\mathscr{A}_n^{(I)}\mathscr{A}_n^{(S)} \sin(\varphi_n^{(I)} - \varphi_n^{(S)})\right]. \tag{4.10}$$

As we shall explore later in Secs. 4.3.4 and 4.3.5 [see Eqs. (4.33) and (4.38)], we have two dependencies

$$\mathscr{A}_n^{(I)}(I, \theta_{\rm fin}) \sim \text{const.} + O(v^4), \qquad \mathscr{A}_n^{(S)}(I, \theta_{\rm fin}) \sim v^2 \sin I + O(v^4) \tag{4.11}$$

where we have omitted specific numerical coefficients that are independent of I and $\theta_{\rm fin}$, and v^2 is a parameter to keep track of the order of approximation (In fact, as we shall show in Sec. 4.3.4, v is the orbital velocity that is widely used in the post-Newtonian theory). Furthermore, we have

$$\varphi_n^{(I)} - \varphi_n^{(S)} \sim \phi_{\rm init} + \text{const.} \tag{4.12}$$

Using the above simple dependences of $[\mathcal{A}_n^{(I)}, \mathcal{A}_n^{(S)}, \varphi_n^{(I)} - \varphi_n^{(S)}]$ on I and $\phi_{\rm init}$, we obtain:

$$\mathcal{A}_{2,\pm 2n} \sim \text{const.} \pm \nu^2 \sin I \sin(\phi_{\rm init} + \text{const.}) + O(\nu^4). \tag{4.13}$$

As a result, for each I-slice (i.e., $\theta_{\rm init}$-slice), the $\mathcal{A}_{2,\pm 20} - \cos\theta_{\rm fin}$ pattern is an approximate Lissajous-like curve (with identical frequencies), distorted by the higher order term containing ν^4. The variation depends on I, which vanishes when $I = 0, \pi$, and is maximal when $I = \pi/2$. Physically speaking, $\mathcal{A}_{2,\pm 2n}$ depends sensitively on $\phi_{\rm init}$ when the spins of two BHs lie entirely in the orbital plane [see Fig. 4.1], but does not change with $\phi_{\rm init}$ as the spins are (anti-)parallel with the orbital angular momentum.

In addition, Eq. (4.13) implies that $\mathcal{A}_{220}$ and $\mathcal{A}_{2,-20}$ are related by a transformation $\phi_{\rm init} \to \phi_{\rm init} + \pi$, i.e., $\cos\theta_{\rm fin} \to -\cos\theta_{\rm fin}$ [see Eq. (4.8)]. This transformation represents the interchange of the in-plane spins for two BHs [see Fig. 4.1]. In fact, as we shall study in Sec. 4.3.2, this conclusion can be generalized to the entire evolution regime (not only the ringdown phase). The symmetry of the SKd system results in [see Eq. (4.26)]

$$\begin{aligned} h_{\ell m}(\pi - I, \phi_{\rm init}) &= (-1)^m h_{\ell m}(I, \phi_{\rm init}), \\ h_{\ell m}(I, \phi_{\rm init} + \pi) &= (-1)^\ell h^*_{\ell,-m}(I, \phi_{\rm init}), \end{aligned}$$

i.e., $\mathcal{A}_{2,\pm 2n}$ remains unchanged when $I \to \pi - I$ (two BHs interchange their z-component spins), and $\mathcal{A}_{2,+2n} \to \mathcal{A}_{2,-2n}$ and $\psi_{2,+20} \to -\psi_{2,-20}$ when $\phi_{\rm init} \to \phi_{\rm init} + \pi$ (two BHs interchange their in-plane spins)[1]. In Fig. 4.5, we can clearly see the patterns for $\mathcal{A}_{220}$ and $\mathcal{A}_{2,-20}$, as well as the patterns for $\psi_{2,+20}$ and $-\psi_{2,-20}$, are symmetric about the $\cos\theta_{\rm fin} = 0$ axis. Meanwhile, the patterns for $\mathcal{A}_{2\pm 20}$ are symmetric about the $I = \pi/2$ axis.

4.3 The feature of mass and current quadrupole waves

In the last section, we explored how QNMs are excited with different initial parameters $(\theta_{\rm init}, \phi_{\rm init})$. We now aim to study the features of ringdown more quantitatively. In particular, we focus on the mass (I_{22}) and current (S_{22}) quadrupole waves of SKd systems, and relate their features to $(\chi_{\rm init}, \theta_{\rm init}, \phi_{\rm init})$. Moreover, since kick velocity is one of the important quantities that reflects SKd systems' properties, we also include it in our study.

[1] Equivalently, $\cos\theta_{\rm fin} \to -\cos\theta_{\rm fin}$.

4.3.1 A brief review

This subsection briefly reviews some facts about gravitational recoil. In particular, we relate the kick velocity to the radiative mass and current quadrupole waves.

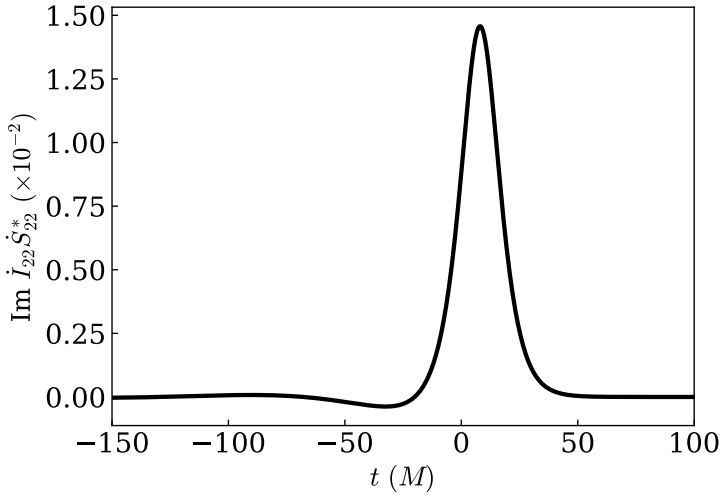

Figure 4.7: The integrand of Eq. (4.17) for the SKd4–'06' system. The majority kick velocity is accumulated around $t \sim 0M$, and the final kick is 4.75×10^{-3}.

It has been shown that for a SKd system, the kick magnitude can be estimated with a simple formula [78–80]

$$v_f \sim \chi_{\rm init} \sin(\phi_{\rm init} - \phi^{(0)}_{\rm init}) \sin\theta_{\rm init}, \tag{4.14}$$

where $\phi^{(0)}_{\rm init}$ is a constant. Eq. (4.14) is based on the computation of linear momentum carried away by GW [117]

$$\dot{P}_z = \lim_{D\to\infty} \frac{1}{24\pi}(\dot{h}_{22}\dot{h}^*_{22} - \dot{h}_{2,-2}\dot{h}^*_{2,-2}), \tag{4.15}$$

where $*$ stands for complex conjugate, D is the distance between the source and the observer, and the z-axis is in the direction of orbital angular momentum. Here we have ignored the effects of other modes since they are negligible.

In terms of I_{22} and S_{22} [Eq. (4.3)], Eq. (4.15) can also be written as

$$\dot{P}_z = -\frac{1}{12\pi}{\rm Im}\ \dot{I}_{22}\dot{S}^*_{22}, \tag{4.16}$$

and the final kick velocity is given by

$$m_f v_f = \frac{1}{12\pi}{\rm Im}\int \dot{I}_{22}\dot{S}^*_{22}dt = \frac{1}{12\pi}{\rm Im}\int |\dot{I}_{22}||\dot{S}_{22}|e^{i\Phi_{i\dot{S}}}dt, \tag{4.17}$$

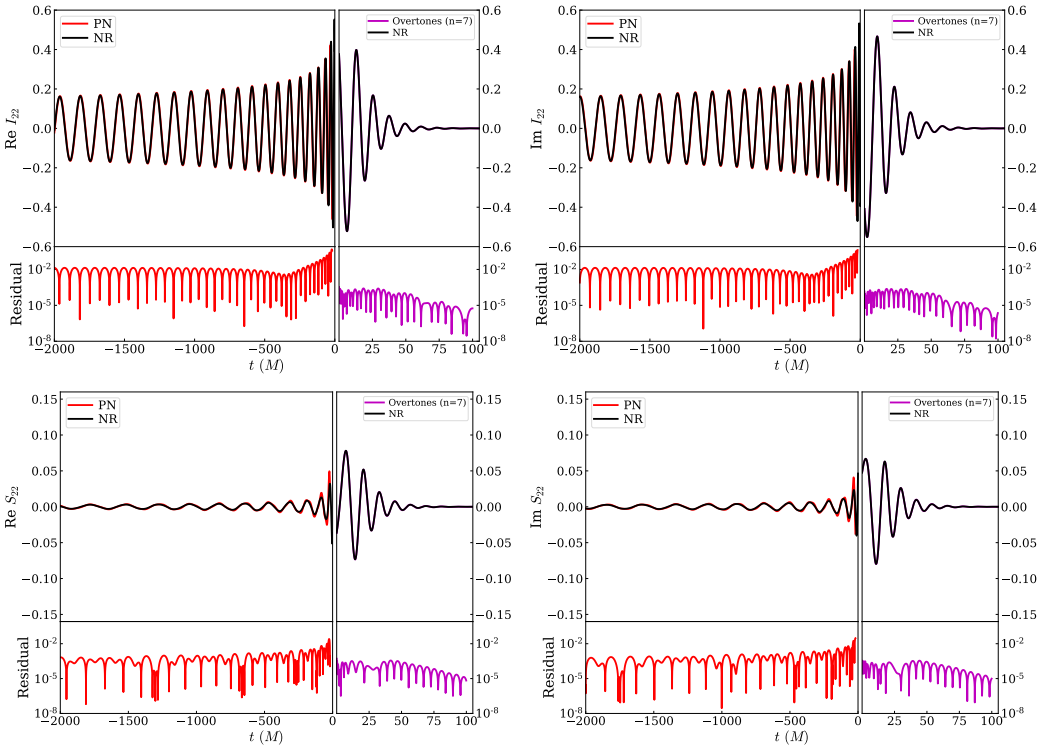

Figure 4.8: The time evolution of I_{22} (upper row) and S_{22} (bottom row) for the SKd4–'03' system, where $t = 0M$ stands for the peak of strain amplitude. The mass (I_{22}) and current (S_{22}) quadrupole waves are compared to PN formulas [Eq. (4.18)] during the inspiral stage, and to QNMs (7 overtones) in the ringdown regime.

with $\Phi_{\dot{I}\dot{S}}$ the phase difference between $\dot{I}_{22}$ and $\dot{S}_{22}$. Note that the change of sign from Eq. (4.16) to (4.17) is a result of linear momentum conservation. In Fig. 4.7, we show the time evolution of the above-mentioned integrand for SKd4–'06' (cf. Table 4.1). We can see that most of the kick velocity is accumulated around $t \sim 0M$.

During the inspiral stage, it was shown that I_{22} and S_{22} are related to the source quadrupole moments[2]. At the leading order, from Refs. [70, 118], we write

$$I_{22}(t) = -\frac{M}{2}\sqrt{\frac{2\pi}{5}}\frac{d^2}{dt^2}r(t)^2 e^{-2i\phi(t)}, \tag{4.18a}$$

$$S_{22}(t) = \sqrt{\frac{2\pi}{5}}\chi \sin\theta(t)\frac{d^2}{dt^2}r(t)e^{-i\phi(t)-i\phi_{\rm pre}(t)}, \tag{4.18b}$$

where M is the total mass of the BBH system; χ is the dimensionless spin of an individual BH; $\phi(t)$ and $r(t)$ are the orbital phase and separation, respectively; $\theta(t)$ is the polar angle of the spin; and $\phi_{pre}(t)$ is the precession angle (the azimuthal

[2]Hereafter we shall not distinguish the source quadrupole moment and the (radiative) quadrupole wave since it will not cause any confusion.

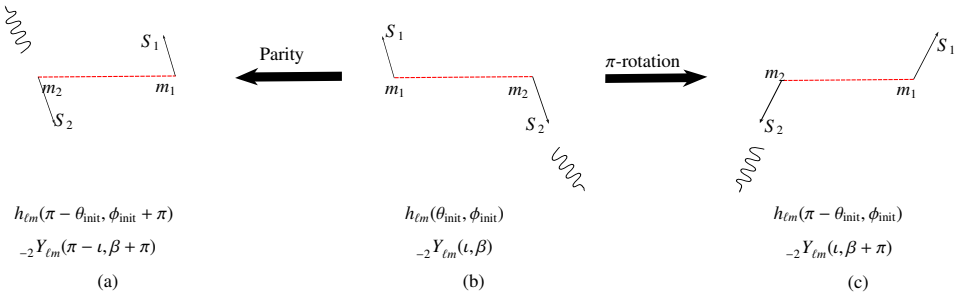

Figure 4.9: Parity inversion of a SKd BBH system. We use arrows to represent the spin direction of BHs, and wavy lines to stand for the GW propagating direction. The complex strain of a SKd system is totally determined by two extrinsic parameters (ι,β), and three intrinsic parameters $(\chi_{\rm init},\theta_{\rm init},\phi_{\rm init})$. Here the intrinsic parameters are the spin of the left BH. The properties of the right BH are determined based on the SKd condition. Figs. 4.9 (a) and (b) are related by a parity inversion: two BHs exchange their locations while having their own spins fixed. As a result, the GW propagation direction and both spins change sign, i.e., $(\iota,\beta)\longleftrightarrow(\pi-\iota,\pi+\beta)$ and $(\theta_{\rm init},\phi_{\rm init})\longleftrightarrow(\pi-\theta_{\rm init},\pi+\phi_{\rm init})$. Figs. 4.9 (b) and (c) are related by a π-rotation about the orbital angular momentum. Thus we have $(\iota,\beta)\longleftrightarrow(\iota,\pi+\beta)$ and $(\theta_{\rm init},\phi_{\rm init})\longleftrightarrow(\pi-\theta_{\rm init},\phi_{\rm init})$.

angle of the in-plane spin component). Note that at the initial time $t_{\rm init}$

$$\theta_{\rm init}\coloneqq\theta(t_{\rm init}),\qquad\qquad \phi_{\rm init}\coloneqq\phi(t_{\rm init}).$$

For instance, we choose SKd4–'03' (see Table 4.1) and compare its radiative multipolar waves I_{22} and S_{22} to PN formulas in Eq. (4.18). We read off the values of $r(t)$, $\theta(t)$, and $\phi(t)$ directly from the outputs of NR simulation. The results are shown in Fig. 4.8. For comparison, we also fit the ringdown signal with QNMs (7 overtones), starting from $t=0M$. We can see the Newtonian formulas can accurately model the phase evolution up to $t\sim-250M$. Meanwhile, both I_{22} and S_{22} are described by 7 overtones accurately from $t=0M$.

In the rest of this section, we shall discuss how I_{22} and S_{22} depend on $(\chi_{\rm init},\theta_{\rm init},\phi_{\rm init})$, and apply our understanding to the gravitational recoil.

4.3.2 Symmetry properties of I_{22} and S_{22}

Before exploring the detailed relations between (I_{22},S_{22}) and $(\chi_{\rm init},\theta_{\rm init},\phi_{\rm init})$, we first take advantage of the symmetry of SKd systems, and study its implication on (I_{22},S_{22}). As shown in Fig. 4.9, there are three SKd binaries, where (a) and (b) are related by a parity transformation, i.e., two BHs interchange their locations while

having their spin directions fixed, recalling that spin is an axial vector, which is not changed by the parity transformation. On the other hand, we rotate the whole system in (b) about the orbital angular momentum by π, and obtain (c). We use wavy lines to stand for the GW propagating direction, and (ι, β) are the coordinates of the observer in (b), as defined in Eq. (4.2). The coordinates of observers in (a) and (c) are transformed accordingly. As discussed in Eq. (4.2), $h(t, \iota, \beta)$ can be decomposed into the extrinsic part ${}_{-2}Y_{\ell m}(\iota, \beta)$ and the intrinsic part $h_{\ell m}(\theta_{\rm init}, \phi_{\rm init})$[3]. Here we omit $\chi_{\rm init}$ in the argument of $h_{\ell m}$ since it has no impact on the transformation in question.

Fig. 4.9 (a) and (b) are related by a parity transformation, hence we have (see Sec. 4.9 for more details)

$$h^{(a)} = h^{(b)*}, \tag{4.19}$$

i.e.,

$$\begin{aligned} &h_{\ell m}(\theta_{\rm init}, \phi_{\rm init}) {}_{-2}Y_{\ell m}(\iota, \beta) \\ &= h^*_{\ell m}(\pi - \theta_{\rm init}, \phi_{\rm init} + \pi) {}_{-2}Y_{\ell m}{}^*(\pi - \iota, \pi + \beta). \end{aligned} \tag{4.20}$$

Using the fact that

$${}_{-2}Y_{\ell m}{}^*(\pi - \iota, \pi + \beta) = (-1)^{\ell+m} {}_{-2}Y_{\ell,-m}(\iota, \beta), \tag{4.21}$$

we obtain

$$h_{\ell m}(\theta_{\rm init}, \phi_{\rm init}) = (-1)^{\ell+m} h^*_{\ell,-m}(\pi - \theta_{\rm init}, \phi_{\rm init} + \pi). \tag{4.22}$$

On the other hand, Fig. 4.9 (b) and (c) are related by a global rotation. Therefore, the observable $h(t, \iota, \beta)$ should not be affected

$$h^{(b)} = h^{(c)}, \tag{4.23}$$

i.e.,

$$\begin{aligned} &h_{\ell m}(\theta_{\rm init}, \phi_{\rm init}) {}_{-2}Y_{\ell m}(\iota, \beta) \\ &= h_{\ell m}(\pi - \theta_{\rm init}, \phi_{\rm init}) {}_{-2}Y_{\ell m}(\iota, \pi + \beta). \end{aligned} \tag{4.24}$$

Recalling that

$${}_{-2}Y_{\ell m}(\iota, \pi + \beta) = (-1)^m {}_{-2}Y_{\ell m}(\iota, \beta), \tag{4.25}$$

[3] We use $(\theta_{\rm init}, \phi_{\rm init})$ to stand for the spin of BH on the left. The other spin is determined uniquely by the SKd condition.

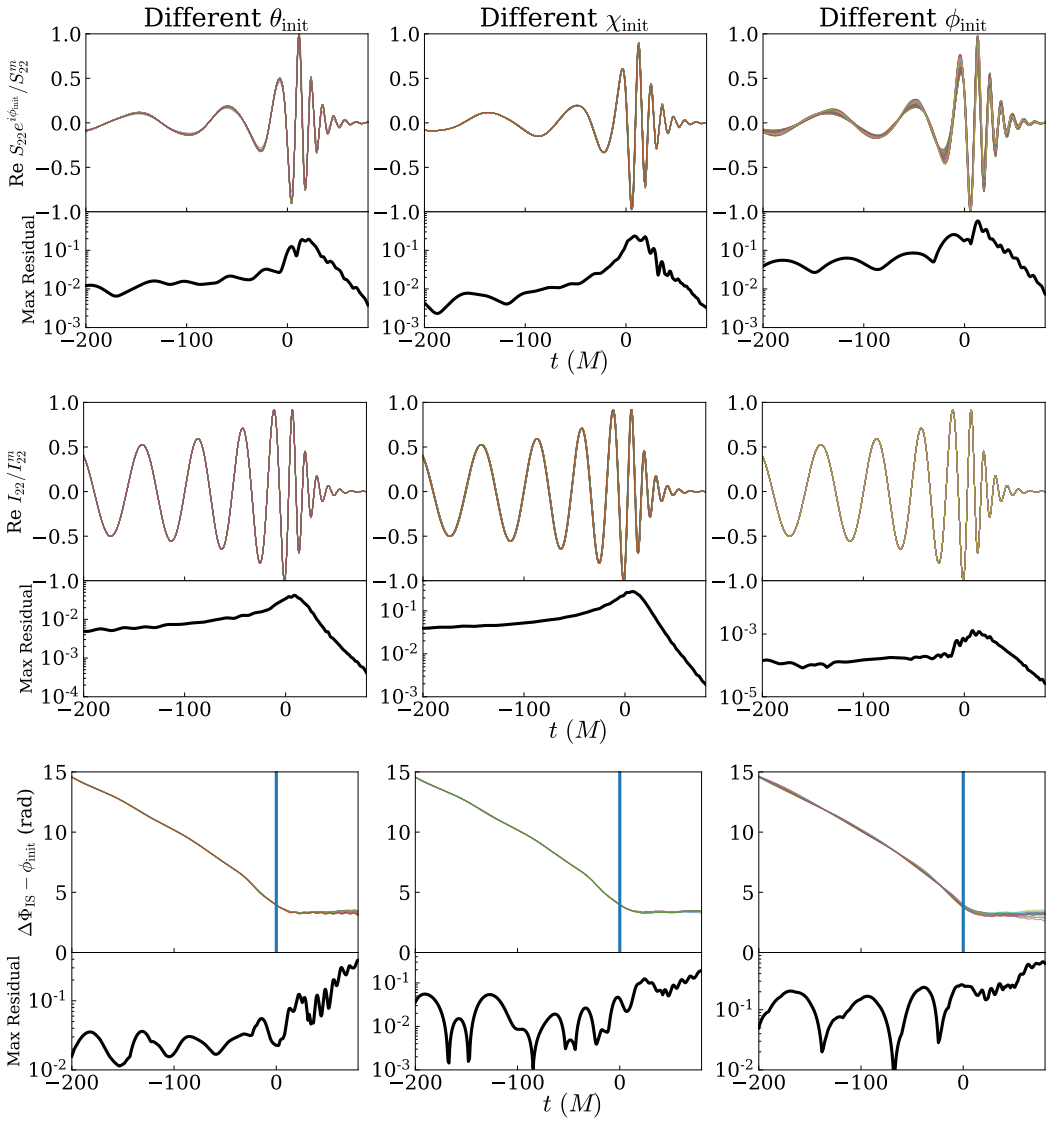

Figure 4.10: The time evolution of the real part of the normalized S_{22} (upper row), the real part of the normalized I_{22} (middle row), as well as $\Delta\Phi_{\rm IS}-\phi_{\rm init}$ (bottom row), using the SKd BBH configuration from NRSur7dq4. The imaginary part is similar. We sample in total of 180 cases with different $\theta_{\rm init}\in[0,\pi]$ (left column), $\chi_{\rm init}\in[0,0.8]$ (middle column), and $\phi_{\rm init}\in[0,2\pi]$ (right column), and plot them on top of each other. 'Max Residual' is defined to be the maximum difference of all cases at each time step. The normalized I_{22} and S_{22} are insensitive to $(\chi_{\rm init},\theta_{\rm init},\phi_{init})$, to the level of $\sim 0.1\%-30\%$.

we then have

$$h_{\ell m}(\pi-\theta_{\rm init},\phi_{\rm init})=(-1)^m h_{\ell m}(\theta_{\rm init},\phi_{\rm init}), \tag{4.26a}$$

$$h_{\ell m}(\theta_{\rm init},\phi_{\rm init}+\pi)=(-1)^\ell h^*_{\ell,-m}(\theta_{\rm init},\phi_{\rm init}), \tag{4.26b}$$

where the first line is the result of Eqs. (4.24) and (4.25), and the second line comes

from the combination of Eq. (4.22) and (4.26a). Eqs. (4.26) give the transformation of $h_{\ell m}$ under $\theta_{\rm init} \to \pi - \theta_{\rm init}$ (two BHs interchange their z-component spins) and $\phi_{\rm init} \to \phi_{\rm init} + \pi$ (two BHs interchange their in-plane spins). As we discussed in Sec. 4.2.3, Eq. (4.26) directly leads to several features revealed in Fig. 4.5: the patterns for $\mathcal{A}_{2\pm 20}$, as well as $\psi_{2,+20}$ and $-\psi_{2,-20}$, have a reflective symmetry about the $\cos\theta_{\rm fin} = 0$ axis; and the patterns for $\mathcal{A}_{2\pm 20}$ are symmetric about the $I = \pi/2$ axis.

We then apply Eqs. (4.26) to the case of $I_{\ell m}$ and $S_{\ell m}$, [see Eqs. (4.3)]

$$I_{\ell m}(\pi - \theta_{\rm init}, \phi_{\rm init}) = (-1)^m I_{\ell m}(\theta_{\rm init}, \phi_{\rm init}), \tag{4.27a}$$

$$S_{\ell m}(\pi - \theta_{\rm init}, \phi_{\rm init}) = (-1)^m S_{\ell m}(\theta_{\rm init}, \phi_{\rm init}), \tag{4.27b}$$

$$I_{\ell m}(\theta_{\rm init}, \phi_{\rm init} + \pi) = (-1)^{\ell+m} I_{\ell m}(\theta_{\rm init}, \phi_{\rm init}), \tag{4.27c}$$

$$S_{\ell m}(\theta_{\rm init}, \phi_{\rm init} + \pi) = (-1)^{\ell+m+1} S_{\ell m}(\theta_{\rm init}, \phi_{\rm init}), \tag{4.27d}$$

One can find the counterpart of Eqs. (4.27) for EMRIs in Eq. (4.6) of Ref. [107]. Those relations imply that the dependence of I_{22} and S_{22} on $\theta_{\rm init}$ is symmetric about $\theta_{\rm init} = \pi/2$ axis, whereas the dependence of $|I_{22}|$ and $|S_{22}|$ on $\phi_{\rm init}$ have a period π[4]. We shall see these features shortly from numercal results.

4.3.3 Time dependence of I_{22} and S_{22}

After the study of $(I_{22}, S_{22}) - (\chi_{\rm init}, \theta_{\rm init}, \phi_{\rm init})$ dependence enforced by the symmetry, we are in a position to carry out more detailed analyses. Based on the discussion around Eq. (4.7), for the post-merger evolution of I_{22} and S_{22}, their $\phi_{\rm init}$ dependence can be factored out. In particular, the spin sector of I_{22} is described by a function $I^m_{22}(\phi_{\rm init})$, and that of S_{22} is given by $S^m_{22}(\phi_{\rm init})e^{-i\phi_{\rm init}}$. In fact, those features are also consistent with PN predictions, as shown in Eqs. (4.18): To the leading PN order, I_{22} is independent of $(\chi_{\rm init}, \theta_{\rm init}, \phi_{\rm init})$, whereas $S_{22} \sim \chi_{\rm init} \sin\theta_{\rm init} e^{-i\phi_{\rm init}}$. In light of the facts, it is reasonable to conjecture that the separability between the spin sector (including $\chi_{\rm init}, \theta_{\rm init}, \phi_{\rm init}$) and the temporal sector is preserved throughout the entire process, i.e.,

$$I_{22}(t, \chi_{\rm init}, \theta_{\rm init}, \phi_{\rm init}) = I^m_{22}(\chi_{\rm init}, \theta_{\rm init}, \phi_{\rm init}) T_I(t), \tag{4.28a}$$

$$S_{22}(t, \chi_{\rm init}, \theta_{\rm init}, \phi_{\rm init}) = S^m_{22}(\chi_{\rm init}, \theta_{\rm init}, \phi_{\rm init}) e^{-i\phi_{\rm init}} T_S(t), \tag{4.28b}$$

where $T_I(t)$ and $T_S(t)$ are two complex functions of time, which are normalized such that they each is equal to 1 at the moment when its magnitude is at maximum.

[4] Here we use the absolute value for future convenience.

As a result, I^m_{22} and S^m_{22} are in fact the peak values of I_{22} and S_{22}, respectively, i.e.,

$$I^m_{22}(\chi_{\rm init},\theta_{\rm init},\phi_{\rm init}) = \max_t |I_{22}(t,\chi_{\rm init},\theta_{\rm init},\phi_{\rm init})|, \tag{4.29a}$$

$$S^m_{22}(\chi_{\rm init},\theta_{\rm init},\phi_{\rm init}) = \max_t |S_{22}(t,\chi_{\rm init},\theta_{\rm init},\phi_{\rm init})|. \tag{4.29b}$$

We want to emphasize that Eq. (4.29) is an approximation based on the observation we made in Fig. 4.3, namely to the leading order $\varphi^{(I)}_n$ is insensitive to $\phi_{\rm init}$, while $\varphi^{(S)}_n \propto -\phi_{\rm init}$. This fact allows us to treat I^m_{22} and S^m_{22} as two real functions [see the context below Eq. (4.7)]. The higher order corrections will lead to additional phase factors for both I^m_{22} and S^m_{22}. This is beyond the scope of this work.

To test the accuracy of Eqs. (4.28) and (4.29), we use NRSur7dq4 to obtain I_{22} and S_{22} with different initial spin configurations. They are normalized by I^m_{22} and $S^m_{22}e^{-i\phi_{\rm init}}$, respectively. The results are shown in the first two rows of Fig. 4.10. To avoid redundancy, we present only the real part since the imaginary part is similar. As we can see, the normalized I_{22} with different $(\chi_{\rm init},\theta_{\rm init},\phi_{\rm init})$ evolves in a similar way, so does the normalized S_{22}. The residuals imply that Eqs. (4.28) are accurate to $\sim 0.1\% - 30\%$ throughout the entire evolution. We remark that the accuracy is limited by the approximation adopted in Eq. (4.29), where I^m_{22} and S^m_{22} are treated as two real functions and their phases (higher order effects) are not included. If we omit these additional phase terms that are functions of $(\chi_{\rm init},\theta_{\rm init},\phi_{\rm init})$, there will be a non-negligible increase in the residual. In fact, if we consider only the absolute value of the normalized I_{22} and S_{22}, the residual can be decreased by a factor of $1.6 \sim 100$.

Nevertheless, the progenitor's information is primarily described by the peak value of mass and current quadrupole waves, I^m_{22} and S^m_{22}. On the other hand, the temporal evolution, $T_I(t)$ and $T_S(t)$, encode the common feature of SKd systems. In particular, as we discussed in Sec. 4.3.1, the phase difference between $T_I(t)$ and $T_S(t)e^{-i\phi_{\rm init}}$, denoted by $\Delta\Phi_{\rm IS}$

$$\Delta\Phi_{\rm IS} \equiv \arg(T_I) - \arg(T_S e^{-i\phi_{\rm init}}) \equiv \arg(I_{22}) - \arg(S_{22}), \tag{4.30}$$

is closely related to gravitational recoil.

We have introduced three quantities, I^m_{22}, S^m_{22} and $\Delta\Phi_{\rm IS}$, which are important characteristics of SKd systems. In the rest of this section, we aim to study I^m_{22}, S^m_{22} and $\Delta\Phi_{\rm IS}$ more carefully and more quantitatively. In particular, we will show that I^m_{22} and S^m_{22} are subject to the periodic condition in both $\theta_{\rm init}-$ and $\phi_{\rm init}-$ directions, as enforced by the symmetry in Eqs. (4.27).

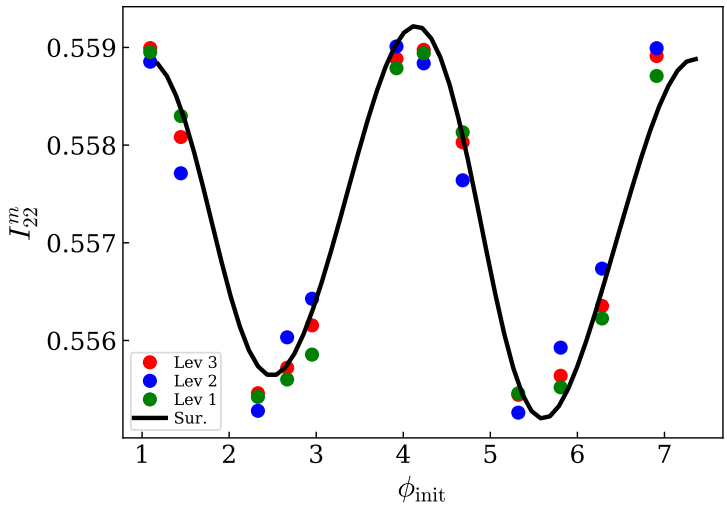

Figure 4.11: The peak value of mass quadrupole wave I^m_{22} as a function of $\phi_{\rm init}$. We use SKd4 systems listed in Table 4.1. The black curve is from NRSur7dq4, whereas points are from NR simulations. Colors (labeled by Lev) correspond to numerical resolutions, where "Lev 1" stands for the lowest resolution. Predictions of NRSur7dq4 are consistent with NR results: I^m_{22} oscillates with $\phi_{\rm init}$ on the level of $\sim 0.36\%$, around a base value ~ 0.557.

4.3.4 The peak of mass quadrupole wave I^m_{22}

We saw that I^m_{22} is an important characteristic quantity for SKd systems. In fact, it was shown that the remnant BH spin is already encoded in the peak amplitude of the gravitational wave strain [56]. Therefore, it is instructive to study how I^m_{22} depends on $(\chi_{\rm init}, \theta_{\rm init}, \phi_{\rm init})$.

We first look at our SKd4 NR runs listed in Table 4.1. Fig. 4.11 shows I^m_{22} as a function of $\phi_{\rm init}$. We can see that I^m_{22} does depend weakly on $\phi_{\rm init}$ for all three numerical resolutions, which verifies that the dependence is not a numerical artifact. For comparison purposes, we also show the prediction of NRSur7dq4 with the same BBH system but varying $\phi_{\rm ini}$. Two results are close. With different $\phi_{\rm init}$, I^m_{22} varies on the level of $\sim 0.36\%$, around a base value ~ 0.557. As discussed earlier, $I^m_{22} - \phi_{\rm init}$ relation is expected to have a period of π [Eq. (4.27)]. However, the black curve is slightly asymmetric. We attribute this to the numerical error of NRSur7dq4. Furthermore, the change of I^m_{22} is much smaller than the base value, which is qualitatively consistent with PN predictions, because the variation caused by spin is 2PN [118] smaller than the leading contribution from the orbital mass quadrupole moment [Eq. (4.18a)].

To explore a larger parameter space, we use NRSur7dq4 and plot I^m_{22} as a function of

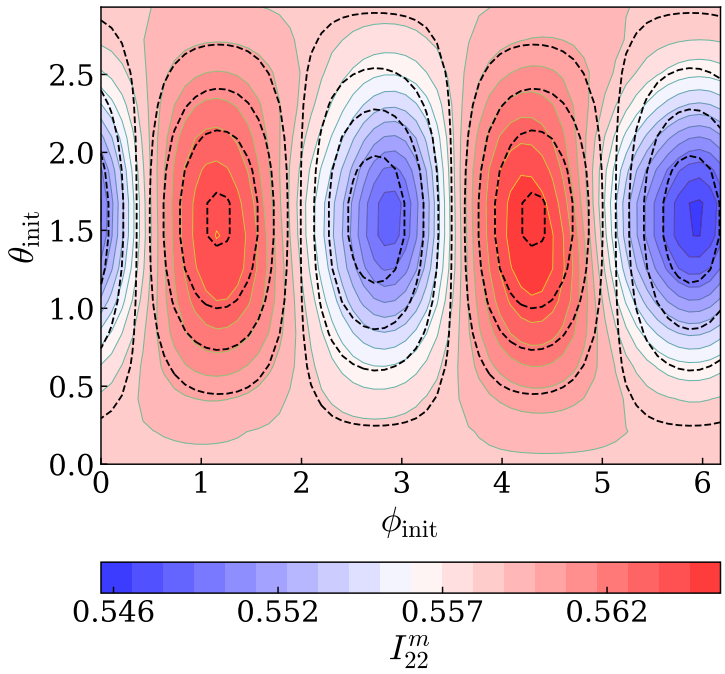

Figure 4.12: The peak value of mass quadrupole wave I^m_{22} as a function of $(\theta_{\rm init}, \phi_{\rm init})$, with $\chi_{\rm init} = 0.8$ (SKd configuration). Results are from NRSur7dq4. The pattern is symmetric about $\theta_{\rm init} = \pi/2$, and has a period π in the $\phi_{\rm init}$-direction, consistent with Eq. (4.27). The contours with dashed lines are the prediction of the PN-inspired counterpart in Eq. (4.33).

$(\theta_{\rm init}, \phi_{\rm init})$ in Fig. 4.12, with $\chi_{\rm init} = 0.8$. The pattern exhibits quadrupolar structure, i.e., symmetric about $\theta_{\rm init} = \pi/2$, and has a period π in the $\phi_{\rm init}$-direction. This is consistent with what we obtained in Eq. (4.27).

To have a better understanding of I^m_{22}, we use PN prediction of mass quadrupole wave during the inspiral stage [118]

$$\mathcal{I}_{22} = \mathcal{I}_{\rm orb} + \mathcal{I}_{S1} + \mathcal{I}_{S2}, \tag{4.31}$$

where

$$\mathcal{I}_{\rm orb} = -\frac{M}{2}\sqrt{\frac{2\pi}{5}} r^2 e^{i\phi}, \tag{4.32a}$$

$$\mathcal{I}_{S1} = \sqrt{\frac{2\pi}{5}}\frac{M^3}{16}\chi^2_{\rm init}\sin^2\theta_{\rm init} e^{-2i\phi_{\rm init}}, \tag{4.32b}$$

$$\mathcal{I}_{S2} = -\sqrt{\frac{2\pi}{5}}\frac{M^3}{16}\chi^2_{\rm init} v^2, \tag{4.32c}$$

with $v \sim \sqrt{M/r}$ the velocity of an individual BH. In Eq. (4.31), the leading contribution from the orbital sector $\mathcal{I}_{\rm orb}$ is modified by the spin sector $\mathcal{I}_{S1,2}$. As discussed

Table 4.2: The coefficients in Eq. (4.33) by fitting to the NRSur7dq4 data. The values of $Q_{\rm orb}/Q_{S1}$ and Q_{S2}/Q_{S1} are close to the PN predictions in Eqs. (4.34).

$Q_{\rm orb}$	Q_{S2}	Q_{S1}	$\tan 2\phi_0$	$Q_{\rm orb}/Q_{S1}$	Q_{S2}/Q_{S1}
0.557	2.72×10^{-3}	12.2×10^{-3}	−0.98	45.7	0.22

in Ref. [119, 120], the amplitudes of ringdown waveforms in different (ℓ, m) modes are related to those of the corresponding modes during the inspiral stage. Therefore, we can write down a fitting formula for the relation $I^m_{22} - (\chi_{\rm init}, \theta_{\rm init}, \phi_{\rm init})$, inspired by Eq. (4.31) and the definition of I_{22} in Eq. (4.3),

$$\begin{aligned} I^m_{22} &= Q_{\rm orb} + Q_{S1}\chi^2_{\rm init}\sin^2\theta_{\rm init}\sin 2(\phi_{\rm init}+\phi_0) \\ &+ Q_{S2}\chi^2_{\rm init}, \end{aligned} \tag{4.33}$$

where $Q_{\rm orb}, Q_{S1}, Q_{S2}$ are constants. Their fitted values are listed in Table 4.2, and the contours of Eq. (4.33) are plotted as dashed lines in Fig. 4.12. We note that Eq. (4.33) was applied to understand the features of $\mathscr{A}^{(I)}_n$ in Sec. 4.2.3 [see Eq. (4.11)], where we used the fact that $\mathscr{A}^{(I)}_n$ is insensitive to the overtone index n and we ignored the mixing between overtones.

Three terms in Eq. (4.33) correspond to $\mathcal{I}_{\rm orb}$, $\mathcal{I}_{S1}$ and $\mathcal{I}_{S2}$, respectively. They imply that

$$Q_{\rm orb}/Q_{S1} \sim |\mathcal{I}_{\rm orb}|\chi^2_{\rm init}/|\mathcal{I}_{S1}| \sim 8\frac{r^2}{M^2} \sim 72, \tag{4.34a}$$

$$Q_{S2}/Q_{S1} \sim |\mathcal{I}^{ij}_{S2}|\sin^2\theta_{\rm init}/|\mathcal{I}^{ij}_{S1}| \sim v^2 \sim 0.3, \tag{4.34b}$$

where the formula is evaluated at $r = 3M$, i.e., the radius of the light ring. In fact, values in Eq. (4.34) are close to the fitted result listed in Table 4.2. Therefore, the peak of mass quadrupole momentum I^m_{22}, as an important characteristic of the ringdown phase, is still qualitatively consistent with the prediction of PN theory.

Although Eq. (4.33) can predict the major pattern of $I^m_{22} - (\theta_{\rm init}, \phi_{\rm init})$ relation, a correction term

$$\sim \chi^4_{\rm init}\sin^4\theta_{\rm init} f(\sin\phi_{\rm init}, \cos\phi_{\rm init}), \tag{4.35}$$

is still needed if one wants to further recover sub-leading features. Here $f(\sin\phi_{\rm init}, \cos\phi_{\rm init})$ is a function of $\phi_{\rm init}$, corresponding to higher PN correction.

4.3.5 The peak of current quadrupole wave S^m_{22}

We now turn our attention to S^m_{22}. In Fig. 4.13, we use NRSur7dq4 and plot $S^m_{22} - (\theta_{\rm init}, \phi_{\rm init})$ with $\chi_{\rm init} = 0.8$. The pattern is still symmetric about $\theta_{\rm init} = \pi/2$

and has a period π in the $\phi_{\rm init}$-direction, consistent with Eq. (4.27). We repeat our previous process and use PN predictions to understand the pattern. With PN theory, we have [118]

$$\mathcal{S}_{22} = \mathcal{S}_{22}^{(1)} + \mathcal{S}_{22}^{(2)}, \tag{4.36}$$

where

$$\mathcal{S}_{22}^{(1)} \sim \chi_{\rm init} \sin\theta_{\rm init} r e^{-i\phi_{\rm init}}, \tag{4.37a}$$
$$\mathcal{S}_{22}^{(2)} \sim -\chi_{\rm init} r v^2 \sin\theta_{\rm init} \cos\phi_{\rm init}. \tag{4.37b}$$

Eqs. (4.37) lead to a fitting formula

$$S_{22}^{m2} = \chi_{\rm init}^2 \sin^2\theta_{\rm init}[Q^{(1)} + Q^{(2)} \sin 2(\phi_{\rm init} + \phi_S)], \tag{4.38}$$

where $Q^{(1)}$ and $Q^{(1)}$ correspond to $\mathcal{S}_{22}^{(1)}$ and $\mathcal{S}_{22}^{(2)}$, respectively. The fitted value of $Q^{(2)}$ and $Q^{(1)}$ are 9.43×10^{-3} and 4.28×10^{-2}. The ratio, $Q^{(2)}/Q^{(1)} \sim 0.22$, is close to v^2 at the light ring (0.33), which is again consistent with the PN prediction $Q^{(2)}/Q^{(1)} \sim v^2$. Therefore, the peak of the current quadrupole wave S_{22}^m also inherits information from the PN regime.

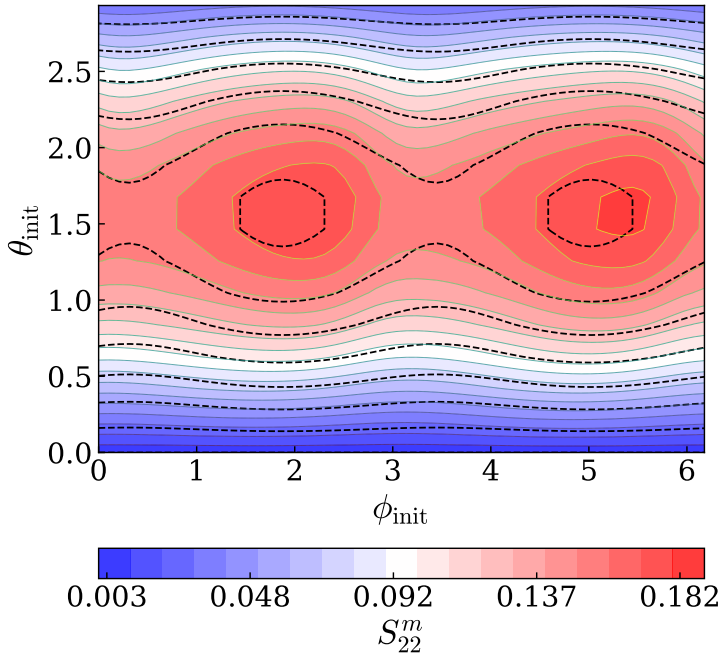

Figure 4.13: The peak value of current quadrupole wave S_{22}^m as a function of $(\theta_{\rm init}, \phi_{\rm init})$, with $\chi_{\rm init} = 0.8$ (SKd configuration). The data are from NRSur7dq4, while dashed lines are the prediction of the PN-inspired counterpart in Eq. (4.38).

4.3.6 The phase difference $\Delta\Phi_{\rm IS}$

We finally study the phase difference between the mass and current quadrupole waves $\Delta\Phi_{\rm IS}$, which is the key factor that determines the final kick velocity. Fig. 4.14 is $\Delta\Phi_{\rm IS}$ of the SKd4–'03' system (Table 4.1). During the inspiral stage, $\Delta\Phi_{\rm IS}$ accumulates monotonically over time. It then gradually settles down to a constant after the merger. In fact, one can use PN theory to understand the evolution of $\Delta\Phi_{\rm IS}$. Before the merger, we have [cf. Eqs. (4.18)]

$$\Delta\Phi_{\rm IS} = \phi_{\rm pre} - \phi. \tag{4.39}$$

Here $\phi_{\rm pre}$ is the precession phase of the spins, and is obtained by measuring the spins of each individual BH; ϕ is the orbital phase. In Fig. 4.14, we compare Eq. (4.39) to the NR result. Two results agree pretty well until $t \sim -50M$. Near the merger, $\phi_{\rm pre}$ is thought to be locked to ϕ [121], in order for the accumulation of $\Delta\Phi_{\rm IS}$ to be halted. An alternative way to think of this is based on the QNM decomposition. For the ringdown portion of I_{22} and S_{22}, they must both be decomposed into $(2,2)$ QNMs. After higher overtones decay away ($t > 20M$), we are left with the fundamental mode [see Eq. (4.5) for more details]

$$I_{22} \sim \mathscr{A}_0^{(I)} e^{i\varphi_0^{(I)}} e^{-i\omega_{220}t}, \qquad S_{22} \sim \mathscr{A}_0^{(S)} e^{i\varphi_0^{(S)}} e^{-i\omega_{220}t}, \tag{4.40}$$

which leads to $\Delta\Phi_{\rm IS} = \varphi_0^{(I)} - \varphi_0^{(S)}$, i.e., a constant. The fact that both I_{22} and S_{22} have the same QNM frequency is a consequence of the *isospectrality* feature of black holes.

Then we study how $\Delta\Phi_{\rm IS}$ depends on the progenitor's parameters. We first choose eight NR runs in Table 4.1, whose $\phi_{\rm init}$ are different. As shown in Fig. 4.15, $\Delta\Phi_{\rm IS}$ with different $\phi_{\rm init}$ are finally locked to different values. The bottom panel is $\sin\Delta\Phi_{\rm IS}$. Recalling that the kick velocity can be roughly estimated by integrating $\sin\Delta\Phi_{\rm IS}$ [Eq. (4.17)], the final value of $\sin\Delta\Phi_{\rm IS}$ is a strong signature for the final kick velocity. For instance, one can directly read that SKd4–'07' leads to a positive largest kick, consistent with NR results (Table 4.1). Interestingly, $\Delta\Phi_{\rm IS}$ of several runs (e.g., '03') do not settle into a constant. Instead, there are slow changes over time. This is because the final BHs are boosted with relatively large kick velocities. As a result, there is a Doppler shift between the mode frequency of h_{22} and of $h_{2,-2}$, recalling that h_{22} is dominantly emitted upward, while $h_{2,-2}$ downward [96]. To test our statement, we pick four of SKu systems that are listed in Table 4.5. Here we choose SKu systems since they lead to larger kicks, thus the comparison is less impacted by numerical noises. The results are summarized in Table 4.3. We can

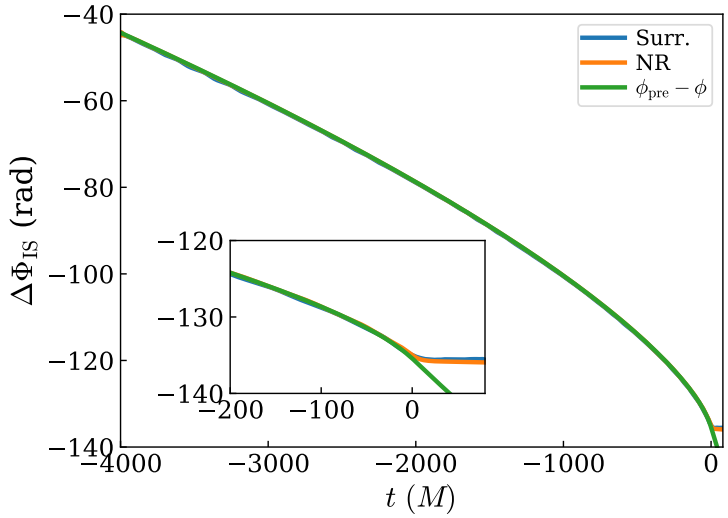

Figure 4.14: The time evolution of $\Delta\Phi_{\rm IS}$ for the SKd4–'03' system (orange curve). It is compared to NRSur7dq4 (blue curve) with the same initial condition. As expected, their results are close. Within the inspiral regime, PN theory predicts $\Delta\Phi_{\rm IS} = \phi_{\rm pre} - \phi$, which is shown as the green curve.

see relative mass differences are close to the kick of final BHs. A slight difference in mass leads to a deviation between the mode frequency of h_{22} and $h_{2,-2}$, i.e., [see Eq. (4.4)]

$$h_{22} \sim \mathcal{A}_{220} e^{i\psi_{220}} e^{-i\omega_{220}(1+\delta)t}, \tag{4.41a}$$

$$h^*_{2,-2} \sim \mathcal{A}_{2,-20} e^{-i\psi_{2,-20}} e^{-i\omega_{220}(1-\delta)t}, \tag{4.41b}$$

where δ is a small parameter, and is proportional to the kick velocity. In the late time regime, Eq. (4.41) implies

$$\begin{aligned}\sin\Delta\Phi_{\rm IS} = \sin[\varphi_0^{(I)} - \varphi_0^{(S)}] \\ + \frac{4(\mathcal{A}^2_{220} - \mathcal{A}^2_{2,-20})\mathcal{A}_{220}\mathcal{A}_{2,-20}}{|\mathcal{A}^2_{220} e^{-i(\psi_{220}+\psi_{2,-20})} - \mathcal{A}^2_{2,-20} e^{i(\psi_{220}+\psi_{2,-20})}|^2} \\ \times \cos(\psi_{220} + \psi_{2,-20})\omega_{220} t\delta + O(\delta^2).\end{aligned} \tag{4.42}$$

The new term above gives rise to a linear change in time, and it is consistent with the feature which we observe in Fig. 4.15.

We then use NRSur7dq4 to explore more parameter space of SKd systems, by varying three free parameters $\chi_{\rm init}$, $\theta_{\rm init}$ and $\phi_{\rm init}$, respectively. Results are shown in the bottom row of Fig. 4.10. We can see that $\chi_{\rm init}$ and $\theta_{\rm init}$ do not affect $\Delta\Phi_{\rm IS}$, even near and after the merger. Meanwhile, $\phi_{\rm init}$ gives rise to only a constant phase

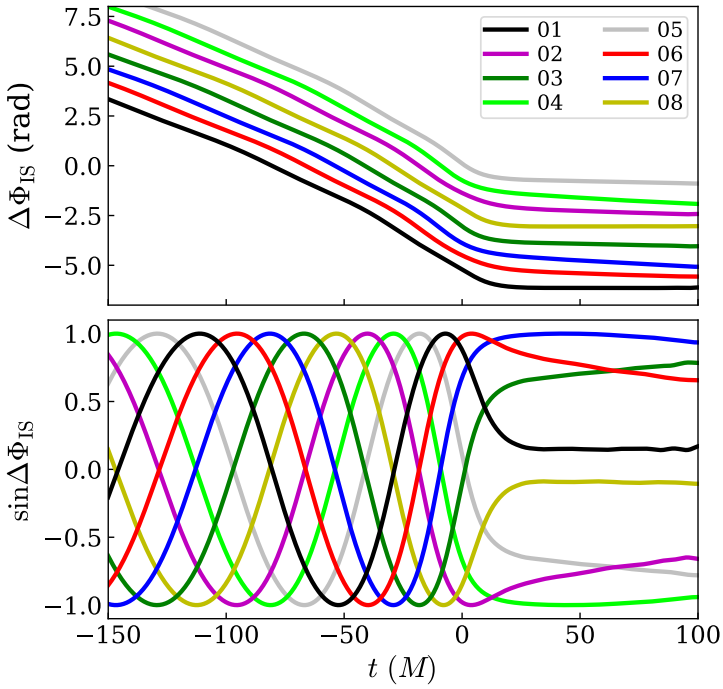

Figure 4.15: The evolution of $\Delta\Phi_{\rm IS}$ for SKd4 systems (Table 4.1). Eight runs start with different $\phi_{\rm init}$, and their $\Delta\Phi_{\rm IS}$ are finally locked to different values. The bottom panel is $\sin\Delta\Phi_{\rm IS}$. One can directly estimate the kick velocity from the final value of $\sin\Delta\Phi_{\rm IS}$, since the kick is roughly proportional to the integration of $\sin\Delta\Phi_{\rm IS}$ [Eq. (4.17)]. As for high-kick cases, their $\Delta\Phi_{\rm IS}$ change slowly during the late post-merger stage. This is due to the Doppler shift.

shift for $\Delta\Phi_{\rm IS}$, consistent with what we obtained in Sec. 4.3.3 [Eq. (4.30)]. In fact, if we subtract $\phi_{\rm init}$ from $\Delta\Phi_{\rm IS}$, the rest of time dependence is still insensitive to $\phi_{\rm init}$, although not as good as the cases of $\chi_{\rm init}$ and $\theta_{\rm init}$.

Recalling that the final kick velocity is given by [Eqs. (4.17) and (4.28)]

$$\begin{aligned} v_f &\sim \mathrm{Im}\int \dot{I}_{22}\dot{S}^*_{22}dt \sim I^m_{22}S^m_{22}\mathrm{Im}\, e^{i\phi_{\rm init}}\int \dot{T}_I(t)\dot{T}^*_S(t)dt \\ &\sim \chi_{\rm init}\sin\theta_{\rm init}\sin(\phi_{\rm init}-\phi^{(0)}_{\rm init}), \end{aligned} \tag{4.43}$$

where we have used the leading terms in Eq. (4.33) and (4.38). This result is the same as Eq. (4.14), as discussed in [78–80]. To offer an illustration, we use NRSur7dq4Remnant to plot v_f as a function of $(\theta_{\rm init}, \phi_{\rm init})$ in Fig. 4.16, with $\chi_{\rm init} = 0.76$. Meanwhile, we use Eq. (4.43) to fit the $v_f - (\chi_{\rm init}, \theta_{\rm init}, \phi_{\rm init})$ dependence, and the result is shown as dashed lines in Fig. 4.16. We can see Eq. (4.43) works properly.

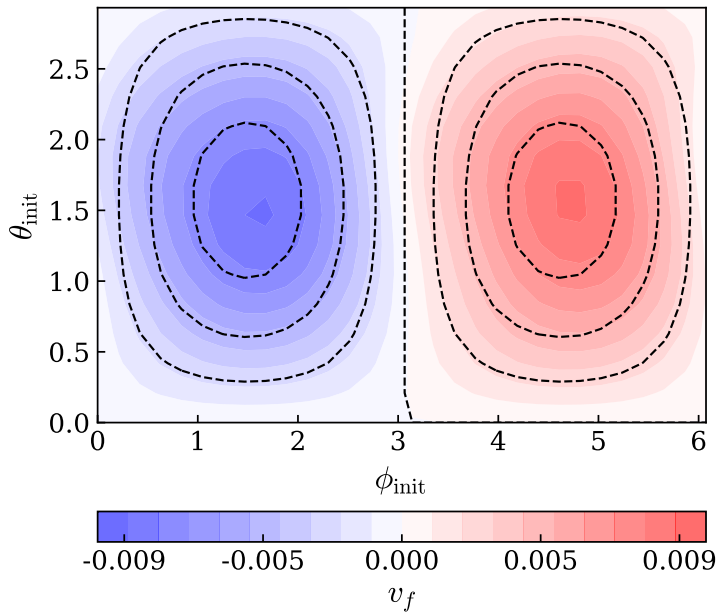

Figure 4.16: The final kick velocity as a function of $(\theta_{\rm init}, \phi_{\rm init})$, predicted by NRSur7dq4Remnant. The component spin $\chi_{\rm init}$ is chosen to be 0.76. The contours with dashed lines are from Eq. (4.43)

Table 4.3: The mass of remnant BHs inferred from h_{22} and $h_{2,-2}$, by fitting with QNMs (7 overtones, see Sec. 4.2 for more details). Four runs below are in the SKu configuration (Table 4.5) with $\chi_{\rm init} = 0.8$ and different $\phi_{\rm init}$. Among them, SKu8–'02' and SKu8–'04' are high-kick cases. The masses inferred from h_{22} and $h_{2,-2}$ are quite different, and the relative difference are close to the final kick velocity.

Runs (SKu8)	'01'	'02'	'03'	'04'
Mass from NR	0.941	0.939	0.941	0.939
Mass from $h_{2,2}$	0.940	0.945	0.941	0.931
Mass from $h_{2,-2}$	0.940	0.931	0.940	0.945
Relative mass difference between $h_{2,\pm2}$	-7.8×10^{-5}	-0.015	3.3×10^{-4}	0.015
Final kick	-1.6×10^{-3}	-0.011	1.3×10^{-3}	0.011

4.4 Backwards One-Body model

In this section, we shall focus on the time evolution of the mass and current quadrupole waves, $T_I(t)$ and $T_S(t)$, as defined in Eq. (4.28). In particular, we use an analytic phenomenological model BOB, conceived by McWilliams [111], to model the ringdown evolution. We first give a brief introduction to BOB in Sec. 4.4.1, and then compare it to NR results in Sec. 4.4.2.

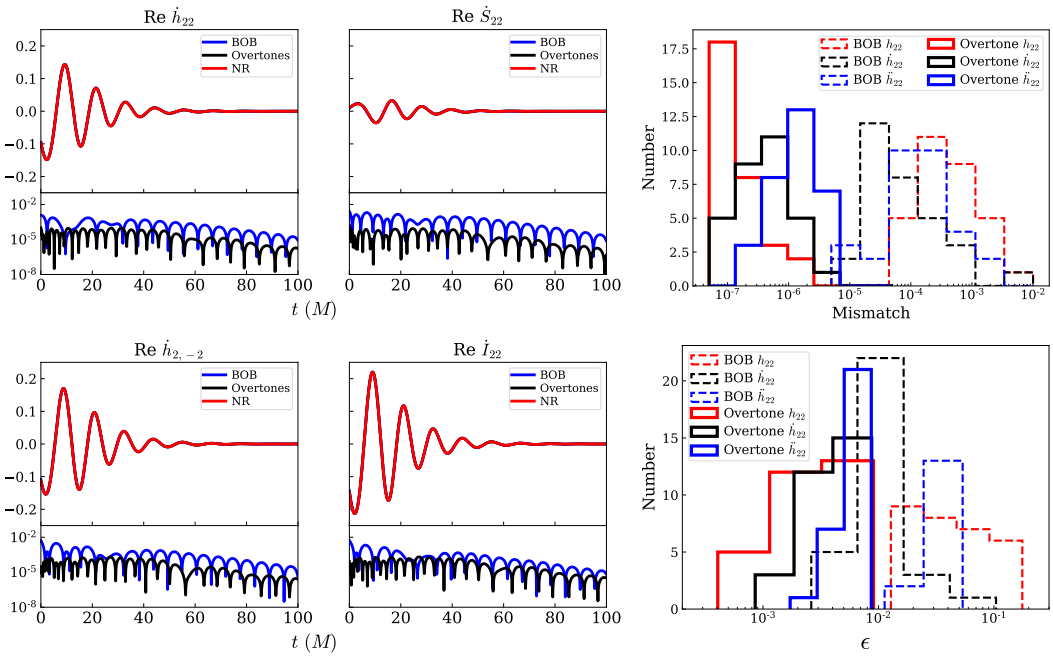

Figure 4.17: The BOB model for $\dot{h}_{22}$, $\dot{h}_{2,-2}$, $\dot{I}_{22}$ and $\dot{S}_{22}$ (the left and middle columns). They are compared to the ringdown portion of SKd4–'03'. We also fit data with QNMs. The residuals of BOB for four variables are all on the order of $\sim 10^{-3}$, an order of magnitude worse than the fitting of QNMs. The right column corresponds to the distribution of mismatch [top panel, see Eq. (4.53)], and parameter deviation [bottom panel, see Eq. (4.55)] for QNM decomposition and BOB, using our NR simulations listed in Table 4.1 and 4.5. BOB is always worse than QNM fitting.

4.4.1 A brief review of BOB

The BOB model is an accurate, fully analytical GW waveform model for the late inspiral, merger and ringdown of BBH [111], which is able to match the waveform $\sim 20M$ before the peak of strain. This feature enables people to avoid the extrapolation of inspiral models beyond their domain of validity. Here we restrict our attention to the ringdown portion.

As discussed in Refs. [111, 122], the amplitude of the News $|\dot{h}_{\ell m}|$ is related to its frequency $\Omega_{\ell m}$ by

$$|\dot{h}_{\ell m}|^2 \propto \frac{d}{dt}\Omega_{\ell m}^2, \tag{4.44}$$

where the coefficient remains (approximately) constant throughout the merger and ringdown phase. It was found[5] that either $|h_{2,\pm 2}|$, $|\dot{h}_{2,\pm 2}|$ or $|\ddot{h}_{2,\pm 2}|$ can be modeled

[5] In Ref. [111], the author pointed out that this phenomenological formula works best for $|\ddot{h}_{\ell m}|$. For now, we try to make our statement general, and make comparisons later.

by

$$X\,\mathrm{sech}[\gamma(t-t_p)], \tag{4.45}$$

with two free variables X and t_p, where $\gamma = -\mathrm{Im}\,\omega_{220}$ is the decay rate of the fundamental mode, determined by the final mass m_f and spin χ_f. Applying Eq. (4.45) to $|\ddot{h}_{2,\pm2}|$, $|\dot{h}_{2,\pm2}|$, and $|h_{2,\pm2}|$ leads to three classes of BOB. Below we shall discuss the model for $\dot{h}_{2,\pm2}$, and refer the interested reader to Sec. 4.8 for $\ddot{h}_{2,\pm2}$ and $h_{2,\pm2}$.

We first write the News $\dot{h}_{22}$ as

$$\dot{h}_{22} = X\,\mathrm{sech}[\gamma(t-t_p)]e^{-i\phi_{22}(t)} \tag{4.46}$$

where X is essentially the peak value of $|\dot{h}_{22}|$, and $t_p(>0M)$ is its peak time. Using the relation in Eq. (4.44), we obtain

$$\dot{\phi}_{22}(t) = \Omega_{22}(t) = \left\{\Omega_0^2 + \frac{\omega_0^2-\Omega_0^2}{2}\left[\tanh\gamma(t-t_p)+1\right]\right\}^{1/2}, \tag{4.47}$$

where Ω_0 is an integration constant and $\omega_0 = \mathrm{Re}\,\omega_{220}$. Eq. (4.47) indicates that

$$\lim_{t\to\infty}\dot{\phi}_{22}(t) = \omega_0, \tag{4.48}$$

i.e., $\dot{h}_{22}$ oscillates at the fundamental QNM frequency during the late time of post-merger portion. Integrating Eq. (4.47) again gives

$$\phi_{22} = \frac{1}{\gamma}\left(\omega_0\,\mathrm{arctanh}\,\frac{\dot{\phi}_{22}}{\omega_0} - \Omega_0\,\mathrm{arctanh}\,\frac{\Omega_0}{\dot{\phi}_{22}}\right) - \phi_0, \tag{4.49}$$

where ϕ_0 is another integration constant. We can see that $\dot{h}_{22}$ depends on 6 parameters

$$X, m_f, \chi_f, t_p, \Omega_0, \phi_0. \tag{4.50}$$

Similarly, Eqs. (4.46)–(4.49) can also be applied to $\dot{h}^*_{2,-2}$, $\dot{I}_{22}$ and $\dot{S}_{22}$.

As $t \gg t_p$, we obtain an asymptotic expansion for $\dot{h}_{22}$

$$\dot{h}_{22} = (2Xe^{\gamma t_p})e^{i\psi_0}e^{-i\omega_{220}t}, \tag{4.51}$$

where

$$\psi_0 = \omega_0 t_p + \phi_0 + \frac{\Omega_0}{\gamma}\,\mathrm{arctanh}\,\frac{\Omega_0}{\omega_0} - \frac{\omega_0}{\gamma}\frac{1}{2}\log\frac{4\omega_0^2}{\omega_0^2-\Omega_0^2}. \tag{4.52}$$

By comparing Eq. (4.51) with the overtone decomposition [e.g., Eq. (4.4)], $(2Xe^{\gamma t_p})$ is supposed to be equal to $|\omega_{220}\mathcal{A}_{220}|$.

Table 4.4: Fitting $\dot{h}_{22}$, $\dot{h}_{2,-2}$, $\dot{I}_{22}$, $\dot{S}_{22}$ to the BOB model, respectively. The original data is the ringdown portion of SKd4–'03'. The first four rows are the free parameters of BOB: peak magnitude X, peak time t_p, final spin χ_f, and final mass m_f. Comparing with the NR prediction of final spin (0.685) and final mass (0.951), the BOB for $\dot{I}_{22}$ and $\dot{h}_{22}$ are more accurate to recover the final properties than the other two. The model for $\dot{S}_{22}$ is the worst. Using the BOB's asymptotic expansion in the late time limit [Eq. (4.51)], $2Xe^{\gamma t_p}$ (the sixth row) is expected to be equal to $|\omega_{220}\mathcal{A}_{220}|$ (the seventh row). The agreement for $\dot{S}_{22}$ is the worst. The last row is the mismatch between BOB and the original NR data.

	$\dot{h}_{22}$	$\dot{h}_{2,-2}$	$\dot{I}_{22}$	$\dot{S}_{22}$
X	0.153	0.171	0.227	0.035
t_p/M	5.13	7.31	6.21	12.53
χ_f	0.684	0.681	0.686	0.559
m_f/M	0.954	0.944	0.951	0.857
$2Xe^{\gamma t_p}$	0.474	0.644	0.771	0.247
$\lvert\omega_{220}\mathcal{A}_{220}\rvert$	0.470	0.622	0.759	0.175
Mismatch ($\times 10^{-5}$)	2.6	9.9	3.1	204.0

4.4.2 Numerical comparisons

In this subsection, we use our NR simulations (Tables 4.1 and 4.5) to study the accuracy of BOB. To begin with, we take the ringdown portion of SKd4–'03' (Tables 4.1), and fit $\dot{h}_{2,\pm2}$, $\dot{I}_{22}$, $\dot{S}_{22}$ to Eq. (4.46), respectively. Similar to the previous QNM fitting algorithm (Sec. 4.2), we fit X and ϕ_0 with unweighted linear least squares, and fit m_f, χ_f, t_p, Ω_0 with nonlinear least squares. To give a comparison, we also fit the ringdown sector with QNMs. As shown in Fig. 4.17, the BOB can capture the major feature of $\dot{h}_{2,\pm2}$, $\dot{I}_{22}$, $\dot{S}_{22}$. Their residuals are all on the order of $\sim 10^{-3}$, an order of magnitude worse than the fitting of QNMs. Note that there are fewer free parameters for the fitting of BOB than the QNM decomposition, a fairer comparison would be restricting to only 2 QNMs (so that there are 6 free parameters for both models) and studying the late ringdown portion[6]. This is beyond the scope of this chapter, and we leave the relevant discussions for future study. Table 4.4 is a summary for the fitting results, where the last row is the mismatch between BOB and NR, defined by

$$\text{Mismatch} = 1 - \frac{(h_{\rm B}, h_{\rm NR})}{\sqrt{(h_{\rm NR}, h_{\rm NR})(h_{\rm B}, h_{\rm B})}}, \tag{4.53}$$

[6]Based on TABLE I of Ref. [22], it corresponds to $\sim 20M$ after the peak of strain.

with

$$(h_{\rm B}, h_{\rm NR}) = {\rm Re}\int_{0M}^{100M} h_{\rm B} h^*_{\rm NR} dt, \tag{4.54}$$

where $h_{\rm B}$ and $h_{\rm NR}$ are the complex strains of BOB and NR in the time domain, respectively. The integration limit is taken to be the ringdown sector. We can see that the BOB for $\dot{I}_{22}$ and $\dot{h}_{22}$ lead to smaller mismatches than the other two. Meanwhile, the BOB behaves worst for $\dot{S}_{22}$: even though the mismatches can reach 2×10^{-3}, this is much higher than those achievable by $\dot{I}_{22}$ and $\dot{h}_{22}$; furthermore, the recovered estimations for spin and mass of the final black hole are substantially biased.

We then use Eq. (4.51) to make a connection between BOB and QNM decomposition, i.e., expanding BOB for the late-time ringdown ($t \gg t_p$). The value of $(2Xe^{\gamma t_p})$ is expected to be close to $|\omega_{220}\mathcal{A}_{220}|$, so we make such a comparison in the sixth and seventh rows of Table 4.4. We can see that $\dot{h}_{22}$ leads to the best agreement, while $\dot{S}_{22}$ the worst.

As we mentioned earlier, $X\,{\rm sech}[\gamma(t-t_p)]$ can also be used to describe the magnitude of $\ddot{h}_{2,\pm2}$ or h_{22}. Each of them leads to a class of BOB model (see Sec. 4.8 for more details). We study their accuracy by fitting our simulations (cf. Table 4.1 and 4.5) to those three classes of BOB, and showing the distribution of mismatches (with NR waveforms) in the third column of Fig. 4.17. Generally speaking, the mismatches of BOB are 10^{-5} – 10^{-2}, which are worse than those of QNM decomposition. Among the three classes, $\ddot{h}_{22}$ gives the smallest mismatch, while h_{22} the largest.

Another way to quantify the accuracy of BOB is to compare the inferred spin and mass (from the fitting) to NR predictions. Similar to Ref. [22], we define a parameter deviation

$$\epsilon = \sqrt{(\delta M_f/M)^2 + (\delta\chi_f)^2}, \tag{4.55}$$

and plot its distribution in Fig. 4.17. We can see ϵ for BOB is also worse than the QNM decomposition. In addition, the distribution of ϵ show that the BOB works worst for h_{22}, and best for $\dot{h}_{22}$.

4.5 Parameter-estimation contributions from inspiral and ringdown stages

In this section, we demonstrate, with a few example sources, the impact of the ringdown portion of the waveforms—as well as the correlation between the ringdown and the inspiral phases—to parameter estimation errors. To do this, we will apply

the Fisher-matrix formalism to the NRSur7dq4 surrogate waveforms (for BBHs with $1 < q < 4$ and individual dimensionless spin $\chi < 0.8$) [46, 47].

In Sec. 4.5.1, we will give a brief review of the Fisher-matrix formalism. In Sec. 4.5.2, we discuss non-precessing BBH systems with varying total mass, illustrating how information contribution from the ringdown stage gains more importance for more massive systems. Finally, in Sec. 4.5.3, we study parameter estimation errors of precessing systems, illustrating how estimations of individual spin components will benefit from information from the ringdown stage.

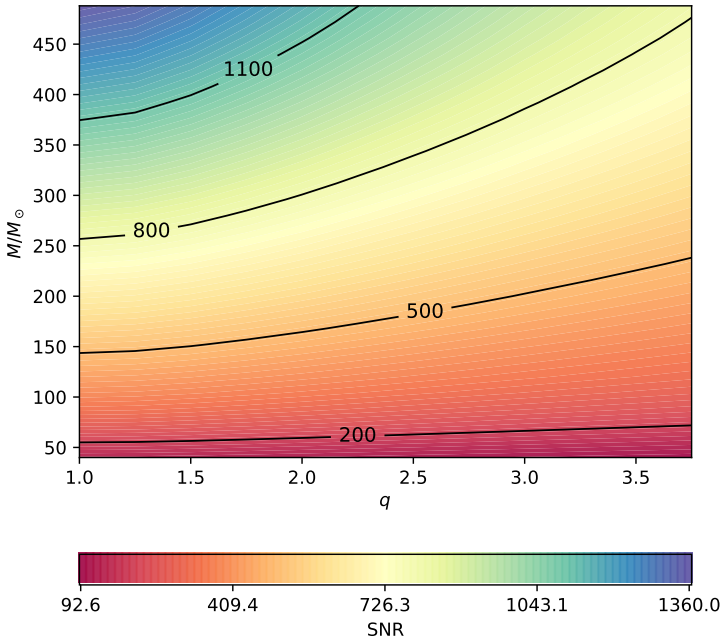

Figure 4.18: The SNR of an optimally oriented GW event with varying total (detector-frame) mass M and mass ratio q, assuming the system is at redshift $z = 1$ (6.7 Gpc) and using $S_n(f)$ of the CE.

4.5.1 The Fisher-Matrix Formalism and Waveform Models

For a gravitational waveform $h(\theta^j)$ that depends on a list of parameters θ^j, the Fisher matrix is given by

$$\Gamma_{ij} = \left(\frac{\partial h}{\partial \theta^i} \middle| \frac{\partial h}{\partial \theta^j} \right). \tag{4.56}$$

Here the inner product between two waveforms $(h|g)$ is defined as

$$(h|g) = 4\mathrm{Re} \int \frac{\tilde{h}^*(f)\tilde{g}(f)}{S_n(f)} df, \tag{4.57}$$

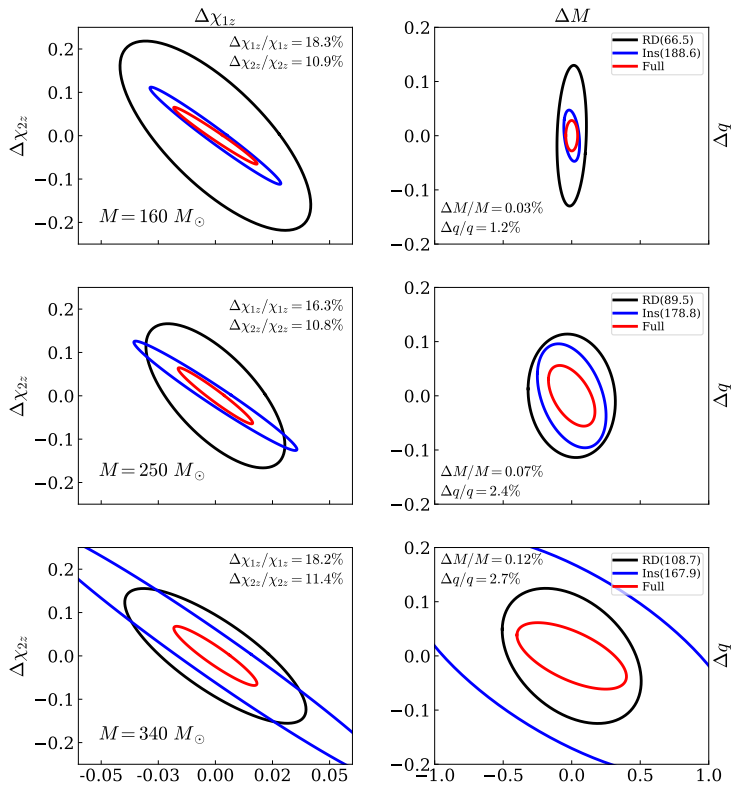

Figure 4.19: The error ellipses of χ_{1z} and χ_{2z} (the left column), as well as M and q (the right column), using the data from NRSur7dq4. Two individual spins are both aligned with the orbital angular momentum, and other parameters are $q = 2.3$, $\chi_{1z} = 0.1$, $\chi_{2z} = 0.6$, $\iota = 3\pi/10$, $\beta = \pi/2$, $\chi_{1p} = \chi_{2p} = 0$. The total mass is chosen to be $160M_\odot$ (the upper row), $250M_\odot$ (the middle row) and $340M_\odot$ (the bottom row). Three colors stand for the ringdown (black), inspiral (blue), and full sector (red), respectively. The numbers in parentheses are SNRs, where we normalize the total SNR of each event to 200 for comparison.

with the superscript $*$ standing for complex conjugation, and $S_n(f)$ the spectral density of the noise when detecting h. In terms of this inner product, the signal-to-noise ratio (SNR) of a signal h is given by $\sqrt{(h|h)}$.

The covariance matrix for the estimated values of θ^j, in presence of noise, is given by the inverse of the Fisher matrix,

$$\mathrm{Var}(\theta^i, \theta^j) = \left(\Gamma^{-1}\right)_{ij} . \tag{4.58}$$

From this, we obtain the individual estimation error for θ^j,

$$\Delta\theta^i = \sqrt{(\Gamma^{-1})_{ii}}. \tag{4.59}$$

and the correlation coefficient between θ^i and θ^j,

$$\mathrm{Corr}(\theta^i, \theta^j) = \frac{(\Gamma^{-1})_{ij}}{\sqrt{(\Gamma^{-1})_{ii}(\Gamma^{-1})_{jj}}}. \tag{4.60}$$

Waveforms described by the NRSur7dq4 surrogate model are parametrized by 13 parameters:

$$\chi_{1z}, \chi_{1p}, \phi_1, \chi_{2z}, \chi_{2p}, \phi_2, M, q, \iota, \beta, t_c, \phi_c, D,$$

Correspondingly, we have a 13-dimensional Fisher matrix. Here, the subscripts '1' and '2' stand for the two individual black holes in the binary system, χ_z is the spin component in the direction of orbital angular momentum, M is the total mass in the detector frame, $q > 1$ is the mass ratio, D is the luminosity distance between the source and the detector, and ι and β describe the wave emission direction in the frame of the source. The spin component in the orbital plane is parameterized by the magnitude χ_p and the azimuthal angle ϕ. Finally, t_c and ϕ_c are the coalescence time and phase, respectively.

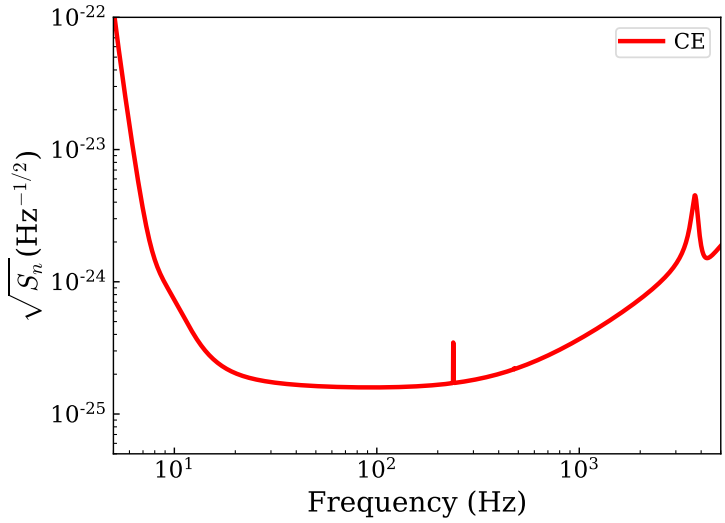

Figure 4.20: The noise spectral density of Cosmic Explorer.

Throughout this chapter, we adopt the Ansatz that the two gravitational-wave polarizations, h_+ and $h_\times$, can be individually measured, both with the noise spectrum S_n. This simplification allows us not to explicitly include the sky location and orientation of the source; it can be justified in the situation of a three-detector network that can provide good source localization. In this way, the results given in this section should be more optimistic than the actual situation.

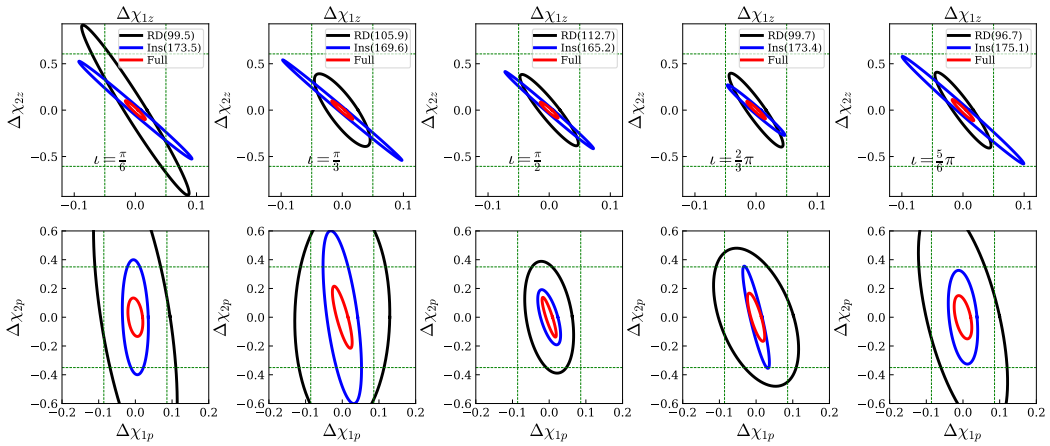

Figure 4.21: Similar to Fig. 4.19, the error ellipses of χ_{1z} and χ_{2z} (the first row), and χ_{1p} and χ_{2p} (the second row), with different ι (each column). The green dashed lines stand for the original value of each parameter. Thus we have a meaningful measurement (<100%) on a parameter if the error ellipse is within the dashed lines. The BBH systems have parameters $M = 300M_\odot$, $q = 3.5$, $\chi_{1z} = 0.05$, $\chi_{1p} = 0.086$, $\chi_{2z} = 0.606$, $\chi_{2p} = 0.35$, $\phi_1 = \pi/13$, $\phi_2 = 43\pi/52$, $\beta = \pi/2$. The error ellipses of ringdown and inspiral portions are not in the same direction, which implies different parameter correlations. After including the information of ringdown, the measurement accuracy of χ_z is improved by a factor of $\sim 4-5$, whereas χ_p is improved by a factor of ~ 1.4.

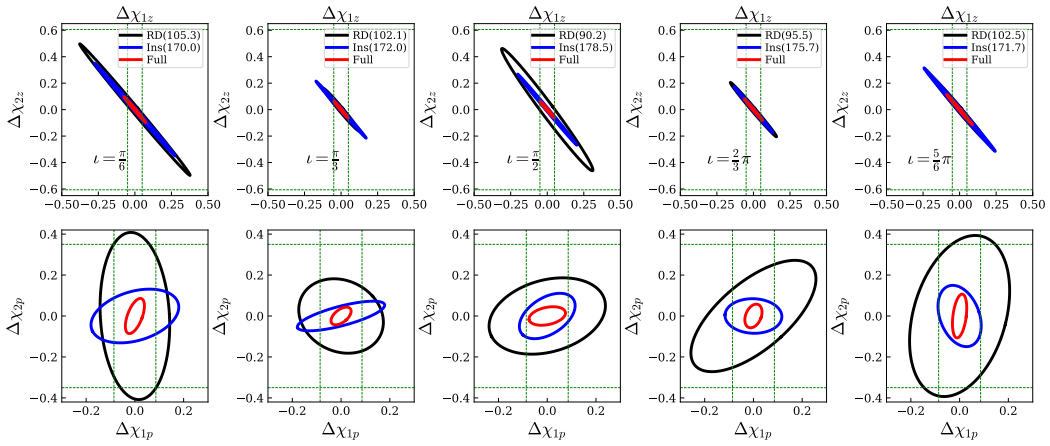

Figure 4.22: Same as Fig. 4.21, except $q = 1.2$.

4.5.2 Inspiral versus Ringdown: Non-precessing Binaries

In this section, we will focus mainly on the Cosmic Explorer (CE) [123], whose $S_n(f)$ is shown in Fig. 4.20. Using this sensitivity, in Fig. 4.18, we show the SNR of an optimally oriented BBH with varying total (detector-frame) mass M and mass ratio q, assuming the system is at redshift $z = 1$ ($D_L = 6.7\,\mathrm{Gpc}$). Note that the intrinsic total mass $M_\bullet$ is given by $M/(1+z)$. The high SNR shown in this figure

indicates that in the 3G era, we will be most frequently be detecting binaries at cosmological distances of around $1 \lesssim z \lesssim 3$. Correspondingly, we will be observing these binaries with higher detector-frame masses, with factor 2 to 4. In this way, events like GW150914 can be redshifted to around $\sim$ 130–260 $M_\odot$, while heavy binaries like GW190521 can be shifted to 302–604 $M_\odot$. In the rest of this section, we shall study BBH systems with increasing total mass, in order to observe the increased importance of information contribution from the ringdown stage.

In order to study the ringdown and the inspiral portions individually, we separate two sectors (in the frequency domain) with the instantaneous h_{22} frequency at $t = 0M$ (where $\sqrt{\sum_{l,m} |h_{lm}|^2}$ is maximum). For non-precessing binaries, we will fix $q = 2.3$, $\chi_{1z} = 0.1$, $\chi_{2z} = 0.6$, $\chi_{1p} = \chi_{2p} = 0$, $\iota = 3\pi/10$, $\beta = \pi/2$, and consider $M/M_\odot = 160,\ 250,\ 340$. For comparison purposes, we normalize all waveforms so that the SNR of the entire waveform is 200. We consider joint parameter estimations errors of (χ_{1z}, χ_{2z}) and (M, q), with results shown in Fig. 4.19 (blue for inspiral alone, black for ringdown alone, and red for combined). As a reference, we also list the SNR of each sector in the figure (cf. numbers in parentheses).

Regarding the overall size of the error ellipses, for the BBH system with total mass $M = 160M_\odot$, constraints from the ringdown sector are worse than those from the inspiral portion. As M increases to $250M_\odot$, constraints from the two sectors become comparable. For more massive systems, the ringdown portion begins to dominate. It is remarkable that substantial parameter estimation can already be obtained from ringdown alone: this means not only the quasi-normal mode frequency, but also the excitation amplitudes, are providing the information [35, 119, 120, 124, 125]. We also note that detector-frame mass of 250 $M_\odot$ corresponds to intrinsic total mass of $\sim 125M_\odot$ at $z = 1$, which will not be a rare type of event in third-generation detectors.

For spin measurements, both ringdown and inspiral sectors lead to somewhat degenerate measurement of χ_{1z} and χ_{2z}. In particular, the inspiral stage accurately measures the $\sim [q\chi_{1z} + (1-q)\chi_{2z}]$ direction (as can be argued from PN treatments [126]), while the ringdown has a less degenerate measurement, although with a most accurately measured combination similar to that from the inspiral. As for mass measurements, the ringdown and inspiral sectors lead to $M - q$ error ellipses with different directions, but no substantial degeneracy breaking.

4.5.3 Precessing BBH systems

We now turn our attention to precessing systems. We set the total mass of the systems to $300M_\odot$, in order to make the contribution of the ringdown sector comparable to the inspiral portion. Meanwhile, we choose $\chi_{1z} = 0.05$, $\chi_{2z} = 0.606$, $\chi_{1p} = 0.086$, $\chi_{2p} = 0.35$, $\phi_1 = \pi/13$, $\phi_2 = 43\pi/52$. The observation is made at $\beta = \pi/2$, with varying ι.

We first study a BBH system with $q = 3.5$. The results are shown in Figs. 4.21. We can see the relative size of ringdown and inspiral ellipses change with ι. This is because the weights of different GW modes $h_{\ell m}$, i.e., ${}_{-2}Y_{\ell m}(\iota, \beta)$, are functions of ι. At different observational locations, the contributions from different GW modes $h_{\ell m}$ are different. Secondly, the $\chi_{1z} - \chi_{2z}$ error ellipse computed from the ringdown portion is tilted relative to that of the inspiral sector, which implies that the parameter correlation of these two sectors is different. After combining the information of ringdown and inspiral, the measurement accuracy of χ_z is around 30%, improved by a factor of $\sim 4 - 5$ compared with using the inspiral signal only. This result agrees qualitatively with the discussion in Ref. [14]. We note that SNR is 1.14 times greater after incorporating the ringdown signal. Hence most of the improvement is contributed by the correlation between the inspiral and ringdown, which leads to a reduction of parameter degeneracy. On the other hand, the measurement accuracy of χ_p is only improved by a factor of ~ 1.4, not as good as the one of χ_z. Nevertheless, the fractional error of χ_p is smaller than 100%, hence we can still put meaningful constraints on χ_p.

We want to remark that the values mentioned above depend heavily on the properties of the BBH system in question. For instance, for a low-mass-ratio BBH system with $q = 1.2$, as shown in Fig. 4.22, the $\chi_{1z} - \chi_{2z}$ error ellipses computed from individual inspiral and ringdown sectors point along more similar directions. This leads to much less degeneracy breaking between χ_{1z} and χ_{2z} than in the $q = 3.5$ case above, in particular making the measurement error $\Delta\chi_{1z}$ greater than the value of χ_{1z}. Even so, incorporating ringdown, in addition to inspiral improves $\Delta\chi_z/\chi_z$ a factor of 2.8, substantially greater than the SNR improvement factor of around 1.16.

4.6 Conclusions

In this chapter, we studied the gravitational waveforms of SKd systems, using both NR simulations (SpEC) and surrogate models (NRSur7dq4, NRSur7dq4Remnant). We first decomposed the ringdown portion of GW signal into QNMs, and explored

how mode amplitudes of overtones depend on the progenitor's parameters (for I_{22}, S_{22}, as well as $h_{2\pm2}$ contents). We then studied the features of the mass and current quadrupole waves, focusing on their time evolutions and peak values. This leads to a qualitative understanding of kick velocity. Next, we fitted the evolution of $I_{22}(t)$ and $S_{22}(t)$ to the Backward-One-Body (BOB) model. Finally, we used Fisher information matrix to study the role of the ringdown state in parameter correlation. Here we summarize our main results:

(i) For SKd systems, the dependences of I_{22} and S_{22} on angular parameters $(\chi_{\rm init}, \theta_{\rm init}, \phi_{\rm init})$ can be separated from their temporal dependences [Eq. (4.28)].

(ii) Similar to the case of EMRI [105], the QNM amplitudes of SKd systems encode the information of progenitors' parameters. As an extension to Ref. [105], we included more overtones to the QNM decomposition. We found that the spectra peak at the fourth overtone, and that the dependence of mode magnitudes on $\phi_{\rm init}$ is insensitive to the overtone index n (up to a scaling factor). We found that the dependence of mode amplitudes on progenitor parameters is more easily understood when decomposed into mass and current quadrupole waves, instead of $(2, 2)$ and $(2, -2)$ modes.

(iii) Peak values of mass (I^m_{22}) and current (S^m_{22}) quadrupole waves encode the information of progenitors' spin. Enforced by the parity symmetry, the $(I^m_{22}, S^m_{22}) - (\chi_{\rm init}, \theta_{\rm init}, \phi_{\rm init})$ pattern is symmetric about $\theta_{\rm init} = \pi/2$ axis and has a period of π in the direction of $\phi_{\rm init}-$axis. Quantitatively speaking, the $(I^m_{22}, S^m_{22}) - (\chi_{\rm init}, \theta_{\rm init}, \phi_{\rm init})$ dependence are consistent with the PN-inspired formulas.

(iv) The phase difference between mass and current quadrupole waves $\Delta\Phi_{\rm IS}$ can lead to a qualitative understanding of kick velocity. Its time evolution can be anticipated from PN and black-hole perturbation theories: in the inspiral regime, $\Delta\Phi_{\rm IS}$ is equal to the difference between the orbital and precession phases; near the merger, the spin precession rate is gradually locked to the orbital frequency—until well into the ringdown regime, when $\Delta\Phi_{\rm IS}$ should become constant since both I_{22} and S_{22} oscillate at the fundamental QNM frequency. However, we found that $\Delta\Phi_{\rm IS}$ does not always settle down to a constant value during the post-merger stage, especially for high-kick cases. Instead, there is a slow change over time. This is due to the Doppler shift caused by the kick. The QNM frequency of h_{22} (emitted upwards) is slightly different from the one of $h_{2,-2}$ (emitted downwards), which leads to a slow time evolution. In fact, the relative frequency difference is on the same order as the kick velocity.

(v) We verified that the BOB phenomenological model is accurate for the ringdown evolution of $\dot{h}_{2,\pm2}$, $\ddot{h}_{2,\pm2}$ and I_{22}, but much less so for S_{22} and $h_{2,\pm2}$. This calls for further, qualitative improvements of the current-quadrupole sector of the BOB model.

(vi) We found that in 3G detectors, the contribution of the ringdown part dominates over the inspiral part as the total detector-frame mass exceeds $\gtrsim 250 - 300M_\odot$. We found that, as we combine both parts, the improvement in parameter estimation error is larger than the increase in SNR, indicating that the reduction of degeneracy due to the additional ringdown signal is the main reason for such improvement. As for χ_z, in our examples, incorporating the information from ringdown signal can lead to $\sim 4-5$ times improvement on the measurement accuracy, while the accuracy for χ_p is improved by a factor of ~ 1.4.

Our results indicate that the ringdown sector of a BBH event encodes plenty of information about the progenitor. It also plays a complementary role to PN theory in the study of BBH evolution. In our study, we primarily focused on the SKd configuration. Future work could include more generic BBH systems and other GW modes, which can lead to more comprehensive understanding of the ringdown signals. Another possible avenue for future work is to increase the precision of NR surrogate models for the ringdown sector, since our work has revealed that the current NR surrogate models are not accurate enough for BH spectroscopy. A more accurate ringdown surrogate model will be beneficial for both data analysis and theoretical studies.

Meanwhile, as revealed in Fig. 4.5, as well as Eqs. (4.7) and (4.10), it might also be interesting for future work to investigate the features of mass and current quadrupole waves of EMRIs, which may turn out to be simpler than features found in Refs. [105–107]. Those further explorations could potentially provide us a more physical understanding of EMRI ringdown spectra.

4.7 Appendix: SpEC runs—SKu configuration

We summarize our NR simulations of SKu BBHs in Table 4.5. We remark that the SKu condition is not well preserved after the junk-radiation regime. Nevertheless, the maximum recoil velocity v_f^z is 4050 km s^{-1}, and it is roughly proportional to $\chi_{\rm init}$.

Table 4.5: A summary for SKu configurations. The convention is the same as the one used in Table 4.1, except that the fifth and sixth columns are the components of individual spin in the Cartesian coordinates, where the z-axis is in the direction of orbital angular momentum; the line of two BHs determines the x-axis; and the right-handed rule determines the y-axis. The dimensionless spin ranges from 0.6 to 0.95, specified at the orbital frequency $\Omega_{\rm orb}$.

	Run label This chapter	SXS:BBH	$\Omega_{\rm orb}$ ($\times 10^{-2}$)	χ_1	χ_2	$\lvert\chi_1\rvert = \lvert\chi_2\rvert$	m_f	v_f^z ($\times 10^{-3}$)	χ_f
SKu6	'01'	2428	1.63	(0.378, −0.378, 0.273)	(−0.413, 0.389, 0.200)	0.6	0.944	−1.46	0.754
	'02'	2429	1.62	(0.390, 0.359, 0.281)	(−0.402, −0.398, 0.199)	0.6	0.942	−8.04	0.749
	'03'	2430	1.63	(−0.374, 0.383, 0.271)	(0.406, −0.395, 0.199)	0.6	0.944	−0.34	0.754
	'04'	2431	1.62	(−0.386, −0.364, 0.281)	(0.397, 0.402, 0.201)	0.6	0.942	8.03	0.749
	'05'	2432	1.63	(0.254, 0.465, 0.282)	(−0.254, −0.504, 0.202)	0.6	0.942	−7.54	0.749
	'06'	2448	1.63	(0.533, −0.0207, 0.275)	$(-0.568, 2.00\times10^{-3}, 0.193)$	0.6	0.944	−6.80	0.752
	'07'	2449	1.63	$(-4.75\times10^{-3}, 0.531, 0.279)$	(0.0218, −0.564, 0.203)	0.6	0.942	−6.01	0.750
	'08'	2450	1.63	(0.0120, −0.531, 0.280)	(−0.0312, 0.564, 0.202)	0.6	0.942	5.91	0.750
SKu8	'01'	2433	1.63	(0.666, 0.308, 0.320)	(−0.667, −0.314, 0.311)	0.8	0.941	−1.58	0.773
	'02'	2434	1.63	(−0.352, 0.647, 0.312)	(0.360, −0.649, 0.300)	0.8	0.939	−11.0	0.767
	'03'	2435	1.63	(−0.669, −0.306, 0.316)	(0.667, 0.309, 0.316)	0.8	0.941	1.31	0.773
	'04'	2436	1.63	(0.382, −0.629, 0.315)	(−0.390, 0.630, 0.301)	0.8	0.939	11.0	0.766
SKu95	'01'	2437	1.63	(−0.793, −0.437, 0.284)	(0.792, 0.437, 0.290)	0.95	0.942	2.43	0.765
	'02'	2438	1.62	(0.422, −0.803, 0.280)	(−0.423, 0.804, 0.279)	0.95	0.938	13.5	0.752
	'03'	2439	1.63	(0.800, 0.423, 0.288)	(−0.800, −0.426, 0.283)	0.95	0.942	−4.29	0.765
	'04'	2440	1.63	(−0.428, 0.802, 0.277)	(0.425, −0.801, 0.283)	0.95	0.938	−13.5	0.753
	'05'	2441	1.63	(−0.826, −0.377, 0.277)	(0.824, 0.376, 0.284)	0.95	0.941	10.6	0.760
	'06'	2442	1.62	(0.390, −0.821, 0.275)	(−0.390, 0.822, 0.2733)	0.95	0.938	13.5	0.750
	'07'	2443	1.62	(−0.358, 0.837, 0.272)	(0.355, −0.836, 0.278)	0.95	0.938	−13.5	0.751
	'08'	2444	1.64	(0.293, −0.820, 0.380)	(−0.301, 0.825, 0.363)	0.95	0.936	−2.80	0.785
	'09'	2445	1.65	(0.826, 0.279, 0.375)	(−0.829, −0.281, 0.368)	0.95	0.933	13.0	0.776
	'10'	2446	1.64	(−0.229, 0.842, 0.376)	(0.239, −0.850, 0.351)	0.95	0.936	3.35	0.784
	'11'	2447	1.65	(−0.836, −0.252, 0.372)	(0.837, 0.251, 0.372)	0.95	0.933	−12.4	0.776

4.8 Appendix: BOB for h_{22} and $\ddot{h}_{22}$

In this section, we discuss the BOB model for h_{22} and $\ddot{h}_{22}$.

4.8.1 $\ddot{h}_{22}$

Let us start from $\ddot{h}_{22}$. As discussed in Ref. [111]

$$\begin{aligned}\ddot{h}_{22} = \frac{d}{dt}\dot{h}_{22} = \frac{d}{dt}|\dot{h}_{22}|e^{-i\phi_{22}(t)} \sim -i\dot{\phi}_{22}|\dot{h}_{22}|e^{-i\phi_{22}(t)} \\ = -i\Omega_{22}|\dot{h}_{22}|e^{-i\phi_{22}(t)},\end{aligned} \tag{4.61}$$

where we have assumed that $|\dot{h}_{22}|$ changes much slower than ϕ_{22}. The above equation implies that the frequency of $\ddot{h}_{22}$ and $\dot{h}_{22}$ are roughly the same. Therefore, below we do not distinguish the frequency of $\ddot{h}_{22}$ from that of $\dot{h}_{22}$, and use Ω_{22} to stand for both frequencies. Combining Eqs. (4.44) with (4.61), we obtain

$$|\dot{h}_{22}|^2 \sim |\ddot{h}_{22}|^2/\Omega_{22}^2 \propto \frac{d}{dt}\Omega_{22}^2. \tag{4.62}$$

Then applying Eq. (4.45) to $|\ddot{h}_{22}|$[7], i.e.,

$$|\ddot{h}_{22}| = X\,\mathrm{sech}[\gamma(t-t_p)], \tag{4.63}$$

[7]We use the same notation as Eq. (4.46) since this will not cause any confusion.

which leads to

$$\Omega_{22} = \left\{\Omega_0^4 + \frac{\omega_0^4 - \Omega_0^4}{2}\left[\tanh\gamma(t-t_p)+1\right]\right\}^{1/4}. \tag{4.64}$$

The above equation implies

$$\lim_{t\to\infty}\Omega_{22}^{(2)} = \omega_0, \tag{4.65}$$

which is the same as the case of $\dot{h}_{22}$ [Eq. (4.48)]. Integrating Eq. (4.64) again gives the time dependence of ϕ_{22}, i.e., the phase of $\ddot{h}_{22}$

$$\begin{aligned}\phi_{22} = \frac{1}{\gamma}\Bigg\{&\omega_0\left(\operatorname{arctanh}\frac{\Omega}{\omega_0} + \arctan\frac{\Omega}{\omega_0}\right)\\ &-\Omega_0\left(\operatorname{arccoth}\frac{\Omega_0}{\Omega} + \operatorname{arccot}\frac{\Omega_0}{\Omega}\right)\Bigg\} - \phi_0.\end{aligned} \tag{4.66}$$

This is the original form of BOB model [cf. Eq. (10) of Ref. [111]]. Clearly, Eq. (4.66) is different from Eq. (4.49).

4.8.2 h_{22}

Following the same line of reasoning, the frequency of h_{22} is also approximately equal to Ω_{22}. Therefore

$$|\dot{h}_{22}|^2 \sim |h_{22}|^2\Omega_{22}^2 \propto \frac{d}{dt}\Omega_{22}^2. \tag{4.67}$$

Then using the assumption

$$|h_{22}| = X\,\mathrm{sech}[\gamma(t-t_p)], \tag{4.68}$$

we obtain

$$\Omega_{22} = \Omega_0 X\gamma^{-1/2}[\tanh\gamma(t-t_p)+1]^{1/2}. \tag{4.69}$$

Integrating the above equation again can lead to a tedious expression of ϕ_{22}, we do not show it here.

The BOB model for h_{22}, $\ddot{h}_{22}$, together with the one for $\dot{h}_{22}$ [Eq. (4.46)], are used to fit NR results, and are compared to QNMs in Fig. 4.17. We can see the model works the worst for h_{22}.

4.9 Appendix: The parity transformation of a complex strain

In this section, we show that the complex strain $h = h_+ - ih_\times$ is transformed to the complex conjugate if the whole system undergoes a parity transformation (including the BBH system and observer).

According to Fig. 4.9, under the parity transformation two BHs exchange their locations, while having their individual spin fixed, since axial vectors are not changed by the parity transformation. Meanwhile, within the detector frame, the orientation of detector arms and the propagation direction are flipped simultaneously, as shown in Fig. 4.23 (a) and (b). We want to emphasize that the GW detector is a 2D plane (formed by two arms). Its parity transformation can be equivalently achieved by a π-rotation about the axis that is perpendicular to the detector plane. Therefore, we further rotate the whole system about the vertical dash line by π, as shown in Fig. 4.23 (c). We can see that the detector configuration changes back to the one of (a), while the sky location of GW source changes from (θ_S, ϕ_S) (the northern hemisphere) to $(\pi - \theta_S, \phi_S)$ (the southern hemisphere).

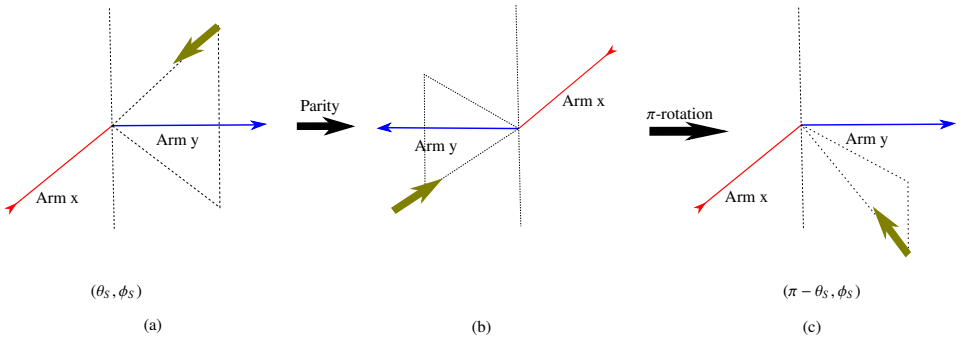

Figure 4.23: Parity inversion of a SKd BBH binary system within the detector frame. The arrow stands for the direction of incoming GW. The system undergoes a parity inversion from (a) to (b). We further rotate the whole system around the vertical dash line by π, which leads to (c). Comparing (a) and (c), the polar angle of sky location θ_S becomes supplementary under the transformation.

Since GR preserves the parity, the strain $h_{\rm obs}$ observed by a detector:

$$h_{\rm obs} = h_+ F_+ + h_\times F_\times,$$

is not affected by the abovementioned transformations. The antenna patterns $F_{+,\times}$ have forms [127]

$$F_+ = \frac{1}{2}(1 + \cos^2\theta_S)\cos 2\phi_S, \quad F_\times = \cos\theta_S \sin 2\phi_S,$$

with (θ_S, ϕ_S) the sky location of GW source relative to the detector. Under the transformation from Fig. 4.23 (a) to (c), i.e., $(\theta_S, \phi_S) \to (\pi - \theta_S, \phi_S)$ the antenna patterns $F_{+,\times}$ transform as

$$F_+ \to F_+, \quad F_\times \to -F_\times.$$

Recalling that the h_{obs} of Fig. 4.23 (a) and (c) are the same, we then have

$$h_+ \to h_+, \quad h_\times \to -h_\times.$$

As a result,

$$h = h_+ - ih_\times \to h^* = h_+ + ih_\times. \tag{4.70}$$

References

[1] Richard Abbott et al. "GW190521: A binary black hole merger with a total mass of 150 $M_\odot$." *Phys. Rev. Lett.* 125.10 (2020), p. 101102. DOI: 10.1103/PhysRevLett.125.101102. arXiv: 2009.01075 [gr-qc].

[2] Richard Abbott et al. "Properties and astrophysical implications of the 150 $M_\odot$ binary black hole merger GW190521." *Astrophys. J.* 900.1 (2020), p. L13. DOI: 10.3847/2041-8213/aba493. arXiv: 2009.01190 [astro-ph.HE].

[3] Matthew J. Graham et al. "Candidate electromagnetic counterpart to the binary black hole merger gravitational wave event S190521g." *Phys. Rev. Lett.* 124.25 (2020), p. 251102. DOI: 10.1103/PhysRevLett.124.251102. arXiv: 2006.14122 [astro-ph.HE].

[4] Stanford E. Woosley. "Pulsational pair-instability supernovae." *Astrophys. J.* 836.2 (2017), p. 244. DOI: 10.3847/1538-4357/836/2/244. arXiv: 1608.08939 [astro-ph.HE].

[5] Stanford E. Woosley. "The evolution of massive Helium Stars, including mass loss." *Astrophys. J.* 878.1, 49 (June 2019), p. 49. DOI: 10.3847/1538-4357/ab1b41. arXiv: 1901.00215 [astro-ph.SR].

[6] Vivekananthaswamy Gayathri et al. "GW190521 as a highly eccentric black hole merger." (Sept. 2020). arXiv: 2009.05461 [astro-ph.HE].

[7] Rossella Gamba et al. "GW190521: A dynamical capture of two black holes." (June 2021). arXiv: 2106.05575 [gr-qc].

[8] Juan Calderón Bustillo et al. "Confusing head-on collisions with precessing intermediate-mass binary black hole mergers." *Phys. Rev. Lett.* 126 (2021), p. 201101. DOI: 10.1103/PhysRevLett.126.201101. arXiv: 2009.01066 [gr-qc].

[9] Juan Calderón Bustillo et al. "GW190521 as a merger of Proca stars: A potential new vector Boson of 8.7×10^{-13} eV." *Phys. Rev. Lett.* 126.8 (2021), p. 081101. DOI: 10.1103/PhysRevLett.126.081101. arXiv: 2009.05376 [gr-qc].

[10] J. Aasi et al. "Advanced LIGO." *Class. Quant. Grav.* 32 (2015), p. 074001. DOI: 10.1088/0264-9381/32/7/074001. arXiv: 1411.4547 [gr-qc].

[11] Fausto Acernese et al. "Advanced Virgo: a second-generation interferometric gravitational wave detector." *Class. Quant. Grav.* 32.2 (2015), p. 024001. DOI: 10.1088/0264-9381/32/2/024001. arXiv: 1408.3978 [gr-qc].

[12] Tomotada Akutsu et al. "KAGRA: 2.5 generation interferometric gravitational wave detector." *Nature Astron.* 3.1 (2019), pp. 35–40. DOI: 10.1038/s41550-018-0658-y. arXiv: 1811.08079 [gr-qc].

[13] Tomotada Akutsu et al. "Overview of KAGRA: Detector design and construction history." (May 2020). arXiv: 2005.05574 [physics.ins-det].

[14] Sylvia Biscoveanu et al. "Measuring the spins of heavy binary black holes." *Phys. Rev. D* 104.10 (2021), p. 103018. DOI: 10.1103/PhysRevD.104.103018. arXiv: 2106.06492 [gr-qc].

[15] Kostas D. Kokkotas and Bernd G. Schmidt. "Quasinormal modes of stars and black holes." *Living Rev. Rel.* 2 (1999), p. 2. DOI: 10.12942/lrr-1999-2. arXiv: gr-qc/9909058.

[16] Brandon Carter. "Axisymmetric black hole has only two degrees of freedom." *Phys. Rev. Lett.* 26 (6 Feb. 1971), pp. 331–333. DOI: 10.1103/PhysRevLett.26.331. URL: https://link.aps.org/doi/10.1103/PhysRevLett.26.331.

[17] Olaf Dreyer et al. "Black hole spectroscopy: Testing general relativity through gravitational wave observations." *Class. Quant. Grav.* 21 (2004), pp. 787–804. DOI: 10.1088/0264-9381/21/4/003. arXiv: gr-qc/0309007 [gr-qc].

[18] Emanuele Berti et al. "Extreme gravity tests with gravitational waves from compact binary coalescences: (II) Ringdown." *Gen. Rel. Grav.* 50.5 (2018), p. 49. DOI: 10.1007/s10714-018-2372-6. arXiv: 1801.03587 [gr-qc].

[19] Richard Brito, Alessandra Buonanno, and Vivien Raymond. "Black-hole spectroscopy by making full use of gravitational-wave modeling." *Phys. Rev. D* 98.8 (2018), p. 084038. DOI: 10.1103/PhysRevD.98.084038. arXiv: 1805.00293 [gr-qc].

[20] Gregorio Carullo et al. "Empirical tests of the black hole no-hair conjecture using gravitational-wave observations." *Phys. Rev. D* 98.10 (2018), p. 104020. DOI: 10.1103/PhysRevD.98.104020. arXiv: 1805.04760 [gr-qc].

[21] Maximiliano Isi et al. "Testing the no-hair theorem with GW150914." *Phys. Rev. Lett.* 123.11 (2019), p. 111102. DOI: 10.1103/PhysRevLett.123.111102. arXiv: 1905.00869 [gr-qc].

[22] Matthew Giesler et al. "Black hole ringdown: The importance of overtones." *Phys. Rev.* X9.4 (2019), p. 041060. DOI: 10.1103/PhysRevX.9.041060. arXiv: 1903.08284 [gr-qc].

[23] Collin D. Capano et al. "Observation of a multimode quasi-normal spectrum from a perturbed black hole." (May 2021). arXiv: 2105.05238 [gr-qc].

[24] Benjamin P. Abbott et al. "Tests of general relativity with the binary black hole signals from the LIGO-Virgo Catalog GWTC-1." *Phys. Rev.* D100.10 (2019), p. 104036. DOI: 10.1103/PhysRevD.100.104036. arXiv: 1903.04467 [gr-qc].

[25] Benjamin P. Abbott et al. "Tests of general relativity with GW150914." *Phys. Rev. Lett.* 116.22 (2016). [Erratum: Phys. Rev. Lett.121,no.12,129902(2018)], p. 221101. DOI: 10.1103/PhysRevLett.116.221101. arXiv: 1602.03841 [gr-qc].

[26] Gregorio Carullo, Walter Del Pozzo, and John Veitch. "Observational black hole spectroscopy: A time-domain multimode analysis of GW150914." *Phys. Rev.* D99.12 (2019). [Erratum: Phys. Rev.D100,no.8,089903(2019)], p. 123029. DOI: 10.1103/PhysRevD.99.123029, 10.1103/PhysRevD.100.089903. arXiv: 1902.07527 [gr-qc].

[27] Emanuele Berti, Vitor Cardoso, and Clifford M. Will. "On gravitational-wave spectroscopy of massive black holes with the space interferometer LISA." *Phys. Rev.* D73 (2006), p. 064030. DOI: 10.1103/PhysRevD.73.064030. arXiv: gr-qc/0512160 [gr-qc].

[28] Miriam Cabero et al. "Observational tests of the black hole area increase law." *Phys. Rev. D* 97.12 (2018), p. 124069. DOI: 10.1103/PhysRevD.97.124069. arXiv: 1711.09073 [gr-qc].

[29] Walter Del Pozzo and Alessandro Nagar. "Analytic family of post-merger template waveforms." *Phys. Rev. D* 95.12 (2017), p. 124034. DOI: 10.1103/PhysRevD.95.124034. arXiv: 1606.03952 [gr-qc].

[30] Emanuele Berti et al. "Matched-filtering and parameter estimation of ringdown waveforms." *Phys. Rev. D* 76 (2007), p. 104044. DOI: 10.1103/PhysRevD.76.104044. arXiv: 0707.1202 [gr-qc].

[31] Sarah Gossan, John Veitch, and Bangalore S. Sathyaprakash. "Bayesian model selection for testing the no-hair theorem with black hole ringdowns." *Phys. Rev.* D85 (2012), p. 124056. DOI: 10.1103/PhysRevD.85.124056. arXiv: 1111.5819 [gr-qc].

[32] Jeroen Meidam et al. "Testing the no-hair theorem with black hole ringdowns using TIGER." *Phys. Rev. D* 90.6 (2014), p. 064009. DOI: 10.1103/PhysRevD.90.064009. arXiv: 1406.3201 [gr-qc].

[33] Emanuele Berti et al. "Testing general relativity with present and future astrophysical observations." *Class. Quant. Grav.* 32 (2015), p. 243001. DOI: 10.1088/0264-9381/32/24/243001. arXiv: 1501.07274 [gr-qc].

[34] Emanuele Berti et al. "Spectroscopy of Kerr black holes with Earth- and space-based interferometers." *Phys. Rev. Lett.* 117.10 (2016), p. 101102. DOI: 10.1103/PhysRevLett.117.101102. arXiv: 1605.09286 [gr-qc].

[35] Vishal Baibhav et al. "Black hole spectroscopy: systematic errors and ringdown energy estimates." *Phys. Rev. D* 97.4 (2018), p. 044048. DOI: 10.1103/PhysRevD.97.044048. arXiv: 1710.02156 [gr-qc].

[36] Vishal Baibhav and Emanuele Berti. "Multimode black hole spectroscopy." *Phys. Rev. D* 99.2 (2019), p. 024005. DOI: 10.1103/PhysRevD.99.024005. arXiv: 1809.03500 [gr-qc].

[37] Vitor Cardoso et al. "Parametrized black hole quasinormal ringdown: Decoupled equations for nonrotating black holes." *Phys. Rev. D* 99.10 (2019), p. 104077. DOI: 10.1103/PhysRevD.99.104077. arXiv: 1901.01265 [gr-qc].

[38] Ryan McManus et al. "Parametrized black hole quasinormal ringdown. II. Coupled equations and quadratic corrections for nonrotating black holes." *Phys. Rev. D* 100.4 (2019), p. 044061. DOI: 10.1103/PhysRevD.100.044061. arXiv: 1906.05155 [gr-qc].

[39] Andrea Maselli et al. "Parametrized ringdown spin expansion coefficients: A data-analysis framework for black-hole spectroscopy with multiple events." *Phys. Rev. D* 101.2 (2020), p. 024043. DOI: 10.1103/PhysRevD.101.024043. arXiv: 1910.12893 [gr-qc].

[40] Luciano Rezzolla et al. "Spin diagrams for equal-mass black-hole binaries with aligned spins." *Astrophys. J.* 679 (2008), pp. 1422–1426. DOI: 10.1086/587679. arXiv: 0708.3999 [gr-qc].

[41] James Healy, Carlos O. Lousto, and Yosef Zlochower. "Remnant mass, spin, and recoil from spin aligned black-hole binaries." *Phys. Rev. D* 90.10 (2014), p. 104004. DOI: 10.1103/PhysRevD.90.104004. arXiv: 1406.7295 [gr-qc].

[42] James Healy and Carlos O. Lousto. "Remnant of binary black-hole mergers: New simulations and peak luminosity studies." *Phys. Rev.* D95.2 (2017), p. 024037. DOI: 10.1103/PhysRevD.95.024037. arXiv: 1610.09713 [gr-qc].

[43] Xisco Jiménez-Forteza et al. "Hierarchical data-driven approach to fitting numerical relativity data for nonprecessing binary black holes with an application to final spin and radiated energy." *Phys. Rev.* D95.6 (2017), p. 064024. DOI: 10.1103/PhysRevD.95.064024. arXiv: 1611.00332 [gr-qc].

[44] Fabian Hofmann, Enrico Barausse, and Luciano Rezzolla. "The final spin from binary black holes in quasi-circular orbits." *Astrophys. J.* 825.2 (2016), p. L19. DOI: 10.3847/2041-8205/825/2/L19. arXiv: 1605.01938 [gr-qc].

[45] James Healy and Carlos O. Lousto. "Hangup effect in unequal mass binary black hole mergers and further studies of their gravitational radiation and remnant properties." *Phys. Rev.* D97.8 (2018), p. 084002. DOI: 10.1103/PhysRevD.97.084002. arXiv: 1801.08162 [gr-qc].

[46] Vijay Varma et al. "High-accuracy mass, spin, and recoil predictions of generic black-hole merger remnants." *Phys. Rev. Lett.* 122.1 (2019), p. 011101. DOI: 10.1103/PhysRevLett.122.011101. arXiv: 1809.09125 [gr-qc].

[47] Vijay Varma et al. "Surrogate models for precessing binary black hole simulations with unequal masses." *Phys. Rev. Research.* 1 (2019), p. 033015. DOI: 10.1103/PhysRevResearch.1.033015. arXiv: 1905.09300 [gr-qc].

[48] Luciano Rezzolla et al. "On the final spin from the coalescence of two black holes." *Phys. Rev.* D78 (2008), p. 044002. DOI: 10.1103/PhysRevD.78.044002. arXiv: 0712.3541 [gr-qc].

[49] Luciano Rezzolla et al. "The final spin from the coalescence of aligned-spin black-hole binaries." *Astrophys. J.* 674 (2008), pp. L29–L32. DOI: 10.1086/528935. arXiv: 0710.3345 [gr-qc].

[50] Alessandra Buonanno, Lawrence E. Kidder, and Luis Lehner. "Estimating the final spin of a binary black hole coalescence." *Phys. Rev. D* 77 (2008), p. 026004. DOI: 10.1103/PhysRevD.77.026004. arXiv: 0709.3839 [astro-ph].

[51] Wolfgang Tichy and Pedro Marronetti. "The Final mass and spin of black hole mergers." *Phys. Rev. D* 78 (2008), p. 081501. DOI: 10.1103/PhysRevD.78.081501. arXiv: 0807.2985 [gr-qc].

[52] Michael Kesden. "Can binary mergers produce maximally spinning black holes?" *Phys. Rev.* D78 (2008), p. 084030. DOI: 10.1103/PhysRevD.78.084030. arXiv: 0807.3043 [astro-ph].

[53] Enrico Barausse and Luciano Rezzolla. "Predicting the direction of the final spin from the coalescence of two black holes." *Astrophys. J.* 704 (2009), pp. L40–L44. DOI: 10.1088/0004-637X/704/1/L40. arXiv: 0904.2577 [gr-qc].

[54] Michael Kesden, Ulrich Sperhake, and Emanuele Berti. "Final spins from the merger of precessing binary black holes." *Phys. Rev. D* 81 (2010), p. 084054. DOI: 10.1103/PhysRevD.81.084054. arXiv: 1002.2643 [astro-ph.GA].

[55] Enrico Barausse, Viktoriya Morozova, and Luciano Rezzolla. "On the mass radiated by coalescing black-hole binaries." *Astrophys. J.* 758 (2012). [Erratum: Astrophys.J. 786, 76 (2014)], p. 63. DOI: 10.1088/0004-637X/758/1/63. arXiv: 1206.3803 [gr-qc].

[56] Deborah Ferguson et al. "Measuring spin of the remnant black hole from maximum amplitude." *Phys. Rev. Lett.* 123.15 (2019), p. 151101. DOI: 10.1103/PhysRevLett.123.151101. arXiv: 1905.03756 [gr-qc].

[57] Thibault Damour and Alessandro Nagar. "Final spin of a coalescing black-hole binary: An effective-one-body approach." *Phys. Rev. D* 76 (2007), p. 044003. DOI: 10.1103/PhysRevD.76.044003. arXiv: 0704.3550 [gr-qc].

[58] Luca Reali et al. "Mapping the asymptotic inspiral of precessing binary black holes to their merger remnants." (May 2020). arXiv: 2005.01747 [gr-qc].

[59] James Healy, Pablo Laguna, and Deirdre Shoemaker. "Decoding the final state in binary black hole mergers." *Class. Quant. Grav.* 31.21 (2014), p. 212001. DOI: 10.1088/0264-9381/31/21/212001. arXiv: 1407.5989 [gr-qc].

[60] Afura Taylor and Vijay Varma. "Gravitational wave peak luminosity model for precessing binary black holes." *Phys. Rev. D* 102.10 (2020), p. 104047. DOI: 10.1103/PhysRevD.102.104047. arXiv: 2010.00120 [gr-qc].

[61] Jacob D. Bekenstein. "Gravitational-Radiation Recoil and runaway black holes." *Astrophys. J.* 183 (July 1973), pp. 657–664. DOI: 10.1086/152255.

[62] Asher Peres. "Classical radiation recoil". *Phys. Rev.* 128 (5 Dec. 1962), pp. 2471–2475. DOI: 10.1103/PhysRev.128.2471. URL: https://link.aps.org/doi/10.1103/PhysRev.128.2471.

[63] William B. Bonnor and Michael A. Rotenberg. "Transport of momentum by gravitational waves: The linear approximation." *Proceedings of the Royal Society of London Series A* 265.1320 (Dec. 1961), pp. 109–116. DOI: 10.1098/rspa.1961.0226.

[64] Alan G. Wiseman. "Coalescing binary systems of compact objects to (post)$^{5/2}$-Newtonian order. II. Higher-order wave forms and radiation recoil". *Phys. Rev. D* 46 (4 Aug. 1992), pp. 1517–1539. DOI: 10.1103/PhysRevD.46.1517. URL: https://link.aps.org/doi/10.1103/PhysRevD.46.1517.

[65] Lawrence E. Kidder. "Coalescing binary systems of compact objects to post-Newtonian 5/2 order. 5. Spin effects." *Phys. Rev. D* 52 (1995), pp. 821–847. DOI: 10.1103/PhysRevD.52.821. arXiv: gr-qc/9506022.

[66] Luc Blanchet, Moh'd S.S. Qusailah, and Clifford M. Will. "Gravitational recoil of inspiralling black-hole binaries to second post-Newtonian order." *Astrophys. J.* 635 (2005), p. 508. DOI: 10.1086/497332. arXiv: astro-ph/0507692.

[67] Jeremy D. Schnittman and Alessandra Buonanno. "The distribution of recoil velocities from merging black holes." *Astrophys. J. Lett.* 662 (2007), p. L63. DOI: 10.1086/519309. arXiv: astro-ph/0702641.

[68] Carlos F. Sopuerta, Nicolas Yunes, and Pablo Laguna. "Gravitational recoil from binary black hole mergers: The close-limit approximation." *Phys. Rev. D* 74 (2006). [Erratum: Phys.Rev.D 75, 069903 (2007), Erratum: Phys.Rev.D 78, 049901 (2008)], p. 124010. DOI: 10.1103/PhysRevD.78.049901. arXiv: astro-ph/0608600.

[69] Bernd Bruegmann et al. "Exploring black hole superkicks." *Phys. Rev.* D77 (2008), p. 124047. DOI: 10.1103/PhysRevD.77.124047. arXiv: 0707.0135 [gr-qc].

[70] Jeremy D. Schnittman et al. "Anatomy of the binary black hole recoil: A multipolar analysis." *Phys. Rev.* D77 (2008), p. 044031. DOI: 10.1103/PhysRevD.77.044031. arXiv: 0707.0301 [gr-qc].

[71] Kip S. Thorne. "Multipole expansions of gravitational radiation." *Rev. Mod. Phys.* 52 (1980), pp. 299–339. DOI: 10.1103/RevModPhys.52.299.

[72] Jose A. Gonzalez et al. "Total recoil: The maximum kick from nonspinning black-hole binary inspiral." *Phys. Rev. Lett.* 98 (2007), p. 091101. DOI: 10.1103/PhysRevLett.98.091101. arXiv: gr-qc/0610154 [gr-qc].

[73] Frank Herrmann et al. "Unequal mass binary black hole plunges and gravitational recoil." *Class. Quant. Grav.* 24.12 (2007), S33–S42. DOI: 10.1088/0264-9381/24/12/S04. arXiv: gr-qc/0601026 [gr-qc].

[74] John G. Baker et al. "Getting a kick out of numerical relativity." *Astrophys. J. Lett.* 653 (2006), pp. L93–L96. DOI: 10.1086/510448. arXiv: astro-ph/0603204.

[75] Carlos O. Lousto and Yosef Zlochower. "Further insight into gravitational recoil." *Phys. Rev.* D77 (2008), p. 044028. DOI: 10.1103/PhysRevD.77.044028. arXiv: 0708.4048 [gr-qc].

[76] John G. Baker et al. "Modeling kicks from the merger of non-precessing black-hole binaries." *Astrophys. J.* 668 (2007), pp. 1140–1144. DOI: 10.1086/521330. arXiv: astro-ph/0702390.

[77] Michael Koppitz et al. “Recoil velocities from equal-mass binary-black-hole mergers.” *Phys. Rev. Lett.* 99 (2007), p. 041102. DOI: 10.1103/PhysRevLett.99.041102. arXiv: gr-qc/0701163 [GR-QC].

[78] Jose A. Gonzalez et al. “Supermassive recoil velocities for binary black-hole mergers with antialigned spins.” *Phys. Rev. Lett.* 98 (2007), p. 231101. DOI: 10.1103/PhysRevLett.98.231101. arXiv: gr-qc/0702052 [GR-QC].

[79] Manuela Campanelli et al. “Large merger recoils and spin flips from generic black-hole binaries.” *Astrophys. J.* 659 (2007), pp. L5–L8. DOI: 10.1086/516712. arXiv: gr-qc/0701164 [gr-qc].

[80] Manuela Campanelli et al. “Maximum gravitational recoil.” *Phys. Rev. Lett.* 98 (2007), p. 231102. DOI: 10.1103/PhysRevLett.98.231102. arXiv: gr-qc/0702133.

[81] Frank Herrmann et al. “Gravitational recoil from spinning binary black hole mergers.” *Astrophys. J.* 661 (2007), pp. 430–436. DOI: 10.1086/513603. arXiv: gr-qc/0701143.

[82] Wolfgang Tichy and Pedro Marronetti. “Binary black hole mergers: Large kicks for generic spin orientations.” *Phys. Rev. D* 76 (2007), p. 061502. DOI: 10.1103/PhysRevD.76.061502. arXiv: gr-qc/0703075.

[83] Frank Herrmann et al. “Binary black holes: Spin dynamics and gravitational recoil.” *Phys. Rev.* D76 (2007), p. 084032. DOI: 10.1103/PhysRevD.76.084032. arXiv: 0706.2541 [gr-qc].

[84] Manuela Campanelli, C.O. Lousto, and Yosef Zlochower. “Spinning-black-hole binaries: The orbital hang up.” *Phys. Rev. D* 74 (2006), p. 041501. DOI: 10.1103/PhysRevD.74.041501. arXiv: gr-qc/0604012.

[85] Carlos O. Lousto and Yosef Zlochower. “Hangup kicks: Still larger recoils by partial spin/orbit alignment of black-hole binaries.” *Phys. Rev. Lett.* 107 (2011), p. 231102. DOI: 10.1103/PhysRevLett.107.231102. arXiv: 1108.2009 [gr-qc].

[86] Carlos O. Lousto and James Healy. “Kicking gravitational wave detectors with recoiling black holes.” *Phys. Rev.* D100.10 (2019), p. 104039. DOI: 10.1103/PhysRevD.100.104039. arXiv: 1908.04382 [gr-qc].

[87] Frans Pretorius. “Binary black hole coalescence.” (Aug. 2007). arXiv: 0710.1338 [gr-qc].

[88] Drew Keppel et al. “Momentum flow in black hole binaries. I. Post-Newtonian analysis of the inspiral and spin-induced bobbing.” *Phys. Rev.* D80 (2009), p. 124015. DOI: 10.1103/PhysRevD.80.124015. arXiv: 0902.4077 [gr-qc].

[89] Geoffrey Lovelace et al. "Momentum flow in black-hole binaries. II. Numerical simulations of equal-mass, head-on mergers with antiparallel spins." *Phys. Rev. D* 82 (2010), p. 064031. DOI: 10.1103/PhysRevD.82.064031. arXiv: 0907.0869 [gr-qc].

[90] Samuel E. Gralla and Frank Herrmann. "Hidden momentum and black hole kicks." *Class. Quant. Grav.* 30 (2013), p. 205009. DOI: 10.1088/0264-9381/30/20/205009. arXiv: 1303.7456 [gr-qc].

[91] David Merritt et al. "Consequences of gravitational radiation recoil." *Astrophys. J.* 607 (2004), pp. L9–L12. DOI: 10.1086/421551. arXiv: astro-ph/0402057 [astro-ph].

[92] Erin Wells Bonning, G.A. Shields, and Sarah Salviander. "Recoiling black holes in quasars." *Astrophys. J. Lett.* 666 (2007), pp. L13–L16. DOI: 10.1086/521674. arXiv: 0705.4263 [astro-ph].

[93] Marta Volonteri. "Gravitational recoil: Signatures on the massive black hole population." *Astrophys. J. Lett.* 663 (2007), p. L5. DOI: 10.1086/519525. arXiv: astro-ph/0703180.

[94] S. Komossa. "Recoiling black holes: electromagnetic signatures, candidates, and astrophysical implications." *Adv. Astron.* 2012 (2012), p. 364973. DOI: 10.1155/2012/364973. arXiv: 1202.1977 [astro-ph.CO].

[95] Katie Chamberlain et al. "Frequency-domain waveform approximants capturing Doppler shifts." *Phys. Rev. D* 99.2 (2019), p. 024025. DOI: 10.1103/PhysRevD.99.024025. arXiv: 1809.04799 [gr-qc].

[96] Davide Gerosa and Christopher J. Moore. "Black hole kicks as new gravitational wave observables." *Phys. Rev. Lett.* 117.1 (2016), p. 011101. DOI: 10.1103/PhysRevLett.117.011101. arXiv: 1606.04226 [gr-qc].

[97] Vijay Varma, Maximiliano Isi, and Sylvia Biscoveanu. "Extracting the gravitational recoil from black hole merger signals." *Phys. Rev. Lett.* 124.10 (2020), p. 101104. DOI: 10.1103/PhysRevLett.124.101104. arXiv: 2002.00296 [gr-qc].

[98] Michael Kesden, Ulrich Sperhake, and Emanuele Berti. "Relativistic suppression of black hole recoils." *Astrophys. J.* 715 (2010), pp. 1006–1011. DOI: 10.1088/0004-637X/715/2/1006. arXiv: 1003.4993 [astro-ph.CO].

[99] Jonathan Blackman et al. "Fast and accurate prediction of numerical relativity waveforms from binary black hole coalescences using surrogate models." *Phys. Rev. Lett.* 115.12 (2015), p. 121102. DOI: 10.1103/PhysRevLett.115.121102. arXiv: 1502.07758 [gr-qc].

[100] Jonathan Blackman et al. "A surrogate model of gravitational waveforms from numerical relativity Simulations of precessing binary black hole mergers." *Phys. Rev.* D95.10 (2017), p. 104023. DOI: 10.1103/PhysRevD.95.104023. arXiv: 1701.00550 [gr-qc].

[101] Jonathan Blackman et al. "Numerical relativity waveform surrogate model for generically precessing binary black hole mergers." *Phys. Rev.* D96.2 (2017), p. 024058. DOI: 10.1103/PhysRevD.96.024058. arXiv: 1705.07089 [gr-qc].

[102] Vijay Varma et al. "Surrogate model of hybridized numerical relativity binary black hole waveforms." *Phys. Rev. D* 99.6 (2019), p. 064045. DOI: 10.1103/PhysRevD.99.064045. arXiv: 1812.07865 [gr-qc].

[103] Davide Gerosa, François Hébert, and Leo C. Stein. "Black-hole kicks from numerical-relativity surrogate models." *Phys. Rev.* D97.10 (2018), p. 104049. DOI: 10.1103/PhysRevD.97.104049. arXiv: 1802.04276 [gr-qc].

[104] Hang Yu et al. "Spin and eccentricity evolution in triple systems: from the Lidov-Kozai interaction to the final merger of the inner binary." *Phys. Rev. D* 102 (2020), p. 123009. DOI: 10.1103/PhysRevD.102.123009. arXiv: 2007.12978 [gr-qc].

[105] Scott A. Hughes et al. "Learning about black hole binaries from their ringdown spectra." *Phys. Rev. Lett.* 123.16 (2019), p. 161101. DOI: 10.1103/PhysRevLett.123.161101. arXiv: 1901.05900 [gr-qc].

[106] Anuj Apte and Scott A. Hughes. "Exciting black hole modes via misaligned coalescences: I. Inspiral, transition, and plunge trajectories using a generalized Ori-Thorne procedure." *Phys. Rev. D* 100.8 (2019), p. 084031. DOI: 10.1103/PhysRevD.100.084031. arXiv: 1901.05901 [gr-qc].

[107] Halston Lim et al. "Exciting black hole modes via misaligned coalescences: II. The mode content of late-time coalescence waveforms." *Phys. Rev. D* 100.8 (2019), p. 084032. DOI: 10.1103/PhysRevD.100.084032. arXiv: 1901.05902 [gr-qc].

[108] *https://www.black-holes.org/code/SpEC.html*. URL: https://www.black-holes.org/code/SpEC.html.

[109] Michael Boyle et al. "The SXS collaboration catalog of binary black hole simulations." *Class. Quant. Grav.* 36.19 (2019), p. 195006. DOI: 10.1088/1361-6382/ab34e2. arXiv: 1904.04831 [gr-qc].

[110] Abdul H. Mroue et al. "Catalog of 174 binary black hole simulations for gravitational wave astronomy." *Phys. Rev. Lett.* 111.24 (2013), p. 241104. DOI: 10.1103/PhysRevLett.111.241104. arXiv: 1304.6077 [gr-qc].

[111] Sean T. McWilliams. "Analytical black-hole binary merger waveforms." *Phys. Rev. Lett.* 122.19 (2019), p. 191102. DOI: 10.1103/PhysRevLett.122.191102. arXiv: 1810.00040 [gr-qc].

[112] Charles W Misner, Kip S Thorne, and John Archibald Wheeler. *Gravitation*. Macmillan, 1973.

[113] William H. Press and Saul A. Teukolsky. "Perturbations of a rotating black hole. II. Dynamical Stability of the Kerr Metric." *Astrophys. J.* 185 (Oct. 1973), pp. 649–674. DOI: 10.1086/152445.

[114] Emanuele Berti and Antoine Klein. "Mixing of spherical and spheroidal modes in perturbed Kerr black holes." *Phys. Rev. D* 90.6 (2014), p. 064012. DOI: 10.1103/PhysRevD.90.064012. arXiv: 1408.1860 [gr-qc].

[115] Leo C. Stein. "qnm: A Python package for calculating Kerr quasinormal modes, separation constants, and spherical-spheroidal mixing coefficients." *J. Open Source Softw.* 4.42 (2019), p. 1683. DOI: 10.21105/joss.01683. arXiv: 1908.10377 [gr-qc].

[116] Eliot Finch and Christopher J. Moore. "Modelling the ringdown from precessing black hole binaries." (Feb. 2021). arXiv: 2102.07794 [gr-qc].

[117] Milton Ruiz et al. "Multipole expansions for energy and momenta carried by gravitational waves." *Gen. Rel. Grav.* 40 (2008), p. 2467. DOI: 10.1007/s10714-007-0570-8. arXiv: 0707.4654 [gr-qc].

[118] Rafael A. Porto, Andreas Ross, and Ira Z. Rothstein. "Spin induced multipole moments for the gravitational wave flux from binary inspirals to third post-Newtonian order." *JCAP* 03 (2011), p. 009. DOI: 10.1088/1475-7516/2011/03/009. arXiv: 1007.1312 [gr-qc].

[119] Ioannis Kamaretsos et al. "Black-hole hair loss: Learning about binary progenitors from ringdown signals." *Phys. Rev. D* 85 (2012), p. 024018. DOI: 10.1103/PhysRevD.85.024018. arXiv: 1107.0854 [gr-qc].

[120] Ioannis Kamaretsos, Mark Hannam, and Bangalore Sathyaprakash. "Is black-hole ringdown a memory of its progenitor?" *Phys. Rev. Lett.* 109 (2012), p. 141102. DOI: 10.1103/PhysRevLett.109.141102. arXiv: 1207.0399 [gr-qc].

[121] David A. Nichols and Yanbei Chen. "Hybrid method for understanding black-hole mergers: Inspiralling case." *Phys. Rev. D* 85 (2012), p. 044035. DOI: 10.1103/PhysRevD.85.044035. arXiv: 1109.0081 [gr-qc].

[122] John G. Baker et al. "Mergers of non-spinning black-hole binaries: Gravitational radiation characteristics." *Phys. Rev. D* 78 (2008), p. 044046. DOI: 10.1103/PhysRevD.78.044046. arXiv: 0805.1428 [gr-qc].

[123] Benjamin P Abbott et al. "Exploring the sensitivity of next generation gravitational wave detectors." *Class. Quant. Grav.* 34.4 (2017), p. 044001. DOI: 10.1088/1361-6382/aa51f4. arXiv: 1607.08697 [astro-ph.IM].

[124] Lionel London, Deirdre Shoemaker, and James Healy. "Modeling ringdown: Beyond the fundamental quasinormal modes." *Phys. Rev. D* 90.12 (2014). [Erratum: Phys.Rev.D 94, 069902 (2016)], p. 124032. DOI: 10.1103/PhysRevD.90.124032. arXiv: 1404.3197 [gr-qc].

[125] Vishal Baibhav, Emanuele Berti, and Vitor Cardoso. "LISA parameter estimation and source localization with higher harmonics of the ringdown." *Phys. Rev. D* 101.8 (2020), p. 084053. DOI: 10.1103/PhysRevD.101.084053. arXiv: 2001.10011 [gr-qc].

[126] Etienne Racine. "Analysis of spin precession in binary black hole systems including quadrupole-monopole interaction." *Phys. Rev. D* 78 (2008), p. 044021. DOI: 10.1103/PhysRevD.78.044021. arXiv: 0803.1820 [gr-qc].

[127] Eric Poisson and Clifford M. Will. *Gravity: Newtonian, Post-Newtonian, relativistic*. Cambridge: Cambridge University Press, 2014. DOI: 10.1017/CBO9781139507486.

Part II

Dynamical tides of neutron stars

Chapter 5

EXCITATION OF f-MODES DURING MERGERS OF SPINNING BINARY NEUTRON STAR

[1] Sizheng Ma, Hang Yu, and Yanbei Chen. "Excitation of f-modes during mergers of spinning binary neutron star." *Phys. Rev. D* 101.12 (2020), p. 123020. DOI: 10.1103/PhysRevD.101.123020. arXiv: 2003.02373 [gr-qc].

5.1 Introduction

The detection of gravitational waves (GWs) and their electromagnetic counterparts from binary neutron star (BNS) coalescence GW170817 [1–4], as well as the recent event GW190425 [5], has started a new approach to study the physics of NSs. The observations have already provided new constraints on tidal deformabilities [6–9], the maximum mass [7, 10–13], radii [6, 9] and f-mode frequencies [14] of NSs. With the improvement of detector sensitivity, more BNS coalescence detections are expected for the near future [15–18]. Furthermore, 3G detectors, like the Einstein Telescope (ET) [19, 20] and the Cosmic Explorer (CE) [21], are being planned for operation in the 2030s. These 3G detectors may increase neutron star black-hole (NSBH) and BNS detection rates by 3-4 orders of magnitude [22]. As a result, accurately modeling NSs in binary systems is necessary and timely.

During the inspiral process, NSs in binaries are distorted due to the tidal field of their companions. Tidal coupling between compact objects in binaries allows the equation of state (EoS) of these objects to leave an imprint on GW signals, both during the early inspiral stage [23] and during the late inspiral stage [24, 25]. Under the equilibrium-tide approximation, the effect of tidal interaction can be characterized by the relativistic tidal Love number. Hinderer *et al.* studied the effect of equilibrium tide on gravitational waveforms, both using polytropic [23, 26] and more realistic EoS [27]. They found that 3G detectors are likely able to probe the clean tidal signatures from the early stage of inspirals. The post-Newtonian (PN) [28–32] tidal effects were studied by Vines and Flanagan [33], who explicitly obtained equations of motion with quadrupolar tidal interactions up to 1PN order. They pointed out that spin-orbit coupling must be included at this order in order to

conserve angular momentum. The spin-tidal couplings and higher PN orders were studied later by Abdelsalhin *et al.* [34].

In the late stage of an inspiral, the binary's orbital frequency sweeps through from hundreds of Hz to thousands of Hz. As the tidal driving frequency comes close to a normal mode frequency of the NS, internal stellar oscillations can be excited—giving rise to dynamical tide (DT). Exchanges of energy and angular momentum between orbital motion and stellar oscillations cause changes in orbital motion, leading to additional features in the gravitational waveform.

The tidal excitation of f-modes of stars was first investigated by Cowling [35]. Later, several authors studied the DTs of non-spinning stars in the context of Newtonian physics [36–38], and in the context of general relativity (incorporating gravitational radiation reaction and treating the NS relativistically) [39–42]. In particular, Lai (hereafter L94) [36] split the whole process into three regimes: the adiabatic, resonant, and post-resonance regimes. The first one is described by the well-known adiabatic approximation to high accuracy. At the post-resonance stage, they assumed that each stellar mode oscillates mainly at its own eigenfrequency; by factoring out the eigenfrequency, the motion can then be described by a slowly varying amplitude. This allowed them to obtain a simple form of post-resonance tidal amplitude with the stationary-phase approximation (SPA), which further leads to changes in the orbital separation, energy, angular momentum and the phase of GWs. They found that the amount of energy transfer due to resonance and the induced GW phase shift are negligible, since the coupling between g-mode and tidal potential is weak. They also pointed out that f-mode frequency is too high for resonance to take place.

As it turns out, the effect of DT can be strengthened by stellar rotation[1] [43, 44] and orbital eccentricity [45–48]. In this chapter, we mainly focus on the significance of stellar rotation. It is conventionally believed that a high rotation rate is unlikely when binaries which enter the LIGO band, since such systems usually have had enough time to evolve and spin down. For example, recent events GW170817 [1] and GW190425 [5] are all consistent with low spin configurations. The fastest spinning pulsar observed in BNS is PSR J0737-3039A, which spins at 44Hz [49]. Andersson *et al.* [50] estimated that it will spin down to 35 Hz as it enters the LIGO band. However, a high spin rate is still physically allowed. In such systems, retrograde rotation (with respect to the orbit) drags the mode frequency to a lower value in the

[1] In the inertial frame, mode frequencies are shifted by the spin frequency to a lower value. As a result, those modes become easier to be excited. See Fig. 5.2 for more details.

inertial frame. This makes the tidal resonance take place earlier. The energy and angular momentum transfers due to DTs in spinning stars were calculated in Ref. [43]. Ho and Lai [44] found that the resonance of the dominant g-mode is enhanced by spin if the star rotates faster than 100Hz, it can induce a phase shift of ~0.05 rad in the waveform. Additionally, f-mode resonance can produce a significant phase shift if the spin frequency is higher than 500Hz (depending on the EoS).

However, Ref. [43] was based on a configuration-space decomposition of the stellar oscillation, which does not use an orthonormal basis for a spinning star. This problem can be fixed by a phase-space mode expansion method [51]. Within this formalism, Lai and Wu [52] investigated the effect of the inertial modes[2], and found that the phase shift is of order 0.1 rad when the spin frequency is lower than 100Hz. The exception is $m = 1$ mode, which can be excited at tens of Hz for nonvanishing spin-orbit inclinations, and hence, generate a large phase shift in GW phase.

Accurate theoretical templates are needed in order to extract tidal information from GWs. Although extensive work has been done on adiabatic tide (AT), the study on DTs still requires improvements. For example, L94 [36] only estimated the changes of several parameters due to DTs. Their work did not explicitly treat the effect of tidal back-reaction on the orbit. The treatment did not provide detailed time evolution near the resonance, either. One approximate model was provided by Flanagan and Racine (hereafter FR07) [53]. They approximated the post-resonance orbit by a point particle (PP) trajectory, since the energy and angular momentum transfers only take place near the resonance. After that, the NS is treated as freely oscillating without interacting with the orbit. This model averages the dynamics over the tide-oscillation timescale, therefore does not describe the tidal perturbation at shorter timescales.

More recently, Hinderer *et al.* (hereafter, H+16) [54, 55] incorporated DT, in particular, the resonance of the f-mode in non-spinning NS, into the Effective-One-Body (EOB) formalism. A frequency domain model was developed later in Ref. [56]. In these works, DT is described by effective Love number

$$\lambda_{\rm eff} = -\frac{E_{ij}Q^{ij}}{E_{kl}E^{kl}}, \tag{5.1}$$

where E_{ij} is the tidal field induced by the companion and Q^{ij} is the quadrupole moment of the NS. To evaluate this quantity, they expanded the NS's response

[2]Inertial modes, or generalized r-modes, are a class of modes in spinning NSs who are not purely axial when spin frequency goes to 0, whereas r-modes are axial in this limit.

function near resonance; and described the evolution of DT by Fresnel functions in the resonant regime. They then used asymptotic analyses to piece adiabatic expressions and Fresnel functions together to obtain a single formula. The formula is precise prior to resonance. But it does not describe the phasing of the post-resonance regime. This is not a big issue for slowly spinning NSs, since in this case the mode is not excited until the end of coalescence, and post-resonance dynamics is extremely short. Furthermore, because current detections are all consistent with low spin configuration [1, 5], this model is accurate enough for current data analysis. However, this method cannot describe rapidly spinning NSs [57]; given the fact that rapidly spinning NSs are physically allowed, an accurate GW model for these systems is still necessary. In this chapter, we extend H+16 [54, 55] to arbitrary spin, by deriving new analytic formulae to describe the entire process of DT, accurate throughout the adiabatic, resonant and post-resonance regimes. The formulae agree with numerical integrations to high accuracies. We then carry out a systematic study on the post-resonance dynamics, by using the tidal response formulae and the method of osculating orbits. Finally, we analyze the impact of DT on parameter estimations by Fisher information matrices formalism. In order to more optimistically illustrate a best-case scenario in which f-mode DT might bring more information, we will be assuming high NS spin frequencies and stiff EoS. However, as we will discuss later, the qualitative features of DT shown in this chapter do not depend on the specific properties of NSs.

This chapter is organized as follows. In Sec. 5.2.1, we introduce the EoS used in this chapter, and construct approximations for the spin's effect on mode frequencies using the Maclaurin spheroid model. In Sec. 5.2.2 we derive equations of motion using the phase-space mode expansion method and a Hamiltonian approach. With these at hand, we give a comprehensive discussion on DT in Secs. 5.3 and 5.4. In Sec. 5.3, we mainly work on the stellar part. We first review previous studies on DT in Sec. 5.3.1 and propose our new approach in Sec. 5.3.2, where we also compare these models with numerical integrations. In Sec. 5.4, we use our new formulae and the method of osculating orbits to study post-resonance orbital dynamics. We get a set of first-order differential equations to describe the time evolution of osculating variables (e.g., Runge-Lenz vector, angular momentum, and orbital phase). These equations can provide rich information of the orbit near resonance, as discussed in Sec. 5.4.3. Then in Sec. 5.4.4, we compare our osculating equations with numerical integrations and provide a new way to obtain the post-resonance averaged orbit over the tide-oscillation timescale, which agrees with FR07 [53] to the leading order in

of tidal interaction. By combining our new method and FR07 [53], we obtain an analytic expression for the time of resonance. Sec. 5.5 mainly focuses on GWs. We first quantify the accuracy of several models by mismatch between waveforms. Then in Sec. 5.5.2 we use the Fisher information matrix formalism to discuss the influence of DT on parameter estimation. Finally, in Sec. 5.6 we summarize our results.

Throughout this chapter we use the following conventions unless stated otherwise. We use the geometric units with $G = c = 1$. We use Einstein summation notation, i.e., summation over repeated indexes.

5.2 Basic equations of dynamical tides

This section will provide equations of motion of the system undergoing DT. In Sec. 5.2.1, we construct approximations on spin's influence on f-mode frequencies, based on the Maclaurin spheroid model. In Sec. 5.2.2 we use the phase-space mode expansion method and a Hamiltonian approach to obtain the coupled equations of motion.

5.2.1 Neutron star equations of state and properties

In this chapter, we shall use, as input for our studies, properties of spinning neutron stars such as values of f-mode frequencies and tidal Love numbers.

The properties of non-spinning NSs have been studied extensively. In this chapter, we use two of them for comparison purposes. One is the H4 model [27], which gives dimensionless Love number $k_2 = 0.104$ for a NS with mass $M_{\rm NS} = 1.4M_\odot$ and radius $R_{\rm NS} = 13.76$km. Here k_2 is defined as [23]

$$k_2 = \frac{3}{2}\frac{\lambda}{R_{\rm NS}^5}, \tag{5.2}$$

where λ is the value of $\lambda_{\rm eff}$ in the equilibrium limit [Eq. (5.1)]. The other one is a $\Gamma = 2$ polytrope with $M_{\rm NS} = 1.4M_\odot$ and $R_{\rm NS} = 14.4$km, which has $k_2 = 0.07524$. The latter model is the same as the one used in H+16 [54, 55]. Their f-mode frequencies are $2\pi \times 1.51$kHz and $2\pi \times 1.55$kHz, respectively, consistent with the universal relation of NS properties [58–61]. We want to note that H4 is a stiff EoS that is not favored by GW170817 [7], yet our focus is on exploring what information DT might bring, hence the H4 EoS will be more "optimistic," since it leads to stronger tidal features than the softer, more compact EoS.

For spinning NSs, f-mode frequencies will split, and the Love number will also change. Unlike the non-spinning case, there is not yet a systematic parameterization of spinning NS properties, depending on EoS. For Love number, we shall simply use their non-spinning values; we will justify the validity of this treatment later [below Eq. (5.35)]. On the other hand, since the f-mode frequency split is important for bringing down the orbital frequency required for resonance, we will need more accurate input. Oscillation of spinning NS has been studied extensively in different limits, such as the (post-)Newtonian limit [62–68], the slow-rotation limit [69–73] and the Cowling approximation [74–77] (see Sec. 8.6.1 of Ref. [78] and references therein). The case of full relativistic NS with arbitrary high rotation rate has also been studied, for example, by Zink *et al.* [79], by using nonlinear time-evolution code. In this chapter, for simplicity, we shall use the features of Maclaurin spheroid to construct an approximation on how spin influences f-mode frequencies.

The Maclaurin spheroid describes a self-gravitating, rigidly rotating body of uniform density in Newton's theory. In the coordinate system (x', y', z') which co-rotates with the NS, the NS surface in hydrostatic equilibrium is described by [80]

$$\frac{x'^2 + y'^2}{a_1^2} + \frac{z'^2}{a_3^2} = 1, \tag{5.3}$$

where we assume that the spin vector is along the z'-axis. The spheroid's semi-axes in the $x'(y')$- and z'-directions are denoted by a_1 and a_3, respectively. They are related to the eccentricity e_s of the star by

$$e_s = \sqrt{1 - \frac{a_3^2}{a_1^2}}. \tag{5.4}$$

Note that the NS surface is oblate due to the spin ($a_3 < a_1$), so the stellar eccentricity is always smaller than 1. Hydrostatic equilibrium lead to a one-to-one mapping between the spin angular frequency Ω_s and the stellar eccentricity e_s [80]

$$\Omega_s^2 = \frac{2\pi\rho}{e_s^3}\left[(1 - e_s^2)^{1/2}(3 - 2e_s^2)\sin^{-1} e_s - 3e_s(1 - e_s^2)\right], \tag{5.5}$$

where ρ is the mass density of the star. For a Maclaurin spheroid, f-mode frequencies are specified in terms of the stellar eccentricity e_s, which is further determined by ρ and Ω_s. In this chapter we mainly focus on the $(j = 2, k = \pm 2)$ and $(j = 2, k = 0)$ modes. Here (j, k) are the angular quantum numbers of multipole expansion. Their mode frequencies (in the co-rotating frame) are given by [see Eq. (32) of Ref. [81]

and Eqs. (12)–(13) of Ref. [82]]

$$\frac{\omega_0^2}{\Omega_s^2} = \frac{1+\zeta_0^2}{1+3\zeta_0^2}\left[(1-9\zeta_0^2) + \frac{12\zeta_0(1-\zeta_0 \mathrm{arccot}\zeta_0)}{(1+3\zeta_0^2)\mathrm{arccot}\zeta_0 - 3\zeta_0}\right], \tag{5.6a}$$

$$\frac{\omega_{2\pm}}{\Omega_s} = -1 \pm \left[1 - \frac{4e_s^2 R_2}{(3-2e_s^2)\sin^{-1} e_s - 3e_s(1-e_s^2)^{1/2}}\right]^{1/2}, \tag{5.6b}$$

where $\zeta_0 = \sqrt{1-e_s^2}/e_s$ and

$$\begin{aligned} R_2 &= \frac{3(1-e_s^2)^{1/2}}{8e_s}\sum_{p=3}^{\infty}\frac{(2p-2)!!}{(2p-1)!!}e_s^{2(p-2)} + \frac{1-e_s^2}{e_s^2}\left[\arcsin e_s - \frac{e_s}{(1-e_s^2)^{1/2}}\right], \\ &= \frac{10e_s^4 - 7e_s^2 - 3}{8e_s^3\sqrt{1-e_s^2}} + \frac{3+8e_s^2-8e_s^4}{8e_s^4}\arcsin e_s. \end{aligned} \tag{5.7}$$

It is straightforward to see that each mode has two frequencies with opposite signs. The positive (negative) one corresponds to the prograde (retrograde) mode. The absolute value of two $(2,2)$ mode eigenfrequencies split due to the spin. This is an analog to the Zeeman split.

Eqs. (5.5)–(5.7) are valid for any $0 \le e_s < 1$[3]. In the small-eccentricity (low-rotation) regime, we have

$$\Omega_s = \sqrt{\frac{8\pi\rho}{15}}e_s + O(e_s^3), \qquad R_2 = -\frac{2}{15}e_s + O(e_s^3). \tag{5.8}$$

As a result, $\omega_{0,2\pm}/\Omega_s$ in Eqs. (5.6) diverge when $e_s \to 0$. However, mode frequencies $\omega_{0,2\pm}$ themselves converge to finite values, which are given by

$$\omega_{2\pm} = \pm\sqrt{\frac{16\pi\rho}{15}} - \sqrt{\frac{8\pi\rho}{15}}e_s + O(e_s^2), \tag{5.9a}$$

$$\omega_0 = \sqrt{\frac{16\pi\rho}{15}} + O(e_s^2), \tag{5.9b}$$

where the leading term $\sqrt{16\pi\rho/15}$ is the mode frequency of a non-spinning NS. But it turns out that this prediction differs from the true f-mode frequencies for a realistic EoS, if we use the mean density of the star as ρ. This is due to the assumption of homogeneity and incompressibility in the Maclaurin case. We refer the interested readers to Ref. [69] for a comprehensive comparison between the Maclaurin spheroid and the relativistic NS in the slow-rotation limit. Therefore, one should not directly

[3]Maclaurin spheroids become unstable as $e_s > 0.813$, corresponds to $\sim$ 900 Hz. Such a high rotation rate, however, is not of our interest.

use Eqs. (5.6). To obtain f-mode frequency for a NS with generic spin, we define an effective density $\rho_{\rm eff}$, such that $\sqrt{16\pi\rho_{\rm eff}/15}$ coincides with f-mode frequency of a non-spinning NS with realistic EoS (H4 EoS or $\Gamma = 2$ polytropic EoS). Meanwhile, we still assume the functional dependence of the mode frequencies $\omega_{0,2\pm}$ on Ω_s and $\rho_{\rm eff}$ to be the same as Eqs. (5.6). With such approximation, f-mode frequencies for non-spinning NSs can be extended to NSs with generic spins. In Fig. 5.1, we plot $\omega_0, |\omega_{2\pm}|$ as functions of Ω_s with both H4 EoS and $\Gamma = 2$ polytropic EoS. Results agree qualitatively with previous studies [see Fig. 5 of Ref. [79]].

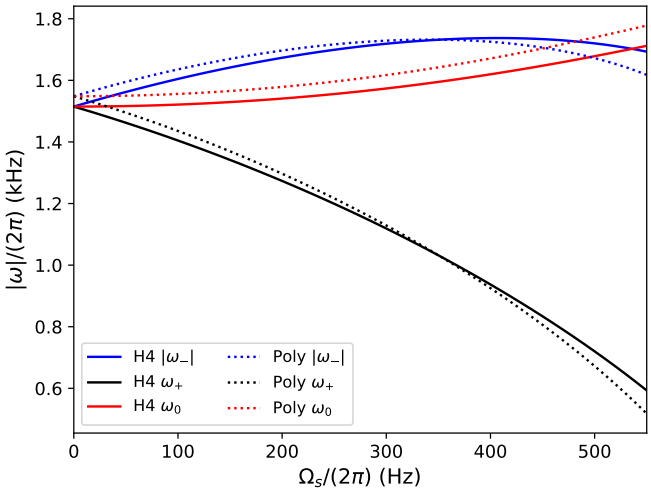

Figure 5.1: The dependence of f-mode frequencies (in the co-rotating frame) on the spin for NS with mass $1.4M_\odot$, following our prescription. The H4 EoS, represented by solid lines, gives $\omega_0, |\omega_{2\pm}| = 2\pi \times 1.51$Hz for non-spinning NS, while $\Gamma = 2$ polytrope gives $2\pi\times1.55$Hz. The frequencies of prograde (black line) and retrograde (blue line) modes split due to spin.

5.2.2 Equations of motion

Using the same convention as Ref. [44], we consider a BNS system with individual masses M_1 and M_2 moving in the $x-y$ plane, whose orbital angular momentum is along the z-axis. For simplicity, we assume that only M_1 is tidally deformed. We still use (x', y', z') as the body coordinate system that co-rotates with M_1. Two coordinate planes $x'-y'$ and $x-y$ intersect at the line ℓ. The angle between the z-axis and the z'-axis is β and the angle between ℓ and the y-axis is α. And let γ be the angle that the star rotates about z'-axis. Therefore two coordinate systems are related by Euler angles $(\alpha, \beta, \gamma = \Omega_s t)$.

5.2.2.1 *The evolution of stellar oscillation*

In the co-rotating frame, the oscillation of the rotating star is governed by[4] [44, 51]

$$\frac{\partial^2 \boldsymbol{\xi}}{\partial t^2} + 2\boldsymbol{\Omega}_s \times \frac{\partial \boldsymbol{\xi}}{\partial t} + \boldsymbol{C} \cdot \boldsymbol{\xi} = -\nabla U, \tag{5.10}$$

where $\boldsymbol{\xi}$ is the Lagrangian displacement of fluid elements, and $\boldsymbol{C}$ is a self-adjoint operator. The external gravitational potential U can be expanded in terms of spherical harmonics

$$\begin{aligned} U &= -GM_2 \sum_{lm} \frac{W_{lm} r_s^l}{r^{l+1}} e^{-im\phi(t)} Y_{lm}(\theta, \iota), \\ &= -GM_2 \sum_{lmm'} \frac{W_{lm} r_s'^l}{r^{l+1}} e^{-im\phi(t)+im'\Omega_s t} Y_{lm'}(\theta', \iota') \mathcal{D}^{(l)}_{m'm}(\alpha, \beta), \end{aligned} \tag{5.11}$$

where r is the separation between the two stars, $\phi(t)$ is the orbital phase, and $r_s = r_s' = \sqrt{x^2 + y^2 + z^2}$ is the distance of fluid element to the origin. Here (l, m) are the angular quantum numbers of multipole expansion; for example $l = 0, 1$ are the monopole and dipole pieces, which do not couple to NS internal oscillations, while tidal effects start from $l = 2$. Variables θ, ι are the angular coordinates of fluid elements in the inertial (unprimed) coordinate system; and θ', ι' are in the co-rotating (primed) coordinate system. We should note that Ω_s is always positive in our convention. The quantity W_{lm} is given by [86]

$$W_{lm} = (-1)^{(l+m)/2} \left[\frac{4\pi}{2l+1}(l+m)!(l-m)!\right]^{1/2} \left[2^l \left(\frac{l+m}{2}\right)! \left(\frac{l-m}{2}\right)!\right]^{-1}, \tag{5.12}$$

which is non-vanishing only when $l + m =$ even. We have used the Wigner $\mathcal{D}$-functions to transform spherical harmonics between the unprimed and primed coordinate systems.

Using the phase-space mode expansion method developed in Ref. [51], the Lagrangian displacement and its time derivative can be expressed as

$$\begin{pmatrix} \boldsymbol{\xi} \\ \dot{\boldsymbol{\xi}} \end{pmatrix} = \sum_\sigma c_\sigma(t) \begin{pmatrix} \boldsymbol{\xi}_\sigma \\ -i\omega_\sigma \boldsymbol{\xi}_\sigma \end{pmatrix}, \tag{5.13}$$

[4] Throughout this chapter we ignore the effect of dissipation. For f-modes, the most significant dissipation comes from the GW radiation of the mode itself, with a damping timescale of ~ 0.03 s [83], which is much longer than the mode period in the co-rotating frame. Shear and bulk viscosity due to electron scattering [36], as well as Urca reactions [84] have even more negligible effects on the dynamics. Therefore, we also assume that the background star's spin is unaffected by the tidal interaction (see also Ref. [85]).

where modes are labeled by $\sigma = (j, k, \nu = \pm)$. The angular quantum numbers j and k are integers with $k = \pm j, \pm(j-1) \ldots 0$. In our case the mode functions with negative k are related to the positive ones by complex conjugate (up to a constant), therefore we restrict ourselves to $k \geq 0$. The label ν stands for the propagation direction of modes, as mentioned in Sec. 5.2.1.

The modes in Eq. (5.13) are normalized by the condition

$$\langle \boldsymbol{\xi}_\alpha, \boldsymbol{\xi}_\alpha \rangle = 1 \tag{5.14}$$

where the inner product is defined by

$$\langle \boldsymbol{\xi}_\sigma, \boldsymbol{\zeta}_\tau \rangle = \int d^3x' \rho(x') \boldsymbol{\xi}^*_\sigma \cdot \boldsymbol{\zeta}_\tau. \tag{5.15}$$

The amplitudes $c_\sigma(t)$ satisfy the equation

$$\dot{c}_\sigma(t) + i\omega_\sigma c_\sigma(t) = -\frac{i}{b_\sigma} \langle \boldsymbol{\xi}_\sigma, \nabla U \rangle , \tag{5.16}$$

where b_σ depends on the structure of the star

$$b_\sigma = \langle \boldsymbol{\xi}_\sigma, 2i\boldsymbol{\Omega}_s \times \boldsymbol{\xi}_\sigma \rangle + 2\omega_\sigma \langle \boldsymbol{\xi}_\sigma, \boldsymbol{\xi}_\sigma \rangle . \tag{5.17}$$

Henceforth we restrict our discussions to systems where the spin is anti-aligned with the orbital angular momentum, with $(\alpha, \beta) = (0, \pi)$. In this case, the Wigner $\mathcal{D}$-functions reduce to $\mathcal{D}^{(2)}_{m'm} = \delta_{m',-m}$, and Eq. (5.11) becomes

$$U = -GM_2 \sum_{lm} \frac{W_{lm} r_s^l}{r^{l+1}} e^{-im(\phi + \Omega_s t)} Y_{l,-m}(\theta', \iota'). \tag{5.18}$$

Here we focus on $(j = 2, k = 2, 0)$ modes coupled to the gravitational fields labeled by $(l = 2, m = -2, 0)$, since they are the leading order terms in $R_{\rm NS}/r$, and give the strongest effects.

The amplitudes of these modes are denoted by $c_0, c_{2,+}$ and $c_{2,-}$, where we have suppressed the mode index j. The equations of motion of these amplitudes are given by

$$\dot{c}_0 + i\omega_0 c_0 = f_0, \tag{5.19a}$$

$$\dot{c}_{2,\nu} + i\omega_{2,\nu} c_{2,\nu} = f_{2,\nu}, \tag{5.19b}$$

with the driving force $f_{2,\nu}$ and f_0 given by the RHS of Eq. (5.16). In particular, for the f-mode of Maclaurin spheroid we know [44, 81]

$$\boldsymbol{\xi}_{2,2} = \frac{1}{\sqrt{2I^s_{xy}}} [(x' + iy'), i(x' + iy'), 0], \tag{5.20a}$$

$$\boldsymbol{\xi}_{2,0} = iV\left[-x' - 2\frac{i\Omega_s}{\omega_0}y', -y' + 2\frac{i\Omega_s}{\omega_0}x', 2z'\right], \tag{5.20b}$$

where the coefficients V and $I^s_{xy} = I_{xx} + I_{yy}$ are determined by the normalization condition Eq. (5.14). Here I_{xx} and I_{yy} are the components of the moment of inertia $I_{ij} = \int \rho x'_i x'_j dV'$. We do not provide the expressions of V and I^s_{xy} since they are not needed in the future—in the final equations of motion, these quantities will absorbed into tidal Love number and f-mode frequency of the NS, see Eq. (5.34), (5.35) and text around them. Then we get

$$f_{2,\pm} = \frac{i\sqrt{I^s_{xy}}}{\omega_{2,\pm} + \Omega_s}\frac{3M_2}{4\sqrt{2}r^3}e^{2i(\phi+\Omega_s t)}, \tag{5.21a}$$

$$f_0 = \frac{-iM_2}{r^3}\frac{\Omega_s}{4V\omega_0^2}. \tag{5.21b}$$

In fact, Eqs. (5.21) are not limited to Maclaurin spheroid. For a non-Maclaurin NS with low spin, we have [based on the definition of $(j = 2, k = 2)$ mode]

$$\boldsymbol{\xi}_{22} = h_{22}(r_s)\boldsymbol{\nabla}Y_{22}(\theta', \iota'), \tag{5.22}$$

where $h_{22}(r_s)$ depends on the EoS. This always leads to

$$f_{2,\pm} \sim \frac{1}{r^3}e^{2i(\phi+\Omega_s t)}, \tag{5.23}$$

with the coefficient eventually absorbed into tidal Love numbers. For larger spins, the NS's $j = 2$ modes will couple to $j \neq 2$ tidal gravity field (which are weaker), we ignore this coupling in this chapter.

5.2.2.2 *Orbital evolution*

By coupling the orbital motion to the NS modes, one can write the Hamiltonian of the whole system as [53]

$$\begin{aligned} H = &\frac{p_r^2}{2\mu} + \frac{p_\phi^2}{2\mu r^2} - \frac{\mu M_t}{r} + b_0(\omega_0|c_0|^2 + if_0c_0^* - if_0^*c_0) \\ &+ \sum_{\nu=\pm} b_{2,\nu}(\omega_{2,\nu}|c_{2,\nu}|^2 + if_{2,\nu}c_{2,\nu}^* - if_{2,\nu}^*c_{2,\nu}), \end{aligned} \tag{5.24}$$

where μ is the reduced mass and M_t is the total mass. The generalized coordinates of the system consists of $(r, \phi, c_0, c_{2,\pm})$, and the conjugate momenta $(p_r, p_\phi, ib_0c_0^*, ib_{2,\pm}c_{2,\pm}^*)$. From Hamilton's equations we obtain the equations of motion

$$\ddot{r} - r\dot{\phi}^2 = -\frac{M_t}{r^2} + \frac{3ib_0}{\mu r}(c_0^*f_0 - c_0f_0^*)$$

$$+\sum_{\nu=\pm}\frac{3ib_{2,\nu}}{\mu r}(c^*_{2,\nu}f_{2,\nu}-c_{2,\nu}f^*_{2,\nu}), \tag{5.25a}$$

$$r\ddot{\phi}+2\dot{r}\dot{\phi}=\sum_{\nu=\pm}\frac{2b_{2,\nu}}{\mu}(c^*_{2,\nu}f_{2,\nu}+c_{2,\nu}f^*_{2,\nu}). \tag{5.25b}$$

Equations (5.19), together with Eqs. (5.25), are a complete set of equations that describe the conservative evolution of the inspiraling BNS system. To include the effect of gravitational radiation, we add the Burke-Thorne dissipation term to the orbital evolution [23]

$$a_i=-\frac{2}{5}x_j\frac{d^5Q^{\rm Total}_{ij}}{dt^5}, \tag{5.26}$$

where $Q^{\rm Total}_{ij}$ is the total quadrupole moment of the system in the inertial frame, which consists of the orbital part and the stellar part, i.e., $Q^{\rm Total}_{ij}=Q_{ij}+\mu(x_ix_j-r^2\delta_{ij}/3)$. For simplicity, we neglect the effect of radiation reaction on the mode evolution.

To express Q_{ij} in terms of the mode amplitudes, we start from the definition of the stellar quadrupole moment in the co-rotating frame

$$Q'^{ij}=\int d^3x'\rho\left(x'^ix'^j-\frac{1}{3}r'^2\delta^{ij}\right). \tag{5.27}$$

The unperturbed quadrupole moment vanishes under the axisymmetric assumption. To linear order in perturbation, we get[5] [87]

$$\begin{aligned}\delta Q'^{ij}&=\int d^3x'\delta\rho\left(x'^ix'^j-\frac{1}{3}r'^2\delta^{ij}\right)+\int d^3x'\nabla\cdot\left[\rho\boldsymbol{\xi}\left(x'^ix'^j-\frac{1}{3}r'^2\delta^{ij}\right)\right]\\&=\int d^3x'\rho\left(x'^i\xi'^j+x'^j\xi'^i-\frac{2r'}{3}\xi'_r\delta^{ij}\right),\end{aligned} \tag{5.28}$$

where we have used $\delta\rho=-\nabla\cdot(\rho\boldsymbol{\xi})$ to simplify the expression. The tensorial components of symmetric tracefree tensors are related to their harmonic components q'_{lm} through Clebsch-Gordan coefficients. The transformation can be expressed in a compact form [88]

$$\delta Q'^{ij}=J^{ij}_m q'_m, \tag{5.29a}$$

$$q'_m=(J^{ij}_m)^*\delta Q'^{ij}, \tag{5.29b}$$

where we suppress the index l of q' since we only consider $l=2$ components, and

$$J^*_{-2}=J_2=\frac{1}{2}\begin{pmatrix}1&i&0\\i&-1&0\\0&0&0\end{pmatrix},\ J_0=\frac{1}{\sqrt{6}}\begin{pmatrix}-1&0&0\\0&-1&0\\0&0&2\end{pmatrix}.$$

[5]The symbol δ on the RHS represents Eulerian perturbation, however, the symbol on the LHS only means the perturbation of the integral.

Combining Eqs. (5.20), (5.28) and (5.29b), we obtain

$$q'^{*}_{-2} = q'_2 = \sqrt{2I^s_{xy}}(c_{2,+} + c_{2,-}), \tag{5.30a}$$

$$q'_0 = \sqrt{\frac{2}{3}}\frac{V\omega_0}{\Omega_s}\left(c_{0,+} + c^*_{0,+}\right). \tag{5.30b}$$

Note that the harmonic component q'_2 is a linear combination of retrograde and prograde modes, which oscillates at two different mode frequencies. So one can expect that q'_2 satisfies a second order differential equation.

So far the expressions are in the co-rotating frame; to transform them to the inertial coordinate system, one can use the relationship between tensor components in the two frames

$$Q^{ij} = R^i_m R^j_n Q'^{mn},$$

where the operator R first rotates Q'^{mn} along the z'-axis by $-\Omega_s t$, and does the other rotation along the new x-axis by π, i.e.,

$$R = \begin{pmatrix} \cos\Omega_s t & -\sin\Omega_s t & 0 \\ -\sin\Omega_s t & -\cos\Omega_s t & 0 \\ 0 & 0 & -1 \end{pmatrix}.$$

This results in

$$q_2 = e^{2i\Omega_s t} q'_{-2}, \tag{5.31a}$$

$$q_0 = q'_0. \tag{5.31b}$$

Plugging Eqs. (5.30) and (5.31) into Eqs. (5.25), we finally get

$$\begin{aligned} \ddot{r} - r\dot{\phi}^2 = &-\frac{M_t}{r^2} + \frac{3M_2}{2\mu r^4}\sqrt{\frac{3}{2}}q'_0 - \frac{9M_2}{2\mu r^4}A + \frac{1}{5}\sqrt{\frac{2}{3}}\frac{d^5 q'_0}{dt^5}r \\ &- \frac{2r}{5}\mathrm{Re}\left[e^{-2i\phi}\frac{d^5}{dt^5}(q'_2 e^{-2i\Omega_s t})\right] - \frac{\mu}{15}\frac{d^5 r^2}{dt^5}r - \frac{\mu r}{5}\mathrm{Re}\left[e^{-2i\phi}\frac{d^5}{dt^5}(r^2 e^{2i\phi})\right], \end{aligned} \tag{5.32a}$$

$$r\ddot{\phi} + 2\dot{r}\dot{\phi} = \frac{3M_2}{\mu r^4}B - \frac{2r}{5}\mathrm{Im}\left[e^{-2i\phi}\frac{d^5}{dt^5}(q'_2 e^{-2i\Omega_s t})\right] - \frac{\mu r}{5}\mathrm{Im}\left[e^{-2i\phi}\frac{d^5}{dt^5}(r^2 e^{2i\phi})\right], \tag{5.32b}$$

$$\begin{aligned} \ddot{q}'_2 - 2i\omega_3\dot{q}'_2 + \omega_2^2 q'_2 = &\frac{3}{2}\frac{\omega_2^2\lambda_2 M_2}{r^3}e^{2i\phi+2i\Omega_s t} - \frac{3M_2}{2r^3}e^{2i\phi+2i\Omega_s t} \\ &\times \frac{\omega_2^2\lambda_2(\Omega_s - \omega_3)}{\Omega_s^2 - 2\Omega_s\omega_3 - \omega_2^2}\left(2\dot{\phi} + 2\Omega_s - \omega_3 + 3i\frac{\dot{r}}{r}\right), \end{aligned} \tag{5.32c}$$

$$\ddot{q}'_0 + \omega_0^2 q'_0 = -\sqrt{\frac{3}{2}}\frac{\omega_0^2 \lambda_0 M_2}{r^3}, \tag{5.32d}$$

where we have defined two real variables A and B as

$$q'_2 e^{-2i\phi - 2i\Omega_s t} = A + iB. \tag{5.33}$$

In Eqs. (5.32), A is proportional to the radial force while B to the azimuthal torque. We have also defined

$$\lambda_2 = I^s_{xy}/\omega_2^2, \tag{5.34}$$

$$\lambda_0 = (I^s_{xy} + 4I_{zz})/(3\omega_0^2). \tag{5.35}$$

It is straightforward to identify these two quantities as the Love numbers of the $(2, 2)$ and $(2, 0)$ modes, respectively.

When deriving Eqs. (5.32), we have assumed the star is described as a Maclaurin spheroid. Nonetheless, this affects only the values of the coupling constants, λ_0 and λ_2. The form of Eqs. (5.32) holds generically [as we discussed in Eqs. (5.22) and (5.23)]. To generailize the result to a realistic EoS, one only needs to replace the values of λ_0 and λ_2 accordingly—our equation of motion is an effective theory for the evolution of binary system (without relativistic corrections). Under the assumption of homogeneity and incompressibility, the Love numbers become $\lambda_0 = \lambda_2 = R^5_{\rm NS}/2$ for a non-spinning NS. This leads to $k_2 = 3/4$ [see Eq. (5.2) and Ref. [89]]. However, this value differs significantly from those obtained from more realistic EoS (cf. numbers provided in Sec. 5.2.1). Hence in this chapter, we obtain values of λ_0 and λ_2 by inserting values of $R_{\rm NS}$ and k_2 from H4 and $\Gamma = 2$ polytropic EoS into Eq. (5.2); and we ignore the spin corrections to them. As a result, our calculations do not rely on the expressions of the auxiliary variables we introduced in Eq. (5.20).

The two frequency parameters ω_2 and ω_3 in Eqs. (5.32) are given by

$$\omega_2^2 = -\omega_{2+}\omega_{2-}, \tag{5.36}$$

$$\omega_3 = -\frac{\omega_{2+} + \omega_{2-}}{2}. \tag{5.37}$$

The minus sign appears in Eq. (5.36) because $\omega_{2\pm}$ have opposite signs. As discussed in the last subsection, we assume the mode frequencies dependence on Ω_s, given in Eqs. (5.6), is still valid, which implies

$$\omega_3 = \Omega_s, \tag{5.38}$$

and the second term on the RHS of Eq. (5.32c) vanishes in our case.

We can see that Eqs. (5.32) reduce to the conventional mode-orbit equations when $\Omega_s \to 0$ [cf. Eq. (6) of Ref. [23]]. As discussed by Ref. [23], high order time derivatives in the radiation reaction terms can be lowered by repeatedly replacing the second time derivatives by contributions from the conservative part alone. In this way, Eqs. (5.32) become a set of second-order ordinary differential equations.

5.3 Model of DT: Stellar oscillations

As we have discussed in the introduction, both L94 [36] and FR07 [53] focused on the total change in the orbital phase when the system evolves through a DT resonance. This is because for g- and/or r-modes that have weak tidal couplings, only the resonant regime plays a significant role in affecting the orbital evolution. On the other hand, H+16 [54, 55] proposed an EOB formalism to study the strongly tidal-coupled f-mode by introducing an effective Love number, which works well when the driving frequency is comparable yet still less than the eigenfrequency of the f-mode. In this and the next sections, we will use semi-analytic methods to carry out a systematic study of DT, and provide an alternative way to describe the full dynamics of DT, including both stellar and orbital evolutions. This section mainly focuses on the stellar part, where we extend H+16 [54, 55] and find analytic solutions of stellar evolution that are valid in all regimes (adiabatic, resonant and post-resonance) and for arbitrary spins. With the new analytic expressions, we can have a better understanding on DT. We first review the approximations presented in L94 [36] and H+16 [54, 55] in Sec. 5.3.1, and then in Sec. 5.3.2 we propose our new approximations and compare them with numerical integrations. In the next section (Sec. 5.4), we will apply our approximation to describe tidal back-reaction.

5.3.1 Previous studies on DT

As studied in L94 [36], the $(2, 2)$ mode q'_2 in a non-spinning NS can be treated as a harmonic oscillator driven by tidal force

$$\ddot{q}'_2 + \omega_2^2 q'_2 = \frac{3}{2}\frac{\omega_2^2 \lambda_2 M_2}{r^3} e^{2i\phi}. \tag{5.39}$$

When the orbital frequency $\Omega \ll \omega_2$, the NS adiabatically follows the tidal driving, with its main time dependence given by $e^{2i\phi}$. Therefore it is appropriate to define a variable $b = q'_2 e^{-2i\phi}$, which satisfies

$$\ddot{b} + 4i\Omega\dot{b} + (\omega_2^2 - 4\Omega^2)b = \frac{3}{2}\frac{\omega_2^2 \lambda_2 M_2}{r^3}. \tag{5.40}$$

Here we have ignored time derivative of orbital frequency since its rate of change due to GW radiation is small compared with other variables. Note that the quantity $A+iB$ we defined in the last section reduces to b when the spin vanishes. Since the major time dependence $e^{-2i\phi}$ has been factored out, we have $\ddot{b} \ll 4\Omega\dot{b} \ll (\omega_2^2 - 4\Omega^2)b$, it is safe to ignore $\ddot{b}$ and $\dot{b}$, leading to the well-known adiabatic approximation

$$b = \frac{3\omega_2^2\lambda_2 M_2}{2r^3}\frac{1}{\omega_2^2 - 4\Omega^2}. \tag{5.41}$$

As Ω approaches $\omega_2/2$, the mode gets resonantly excited. L94 [36] assumed that near resonance, the mode mainly oscillates at its natural frequency ω_2, so they defined a slowly varying complex amplitude $c = q_2' e^{-i\omega_2 t}$, which satisfies[6]

$$\ddot{c} + 2i\omega_2\dot{c} = \frac{3}{2}\frac{\omega_2^2\lambda_2 M_2}{r^3}e^{2i\phi - i\omega_2 t}. \tag{5.42}$$

Similarly, by neglecting $\ddot{c}$, this equation can be solved as

$$c = \frac{3}{4i\omega_2}\int^t \frac{\omega_2^2\lambda_2 M_2}{r'^3}e^{2i\phi' - i\omega_2 t'}dt', \tag{5.43}$$

which can in turn be evaluated with SPA, giving the post-resonance amplitude:

$$|c| = \frac{3}{4\omega_2}\frac{\omega_2^2\lambda_2 M_2}{r_r^3}\sqrt{\frac{\pi}{\dot{\Omega}_r}}. \tag{5.44}$$

Hereafter we use the subscript r to refer to the point of resonance. As we can see, the treatment in L94 [36] is piecewise: they separated out distinct time dependence in different regimes. This is enough for evaluating the energy and angular momentum transfers from orbital motion to NS mode since they only depend on the post-resonance amplitude. However, neither the detailed time evolution of the mode, nor the orbital dynamics in the resonant regime were provided.

L94 [36] was improved by H+16 [54, 55], who solved Eq. (5.39) with the Green function, obtaining

$$q_2'(t) = \frac{3}{2\omega_2}\int^t \frac{\omega_2^2\lambda_2 M_2}{r'^3}e^{2i\phi'}\sin\omega_2(t-t')dt'. \tag{5.45}$$

Near resonance, Eq. (5.45) reduces to Eq. (5.43) if one writes $\sin\omega_2(t-t') = \frac{1}{2i}[e^{2i\omega_2(t-t')} - e^{-2i\omega_2(t-t')}]$ and neglects the term that does not contribute to SPA. However, Eq. (5.45) is exact in all regimes. This lays the foundation to obtain a

[6] The other term proportional to $q_2' e^{i\omega_2 t}$ doesn't contribute to SPA in Eq. (5.44)

single continuous function to represent the stellar motion during DT. Instead of using SPA to get the final amplitude of the mode, H+16 [54, 55] expanded the integrand in Eq. (5.43) near resonance

$$c = \frac{3}{4i\omega_2}\frac{\omega_2^2\lambda_2 M_2}{r_r^3}\int^t e^{i\dot{\Omega}_r(t'-t_r)^2}t', \tag{5.46}$$

which becomes a Fresnel function. This approximation is accurate within the duration of the resonance $T_{\rm dur}$

$$|t - t_r| \ll T_{\rm dur}, \tag{5.47}$$

where $T_{\rm dur} = \sqrt{\frac{\pi}{\dot{\Omega}_r}}$. They then asymptotically matched Eq. (5.46) to Eq. (5.41). More specifically, they first observed that Eq. (5.41) diverges as $(t - t_r)^{-1}$ as $\Omega \to \omega_2/2$

$$be^{2i\phi - i\omega_2 t} \sim -M_2\lambda_2\omega_2^2\frac{3}{8\omega_2 r_r^3}\frac{e^{2i\phi_r - i\omega_2 t}}{\dot{\Omega}_r(t - t_r)}. \tag{5.48}$$

H+16 [54, 55] used the RHS of Eq. (5.48) as a counterterm: they added the adiabatic solution in Eq. (5.41) and the resonant one in Eq. (5.46) up and then subtracted the counterterm. In this way, the divergence is cured, and the sum has the correct asymptotic behavior in both the adiabatic and resonant regimes. This new solution cannot describe the post-resonance evolution, as is expected because the asymptotic behavior in that regime was not yet considered. As pointed out in the introduction, this approximation is sufficient for non-spinning NS if the post-resonance regime is short. However, for highly spinning systems, we must extend this method to the post-resonance regime.

5.3.2 New approximation and numerical comparisons

Let us start from the equation that governs the $(2, 2)$ mode [Eq. (5.32c)]. By defining $x = q_2' e^{-i\Omega_s t}$, it becomes

$$\ddot{x} + \zeta^2 x = \frac{3}{2}\frac{\omega_2^2\lambda_2 M_2}{r^3}e^{2i\phi + i\Omega_s t}, \tag{5.49}$$

where

$$\zeta^2 = \Omega_s^2 + \omega_2^2. \tag{5.50}$$

Note that the second term on the RHS of Eq. (5.32c) vanishes because $\omega_3 = \Omega_s$ [Eq. (5.38)]. The resonance is determined by the condition

$$\dot{\phi} = \Omega_r = \frac{\zeta - \Omega_s}{2}. \tag{5.51}$$

Under the assumed $\omega_2 - \Omega_s$ relation, ζ can be simplified to $(\omega_+ - \omega_-)/2$, then we have

$$\dot{\phi} = \Omega_r = -\Omega_s - \frac{\omega_{2-}}{2}, \tag{5.52}$$

but here we keep ζ for generality. Eq. (5.52) shows that only the retrograde mode is excited. The dependence of Ω_r on Ω_s is shown in Fig. 5.2.

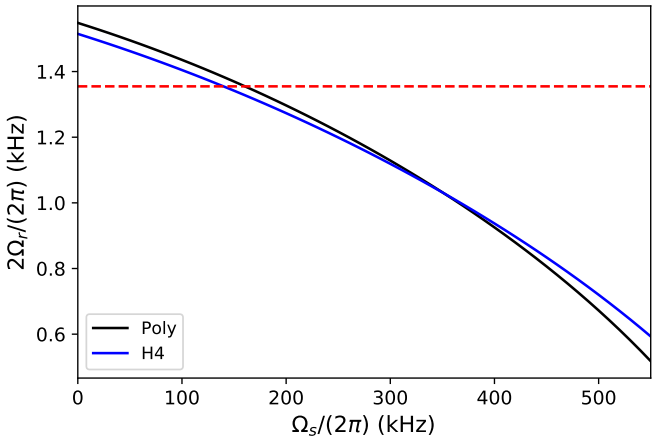

Figure 5.2: The resonant GW frequency ($2\Omega_r$) as functions of spin frequency for two EoS. We also plot the contact GW frequency as a red dashed line for comparison. The retrograde mode frequency is shifted by spin to a smaller value, which makes DT possible during the inspiral.

By incorporating spin into procedures discussed in the previous subsection, H+16's result [54, 55] can be written as

$$A(t) = \frac{3M_2\lambda_2\omega_2^2}{2r^3}\frac{1}{\zeta^2 - (\Omega_s + 2\Omega)^2} + \frac{3M_2\lambda_2\omega_2^2}{8\sqrt{\dot{\Omega}_r}\zeta r_r^3}\frac{1}{\hat{t}}$$
$$+ \frac{3M_2\lambda_2\omega_2^2}{4r_r^3\zeta}\sqrt{\frac{\pi}{2\dot{\Omega}_r}}\left[-\frac{1}{\sqrt{2}}\sin\left(\hat{t}^2 - \frac{\pi}{4}\right) - \mathrm{FC}\left(\sqrt{\frac{2}{\pi}}\hat{t}\right)\sin\hat{t}^2 + \mathrm{FS}\left(\sqrt{\frac{2}{\pi}}\hat{t}\right)\cos\hat{t}^2\right], \tag{5.53a}$$

$$B(t) = \frac{3M_2\lambda_2\omega_2^2}{4r_r^3\zeta}\sqrt{\frac{\pi}{2\dot{\Omega}_r}}\left[-\frac{1}{\sqrt{2}}\sin\left(\hat{t}^2 + \frac{\pi}{4}\right) - \mathrm{FC}\left(\sqrt{\frac{2}{\pi}}\hat{t}\right)\cos\hat{t}^2 - \mathrm{FS}\left(\sqrt{\frac{2}{\pi}}\hat{t}\right)\sin\hat{t}^2\right], \tag{5.53b}$$

where variables A and B are defined in Eq. (5.33). We can see that the phase of A and B's oscillations is governed by:

$$\hat{t} = \sqrt{\dot{\Omega}_r}(t - t_r). \tag{5.54}$$

FC and FS in Eqs. (5.53) are Fresnel functions defined as $\int_{-\infty}^{\hat{t}} \sin s^2 ds = \sqrt{\pi/8}[1 + 2\mathrm{FS}(\hat{t}\sqrt{2/\pi})]$ and $\int_{-\infty}^{\hat{t}} \cos s^2 ds = \sqrt{\pi/8}[1 + 2\mathrm{FC}(\hat{t}\sqrt{2/\pi})]$.

To check the accuracies of these formulae, we compare them with numerical integrations of Eqs. (5.32). We choose the H4 EoS and spin frequency of 550Hz. This gives $e_0 = 0.63$, $\omega_0 = 2\pi \times 1.71\mathrm{kHz}$, $\omega_+ = 2\pi \times 0.59\mathrm{kHz}$ and $\omega_- = -2\pi \times 1.69\mathrm{kHz}$. Eq. (5.51) indicates that resonance happens at the orbital angular frequency $2\pi \times 0.30\mathrm{kHz}$. Using these numbers, we solve Eqs. (5.32) numerically with the following initial conditions:

$$\begin{aligned}
&\dot{\phi}^{(0)} = 2\pi F_0 = 2\pi \times 18\mathrm{Hz},\ r^{(0)} = \left(\frac{M_t}{\dot{\phi}^{(0)2}}\right)^{1/3},\\
&\dot{r}^{(0)} = -\frac{64}{5}\eta\left(\frac{M_t}{r^{(0)}}\right)^3,\ q_0^{(0)} = -M_2\lambda_0\sqrt{\frac{3}{2}}\frac{1}{r_0^3},\\
&\dot{q}_0^{(0)} = -3\frac{\dot{r}_r^{(0)}}{r_r^{(0)}}q_0^{(0)},\ A^{(0)} = \frac{3M_2\lambda_2\omega_2^2}{2r^{(0)3}}\frac{1}{\zeta^2 - (2\dot{\phi}^{(0)} + \Omega_s)^2},\\
&\dot{A}^{(0)} = 0, B^{(0)} = 0,\ \dot{B}^{(0)} = 0.
\end{aligned} \tag{5.55}$$

The evaluation of Eq. (5.53) requires the information of orbital evolution, like $r(t)$, $\Omega(t)$, and $\dot{\Omega}_r$. Here we take them from the numerical integrations (with tidal backreaction). In Fig. 5.3, we plot the numerical solutions (red) versus predictions of Eqs. (5.53) (black). Dimensionless variables $\tilde{A}$ and $\tilde{B}$ are defined by

$$\tilde{A} = \frac{3}{2}\frac{A}{R_{\mathrm{NS}}^3}, \quad \tilde{B} = \frac{3}{2}\frac{B}{R_{\mathrm{NS}}^3}. \tag{5.56}$$

The vertical dashed line labels the time of resonance. We can see that Eqs. (5.53) can describe pre-resonance evolutions of A and B to high accuracy, despite a small discrepancy in $\tilde{A}$ at t_r. They smoothly connect the adiabatic and resonant regimes. In the post-resonance regime, the formulae give the correct amplitude of mode oscillation, same as L94 [36], but do not predict the correct phasing of post-resonance oscillation. Let us attempt to improve the treatment in H+16 [54, 55], in several steps.

The post-resonance oscillation can be viewed as trigonometric functions modulated by Fresnel functions FC and FS. In this regime, FC and FS both approach $1/2$ when $\hat{t} \to \infty$, Eqs. (5.53) then predict

$$A \sim \frac{3M_2\lambda_2\omega_2^2}{4r_r^3\zeta}\sqrt{\frac{\pi}{\dot{\Omega}_r}}\cos(\hat{t}^2 + \frac{\pi}{4}), \tag{5.57a}$$

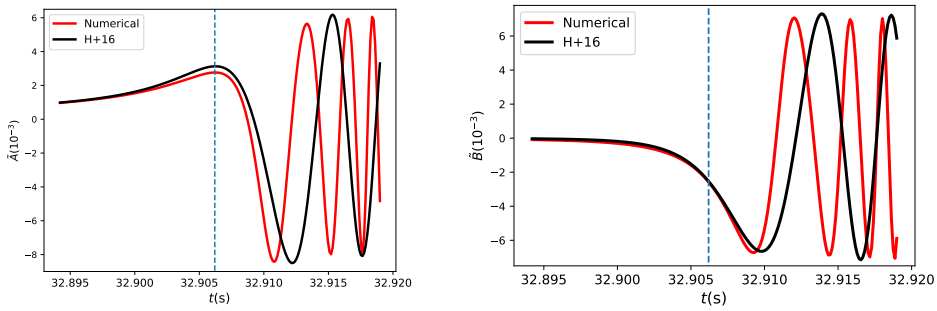

Figure 5.3: Dimensionless quadrupole moments [normalized by $R_{\rm NS}^3$ in Eq. (5.56)] induced by DT as functions of time. Red curves are results from fully numerical evolution and black curves are from Eqs. (5.53). The vertical dashed blue line denotes the time of resonance. Eqs. (5.53) are accurate in the pre-resonance regime, but fail to describe the phasing of post-resonance oscillation.

$$B \sim -\frac{3M_2\lambda_2\omega_2^2}{4r_r^3\zeta}\sqrt{\frac{\pi}{\dot{\Omega}_r}}\sin(\hat{t}^2+\frac{\pi}{4}), \tag{5.57b}$$

which lead to

$$x \sim \frac{3M_2\lambda_2\omega_2^2}{4r_r^3\zeta}\sqrt{\frac{\pi}{\dot{\Omega}_r}}e^{-i\hat{t}^2-i\pi/4+2i\phi+i\Omega_s t}. \tag{5.58}$$

However, as pointed out by L94 [36], x should oscillate at its eigenfrequency ζ in the post-resonance regime. Re-writing the phase of x in Eq. (5.58) as $(2\phi-\zeta t+\Omega_s t-\hat{t}^2)+\zeta t-\pi/4$, it is straightforward to see that the term in the bracket is supposed to vanish in order to meet this requirement. Therefore we can attempt to replace all $\hat{t}^2$ in trigonometric functions in Eq. (5.53) by

$$\Theta = -\chi_r - \zeta t + 2\phi + \Omega_s t, \tag{5.59}$$

where $\chi_r = 2\phi_r - \zeta t_r + \Omega_s t_r$. The constant χ_r is chosen so that Θ is 0 at t_r to match $\hat{t}$. Note that $\hat{t}^2$ is the leading order of Taylor expansion of Θ around t_r. Figure 5.4 shows the result of our new approximation, which gives the correct phasing in the post-resonance regime, but still fails to explain the amplitude of the first cycle as well as the evolution in the adiabatic regime.

These undesired features can be cured by making a further change to the counterterm Eq. (5.48) and adding a new term to B, resulting in:

$$A = \frac{3M_2\lambda_2\omega_2^2}{2r^3}\frac{1}{\zeta^2-(2\Omega+\Omega_s)^2} + \frac{3M_2\lambda_2\omega_2^2}{8\sqrt{\dot{\Omega}_r}\zeta r_r^3}\frac{\cos(\hat{t}^2-\Theta)}{\hat{t}}$$

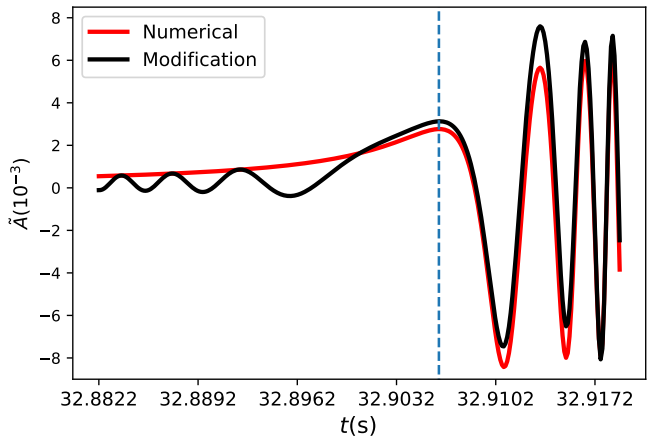

Figure 5.4: Time evolution of dimensionless quadrupole moment $\tilde{A}$. The black line represents the formula in Eq. (5.53a) with $\hat{t}^2$ that appears in trigonometric functions replaced by Θ [Eq. (5.59)], while the red line is from numerical integrations. The vertical dashed line is the time of resonance. This modification gives the correct post-resonance phasing, but does not give accurate post-resonance amplitude nor adiabatic evolution.

$$+\frac{3M_2\lambda_2\omega_2^2}{4r_r^3\zeta\dot{\Omega}_r}\sqrt{\frac{\pi}{2\dot{\Omega}_r}}\left[-\frac{1}{\sqrt{2}}\sin(\Theta-\frac{\pi}{4})-\mathrm{FC}\left(\sqrt{\frac{2}{\pi}}\hat{t}\right)\sin\Theta+\mathrm{FS}\left(\sqrt{\frac{2}{\pi}}\hat{t}\right)\cos\Theta\right], \tag{5.60a}$$

$$B=\frac{3M_2\lambda_2\omega_2^2}{8r_r^3\zeta\sqrt{\dot{\Omega}_r}}\frac{\sin(\hat{t}^2-\Theta)}{\hat{t}}+\frac{3M_2\lambda_2\omega_2^2}{4r_r^3\zeta}\sqrt{\frac{\pi}{2\dot{\Omega}_r}}\left[-\frac{1}{\sqrt{2}}\sin(\Theta+\frac{\pi}{4})\right.$$
$$\left.-\mathrm{FC}\left(\sqrt{\frac{2}{\pi}}\hat{t}\right)\cos\Theta-\mathrm{FS}\left(\sqrt{\frac{2}{\pi}}\hat{t}\right)\sin\Theta\right]. \tag{5.60b}$$

We refer interested readers to Sec. 5.7 for detailed derivations. The new expressions still need orbital information as input. For example, one cannot obtain $A(t)$ and $B(t)$ without the knowledge of $\dot{\Omega}_r$, t_r, and so on. In the next section, we will combine our new formulae with orbital evolutions to give analytic estimations on these parameters.

Results from Eq. (5.60) are plotted as blue dots in Fig. 5.5, and compared with numerical solutions (red lines). We can see that our new results are more accurate. In comparison with H+16 [54, 55], the second term in the first line of Eq. (5.60a) is multiplied by $\cos(\hat{t}^2-\Theta)$. The modification can be understood as follows. The adiabatic term, i.e., the first term in Eq. (5.60a), diverges as the system reaches the resonance point. H+16 [54, 55] chose Eq. (5.48) as the counterterm to cancel the

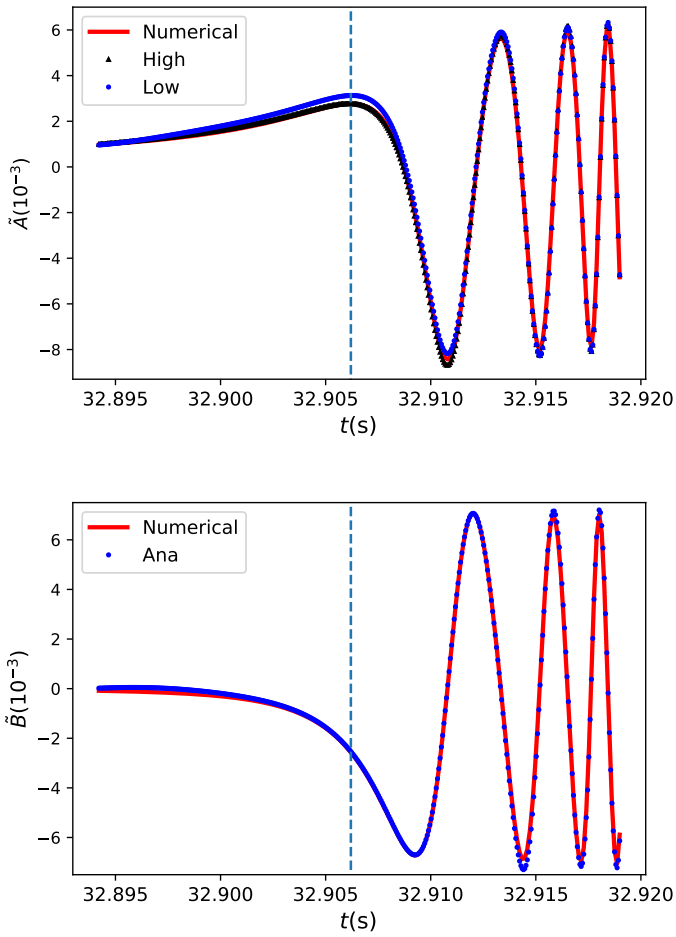

Figure 5.5: Same as Fig. 5.3, but the numerical solutions are compared with Eqs. (5.60) and (5.61). The formula of $\tilde{B}$ is already accurate enough to fit the numerical results. While the formula of $\tilde{A}$ without higher order correction (blue dots) predicts a larger value near t_r. The problem is fixed after the inclusion of Eq. (5.61), which we plot as black triangles.

undesired infinity. Our better counterterm, $\cos(\hat{t}^2 - \Theta)/\hat{t}$, not only diverges as $1/\hat{t}$, but also has the correct oscillatory behavior. This cures the problems shown in Fig. 5.4. In B, we have a new term $\sim \sin(\hat{t}^2 - \Theta)/\hat{t}$ [the first line in Eq. (5.60b)], which vanishes both as $|t_r| \to \infty$ and at t_r (recall that $\lim_{x\to 0} \sin x^3/x = 0$, hence no infinity issue at t_r), therefore does not modify the asymptotic behaviors of B in the adiabatic or in the post-resonance regimes.

In comparison with Fig. 5.4, changes in Fig. 5.5 not only cancel the undesired features in the adiabatic regime, but also move the first cycle of post-resonance evolution downward to match the amplitude. Prior to resonance, A gradually grows

while B remains 0. Approximately, the resonance time is the local maximum of A, but the value of A on resonance is less than its final amplitude, only reaching it after one cycle. The evolution of B is similar but lags behind A. Although Eq. (5.60a) predicts slightly larger A in the resonant regime, they are accurate enough for the purpose of studying the tidal back-reaction onto the orbital motion, as we shall see in the next section.

If one wants to obtain more accurate expressions, especially to remove the discrepancy near resonance, a higher order correction can be made by adding

$$\Delta A(t) = \frac{3M_2\lambda_2\omega_2^2}{16\zeta r_r^3\sqrt{\dot{\Omega}_r}}\frac{\sin(\hat{t}^2-\Theta)}{\hat{t}^3}, \tag{5.61}$$

into Eq. (5.60a). Readers can find derivations in Sec. 5.7. The result is shown in Fig. 5.5 with black triangles, where we can see the formula with higher order correction gives a more accurate description on A near t_r.

To quantify the accuracies of the analytic results, we calculate the values of A and B at t_r

$$A_r = \frac{3M_2\lambda_2\omega_2^2}{8\zeta r_r^3}\left(\sqrt{\frac{\pi}{2\dot{\Omega}_r}} + \frac{3}{\dot{\Omega}_r}\frac{\dot{r}_r}{r_r} + \frac{1}{\zeta}\right) + \frac{M_2\lambda_2\omega_2^2}{8\zeta r_r^3}\frac{\ddot{\Omega}_r}{\dot{\Omega}_r^2}, \tag{5.62a}$$

$$B_r = -\frac{3M_2\lambda_2\omega_2^2}{8\zeta r_r^3}\sqrt{\frac{\pi}{2\dot{\Omega}_r}}, \tag{5.62b}$$

where the last term in A_r comes from the higher order correction Eq. (5.61). It is interesting to see that B_r is equal to half of the final amplitude [cf. Eq. (5.57b)]. For completeness, we also list q_0 below

$$q_0 = -M_2\lambda_0\sqrt{\frac{3}{2}}\frac{1}{r^3}, \tag{5.63}$$

which comes from the adiabatic approximation. These values are compared with numerical results in Table 5.1, which shows that our analytic results of A with higher order correction and B only differ from numerical results by several percent. We can see the error decreases as spin rises. We also compare the formula of A without the higher correction Eq. (5.61), errors are around tens of percent. Hence the correction is important if we require high accuracy around the resonance.

Finally, we want to note that discussions in this subsection may not be useful in practice, because one can get tidal evolution by directly integrating Eqs. (5.32). However, the structure of Eqs. (5.60) helps us gain more physical insights, especially after combining with orbital dynamics in the next section.

Table 5.1: Relative errors of Eqs. (5.62) and (5.63) for different spins, where 'High' and 'Low' means including and not including the higher order correction Eq. (5.61), respectively.

$\Omega_s/(2\pi)$ (Hz)	$\lvert\Delta q_0\rvert/q_0$ ($\times 0.1\%$)	$\lvert\Delta A\rvert/A$ ($\times 1\%$)		$\lvert\Delta B\rvert/B$ ($\times 1\%$)
		High	Low	
550	0.2	0.2	13.1	1.4
450	1.3	1.1	14.0	0.6
350	4.0	2.2	14.4	0.1
250	8.7	3.2	14.4	0.8
150	15.1	4.0	14.4	1.4

5.4 Model of DT: Orbital dynamics near resonance

In this section we will discuss the post-resonance orbital dynamics. As we will review in Sec. 5.4.1, currently there are mainly two analytic approximations to DTs: the method of averaged PP orbit in FR07 [53] and the method of effective Love number in H+16 [54, 55]. Here we provide an alternative way to describe the post-resonance dynamics. In Sec. 5.4.2, we derive a set of first order differential equations for osculating variables: the Runge-Lenz vector (whose magnitude is proportional to the eccentricity of the orbit), angular momentum and the orbital phase. These equations, with our new formulae for A and B [Eq. (5.60)], are self-contained except that they need $\dot{\Omega}_r$ as input. But as we will discuss in Sec. 5.4.3, osculating equations lead to an analytic expression (or more accurately, a quintic equation) for $\dot{\Omega}_r$, which is accurate for the systems we study. Therefore we do not need to use non-tidal orbit as a prior knowledge to feed into the formulae of A and B. Then in Sec. 5.4.4, we compare our analyses and the method of effective Love number with fully numerical results. Finally in Sec. 5.4.5, we propose an alternative way to obtain the post-resonance PP orbit, which turns out to agree with FR07 [53] to the leading order in tidal interaction. By combining our approach and FR07 [53], we derive an analytic expression for t_r, i.e., the time of resonance.

5.4.1 Review of previous works

The model in FR07 [53] is based on the fact that the DT only causes significant energy and angular momentum transfers to the star near resonance, within the time

$$\Delta t = \frac{\Delta L}{\dot{L}_{\rm GW}}, \tag{5.64}$$

where ΔL is the angular momentum transfer from the orbit to the star due to resonance and $\dot{L}_{\rm GW}$ is the rate at which angular momentum radiated in GWs [90]

$$\dot{L}_{\rm GW} = \frac{32}{5}\mu^2 \frac{{M_t}^{5/2}}{r_r^{7/2}}. \tag{5.65}$$

We note that r_r in Eq. (5.65) should be the actual separation of the star at t_r, instead of the one predicted by pre-resonance PP orbit. After resonance, the NS is treated as freely oscillating, with the interaction between the star and the orbit neglected, and the post-resonance orbit is another PP trajectory. The pre- and post-resonance orbital separations are related by the time shift Δt

$$r(t) = \begin{cases} r^{\rm PP}(t) & t - t_r \ll T_{\rm dur}, \\ r^{\rm PP}(t + \Delta t) & t - t_r \gg T_{\rm dur}, \end{cases} \tag{5.66}$$

where $T_{\rm dur}$ comes from the same reasoning that leads to Eq. (5.47). We can see that this method is based on the estimation of time shift Δt due to resonance, where the non-tide $\dot{L}_{\rm GW}$ is used. We will discuss these in details in Sec. 5.4.5.

A more detailed model was developed in H+16 [54, 55], where the authors incorporated DT to the EOB formalism by introducing an effective Love number $\lambda_{\rm eff}$, as defined in Eq. (5.1). This quantity is based on the non-tidal orbit as a prior knowledge, and does not incorporate the imaginary part of $q_2' e^{-2i\phi - 2i\Omega_s t}$. In fact, with the help of Eqs. (5.29a), the effective Love number can be written in our notation as

$$\lambda_{\rm eff} = -\frac{r^3}{2M_2}\Re(q_2' e^{-2i\phi - 2i\Omega_s t}) = -\frac{r^3}{2M_2}A. \tag{5.67}$$

This term does not contain the full information of the NS oscillation, since B is missing. By comparing this term with the RHS of Eq. (5.32a), one can find that the effective Love number only describes the radial force due to the star's deformation. The ignored part, which characterizes the torque between the star and the orbit, actually plays an important role, as we shall see in Sec. 5.4.4. Furthermore, their calculations of effective Love number were obtained from non-tidal orbital evolution. This will cause inaccuracy when the spin is large.

5.4.2 Osculating equations

Since the traditional method of osculating orbits (cf. Ref. [90]) is singular for vanishing orbital eccentricity, we need to adopt a special perturbation method here [91]. This method uses specific angular momentum $\boldsymbol{h}$, the Runge-Lenz vector $\boldsymbol{\epsilon}$ and

the orbital phase ϕ as osculating variables. Assume that the perturbation force $\boldsymbol{F}$ is described by

$$\frac{\boldsymbol{F}}{\mu} = \mathcal{W}\boldsymbol{n} + S\boldsymbol{\lambda}, \tag{5.68}$$

where $\boldsymbol{n}$ is the unit vector along the radial direction and $\boldsymbol{\lambda}$ the unit vector along the azimuthal direction. $\mathcal{W}$ and S are the components of the acceleration. Equations of motion in terms of the osculating variables are given by

$$\begin{aligned} \frac{d\boldsymbol{h}}{dt} &= \boldsymbol{r} \times \boldsymbol{F}, \\ \frac{d\boldsymbol{\epsilon}}{dt} &= \boldsymbol{F} \times \boldsymbol{h} + \boldsymbol{r} \times \boldsymbol{h}, \\ \frac{d\phi}{dt} &= \frac{h}{r^2}. \end{aligned} \tag{5.69}$$

Note that the magnitude of $\boldsymbol{\epsilon}$ is proportional to the orbital eccentricity. In our case, only the z component of $\boldsymbol{h}$, denoted by h, and in-plane components of $\boldsymbol{\epsilon}$=(ϵ_r, ϵ_ϕ) matter. The orbital separation r, and its rate of change $\dot{r}$, can be expressed as

$$r = \frac{h^2}{M_t + \epsilon_r}, \tag{5.70a}$$

$$\dot{r} = -\frac{\epsilon_\phi}{h}. \tag{5.70b}$$

Equations of motion of the osculating variables can then be re-written as

$$\frac{d\phi}{dt} = \frac{h}{r^2}, \tag{5.71a}$$

$$\frac{dh}{dt} = rS, \tag{5.71b}$$

$$\frac{d\epsilon_r}{dt} = \frac{h}{r^2}\epsilon_\phi + 2Sh, \tag{5.71c}$$

$$\frac{d\epsilon_\phi}{dt} = -\frac{h}{r^2}\epsilon_r - \mathcal{W}h - \dot{r}rS. \tag{5.71d}$$

The perturbation forces S and $\mathcal{W}$ can be separated into radiation and tidal parts. The former comes from the Burke-Thorne radiation reaction potential. By neglecting tidal corrections, they are given by

$$\mathcal{W}_{\rm orb} = \frac{2}{5}\mu\left(\frac{32{M_t}^2\dot{r}}{3r^4} + \frac{48M_t\dot{r}\dot{\phi}^2}{r} + \frac{8M_t\dot{r}^3}{r^3}\right), \tag{5.72a}$$

$$S_{\rm orb} = \frac{2}{5}M_t\mu\left(\frac{8M_t\dot{\phi}}{r^3} + \frac{36\dot{r}^2\dot{\phi}}{r^2} - 24\dot{\phi}^3\right). \tag{5.72b}$$

The tidal perturbation forces $\mathcal{W}_{\rm tid}$ and $S_{\rm tid}$ are given by

$$\mathcal{W}_{\rm tid} = \frac{3M_2}{2\mu}\frac{(M_t+\epsilon_r)^4}{h^8}\left(\sqrt{\frac{3}{2}}q_0 - 3A\right), \tag{5.73a}$$

$$S_{\rm tid} = \frac{3M_2}{\mu}B\frac{(M_t+\epsilon_r)^4}{h^8}. \tag{5.73b}$$

For the time evolution of q_0, A, and B we use our analytic formulae, as shown in Eqs. (5.60) and (5.63). Here we do not include the higher order correction to A in Eq. (5.61) since the leading order already turns out to be accurate enough. By plugging Eqs. (5.70) into equations above we get

$$\frac{d\phi}{dt} = \frac{(M_t+\epsilon_r)^2}{h^3}, \tag{5.74a}$$

$$\frac{dh}{dt} = \frac{2}{5}M_t\mu\frac{(M_t+\epsilon_r)^3}{h^7}\left[8M_t(M_t+\epsilon_r) + 36\epsilon_\phi^2 - 24(M_t+\epsilon_r)^2\right] + \frac{h^2}{M_t+\epsilon_r}S_{\rm tid}, \tag{5.74b}$$

$$\frac{d\epsilon_r}{dt} = 2hS_{\rm tid} + \frac{(M_t+\epsilon_r)^2}{h^3}\epsilon_\phi + \frac{4}{5}M_t\mu\frac{(M_t+\epsilon_r)^4}{h^8}[8M_t(M_t+\epsilon_r) + 36\epsilon_\phi^2 - 24(M_t+\epsilon_r)^2], \tag{5.74c}$$

$$\begin{aligned}\frac{d\epsilon_\phi}{dt} &= -h\mathcal{W}_{\rm tid} + \frac{h\epsilon_\phi}{M_t+\epsilon_r}S_{\rm tid} - \epsilon_r\frac{(M_t+\epsilon_r)^2}{h^3} \\ &\quad + \frac{2}{5}\mu M_t\epsilon_\phi\frac{(M_t+\epsilon_r)^3}{h^8}\left[\frac{56M_t}{3}(M_t+\epsilon_r) + 24(M_t+\epsilon_r)^2 + 44\epsilon_\phi^2\right],\end{aligned} \tag{5.74d}$$

Eqs. (5.72)—(5.74) are a complete set of equations of ϕ, h, ϵ_r and ϵ_ϕ, except that we are missing the value of $\dot{\Omega}_r$ that appears in the formulae of A and B, this will be determined in Sec. 5.4.3. With these at hand, one can obtain the post-resonance orbital dynamics without solving tidal variables (e.g., q_0, A, and B) simultaneously.

In practice, we numerically evolve the system slightly after the resonance point, i.e., $t_r + \delta$, to get rid of the numerical infinity due to the term $\sin(\hat{t}^2 - \Theta)/\hat{t}$ in B. In our code, $\delta = 10^{-8}$s. Two infinities in A (adiabatic term and the counterterm) needs more care. The cancellation of these two infinities requires they have the exact the same behavior near the resonance point, this is difficult to achieve in practice, especially when there are osculating variables in A. In our simulations, we approximate the first divergence term by the following formula

$$\frac{3M_2\lambda_2\omega_2^2}{2r^3}\frac{1}{\zeta^2 - (2\Omega+\Omega_s)^2} = -\frac{3M_2\lambda_2\omega_2^2}{8\sqrt{\dot{\Omega}_r}\zeta r^3\hat{t}}, \tag{5.75}$$

where the denominator is expanded around t_r. In this manner, both divergence terms go to infinity as $1/\hat{t}$, so they cancel each other nicely. In order to improve the accuracy, one can include more terms of the Taylor expansion. However, this only works well for low spin, since the time for post-resonance evolution should be short enough such that the series converges. For high spin we only keep the leading term[7].

We should note that one can evolve the post-resonance system without knowing the value of t_r, of which our analytic estimations are not very accurate in some regimes of spin (we will discuss the estimation on it in Sec. 5.4.4), since the formulae of $A(t)$ and $B(t)$ only depend on $\hat{t}$. One can shift the time of resonance to $t = 0$ and simultaneously set $t_r = 0$. Similarly, the orbital phase of the resonance ϕ_r in Eq. (5.59) can be eliminated by an appropriate initial condition for ϕ, here we choose $\phi_r = 0$ and $\phi^{(0)} = 0$, where $\phi^{(0)}$ is the initial value of ϕ. Correspondingly, the constant χ_r becomes 0. What remains unknown in the osculating equations are $\dot{\Omega}_r$ and the initial conditions for $(\epsilon_{r,\phi}, h, \phi)$. We will address them in the next subsection.

5.4.3 The applications of osculating equations

In this subsection, we will discuss the applications of osculating equations introduced in the previous subsection.

5.4.3.1 *Orbit at resonance*

Let us first derive algebraic equations for $\dot{\Omega}_r$, $\dot{r}_r$ and the initial conditions of Eqs. (5.74). The basic idea is that variables like $\dot{\Omega}_r$ and $\dot{r}_r$ at resonance are determined by the tidal variables A and B through the osculating equations. Conversely, A and B are governed by $\dot{\Omega}_r$ in Eqs. (5.62). The relationship allows us to write down equations of $\dot{\Omega}_r$ and $\dot{r}_r$.

To calculate $\dot{r}$, we start with Eq. (5.70a). In our cases, the value of ϵ_r rises as the spin of the NS decrease, but it remains a small number. So we can approximate r by h^2/M_t. Using the equation of $\dot{h}$ [Eq. (5.74b)], we get

$$\frac{dr}{dt} = 2\sqrt{\frac{r^3}{M_t}}S. \tag{5.76}$$

[7] As we shall see in Sec. 5.4.4, the orbital frequency is oscillatory for high spin in the post-resonance regime. Under this situation, the leading term alone is more accurate than including higher order corrections.

For a quasicircular orbit, the radius and orbtial frequency approximately satisfy:

$$r_r = \left(\frac{M_t}{\Omega_r^2}\right)^{1/3}. \tag{5.77}$$

In Table 5.2 we verify that the error of Eq. (5.77) is less than 0.4% within the regime we concern. With this observation, together with B_r in Eqs. (5.62), one can simplify the expression of S into

$$\begin{aligned} S = S_{\rm tid} + S_{\rm orb} &= -\frac{3{M_2}^2\lambda_2}{\mu\zeta}\frac{3\omega_2^2}{8r_r^7}\sqrt{\frac{\pi}{2\dot{\Omega}_r}} \\ &+ \frac{4}{5}M_t\mu\Omega_r\left(\frac{18\dot{r}_r^2}{r_r^2} - 8\Omega_r^2\right), \end{aligned} \tag{5.78}$$

which is completely determined by $\dot{r}_r$ and $\dot{\Omega}_r$. Substituting this into Eq. (5.76) leads to a equation for $\dot{r}_r$ and $\dot{\Omega}_r$

$$\dot{r}_r = -\frac{3{M_2}^2\lambda_2}{\Omega_r\mu\zeta}\frac{3\omega_2^2}{4r_r^7}\sqrt{\frac{\pi}{2\dot{\Omega}_r}} + \frac{8}{5}M_t\mu\left(\frac{18\dot{r}_r^2}{r_r^2} - 8\Omega_r^2\right). \tag{5.79}$$

In order to solve for these two variables, one can use Eqs. (5.71a) and (5.71b) to establish another equation

$$\dot{\Omega}_r = \frac{\dot{h}}{r_r^2} - 2\frac{\dot{r}_r}{r_r^3}h = \frac{S}{r_r} - 2\Omega_r\frac{\dot{r}_r}{r_r}, \tag{5.80}$$

which gives

$$2r_r\dot{\Omega}_r = -3\Omega_r\dot{r}_r. \tag{5.81}$$

This relation can also be directly obtained by differentiating Eq. (5.77). Plugging Eq. (5.81) back into Eq. (5.79) gives a quintic function for $\dot{\Omega}_r$. The calculation can be simplified by the approximation $\dot{r}_r/r_r \ll \Omega_r$, so that the first term in the bracket of Eq. (5.79) can be neglected. In this manner, we obtain an explicit expression for $\dot{\Omega}_r$:

$$\dot{\Omega}_r = \left(\frac{u}{2} + \sqrt{\frac{u^2}{4} - \frac{v^3}{27}}\right)^{1/3} + \left(\frac{u}{2} - \sqrt{\frac{u^2}{4} - \frac{v^3}{27}}\right)^{1/3}, \tag{5.82}$$

where

$$u = \frac{27{M_2}^2\lambda\omega_2^2}{8r_r^8\zeta\mu}\sqrt{\frac{\pi}{2}}, \qquad v = \frac{96M_t\mu}{5r_r}\Omega_r^3 = \frac{3}{\mu r_r^2}\dot{L}_{\rm GW}^{(r)}. \tag{5.83}$$

Table 5.2: Comparisons between results from our formulae for $\dot{\Omega}_r$, $\dot{r}$, ϵ_ϕ, r and numerical integrations, where "Num." of $\Delta\dot{\Omega}_r/\dot{\Omega}_r$ are the results by numerical solving Eqs. (5.79) and (5.81); "Appr." are the results of Eq. (5.85). The parameters of NSs are still the H4 EoS with component masses $(1.4, 1.4)M_\odot$. The relative error becomes large when the spin decreases. The last column is the ratio of the non-tidal $\dot{\Omega}_r$ to the realistic $\dot{\Omega}_r$ when the orbital frequencies satisfy the resonance condition in Eq. (5.51).

$\Omega_s/(2\pi)$ (Hz)	$\Delta\dot{\Omega}_r/\dot{\Omega}_r(\times10^{-2})$ Num.	Appr.	$\Delta\dot{r}/\dot{r}$ $(\times10^{-2})$	$\Delta\epsilon_\phi/\epsilon_\phi$ $(\times10^{-2})$	$\Delta r/r$ $(\times10^{-2})$	$\frac{\dot{\Omega}_r^{\rm non}}{\dot{\Omega}_r^{\rm tide}}$
550	0.9	0.8	0.4	0.1	0.1	0.56
450	2.7	2.7	1.6	1.8	0.2	0.53
350	4.4	4.5	2.7	2.2	0.3	0.52
250	5.9	6.1	3.7	3.0	0.4	0.52
150	7.1	7.3	4.5	3.6	0.4	0.52

Eq. (5.82) can be further simplified by Taylor expanding in w, defined by

$$w = \frac{2^{1/3}v}{3u^{2/3}}, \tag{5.84}$$

leading to

$$\dot{\Omega}_r = u^{2/3}\left[1 + 2^{2/3}w + w^2 - \frac{w^3}{3} + O(w^4)\right]. \tag{5.85}$$

Recall that the duration of the resonance is $T_{\rm dur} = \sqrt{\pi/\dot{\Omega}_r}$ [Eqs. (5.47) and (5.66)], Eq. (5.85) is in fact an analytic relation between $T_{\rm dur}$ and the orbital time shift Δt due to resonance. The variable $\dot{r}_r$ is determined once $\dot{\Omega}_r$ is known. Finally, the initial value of ϵ_ϕ is related to $\dot{r}_r$ through its definition in Eq. (5.70b). With the values of $\dot{\Omega}_r$ and $\dot{r}_r$, Eq. (5.60) for $A(t)$ and $B(t)$ does not require input from numerical integrations.

In Table 5.2, we compare predictions of our formulae with numerical results. The parameters of NSs are the H4 EoS with component masses $(1.4, 1.4)M_\odot$. Results show that the accuracies of our analyses are higher than 93%. We can also see that accuracy is lower for low spins. Since H+16 [54, 55] used non-tidal $\dot{\Omega}_r$ in the effective Love number, we compare $\dot{\Omega}_r$ of non-tide orbits with realistic ones. The ratios of two quantities are shown in the last column of Table 5.2, we can see that $\dot{\Omega}_r^{\rm non}$ is only half of $\dot{\Omega}_r^{\rm tide}$, hence the use of $\dot{\Omega}_r^{\rm non}$ will cause inaccuracies.

5.4.3.2 *Angular momentum and energy transfers*

Another application of the osculating equations is to calculate the angular momentum and energy exchange between the star and the orbit. The transfer in L can be directly calculated from Eq. (5.71b). Following the procedure in Ref. [36], we get

$$\begin{aligned}\Delta L &= -\mu h_t = -\int \mu r S_{\rm tid} dt = -\int 3M_2 \frac{B}{r^3} dt \\ &= -\mathrm{Im}\int 3M_2 \frac{q_2' e^{-2i\phi - 2i\Omega_s t}}{r^3} dt \\ &= -\frac{2}{\mu\omega_2^2\lambda_2}\mathrm{Im}\int q_2'(\ddot{q}_{-2}' + 2i\Omega_s \dot{q}_{-2}' + \omega_2^2 q_{-2}') dt \\ &= -\frac{2}{\mu\omega_2^2\lambda_2}\left[\dot{A}B - \dot{B}A - (A^2+B^2)(\Omega_s + 2\Omega)\right], \end{aligned} \tag{5.86}$$

where we have used Eq. (5.32c). Assuming the deformation of the star is small initially, this exact formula gives the angular momentum deposited in the star. In fact, the quantity is the generalization of the "tidal spin," defined by (up to a constant) $\epsilon_{ijs} Q^{mi} \dot{Q}^{jm}$ for a non-spinning star [54].

By combining our formulae for A and B with the ΔL shown above, one can obtain a lengthy expression of angular momentum transfer as a function of time, but little can be learned from it. To give a more useful description, we follow the idea of FR07 [53], who assumed the net transfer only takes place near resonance. Within the post-resonance regime, ΔL is periodic and the net transfer is zero. In fact, we can see this clearly with the asymptotic behavior of A and B. From Eqs. (5.60) we know

$$A \sim \frac{3M_2\lambda_2\omega_2^2}{4r_r^3\zeta}\sqrt{\frac{\pi}{\dot{\Omega}_r}}\cos(\chi_r + \zeta t - 2\phi - \Omega_s t - \frac{\pi}{4}), \tag{5.87a}$$

$$B \sim \frac{3M_2\lambda_2\omega_2^2}{4r_r^3\zeta}\sqrt{\frac{\pi}{\dot{\Omega}_r}}\sin(\chi_r + \zeta t - 2\phi - \Omega_s t - \frac{\pi}{4}), \tag{5.87b}$$

where we have used the fact that the Fresnel functions go to $1/2$ as $\hat{t} \to \infty$. Plugging the above equations into Eq. (5.86) and averaging over orbital phase, we get the net angular momentum transfer as

$$\Delta L = \frac{9{M_2}^2\pi\lambda_2\omega_2^2}{8\dot{\Omega}_r r_r^6\zeta}. \tag{5.88}$$

This formula reduces to the result in L94 [36] when spin vanishes. The energy transfer is related to the angular momentum transfer by

$$\Delta E = \Omega_r \Delta L. \tag{5.89}$$

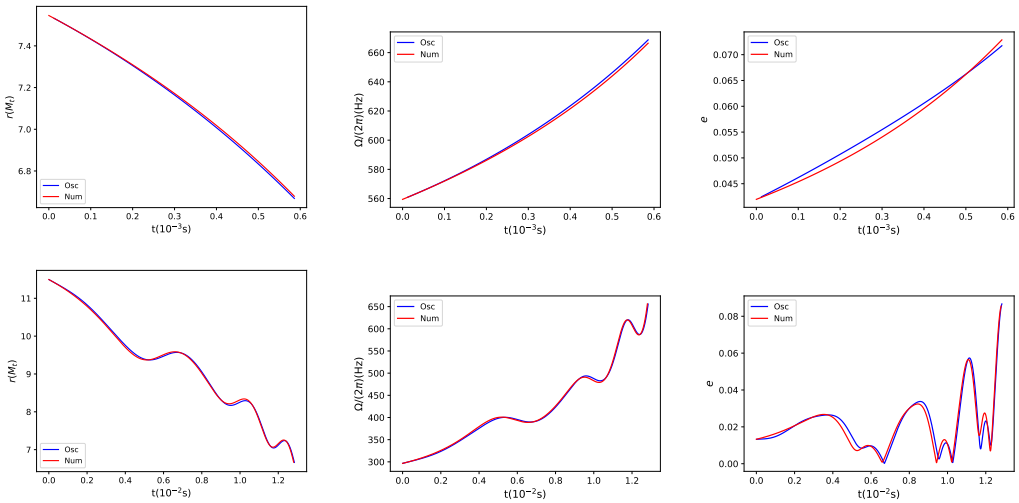

Figure 5.6: The seperation r, orbital frequency $\Omega/(2\pi)$ and the eccentricity e as functions of time. The initial time $t = 0$ represents the location of resonance and the endpoint corresponds to the contact separation. Red lines are from fully numerical solutions and blue lines are the results of osculating equations Eqs. (5.74). The spin of the upper panel is 300Hz, and the bottom one is 550Hz. We keep both the leading and the sub-leading terms in Eq. (5.75) in the low spin case while only the leading term in the high spin case.

By the expression of ΔL in Eq. (5.88), variables u and w defined in Eqs. (5.83) and (5.84) can be expressed as:

$$u = \frac{9\Omega_r^2}{\sqrt{2\pi}} \frac{\Delta L}{L_r} \frac{\dot{L}_{\rm GW}^{(r)}}{L_r}, \qquad w = \left(\frac{2}{81} \frac{T_{\rm orb}}{\Delta t} \frac{L_r}{\Delta L} \right)^{1/3}, \tag{5.90}$$

with $T_{\rm orb} = 2\pi\Omega_r$ and L_r the orbital angular momentum at resonance.

5.4.4 Comparisons with numerical results

In this subsection we will compare our approximations, as well as the method of effective Love number in H+16 [54, 55], with fully numerical results, in the post-resonance regime. We still choose the H4 EoS with spin frequencies 300Hz and 550Hz.

5.4.4.1 *Validating osculating equations*

We numerically solve Eqs. (5.74) starting from $t = \delta = 10^{-8}$s, where we have shifted the resonance time to 0 and set $t_r = 0$. The initial values of h, ϵ_r and ϵ_ϕ are from Eqs. (5.70b), (5.71a), (5.77), (5.79) and the resonance condition in Eq. (5.51). In the absence of analytic estimations for ϵ_r, we assume ϵ_r is 0 in Eq. (5.77), since it remains small within the domain we are interested in.

In Fig. 5.6, we plot orbital separation r (left panels), orbital frequency $\Omega/(2\pi)$ (middle panels), and eccentricity e (right panels) as functions of time, for NS spins 300Hz (upper panels) and 550Hz (lower panels). For the low spin case, we approximate the adiabatic term in Eq. (5.75) by both the leading and sub-leading terms, while for the high spin case we only keep the leading term. Predictions of our osculating equations agree well with the real post-resonance orbital dynamics. This again verifies that our formulae for $A(t)$ and $B(t)$ are accurate enough to describe the star's oscillation and its back reaction on the orbit. Furthermore, in our osculating equations we have only included the orbital part of the radiation-reaction force. The comparison confirms that the other part, i.e., the stellar radiation-reaction force, can be safely ignored. One interesting feature of the post-resonance dynamics is the eccentricity of the orbit. Once the oscillations of NSs are excited, the tidal torque and the radial tidal force lead to energy and angular momentum exchanges between the orbit and the star periodically. As a result, the eccentricity of the orbit increases and oscillates. Results show that the final eccentricities are nearly 0.08 for both cases.

5.4.4.2 *Deficiency of the method of effective Love number*

According to the definition of effective Love number in Eq. (5.67), we first construct the non-tidal binary orbit with the same initial conditions in Eq. (5.55)

$$\phi(t) = \frac{1}{32\eta}\frac{1}{(2\pi M_t F_0)^{5/3}}\left\{1-\left[1-\frac{256}{5}tM_t{}^{2/3}\mu(2\pi F_0)^{8/3}\right]^{5/8}\right\}, \tag{5.91a}$$

$$r(t) = \left(r^{(0)4} - \frac{256\eta M_t{}^3}{5}t\right)^{1/4}, \tag{5.91b}$$

with initial value $r^{(0)}$ obtained from Eq. (5.55). Following the procedure in H+16 [54, 55], we use the PP orbit's time of resonance $t_r^{(\mathrm{PP})}$ and the time derivative of angular frequency as the true t_r and $\dot{\Omega}_r$. Substituting them and the formulae of A and B into the equation of the effective Love number in Eq. (5.67) gives the time evolution of the effective Love number. In Fig. 5.7, we plot the results by using both H+16 [54, 55] and our new formulae of A and B. The dotted one represents the resonance time from the full numerical integrations, and the dash-dotted line is from the PP orbit. We can see that the true resonance time is earlier than that of the PP orbit. This is expected because the mode excitation extracts energy and angular momentum from the orbit, accelerating the inspiraling process. The amplitude of

the two models decays at the same rate but has different phases. Our formulae predict more oscillation cycles.

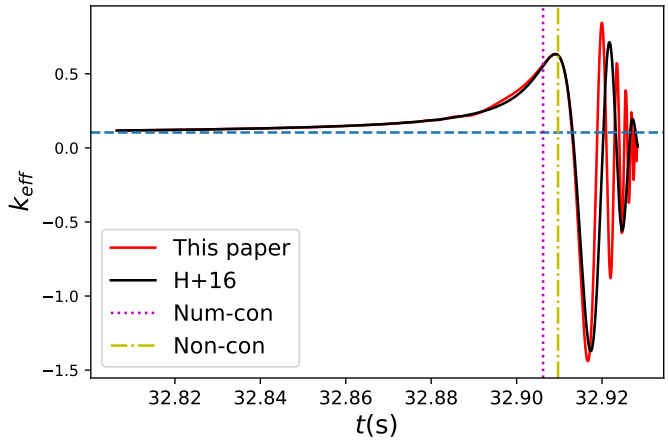

Figure 5.7: The time evolution of effective Love number based on the PP orbit. The red line is from our new formulae of A and B while the black one is from H+16 [54, 55]. As represented by the horizontal dash line, the effective k asymptotically approaches $k_2 = 0.104$ in the adiabatic regime. The dotted vertical line represents the real resonant time and the dash-dotted vertical line is from the pre-resonance PP orbit.

By feeding $k_{\rm eff}(t)$ into the orbital dynamics, we obtain the evolution of orbital separation $r(t)$ in Fig. 5.8. We can see that neither formula could capture the feature of post-resonance dynamics. The similarity between the two results shows that it is the formalism of the effective love number itself that is inaccurate. Such inaccuracy mainly comes from the fact that the torque is missing, and the orbit does not shrink as fast as it should, as we have discussed around Eq. (5.67).

5.4.5 The averaged orbit in the post-resonance regime

As discussed in FR07 [53], there are three timescales in the system's dynamics, although their values in our case may not be well-separated. The shortest one is orbital timescale, characterized by the orbital angular frequency Ω; the middle one is the tidal timescale, characterized by the angular frequency $\sim \dot{\Theta} = 2\Omega + \Omega_s - \zeta$ [Eq. (5.59)]; and the final one is the gravitational radiation reaction timescale, characterized by the frequency $\dot{L}_{\rm GW}/L$. The separation between tidal and radiation reaction timescales is shown more clearly in Fig. 5.9, where we plot $r(t)$ near resonance with $\Omega_s = 2\pi \times 550$Hz. Let us first focus on the upper panel, which is from FR07 [53]. The vertical dashed line indicates the time of resonance, and the

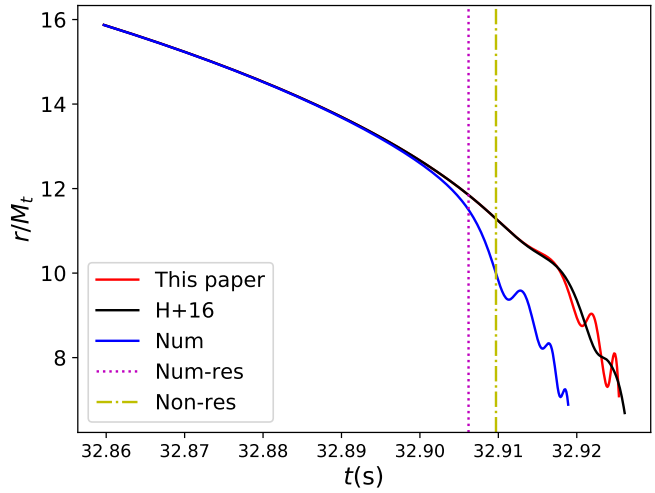

Figure 5.8: The orbital dynamics near the resonance, by means of effective Love number. The blue line is the result of fully numerical integration. The red line is from our new formulae of DT, while the black one is from H+16 [54, 55]. Same as Fig. 5.7, the dotted line and dash-dotted line represent the resonance condition of numerical and PP evolution, respectively.

horizontal dashed line represents the actual separation of the system at resonance. Both quantities are obtained from the numerical integration. In the radiation-reaction timescale, the system evolves as PP. The upper blue curve corresponds to the non-tidal quasi-circular orbit with the same initial conditions as our system. It intersects with the vertical and horizontal dashed lines at "a" and "d." We can see that there is little difference between full orbit and the PP orbit in the adiabatic regime. After resonance, the actual separation oscillates around another PP orbit in the tidal timescale, which is determined by Eq. (5.66) and shown as the lower blue curve; this curve intersects with the vertical and horizontal dash lines at "b" and "c." The pre- and post-resonance PP orbits are related by an instantaneous time shift Δt [see Eq. (5.64)] when the pre-resonance PP orbit satisfies the resonance condition Eq. (5.51), i.e., the horizontal line between "c" and "d." We should note that the regimes between "ad" and "cb" are not real evolution stages that the system undergoes. This is only an effective way to describe the resonance between two PP orbits. The time of "d," t_d, is actually $t_r^{(\mathrm{PP})}$ that we used to construct the effective Love number in Sec. 5.4.4.2, it is larger than the actual resonance time t_r because the tide effect accelerates the inspiral process and makes resonance earlier. We can see that FR07 [53] can track the post-resonance PP orbit to a high accuracy.

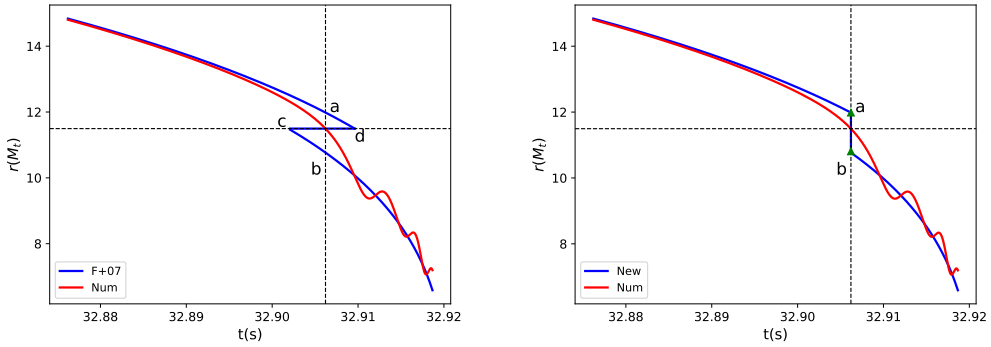

Figure 5.9: The orbital separation as a function of time, with NS spinning at 550Hz. The vertical dashed lines indicate the time of resonance, and the horizontal dashed lines represent the actual separation of the system at resonance. The red curves are from numerical integrations, while the blue curves are predictions of PP orbits. The upper blue curves have the same initial conditions as the system we study. They intersect with the vertical and horizontal dashed lines at "a" and "d." The lower blue curves are predictions of FR07 [53] (upper panel) and our new method (lower panel), which intersect with the vertical and horizontal dash lines at "b" and "c." To connect the pre- and post-resonance PP orbits, FR07 [53] proposed the time jump Δt from "d" to "c" at the fixed separation, while we use the angular momentum jump (or equivalently, the separation jump) from "a" to "b" at the fixed time t_r.

Here we provide an additional description of the averaged orbit. As shown in the lower panel of Fig. 5.9, instead of evolving the pre-resonance PP orbit to "d" and making a jump in time at a fixed separation, we propose that the orbit has an immediate jump in angular momentum (or equivalently, separation) at the fixed time t_r, i.e., the vertical line between "ab." The jump can be determined as follows. The orbital angular momentum at "a" is given by

$$L_{\rm PP}^{(a)} = \mu M_t{}^{1/2} r_{\rm PP}^{(a)1/2}, \tag{5.92}$$

while at "b" the angular momentum is determined by the angular momentum transfer in Eq. (5.88),

$$L_{\rm PP}^{(b)} = L_{\rm PP}^{(a)} - \Delta L, \tag{5.93}$$

which leads to the orbital separation $r_{\rm PP}^{(b)}$

$$r_{\rm PP}^{(b)} = r_{\rm PP}^{(a)} \left(1 - \frac{\Delta L}{L_{\rm PP}^{(a)}}\right)^2. \tag{5.94}$$

Evolving the PP orbit with the above initial condition gives the lower panel of Fig. 5.9. This method is very similar to FR07 [53]. However, it also has a disadvantage: since so far we do not have an independent analytic estimation on the time of resonance, we cannot know the value of $r_{\rm PP}^{(a)}$ without solving the full equations. Nevertheless, this method provide us an alternative understanding on the post-resonance PP orbit, i.e., it is related to the pre-resonance PP orbit by an instantaneous jump in a angular momentum, by contrast to a time shift Δt at a fixed separation. In fact, one can prove that two methods agree with each other to the leading order in Δt. By expanding Eq. (5.94), we find the jump between "a" and "b" to be

$$r_{\rm PP}^{(a)} - r_{\rm PP}^{(b)} = \frac{2\Delta L}{L_{\rm PP}^{(a)}} r_{\rm PP}^{(a)} = \dot{r}_{\rm PP}^{(a)} \Delta t, \tag{5.95}$$

where the last equality comes from the fact that $L \propto r^{1/2}$ and the relation between ΔL and Δt in Eq. (5.64). The result is exactly the jump predicted by Eq. (5.66) if one expands $r(t_r + \Delta t) - r(t_r)$ to the leading order in Δt. In fact, we can work conversely. By imposing that the two methods predict the same orbital separation for the post-resonance PP orbit at resonance, we get an analytic equation for t_r

$$r_{\rm PP}^{(b)} = r(t_r + \Delta t) = r(t_r) \left(1 - \frac{\Delta L}{L_r}\right)^2, \tag{5.96}$$

Table 5.3: The comparisons between our analytic estimates for t_r in Eq. (5.96) and full numerical integrations. For reference, the errors of results are compared with $|t_d - t_r|$, i.e., the time difference between "d" and "a" in Fig. 5.9.

$\Omega_s/(2\pi)$(Hz)	550	450	350	250	150
$\frac{\lvert\Delta t_r\rvert}{\lvert t_r - t_a\rvert}$ ($\times 10^{-2}$)	20.3	5.3	5.4	13.6	20

where

$$L_r = \mu M_t^{1/2} r(t_r)^{1/2}, \tag{5.97}$$

and $r(t)$ is shown in Eq. (5.91b). Eq. (5.96) is an algebraic equation for t_r. In Table 5.3, we show the accuracies of results by calculating the ratio between Δt and $|t_d - t_r|$, where Δt is the difference between t_r obtained from Eq. (5.96) and the true t_r; and $|t_d - t_r|$ is the time difference between "a" and "d" in Fig. 5.9. The ratios are between 5%—20%.

From the above discussion, we can see the method of the averaged orbit is qualitatively accurate. By connecting two PP orbits with a jump, one can already extract some information about the system (e.g., t_r) without solving fully coupled differential equations. However, this method has two disadvantages. The first one is that it ignores the oscillation on the top of the averaged orbit in the post-resonance regime, which carries the information of f-mode. Secondly, averaging is only valid when the spin is large. As shown in Fig. 5.6, since the system does not undergo a full tidal oscillation cycle when spin is 300Hz or below, it is not appropriate to discuss the averaged orbit in this case.

5.5 Gravitational waveforms and extraction of parameters

In the last two sections, we mainly discussed near-zone dynamics. We obtained new formulae Eqs. (5.60) for the tidal deformation amplitudes A and B; obtained osculating equations Eqs. (5.74) for the orbit; and developed analytic treatments that coupled stellar and orbital motions and carried out comparisons between analytic and numerical results.

In this section, we will go to the far zone to study GWs. We first quantify the accuracy of the method of effective Love number and the method of averaged PP orbit in the framework of match filtering. We then compute the SNR of GWs emitted during and after resonance. Results show that post-resonance GWs may be strong enough to be observed by future GW detectors. We finally show that DT can provide more precise estimations on the parameters of NSs. We want to emphasize again

that the major goal of this section is to provide a qualitative feature of the impact of DT on GW observations. As we have discussed above, the EoS we used, as well as the high spin rate, might be unlikely in realistic scenarios.

5.5.1 Accuracies of DT models

To the lowest order, GW emitted by a system is related to the near-zone dynamics through [90]

$$h_{ij}^{\rm TT} = \frac{2}{D_L}\ddot{Q}_{ij}^{\rm TT}, \tag{5.98}$$

where D_L is the distance between the detector and the source, which we choose as 100Mpc. Q_{ij} is the quarupole moment of the system. The superscript "TT" stands for the transverse-traceless components of the tensor. Amplitudes of the two polarizations of the GW are given by [90]

$$\begin{aligned} h_+ &= -\frac{1}{4}s_i^2(Q_{xx}+Q_{yy}) + \frac{1}{4}(1+c_i^2)c_{2\beta}(Q_{xx}-Q_{yy}) + \frac{1}{2}(1+c_i^2)s_{2\beta}Q_{xy} \\ &\quad - s_i c_i c_\beta Q_{xz} - s_i c_i s_\beta Q_{yz} + \frac{1}{2}s_i^2 Q_{zz}, \end{aligned} \tag{5.99a}$$

$$h_\times = -\frac{1}{2}c_i s_{2\beta}(Q_{xx}-Q_{yy}) + c_i c_{2\beta}Q_{xy} + s_i s_\beta Q_{xz} - s_i c_\beta Q_{yz}, \tag{5.99b}$$

where $c_i = \cos\iota$, $s_i = \sin\iota$, $c_{2\beta} = \cos 2\beta$, and $s_{2\beta} = \sin 2\beta$. The angle ι is the inclination of the orbital plane with respect to the line of sight toward the detector, and β is azimuthal angle of the line of nodes. The detector measures the linear combination of the two polarizations

$$h(t) = F_+ h_+ + F_\times h_\times, \tag{5.100}$$

where the detector antenna pattern functions F_+ and $F_\times$ are given by

$$F_+ = \frac{1}{2}(1+\cos^2\theta)\cos 2\phi\cos 2\psi - \cos\theta\sin 2\phi\sin 2\psi, \tag{5.101a}$$

$$F_\times = \frac{1}{2}(1+\cos^2\theta)\cos 2\phi\sin 2\psi + \cos\theta\sin 2\phi\cos 2\psi, \tag{5.101b}$$

with θ and ϕ the angular location of the source relative to the detector, ψ the polarization angle [90].

In order to measure the similarity between two waveforms h and g, we define their match [92]

$$O[h,g] = \max_{t_c,\phi_c}\frac{(h|g)}{\sqrt{(h|h)(g|g)}}, \tag{5.102}$$

and mismatch $1-\mathcal{O}$. The inner product $(h|g)$ between two waveforms is defined as

$$(h|g) = 4\Re \int \frac{\tilde{h}^*(f)\tilde{g}(f)}{S_n(f)} df, \tag{5.103}$$

with the superscript $*$ standing for complex conjugation, and $S_n(f)$ the noise spectral density of the detector. In Fig. 5.10, we plot the noise spectral densities of aLIGO [93, 94], aVirgo [94, 95], KAGRA [94, 96], Voyager [97], CE [98], and ET [99].

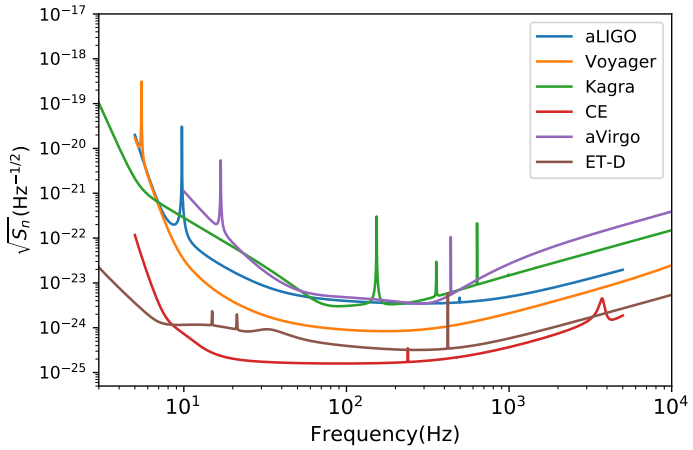

Figure 5.10: The noise spectral densities of several ground-based detectors.

The fully numerical simulated waveforms can be computed in the following way. We first numerically solve the equations of motion Eqs. (5.32), which gives the total quarupole moment of the system $Q_{ij}^{\mathrm{Total}} = Q_{ij} + \mu x_i x_j - \mu r^2 \delta_{ij}/3$ by Eq. (5.29a). We then obtain the waveform $h(t)$ from Eq. (5.98). In this chapter, we choose $\iota = \beta = \theta = \phi = \psi = 0$ for simplicity. We then sample the solutions in the time domain with the rate $1/8192$s, and use the fast Fourier Transform (FFT) algorithm to perform the discrete Fourier transform on the sampled data. Following the procedure of Ref. [100], we zero-pad the strain data on both sides to satisfy periodic boundary condition before FFT. Our choice of sample rate already ensures that the Nyquist frequency is larger than the contact frequency. We define the frequency-domain waveform within the frequency band $[2F_0, 2F_{\mathrm{contact}}]$ as the full signal and $[2\Omega_r/(2\pi), 2F_{\mathrm{contact}}]$ as post-resonance signal. Here F_{contact} is the orbital contact frequency, the factor of 2 comes from the correspondence between the orbital frequency and GW frequency at quadrupole order.

In Fig. 5.11, we plot the mismatch between post-resonance waveforms obtained from different DT models, as functions of spin frequency. One waveform is calculated

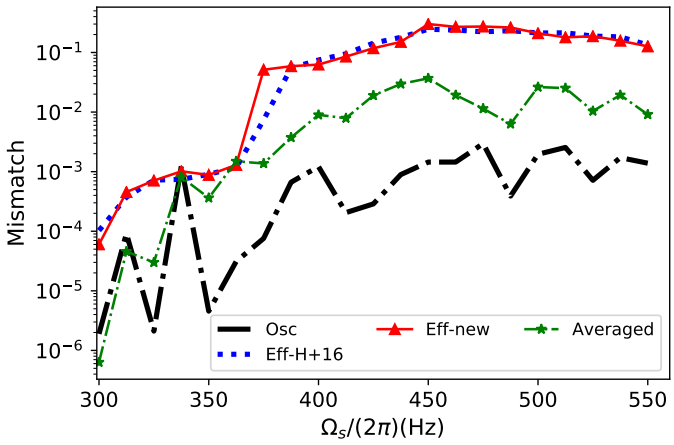

Figure 5.11: The mismatches as functions of spin frequency. We only use the signals with frequency higher than $2\Omega_r/(2\pi)$ because we only focus on the post-resonance dynamics. The fully numerical integrations are compared with four models, effective Love number with H+16 [54, 55] (blue dashed line), effective Love number with our new DT formulae (red line), our new averaged PP orbit (green line), and osculating equations (black line). The mismatches of osculating equations are lower than 10^{-3}, while the method of the effective Love number gives $\sim 0.1-0.2$ for spin higher than 370Hz. This approach is insensitive to which DT model we use. Our new averaged PP orbit, on the other hand, is in the middle of two other approaches. The worst mismatch is around 3×10^{-2}.

from the fully numerical integration; against this target waveform, we compare waveforms obtained from 4 different models: effective Love number with H+16 [54, 55] (blue dashed line), effective Love number with our new formulae Eqs. (5.60) (red line), our new post-resonance averaged PP orbit defined in Eq. (5.94) (green line), and osculating equations (black line). Here we do not include the averaged orbit model in FR07 [53] because it is very close to our model. Since the match depends weakly on detector noise curve, we shall use that of aLIGO. One can see that the mismatches of all models are smaller that 10^{-3} for spins below 370Hz, since in this case the post-resonance signals are very short, such that the phase mismatches does not accumulate with frequency. The mean mismatches of our osculating equations are around 10^{-4}, with the worst one still below 10^{-3}. Accordingly, this approach describes the post-resonance dynamics accurately. This confirms that our new formulae of A and B are precise enough to describe the tidal back-reaction on the orbit. Methods that use the effective Love number, on the other hand, give a large mismatch of around 0.2 when the spin frequency reaches $\sim$ 450Hz. The fact that both versions lead to similar mismatches, even with our

Table 5.4: The SNRs of full GW signals within the band $[2F_0, 2F_{\rm contact}]$ for different detectors. The spin frequency of NS is 300Hz.

aLIGO	aVIRGO	KAGRA	Voyager	ET-D	CE
31.6	25.4	31.4	135.1	305.7	884.0

accurate formulae for A and B, shows that the formalism itself is imprecise. The mismatch of our averaged PP-orbit treatment is less than 0.03 within the entire regime we study. Therefore this approach gives a fairly accurate description of post-resonance GW signals.

5.5.2 Detectability and Fisher analyses

In Fig. 5.12, we plot the signal-to-noise ratios (SNRs) of post-resonance GW (within the band $[2\Omega_r/(2\pi), 2F_{\rm contact}]$) as functions of spin frequency Ω_s. As expected, it grows with spin frequency. For aLIGO, Ω_s needs to be above $\sim$ 425Hz to lead to SNR $>$ 1. For 3G detectors, SNRs are around 4 for spin $\sim$ 300Hz; It can reach 50 if the spin is around 500Hz. For comparison, we also calculate the SNRs of full signals within the band $[2F_0, 2F_{\rm contact}]$ in Table 5.4. Since the full SNRs depend weakly on the spin frequency, here we choose $\Omega_s = 2\pi \times 300$Hz.

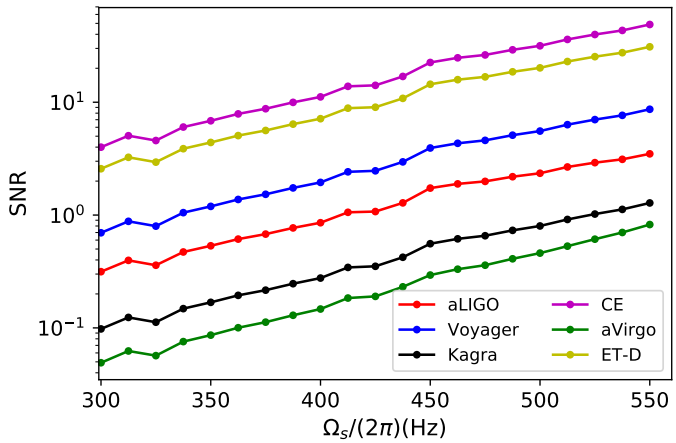

Figure 5.12: The SNRs from the resonant part of GW signals, with frequency higher than $2\Omega_r/(2\pi)$. The faster the NS spins, the higher the SNR. The SNR is around 0.3-3 for current detectors, but $\sim 10-50$ for 3G detectors.

These results of SNRs show the potential to detect post-resonance signals with 3G detectors. This allows us to extract more information from GW signals than AT. As pointed out in Ref. [23], the Love number of non-spinning NS is degenerate with

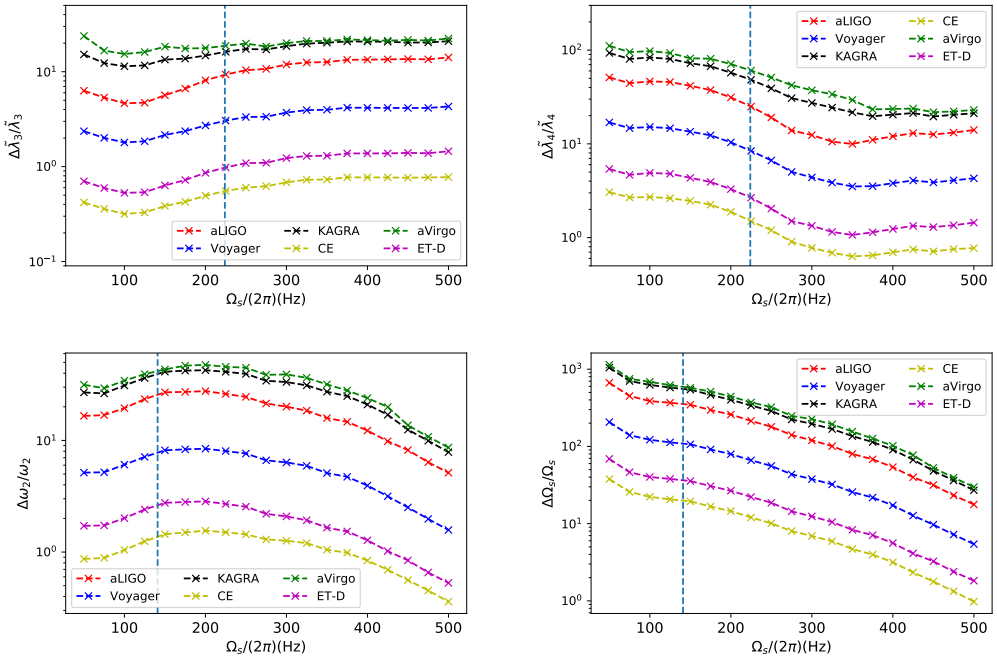

Figure 5.13: Relative errors of $\tilde{\lambda}_3$, $\tilde{\lambda}_4$, ω_2 and Ω_s as functions of spin from Fisher analyses. The GW waveform is at the Newtonian order. The vertical dotted line stands for the location where resonance happens. The system is optimally oriented at 100Mpc, with component masses $(1.4M_\odot, 1.4M_\odot)$. The H4 EoS is used.

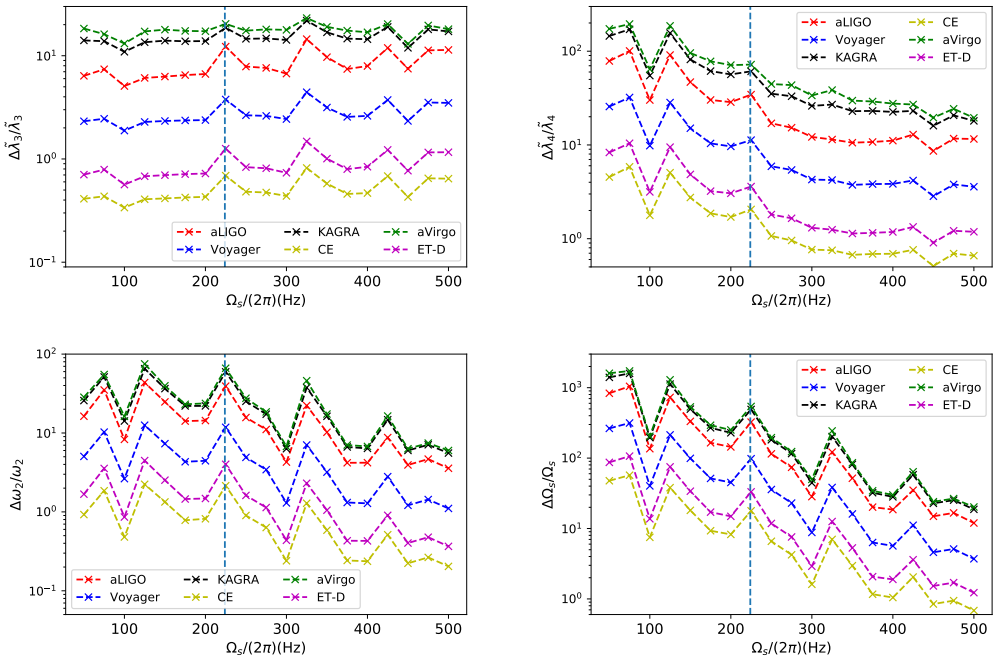

Figure 5.14: Same as Fig. 5.13, except the polytropic EoS is used.

mass ratio $\Xi = M_2/M_t$ at leading order in the adiabatic regime. Only the effective $\tilde{\lambda} = \lambda\Xi(11\Xi+1)$ can be constrained by GWs[8]. This degeneracy persists for spinning NSs in AT. In this case, the phase of GW during AT (up to leading tidal order of the Love number) is given by

$$\Psi = 2\pi f t_c - \phi_c - \frac{\pi}{4} + \frac{3}{128}(\pi\mathcal{M}f)^{-5/3}\left\{1 - \frac{24(\pi f)^{10/3}}{\mathcal{M}^{5/3}} \times \left[\frac{11}{4}\Xi^2\lambda_0 + \frac{\lambda_2\Xi}{1-2\Omega_s^2/\omega_2^2}\left(1+\frac{33}{4}\Xi\right)\right]\right\}. \tag{5.104}$$

Hence the tidal term is governed by the effective Love number

$$\tilde{\lambda}_3 = \frac{11}{4}\Xi^2\lambda_0 + \frac{\lambda_2\Xi}{1-2\Omega_s^2/\omega_2^2}\left(1+\frac{33}{4}\Xi\right). \tag{5.105}$$

It is straightforward to see that $\tilde{\lambda}_3$ reduces to $\tilde{\lambda}$ in the non-spinning limit. Note that our notation of $\tilde{\lambda}_3$ differs from Ref. [23] by a factor of $\eta = \mu/M_t$, since they used total mass M_t while we use the chirp mass $\mathcal{M}$ here. As Ω increases, the motion of $(2,2)$ mode is resonantly getting excited while $(2,0)$ mode is not, their different reactions to the tidal driving from the orbit lead to distinct effects on GW emission, therefore the degeneracy is broken. To describe this effect, we introduce another parameter

$$\tilde{\lambda}_4 = \frac{\lambda_2\Xi}{1-2\Omega_s^2/\omega_2^2}\left(1+\frac{33}{4}\Xi\right), \tag{5.106}$$

i.e., the second part of Eq. (5.105). Accordingly, the numerical waveforms are determined by a 9-dimensional parameter $\boldsymbol{\theta} = \{t_c, \phi_c, D_L, \mathcal{M}, \Xi, \Omega_s, \omega_2, \tilde{\lambda}_3, \tilde{\lambda}_4\}$. Here we ignore ω_0, the mode frequency of $(2,0)$ mode, since this mode does not have DT and its mode frequency is almost degenerate with other parameters.

Let us now turn to parameter estimation, using the Fisher information matrix formalism. Suppose random noise $n(t)$ in observed signal $s(t)$ is stationary and Gaussian, the conditional likelihood function of s given parameters $\boldsymbol{\theta}$ can be written as

$$p(s|\boldsymbol{\theta}) \propto e^{-(s-h|s-h)/2}, \tag{5.107}$$

where $h(\boldsymbol{\theta}, t)$ stands for the true waveform for parameter $\boldsymbol{\theta}$. In the large-SNR approximation, the likelihood function becomes Gaussian,

$$p(s|\boldsymbol{\theta}) \propto e^{-\Gamma_{ij}\Delta\theta^i\Delta\theta^j/2}, \tag{5.108}$$

[8] We still assume only M_1 is tidally deformed.

where Fisher matrix Γ_{ij} is given by

$$\Gamma_{ij} = \left(\frac{\partial h}{\partial \theta^i} \middle| \frac{\partial h}{\partial \theta^j} \right). \tag{5.109}$$

Since waveforms are numerically calculated in our case (from algorithms discussed in the previous subsection), derivatives are computed numerically using the symmetric difference quotient method. The inverse of the Fisher matrix gives the covariance matrix. In particular, the diagonal components are the variances of the estimated parameters

$$\Delta\theta_i = \sqrt{(\Gamma^{-1})_{ii}}, \tag{5.110}$$

which are the projected constraints that we can put on parameters from the observation.

We still use the H4 and the $\Gamma = 2$ polytropic EoS, with $M_1 = M_2 = 1.4M_\odot$. The system is at $D_L = 100$Mpc and optimally oriented. Projected constraints on several parameters as functions of spin frequency are shown in Figs. 5.13 and 5.14, where the vertical lines stand for values of spins for which resonance takes place right on contact. We can see that the two EoS give similar results. The constraints change with detectors since we have fixed the distance of the source, and 3G detectors can benefit from large SNRs. Among the six detectors, CE provides the best parameter estimations because it is the most sensitive in the high-frequency band, where DT takes place. To quantify the effect of DT, we list the projected constraints on several parameters in Table 5.5 under two situations: (i) results evaluated with spin frequencies when resonance takes place right on contact and (ii) constraints with spin frequencies 500Hz. The improvement factor, which is the ratio of estimation accuracies between two situations, characterizes the effect of DT.

Let us discuss each parameter more specifically. First, we can see that for different detectors the relative errors on $\tilde{\lambda}_3$ are of order $\sim 0.4-20$, which depend most weakly on spins when compared to other parameters. The estimation error even becomes worse when spins are high. This is because this parameter is mainly estimated from AT, and the constraints do not benefit from DT. When spins are high, adiabatic waveforms become relatively short, hence the project constraints become worse. By contrast, the estimation error of the other Love number $\tilde{\lambda}_4$, which describes the $(2, 2)$ mode, improves with spin. This is expected since DT introduces the dependence of waveforms on $\tilde{\lambda}_4$. The constraints on this quantity can be improved by a factor of $3-5$, depending on EoS and detectors. In the CE case, the relative error of $\tilde{\lambda}_4$ can

final decrease to ~ 0.8 as spins are around 500Hz. However, this parameter is still degenerate with the mass ratio Ξ. One need to take into account PN corrections to break such degeneracy.

DT also helps us put more stringent constraints on the $(2,2)$ mode frequency, since the oscillations of NSs can react back to orbits and influence GW waveforms. As shown in Table 5.5, the averaged improvement factors are around $6.6-6.9$ for the polytropic EoS, while ~ 5 for the H4 EoS. The current detector, like aLIGO, cannot constrain this parameter well, giving relative errors ~ 5. However, it is improved to 0.2 in the CE case. We have also calculated the effect of DT on constraining spin frequencies. The improvements on spin are the largest among parameters we discuss, since this parameter determines the location of resonance in the time (frequency) domain. The improvements are around $20-27$ for both EoSs. In the CE case, the relative errors are $\sim 0.7-1$ when spins reach 500Hz.

5.6 Conclusions and discussion

We have systematically studied the $(2,2)$ f-mode DT of spinning NSs in coalescing binaries. In particular, the spin is assumed to be anti-aligned with the orbital angular momentum, in which case the effect of DT is the most pronounced. We began by deriving a complete set of coupled equations for mode oscillation and orbital evolution, with the aid of the phase-space mode expansion method and the Hamiltonian approach. We then extended H+16's model [54, 55] for f-mode excitation to spinning NSs and obtained a new approximation which can describe the full dynamics of systems to a high accuracy. One application of this approximation is to study the post-resonance orbital dynamics, where we used the method of osculating orbits and obtained the time evolution of the osculating variables. This framework allowed us to obtain analytic estimations on the orbital information at resonance (e.g., $\dot{r}_r$, $\dot{\Omega}_r$). We also obtained a simple formula of angular momentum transfer due to DT, which is an extension of L94 [36] to the spinning case. Based on this result, we derived the averaged post-resonance orbits over the tide-oscillation timescale in an alternative way. The result of our averaged treatment turns out to agree with that of FR07 [53], to the leading order in angular momentum transfer time Δt [Eq. (5.64)]. By combining the two treatments, we obtained an algebraic equation for t_r. We then compared several DT models by computing the mismatches of waveforms. Finally, we carried out a Fisher matrix analysis to estimate the effect of DT on parameter estimation, with current and 3G detectors.

Table 5.5: Projected constraints on $\tilde{\lambda}_3$, $\tilde{\lambda}_4$, ω_2 and Ω_s with two EoS for six different detectors. Here we compare two situations: (i) constraints with spins when resonance takes place right on contact (Res) and (ii) constraints with NSs spinning at 500Hz (Ω_s^m). The improvement factor is the ratio of Ω_s^m to Res, which characterizes the effect of DT.

	Detectors		aVirgo	KAGRA	aLIGO	Voyager	ET-D	CE
H4	$\frac{\Delta\tilde{\lambda}_3}{\tilde{\lambda}_3}$	Res	18.4	13.4	5.7	2.1	0.6	0.4
		Ω_s^m	22.4	21.0	14.1	4.3	1.5	0.8
		Imp	0.8	0.6	0.4	0.5	0.4	0.5
	$\frac{\Delta\tilde{\lambda}_4}{\tilde{\lambda}_4}$	Res	81.8	72.4	41.6	13.5	4.3	2.5
		Ω_s^m	23.0	21.1	14.1	4.3	1.4	0.8
		Imp	3.6	3.4	3.9	3.1	3.0	3.2
	$\frac{\Delta\omega_2}{\omega_2}$	Res	43.2	41.2	27.0	8.2	2.8	1.4
		Ω_s^m	8.6	7.8	5.1	1.6	0.5	0.4
		Imp	5.0	5.3	5.2	5.2	5.2	4.0
	$\frac{\Delta\Omega_s}{\Omega_s}$	Res	575.7	542.9	346.6	106.4	35.6	19.4
		Ω_s^m	29.9	27.1	17.7	5.4	1.8	1.0
		Imp	19.3	20.1	19.6	19.6	19.5	19.9
Poly	$\frac{\Delta\tilde{\lambda}_3}{\tilde{\lambda}_3}$	Res	17.9	14.0	6.3	2.3	0.7	0.4
		Ω_s^m	18.1	17.2	11.4	3.5	1.2	0.6
		Imp	1.0	0.8	0.6	0.7	0.6	0.6
	$\frac{\Delta\tilde{\lambda}_4}{\tilde{\lambda}_4}$	Res	95.8	81.6	46.8	15.1	4.9	2.8
		Ω_s^m	19.5	18.1	11.6	3.6	1.2	0.7
		Imp	4.9	4.5	4.0	4.2	4.1	4.2
	$\frac{\Delta\omega_2}{\omega_2}$	Res	39.7	36.5	24.8	7.3	2.5	1.3
		Ω_s^m	6.0	5.6	3.6	1.1	0.4	0.2
		Imp	6.6	6.6	6.9	6.6	6.9	6.6
	$\frac{\Delta\Omega_s}{\Omega_s}$	Res	533.4	496.0	332.5	99.2	33.9	18.1
		Ω_s^m	20.2	18.7	12.0	3.7	1.2	0.7
		Imp	26.4	26.5	27.8	26.7	27.6	26.5

We summarize our main conclusions as follows. (i) The $(2,2)$ f-mode in the spinning NS, by defining a new variable x [Eq. (5.49)], can still be treated as a harmonic oscillator, which is oscillating at its eigenfrequency ζ in the post-resonance regime. (ii) The reason that H+16 [54, 55] cannot describe the post-resonance evolution are two folds. The first is that their phasing $\hat{t}^2$ is not accurate and should be replaced by Θ [Eq. (5.59)]. Second, their counterterm Eq. (5.48) does not contain phase information. (iii) The picture of averaged orbit over the tide-oscillation timescale is accurate: the true pre- and post-resonance orbital motion can be tracked accurately by PP orbits. These PP orbits are related by energy and angular momentum transfers, and hence a jump in the orbital separation at t_r.

Within the spin range we studied, the match of GW signals between the prediction using the averaged orbit and numerical integration (post-resonance part) is as high as 99%. Therefore the additional tidal perturbation is a small effect. However, such a description requires that the post-resonant signal is long enough (i.e., large spin) so that the system can undergo several tidal oscillation cycles. Looking at the full orbit, we found that there is an extra oscillation on top of the averaged trajectory. We also found that the eccentricity of the orbit is induced by the tidal interaction and can grow to ~ 0.08 at the end of inspiral, the numbers depend weakly on the spin. (iv) The method of effective Love number is not accurate to describe f-mode when spin is large and when DT is significant: this method essentially ignores the torque between the orbit and the star. The mismatch of GW signals between this formalism and numerical integrations increases to 0.2 when the spin frequency is larger than 450Hz, even when accurate models for tidal amplitudes A and B are used, therefore, it is the method itself that is inaccurate. (v) We found that DT leads to little improvement on estimating $\tilde{\lambda}_3$ in Eq. (5.105), for which constrains are mainly from AT. In our study, they even become worse since the adiabatic part is relatively short when the spin is large. For a system with component masses $(1.4, 1.4)M_\odot$ at 100Mpc, the relative errors of $\tilde{\lambda}_3$ are around 5 for aLIGO and 0.4 for CE. However, DT does break the degeneracy between $\tilde{\lambda}_3$ and $\tilde{\lambda}_4$, because the oscillations of $(2, 2)$ mode are excited while $(2, 0)$ mode are not, hence they contribute differently to GWs. The constraints on $\tilde{\lambda}_4$ can be improved by factor of $3 \sim 4$. In the CE case, the relative errors are $0.7 \sim 0.8$ when the spin frequency is 500Hz. We also calculated the constraints on the mode frequency ω_2 and the spin Ω_s. We found that they improve by factors of $5 \sim 6$ and $19 \sim 27$, respectively. In the CE case, the relative errors of the mode frequency are around $0.2 \sim 0.4$ while for spin, the numbers are $0.7 \sim 1.0$. Hence DT potentially provides an alternative channel for people to study the physics of NSs.

Throughout the chapter, we have assumed that the NS is in the normal-fluid state, whereas in reality the core of a cold NS is expected to be in the superfluid state [101]. Thus a two-fluid formalism should be used to capture the new degree of freedom associated with the superfluidity [102], and the f-mode in particular should split into a doublet [103]. However, as shown in Ref. [103], the new f-mode due to the superfluid degree of freedom typically have a much higher frequency than the ordinary one (i.e., the f-mode we considered here) and consequently we do not expect it to significantly change the results we have here.

In addition to the ignorance of superfluidity, there are three caveats we would like to note. First, the H4 EoS has been shown to be less likely based on the observation of GW170817 [7]. Second, the spin modifications to mode frequencies through Maclaurin spheroid is merely a toy model and might be too simple for the real situation. Finally, the NS spin frequency should be high enough ($\sim$ 500Hz) for DT to have significant effects. Such high frequency is unlikely in astrophysical binaries. However, we here mainly aim to use semi-analytic methods to provide qualitative understandings on DT, different EoS will give similar results. This is because the equations of motion in Eqs. (5.32) are generic. EoS only affects the values of $\lambda_{0,2}$ and $\omega_{0,2,3}$. On the other hand, our derivations of tidal excitations A and B [Eq. (5.60)] are valid for any systems which couple a harmonic oscillator to a Kepler orbit with a dissipative force in the long timescale. The framework presented in the chapter is generic and can be applied to other types of DTs. One possible avenue for future work is to use our discussions to study the excitation of r-modes with more realistic EoS, since they only require NS to spin at tens of Hz, and are more likely to take place in BNS systems.

All of the calculations in this chapter are at the Newtonian order, which has allowed us to reveal the insufficiency of the effective Love number approach, and the possibility of gaining further information on neutron stars—in the regime where the NS has substantial spin, anti-aligned with the orbital angular momentum. This information must still be complemented by contributions from PN corrections. For instance, at the Newtonian order ζ and Ω_s are partially degenerate since they mainly enter equations through the combination $\zeta - \Omega_s$. By introducing PN effect, like spin-orbit and spin-spin coupling, spin will be more constrained, which could break the degeneracy, and consequently, put more stringent constraints on mode frequencies. This is also true for the degeneracy between mass ratio and Love number. In our case, the mass ratio is still badly constrained and degenerates with the Love number. By including the 1PN effect, we could get more accurate estimations of these quantities.

Secondly, the universal relation for NS is also an important fact to break degeneracy. For example, the universality between the Love number and f-mode frequencies was observed in Ref. [58]. With such additional information, constraints on parameters should be improved.

Finally, it is interesting to compare our analytic analyses with recent numerical simulations in Ref. [57]. To do so, one need to append the tidal Hamiltonian Eq. (5.24) to the EOB Hamiltonian, and jointly evolve the orbital motion and the stellar

oscillation, to obtain faithful predictions of waveforms.

5.7 Appendix: The derivation of mode oscillation formulae

In this section, we will give a detailed derivation for our new DT formulae of A and B, following Ref. [104].

As we have shown in Eq. (5.49), the stellar oscillation during DT can be described by a harmonic oscillator after a transformation. Its general solution is the sum of a homogeneous solution and the particular solution. Here we assume that there are no free oscillations in the NS initially, hence the solution can be expressed in terms of the retarded Green function and tidal driving

$$x(t) = \frac{1}{\zeta}\int^t \frac{3M_2\lambda_2\omega_2^2}{2r'^3} e^{i\Omega_s t' + 2i\phi(t')} \sin\zeta(t-t')dt'. \tag{5.111}$$

By integration by part, we get

$$\begin{aligned} x(t) = \frac{3M_2\lambda_2\omega_2^2}{2\zeta}\Bigg[&\frac{\zeta e^{i\Omega_s t + 2i\phi}}{\zeta^2 - (\Omega_s + 2\Omega)^2}\frac{1}{r^3} + e^{-i\zeta t}\int^t \frac{\dot\Omega' e^{i\Omega_s t' + 2i\phi(t') + i\zeta t'}}{(\Omega_s + 2\Omega' + \zeta)^2 r'^3}dt' \\ &- e^{i\zeta t}\int^t \frac{\dot\Omega' e^{i\Omega_s t' + 2i\phi(t') - i\zeta t'}}{(\Omega_s + 2\Omega' - \zeta)^2 r'^3}dt'\Bigg], \end{aligned} \tag{5.112}$$

where we have ignored $\dot r$. However, the method fails once the resonance happens. There is a stationary point within the integration domain. L94 [36] and H+16 [54, 55] expanded $\phi(t')$ in Eq. (5.111) around t_r and estimated the integral with SPA. Our treatment is slightly different. In order to incorporate both the adiabatic and resonant regimes, we start from Eq. (5.112) instead of (5.111), where the adiabatic term is separated out initially. At resonance, this adiabatic term goes to infinity. Hence there should be a counterterm arising from the integration, to cancel out such infinity. H+16 [54, 55] chose Eq. (5.48) as the counterterm. Here we derive a better counterterm by studying the integration in Eq. (5.112).

Since there is no stationary point in the second term on the RHS of Eq. (5.112), it can be ignored. Expanding the integrand of the third term around the resonance point, and neglecting the time derivatives of $\dot\Omega$ and r, the integration becomes

$$\begin{aligned} \int^t \frac{e^{i\chi_r + i\dot\Omega_r(t'-t_r)^2}}{4r_r^3\dot\Omega_r(t'-t_r)^2}dt' = &-\frac{e^{i\chi_r + i\hat t^2}}{4r_r^3\sqrt{\dot\Omega_r}}\frac{1}{\hat t} + \frac{e^{i\chi_r}}{2r_r^3}\sqrt{\frac{\pi}{2\dot\Omega_r}} \\ \times\Bigg[&-\mathrm{FS}\left(\sqrt{\frac{2}{\pi}}\hat t\right) + i\mathrm{FC}\left(\sqrt{\frac{2}{\pi}}\hat t\right) - \frac{1}{\sqrt{2}}e^{-i\pi/4}\Bigg]. \end{aligned} \tag{5.113}$$

The terms in the bracket are the same as H+16 [54, 55]. However, we have a new counterterm

$$-\frac{e^{i\chi_r+i\hat{t}^2}}{4r_r^3\sqrt{\dot{\Omega}_r}}\frac{1}{\hat{t}}, \tag{5.114}$$

which contains the phase $\chi_r + \hat{t}^2$. As we have discussed in Sec. 5.3.2, the real part of this term gives rise to a contribution to A that is proportional to $\cos(\hat{t}^2 - \Theta)/\hat{t}^2$, which reduces to H+16's [54, 55] if we neglect $\cos(\hat{t}^2 - \Theta)$. This term cancels the infinity caused by the adiabatic term. On the other hand, the imaginary part of Eq. (5.114) does not diverge, since

$$\lim_{t\to t_r}\frac{\sin(\hat{t}^2-\Theta)}{\hat{t}} = 0. \tag{5.115}$$

Performing the integration by part again on the third term of Eq. (5.112), we get the next order correction

$$\int^t \frac{\dot{\Omega}' e^{i\Omega_s t'+2i\phi(t')-i\zeta t'}}{(\Omega_s+2\Omega'-\zeta)^2 r'^3}dt' = \frac{\dot{\Omega} e^{i\Omega_s t+2i\phi-i\zeta t}}{i(\Omega_s+2\Omega-\zeta)^3 r^3} + \int^t \frac{6\dot{\Omega}'^2 e^{i\Omega_s t'+2i\phi(t')-i\zeta t'}}{i(\Omega_s+2\Omega'-\zeta)^4 r'^3}dt'. \tag{5.116}$$

Following the same procedure, we obtain a higher-order correction as

$$\Delta A(t) = \frac{M_2\lambda_2}{\zeta}\frac{3\omega_2^2}{16r_r^3\dot{\Omega}_r^{1/2}}\frac{\sin(\hat{t}^2-\Theta)}{\hat{t}^3}. \tag{5.117}$$

The correction term contributes a finite value as $t \to t_r$. As shown in Table 5.1, this term reduces the error of A_r from tens of percent to $\lesssim 4\%$ in the situations we consider.

References

[1] Benjamin P. Abbott et al. "GW170817: Observation of gravitational waves from a binary neutron star Inspiral." *Phys. Rev. Lett.* 119.16 (2017), p. 161101. DOI: 10.1103/PhysRevLett.119.161101. arXiv: 1710.05832 [gr-qc].

[2] Benjamin P. Abbott et al. "Gravitational waves and Gamma-rays from a binary neutron star merger: GW170817 and GRB 170817A." *Astrophys. J.* 848.2 (2017), p. L13. DOI: 10.3847/2041-8213/aa920c. arXiv: 1710.05834 [astro-ph.HE].

[3] Adam Goldstein et al. "An ordinary short gamma-ray burst with extraordinary implications: Fermi-GBM detection of GRB 170817A." *Astrophys. J.* 848.2 (2017), p. L14. DOI: 10.3847/2041-8213/aa8f41. arXiv: 1710.05446 [astro-ph.HE].

[4] Volodymyr Savchenko et al. "INTEGRAL detection of the first prompt gamma-ray signal coincident with the gravitational-wave event GW170817." *Astrophys. J.* 848.2 (2017), p. L15. DOI: 10.3847/2041-8213/aa8f94. arXiv: 1710.05449 [astro-ph.HE].

[5] Benjamin P. Abbott et al. "GW190425: Observation of a compact binary coalescence with total mass $\sim 3.4 M_{\odot}$." *Astrophys. J. Lett.* 892.1 (2020), p. L3. DOI: 10.3847/2041-8213/ab75f5. arXiv: 2001.01761 [astro-ph.HE].

[6] Benjamin P. Abbott et al. "GW170817: Measurements of neutron star radii and equation of state." *Phys. Rev. Lett.* 121.16 (2018), p. 161101. DOI: 10.1103/PhysRevLett.121.161101. arXiv: 1805.11581 [gr-qc].

[7] Benjamin P Abbott et al. "Model comparison from LIGO-Virgo data on GW170817's binary components and consequences for the merger remnant." *Class. Quant. Grav.* 37.4 (2020), p. 045006. DOI: 10.1088/1361-6382/ab5f7c. arXiv: 1908.01012 [gr-qc].

[8] Eemeli Annala et al. "Gravitational-wave constraints on the neutron-star-matter equation of state." *Phys. Rev. Lett.* 120.17 (2018), p. 172703. DOI: 10.1103/PhysRevLett.120.172703. arXiv: 1711.02644 [astro-ph.HE].

[9] Elias R. Most et al. "New constraints on radii and tidal deformabilities of neutron stars from GW170817." *Phys. Rev. Lett.* 120.26 (2018), p. 261103. DOI: 10.1103/PhysRevLett.120.261103. arXiv: 1803.00549 [gr-qc].

[10] Ben Margalit and Brian D. Metzger. "Constraining the maximum mass of neutron stars From multi-messenger observations of GW170817." *Astrophys. J.* 850.2 (2017), p. L19. DOI: 10.3847/2041-8213/aa991c. arXiv: 1710.05938 [astro-ph.HE].

[11] Luciano Rezzolla, Elias R. Most, and Lukas R. Weih. "Using gravitational-wave observations and quasi-universal relations to constrain the maximum mass of neutron stars." *Astrophys. J.* 852.2 (2018). [Astrophys. J. Lett.852,L25(2018)], p. L25. DOI: 10.3847/2041-8213/aaa401. arXiv: 1711.00314 [astro-ph.HE].

[12] Milton Ruiz, Stuart L. Shapiro, and Antonios Tsokaros. "GW170817, General relativistic magnetohydrodynamic simulations, and the neutron star maximum mass." *Phys. Rev.* D97.2 (2018), p. 021501. DOI: 10.1103/PhysRevD.97.021501. arXiv: 1711.00473 [astro-ph.HE].

[13] Masaru Shibata et al. "Modeling GW170817 based on numerical relativity and its implications." *Phys. Rev.* D96.12 (2017), p. 123012. DOI: 10.1103/PhysRevD.96.123012. arXiv: 1710.07579 [astro-ph.HE].

[14] Geraint Pratten, Patricia Schmidt, and Tanja Hinderer. "Gravitational-wave asteroseismology with fundamental modes from compact binary inspirals." (2019). arXiv: 1905.00817 [gr-qc].

[15] Jacques Abadie et al. "Predictions for the rates of compact binary coalescences observable by ground-based gravitational-wave detectors." *Class. Quant. Grav.* 27 (2010), p. 173001. DOI: 10.1088/0264-9381/27/17/173001. arXiv: 1003.2480 [astro-ph.HE].

[16] Vassiliki Kalogera et al. "The cosmic coalescence rates for double neutron star binaries." *Astrophys. J.* 601 (2004). [Erratum: Astrophys. J.614,L137(2004)], pp. L179–L182. DOI: 10.1086/425868. arXiv: astro-ph/0312101 [astro-ph].

[17] Chunglee Kim, Vicky Kalogera, and Duncan R. Lorimer. "The effect of PSR J0737-3039 on the DNS merger rate and implications for gravity-wave detection." *New Astron. Rev.* 54 (2010), pp. 148–151. DOI: 10.1016/j.newar.2010.09.010. arXiv: astro-ph/0608280 [astro-ph].

[18] Richard O'Shaughnessy et al. "Constraining population synthesis models via empirical binary compact object merger and supernova rates." *The Astrophysical Journal* 672.1 (2008), p. 479.

[19] Stefan Hild et al. "A xylophone configuration for a third generation gravitational wave detector." *Class. Quant. Grav.* 27 (2010), p. 015003. DOI: 10.1088/0264-9381/27/1/015003. arXiv: 0906.2655 [gr-qc].

[20] Bangalore Sathyaprakash et al. "Scientific objectives of Einstein Telescope." *Class. Quant. Grav.* 29 (2012). [Erratum: Class. Quant. Grav.30,079501(2013)], p. 124013. DOI: 10.1088/0264-9381/29/12/124013,10.1088/0264-9381/30/7/079501. arXiv: 1206.0331 [gr-qc].

[21] Benjamin P Abbott et al. "Exploring the sensitivity of next generation gravitational wave detectors." *Class. Quant. Grav.* 34.4 (2017), p. 044001. DOI: 10.1088/1361-6382/aa51f4. arXiv: 1607.08697 [astro-ph.IM].

[22] Vishal Baibhav et al. "Gravitational-wave detection rates for compact binaries formed in isolation: LIGO/Virgo O3 and beyond." *Phys. Rev.* D100.6 (2019), p. 064060. DOI: 10.1103/PhysRevD.100.064060. arXiv: 1906.04197 [gr-qc].

[23] Eanna E. Flanagan and Tanja Hinderer. "Constraining neutron star tidal Love numbers with gravitational wave detectors." *Phys. Rev.* D77 (2008), p. 021502. DOI: 10.1103/PhysRevD.77.021502. arXiv: 0709.1915 [astro-ph].

[24] Joshua A. Faber et al. "Measuring neutron star radii with gravitational wave detectors." *Phys. Rev. Lett.* 89 (2002), p. 231102. DOI: 10.1103/PhysRevLett.89.231102. arXiv: astro-ph/0204397 [astro-ph].

[25] Michal Bejger et al. "Impact of the nuclear equation of state on the last orbits of binary neutron stars." *Astron. Astrophys.* 431 (2005), p. 297. DOI: 10.1051/0004-6361:20041441. arXiv: astro-ph/0406234 [astro-ph].

[26] Tanja Hinderer. "Tidal love numbers of neutron stars." *Astrophys. J.* 677 (2008), pp. 1216–1220. DOI: 10.1086/533487. arXiv: 0711.2420 [astro-ph].

[27] Tanja Hinderer et al. "Tidal deformability of neutron stars with realistic equations of state and their gravitational wave signatures in binary inspiral." *Phys. Rev.* D81 (2010), p. 123016. DOI: 10.1103/PhysRevD.81.123016. arXiv: 0911.3535 [astro-ph.HE].

[28] Thibault Damour, Michael Soffel, and Chong-ming Xu. "General relativistic celestial mechanics. 1. Method and definition of reference systems." *Phys. Rev.* D43 (1991), pp. 3273–3307. DOI: 10.1103/PhysRevD.43.3273.

[29] Thibault Damour, Michael Soffel, and Chongming Xu. "General-relativistic celestial mechanics II. Translational equations of motion." *Phys. Rev. D* 45 (4 Feb. 1992), pp. 1017–1044. DOI: 10.1103/PhysRevD.45.1017. URL: https://link.aps.org/doi/10.1103/PhysRevD.45.1017.

[30] Thibault Damour, Michael Soffel, and Chong-ming Xu. "General relativistic celestial mechanics. 3. Rotational equations of motion." *Phys. Rev.* D47 (1993), pp. 3124–3135. DOI: 10.1103/PhysRevD.47.3124.

[31] Thibault Damour, Michael Soffel, and Chong-ming Xu. "General relativistic celestial mechanics. 4: Theory of satellite motion." *Phys. Rev.* D49 (1994), pp. 618–635. DOI: 10.1103/PhysRevD.49.618.

[32] Etienne Racine and Eanna E. Flanagan. "Post-1-Newtonian equations of motion for systems of arbitrarily structured bodies." *Phys. Rev.* D71 (2005). [Erratum: Phys. Rev.D88,no.8,089903(2013)], p. 044010. DOI: 10.1103/PhysRevD.71.044010, 10.1103/PhysRevD.88.089903. arXiv: gr-qc/0404101 [gr-qc].

[33] Justin E. Vines and Eanna E. Flanagan. "Post-1-Newtonian quadrupole tidal interactions in binary systems." *Phys. Rev.* D88 (2013), p. 024046. DOI: 10.1103/PhysRevD.88.024046. arXiv: 1009.4919 [gr-qc].

[34] Tiziano Abdelsalhin, Leonardo Gualtieri, and Paolo Pani. "Post-Newtonian spin-tidal couplings for compact binaries." *Phys. Rev.* D98.10 (2018), p. 104046. DOI: 10.1103/PhysRevD.98.104046. arXiv: 1805.01487 [gr-qc].

[35] Thomas G. Cowling. "The non-radial oscillations of polytropic stars." *Mon. Not. R. Astron Soc.* 101 (1941), p. 367. DOI: 10.1093/mnras/101.8.367.

[36] Dong Lai. "Resonant oscillations and tidal heating in coalescing binary neutron stars." *Mon. Not. Roy. Astron. Soc.* 270 (1994), p. 611. DOI: 10.1093/mnras/270.3.611. arXiv: astro-ph/9404062 [astro-ph].

[37] Andreas Reisenegger and Peter Goldreich. "Excitation of neutron star normal modes during binary inspiral." *Astrophys. J.* 426 (May 1994), pp. 688–691. DOI: 10.1086/174105.

[38] Kostas D. Kokkotas and Gerhard Schaefer. "Tidal and tidal resonant effects in coalescing binaries." *Mon. Not. Roy. Astron. Soc.* 275 (1995), p. 301. DOI: 10.1093/mnras/275.2.301. arXiv: gr-qc/9502034.

[39] Leonardo Gualtieri et al. "Gravitational signals emitted by a point mass orbiting a neutron star: A perturbative approach." *Phys. Rev.* D64 (2001), p. 104007. DOI: 10.1103/PhysRevD.64.104007. arXiv: gr-qc/0107046 [gr-qc].

[40] Jose A. Pons et al. "Gravitational signals emitted by a point mass orbiting a neutron star: Effects of stellar structure." *Phys. Rev. D* 65 (2002), p. 104021. DOI: 10.1103/PhysRevD.65.104021. arXiv: gr-qc/0111104.

[41] Giovanni Miniutti et al. "Non-radial oscillation modes as a probe of density discontinuities in neutron stars." *Mon. Not. Roy. Astron. Soc.* 338 (2003), p. 389. DOI: 10.1046/j.1365-8711.2003.06057.x. arXiv: astro-ph/0206142 [astro-ph].

[42] Emanuele Berti et al. "Are post-Newtonian templates faithful and effectual in detecting gravitational signals from neutron star binaries?" *Phys. Rev. D* 66 (2002), p. 064013. DOI: 10.1103/PhysRevD.66.064013. arXiv: gr-qc/0208011.

[43] Dong Lai. "Dynamical tides in rotating binary stars." *Astrophys. J.* 490 (1997), p. 847. DOI: 10.1086/304899. arXiv: astro-ph/9704132 [astro-ph].

[44] Wynn C. G. Ho and Dong Lai. "Resonant tidal excitations of rotating neutron stars in coalescing binaries." *Mon. Not. Roy. Astron. Soc.* 308 (1999), p. 153. DOI: 10.1046/j.1365-8711.1999.02703.x. arXiv: astro-ph/9812116 [astro-ph].

[45] Cecilia Chirenti, Roman Gold, and M.Coleman Miller. "Gravitational waves from f-modes excited by the inspiral of highly eccentric neutron star binaries." *Astrophys. J.* 837.1 (2017), p. 67. DOI: 10.3847/1538-4357/aa5ebb. arXiv: 1612.07097 [astro-ph.HE].

[46] Huan Yang et al. "Evolution of highly eccentric binary neutron stars including tidal effects." *Phys. Rev.* D98.4 (2018), p. 044007. DOI: 10.1103/PhysRevD.98.044007. arXiv: 1806.00158 [gr-qc].

[47] Huan Yang. "Inspiralling eccentric binary neutron stars: Orbital motion and tidal resonance." *Phys. Rev.* D100.6 (2019), p. 064023. DOI: 10.1103/PhysRevD.100.064023. arXiv: 1904.11089 [gr-qc].

[48] Michelle Vick and Dong Lai. "Tidal effects in eccentric coalescing neutron star binaries." *Phys. Rev.* D100.6 (2019), p. 063001. DOI: 10.1103/PhysRevD.100.063001. arXiv: 1906.08780 [astro-ph.HE].

[49] Andrew G. Lyne et al. “A double pulsar system - A rare laboratory for relativistic gravity and plasma physics.” *Science* 303 (2004), pp. 1153–1157. DOI: 10.1126/science.1094645. arXiv: astro-ph/0401086 [astro-ph].

[50] Nils Andersson and W. C. G. Ho. “Using gravitational-wave data to constrain dynamical tides in neutron star binaries.” *Phys. Rev.* D97.2 (2018), p. 023016. DOI: 10.1103/PhysRevD.97.023016. arXiv: 1710.05950 [astro-ph.HE].

[51] A. Katrin Schenk et al. “Nonlinear mode coupling in rotating stars and the r mode instability in neutron stars.” *Phys. Rev.* D65 (2002), p. 024001. DOI: 10.1103/PhysRevD.65.024001. arXiv: gr-qc/0101092 [gr-qc].

[52] Dong Lai and Yanqin Wu. “Resonant tidal excitations of Inertial Modes in Coalescing neutron star Binaries.” *Phys. Rev.* D74 (2006), p. 024007. DOI: 10.1103/PhysRevD.74.024007. arXiv: astro-ph/0604163 [astro-ph].

[53] Eanna E. Flanagan and Etienne Racine. “Gravitomagnetic resonant excitation of Rossby modes in coalescing neutron star binaries.” *Phys. Rev.* D75 (2007), p. 044001. DOI: 10.1103/PhysRevD.75.044001. arXiv: gr-qc/0601029 [gr-qc].

[54] Jan Steinhoff et al. “Dynamical tides in general relativity: Effective action and effective-one-body hamiltonian.” *Phys. Rev.* D94.10 (2016), p. 104028. DOI: 10.1103/PhysRevD.94.104028. arXiv: 1608.01907 [gr-qc].

[55] Tanja Hinderer et al. “Effects of neutron-star dynamic tides on gravitational waveforms within the effective-one-body approach.” *Phys. Rev. Lett.* 116.18 (2016), p. 181101. DOI: 10.1103/PhysRevLett.116.181101. arXiv: 1602.00599 [gr-qc].

[56] Patricia Schmidt and Tanja Hinderer. “Frequency domain model of f-mode dynamic tides in gravitational waveforms from compact binary inspirals.” *Phys. Rev.* D100.2 (2019), p. 021501. DOI: 10.1103/PhysRevD.100.021501. arXiv: 1905.00818 [gr-qc].

[57] Francois Foucart et al. “Gravitational waveforms from spectral Einstein code simulations: neutron star-neutron star and low-mass black hole-neutron star binaries”. *Phys. Rev. D* 99 (4 Feb. 2019), p. 044008. DOI: 10.1103/PhysRevD.99.044008. URL: https://link.aps.org/doi/10.1103/PhysRevD.99.044008.

[58] Tsang Keung Chan et al. “Multipolar universal relations between f-mode frequency and tidal deformability of compact stars.” *Phys. Rev.* D90.12 (2014), p. 124023. DOI: 10.1103/PhysRevD.90.124023. arXiv: 1408.3789 [gr-qc].

[59] Kent Yagi and Nicolás Yunes. "I-Love-Q: Unexpected universal relations for neutron stars and quark stars". *Science* 341.6144 (2013), pp. 365–368. ISSN: 0036-8075. DOI: 10.1126/science.1236462. eprint: http://science.sciencemag.org/content/341/6144/365.full.pdf. URL: http://science.sciencemag.org/content/341/6144/365.

[60] Kent Yagi and Nicolas Yunes. "I-Love-Q relations in neutron stars and their applications to astrophysics, gravitational waves and fundamental Physics." *Phys. Rev.* D88.2 (2013), p. 023009. DOI: 10.1103/PhysRevD.88.023009. arXiv: 1303.1528 [gr-qc].

[61] Kent Yagi and Nicolás Yunes. "Approximate universal relations for neutron stars and quark stars." *Phys. Rept.* 681 (2017), pp. 1–72. DOI: 10.1016/j.physrep.2017.03.002. arXiv: 1608.02582 [gr-qc].

[62] Robert A. Managan. "Nonaxisymmetric normal modes and secular instabilities of rotating stars." *Astrophys. J.* 309 (Oct. 1986), p. 598. DOI: 10.1086/164628.

[63] James R. Ipser and Lee Lindblom. "The oscillations of rapidly rotating Newtonian stellar models." *Astrophys. J.* 355 (May 1990), p. 226. DOI: 10.1086/168757.

[64] James R. Ipser and Lee Lindblom. "The oscillations of rapidly rotating Newtonian stellar models. II. Dissipative effects." *Astrophys. J.* 373 (May 1991), p. 213. DOI: 10.1086/170039.

[65] Shin'ichirou Yoshida and Yoshiharu Eriguchi. "Gravitational radiation–driven secular instability of rotating polytropes." *Astrophys. J.* 438 (Jan. 1995), p. 830. DOI: 10.1086/175126.

[66] Andrea Passamonti, Brynmor Haskell, and Nils Andersson. "Oscillations of rapidly rotating superfluid stars." *Mon. Not. Roy. Astron. Soc.* 396 (2009), p. 951. DOI: 10.1111/j.1365-2966.2009.14751.x. arXiv: 0812.3569 [astro-ph].

[67] Curt Cutler. "Post-Newtonian effects on the modes of rotating stars." *Astrophys. J.* 374 (June 1991), p. 248. DOI: 10.1086/170113.

[68] Curt Cutler and Lee Lindblom. "Post-Newtonian frequencies for the pulsations of rapidly rotating neutron stars." *Astrophys. J.* 385 (Feb. 1992), p. 630. DOI: 10.1086/170968.

[69] Yasufumi Kojima. "Normal modes of relativistic stars in slow rotation limit." *Astrophys. J.* 414 (Sept. 1993), p. 247. DOI: 10.1086/173073.

[70] Yasufumi Kojima. "Coupled pulsations between polar and axial modes in a slowly rotating relativistic star." *Progress of Theoretical Physics* 90.5 (Sept. 1993), pp. 977–990. ISSN: 0033-068X. DOI: 10.1143/ptp/90.5.977. eprint: https://academic.oup.com/ptp/article-pdf/90/5/977/

5326203/90-5-977.pdf. URL: https://doi.org/10.1143/ptp/90.5.977.

[71] Shijun Yoshida and Yasufumi Kojima. "Accuracy of the relativistic Cowling approximation in slowly rotating stars." *Mon. Not. R. Astron Soc.* 289.1 (July 1997), pp. 117–122. DOI: 10.1093/mnras/289.1.117. arXiv: gr-qc/9705081 [gr-qc].

[72] Adamantios Stavridis, Andrea Passamonti, and Kostas Kokkotas. "Nonradial oscillations of slowly and differentially rotating compact stars". *Phys. Rev. D* 75 (6 Mar. 2007), p. 064019. DOI: 10.1103/PhysRevD.75.064019. URL: https://link.aps.org/doi/10.1103/PhysRevD.75.064019.

[73] Andrea Passamonti, Adamantios Stavridis, and Kostas D. Kokkotas. "Non-axisymmetric oscillations of differentially rotating relativistic stars". *Phys. Rev. D* 77 (2 Jan. 2008), p. 024029. DOI: 10.1103/PhysRevD.77.024029. URL: https://link.aps.org/doi/10.1103/PhysRevD.77.024029.

[74] Shin'ichirou Yoshida and Yoshiharu Eriguchi. "A numerical study of normal modes of rotating neutron star models by the cowling approximation." *Astrophys. J.* 515 (1999), p. 414. DOI: 10.1086/307012. arXiv: astro-ph/9807254.

[75] James R. Ipser and Lee Lindblom. "On the pulsations of relativistic accretion disks and rotating stars: The Cowling approximation." *Astrophys. J.* 389 (Apr. 1992), p. 392. DOI: 10.1086/171214.

[76] Christian Krüger, Erich Gaertig, and Kostas D. Kokkotas. "Oscillations and instabilities of fast and differentially rotating relativistic stars". *Phys. Rev. D* 81 (8 Apr. 2010), p. 084019. DOI: 10.1103/PhysRevD.81.084019. URL: https://link.aps.org/doi/10.1103/PhysRevD.81.084019.

[77] Erich Gaertig and Kostas D. Kokkotas. "Oscillations of rapidly rotating relativistic stars". *Phys. Rev. D* 78 (6 Sept. 2008), p. 064063. DOI: 10.1103/PhysRevD.78.064063. URL: https://link.aps.org/doi/10.1103/PhysRevD.78.064063.

[78] John L. Friedman and Nikolaos Stergioulas. *Rotating relativistic Stars*. Cambridge University Press, 2013.

[79] Burkhard Zink et al. "On the frequency band of the f-mode CFS instability." *Phys. Rev. D* 81 (2010), p. 084055. DOI: 10.1103/PhysRevD.81.084055. arXiv: 1003.0779 [astro-ph.SR].

[80] Subrahmanyan Chandrasekhar. *Ellipsoidal figures of equilibrium*. Vol. 9. Yale University Press New Haven, 1969.

[81] Harry J. Braviner and Gordon I. Ogilvie. "Tidal interactions of a Maclaurin spheroid – I. Properties of free oscillation modes." *Mon. Not. Roy. Astron. Soc.* 441.3 (2014), pp. 2321–2345. DOI: 10.1093/mnras/stu704. arXiv: 1404.2461 [astro-ph.SR].

[82] Neil Comins. "On secular instabilities of rigidly rotating stars in general relativity - 11. Numerical results." *Mon. Not. R. Astron Soc.* 189 (Oct. 1979), pp. 255–272. DOI: 10.1093/mnras/189.2.255.

[83] James R. Ipser and Lee Lindblom. "The oscillations of rapidly rotating Newtonian stellar models. II. Dissipative effects." *Astrophys. J.* 373 (May 1991), p. 213. DOI: 10.1086/170039.

[84] Phil Arras and Nevin N. Weinberg. "Urca reactions during neutron star inspiral." *Mon. Not. R. Astron Soc.* 486.1 (June 2019), pp. 1424–1436. DOI: 10.1093/mnras/stz880. arXiv: 1806.04163 [astro-ph.HE].

[85] Lars Bildsten and Curt Cutler. "Tidal interactions of inspiraling compact binaries." *Astrophys. J.* 400 (Nov. 1992), pp. 175–180. DOI: 10.1086/171983.

[86] William H. Press and Saul A. Teukolsky. "On formation of close binaries by two-body tidal capture." *Astrophys. J.* 213 (Apr. 1977), pp. 183–192. DOI: 10.1086/155143.

[87] Stuart L Shapiro and Saul A Teukolsky. *Black holes, white dwarfs, and neutron stars: The physics of compact objects*. John Wiley & Sons, 2008.

[88] Kip S. Thorne. "Multipole expansions of gravitational radiation." *Rev. Mod. Phys.* 52 (1980), pp. 299–339. DOI: 10.1103/RevModPhys.52.299.

[89] Sean M. Wahl, William B. Hubbard, and Burkhard Militzer. "The concentric Maclaurin spheroid method with tides and a rotational enhancement of Saturn's tidal response." *Icarus* 282 (Jan. 2017), pp. 183–194. DOI: 10.1016/j.icarus.2016.09.011. arXiv: 1602.07350 [astro-ph.EP].

[90] Eric Poisson and Clifford M. Will. *Gravity: Newtonian, Post-Newtonian, relativistic*. Cambridge: Cambridge University Press, 2014. DOI: 10.1017/CBO9781139507486.

[91] Archie E. Roy and P. E. Moran. "Studies in the application of recurrence relations to special perturbation methods. III. Non-singular differential equations for special perturbations." *Celestial Mechanics* 7 (Feb. 1973), pp. 236–255. DOI: 10.1007/BF01229950.

[92] Curt Cutler and Eanna E. Flanagan. "Gravitational waves from merging compact binaries: How accurately can one extract the binary's parameters from the inspiral wave form?" *Phys. Rev.* D49 (1994), pp. 2658–2697. DOI: 10.1103/PhysRevD.49.2658. arXiv: gr-qc/9402014 [gr-qc].

[93] J. Aasi et al. "Advanced LIGO." *Class. Quant. Grav.* 32 (2015), p. 074001. DOI: 10.1088/0264-9381/32/7/074001. arXiv: 1411.4547 [gr-qc].

[94] Benjamin P. Abbott et al. "Prospects for observing and localizing gravitational-wave transients with advanced LIGO, Advanced Virgo and KAGRA." *Living Rev. Rel.* 21.1 (2018), p. 3. DOI: 10.1007/s41114-018-0012-9,10.1007/lrr-2016-1. arXiv: 1304.0670 [gr-qc].

[95] Fausto Acernese et al. "Advanced Virgo: a second-generation interferometric gravitational wave detector." *Class. Quant. Grav.* 32.2 (2015), p. 024001. DOI: 10.1088/0264-9381/32/2/024001. arXiv: 1408.3978 [gr-qc].

[96] Tomotada Akutsu et al. "KAGRA: 2.5 generation interferometric gravitational wave detector." *Nat. Astron.* 3.1 (2019), pp. 35–40. DOI: 10.1038/s41550-018-0658-y. arXiv: 1811.08079 [gr-qc].

[97] *https://dcc.ligo.org/LIGO-T1600119/public*. URL: https://dcc.ligo.org/LIGO-T1600119/public.

[98] Benjamin P Abbott et al. "Exploring the sensitivity of next generation gravitational wave detectors." *Class. Quant. Grav.* 34.4 (2017), p. 044001. DOI: 10.1088/1361-6382/aa51f4. arXiv: 1607.08697 [astro-ph.IM].

[99] Stefan Hild et al. "A xylophone configuration for a third generation gravitational wave detector." *Class. Quant. Grav.* 27 (2010), p. 015003. DOI: 10.1088/0264-9381/27/1/015003. arXiv: 0906.2655 [gr-qc].

[100] Serge Droz et al. "Gravitational waves from inspiraling compact binaries: Validity of the stationary phase approximation to the Fourier transform." *Phys. Rev.* D59 (1999), p. 124016. DOI: 10.1103/PhysRevD.59.124016. arXiv: gr-qc/9901076 [gr-qc].

[101] Dmitrii G. Yakovlev, Kseniya P. Levenfish, and Yurii A. Shibanov. "REVIEWS OF TOPICAL PROBLEMS: Cooling of neutron stars and superfluidity in their cores." *Physics Uspekhi* 42.8 (Aug. 1999), pp. 737–778. DOI: 10.1070/PU1999v042n08ABEH000556. arXiv: astro-ph/9906456 [astro-ph].

[102] Nils Andersson and Greg L. Comer. "On the dynamics of superfluid neutron star cores." *Mon. Not. R. Astron Soc.* 328.4 (Dec. 2001), pp. 1129–1143. DOI: 10.1046/j.1365-8711.2001.04923.x. arXiv: astro-ph/0101193 [astro-ph].

[103] Reinhard Prix and Michel L. E. Rieutord. "Adiabatic oscillations of non-rotating superfluid neutron stars." *Astron. Astrophys.* 393 (2002), pp. 949–964. DOI: 10.1051/0004-6361:20021049. arXiv: astro-ph/0204520.

[104] Carl M Bender and Steven A Orszag. *Advanced mathematical methods for scientists and engineers I: Asymptotic methods and perturbation theory*. Springer Science & Business Media, 2013.

Chapter 6

DETECTING RESONANT TIDAL EXCITATIONS OF ROSSBY MODES IN COALESCING NEUTRON-STAR BINARIES WITH THIRD-GENERATION GRAVITATIONAL-WAVE DETECTORS

[1] Sizheng Ma, Hang Yu, and Yanbei Chen. "Detecting resonant tidal excitations of Rossby modes in coalescing neutron-star binaries with third-generation gravitational-wave detectors." *Phys. Rev. D* 103.6 (2021), p. 063020. DOI: 10.1103/PhysRevD.103.063020. arXiv: 2010.03066 [gr-qc].

6.1 Introduction

Gravitational-wave (GW) astronomy recently provided us with a new way to study neutron star (NS) physics, with events GW170817 [1, 2] and GW190425 [3] already imposing new constraints on NS properties [4–12]. With future upgrades for Advanced LIGO and Virgo [13–24], LIGO-India [25], KAGRA [26, 27], as well as third-generation detectors like the Einstein Telescope [28–31] and the Cosmic Explorer (CE) [32, 33], we expect to detect more events, as well as achieving much higher signal-to-noise ratios [34]. These new opportunities motivate the more accurate modeling of NSs in coalescing binaries, and the GWs they emit [35–40].

During the last few minutes of a binary neutron star inspiral, the orbital frequency sweeps through tens of Hertz to hundreds of Hertz; internal fluid motions of NSs may get resonantly excited by tidal forces exerted by their companions. Such fluid motion will also act back onto the orbital motion. This phenomenon is called dynamical tide (DT), which was first investigated by Cowling [41]. For non-spinning NSs in binaries with circular orbits, only g-modes can be resonantly excited, but their effect on gravitational waveforms is negligible [42–45]. However, DT can be enhanced by orbital eccentricity [46–49] and rotation [50–53].

The effect of rotation on DTs was first studied by Lai *et al.* [50, 51], who aimed to explain the orbital decay of the PSR J0045-7319/B binary system. They pointed out that stellar rotation can excite f-modes and lower-order g-modes. Since these modes couple more strongly to the tidal field, DTs should be more pronounced. The same formalism was then applied to coalescing binaries by Ho and Lai [52] to investigate the impact of DTs on GW. It was found that f-mode resonances require NSs to rotate

at very high frequencies—and only in this case it induces significant GW phase shift. On the other hand, g-mode resonances are still too weak to be detected. Several authors later extended the above Newtonian studies, and discussed the excitation of f-modes and g-modes in the context of general relativity [35, 54–58].

Although f-mode resonances can significantly influence GW, the high rotation rate required here is disfavored by the astrophysics of formation scenarios. It is generally believed that NSs in binaries have already spun down to low frequencies ($\lesssim 40$ Hz) when their GW frequencies enter the band of ground-based detectors [59, 60]. For example, recent events GW170817 [1] and GW190425 [3] were all consistent with low spins. In this way, f-mode resonance might not be very promising for GW observations.

For spinning neutron stars, besides f-, p- and g-modes, there also exist inertial modes (hybrid modes) that are mainly supported by the Coriolis force [61–63]. As pointed out by Lockitch and Friedman [62], for isentropic stars[1], rotation mixes purely axial modes and purely polar modes, and leads to a class of modes that have hybrid parity, where each of them can be classified into axial-led or polar-led For Newtonian stars, there is a special subclass of modes that has a purely axial parity, which is usually referred to as the Rossby modes (or r-modes) [64, 65], although this particular subclass also obtains a polar part for relativistic stars [66–68]. On the other hand, for non-isentropic NSs, the mixing of g-modes and r-modes takes place at a relatively high rotation rate (where the Coriolis force dominates over the buoyancy), leading to the so-called inertial-gravity modes.

Previous studies have shown that inertial modes (including r-modes) and inertial-gravity modes can be excited by the (gravito-electric) Newtonian tidal field [52, 69, 70]. The resonance takes place as the orbital angular velocity becomes comparable to the spin frequency, which requires a minimum NS spin of only tens of Hertz. Although this spin requirement is more likely fulfilled, the effect of such resonances are too weak to be detectable. However, inertial modes (including r-modes) can also be excited by the gravitomagnetic force [71–75]. As pointed out by Flanagan *et al.* (hereafter FR07) [72], this kind of DT can induce ~ 0.1 rad of GW phase shift—detectable by third-generation detectors, like ET and CE. Their studies, though, did not provide detailed discussions on how those DTs impact parameter estimation. Later on, Yu *et al.* [76] proposed that the r-mode DTs can improve the accuracy in

[1] Isentropic stars have no buoyancy; both g-modes and r-modes (purely axial modes) have vanishing mode frequency in the non-spinning limit, and they are mixed even without rotation.

measuring tidal Love numbers. The aim of this chapter is to build upon FR07 and Ref. [76], and study the r-mode DTs with more details, including a Fisher-matrix analysis. Especially, we will investigate the impact of universal relations among NS properties [77, 78].

This chapter is organized as follows. We first give a summary of the implication of r-mode DT on GW parameter estimation in Sec. 6.2, and the rest of this chapter presents the details. In Sec. 6.3, we briefly review the coupling between the r-mode and the gravitomagnetic force. In Sec. 6.4, we discuss features of r-mode excitation and the r-mode's impact on the orbital evolution. We first focus on the orbital part in Sec. 6.4.2, where we compare the model presented in FR07 [Eq. (6.1)] with numerical integration. Next we study the tidal excitation in Sec. 6.4.3, where we give an analytic formula for r-mode tidal evolution that is valid in the entire evolution regime. In Sec. 6.5, we explore the universal relation between the normalized r-mode overlap and the normalized tidal Love number. Sec. 6.6 focuses on the construction of gravitational waveforms. We first propose a hybrid GW waveform in Sec. 6.6.1, which incorporates both r-mode and other PN effects. Next in Sec. 6.6.2 we provide a model for the GW phase of r-mode, following FR07. In Sec. 6.7, we use the Fisher information matrix formalism to discuss the influence of r-mode excitation on parameter estimation. Finally in Sec. 6.8 we summarize our results.

Throughout this chapter we use geometric units with $G = c = 1$.

6.2 Summary of parameter dependencies

In this section, we shall give a brief summary of r-mode resonance's impact on the gravitational waveform, and on how physical parameters of neutron-star and neutron-star–black-hole binaries influence the gravitational waveform, via point-particle, spin-orbit, f-mode tide, and r-mode resonance effects. We shall divide binaries into four categories, and discuss in each category how some, or all, of the physical parameters of the neutron stars can be measured.

6.2.1 The role of r-mode dynamical tide

As discussed in FR07 [72], r-mode excitation is mainly controlled by the spin frequency Ω_s and r-mode coupling coefficient $\mathcal{I}$ [Eq. (6.30)], which play different roles: (i) spin frequency determines the location (both in time and frequency domains) of resonance during orbital evolution, because resonance takes place as the tidal driving frequency (related to the orbital frequency) coincides with the pattern

frequency of the mode (determined by the spin frequency) in the inertial frame; (ii) the r-mode coupling coefficient $\mathcal{I}$ characterizes the strength of the r-mode DT, therefore determines the effect of this DT on orbital evolution [See Sec. 6.4 for details]. As proposed in FR07, the orbital evolution before and after the r-mode resonance can described as two different point-particle (PP) orbits, with orbital-frequency evolution given by

$$\dot{\phi}(t) = \begin{cases} \dot{\phi}_{\rm PP}^{\rm (pre)}(t), & \text{if } t < t_r \\ \dot{\phi}_{\rm PP}^{\rm (post)}(t), & \text{if } t > t_r \end{cases}, \tag{6.1}$$

with t_r the time of resonance[2]. These two frequency evolutions satisfy the same evolution equation, with the same set of parameters (including mass, spin, inclination angles, etc) which, at Newtonian order, reads

$$\frac{d}{dt}\dot{\phi}_{\rm (PP)} = \frac{96}{5}\mathcal{M}^{5/3}\dot{\phi}_{\rm (PP)}^{11/3}, \tag{6.2}$$

where $\mathcal{M}$ is the chirp mass. The two orbits are related to each other by a "jump" at t_r

$$\dot{\phi}_{\rm PP}^{\rm (post)}(t_r) - \dot{\phi}_{\rm PP}^{\rm (pre)}(t_r) = \Delta\dot{\phi}_{\rm tid}, \tag{6.3}$$

where $\Delta\dot{\phi}_{\rm tid}$ depends on $\mathcal{I}$ (see Sec. 6.4.2 for more details). As a result, by studying the GW emitted from the orbit in Eq. (6.1), we can obtain the constraints on Ω_s and $\mathcal{I}$.

6.2.2 The impact of r-mode DT on parameter estimation

In order to explore how the additional information from the r-mode DT can improve parameter estimation, we consider both BNS and BHNS binaries, and distinguish whether *universal relations* between neutron-star properties are used as input. This will divide these binaries into four categories.

6.2.2.1 *BNS systems without r-mode DT and universal relations*

A spinning BNS system is sketched in Fig. 6.1. Without r-mode DT (but with f-mode adiabatic tide), the system has 6 intrinsic parameters: chirp mass $\mathcal{M}$; mass ratio $\Xi = m_1/(m_1+m_2)$; two individual tidal Love numbers $\lambda_f^{(i)}$; and two dimensionless spin along the direction of orbital angular momentum $\chi_i^{(z)}$ (The index

[2]The resonance condition is given by Eq. (6.19). Hereafter we use the subscript r to refer to the value at the resonance time.

Table 6.1: Parameters and constraints for a BNS system without r-mode DT and not applying the universal relations between NS properties. We have 6 parameters and 4 independent constraints; as a result, the two individual Love numbers are degenerate, so are the two individual dimensionless spins.

All variables in GW	Effect	Variables in the effect	Constrainable variable
$\mathcal{M}, \Xi$ $\lambda_f^{(1)}, \lambda_f^{(2)}$ $\chi_1^{(z)}, \chi_2^{(z)}$	PN (PP part)	$\mathcal{M}$	$\mathcal{M}$
	PN (PP part)	Ξ	Ξ
	SO coupling	$\chi_1^{(z)}, \chi_2^{(z)}$	$\chi^{\rm eff}$
	Adiabatic tide (f-mode)	$\lambda_f^{(1)}, \lambda_f^{(2)}$	$\lambda_f^{\rm eff}$

$i = 1, 2$ labels the two NSs). In the absence of DT, the system evolves under four main effects: the Newtonian gravity, post-Newtonian (PN) corrections from mass ratio, PN corrections from spin-orbit (SO) coupling, and the adiabatic (f-mode) tidal effect, as summarized in Table 6.1. Here we do not include the PN spin-spin coupling [79] and PN spin precession [80], because their effects are negligible even for 3G detectors for the range of spins we consider (10 $\sim$ 80 Hz, see Sec. 6.9 for more details). For a BNS system, the waveform only depends on a combination of $\lambda_f^{(i)}$ and a combination of χ_i^z, not individually; as a result, we can only measure four parameters to meaningful accuracy: $\mathcal{M}$, Ξ, $\chi^{\rm eff}$, and $\lambda_f^{\rm eff}$, with $\lambda_f^{\rm eff}$ and $\chi^{\rm eff}$ defined by [81, 82]

$$\chi^{\rm eff} = \frac{m_1\chi_1^{(z)} + m_2\chi_2^{(z)}}{M},$$
$$\lambda_f^{\rm eff} = \left(11\frac{m_2}{m_1} + \frac{M}{m_1}\right)\lambda_f^{(1)} + \left(11\frac{m_1}{m_2} + \frac{M}{m_2}\right)\lambda_f^{(2)},$$

where $M = m_1 + m_2$. The two individual Love numbers $\lambda_f^{(i)}$, as well as the two $\chi_i^{(z)}$, are degenerate. Even among the constrainable parameters, errors in Ξ, $\chi^{\rm eff}$, and $\lambda_f^{\rm eff}$ are highly correlated with each other. In order to obtain a good constraint on $\lambda_f^{\rm eff}$, a low-spin prior based on the observed Galactic binary NS population has to be assumed [1, 4]. As we shall discuss later, such assumption is not necessary if r-mode resonance can be incorporated.

6.2.2.2 *BNS systems with the I-Love universal relation but without DT*

For the same BNS system (without DT), the *I-Love* universal relation of NSs [77, 78] can be used to improve parameter estimation. This is a relation between momentum

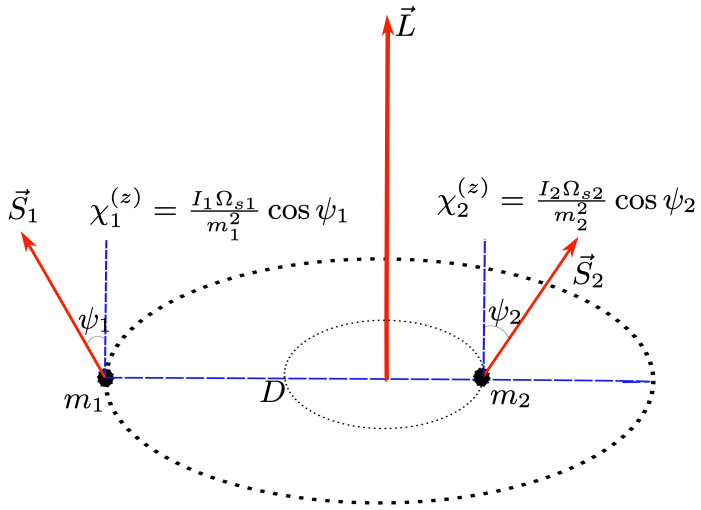

Figure 6.1: A BNS system $m_1 - m_2$ with two spin vectors $\vec{S}_1$ and $\vec{S}_2$. The neutron stars' spin axis are tilted by angles $\psi_{1,2}$ with respect to the direction of the orbital angular momentum $\vec{L}$. Here the azimuthal angle of the spins are unimportant, because the effect of precession is negligible.

of inertia and tidal Love number, that is insensitive to the EoS. To use this relation, we express $\chi^{(z)}$ of each NS as

$$\chi_i^{(z)} = \frac{I_i\Omega_{si}}{m_i^2}\cos\psi_i. \tag{6.4}$$

In this case, we have a total of 10 parameters: chirp mass $\mathcal{M}$; mass ratio Ξ; two Love numbers $\lambda_f^{(i)}$; two moments of inertia I_i; two inclination angles ψ_i; and two spin frequencies Ω_{si}. As listed in Table 6.2 ("Non-DT sector"), there are 6 constraints on these parameters: four are from GW $(\mathcal{M}, \Xi, \chi^{\rm eff}, \lambda_f^{\rm eff})$, as discussed above; and two are from universal relations (each star contributes one constraint). This is still not enough to independently constrain all 10 parameters.

Introducing the universal relations did not reduce the number of degeneracies because more parameters, namely spin frequency and inclination angle for each NS, are needed to be introduced in order to use these relations. The situation will change as we consider r-mode DT.

6.2.2.3 *Resonant BNS systems with universal relations*

Now take the r-mode resonance into account. As shown in Table 6.2 , we have in total 12 parameters: chirp mass $\mathcal{M}$; mass ratio Ξ; two Love numbers $\lambda_f^{(i)}$; two momentum of inertia I_i; two spin frequencies Ω_{si}; two inclination angles ψ_i; and

Table 6.2: Parameters and constraints for a BNS system with universal relations (for both NSs). In the "Non-DT sector," when r-mode DTs do not take place, we have 10 parameters and 6 constraints, with 4 degeneracies. In presence of r-mode DTs, we have 2 more parameters, but 6 more constraints. As a result, we have in total 12 parameters and 12 constraints; the system can in principle be decoded without degeneracy.

Variables in GW	Sector	Effect	Variables in effect	Constrainable variable
$\mathcal{M}, \Xi$ $\lambda_f^{(1)}, \lambda_f^{(2)}$ I_1, I_2 ψ_1, ψ_2 Ω_{s1}, Ω_{s2}	Non-DT sector	PN (PP part)	$\mathcal{M}$	$\mathcal{M}$
		PN (PP part)	Ξ	Ξ
		SO-coupling	$I_1, \Omega_{s1}, \psi_1, \mathcal{M}$ $I_2, \Omega_{s2}, \psi_2, \Xi$	$\chi^{\rm eff}$
		Adiabatic tide (f-mode)	$\lambda_f^{(1)}, \lambda_f^{(2)}$	$\lambda_f^{\rm eff}$
		I-Love universal relation	$\lambda_f^{(1)}, \lambda_f^{(2)}$ I_1, I_2 Ξ	I_1, I_2
		r-mode resonances	Ω_{s1}, Ω_{s2} $\mathcal{I}_1, \mathcal{I}_2$	Ω_{s1}, Ω_{s2} $\mathcal{I}_1, \mathcal{I}_2$
$\mathcal{I}_1, \mathcal{I}_2$	DT sector	r-mode universal relation	$\mathcal{I}_1, \psi_1, \lambda_f^{(1)}$ $\mathcal{I}_2, \psi_2, \lambda_f^{(2)}$ Ξ	ψ_1, ψ_2

two r-mode coupling coefficients $\mathcal{I}_i$. Meanwhile, we can obtain 12 constraints from GW and the universal relations. Six of them ($\mathcal{M}, \Xi, \chi^{\rm eff}, \lambda_f^{\rm eff}, I_{1,2}$) have already been discussed previously. The rest of the six constraints involve the r-mode. Four are constraints on Ω_{si} and $\mathcal{I}_i$, as we discussed in Sec. 6.2.1. The other two constraints come from a new universal relation found in this chapter, namely the relation between the normalized r-mode overlap and the normalized Love number (see Sec. 6.5). As a result, the number of constraints is the same as the number of parameters. In principle, this breaks degeneracy, and allows us to estimate all parameters independently, given a high enough signal-to-noise ratio. However, as it later turns out, even in the era of 3G detectors, for each individual binary, we still may not fully constrain all parameters with relative error less than 100%, since the DT sector is not strong enough.

Table 6.3: Parameters and constraints for a BHNS system with universal relations and r-mode DT. We have 8 parameters and 8 constraints, and the system can be decoded without degeneracy.

All variables in GW	Effect	Variables in the effect	Constrainable variable
$\mathcal{M}, \Xi$ $\lambda_f^{(1)}, I_1$ ψ_1, Ω_{s1} $\mathcal{I}_1, \chi_2^{(z)}$	PN (PP part)	$\mathcal{M}$	$\mathcal{M}$
	PN (PP part)	Ξ	Ξ
	SO coupling	I_1, Ω_{s1}, ψ_1 $\chi_2^{(z)}, \Xi, \mathcal{M}$	$\chi^{\rm eff}$
	Adiabatic tide (f-mode)	$\lambda_f^{(1)}$	$\lambda_f^{(1)}$
	I-Love universal relation	$\lambda_f^{(1)}, I_1$	I_1
	r-mode resonances	$\Omega_{s1}, \mathcal{I}_1$	$\Omega_{s1}, \mathcal{I}_1$
	r-mode universal relation	$\mathcal{I}_1, \psi_1$ $\Xi, \lambda_f^{(1)}$	ψ_1

6.2.2.4 *Resonant BHNS systems with universal relations*

For BHNS systems, the r-mode resonance only takes place once before merger. As shown in Table 6.3, the system has 8 parameters: chirp mass $\mathcal{M}$; mass ratio Ξ; NS Love number $\lambda_f^{(1)}$; NS moment of inertia I_1; NS spin frequency of NS Ω_{s1}; NS inclination angle ψ_1; NS r-mode coupling coefficient $\mathcal{I}_1$, and the spin of BH along the direction of orbital angular momentum $\chi_2^{(z)}$. We can obtain 8 constraints on these parameters, with 6 of them from GW $(\mathcal{M}, \Xi, \chi^{\rm eff}, \lambda_f^{(1)}, \Omega_{s1}, \mathcal{I}_1)$, and 2 from the two universal relations. In this way, the BHNS system is also expected to be decoded without degeneracy, given enough signal-to-noise ratio.

6.3 Basic equations of dynamical tides

In this section, we briefly review the coupling between r-modes and gravitomagnetic force in coalescing binary systems. We refer the reader to Refs. [72, 83] by Flanagan and Racine for further details. In Sec. 6.3.1, we first provide some basic information about r-modes in NSs. All equations are kept to linear order in spin frequency. In Sec. 6.3.2, we show how r-modes are driven by the gravitomagnetic force. Finally in Sec. 6.3.3, we discuss the tidal back reaction to the orbit and present the full equation of motion (EOM). In this section, as done in FR07, the slowly rotating NS is treated in Newtonian gravity. This will lead to the correct form of evolution equations, although parameters may eventually need relativistic corrections. We

shall incorporate PN and f-mode adiabatic tide corrections using a hybrid approach described in Sec. 6.6.

6.3.1 Rossby modes

For a rotating NS with mass m_1, we introduce a co-rotating frame (x', y', z'), in which the spin of the star $\mathbf{\Omega}_{s1}$ is along the z' direction. In this coordinate system, the perturbation equation of the rotating star is given by

$$\frac{\partial^2 \boldsymbol{\xi}}{\partial t^2} + 2\mathbf{\Omega}_{s1} \times \frac{\partial \boldsymbol{\xi}}{\partial t} + \boldsymbol{C} \cdot \boldsymbol{\xi} = \boldsymbol{a}_{\rm ext}, \tag{6.5}$$

where $\boldsymbol{\xi}$ is the Lagrangian displacement of fluid elements, and $\boldsymbol{C}$ is a self-adjoint operator, and $\boldsymbol{a}_{\rm ext}$ the external driving, which will arise from gravitomagnetism in our case. We refer the interested reader to Ref. [84] for more details.

In the phase-space mode expansion framework [71], $\boldsymbol{\xi}$ and its time derivative $\dot{\boldsymbol{\xi}}$ can be expanded as a summation of modes

$$\begin{pmatrix} \boldsymbol{\xi} \\ \dot{\boldsymbol{\xi}} \end{pmatrix} = \sum_{lm} c_{lm}(t) \begin{pmatrix} \boldsymbol{\xi}_{lm} \\ -i\omega_{lm}\boldsymbol{\xi}_{lm} \end{pmatrix}, \tag{6.6}$$

where the angular quantum numbers l and m are integers with $m = \pm l, \pm(l-1) \ldots 0$. Here ω_{lm} is the co-rotating frame eigenfrequency of the mode. Each mode $\boldsymbol{\xi}_{lm}$ satisfies the following eigenvalue problem,

$$-\omega_{lm}^2 \boldsymbol{\xi}_{lm} - 2i\omega_{lm}\mathbf{\Omega}_{s1} \times \boldsymbol{\xi}_{lm} + \mathbf{C} \cdot \boldsymbol{\xi}_{lm} = 0\,, \tag{6.7}$$

and modes with $(l, m) \neq (l', m')$ satisfy the following orthogonality condition,

$$\langle \boldsymbol{\xi}_{lm}, 2i\mathbf{\Omega}_{s1} \times \boldsymbol{\xi}_{l'm'} \rangle + (\omega_{lm} + \omega_{l'm'}) \langle \boldsymbol{\xi}_{lm}, \boldsymbol{\xi}_{l'm'} \rangle = 0, \tag{6.8}$$

with the inner product defined by

$$\langle \boldsymbol{u}, \boldsymbol{v} \rangle = \int d^3x' \rho \boldsymbol{u}^* \cdot \boldsymbol{v}, \tag{6.9}$$

where ρ is the density profile of NS.

In presence of driving, the mode amplitudes satisfy

$$\dot{c}_{lm}(t) + i\omega_{lm} c_{lm}(t) = \frac{i}{b_{lm}} \langle \boldsymbol{\xi}_{lm}, \boldsymbol{a}_{\rm ext} \rangle\,, \tag{6.10}$$

where the coefficient b_{lm} is given by

$$b_{lm} = \langle \boldsymbol{\xi}_{lm}, 2\omega_{lm}\boldsymbol{\xi}_{lm} + 2i\mathbf{\Omega}_{s1} \times \boldsymbol{\xi}_{lm} \rangle\,. \tag{6.11}$$

To linear order in spin frequency, the (l, m) r-mode has Lagrangian displacement vector field as

$$\boldsymbol{\xi}_{lm}(r', \theta', \phi') = -\frac{i f_{lm}(r')}{\sqrt{l(l+1)}} \boldsymbol{r}' \times \nabla Y_{lm}(\theta', \phi'), \tag{6.12}$$

where $Y_{lm}(\theta', \phi')$ are spherical harmonics, and (co-rotating frame) eigenfrequency given by [84]

$$\omega_{lm} = -\frac{2m\Omega_{s1}}{l(l+1)}. \tag{6.13}$$

The radial profile function $f_{lm}(r')$ can only be determined if one includes the next-order correction of spin frequency. For barotropic stars, only the modes $|m| = l$ exist, whose coefficients $f_{lm}(r')$ are given by [84]

$$f_{lm}(r') \propto r'^{l}. \tag{6.14}$$

The constant of proportionality can be determined by the normalization condition

$$\langle \boldsymbol{\xi}_{lm}, \boldsymbol{\xi}_{lm} \rangle = m_1 R_1^2, \tag{6.15}$$

where R_1 the radius of the star. As for other modes with $|m| \neq l$, $f_{lm} = 0$. Henceforth, we restrict our discussions to barotropic stars, and only focus on the $(2, 2)$ r-mode, since it gives the strongest effect [72].

6.3.2 Gravitomagnetic coupling: stellar part

To investigate the coupling between the $(2, 2)$ r-mode and gravitomagnetic force, i.e., the RHS of Eq. (6.10), we place the spinning NS, m_1, in a binary system. It is perturbed by the gravitomagnetic tidal field $\mathcal{B}_{ij}(t)$ exerted by the companion m_2. For convenience, we introduce a non-rotating, co-moving coordinate system (x, y, z) centered at m_1, as shown in Fig. 6.2, with z axis placed along the spin axis. The co-moving frame is related to the co-rotating frame (the primed frame) though a rotation about the z (z') axis by $\Omega_{s1}t$. (Note that the co-moving frame can be non-rotating because in this chapter we treat the spin directions of NSs as fixed.)

Using the same convention as Ref. [72], we parameterize the location of m_2, $\boldsymbol{z}$, as

$$\boldsymbol{z}(t) = D(t)[\cos\psi_1 \cos\phi(t), \sin\phi(t), \sin\psi_1 \cos\phi(t)], \tag{6.16}$$

where ψ_1 is the inclination angle between the stellar spin vector and the orbital angular momentum; $D(t)$ is the separation between two NSs. With this parametrization,

the orbital angular moment, $\vec{L}$, is in the $x-z$ plane. This plane and the orbital plane intersect at $\vec{N}$. The orbital phase of m_2, $\phi(t)$, is the angle between $\vec{z}$ and $\vec{N}$.

The expressions of $\mathcal{B}_{ij}(t)$ and $\boldsymbol{a}_{\rm ext}$ are given in Sec. V C of Ref. [72]. Plugging them and Eq. (6.12) into Eq. (6.10), we obtain the evolution equation for c_{22}

$$\dot{c}_{22} + i\omega_{22}c_{22} = \frac{i}{\omega_{22}}\sqrt{\frac{16\pi}{5}}\frac{I^r_{22}m_2R_1}{D^2}\dot{\phi}(\dot{\phi}-2\Omega_{s1}) \times \sin\psi_1\cos^2\frac{\psi_1}{2}e^{2i\Omega_{s1}t-i\phi}, \tag{6.17}$$

where we have ignored the $\exp[+i\phi]$ part of driving force that does not give rise to resonance, since its effect is negligible. On the RHS of Eq. (6.17), we have used I^r_{22} to denote the $(2,2)$ r-mode overlap. For Newtonian NS, I^r_{22} is given by

$$I^r_{22} = \sqrt{\frac{1}{m_1R_1^4}\int_0^{R_1}\rho r^6 dr}. \tag{6.18}$$

This is an analog of the tidal Love number for f-mode.

In Eq. (6.17), ψ_1 is treated as a constant, because for a typical BNS system, this angle changes on a timescale of $\sim$ 70 s, which is much longer than the duration of resonance ($\sim$ 0.52 s) and the time to the merger ($\sim$ 4 s); see Sec. 6.9 for more details.

From Eq. (6.17), we can obtain the resonant condition in terms of orbital frequency $\dot{\phi}_r$

$$\dot{\phi}_r = 2\Omega_{s1} + \omega_{22} = \frac{4}{3}\Omega_{s1}, \tag{6.19}$$

where we have used Eq. (6.13) to replace the mode frequency by spin frequency. Note that the driving force is porportional to $\sim \sin\psi_1\cos^2\psi_1/2$, therefore no r-mode DT takes place for $\psi_1 = 0, \pi$, when spins are aligned or anti-aligned with the orbital angular momentum.

6.3.3 Gravitomagnetic coupling: orbital part

Let us now use the standard osculating equations to study the orbital evolution. Assume that there is a perturbing force $\boldsymbol{F}$ on the Newtonian binary system, which takes the form of

$$\frac{\boldsymbol{F}}{\mu} = \mathcal{S}\boldsymbol{\lambda}, \tag{6.20}$$

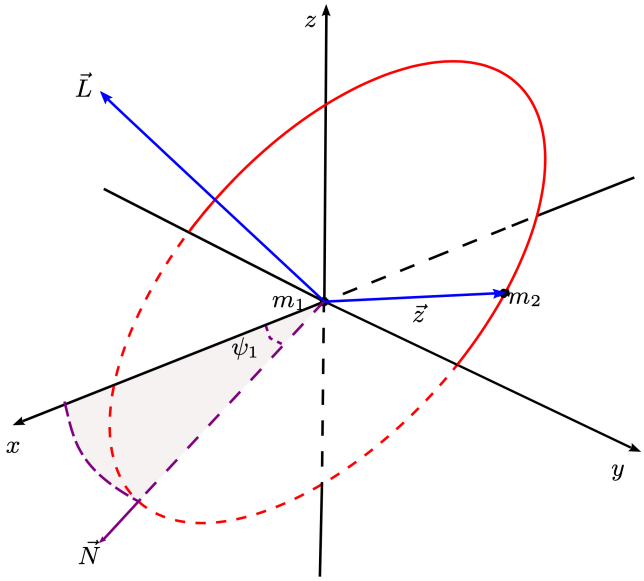

Figure 6.2: A co-moving coordinate system (x, y, z) that centers at m_1. The companion NS m_2 orbits around m_1, whose orbital plane intersects with the $x-z$ plane at $\vec{N}$, and intersects with the $x-y$ plane at the y-axis. The orbital phase $\phi(t)$ is the angle between $\vec{N}$ and the location of m_2, $\vec{z}$. The orbital angular momentum $\vec{L}$ is in the $x-z$ plane, with polar angle ψ_1.

where μ is the reduced mass, and $\boldsymbol{\lambda}$ is the unit azimuthal vector in the orbital plane. The evolution of orbital separation $D(t)$ is given by [85]

$$\frac{dD}{dt} = 2\sqrt{\frac{D^3}{M}}\mathcal{S}. \tag{6.21}$$

In our case, $\mathcal{S}$ contains two parts. The first one is the back-reaction force due to GW radiation, given by the averaged (over orbital timescale) Burke-Thorne dissipation term [85]:

$$\mathcal{S}_{\rm GW} = -\frac{32}{5}\eta\left(\frac{M}{D}\right)^3\sqrt{\frac{M}{D^3}}. \tag{6.22}$$

The other part is the stellar induced force. The current quadrupole moment J_{ij} induced by the r-mode (to the linear order in $\boldsymbol{\xi}_{22}$) is given by[3] [72]

$$J_{ij} \sim I^r_{22} m_1 R_1^3 \omega_{22} e^{-2i\Omega_{s1}t} c_{22} + c.c., \tag{6.23}$$

leading to an azimuthal acceleration $\mathcal{S}_{\rm tide}$ [83]

$$\mathcal{S}_{\rm tide} = \frac{8}{3}\sqrt{\frac{\pi}{5}} I^r_{22}\frac{\Omega_{s1}(\omega_{22}+2\Omega_{s1})}{D^3} M R_1^3 \sin\psi_1 \cos^2\frac{\psi_1}{2} \times 2\Re(-ie^{i\phi-2i\Omega_s t}c_{22}). \tag{6.24}$$

[3] This is different from the f-mode dynamical tides, where the leading term is mass quadrupole moment.

The total acceleration is given by

$$\mathcal{S} = \mathcal{S}_{\rm tide} + \mathcal{S}_{\rm GW}. \tag{6.25}$$

Note that the current quadrupole moment also induces forces along the radial axis, and along the axis of orbital angular momentum. These will lead to the evolution in orbital eccentricity and semi-latus rectum. However, as argued in Ref. [72], these effects are negligible, and the orbit keeps quasicircular within the entire evolution process. We have also confirmed this numerically. Here we do not include those effects.

So far we have only considered the r-mode of m_1. The resonance for m_2 can be treated by a direct replacement $(1 \leftrightarrow 2)$. Since we only consider the $(2,2)$ r-mode in the two stars, henceforth we will drop the labels of (l,m), and add a new subscript to refer to individual star. For example, I_1^r and ω_1 stand for the r-mode overlap and frequency of m_1, respectively.

Combining Eqs. (6.17), (6.21), (6.22) and (6.24), we finally arrive at a complete set of EOM for the binary system

$$\frac{d\phi}{dt} = \sqrt{\frac{M}{D^3}}, \tag{6.26a}$$

$$\begin{aligned}\frac{dD}{dt} =& -\frac{64}{5}\eta\left(\frac{M}{D}\right)^3 + \frac{16}{3}\sqrt{\frac{\pi}{5}}I_1^r\frac{\Omega_{s1}(\omega_1+2\Omega_{s1})}{D^{3/2}}M^{1/2}R_1^3 \\ &\times 2\sin\psi_1\cos^2\frac{\psi_1}{2}\Re(-ie^{i\phi-2i\Omega_{s1}t}c_1) \\ &+ \frac{32}{3}\sqrt{\frac{\pi}{5}}I_2^r\frac{\Omega_{s2}(\omega_2+2\Omega_{s2})}{D^{3/2}}M^{1/2}R_2^3\sin\psi_2\cos^2\frac{\psi_2}{2}\Re(-ie^{i\phi-2i\Omega_{s2}t}c_2),\end{aligned} \tag{6.26b}$$

$$\dot{c}_1 = -i\omega_1 c_1 + \frac{i}{\omega_1}\sqrt{\frac{16\pi}{5}}\frac{I_1^r m_2 R_1}{D^2}\dot{\phi}(\dot{\phi}-2\Omega_{s1})\sin\psi_1\cos^2\frac{\psi_1}{2}e^{2i\Omega_{s1}t-i\phi}, \tag{6.26c}$$

$$\dot{c}_2 = -i\omega_2 c_2 + \frac{i}{\omega_2}\sqrt{\frac{16\pi}{5}}\frac{I_2^r m_1 R_2}{D^2}\dot{\phi}(\dot{\phi}-2\Omega_{s2})\sin\psi_2\cos^2\frac{\psi_2}{2}e^{2i\Omega_{s2}t-i\phi}. \tag{6.26d}$$

By simultaneously integrating stellar and orbital parts, we can obtain the evolution of the system, and the gravitational waves it emits.

6.4 Dynamics of r-mode excitation

In this section, we discuss features of r-mode excitation and its back action onto orbital motion. In Sec. 6.4.1, we first cast equations of motion Eqs. (6.26) into

forms that only depend on independent parameters, and provide the appropriate initial conditions. In Sec. 6.4.2, we analytically describe orbital motion across tidal resonance, and compare it with the results in FR07. In Sec. 6.4.3, we provide analytical formulas for tidal excitation.

6.4.1 Equation of motion

Although Eqs. (6.26) are complete, and can be integrated straightforwardly, it is difficult to see the actual dependence of solutions on specific parameters. For example, it is well known that the inspiraling process of a binary system is controlled by the chirp mass $\mathcal{M} = M\eta^{3/5}$ at the leading order, since the direct observable is GW phase as a function of frequency. However both the total mass M and the symmetric mass ratio η appears in equations. The degeneracy between them is hidden. This problem can be fixed by rescaling parameters in the following way:

$$c_1 = \bar{c}_1 \frac{I_1^r m_2 R_1}{\omega_1 M^{2/3}} \sin\psi_1 \cos^2\frac{\psi_1}{2}, \tag{6.27}$$

$$c_2 = \bar{c}_2 \frac{I_2^r m_1 R_2}{\omega_2 M^{2/3}} \sin\psi_2 \cos^2\frac{\psi_2}{2}, \tag{6.28}$$

and replace separation D by orbital frequency $\dot{\phi}$. In terms of these new parameters, the equations of motion become:

$$\begin{aligned}\frac{d\dot{\phi}}{dt} &= \frac{96}{5}\mathcal{M}^{5/3}\dot{\phi}^{11/3} + 32\sqrt{\frac{\pi}{5}}\mathcal{I}_1\Omega_{s1}\dot{\phi}^{8/3}\Re(-ie^{i\phi-2i\Omega_{s1}t}\bar{c}_1) \\ &+ 32\sqrt{\frac{\pi}{5}}\mathcal{I}_2\Omega_{s2}\dot{\phi}^{8/3}\Re(-ie^{i\phi-2i\Omega_{s2}t}\bar{c}_2),\end{aligned} \tag{6.29a}$$

$$\dot{\bar{c}}_1 - \frac{2}{3}i\Omega_{s1}\bar{c}_1 = i\sqrt{\frac{16\pi}{5}}(\dot{\phi} - 2\Omega_{s1})\dot{\phi}^{7/3}e^{2i\Omega_{s1}t-i\phi}, \tag{6.29b}$$

$$\dot{\bar{c}}_2 - \frac{2}{3}i\Omega_{s2}\bar{c}_2 = i\sqrt{\frac{16\pi}{5}}(\dot{\phi} - 2\Omega_{s2})\dot{\phi}^{7/3}e^{2i\Omega_{s2}t-i\phi}. \tag{6.29c}$$

Here we have defined the r-mode coupling coefficient for each individual NS as :

$$\mathcal{I}_i = \bar{I}_i^{r2} m_i^4 \sin^2\psi_i \cos^4\frac{\psi_i}{2}\left(1 - \frac{m_i}{M}\right), \tag{6.30}$$

with the normalized r-mode overlap $\bar{I}^r$ defined by

$$\bar{I}^r = \sqrt{\frac{1}{m_{\rm NS}^5}\int_0^{R_{\rm NS}} \rho r^6 dr}, \tag{6.31}$$

where $m_{\rm NS}$ and $R_{\rm NS}$ are the mass and the radius of the NS. In Eqs. (6.29), $\mathcal{I}_i$ characterizes the tidal backreaction of NS i onto the orbit. Note that $\mathcal{I}$ (the effect of r-mode DT) vanishes when $\psi = 0, \pi$, and its maximized when $\psi = \pi/3$.

Initial conditions for Eqs. (6.29) are chosen such that the orbit is quasicircular and tides are in equilibrium:

$$\begin{aligned}
&\dot{\phi}^{(0)} = 2\pi F_0, \quad \phi^{(0)} = 0,\\
&\bar{c}_1^{(0)} = (2\pi F_0)^{4/3}\sqrt{\frac{16\pi}{5}}\frac{(2\pi F_0)^2 - 4\Omega_{s1}\pi F_0}{\frac{4}{3}\Omega_{s1} - 2\pi F_0},\\
&\bar{c}_2^{(0)} = (2\pi F_0)^{4/3}\sqrt{\frac{16\pi}{5}}\frac{(2\pi F_0)^2 - 4\Omega_{s2}\pi F_0}{\frac{4}{3}\Omega_{s2} - 2\pi F_0}.
\end{aligned}$$

Written in this way, the EOM (as well as initial conditions) depend on five parameters of the binary system: $\mathcal{M}$, $\mathcal{I}_i$, Ω_{si}, with $i = 1, 2$.

In the rest of this section, we shall numerically integrate the EOM and discuss features of solutions. For example, we choose a $(1.4, 1.4)M_\odot$ BNS system, with one of the stars spinning at frequency $\Omega_{s1} = 2\pi \times 30$Hz, and the other one non-spinning. We choose an inclination angle ψ_1 of $\pi/3$. The EoS is polytopic with $\Gamma = 2$, and the radii of both stars are chosen to be $R_{\rm NS} = 13$km. This gives the r-mode overlap of $I_1^r = 0.185$. There is only one resonance during the inspiral whose resonant orbital frequency is given by

$$\dot{\phi}(t_r) = \frac{4}{3}\Omega_s = 2\pi \times 40 \text{ Hz}. \tag{6.32}$$

We set an initial orbital frequency F_0 as 4.5 Hz, and evolve the system up to the contact separation of $r^{\rm stop} = 2R_{\rm NS}$.

6.4.2 Orbital evolution

As argued in FR07, the pre- and post-resonance orbit can be well approximated as two point-particle (PP) orbits, with orbital phase given by

$$\phi^{(\rm ana)}(t) = \begin{cases} \phi_{\rm PP}^{(\rm pre)}(t), & \text{if } t < t_r \\ \phi_{\rm PP}^{(\rm post)}(t), & \text{if } t > t_r \end{cases}, \tag{6.33}$$

Both $\phi^{(\rm post,pre)}(t)$ evolve without being affected by tides, following the *same equation*:

$$\frac{d}{dt}\dot{\phi}^{(\rm post,pre)} = \frac{96}{5}\mathcal{M}^{5/3}\left[\dot{\phi}^{(\rm post,pre)}\right]^{11/3}. \tag{6.34}$$

The initial condition for pre-resonance orbit is simply (the same as the one we used for numerical integration)

$$\phi^{(\rm pre)}(t = 0) = 0\,, \quad \dot{\phi}^{(\rm pre)}(t = 0) = 2\pi F_0, \tag{6.35}$$

the resonance orbital frequency is given by

$$\dot{\phi}_{\rm PP}^{\rm (pre)}(t_r) = \frac{4}{3}\Omega_{s1}\,. \tag{6.36}$$

At resonance, $\phi_{\rm PP}^{\rm (post)}(t_r)$ is related to $\phi_{\rm PP}^{\rm (pre)}(t_r)$ with continuity in value and a jump in derivative, and one can write

$$\phi_{\rm PP}^{\rm post}(t_r) = \phi_{\rm PP}^{\rm pre}(t_r), \tag{6.37}$$

$$\Delta\dot{\phi}_{\rm tid} = \dot{\phi}_{\rm PP}^{\rm (post)}(t_r) - \dot{\phi}_{\rm PP}^{\rm (pre)}(t_r) = \ddot{\phi}_{\rm PP}^{\rm (pre)}(t_r)\delta t_r. \tag{6.38}$$

In fact, Eqs. (6.37) and (6.38) can be grouped into a compact form [cf. Eq. (1.6) in FR07]

$$\phi_{\rm PP}^{\rm post}(t) = \phi_{\rm PP}^{\rm pre}(t + \delta t_r) - \delta\phi_r, \tag{6.39}$$

with [cf. Eq. (5.37) in FR07]

$$\begin{aligned}\delta t_r &= -\frac{5\pi^2}{192}\left(\frac{4}{3}\right)^{-1/3}\frac{\Omega_{s1}^{-1/3}}{\mathcal{M}^{10/3}}\mathcal{I}_1 \\ &= -2.64\times10^{-4}\ {\rm s}\left(\frac{\Omega_{s1}}{2\pi\times30\ {\rm Hz}}\right)^{-1/3}\left(\frac{\sin^2\psi_1\cos^4\psi_1/2}{0.422}\right) \\ &\times\left(\frac{m_1}{1.4\ M_\odot}\right)^3\left(\frac{M}{2.8\ M_\odot}\right)^{-7/3}\left(\frac{\eta}{0.25}\right)^{-1}\left(\frac{\bar{I}_1^r}{7.32}\right)^2.\end{aligned} \tag{6.40a}$$

$$\begin{aligned}\delta\phi_r &= \dot{\phi}(t_r)\delta t_r = -\frac{5\pi^2}{192}\left(\frac{4}{3}\right)^{2/3}\frac{\Omega_{s1}^{2/3}}{\mathcal{M}^{10/3}}\mathcal{I}_1 \\ &= -6.65\times10^{-2}\ {\rm rad}\left(\frac{\Omega_{s1}}{2\pi\times30\ {\rm Hz}}\right)^{2/3}\left(\frac{\sin^2\psi_1\cos^4\psi_1/2}{0.422}\right) \\ &\times\left(\frac{m_1}{1.4\ M_\odot}\right)^3\left(\frac{M}{2.8\ M_\odot}\right)^{-7/3}\left(\frac{\eta}{0.25}\right)^{-1}\left(\frac{\bar{I}_1^r}{7.32}\right)^2,\end{aligned} \tag{6.40b}$$

Here δt_r and $\delta\phi_r$ are effective orbital time and phase shifts between the pre- and post-resonance PP orbits.

Note that $\Delta\dot{\phi}_{\rm tid} < 0$, and $\dot{\phi}_{\rm PP}^{\rm (post)}(t_r) < \dot{\phi}_{\rm PP}^{\rm (pre)}(t_r)$, the resonance transfers the energy from star to orbit, which is different from the case for f-mode (cf. Fig. 8 in Ref. [53]). This can be understood by the relation [71, 72]

$$\begin{aligned}\Delta E_{\rm star} &= \frac{E_{\rm mode}}{\omega_{lm}}(\omega_{lm} + m\Omega_{s1}) \\ &= -9.9\times10^{46}\ {\rm erg}\left(\frac{\Omega_{s1}}{2\pi\times30\ {\rm Hz}}\right)^3\left(\frac{\bar{I}_1^r}{7.32}\right)^2\left(\frac{m_1}{1.4M_\odot}\right)^4\end{aligned}$$

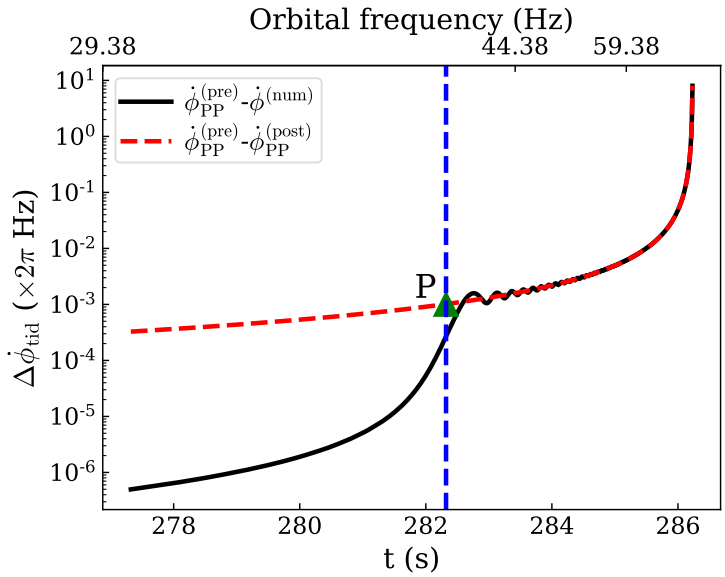

Figure 6.3: The orbital dynamics near the r-mode resonance. The BNS system has individual masses $(1.4, 1.4)M_\odot$. One of them spins at $\Omega_{s1} = 30$Hz with the inclination angle $\psi_1 = \pi/3$, whereas the other one is non-spinning. The EoS is $\Gamma = 2$ polytrope with radius $R_{\rm NS} = 13$km. The vertical dashed line represents for the time of resonance t_r. The pre-resonance PP orbit $\dot{\phi}_{\rm PP}^{\rm (pre)}(t)$, which has the same initial condition as the numerical one, is compared with the numerical integration, as shown by black curve. Before the resonance, $|\Delta\dot{\phi}_{\rm tid}|$ is below $\sim 2\pi \times 10^{-4}$ Hz, which is mainly caused by the adiabatic r-mode. After the resonance, there are some oscillatory features, which are from the r-mode oscillation. Eq. (6.38) gives the new orbital frequency after the r-mode is excited, which is labeled by "P" in the figure. Using "P" as a new initial condition, we obtain the other PP orbit $\dot{\phi}_{\rm PP}^{\rm (post)}(t)$. The difference between $\dot{\phi}_{\rm PP}^{\rm (pre)}(t)$ and $\dot{\phi}_{\rm PP}^{\rm (post)}(t)$ is shown as red dashed line, which tracks the averaged numerical result very well.

$$\times \left(\frac{\sin^2\psi_1 \cos^4\psi_1/2}{0.422}\right)\left(\frac{1-\Xi}{0.5}\right), \tag{6.41}$$

where $E_{\rm mode} = b_{lm}\omega_{lm}|c_{lm}|^2 > 0$, and $\Delta E_{\rm star}$ is the change of stellar energy. Therefore, for any mode that is subjected to the Chandrasekhar-Friedman-Schutz instability condition [86, 87]

$$\omega_{lm}(\omega_{lm} + m\Omega_{s1}) < 0, \tag{6.42}$$

the tidal excitation leads to the loss of stellar energy, and the decrease of spin frequency.[4] For completeness, the angular momentum transfer can be written as

$$\Delta L_{\rm star} = \frac{E_{\rm mode}}{\omega_{lm}} = -3.9\times10^{44}\ erg\cdot s\left(\frac{\Omega_{s1}}{2\pi\times 30\ {\rm Hz}}\right)^2\left(\frac{\bar{I}_1^r}{7.32}\right)^2\left(\frac{m_1}{1.4M_\odot}\right)^4 \times\left(\frac{\sin^2\psi_1\cos^4\psi_1/2}{0.422}\right)\left(\frac{1-\Xi}{0.5}\right), \tag{6.43}$$

and the change of spin frequency is given by

$$\Delta\Omega_s = -2\pi\times3.6\times10^{-2}\ {\rm Hz}\left(\frac{\Omega_{s1}}{2\pi\times 30\ {\rm Hz}}\right)^2\left(\frac{\bar{I}_1^r}{7.32}\right)^2 \times\left(\frac{m_1}{1.4M_\odot}\right)^4\left(\frac{\sin^2\psi_1\cos^4\psi_1/2}{0.422}\right)\left(\frac{1-\Xi}{0.5}\right)\left(\frac{\bar{I}}{14.6}\right)^{-1}, \tag{6.44}$$

which is negligible in our study.

Using the binary system above, we first investigate how the numerical integration of the EOM deviates from $\dot{\phi}_{\rm PP}^{\rm (pre)}(t)$. In Fig. 6.3, we plot $\dot{\phi}_{\rm PP}^{\rm (pre)}(t)-\dot{\phi}^{\rm (num)}(t)$ in the black line. The vertical, blue-dashed line stands for the time of resonance. In the pre-resonance regime $t<t_r$, $|\Delta\dot{\phi}_{\rm tid}|<2\pi\times10^{-4}$ Hz, and is mainly contributed by the adiabatic tide. During the resonance, $|\Delta\dot{\phi}_{\rm tid}|$ quickly grows to $2\pi\times10^{-3}$ Hz. Then in the post-resonance regime, there is a small oscillation on the top of major deviation, which is caused by the r-mode oscillation. We also saw this feature in the case of f-mode [53]. Note that $\dot{\phi}^{\rm (num)}\sim 2\pi\times10^2-2\pi\times10^3$ Hz for the time interval we present, the deviation caused by the resonance is extremely small.

Eqs. (6.40) show that typical values for $\delta\phi_r$ and δt_r are -6.65×10^{-2} rad and -2.64×10^{-4} s, respectively. The induced change in orbital frequency $|\Delta\dot{\phi}_{\rm tid}(t_r)|$ is $2\pi\times10^{-3}$ Hz, which corresponds to "P" in Fig. 6.3. With "P" as a new initial condition, we obtain $\dot{\phi}_{\rm PP}^{\rm (post)}(t)$ by solving Eq. (6.34). In Fig. 6.3, we show $\dot{\phi}_{\rm PP}^{\rm (pre)}(t)-\dot{\phi}_{\rm PP}^{\rm (post)}(t)$ as red dashed line. We can see $\dot{\phi}_{\rm PP}^{\rm (post)}(t)$ tracks the averaged $\dot{\phi}^{\rm (num)}(t)$ well in the post-resonance regime.

6.4.3 Tidal evolution

Let us move on to the stellar part. Following the procedure in Sec. III of Ref. [53], we define two real-valued quadratures, A and B, from the r-mode amplitude,

$$A+iB=\bar{c}_1 e^{i\phi-im\Omega_{s1}t}\quad\text{and}\quad m=2, \tag{6.45}$$

[4] For a given baryon number and total angular momentum, uniform angular velocity is the minimum-energy state [88, 89].

with A determining the radial force, and B the torque back-reacting onto the orbit, respectively. Here $m = 2$ since we are focusing on the $(l = 2, m = 2)$ mode. Using integration by parts, we obtain analytic expressions of A and B as

$$A = -\dot{\phi}^{7/3}\sqrt{\frac{16\pi}{5}}\frac{(2\Omega_{s1}-\dot{\phi})}{-\dot{\phi}+\frac{4}{3}\Omega_{s1}} + \frac{\dot{\phi}_r^{10/3}}{\sqrt{\dot{\Omega}_r}}\sqrt{\frac{4\pi}{5}}\left[\sqrt{\pi}FC\left(\frac{\hat{t}}{\sqrt{\pi}}\right)\sin\Theta + \sqrt{\frac{\pi}{2}}\sin\left(\Theta-\frac{\pi}{4}\right)\right.$$
$$\left. - \sqrt{\pi}FS\left(\frac{\hat{t}}{\sqrt{\pi}}\right)\cos\Theta - \frac{\cos(\Theta-\frac{1}{2}\hat{t}^2)}{\hat{t}}\right], \tag{6.46a}$$

$$B = -\frac{\dot{\phi}_r^{10/3}}{\sqrt{\dot{\Omega}_r}}\sqrt{\frac{4\pi}{5}}\left[\sqrt{\pi}FC\left(\frac{\hat{t}}{\sqrt{\pi}}\right)\cos\Theta + \sqrt{\frac{\pi}{2}}\cos\left(\Theta-\frac{\pi}{4}\right)\right.$$
$$\left. + \sqrt{\pi}FS\left(\frac{\hat{t}}{\sqrt{\pi}}\right)\sin\Theta + \frac{\sin(\Theta-\frac{1}{2}\hat{t}^2)}{\hat{t}}\right]. \tag{6.46b}$$

where [Eq. (6.34)]

$$\frac{1}{\dot{\Omega}_r^{1/2}} = \left[\frac{96}{5}\mathcal{M}^{5/3}\left(\frac{4}{3}\Omega_{s1}\right)^{11/3}\right]^{-1/2} = 0.2\ \mathrm{s}\left(\frac{\mathcal{M}}{1.22\ M_\odot}\right)^{-5/6}\left(\frac{\Omega_{s1}}{2\pi\times 30\ \mathrm{Hz}}\right)^{-11/6}. \tag{6.47}$$

The phases of A and B in the post-resonance regime are controlled by two quantities,

$$\Theta = \chi_r - \omega_1 t + \phi - 2\Omega_{s1}t, \tag{6.48a}$$

$$\hat{t} = \sqrt{\dot{\Omega}_r}(t - t_r), \tag{6.48b}$$

with the constant defined by $\chi_r = \omega_1 t_r - \phi_r + 2\Omega_{s1}t_r$, which results in $\Theta_r = 0$ on resonance. Note that $1/\sqrt{\dot{\Omega}_r} \sim 0.2$ s in Eq. (6.48b) is the duration of tidal excitation, which is much longer than the effective orbital time shift $\delta t_r \sim 10^{-4}$ s induced by tide [Eq. (6.40a)].

In Fig. 6.4, we compare Eqs. (6.46) with numerical integration, for the same binary system mentioned above. We can see that our formulas are accurate in all regimes: adiabatic, resonance, and post-resonance. The evolutions of A and B are similar to those of f-mode [53], except the fact that A increases toward infinity as the two stars become close to each other (recall that the amplitude of A for f-mode remains constant after the resonance.) This can be easily understood from Eq. (6.46a). The first line of Eq. (6.46a), i.e, the adiabatic part, diverges as $\dot{\phi}^{7/3}$ when $\dot{\phi} \to \infty$. On the other hand, the term remains ~ 1 for f-mode, which stays constant as two stars contact. In spite of the diverging feature of r-mode in the late time evolution, our

numerical calculation shows that it does not lead to any detectable effect (for 3G detectors).

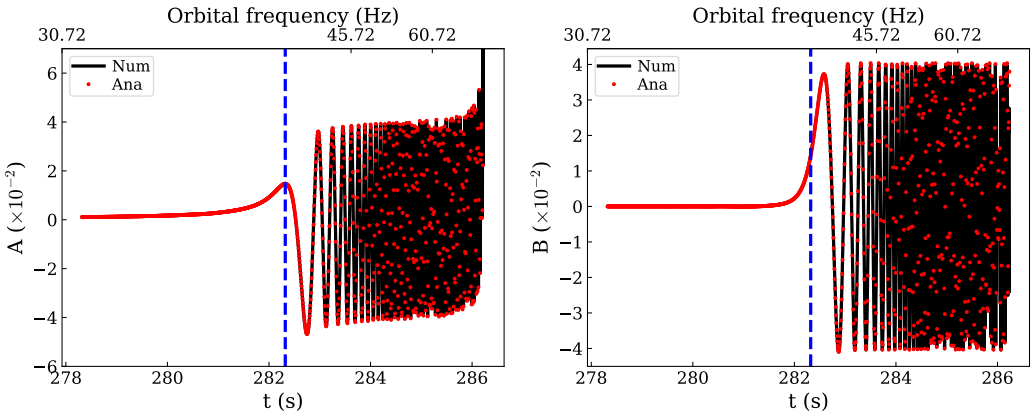

Figure 6.4: Time evolution of r-mode amplitudes, A (upper panel) and B (lower panel). Black curves are from the numerical integration of Eqs. (6.29), and red dots are from our analytic approximations in Eqs. (6.46). The vertical dashed line is the time of resonance from numerical simulation. Our analytic results agree with numerical ones to high accuracies. Unlike f-mode, the variable A diverges as two NSs become close to each other, this is caused by differences in adiabatic tide. [see first line of Eq. (6.46a)].

6.5 Rossby-mode overlaps for different equations of state: A new universal relation

In the last section, we have seen that the effect of r-mode enters into the EOM through the normalized overlap $\bar{I}^r$. Here we shall identify a new universal relation between $\bar{I}^r$ and the tidal Love number λ_f. We consider five realistic EoS for cold NSs: APR [90], FPS [91], GM1 [92, 93], QHC19 [94–96], SLY [93], which are shown in Fig. 6.5. Among them, the data of FPS are from Ref. [97] and the rest of them are obtained from a EoS database CompOSE [98]. For comparison, we also include a polytropic EoS with $P \propto \rho^\Gamma$ and $\Gamma = 2$. The mass-radius relations from those EoS are shown in Fig. 6.6.

In Sec. 6.5.1, we first calculate $\bar{I}^r$ by solving Tolman–Oppenheimer–Volkoff (TOV) equations. Then in Sec. 6.5.2, we explore the universal relation between I^r and λ_f.

6.5.1 The calculation of I^r

We calculate I^r at the zeroth order, i.e., using an unperturbed NS with spherical symmetry. Its metric is given by

$$ds^2 = -e^\nu dt^2 + e^\lambda dr^2 + r^2(d\theta^2 + \sin^2\theta d\phi^2), \tag{6.49}$$

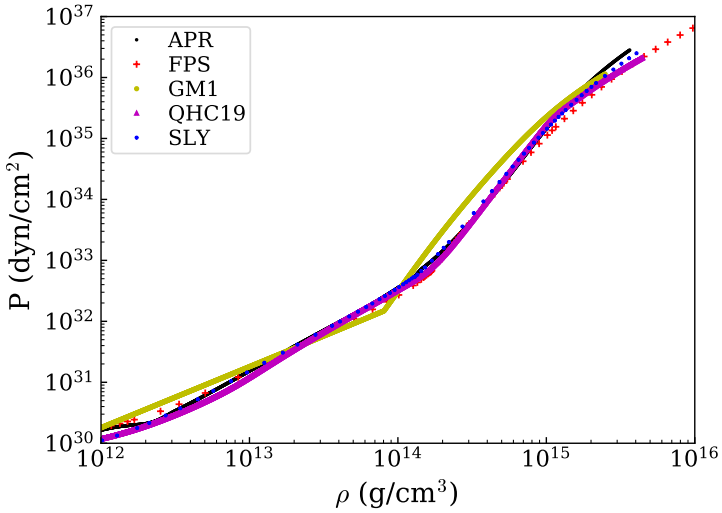

Figure 6.5: Several EoS for NSs used in this chapter.

we can obtain the density profile $\rho(r)$ by solving the TOV equations (see Sec. 6.10 for more details). We then perform a numerical integration to get I^r based on its definition in Eq. (6.18). $\bar{I}^r$ is related to I^r by

$$I^r = \bar{I}^r C^2, \tag{6.50}$$

where C is the compactness of the NS

$$C = \frac{m_{\rm NS}}{R_{\rm NS}}. \tag{6.51}$$

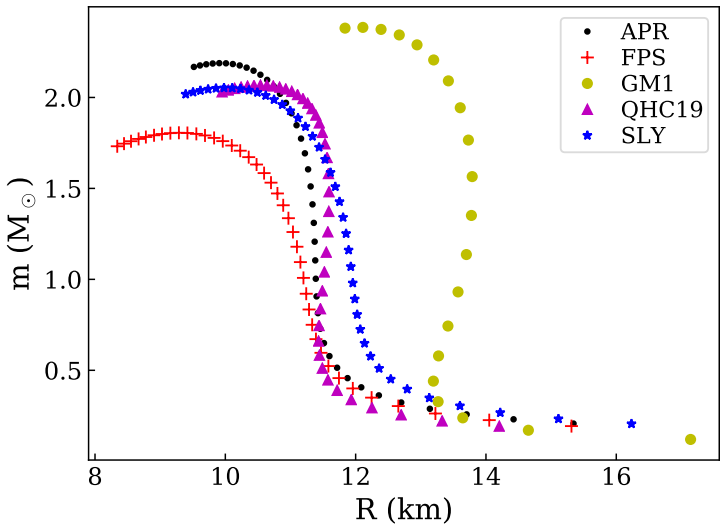

Figure 6.6: NS mass-radius relation with different EoS.

6.5.2 Universal relations

To establish the universal relation between the tidal Love number and the moment of inertia, Yagi *et al.* [77, 78] normalized the tidal Love number λ_f and the moment of inertia I as: $\bar{\lambda}_f = \lambda_f / m_{\rm NS}^5$ and $\bar{I} = I/m_{\rm NS}^3$ (The calculation of $\bar{\lambda}_f$ is summarized in Sec. 6.11.). Universal relation between λ_f and $\bar{I}$ are shown in the left panel of Fig. 6.7.

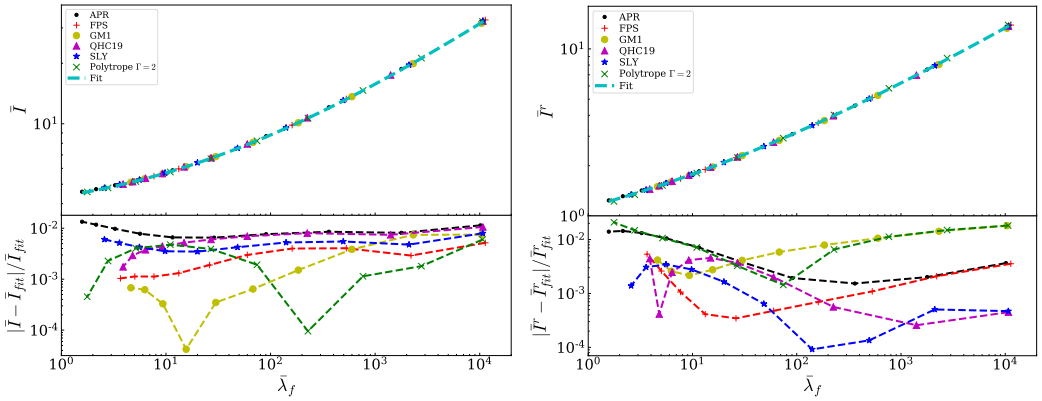

Figure 6.7: The I-Love and $\bar{I}^r$-Love universal relations for several EoS, as well as the fitting formulae in Eq. (6.52). The bottom two plots are fractional errors between true values and fitted results; errors of both relations are within 10^{-2} for $\bar{\lambda}_f$ ranging from $O(1)$ to $O(10^4)$.

Similarly, we plot $\bar{I}^r$ as functions of $\bar{\lambda}_f$ for various EoS in the right panel of Fig. 6.7. We can see that their relation is also insensitive to EoS. Same as Yagi *et al.*, we fit the relation with a polynomial on a log-log scale

$$\log y = a + b \log \bar{\lambda}_f + c(\log \bar{\lambda}_f)^2 + d(\log \bar{\lambda}_f)^3 + e(\log \bar{\lambda}_f)^4, \tag{6.52}$$

where $y = \bar{I}^r$ or $\bar{I}$. Results are shown in Table 6.4, where we also list the I-Love relation for comparison. In Fig. 6.7 we compare fitted results with true values. We can see that relative errors for both relations are similar and within 10^{-2}.

Note that although the profile of ρ comes from the solution of Einstein's equation (i.e., TOV equations), our definition of $\bar{I}^r$ in Eq. (6.31) still used a Newtonian model of the NS, and post-Newtonian equations for the gravitomagnetic coupling. We conjecture that a universal relation will still exist after relativistic corrections are made, but we anticipate systematic corrections to the form of the relation.

6.6 Gravitational waves

This section focuses on gravitational waves emitted by binaries that contain at least one spinning NS with r-mode resonance. In Sec. 6.6.1, we construct a hybrid

Table 6.4: Coefficients for the fitting formulae of the NS I-Love and $\bar{I}^r$-Love relations.

y	a	b	c	d	e
$\bar{I}^r$	0.121	0.169	1.25×10^{-2}	-9.38×10^{-5}	-1.92×10^{-5}
$\bar{I}$	1.47	8.17×10^{-2}	1.49×10^{-2}	2.87×10^{-4}	-3.64×10^{-5}

waveform model that incorporates both r-mode and PN effects. In Sec. 6.6.2, we compare Flanagan and Racine's analytical formula for r-mode-resonance-induced GW phase with numerical results.

6.6.1 A hybrid PN-r-mode waveform model

Once we obtain the orbital evolution from the EOM, we can extract numerical GW waveform through the (mass) quadrupole formula [85]

$$h(t) = \frac{1}{D_L}(\ddot{Q}_{xx} - \ddot{Q}_{yy}), \tag{6.53}$$

where D_L is the distance between the detector and the source. Here we assume the BNS is optimally oriented for the plus polarization. The quadrupole moment of the system is given by

$$Q_{ij} = \mu(x_i x_j - r^2\delta_{ij}/3), \tag{6.54}$$

where only the orbital part is included, because r-mode does not induce additional mass quadrupole moment[5].

It is usually convenient to analyze data in the frequency domain (FD). Following Ref. [53], we first sample the numerical $h(t)$ in the time domain with a rate of 8192 Hz, and then use the fast Fourier Transform algorithm to transform the data to FD. Finally, we select data in the frequency band $[2F_0, 2F_{\rm contact}]$. (Note that at the mass quadrupole order, GW freuqency is twice the orbital frequency.)

Our numerical FD waveform $\tilde{h}^{N+r}(f)$ contains the leading-order PP contribution as well as the effect of r-mode resonance; its phase Ψ_{N+r} can be written as

$$\Psi_{N+r} = \Psi_N + \Psi_r. \tag{6.55}$$

where Ψ_r is the phase induced by the r-mode resonance; and Ψ_N corresponds to the leading order of PP waveform. With the stationary phase approximation (SPA), Ψ_N

[5]R-mode does contribute to gravitational radiation through the current quadrupole moment [Eq. (6.23)]. However, it is 10^{-7} smaller than the orbital mass quadrupole moment, which is negligible in our case.

can be written as $\Psi_N = 2\pi f t_c - \phi_c + \frac{3}{128}(\pi \mathcal{M} f)^{-5/3}$, where t_c and ϕ_c are the time and GW phase of coalescence.

To incorporate other PN and (f-mode) tidal effects into the waveform, we introduce a phase correction within the SPA framework, writing

$$\tilde{h}(f) = \tilde{h}^{N+r}(f) e^{i\Psi_{\rm SPA}}. \tag{6.56}$$

The total phase of $\tilde{h}(f)$, $\Psi_{\rm tot}$, can be written as

$$\Psi_{\rm tot} = \Psi_N + \Psi_r + \Psi_{\rm SPA}\,, \tag{6.57}$$

with

$$\Psi_{\rm SPA} = \Psi_{\rm PP} + \Psi_{SO} + \Psi_{\bar{\lambda}_f^{(1)}} + \Psi_{\bar{\lambda}_f^{(2)}}\,. \tag{6.58}$$

Here $\Psi_{\rm PP}$ is the PN correction to the phase of non-spinning PP, up to 3.5PN[6] [99]; Ψ_{SO} is the spin-orbit coupling term [100–103]; and $\Psi_{\bar{\lambda}_f^{(1)}}$ and $\Psi_{\bar{\lambda}_f^{(2)}}$ are f-mode tidal effects from m_1 and m_2, respectively [104–106]. We have ignored the spin-spin coupling and the spin precession, because their effects are negligible (cf. Sec. 6.9). Expressions of phase terms are shown in Sec. 6.12.

Let us briefly review the parameter dependence of our waveforms. The Newtonian-plus-r-mode part of the waveform, $\tilde{h}^{N+r}$, depends on 8 independent parameters: chirp mass $\mathcal{M}$; two individual spin frequencies Ω_{si}; two individual r-mode coupling coefficients $\mathcal{I}_i$; luminosity distance, D_L; the coalescing time and phase, t_c and ϕ_c. The phase correction, $\Psi_{\rm SPA}$, depends on 5 additional parameters: mass ratio $\Xi = m_1/M$; the (anti-)symmetric tidal Love numbers $\bar{\lambda}_f^{s(a)} = (\bar{\lambda}_f^1 \pm \bar{\lambda}_f^2)/2$; the (anti-)symmetric dimensionless spin along the orbital angular momentum $\chi_{s(a)}^{(z)} = (\chi_1^{(z)} \pm \chi_2^{(z)})/2$. Here we use the normalized Love number (Sec. 6.5.2) because in this way it is more convenient to incorporate universal relations into the calculation.

6.6.2 Analytic model for Ψ_r

As discussed in Sec. 6.4.2, DTs only affect the orbital evolution significantly near the resonance. In the post-resonance regime, the orbit is well described by a PP orbit. Similarly, in the FD, resonance only leads to a phase shift $\delta\Phi_r$ and a time shift δt_r to the waveform, i.e., [72]

$$\Psi_r = (\delta\Phi_r - 2\pi f \delta t_r)\Theta(f - f_r), \tag{6.59}$$

[6] It excludes the leading-order contribution which is already contained in Ψ_N.

where the resonant GW frequency is given by [Eq. (6.19)]

$$f_r = \frac{\dot{\phi}_r}{\pi} = \frac{4}{3\pi}\Omega_{s1}. \tag{6.60}$$

The Heaviside step function $\Theta(f - f_r)$ is introduced here because there is no DT when $f < f_r$[7]. Using Eqs. (6.40b), (6.40a) and the relation

$$\delta\Phi_r = 2\delta\phi_r, \tag{6.61}$$

we obtain

$$\delta t_r = \frac{\delta\Phi_r}{2\pi f_r}, \tag{6.62}$$

we arrive at

$$\Psi_r = \left(1 - \frac{f}{f_r}\right)\delta\Phi_r\Theta(f - f_r). \tag{6.63}$$

We refer the interested reader to Appendix B in Ref. [45] for a strict derivation. In Fig. 6.8, we compare Eq. (6.63) with the numerical result, using the same BNS system as Fig. 6.3, except that $\Omega_{s1} = 80$ Hz. We can see that the phase difference induced by the r-mode, $\Psi_{\rm GW}^{\rm (num)} - \Psi_{\rm GW}^{\rm (pre)}$, agrees well with the expression of Ψ_r in Eq. (6.63). Here $\Psi_{\rm GW}^{\rm (num)}$ stands for the real GW phase, and $\Psi_{\rm GW}^{\rm (pre)}$ is the GW phase of the pre-resonance PP orbit (extending to the post-resonance regime).

The expression of Ψ_r results in

$$\frac{\partial\tilde{h}^{N+r}}{\partial\mathcal{I}} \sim \frac{\partial\tilde{h}^{N+r}}{\partial\delta\Phi_r} = i\left(1 - \frac{f}{f_r}\right)\Theta(f - f_r)\tilde{h}^{N+r}, \tag{6.64a}$$

$$\frac{\partial\tilde{h}^{N+r}}{\partial\Omega_s} \sim \frac{\partial\tilde{h}^{N+r}}{\partial f_r} + \frac{\partial\tilde{h}^{N+r}}{\partial\delta\Phi_r}\frac{\partial\delta\Phi_r}{\partial\Omega_{s1}} \sim \frac{f}{f_r^2}\delta\Phi_r\Theta(f - f_r)\tilde{h}^{N+r}, \tag{6.64b}$$

which are important to understand the result Fisher analysis, as we will discuss in the next section. In Eq. (6.64b), we have ignored the term $\partial\tilde{h}^{N+r}/\partial\delta\Phi_r$, because it is suppressed by the factor $(1 - f/f_r)$ when $f \sim f_r$.

With Eqs. (6.64), we can learn two things. First, $\partial\tilde{h}^{N+r}/\partial\delta\mathcal{I}$ is proportional to $(1 - f/f_r)$, which is close to 0 when $f \sim f_r$, so the constraint for $\mathcal{I}$ from GW detection is weaker than the one for Ω_s. Second, the constraint for $\mathcal{I}$ is independent from the magnitude of $\delta\Phi_r$ (or $\mathcal{I}$); while the constraint for Ω_s is proportional to $\delta\Phi_r^{-1} \sim \mathcal{I}^{-1}$ (see also Ref. [45]).

[7]Here we assume that the pre-resonance PP orbit is aligned with the true orbit, so the phase and time shifts appear after the resonance. It is also equivalent to align the post-resonance PP orbit with the real orbit. Then the Heaviside step function should be changed to $\Theta(f_r - f)$.

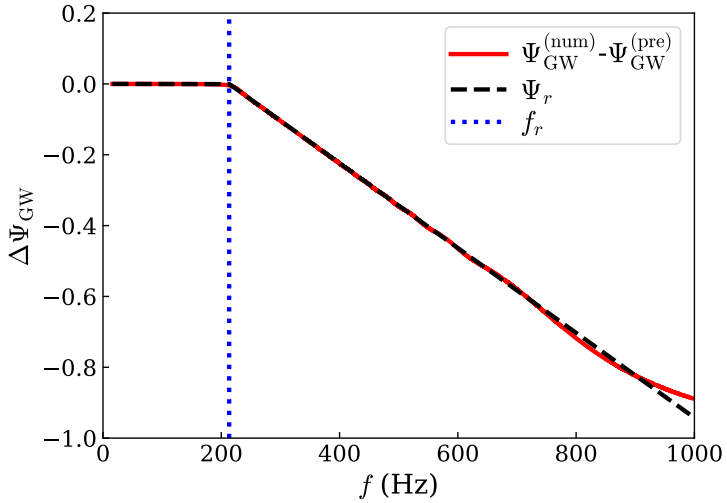

Figure 6.8: The GW phase difference induced by the r-mode DT versus GW frequency. It is compared with the expression of Ψ_r in Eq. (6.63). The BNS system is the same as the one we used in Fig. 6.3, except that $\Omega_{s1} = 80$ Hz.

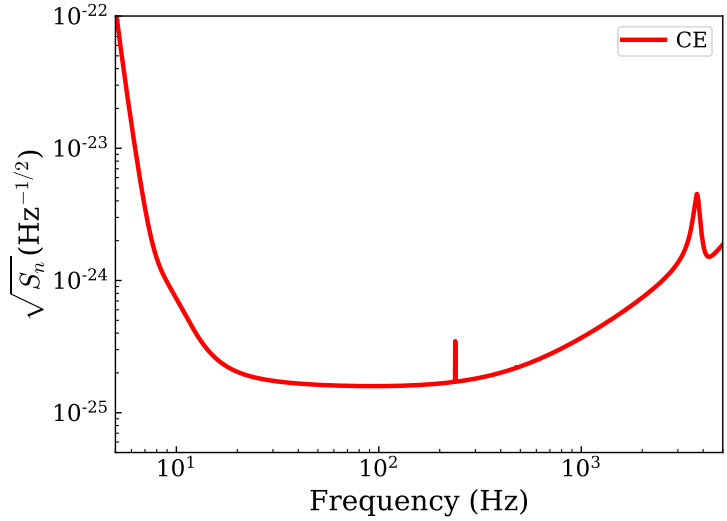

Figure 6.9: The noise spectral density of CE.

6.7 Constraints of parameters using r-mode dynamical tide

In this section, we discuss parameter estimation based on the hybrid PN-r-mode waveform obtained in Sec. 6.6.1.

6.7.1 Fisher-matrix formalism and signal strength

We shall do this by computing the Fisher information matrix, defined by

$$\Gamma_{ij} = \left(\frac{\partial h}{\partial \theta^i} \middle| \frac{\partial h}{\partial \theta^j} \right), \tag{6.65}$$

where θ^i are parameters of the waveform, and the derivative will be computed numerically. The inner product between two waveforms $(h|g)$ is defined as

$$(h|g) = 4\Re \int \frac{\tilde{h}^*(f)\tilde{g}(f)}{S_n(f)} df, \tag{6.66}$$

with the superscript $*$ standing for complex conjugation, and $S_n(f)$ the noise spectral density of the detector. By inverting the Fisher information matrix, we obtain projected constraints on θ^i as

$$\Delta\theta^i = \sqrt{(\Gamma^{-1})_{ii}}, \tag{6.67}$$

and the covariance between θ^i and θ^j is characterized by the off-diagonal term $(\Gamma^{-1})_{ij}$. In this section, we will mainly focus on the Cosmic Explorer (CE), whose $S_n(f)$ is shown in Fig. 6.9 [107].

To see the loudness of BNS signals, we choose a $(1.4, 1.35)M_\odot$ BNS system as an example, and plot the SNR of pre- and post-resonance signals as functions of spin frequency in Fig. 6.10. The system is assumed to be 100Mpc away and optimally oriented. Unless stated otherwise, our lower limit of GW frequency band is $2F_0 = 9$ Hz. We note that CE is also sensitive to the frequency below 9 Hz, yet it is computationally expensive to simulate the low-frequency evolution. We have checked that neglecting those signals does not lead to a significant change on parameter estimation if $\Omega_s \gtrsim 2\pi \times 10$ Hz (cf. Fig. 6.12). On the other hand, low-frequency signals are important if $\Omega_s < 3/4F_0 = 3.38$ Hz. Nonetheless, as we will show shortly, r-mode sector does not provide as strong constraints in that regime, hence that part of parameter space is not of our interest. Because the resonant orbital frequency is proportional to spin frequency, SNR of the pre-resonance signals increases with the spin frequency, and there is no pre-resonance signals when the spin frequency is below $3/4F_0 = 3.38$ Hz. For 10 Hz $\lesssim \Omega_s \lesssim$ 80 Hz, both the pre- and post-resonance signals are loud enough to be detected. Thus phase and time shift induced by the r-mode resonance (Sec. 6.6.2) can be extracted from the waveform, and can be used for parameter estimation. This is the foundation for our later discussions.

In the rest of this section, we use the same BNS system to explore the effect of r-mode resonance on parameter estimation. Since the sky location, the inclination between the orbital angular momentum and the line of sight, and the polarization angle are not of our interest, below we simply fix their values and consider Fisher matrices involving only the intrinsic parameters. We mainly consider three situations. In

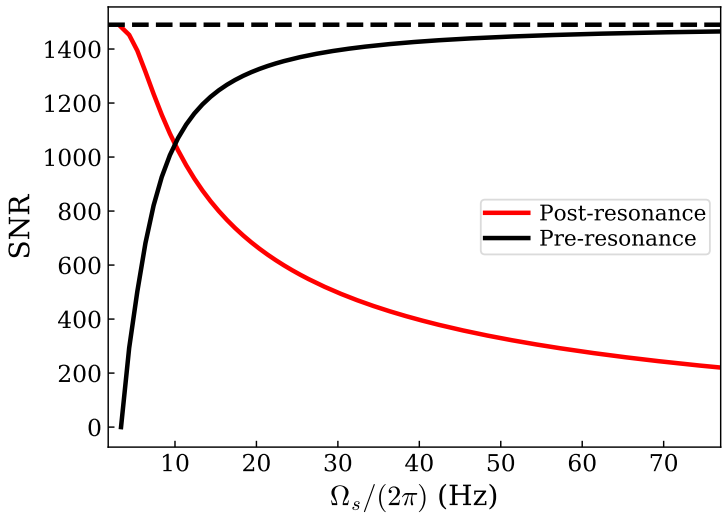

Figure 6.10: SNR of pre- and post-resonance GW signals as functions of spin frequency. The BNS system is $(1.4, 1.35)M_\odot$, optimally oriented at 100Mpc. EoS is GM1. As a comparison, the horizontal dash line is the SNR of the entire in-band signals. There is no pre-resonance signals when $3/4F_0 = 3.38$ Hz, because our frequency band starts from there. Recalling that the resonant orbital frequency is proportional to the spin frequency, then the SNR of pre-resonance signal increases with the spin frequency.

Table 6.5: A summary of properties of NS for GM1 and FPS.

EOS	$m/M_\odot$	R/km	k_2	$\bar{I}^r$	$\bar{I}$
GM1	1.4	13.79	0.116	6.151	15.85
GM1	1.35	13.78	0.121	6.578	16.87
FPS	1.4	10.90	0.0668	3.709	10.09
FPS	1.35	10.95	0.0711	4.000	10.77

Sec. 6.7.2, we first investigate the case where resonances take place in both NSs. The r-mode DTs are treated as an independent degree of freedom (i.e., the universal relations between NS properties are not used). Then in Sec. 6.7.3, we discuss the improvements on parameter estimation by incorporating the universal relations. Finally in Sec. 6.7.4, we study BHNS systems. For comparison, we consider two EoSs, GM1 and FPS, as they, respectively, give the largest and smallest radii for the same mass (see Fig. 6.6). The NS properties for these two EoSs are summarized in Table 6.5. Because the features for both EoSs are similar, we mainly discuss GM1 in the main text, and put the results of FPS in Secs. 6.13 and 6.14.

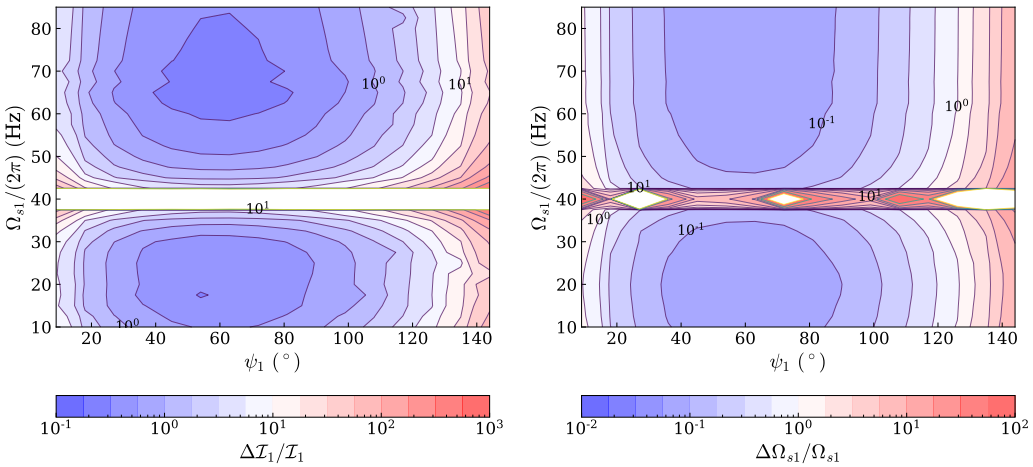

Figure 6.11: Case I: relative errors of $\mathcal{I}_1$ (left) and Ω_{s1} (right) as functions of ψ_1 and Ω_{s1}, i.e., the spin configuration of m_1. The errorbar is in log scale. For m_2, we fix its spin configuration as $\Omega_{s2} = 40$ Hz, $\psi_2 = 7\pi/18$. The EoS is GM1. Eq. (6.68) shows that both $\Delta\mathcal{I}_1/\mathcal{I}_1$ annd $\Delta\Omega_{s1}/\Omega_{s1}$ have ψ_1 dependence: $\sin^{-2}\psi_1 \cos^{-4}\psi_1/2$. Therefore they diverge to infinite as $\psi_1 \to 0, \pi$, and become the best when $\psi = \pi/3$. In the best scenario, the constraint on Ω_{s1} is around 6%, and the one on $\mathcal{I}_1$ is 21.7%. $\mathcal{I}_1$ is less constrained because $\partial h/\partial\mathcal{I}_1$ is suppressed by the factor $(1 - f/f_r)$ as $f \sim f_r$ [Eq. (6.64a)]. Constraints get bad when $\Omega_{s1} \sim \Omega_{s2} = 40$ Hz, because two resonances are degenerated in GW.

6.7.2 Case I: two resonant NSs without the universal relations

As we discussed in Sec. 6.2.1, for a BNS system where r-mode excitation takes place in each NS, Ω_{si} and $\mathcal{I}_i$ can be constrained by GW. Since r-mode DT adds independent contributions to the GW phase evolution, simply adding this effect does not improve the existing measurement accuracy provided by other PN effects. For example, individual tidal Love numbers, as well as individual dimensionless spins, are still degenerate. Therefore, in this subsection, we mainly focus on the measurement of r-mode sector itself, and study estimation accuracy for Ω_{si} and $\mathcal{I}_i$. The full waveform depends on 13 parameters, including 9 PP parameters, $\mathcal{M}$, Ξ, $\chi^{(z)}_{s(a)}$, $\bar{\lambda}^{s(a)}_f$, D_L, t_c, ϕ_c, and 4 r-mode parameters Ω_{si}, and $\mathcal{I}_i$. The Fisher matrix is 13 dimensional. We note again that here we use the normalized Love number [Eq. (6.31)] instead of the Love number listed in Table 6.2.

To be concrete, let us fix the spin vector of m_2, $\Omega_{s2} = 40$ Hz and $\psi_2 = 7\pi/18$, and explore the following parameter space: $\Omega_{s1} \in [10, 85]$ Hz, $\psi_1 \in [\frac{1}{20}\pi, \frac{17}{20}\pi]$. In Fig. 6.11, we show the relative errors of $\mathcal{I}_1$ and Ω_{s1} as functions of Ω_{s1} and ψ_1. We first observe that the relative errors of $\mathcal{I}_1$ and Ω_{s1} depend on ψ_1 in a similar way; both become worse as $\psi_1 \to 0$ and π. However, their behaviors are caused

Table 6.6: The comparison between constraints for Ω_{si} and $\mathcal{I}_i$ with two EoS: FPS and GM1. We explore the parameter space: $\Omega_{s1} \in [10, 85]$ Hz, $\psi_1 \in [\frac{\pi}{20}, \frac{17}{20}\pi]$, while choose $\Omega_{s2} = 40$ Hz and $\psi_2 = 7\pi/18$. The median values of the ratio between two EoS for several parameters are shown in the first four columns. Eq. (6.68) shows that the constraint is proportional to $(\bar{I}_i^r)^{-2}$, so we also show their ratios in the last two columns, for comparison. All numbers are close.

Parameters	$\Delta\Omega_{s1}$	$\Delta\Omega_{s2}$	$\Delta\mathcal{I}_1$	$\Delta\mathcal{I}_2$	$(\bar{I}_1^r)^{-2}$	$(\bar{I}_2^r)^{-2}$
FPS/GM1	2.67	2.65	3.23	2.78	2.77	2.72

by different reasons. Recall the discussion in Sec. 6.6.2, $\Delta\mathcal{I}_1$ is independent of $\mathcal{I}_1$, while $\Delta\Omega_{s1} \propto \mathcal{I}_1^{-1}$, hence we can obtain

$$\frac{\Delta\mathcal{I}_1}{\mathcal{I}_1} \sim \frac{\Delta\Omega_{s1}}{\Omega_{s1}} \sim \mathcal{I}_1^{-1} \sim (\bar{I}_i^r)^{-2} \sin^{-2}\psi_1 \cos^{-4}\psi_1/2, \tag{6.68}$$

where Eq. (6.30) is used. We have checked that the dependence above is consistent with our numerical calculation. With this knowledge, we can know that constraints become the best when $\psi_1 = \pi/3$, where $\mathcal{I}_1$ is maximal. In the best case, the constraint on Ω_{s1} is around 6%, and on $\mathcal{I}_1$ around 22%. Meanwhile, the measurement error $\Delta\mathcal{I}_1/\mathcal{I}_1$ is less than 1 when $\psi_1 \in [18°, 110°]$, therefore there is a large range of parameter space where one can extract meaningful constraints from GW.

Secondly, constraints on both Ω_{si} and $\mathcal{I}_i$ become worse when $\Omega_{s1} \sim \Omega_{s2} = 40$ Hz, because two resonances take place at similar locations, and are therefore indistinguishable from each other. In this regime, Fisher-matrix based analysis becomes invalid, and a more detailed Bayesian analysis will be required. Out of this regime, two resonances do not interfere anymore. We have checked that constraints on Ω_{s2} and $\mathcal{I}_2$ are insensitive to the values of ψ_1 and Ω_{s1} (except when $\Omega_{s1} \sim \Omega_{s2}$). In the best-case scenario, $\Delta\Omega_{s2}/\Omega_{s2}$ is around 5%, and $\Delta\mathcal{I}_2/\mathcal{I}_2$ around 17%.

Thirdly, constraints on Ω_s are better than those on $\mathcal{I}$, because $\partial\tilde{h}^{N+r}/\partial\mathcal{I}$ is suppressed by the factor $(1 - f/f_r)$ as $f \sim f_r$ [Eq. (6.64a)]. Recalling that the spin frequency determines where the resonance takes place (in time or frequency domain), while $\mathcal{I}$ characterizes the phase shift (strength of the DT), therefore we can conclude that GW signals are more sensitive to the location of resonance than the strength of the resonance.

Finally, we investigate the effect of EoS. We compute the ratio of relative errors with FPS to those with GM1: $\left[\Delta\Omega_{si}^{(\mathrm{FPS})}/\Omega_{si}^{(\mathrm{FPS})}\right] \Big/ \left[\Delta\Omega_{si}^{(\mathrm{GM1})}/\Omega_{si}^{(\mathrm{GM1})}\right]$ and $\left[\Delta\mathcal{I}_i^{(\mathrm{FPS})}/\mathcal{I}_i^{(\mathrm{FPS})}\right] \Big/ \left[\Delta\mathcal{I}_i^{(\mathrm{GM1})}/\mathcal{I}_i^{(\mathrm{GM1})}\right]$. In Table 6.6, we provide the median values

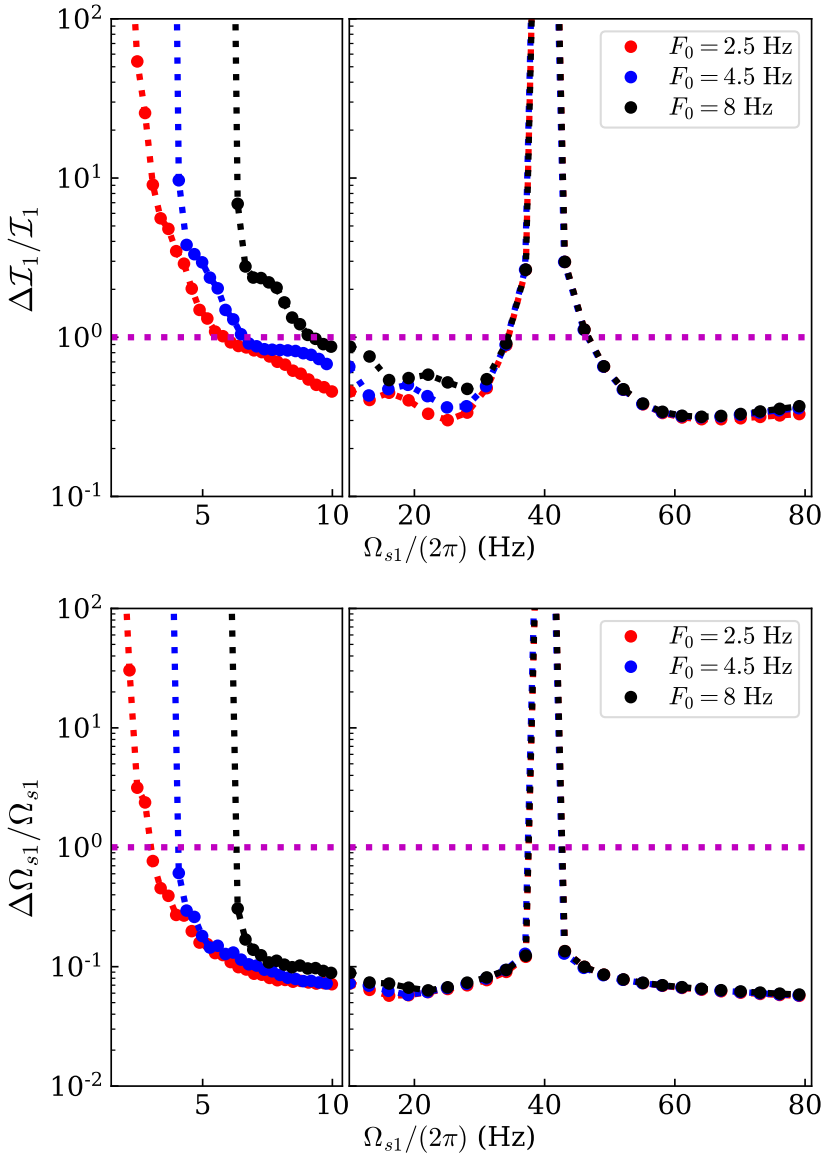

Figure 6.12: Fractional errors of Ω_{s1} and $\mathcal{I}_1$ as functions of Ω_{s1}, with different values of F_0. We set the spin configuration for m_2 to be the same as Fig. 6.11, and $\psi_1 = \pi/3$. Fractional errors first decrease with Ω_{s1}, because there are more in-band pre-resonance signals. Then it becomes bad as $\Omega_{s1} \sim \Omega_{s2}$, since two resonances are not distinguishable. The lower limit of $\Omega_{s1}/(2\pi)$ is taken to be $3/4F_0$, i.e., resonance takes place initially (at orbital frequency F_0). We cannot get constraints on $\mathcal{I}_1$ and Ω_{s1} if we further decrease the spin frequency. Those curves show that the value of F_0 only affects these constraints mildly.

of these ratios over the parameter space we have explored. The results for different parameters are similar: those for GM1 are better than FPS by a factor of $2.6 \sim 3.2$. The numbers are also close to the ratio of $(\bar{I}^r)^{-2}$, recalling that the relative errors

are proportional to $\mathcal{I}^{-1} \sim (\bar{I}^r)^{-2}$. We can then conclude that, constraints are more stringent for less compact NSs, i.e., those with harder EoS, with error inversely proportional to r-mode overlap. Detailed results for FPS are shown in Sec. 6.13. Since the two EoSs are representative for hard and soft EoSs, the fractional error on the spin for other EoSs can be between 6% to 16%. As a result, the r-mode resonance provides an important channel to put constraints on the spin frequency.

If Ω_{s1} is further decreased to below 3.38 Hz, we need to lower the value of F_0 to include enough pre-resonance signals[8]. In Fig. 6.12, we compare $\Delta\mathcal{I}_1/\mathcal{I}_1 - \Omega_{s1}$ and $\Delta\Omega_{s1}/\Omega_{s1} - \Omega_{s1}$ relations with different values of F_0. We can see that the value of F_0 affects the constraint mildly if $\Omega_s > 10$ Hz. Furthermore, the fractional error of $\mathcal{I}_1$ exceeds 100% when $\Omega_{s1} \lesssim 6$ Hz. In this parameter regime, the r-mode cannot be unambiguously detected. Therefore, we here only focus on $\Omega_s > 10$ Hz, and it is enough to choose $F_0 = 4.5$ Hz for a general calculation.

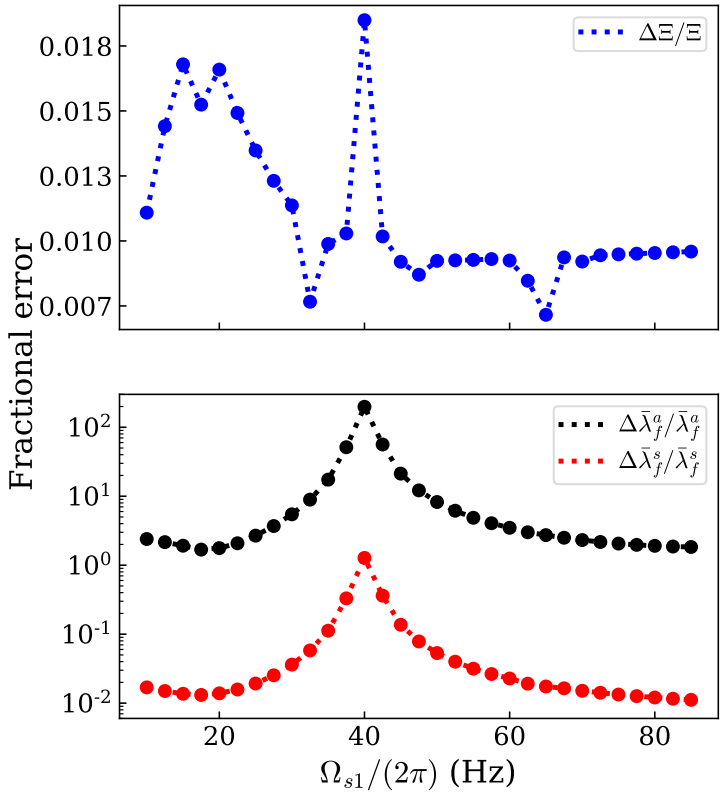

Figure 6.13: Case II: fractional errors as functions of Ω_{s1} after incorporating universal relations. The spin configuration for m_2 is same as Fig. 6.11, and $\psi_1 = 3\pi/10$. EoS is still GM1. The top panel is for Ξ while the bottom one corresponds to $\bar{\lambda}_f^{s(a)}$.

[8]Constraints on Ω_{s2} and $\mathcal{I}_2$ are unaffected, because the two resonances are independent from each other.

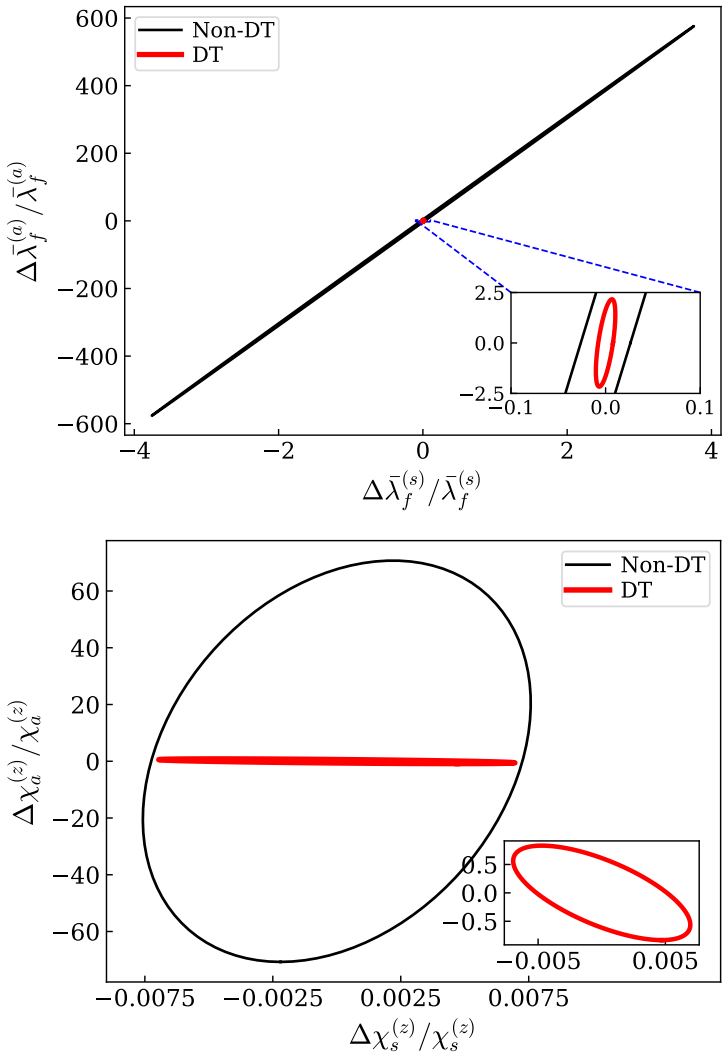

Figure 6.14: The error ellipses of $(\Delta\bar{\lambda}_f^a, \Delta\bar{\lambda}_f^s)$ and $(\Delta\chi_a^{(z)}, \Delta\chi_s^{(z)})$, with $\Omega_{s1} = 80$ Hz, $\Omega_{s2} = 40$ Hz, $\psi_1 = \pi/3$ and $\psi_2 = 7\pi/18$. The black curve is the result of PN effects (including adiabatic tidal effect and spin-orbit coupling). The red curve is the result after including r-mode resonances (with universal relations). For those ellipses, both directions are improved by resonances.

6.7.3 Case II: two resonant NSs + universal relations

In the previous subsection, we only studied the estimation of parameters in the r-mode sector because this sector is independent of other PN effects. However, if we take into account the universal relations between NS properties, the r-mode sector will behave like a bridge that connects tidal and spin parameters. We will then have enough number of degrees of freedom in the waveform to constrain all parameters, as summarized in Table 6.2.

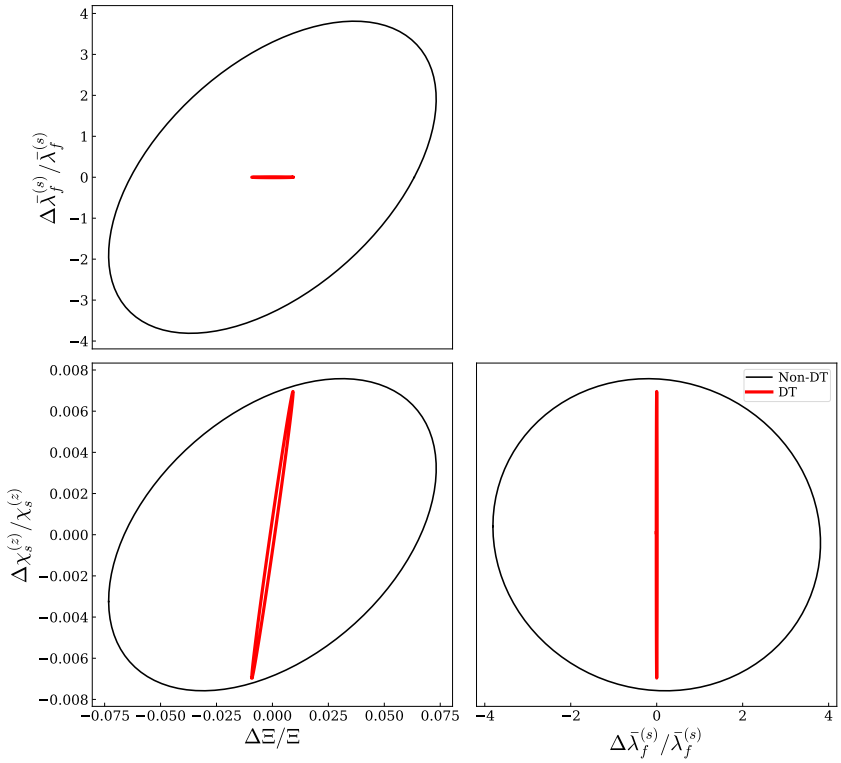

Figure 6.15: Same as Fig. 6.14. The error ellipses between $\Xi - \bar{\lambda}_f^s - \chi_s^{(z)}$.

6.7.3.1 *Neutron-Star Parameters*

To begin with, we need to express $\chi_{s(a)}^{(z)}$ in terms of spin frequency and (normalized) moment of inertia [Sec. 6.5.2]:

$$\chi_{s(a)}^{(z)} = \frac{1}{2}\left(\bar{I}_1\Omega_{s1}m_1\cos\psi_1 \pm \bar{I}_2\Omega_{s2}m_2\cos\psi_2\right), \tag{6.69}$$

We will then have 12 intrinsic parameters, including: chirp mass $\mathcal{M}$; mass ratio Ξ; (anti-)symmetric normalized Love numbers $\bar{\lambda}_f^{s(a)}$; two inclination angles ψ_i; two spin frequencies Ω_{si}; two r-mode coupling coefficients $\mathcal{I}_i$; and two normalized momentum of inertia $\bar{I}_i$. Meanwhile, we have 8 constraints from GW

$$\mathcal{M}, \quad \Xi, \quad \chi^{\rm eff}, \quad \lambda_f^{\rm eff}, \quad \Delta\Omega_{si}, \quad \Delta\mathcal{I}_i, \tag{6.70}$$

and 4 constraints from the two universal relations

$$\mathcal{I}_i = \mathcal{I}_i(\bar{\lambda}_f^{s(a)}, \Xi, \psi_i, \mathcal{M}), \qquad \bar{I}_i = \bar{I}_i(\bar{\lambda}_f^{s(a)}), \tag{6.71}$$

where we have used the definitions of $\mathcal{I}$ in Eq. (6.30). In principle, these 12 constraints are enough to decode the BNS system. However, as we have seen in the last subsection, constraints in Eq. (6.70) in practice may not be measured with

extremely high statistical accuracy; the relative error on $\mathcal{I}$ can be as bad as 100%. Therefore, we should be prepared that degeneracy may not be completely broken in practice.

After using the universal relations, the Fisher matrix is 11D, corresponds to $\mathcal{M}$, Ξ, Ω_{si}, $\bar{\lambda}_f^{s(a)}$, ψ_i, t_c, ϕ_c, D_L.

6.7.3.2 *Parameter Constraints: tidal Love numbers* $\bar{\lambda}_f^{s,a}$

In the lower panel of Fig. 6.13, we plot the dependence of $\Delta\bar{\lambda}_f^{s(a)}/\bar{\lambda}_f^{s(a)}$ on Ω_{s1}, with $\psi_1 = 3\pi/10$, $\psi_2 = 7\pi/18$ and $\Omega_{s2} = 2\pi \times 40$ Hz. (we use the GM1 EoS; data for the FPS EoS are shown in Sec. 6.14.) Constraints become worse when $\Omega_{s1} \sim \Omega_{s2} = 2\pi \times 40$ Hz because two resonances take place simultaneously, making it impossible to resolve their individual features. For favorable values of Ω_{s1}, $\Delta\bar{\lambda}_f^s$ can be constrained as well as $\sim 1.0\%$, while $\Delta\bar{\lambda}_f^a/\bar{\lambda}_f^a$ is ~ 1.7. The degeneracy between two individual tidal Love numbers is still not broken, but substantially reduced. To see this more clearly, we plot the error ellipses between $\Delta\bar{\lambda}_f^a$ and $\Delta\bar{\lambda}_f^s$ in Fig. 6.14, for $\Omega_{s1} = 80$ Hz and $\psi_1 = \pi/3$, when r mode is either included or not included. Constraints on both directions are substantially improved by r-mode, but the fractional error of $\bar{\lambda}_f^a$ is still greater than 1.

Let us note that breaking of $\bar{\lambda}_f^a$ degeneracy is difficult because the predicted values of $\bar{\lambda}_f^a$ is intrinsically very small, if we make the tacit assumption that neutron stars all have the *same*, albeit unknown, EoS. For example, in our case, the two neutron stars are $(1.4, 1.35)\, M_\odot$, and with the GM1 EoS, $\bar{\lambda}_f^a/\bar{\lambda}_f^s \approx 0.1$. Nevertheless, it is theoretically possible that the two neutron stars do not follow the same EoS—and for this reason, it is still very meaningful to dramatically reduce $\Delta\bar{\lambda}_f^a$, even if our measurement error is somewhat larger than the predicted value of $\bar{\lambda}_f^a$.

As we turn to the individual Love numbers of the two neutron stars, $\bar{\lambda}_f^{(i)}$, we find that their errors are still correlated in general. For some special cases, the individual Love numbers can be sufficiently well constrained. In Table 6.7, we show one example with $\Omega_{s1} = 80$ Hz, $\psi_1 = \pi/3$, $\Omega_{s2} = 40$ Hz, $\psi_1 = 7\pi/18$, and GM1 EoS. Relative errors of two individual tidal Love numbers are around 20%.

We then study the improvement of constraints by comparing results above with those of pure PN effects (i.e., adiabatic tidal effect). The improvement factor, Imp. $\Delta\bar{\lambda}_f^{s(a)}/\bar{\lambda}_f^{s(a)}$, is defined to be the ratio between constraints from two sides (the factor is larger than 1 when the r-mode enhances the constraint). Results are shown in

Table 6.7: A special case where the individual normalized Love numbers and inclination angles are well constrained. Two NSs have spin $\Omega_{s2} = 40$Hz, $\psi_2 = 7\pi/18$, $\Omega_{s1} = 80$Hz and $\psi_1 = \pi/3$. EoS is GM1.

Parameters	$\Delta\bar{\lambda}_f^{(1)}/\bar{\lambda}_f^{(1)}$	$\Delta\bar{\lambda}_f^{(2)}/\bar{\lambda}_f^{(2)}$	$\Delta\psi^{(1)}$ (rad)	$\Delta\psi^{(2)}$ (rad)
Constraints	0.26	0.22	0.18	0.28

Table 6.8: A summary of the effect of including r-mode resonance on parameter constraints. The second column gives the best fractional errors for Ξ and $\bar{\lambda}_f^{s(a)}$ achievable when we vary ψ_1 and Ω_{s1}. These fractional errors are generally improved, when compared with those achievable only including PN effects. In the third and forth columns, we list the best and worst improvement factors for each parameter, as we vary ψ_1 and Ω_{s1}.

Parameters	Best constraints	Best improvement	Worst improvement
$\Delta\bar{\lambda}_f^s/\bar{\lambda}_f^s$	10^{-2}	389	1
$\Delta\bar{\lambda}_f^a/\bar{\lambda}_f^a$	1.84	336	1
$\Delta\Xi/\Xi$	5×10^{-3}	11.6	1

Table 6.8. We can see constraints on $\Delta\bar{\lambda}_f^{s(a)}/\bar{\lambda}_f^{s(a)}$ are improved. In the best case, the factor is around 300–400.

6.7.3.3 *Parameter Constraints: mass ratio Ξ and spins $\chi_{a,s}^{(z)}$*

The measurement of $\Delta\chi_a^{(z)}$ and $\Delta\chi_s^{(z)}$ can also benefit from universal relations[9]. As shown in the lower panel of Fig. 6.14, while the improvement in $\chi_s^{(z)}$ is mild, the constraint on $\chi_a^{(z)}$ is improved by a factor of ~ 120. Therefore, the degeneracy between individual dimensionless spin is also reduced.

The case for Ξ is similar. Its correlation with other parameters is reduced by the r-mode DT and the universal relations. Compared with constraints from pure PN effects, the error in Ξ can be improved by a factor of $1-11.6$, as summarized in Table 6.8. In the first row of Fig. 6.13, we also present its fractional error as a function of Ω_{s1}. We can see $\Delta\Xi/\Xi$ is insensitive to Ω_s. Generally, it can be constrained to $\sim 1.3\%$.

It is also well-known that the estimation errors of Ξ, $\bar{\lambda}_f^s$ and $\chi_s^{(z)}$ are correlated in absence of r-mode resonance. The effects of incorporating r-mode resonances are

[9]These are not independent variables in this subsection, their constraints are obtained by error propagation.

shown in Fig. 6.15. Whereas in Refs. [1, 4] the error reduction relies on imposing an observational-based prior on χ_z, once the r-mode resonances are taken into account, the mutual correlations between parameters are significantly reduced. As suggested in Ref. [76], the r-mode DT indeed improves dramatically the inference accuracy on both the tidal deformability and the NS component masses. The later can be further converted to an indication of the maximum mass of NSs with a population of events. We thus conclude that the r-mode DT plays a crucial role in constraining the nature of NS EoS.

6.7.3.4 *Parameter Constraints: inclination angles*

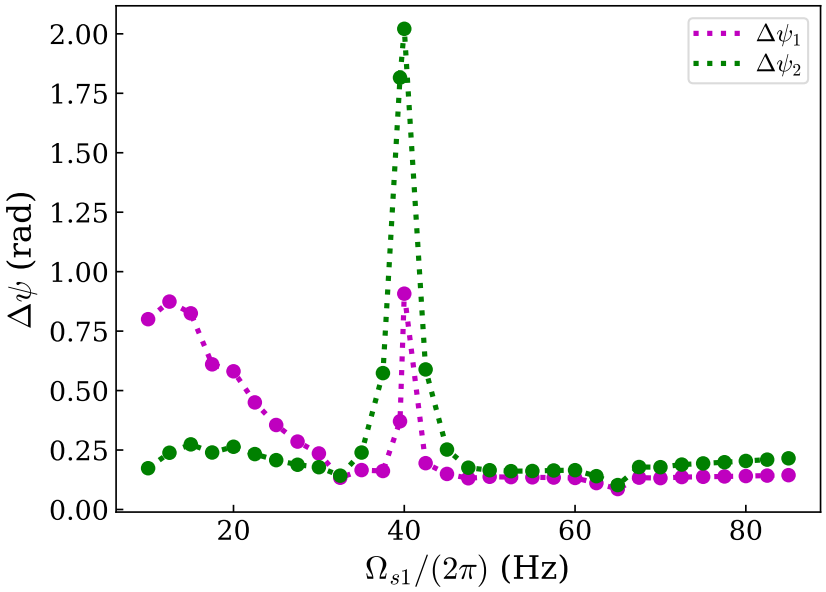

Figure 6.16: Case II: constraints on inclination angles ψ_i as functions of Ω_{s1}. Spin configurations are same as Fig. 6.11 and $\psi_1 = 3\pi/10$. Generally speaking, ψ_1 and ψ_2 are correlated. In the best case, $\Delta\psi_1 \sim \Delta\psi_2 \sim 0.09$ rad.

Besides improving constraints, universal relations also provide information of inclination angles ψ_i, which is hard to be accessible by other PN effects. In Figs. 6.16, we show $\Delta\psi_i$ as functions of Ω_{s1}. Generally speaking, ψ_1 and ψ_2 are correlated. In the best case, $\Delta\psi_1 \sim \Delta\psi_2 \sim 0.09$ rad. We note that determining this angle may play significant roles in astrophysics, as it allows the constraining of the NS natal kicks, i.e., kicks received by NSs at their formation due to asymmetric supernova explosions (see, e.g., Refs. [108–110]). This may further shed light on models and theories of core-collapse supernova [111, 112].

6.7.3.5 *If only one of NS is resonant*

If one of NS (e.g., m_2) in the binary system rotates at very low frequency, its r-mode resonance is not in-band anymore, and r-mode resonance does not provide enough constraints to decode the whole system. In fact, we find that the two inclination angles ψ_i are highly correlated and are totally unmeasurable. Nevertheless, the measurement of Love number can still benefit from the single, in-band resonance. As an example, we still adopt a BNS system with $(1.4, 1.35)M_\odot$ and $\psi_1 = \pi/3$, $\Omega_{s1} = 40$ Hz. The value of Ω_{s2} is taken to be small enough such that the r-mode of m_2 is not excited in-band. In Fig. 6.17, we show contours between $\bar{\lambda}^s_f$ and $\bar{\lambda}^a_f$ with or without DT. We can see they are similar to the case of two resonances in Fig. 6.14: even with only one resonance, the degeneracy between $\bar{\lambda}^{s(a)}_f$ can still be substantially reduced.

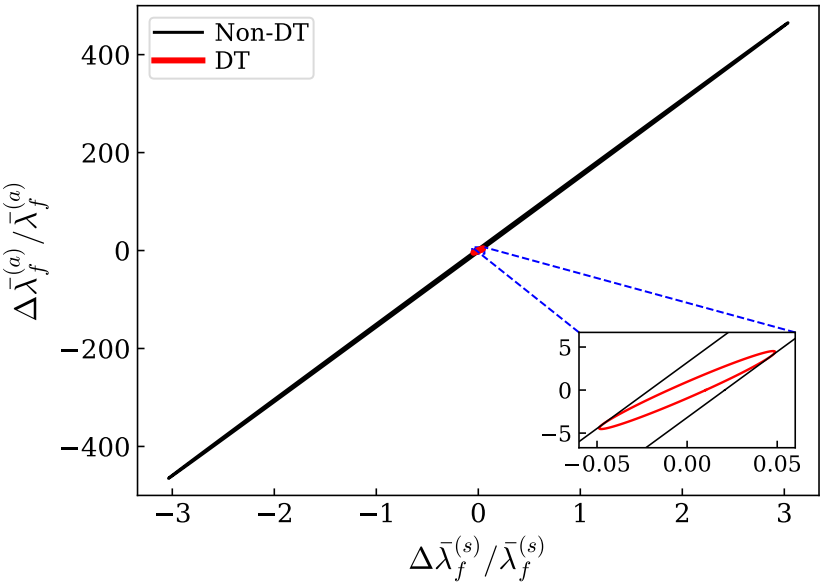

Figure 6.17: Similar to the top panel of Fig. 6.14. But with only one in-band r-mode resonance. For the binary system, we choose $\Omega_{s1} = 40$ Hz, $\psi_1 = \pi/3$. The value of Ω_{s2} is taken to be small enough such that the r-mode of m_2 is not excited in-band. The degeneracy between $\bar{\lambda}^{s(a)}_f$ can still be reduced a lot.

6.7.4 Case III: BHNS

For a BHNS system, the r-mode resonance only takes place once before the merger. As shown in Table 6.3, there are 8 parameters for the system: $\mathcal{M}$, Ξ, $\bar{\lambda}^{(1)}_f$, $\bar{I}_1$, Ω_{s1}, $\bar{\mathcal{I}}_1$, ψ_1 and $\chi^{(z)}_2$. And there are 8 constraints from GW and universal relations. Hence the degeneracies can be reduced, even broken.

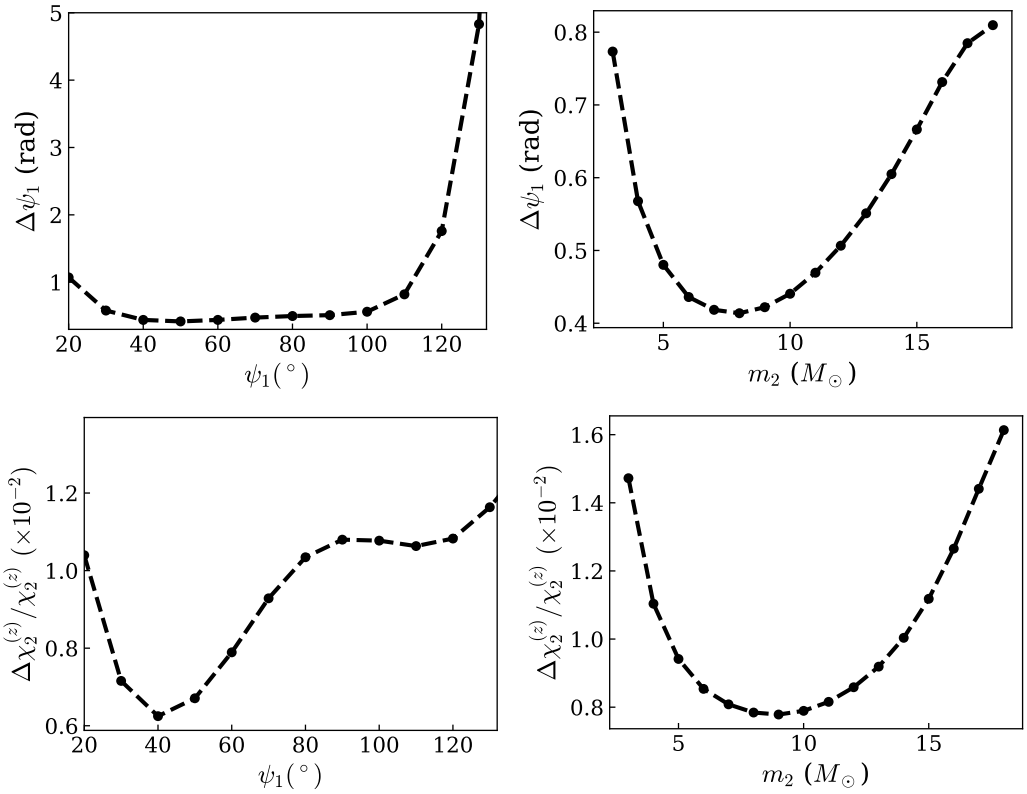

Figure 6.18: Case III: constraints on several parameters in the case of BHNS system. We choose $\Omega_{s1} = 30$ Hz and $\chi_2^{(z)} = 0.1$. The EoS is GM1, and the binary system is 100Mpc away from the detector. In the left panel, we show constraints as functions of ψ_1, where we fix the mass of BH to be $10M_\odot$; whereas in the right panel, we study their dependence on the mass of BH m_2, with $\psi_1 = \pi/3$. Using universal relations, the degeneracy of parameters is totally broken, where $\Delta\psi$ is ~ 1 rad, and the relative errors of $\chi_2^{(z)}$ are $\sim 1\%$.

To study this case, we choose a BHNS system with $(1.4, 10)M_\odot$. The NS is assumed to spin at 30 Hz, and EoS is GM1. As for BH, we assume $\chi_2^{(z)} = 0.1$. The distance of the system is 100 Mpc. Results are shown in the left column of Fig. 6.18. In this case, the degeneracy between two individual spins is completely broken. For $\chi_2^{(z)}$, it is constrained to $\sim 1\%$, and ψ_1 is constrained to ~ 1 rad.

We further investigate the effect of BH mass on constraints by varying m_2, while fixing Ω_{s1}=30 Hz and $\psi_1 = \pi/3$. The distance of the system is still 100 Mpc. In the right column of Fig. 6.18, we show constraints as functions of BH mass. We can see both constraints first decrease with m_2, because of the increase of SNR. If we further increase m_2, post-resonance signals then will be reduced, and the constraints will become worse accordingly.

6.8 Conclusion

In this chapter, we studied the tidal excitation of r-mode by the gravitomagnetic force in coalescencing NS binaries. We began by a brief review on the dynamics of these systems: the r-mode is excited by the gravitomagnetic field from the companion, while the induced current quadrupole moment gives rise to an acceleration back to the orbit. By assuming the orbit to be quasicircular, we obtained a coupled EOM. Next, we numerically integrated the coupled set of EOM and discussed features of solutions. We confirmed that the pre- and post-resonance orbital evolution can be well described by two PP orbits, as proposed in FR07 [72]. The post-resonance PP orbit is related to the pre-resonance one through a "jump" in orbital frequency at the resonance. We subsequently investigated the tidal evolution, by extending Ref. [53] to the r-mode, and providing analytic formulae for tidal evolution that are accurate in all regimes: adiabatic, resonance and post-resonance. Separately, using the TOV equation, we found a universal relation between the normalized r-mode overlap $\bar{I}^r$ of a neutron star and its normalized tidal Love number $\bar{\lambda}_f$.

We then moved on to the wave zone and studied gravitational waves emitted by such binaries. We constructed a hybrid GW waveform that combines several SPA models with results from numerical integrations of the coupled EOM. This waveform contains information from r-mode resonance, adiabatic tidal effect, and spin-orbit coupling. To understand the effect of r-mode DT on GW waveforms, we adopted the model in FR07: the r-mode induces phase and time shifts in GW. We found this model to be quantitatively accurate. Finally, with the hybrid waveform, we calculated Fisher information matrix to investigate how r-mode resonances improves parameter

estimation accuracy. We mainly studied three cases: binary NS systems with r-mode resonances in NSs, binary NS systems including r-mode resonances together with universal relations between NS properties, and BHNS binary systems.

We found a variety of interesting results. First, the excitation of r-mode is mainly described by two parameters: spin frequency Ω_s and r-mode coupling coefficient $\mathcal{I}$. The spin frequency Ω_s determines when the resonance takes place during the inspiral, and $\mathcal{I}$ determines the phase and time shifts induced by the r-mode resonance. Choosing a $(1.4, 1.35)M_\odot$ BNS system at 100Mpc away as example, we found that when the inclination angle is within the range of $[18°, 110°]$ (and if $\Omega_{s1,2}$ are not too close), the measurements errors of $\mathcal{I}_i$ and Ω_{si} are less than 100%, where Fisher analysis is valid and we can extract meaningful information from GW. The best constraint on Ω_s is around 6% with 3G detectors; whereas for $\mathcal{I}$, the value is around 22%. The constraint on $\mathcal{I}$ is worse than Ω_s because $\partial\tilde{h}^{N+r}/\partial\mathcal{I}$ is suppressed by the factor $(1 - f/f_r)$ as $f \sim f_r$ [Eq. (6.64a)]. In other words, the waveform is more sensitive to the location of the resonance than to the phase shift. With the analytic model for the r-mode, we found $\Delta\mathcal{I}/\mathcal{I} \sim \Delta\Omega_s/\Omega_s \sim \sin^{-2}\psi\cos^{-4}\psi/2$ [Eq. (6.68)]. This is consistent with our numerical calculations. The formula shows that the constraint is the best when $\psi = \pi/3$, while there is no constraint as $\psi \to 0, \pi$. We also found that two resonances in each star do not get strongly correlated except for $\Omega_{s1} \sim \Omega_{s2}$, when effects from the two resonances become indistinguishable.

Secondly, with the help of the universal relations, r-mode resonance behaves like a bridge that connects adiabatic tidal effect and the spin-orbit coupling. In principle, for systems which have two r-mode resonances, we can obtain as many constraints as free parameters in GW. This situation is in contrary to the case without DT, where the universal relation requires additional parameters to be incorporated. This is because if one wants to use I-Love relation to connect adiabatic tidal effect and the spin-orbit coupling, four more free parameters: inclination angle ψ_i and spin frequency Ω_{si} should be introduced. In the absence of r-mode resonance, they cannot be constrained at all.

Although the r-mode resonance provides enough constraints to decode the BNS system, some constraints are not very accurate in practice. For example, errors on $\mathcal{I}_i$ sometimes are as large as 100%, where the information is not meaningful. This will diminish the role of r-mode in degeneracy breaking. Nevertheless, our calculations show that two individual normalized Love numbers are still significantly correlated in the most cases. The best relative errors of symmetric normalized Love number

is $\sim 1.3\%$, while is 1.84 for the anti-symmetric normalized Love number. Both of them are improved by factors of $\sim 300 - 400$ in the best-case scenario, comparing with those that come solely from PN effects. In favorable cases, the normalized Love numbers of individual NS can be sufficiently well constrained. As shown in Table 6.7, each normalized Love number is constrained to 20%, significantly improve our understanding on the NS EoS. Meanwhile, the r-mode DT allows us to put constraints on the inclination angle between the spin and orbital angular momentum, which is hard to be accessible by other PN effects. In the best-case scenario, each inclination angle is constrained to 0.09 rad. This could potentially constrain the NS natal kick and hence the supernovae explosion mechanism. The other benefit from the universal relations is constraints on mass ratio Ξ, which is known to have correlated errors with $\bar{\lambda}^s_f$ and $\chi^{(z)}_s$ in absence of DT. After including r-mode DT and universal relations, Ξ measurement can be improved by actors of $1 - 11.6$. For most cases, its fractional error is around $\sim 1\%$. An improved estimation accuracy on Ξ means better accuracy on the component masses. This could constrain the maximum mass of NSs with a large number of detection and shed light on the NS EoS in a way complementary to the information derived from tidal deformability.

Thirdly, for BHNS systems, we can also obtain as many constraints as parameters. As a result, degeneracies are totally broken. Choosing a BHNS system as example, we found $\Delta\psi_1 \sim 1$ rad, and $\Delta\chi^{(z)}_2/\chi^{(z)}_2 \sim 1\% - 2\%$.

Our results show that r-mode resonance will be an important channel for 3G detectors to extract information of NSs. Since the excitation only requires NSs to spin at tens of Hertz, these events are quite generic in coalescing binaries that have NSs. Therefore, to develop an accurate GW waveform from these systems seems necessary in the future. Our numerical calculations of r-mode are only on Newtonian order, and PN effects are incorporated in a naive way. Also, the corrections of DT onto PN terms are not considered here. Therefore, one possible avenue for future work is to perform a systematic study on the scenario with relativity. This includes to couple the gravitomagnetic force with rotational modes of relativistic stars[10] by the formalism in Ref. [66], and to study the orbital evolution with either PN approach [83] or EOB formalism [35, 57]. As pointed out by Idrisy *et al.* [68], there is more than 10% variance for the mode frequency of relativistic stars, depending on the compactness. This is on the same order as the statistical accuracy of Ω_s in this

[10]There is no pure r-mode in relativistic barotropic stars.

chapter. Therefore, relativistic corrections would be important in this case. It is also interesting to see how relativistic corrections to the $\bar{I}^r - \bar{\lambda}_f$ universal relation changes the parameter estimation.

The other direction would be numerical relativity. Although the excitation of f-mode has been observed by recent study [113], the simulation of r-mode is more difficult to achieve with the current version of numerical relativity code, such as SpEC [114], since the mode amplitude of r-mode is much smaller. A typical Lagrangian displacement of r-mode is only 10^{-4} of the radius of a NS. This requires much more resolutions to resolve r-mode. However, with the upgraded version of SpEC, SpECTRE [115], this may be doable in the near future.

Furthermore, our study mainly focuses on the $(2,2)$ r-mode in barotropic NSs. As pointed out by Poisson *et al.* recently [73], four inertial modes can be excited by the gravitomagnetic force before the merger. Meanwhile, for NSs with buoyancy, there is also the $(2,1)$ r-mode, which plays a role as important as the $(2,2)$ mode [72]. These modes have different ψ-dependence, and contain different information about NSs. Therefore, they can further reduce the degeneracy of parameters, and put more constraints on the inclination angle ψ. On the other hand, the detection of $(2,1)$ mode can confirm the existence of buoyancy in cold NSs, so it is worth incorporating these modes in the future.

A caveat, however, is that our analysis as well as the studies mentioned above, all assumed that the matter inside the NS behaves as a normal fluid. In reality, superfluidity may be expected in cold NSs [116] and may lead to richer dynamics than what we considered here thanks to its two-fluid nature (see e.g., Ref. [117]). Ref. [118] showed that the superfluid r-modes characterized by a common flow of neutrons and protons reduce to their normal-fluid counterparts (i.e., the r-mode studied in our work) in the slow-rotation limit. On the other hand, Ref. [117] argued the existence of a new class of r-modes whose fluid motion is such that neutrons and protons are counter-moving. This new class of r-modes is not accounted for in our current study and is deferred to future studies.

Meanwhile, we ignored damping on the r-mode due to microphysical processes in the NS. While viscous damping and nonlinear saturation may play a critical role for the r-mode instability in newly-born NSs and/or X-ray binaries [119], its effect might be subdominant in coalescing NS binaries given the very short duration of tidal excitation (< 1s, see [120]) compared to the typical viscous damping timescale of 10^4 s [118]. Nevertheless, sufficiently large uncertainty remains in our current

understanding of NS microphysics, and future explorations on the dissipation of saturation of r-modes under various astrophysical contexts will be of great value.

Finally, we want to emphasize that we treated the two universal relations as exact relations. However, as pointed out in Ref. [121], even the most insensitive relations still have residual variability with respect to EoSs and could lead to systematic bias in parameter estimations for 3G detectors potentially comparable to the statistical uncertainties. Therefore, studying the impact of such EoS variability would be another interesting direction to go.

6.9 Appendix: Justification of ignoring the PP precession

When the spins $\boldsymbol{S}_{1,2}$ are misaligned with respect to the orbital angular momentum $\boldsymbol{L}$, various precession effects will happen and, in principle, modify the dynamics when the orbit is both close to and far away from a mode's resonance. We will show quantitatively that all the precession-induced corrections are small and therefore can be safely ignored.

Specifically, we have [80, 122]

$$\frac{d\hat{\boldsymbol{S}}_1}{dt} = \boldsymbol{\Omega}^{(1)}_{\rm dS} \times \hat{\boldsymbol{S}}_1, \tag{6.72}$$

$$\frac{d\hat{\boldsymbol{S}}_2}{dt} = \boldsymbol{\Omega}^{(2)}_{\rm dS} \times \hat{\boldsymbol{S}}_2, \tag{6.73}$$

$$\frac{d\hat{\boldsymbol{L}}}{dt} = \left[\boldsymbol{\Omega}^{(1)}_{\rm LT} + \boldsymbol{\Omega}^{(2)}_{\rm LT}\right] \times \hat{\boldsymbol{L}}, \tag{6.74}$$

where

$$\boldsymbol{\Omega}^{(1,2)}_{\rm dS} = \frac{3\left(m_{2,1} + \mu/3\right)}{2D}\Omega_{\rm orb}\hat{\boldsymbol{L}}, \tag{6.75}$$

is the rate of the leading-order de Sitter precession of the spins induced by the orbital angular momentum $\boldsymbol{L}$ and

$$\boldsymbol{\Omega}^{(1,2)}_{\rm LT} = \frac{S_{1,2}\left(4 + 3m_{2,1}/m_{1,2}\right)}{2D^3}\hat{\boldsymbol{S}}_2, \tag{6.76}$$

is the rate of the Lense-Thirring precession of $\boldsymbol{L}$ due to $\boldsymbol{S}_{1,2}$. The hat stands for the unit vector along the direction of the corresponding quantity.

As a result of the de Sitter precession of $\boldsymbol{S}_1$, the resonance frequency of the r-mode in m_1 should be shifted by $\Omega^{(1)}_{\rm dS}$ with

$$\frac{\Omega^{(1)}_{\rm dS}}{2\pi} \simeq 0.8 \times \left(\frac{f_r}{80\,{\rm Hz}}\right)^{5/3}, \tag{6.77}$$

assuming a binary with $m_1 \simeq m_2 \simeq 1.4\,M_\odot$ and evaluating at $f = f_r$ with f_r the resonant frequency [Eq. (6.60)]. The above shift is $\sim 1\%$ of the spin frequency, about 10 times smaller than the typical statistical error of $\sim 10\%$ (e.g., Fig. 6.11), it can thus be neglected.

Meanwhile, the Lense-Thirring precession of the orbital angular momentum together with the spin-spin interaction will cause the inclination angle of the spin of NS, $\psi_{1(2)}$, evolves slowly as [123]

$$\frac{d}{dt}\cos\psi_1 = \Omega_{\Delta\psi_1}\hat{\boldsymbol{S}}_1 \cdot \left(\hat{\boldsymbol{S}}_2 \times \hat{\boldsymbol{L}}\right), \tag{6.78}$$

where $\Omega_{\Delta\psi_1} = 3(1+q)S_2/2qD^3 \simeq (6/7)\Omega_{\rm LT}^{(2)}$ for nearly equal-mass binaries with $q \equiv m_2/m_1 \simeq 1$. We can thus define a timescale $\tau_{\Delta\psi_1} = 1/\Omega_{\Delta\psi_1}$, which is given by

$$\tau_{\Delta\psi_1} \simeq 70\,{\rm s}\left(\frac{f_r}{80\,{\rm Hz}}\right)^{-2}\left(\frac{\chi_2\sin\psi_2}{0.02}\right)^{-1}. \tag{6.79}$$

On the other hand, the duration of resonance is given by [Eq. (6.48b)]

$$\tau_{\rm r} \simeq \left(\frac{1}{\dot{\Omega}_r}\right)^{1/2} = 0.52\,{\rm s}\left(\frac{f_r}{80\,{\rm Hz}}\right)^{-11/6}. \tag{6.80}$$

We thus see that ψ_1 is a well-defined quantity at resonance. Moreover, it is well defined throughout the entire post-resonance evolution which lasts about 4 s (Fig. 6.4), much shorter than $\tau_{\Delta\psi_1}$.

The above two points allow us to conclude that the modifications due to precession is indeed negligible during mode resonances. We now consider their effects away from resonance. To do so, we drop the r-mode effects and use the `LALSuite` [124] to generate PP waveforms with `IMRPhenomPv2` approximation [80, 125].

In Fig. 6.19 we compute the mismatch of a precessing waveform (parameterized in terms of $\chi_{\rm p}$) with a non-precessing but otherwise identical one. Here the mismatch is defined as

$$\text{Mismatch}(h_1, h_2) = 1 - \max_{t_c,\phi_c}\frac{(h_1|h_2)}{\sqrt{(h_1|h_1)(h_2|h_2)}}. \tag{6.81}$$

For a typical NS with spin < 100 Hz, it corresponds to a precession parameter $\chi_{\rm p} \lesssim 0.1$ (even assuming $\psi = \pi/2$; $\chi_{\rm p}$ is smaller for harder EOSs). Consequently, neglecting precessions will only cause small errors on the PP waveforms.

Lastly, we show in Fig. 6.20 the parameter estimation uncertainties of $\chi_{\rm p}$ using the PP waveform alone. Here we have assumed a fiducial relation of $\chi_{\rm p} =$

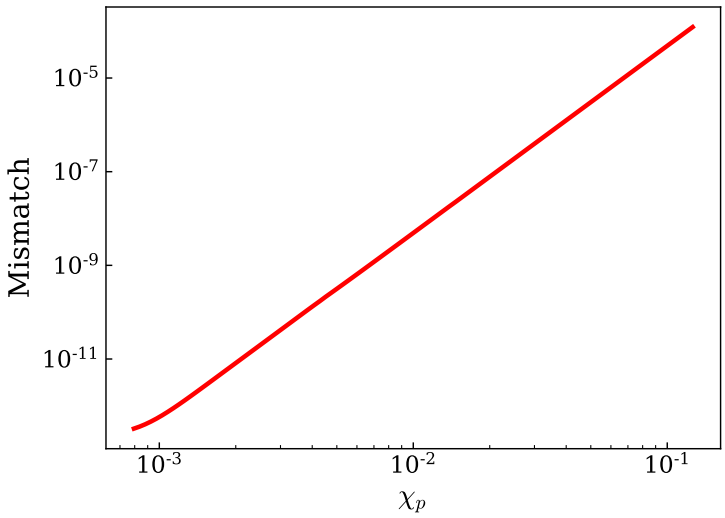

Figure 6.19: Mismatch between a precessing waveform $\chi_{\rm p} \neq 0$ and an a non-precessing but otherwise identical one.

$0.06\Omega_{s_1} \sin\psi_1/(2\pi \times 100\,\mathrm{Hz})$ so that we can show the y-axis in physical spin units. As the fractional error $\Delta\chi_{\rm p}/\chi_{\rm p} > 10$ for the parameter space of interest, we thus do not expect we would be able to further improve the parameter estimation accuracy by incorporating the precession effects.

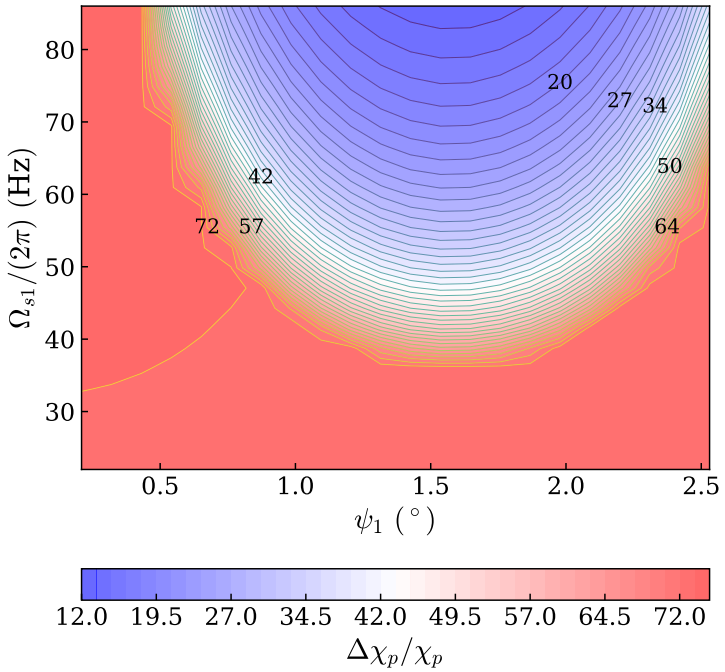

Figure 6.20: The fractional error in inferring the PP precession parameter χ_p.

6.10 Appendix: The Tolman–Oppenheimer–Volkoff equations

The stress-energy tensor $T_{\mu\nu}$ for a perfect fluid is given by

$$T_{\mu\nu} = (\rho + p)u_\mu u_\nu + p g_{\mu\nu}, \tag{6.82}$$

where p and ρ stand for the pressure and energy density of the star, and u_μ is four-velocity. The metric $g_{\mu\nu}$ is given by Eq. (6.49). With Einstein field equation, quantities shown above can be solved by the TOV equations

$$\frac{dm}{dr} = 4\pi r^2 \rho, \tag{6.83}$$

$$\frac{dp}{dr} = -\frac{(4\pi r^3 p + m)(\rho + p)}{r(r - 2m)}, \tag{6.84}$$

$$\frac{d\nu}{dr} = 2\frac{4\pi r^3 p + m}{r(r - 2m)}, \tag{6.85}$$

where

$$m \equiv \frac{1 - e^{-\lambda}}{2} r. \tag{6.86}$$

In practice, it is preferable to cast them into a new form for numerical integration. Following the procedure of Ref. [126], we use the specific enthalpy h, defined by

$$dh = \frac{dp}{\rho + p}, \tag{6.87}$$

to replace r, where the integration constant is set by the condition $h \to 0$ as $\rho \to 0$ and $p \to 0$. Defining two new dependent variables, $u = r^2$ and $v = m/r$, then we have

$$\frac{du}{dh} = -\frac{2u(1 - 2v)}{4\pi u p + v}, \tag{6.88}$$

$$\frac{dv}{dh} = -(1 - 2v)\frac{4\pi u \rho - v}{4\pi u p + v}, \tag{6.89}$$

$$\frac{d\nu}{dh} = -2. \tag{6.90}$$

At the center of the star, we have

$$h = h_c, \quad u = 0, \quad v = 0, \tag{6.91}$$

with h_c a free parameter. The surface of star locates at $h = 0$.

Therefore, we can find the structure of the star by integrating Eqs. (6.88)–(6.90) from $h = h_c$ to $h = 0$, with the initial conditions in Eq. (6.91). The total mass of the star can be obtained from the formula $m_{\rm NS} = \sqrt{u}v|_{h=0}$, and the radius is given by $R_{\rm NS} = \sqrt{u}|_{h=0}$. The quantity ν is linear in h, where the integration constant is set by the condition $\nu|_{h=0} = \log(1 - 2m_{\rm NS}/R_{\rm NS})$, to connect the value outside of star.

6.11 Appendix: The calculation of tidal Love number λ_f

Let us consider linearized even-parity perturbations to the equilibrium metric in Eq. (6.49). Following Refs. [127–129], the perturbed metric in the Regge-Wheeler gauge can be written as

$$g_{\mu\nu} = g^{(0)}_{\mu\nu} + h_{\mu\nu}, \tag{6.92}$$

with

$$h_{\mu\nu} = \mathrm{diag}[e^{-\nu}H_0, e^{\lambda}H_2, r^2K, r^2\sin^2\theta K]Y_{lm}(\theta,\phi), \tag{6.93}$$

where H_0, H_2, K are functions of r. The perturbation on the stress-energy tensor is given by [127]

$$\delta T^0_0 = -\delta\rho_l Y_{lm}(\theta,\phi) = -\frac{d\rho}{dp}\delta p_l Y_{lm}(\theta,\phi), \tag{6.94}$$

$$\delta T^i_i = \delta p_l Y_{lm}(\theta,\phi). \tag{6.95}$$

With Einstein's field equations, we obtain [129]

$$H_2 = H_0 = H, \tag{6.96}$$

$$\begin{aligned} &H'' + H'\left\{\frac{2}{r} + e^{\lambda}\left[\frac{2m}{r^2} + 4\pi r(p-\rho)\right]\right\} \\ &+ H\left\{e^{\lambda}\left[-\frac{6}{r^2} + 4\pi(\rho+p)\frac{d\rho}{dp} + 4\pi(5\rho+9p)\right] - \left(\frac{d\nu}{dr}\right)^2\right\} = 0, \end{aligned} \tag{6.97}$$

where we only focus on the $l = 2$ component. The mass function m is related to the metric function λ by Eq. (6.86).

Imposing regularity condition at $r = 0$ yields the initial condition $H \propto r^2$. The proportionality constant does not matter here, so we simply choose it as 1. Functions λ, m, p, ρ in the above equation can be obtained from the solutions of TOV equations.

Integrating Eq. (6.97) from $r = 0$ to $r = R_{\rm NS}$ leads to the dimensionless tidal Love number k_2 as [130]

$$\begin{aligned} k_2 = {} & \frac{8}{5}C^5(1-2C)^2[2+2C(y-1)-y]\,\{2C[6-3y \\ & + 3C(5y-8)] + 4C^3[13-11y+C(3y-2)+2C^2(1+y)] \\ & + 3(1-2C)^2[2-y+2C(y-1)]\log(1-2C)\}^{-1}, \end{aligned} \tag{6.98}$$

where $y = R_{\rm NS}H'(R_{\rm NS})/H(R_{\rm NS})$, and the tidal Love number λ_f is given by

$$\lambda_f = \frac{2}{3}k_2 R^5_{\rm NS}. \tag{6.99}$$

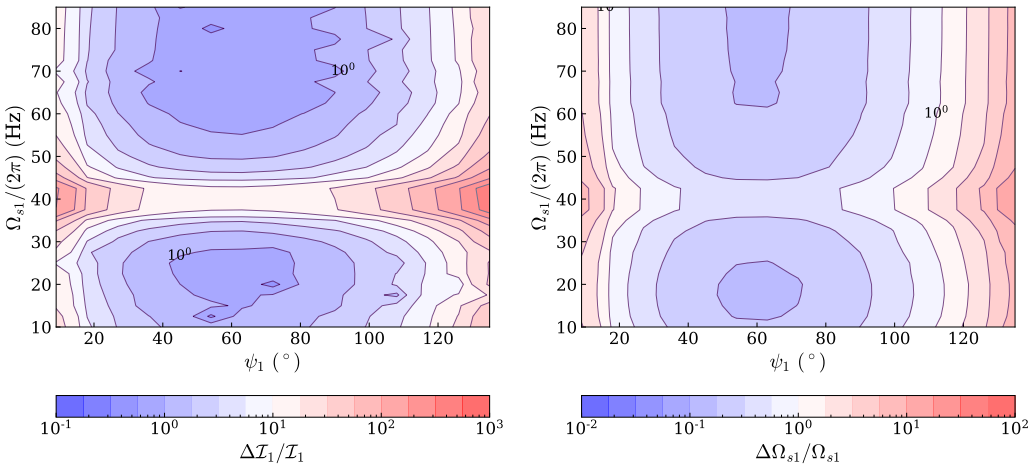

Figure 6.21: Same as Fig. 6.11, but with FPS EoS. The constraints are worse than those for GM1 by factors of $\sim 2.6 - 2.7$

6.12 Appendix: The GW phase with SPA

From Ref. [99–106], we obtain the frequency-domain gravitational-wave phasing, up to 3.5 PN order for point-particle contributions, up to 3PN for spin terms, and up to 2.5 PN for adiabatic, f-mode tide. Here are terms *in addition to* the leading Newtonian phasing Ψ_N:

$$\Psi_{\rm PP} = \frac{3}{128}(\pi\mathcal{M}f)^{-5/3}\left\{\left(\frac{3715}{756}+\frac{55}{9}\eta\right)x - 16\pi x^{3/2} + \left(\frac{15293365}{508032}+\frac{27145}{504}\eta+\frac{3085}{72}\eta^2\right)x^2 \right.$$
$$+\left(\frac{38645}{756}\pi-\frac{65}{9}\pi\eta\right)(1+3\log v)x^{5/2} + \left[\frac{11583231236531}{4694215680}-\frac{640\pi^2}{3}-\frac{6848}{21}\gamma_E\right.$$
$$\left.-\left(\frac{15737765635}{3048192}-\frac{2255}{12}\pi^2\right)\eta+\frac{76055}{1728}\eta^2-\frac{127825}{1296}\eta^3-\frac{6848}{21}\log(4v)\right]x^3$$
$$\left.+\left(\frac{77096675}{254016}+\frac{1014115}{3024}\eta-\frac{36865}{378}\eta^2\right)\pi x^{7/2}\right\}, \tag{6.100a}$$

$$\Psi_{SO} = \frac{3}{128}(\pi\mathcal{M}f)^{-5/3}\left\{4\left(\frac{113}{12}-\frac{19}{3}\eta\right)(\hat{\boldsymbol{L}}\cdot\boldsymbol{\chi}_s)x^{3/2} - 10\left[\frac{719}{48}\delta_m(\hat{\boldsymbol{L}}\cdot\boldsymbol{\chi}_s)(\hat{\boldsymbol{L}}\cdot\boldsymbol{\chi}_a)\right.\right.$$
$$\left.+\left(\frac{719}{96}+\frac{\eta}{24}\right)(\hat{\boldsymbol{L}}\cdot\boldsymbol{\chi}_s)^2+\left(\frac{719}{96}-30\eta\right)(\hat{\boldsymbol{L}}\cdot\boldsymbol{\chi}_a)^2\right]x^2 - (1+3\log v)$$
$$\times\left[\left(\frac{732985}{2268}-\frac{24260}{81}\eta-\frac{340}{9}\eta^2\right)(\hat{\boldsymbol{L}}\cdot\boldsymbol{\chi}_s)+\left(\frac{732985}{2268}+\frac{140}{9}\eta\right)\delta_m(\hat{\boldsymbol{L}}\cdot\boldsymbol{\chi}_a)\right]x^{5/2}$$
$$\left.+\frac{2270\pi}{3}\left[\left(1-\frac{227}{156}\eta\right)(\hat{\boldsymbol{L}}\cdot\boldsymbol{\chi}_s)+\delta_m(\hat{\boldsymbol{L}}\cdot\boldsymbol{\chi}_a)\right]x^3\right\}, \tag{6.100b}$$

$$\Psi_{\bar{\lambda}_f^{(1)}} = -\frac{3}{16\eta}x^{5/2}(12-11\Xi)\bar{\lambda}_f^{(1)}\Xi^4\left\{1+\frac{5(3179-919\Xi-2286\Xi^2+260\Xi^3)}{672(12-11\Xi)}x-\pi x^{3/2}\right.$$

$$+\frac{1}{12-11\Xi}\left[\frac{39927845}{508032}-\frac{480043345}{9144576}\Xi+\frac{9860575}{127008}\Xi^2-\frac{421821905}{2286144}\Xi^3+\frac{4359700}{35721}\Xi^4\right.$$
$$\left.-\frac{10578445}{285768}\Xi^5\right]x^2-\frac{\pi(27719-22127\Xi+7022\Xi^2-10232\Xi^3)}{672(12-11\Xi)}x^{5/2}\Bigg\}, \quad (6.100c)$$

$$\Psi_{\bar{\lambda}_f^{(2)}} = (1\to 2 \text{ and } \Xi\to 1-\Xi). \quad (6.100d)$$

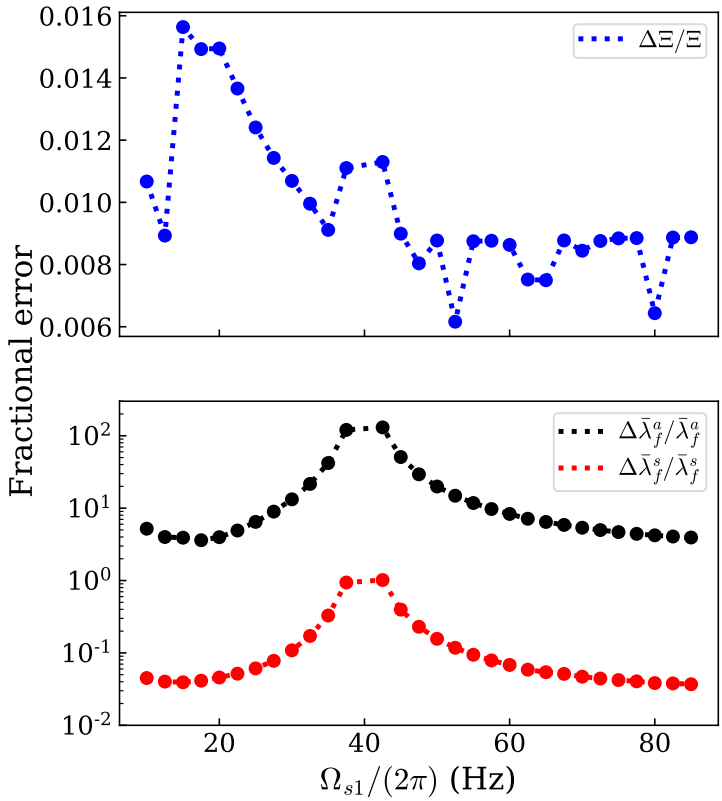

Figure 6.22: Same as Fig. 6.13, but with FPS EoS.

Here we have defined $x = v^2 = (\pi M f)^{2/3}$, $\Xi = m_1/M$, $\delta_m = (m_1 - m_2)/M$. $\hat{L}$ is the unit vector along the orbital angular momentum. Symmetric and anti-symmetric dimensionless spins are defined as $\boldsymbol{\chi}_s = (\boldsymbol{\chi}_1 + \boldsymbol{\chi}_2)/2$ and $\boldsymbol{\chi}_a = (\boldsymbol{\chi}_1 - \boldsymbol{\chi}_2)/2$ with $\boldsymbol{\chi}_i = \bar{I}_i \boldsymbol{\Omega}_{si} m_i$. Here we use the normalized momentum of inertia, as well as the normalized tidal Love number in Eqs. (6.100c) and (6.100d), in order to use the I-Love universal relation.

6.13 Appendix: Case I for FPS EoS (without universal relations)

In Fig. 6.21, we present the results for a BNS system with FPS EoS. Following Sec. 6.7.2, we still assume that both NSs are excited before merger. The spin vector of m_2 is fixed at $\Omega_{s2} = 2\pi \times 40$ Hz and $\psi_2 = 7\pi/18$. And we vary the spin of m_1:

$\Omega_{s1} \in 2\pi \times [10, 85]$ Hz, $\psi_1 \in [\frac{1}{20}\pi, \frac{17}{20}\pi]$. Without universal relations, we can put constraints on Ω_{si} and $\mathcal{I}_i$. From Table 6.6, we know that the constraints for FPS are worse than those for GM1 by factors of $\sim 2.6 - 3.2$. But their dependence on Ω_{s1} and ψ_{s1} is the same as the case of GM1.

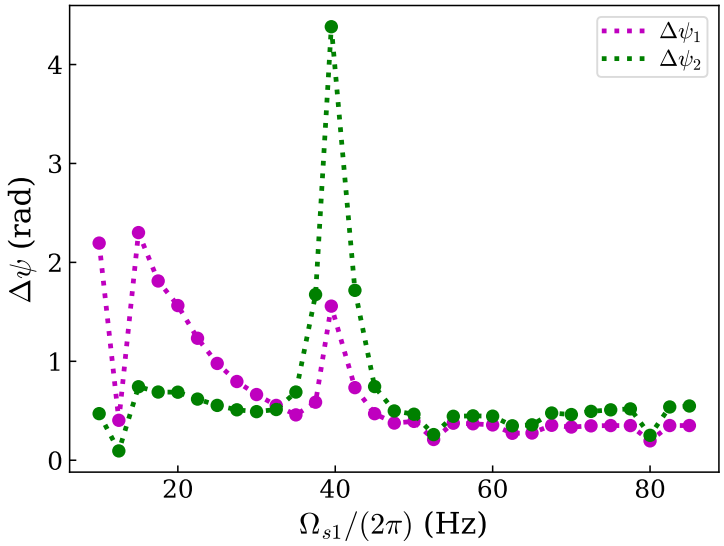

Figure 6.23: Same as Fig. 6.16, but with FPS EoS.

6.14 Appendix: Case II for FPS EoS (with universal relations)

After incorporating universal relations into the calculations of Appendix 6.13, we can obtain the constraints on $\bar{\lambda}_f^{s(a)}$, Ξ, and ψ_i, as shown in Fig. 6.22 and 6.23.

References

[1] Benjamin P. Abbott et al. "GW170817: Observation of gravitational waves from a binary neutron star inspiral." *Phys. Rev. Lett.* 119.16 (2017), p. 161101. DOI: 10.1103/PhysRevLett.119.161101. arXiv: 1710.05832 [gr-qc].

[2] Benjamin P. Abbott et al. "Gravitational waves and gamma-rays from a binary neutron star merger: GW170817 and GRB 170817A." *Astrophys. J.* 848.2 (2017), p. L13. DOI: 10.3847/2041-8213/aa920c. arXiv: 1710.05834 [astro-ph.HE].

[3] Benjamin P. Abbott et al. "GW190425: Observation of a compact binary coalescence with total mass $\sim 3.4 M_\odot$." *Astrophys. J. Lett.* 892.1 (2020), p. L3. DOI: 10.3847/2041-8213/ab75f5. arXiv: 2001.01761 [astro-ph.HE].

[4] Benjamin P. Abbott et al. "GW170817: Measurements of neutron star radii and equation of state." *Phys. Rev. Lett.* 121.16 (2018), p. 161101. DOI: 10.1103/PhysRevLett.121.161101. arXiv: 1805.11581 [gr-qc].

[5] Benjamin P Abbott et al. "Model comparison from LIGO-Virgo data on GW170817's binary components and consequences for the merger remnant." *Class. Quant. Grav.* 37.4 (2020), p. 045006. DOI: 10.1088/1361-6382/ab5f7c. arXiv: 1908.01012 [gr-qc].

[6] Eemeli Annala et al. "Gravitational-wave constraints on the neutron-star-matter equation of state." *Phys. Rev. Lett.* 120.17 (2018), p. 172703. DOI: 10.1103/PhysRevLett.120.172703. arXiv: 1711.02644 [astro-ph.HE].

[7] Elias R. Most et al. "New constraints on radii and tidal deformabilities of neutron stars from GW170817." *Phys. Rev. Lett.* 120.26 (2018), p. 261103. DOI: 10.1103/PhysRevLett.120.261103. arXiv: 1803.00549 [gr-qc].

[8] Ben Margalit and Brian D. Metzger. "Constraining the maximum mass of neutron stars from multi-messenger observations of GW170817." *Astrophys. J.* 850.2 (2017), p. L19. DOI: 10.3847/2041-8213/aa991c. arXiv: 1710.05938 [astro-ph.HE].

[9] Luciano Rezzolla, Elias R. Most, and Lukas R. Weih. "Using gravitational-wave observations and quasi-universal relations to constrain the maximum mass of neutron stars." *Astrophys. J.* 852.2 (2018). [Astrophys. J. Lett.852,L25(2018)], p. L25. DOI: 10.3847/2041-8213/aaa401. arXiv: 1711.00314 [astro-ph.HE].

[10] Milton Ruiz, Stuart L. Shapiro, and Antonios Tsokaros. "GW170817, general relativistic magnetohydrodynamic simulations, and the neutron star maximum mass." *Phys. Rev.* D97.2 (2018), p. 021501. DOI: 10.1103/PhysRevD.97.021501. arXiv: 1711.00473 [astro-ph.HE].

[11] Masaru Shibata et al. "Modeling GW170817 based on numerical relativity and its implications." *Phys. Rev.* D96.12 (2017), p. 123012. DOI: 10.1103/PhysRevD.96.123012. arXiv: 1710.07579 [astro-ph.HE].

[12] Geraint Pratten, Patricia Schmidt, and Tanja Hinderer. "Gravitational-wave asteroseismology with fundamental modes from compact binary inspirals." (2019). arXiv: 1905.00817 [gr-qc].

[13] J. Aasi et al. "Advanced LIGO." *Class. Quant. Grav.* 32 (2015), p. 074001. DOI: 10.1088/0264-9381/32/7/074001. arXiv: 1411.4547 [gr-qc].

[14] Fausto Acernese et al. "Advanced Virgo: a second-generation interferometric gravitational wave detector." *Class. Quant. Grav.* 32.2 (2015), p. 024001. DOI: 10.1088/0264-9381/32/2/024001. arXiv: 1408.3978 [gr-qc].

[15] Fausto Acernese et al. "Increasing the astrophysical reach of the advanced Virgo detector via the application of squeezed vacuum states of light." *Phys. Rev. Lett.* 123.23 (2019), p. 231108. DOI: 10.1103/PhysRevLett.123.231108.

[16] *https://tds.ego-gw.it/ql/?c=8940*. URL: https://tds.ego-gw.it/ql/?c=8940.

[17] Maggie Tse et al. “Quantum-enhanced advanced LIGO detectors in the era of gravitational-wave astronomy.” *Phys. Rev. Lett.* 123.23 (2019), p. 231107. DOI: 10.1103/PhysRevLett.123.231107.

[18] Gregory M. Harry. “Advanced LIGO: The next generation of gravitational wave detectors.” *Class. Quant. Grav.* 27 (2010). Ed. by Zsuzsa Marka and Szabolcs Marka, p. 084006. DOI: 10.1088/0264-9381/27/8/084006.

[19] Benjamin P. Abbott et al. “Prospects for observing and localizing gravitational-wave transients with advanced LIGO, Advanced Virgo and KAGRA.” *Living Rev. Rel.* 21.1 (2018), p. 3. DOI: 10.1007/s41114-018-0012-9,10.1007/lrr-2016-1. arXiv: 1304.0670 [gr-qc].

[20] *https://dcc.ligo.org/LIGO-M060056/public*. URL: https://dcc.ligo.org/LIGO-M060056/public.

[21] *https://dcc.ligo.org/LIGO-T1800044/public*. URL: https://dcc.ligo.org/LIGO-T1800044/public.

[22] David Shoemaker. “Gravitational wave astronomy with LIGO and similar detectors in the next decade.” (Apr. 2019). arXiv: 1904.03187 [gr-qc].

[23] *https://dcc.ligo.org/LIGO-T1600119/public*. URL: https://dcc.ligo.org/LIGO-T1600119/public.

[24] *https://tds.virgo-gw.eu/?call_file=VIR-0027A-09.pdf*. URL: https://tds.virgo-gw.eu/?call%5C_file=VIR-0027A-09.pdf.

[25] *https://dcc.ligo.org/LIGO-M1100296/public*. URL: https://dcc.ligo.org/LIGO-M1100296/public.

[26] Yoichi Aso et al. “Interferometer design of the KAGRA gravitational wave detector.” *Phys. Rev. D* 88.4 (2013), p. 043007. DOI: 10.1103/PhysRevD.88.043007. arXiv: 1306.6747 [gr-qc].

[27] Kentaro Somiya. “Detector configuration of KAGRA: The Japanese cryogenic gravitational-wave detector.” *Class. Quant. Grav.* 29 (2012). Ed. by Mark Hannam et al., p. 124007. DOI: 10.1088/0264-9381/29/12/124007. arXiv: 1111.7185 [gr-qc].

[28] Michele Punturo et al. “The third generation of gravitational wave observatories and their science reach.” *Class. Quant. Grav.* 27 (2010). Ed. by Zsuzsa Marka and Szabolcs Marka, p. 084007. DOI: 10.1088/0264-9381/27/8/084007.

[29] Stefan Hild et al. “Sensitivity studies for third-generation gravitational wave observatories.” *Class. Quant. Grav.* 28 (2011), p. 094013. DOI: 10.1088/0264-9381/28/9/094013. arXiv: 1012.0908 [gr-qc].

[30] *http://www.et-gw.eu/index.php/etdsdocument*. URL: http://www.et-gw.eu/index.php/etdsdocument.

[31] Stefan Hild et al. "A xylophone configuration for a third generation gravitational wave detector." *Class. Quant. Grav.* 27 (2010), p. 015003. DOI: 10.1088/0264-9381/27/1/015003. arXiv: 0906.2655 [gr-qc].

[32] Benjamin P Abbott et al. "Exploring the sensitivity of next generation gravitational wave detectors." *Class. Quant. Grav.* 34.4 (2017), p. 044001. DOI: 10.1088/1361-6382/aa51f4. arXiv: 1607.08697 [astro-ph.IM].

[33] David Reitze et al. "Cosmic Explorer: The U.S. contribution to gravitational-wave astronomy beyond LIGO." *Bull. Am. Astron. Soc.* 51 (July 2019), p. 035. arXiv: 1907.04833 [astro-ph.IM].

[34] Vishal Baibhav et al. "Gravitational-wave detection rates for compact binaries formed in isolation: LIGO/Virgo O3 and beyond." *Phys. Rev.* D100.6 (2019), p. 064060. DOI: 10.1103/PhysRevD.100.064060. arXiv: 1906.04197 [gr-qc].

[35] Tanja Hinderer et al. "Effects of neutron-star dynamic tides on gravitational waveforms within the effective-one-body approach." *Phys. Rev. Lett.* 116.18 (2016), p. 181101. DOI: 10.1103/PhysRevLett.116.181101. arXiv: 1602.00599 [gr-qc].

[36] Tim Dietrich, Sebastiano Bernuzzi, and Wolfgang Tichy. "Closed-form tidal approximants for binary neutron star gravitational waveforms constructed from high-resolution numerical relativity simulations." *Phys. Rev. D* 96.12 (2017), p. 121501. DOI: 10.1103/PhysRevD.96.121501. arXiv: 1706.02969 [gr-qc].

[37] Sarp Akcay et al. "Effective-one-body multipolar waveform for tidally interacting binary neutron stars up to merger." *Phys. Rev. D* 99.4 (2019), p. 044051. DOI: 10.1103/PhysRevD.99.044051. arXiv: 1812.02744 [gr-qc].

[38] Alessandro Nagar et al. "Time-domain effective-one-body gravitational waveforms for coalescing compact binaries with nonprecessing spins, tides and self-spin effects." *Phys. Rev. D* 98.10 (2018), p. 104052. DOI: 10.1103/PhysRevD.98.104052. arXiv: 1806.01772 [gr-qc].

[39] Kevin Barkett et al. "Gravitational waveforms of binary neutron star inspirals using post-Newtonian tidal splicing." *Phys. Rev. D* 102.2 (2020), p. 024031. DOI: 10.1103/PhysRevD.102.024031. arXiv: 1911.10440 [gr-qc].

[40] Francesco Messina et al. "Quasi-5.5PN TaylorF2 approximant for compact binaries: point-mass phasing and impact on the tidal polarizability inference." *Phys. Rev. D* 99.12 (2019), p. 124051. DOI: 10.1103/PhysRevD.99.124051. arXiv: 1904.09558 [gr-qc].

[41] Thomas G. Cowling. "The non-radial oscillations of polytropic stars." *Mon. Not. R. Astron Soc.* 101 (1941), p. 367. DOI: 10.1093/mnras/101.8.367.

[42] Andreas Reisenegger and Peter Goldreich. "Excitation of neutron star normal modes during binary inspiral." *Astrophys. J.* 426 (May 1994), pp. 688–691. DOI: 10.1086/174105.

[43] Dong Lai. "Resonant oscillations and tidal heating in coalescing binary neutron stars." *Mon. Not. Roy. Astron. Soc.* 270 (1994), p. 611. DOI: 10.1093/mnras/270.3.611. arXiv: astro-ph/9404062 [astro-ph].

[44] Hang Yu and Nevin N. Weinberg. "Resonant tidal excitation of superfluid neutron stars in coalescing binaries." *Mon. Not. R. Astron Soc.* 464.3 (Jan. 2017), pp. 2622–2637. DOI: 10.1093/mnras/stw2552. arXiv: 1610.00745 [astro-ph.HE].

[45] Hang Yu and Nevin N. Weinberg. "Dynamical tides in coalescing superfluid neutron star binaries with hyperon cores and their detectability with third generation gravitational-wave detectors." *Mon. Not. Roy. Astron. Soc.* 470.1 (2017), pp. 350–360. DOI: 10.1093/mnras/stx1188. arXiv: 1705.04700 [astro-ph.HE].

[46] Cecilia Chirenti, Roman Gold, and M.Coleman Miller. "Gravitational waves from f-modes excited by the inspiral of highly eccentric neutron star binaries." *Astrophys. J.* 837.1 (2017), p. 67. DOI: 10.3847/1538-4357/aa5ebb. arXiv: 1612.07097 [astro-ph.HE].

[47] Huan Yang et al. "Evolution of highly eccentric binary neutron stars including tidal effects." *Phys. Rev.* D98.4 (2018), p. 044007. DOI: 10.1103/PhysRevD.98.044007. arXiv: 1806.00158 [gr-qc].

[48] Huan Yang. "Inspiralling eccentric binary neutron stars: Orbital motion and tidal resonance." *Phys. Rev.* D100.6 (2019), p. 064023. DOI: 10.1103/PhysRevD.100.064023. arXiv: 1904.11089 [gr-qc].

[49] Michelle Vick and Dong Lai. "Tidal effects in eccentric coalescing neutron star binaries." *Phys. Rev.* D100.6 (2019), p. 063001. DOI: 10.1103/PhysRevD.100.063001. arXiv: 1906.08780 [astro-ph.HE].

[50] Dong Lai. "Orbital decay of the psr j0045-7319/b star binary system: age of radio pulsar and initial spin of neutron star." *Astrophys. J.* 466 (1996), p. L35. DOI: 10.1086/310166. arXiv: astro-ph/9605096 [astro-ph].

[51] Dong Lai. "Dynamical tides in rotating binary stars." *Astrophys. J.* 490 (1997), p. 847. DOI: 10.1086/304899. arXiv: astro-ph/9704132 [astro-ph].

[52] Wynn C. G. Ho and Dong Lai. "Resonant tidal excitations of rotating neutron stars in coalescing binaries." *Mon. Not. Roy. Astron. Soc.* 308 (1999), p. 153. DOI: 10.1046/j.1365-8711.1999.02703.x. arXiv: astro-ph/9812116 [astro-ph].

[53] Sizheng Ma, Hang Yu, and Yanbei Chen. "Excitation of f-modes during mergers of spinning binary neutron star." *Phys. Rev. D* 101 (12 June 2020), p. 123020. DOI: 10.1103/PhysRevD.101.123020. URL: https://link.aps.org/doi/10.1103/PhysRevD.101.123020.

[54] Leonardo Gualtieri et al. "Gravitational signals emitted by a point mass orbiting a neutron star: A perturbative approach." *Phys. Rev.* D64 (2001), p. 104007. DOI: 10.1103/PhysRevD.64.104007. arXiv: gr-qc/0107046 [gr-qc].

[55] Jose A. Pons et al. "Gravitational signals emitted by a point mass orbiting a neutron star: Effects of stellar structure." *Phys. Rev. D* 65 (2002), p. 104021. DOI: 10.1103/PhysRevD.65.104021. arXiv: gr-qc/0111104.

[56] Giovanni Miniutti et al. "Non-radial oscillation modes as a probe of density discontinuities in neutron stars." *Mon. Not. Roy. Astron. Soc.* 338 (2003), p. 389. DOI: 10.1046/j.1365-8711.2003.06057.x. arXiv: astro-ph/0206142 [astro-ph].

[57] Jan Steinhoff et al. "Dynamical tides in general relativity: Effective action and effective-one-body hamiltonian." *Phys. Rev.* D94.10 (2016), p. 104028. DOI: 10.1103/PhysRevD.94.104028. arXiv: 1608.01907 [gr-qc].

[58] Patricia Schmidt and Tanja Hinderer. "Frequency domain model of f-mode dynamic tides in gravitational waveforms from compact binary inspirals." *Phys. Rev.* D100.2 (2019), p. 021501. DOI: 10.1103/PhysRevD.100.021501. arXiv: 1905.00818 [gr-qc].

[59] Andrew G. Lyne et al. "A double pulsar system - A rare laboratory for relativistic gravity and plasma physics." *Science* 303 (2004), pp. 1153–1157. DOI: 10.1126/science.1094645. arXiv: astro-ph/0401086 [astro-ph].

[60] Nils Andersson and W. C. G. Ho. "Using gravitational-wave data to constrain dynamical tides in neutron star binaries." *Phys. Rev.* D97.2 (2018), p. 023016. DOI: 10.1103/PhysRevD.97.023016. arXiv: 1710.05950 [astro-ph.HE].

[61] Lee Lindblom and James R. Ipser. "Generalized r modes of the Maclaurin spheroids." *Phys. Rev.* D59 (1999), p. 044009. DOI: 10.1103/PhysRevD.59.044009. arXiv: gr-qc/9807049 [gr-qc].

[62] Keith H. Lockitch and John L. Friedman. "Where are the r modes of isentropic stars?" *Astrophys. J.* 521 (1999), p. 764. DOI: 10.1086/307580. arXiv: gr-qc/9812019 [gr-qc].

[63] Shijun Yoshida and Umin Lee. "Inertial modes of slowly rotating isentropic stars." *Astrophys. J.* 529 (2000), p. 997. DOI: 10.1086/308312. arXiv: astro-ph/9908197 [astro-ph].

[64] John Papaloizou and James E. Pringle. "Non-radial oscillations of rotating stars and their relevance to the short-period oscillations of cataclysmic variables." *Mon. Not. Roy. Astron. Soc.* 182 (1978), pp. 423–442. DOI: 10.1093/mnras/182.3.423.

[65] Hideyuki Saio. "R-mode oscillations in uniformly rotating stars." *Astrophys. J.* 256 (May 1982), pp. 717–735. DOI: 10.1086/159945.

[66] Keith H. Lockitch, Nils Andersson, and John L. Friedman. "The rotational modes of relativistic stars. 1. Analytic results." *Phys. Rev.* D63 (2001), p. 024019. DOI: 10.1103/PhysRevD.63.024019. arXiv: gr-qc/0008019 [gr-qc].

[67] Keith H. Lockitch, John L. Friedman, and Nils Andersson. "The rotational modes of relativistic stars: Numerical results." *Phys. Rev.* D68 (2003), p. 124010. DOI: 10.1103/PhysRevD.68.124010. arXiv: gr-qc/0210102 [gr-qc].

[68] Ashikuzzaman Idrisy, Benjamin J. Owen, and David I. Jones. "*R*-mode frequencies of slowly rotating relativistic neutron stars with realistic equations of state." *Phys. Rev.* D91.2 (2015), p. 024001. DOI: 10.1103/PhysRevD.91.024001. arXiv: 1410.7360 [gr-qc].

[69] Dong Lai and Yanqin Wu. "Resonant tidal excitations of inertial modes in coalescing neutron star binaries." *Phys. Rev.* D74 (2006), p. 024007. DOI: 10.1103/PhysRevD.74.024007. arXiv: astro-ph/0604163 [astro-ph].

[70] Wenrui Xu and Dong Lai. "Resonant tidal excitation of oscillation modes in merging binary neutron stars: Inertial-gravity modes." *Phys. Rev.* D96.8 (2017), p. 083005. DOI: 10.1103/PhysRevD.96.083005. arXiv: 1708.01839 [astro-ph.HE].

[71] A. Katrin Schenk et al. "Nonlinear mode coupling in rotating stars and the r mode instability in neutron stars." *Phys. Rev.* D65 (2002), p. 024001. DOI: 10.1103/PhysRevD.65.024001. arXiv: gr-qc/0101092 [gr-qc].

[72] Eanna E. Flanagan and Etienne Racine. "Gravitomagnetic resonant excitation of Rossby modes in coalescing neutron star binaries." *Phys. Rev.* D75 (2007), p. 044001. DOI: 10.1103/PhysRevD.75.044001. arXiv: gr-qc/0601029 [gr-qc].

[73] Eric Poisson. "Gravitomagnetic tidal resonance in neutron-star binary inspirals." *Phys. Rev. D* 101.10 (2020), p. 104028. DOI: 10.1103/PhysRevD.101.104028. arXiv: 2003.10427 [gr-qc].

[74] Eric Poisson. "Gravitomagnetic Love tensor of a slowly rotating body: post-Newtonian theory." (July 2020). arXiv: 2007.01678 [gr-qc].

[75] Eric Poisson and Cyann Buisson. "Tidal driving of inertial modes of Maclaurin spheroids." (July 2020). arXiv: 2007.03050 [gr-qc].

[76] Hang Yu et al. "Prospects for detecting gravitational waves at 5 Hz with ground-based detectors." *Phys. Rev. Lett.* 120.14 (2018), p. 141102. DOI: 10.1103/PhysRevLett.120.141102. arXiv: 1712.05417 [astro-ph.IM].

[77] Kent Yagi and Nicolas Yunes. "I-Love-Q Relations in neutron stars and their applications to Astrophysics, gravitational waves and fundamental physics." *Phys. Rev.* D88.2 (2013), p. 023009. DOI: 10.1103/PhysRevD.88.023009. arXiv: 1303.1528 [gr-qc].

[78] Kent Yagi and Nicolás Yunes. "I-Love-Q: Unexpected universal relations for neutron stars and quark stars." *Science* 341.6144 (July 2013), pp. 365–368. DOI: 10.1126/science.1236462. arXiv: 1302.4499 [gr-qc].

[79] Alessandro Nagar et al. "Nonlinear-in-spin effects in effective-one-body waveform models of spin-aligned, inspiralling, neutron star binaries." *Phys. Rev.* D99.4 (2019), p. 044007. DOI: 10.1103/PhysRevD.99.044007. arXiv: 1812.07923 [gr-qc].

[80] Patricia Schmidt, Frank Ohme, and Mark Hannam. "Towards models of gravitational waveforms from generic binaries II: Modelling precession effects with a single effective precession parameter." *Phys. Rev. D* 91.2 (2015), p. 024043. DOI: 10.1103/PhysRevD.91.024043. arXiv: 1408.1810 [gr-qc].

[81] Eanna E. Flanagan and Tanja Hinderer. "Constraining neutron star tidal Love numbers with gravitational wave detectors." *Phys. Rev. D* 77 (2008), p. 021502. DOI: 10.1103/PhysRevD.77.021502. arXiv: 0709.1915 [astro-ph].

[82] Etienne Racine. "Analysis of spin precession in binary black hole systems including quadrupole-monopole interaction." *Phys. Rev. D* 78 (2008), p. 044021. DOI: 10.1103/PhysRevD.78.044021. arXiv: 0803.1820 [gr-qc].

[83] Etienne Racine and Eanna E. Flanagan. "Post-1-Newtonian equations of motion for systems of arbitrarily structured bodies." *Phys. Rev.* D71 (2005). [Erratum: Phys. Rev.D88,no.8,089903(2013)], p. 044010. DOI: 10.1103/PhysRevD.71.044010, 10.1103/PhysRevD.88.089903. arXiv: gr-qc/0404101 [gr-qc].

[84] J. Provost, G. Berthomieu, and A. Rocca. "Low frequency oscillations of a slowly rotating star - Quasi toroidal modes." *Astron. Astrophys.* 94 (Jan. 1981), p. 126.

[85] Eric Poisson and Clifford M. Will. *Gravity: Newtonian, Post-Newtonian, relativistic*. Cambridge: Cambridge University Press, 2014. DOI: 10.1017/CBO9781139507486.

[86] Subrahmanyan Chandrasekhar. "Solutions of two problems in the theory of gravitational radiation." *Phys. Rev. Lett.* 24.11 (Mar. 1970), pp. 611–615. DOI: 10.1103/PhysRevLett.24.611.

[87] John L. Friedman and Bernard F. Schutz. "Secular instability of rotating Newtonian stars." *Astrophys. J.* 222 (May 1978), pp. 281–296. DOI: 10.1086/156143.

[88] Robert H. Boyer and Richard W. Lindquist. "A variational principle for a rotating relativistic fluid." *Physics Letters* 20.5 (1966), pp. 504–506. ISSN: 0031-9163. DOI: https://doi.org/10.1016/0031-9163(66)90975-9. URL: http://www.sciencedirect.com/science/article/pii/0031916366909759.

[89] James B. Hartle and David H. Sharp. "Variational principle for the equilibrium of a relativistic, rotating star." *Astrophys. J.* 147 (Jan. 1967), p. 317. DOI: 10.1086/149002.

[90] Arya Akmal, Vijay R. Pandharipande, and David G. Ravenhall. "The equation of state of nucleon matter and neutron star structure." *Phys. Rev.* C58 (1998), pp. 1804–1828. DOI: 10.1103/PhysRevC.58.1804. arXiv: nucl-th/9804027 [nucl-th].

[91] Vijay R Pandharipande and David G Ravenhall. "Hot nuclear matter." *Nuclear matter and heavy ion collisions*. Springer, 1989, pp. 103–132.

[92] Norman K. Glendenning and Steven A. Moszkowski. "Reconciliation of neutron star masses and binding of the lambda in hypernuclei." *Phys. Rev. Lett.* 67 (1991), pp. 2414–2417. DOI: 10.1103/PhysRevLett.67.2414.

[93] Fabrice Douchin and Paweł Haensel. "A unified equation of state of dense matter and neutron star structure." *Astron. Astrophys.* 380 (2001), p. 151. DOI: 10.1051/0004-6361:20011402. arXiv: astro-ph/0111092 [astro-ph].

[94] Hajime Togashi et al. "Nuclear equation of state for core-collapse supernova simulations with realistic nuclear forces." *Nucl. Phys.* A961 (2017), pp. 78–105. DOI: 10.1016/j.nuclphysa.2017.02.010. arXiv: 1702.05324 [nucl-th].

[95] Gordon Baym et al. "From hadrons to quarks in neutron stars: a review." *Rept. Prog. Phys.* 81.5 (2018), p. 056902. DOI: 10.1088/1361-6633/aaae14. arXiv: 1707.04966 [astro-ph.HE].

[96] Gordon Baym et al. "New neutron star equation of state with quark-hadron crossover." *Astrophys. J.* 885 (2019), p. 42. DOI: 10.3847/1538-4357/ab441e. arXiv: 1903.08963 [astro-ph.HE].

[97] Paweł Haensel and Alexander Y. Potekhin. "Analytical representations of unified equations of state of neutron-star matter." *Astron. Astrophys.* 428 (2004), pp. 191–197. DOI: 10.1051/0004-6361:20041722. arXiv: astro-ph/0408324 [astro-ph].

[98] *https://compose.obspm.fr/home/*. URL: https://compose.obspm.fr/home/.

[99] Kodanad G. Arun et al. "Parameter estimation of inspiralling compact binaries using 3.5 post-Newtonian gravitational wave phasing: The non-spinning case." *Phys. Rev.* D71 (2005). [Erratum: Phys. Rev.D72,069903(2005)], p. 084008. DOI: 10.1103/PhysRevD.71.084008,10.1103/PhysRevD.72.069903. arXiv: gr-qc/0411146 [gr-qc].

[100] Lawrence E. Kidder, Clifford M. Will, and Alan G. Wiseman. "Spin effects in the inspiral of coalescing compact binaries." *Phys. Rev.* D47.10 (1993), R4183–R4187. DOI: 10.1103/PhysRevD.47.R4183. arXiv: gr-qc/9211025 [gr-qc].

[101] Kodanad G. Arun et al. "Higher-order spin effects in the amplitude and phase of gravitational waveforms emitted by inspiraling compact binaries: Ready-to-use gravitational waveforms." *Phys. Rev.* D79 (2009). [Erratum: Phys. Rev.D84,049901(2011)], p. 104023. DOI: 10.1103/PhysRevD.79.104023,10.1103/PhysRevD.84.049901. arXiv: 0810.5336 [gr-qc].

[102] Luc Blanchet, Alessandra Buonanno, and Guillaume Faye. "Tail-induced spin-orbit effect in the gravitational radiation of compact binaries." *Phys. Rev.* D84 (2011), p. 064041. DOI: 10.1103/PhysRevD.84.064041. arXiv: 1104.5659 [gr-qc].

[103] Balázs Mikóczi, Mátyás Vasúth, and László Á. Gergely. "Self-interaction spin effects in inspiralling compact binaries." *Phys. Rev. D* 71.12, 124043 (June 2005), p. 124043. DOI: 10.1103/PhysRevD.71.124043. arXiv: astro-ph/0504538 [astro-ph].

[104] Tanja Hinderer. "Tidal love numbers of neutron stars." *Astrophys. J.* 677.2 (Apr. 2008), pp. 1216–1220. DOI: 10.1086/533487. arXiv: 0711.2420 [astro-ph].

[105] Thibault Damour, Alessandro Nagar, and Loic Villain. "Measurability of the tidal polarizability of neutron stars in late-inspiral gravitational-wave signals." *Phys. Rev. D* 85.12, 123007 (June 2012), p. 123007. DOI: 10.1103/PhysRevD.85.123007. arXiv: 1203.4352 [gr-qc].

[106] Quentin Henry, Guillaume Faye, and Luc Blanchet. "Tidal effects in the gravitational-wave phase evolution of compact binary systems to next-to-next-to-leading post-Newtonian order." *Phys. Rev. D* 102.4 (2020), p. 044033. DOI: 10.1103/PhysRevD.102.044033. arXiv: 2005.13367 [gr-qc].

[107] Benjamin P Abbott et al. "Exploring the sensitivity of next generation gravitational wave detectors." *Class. Quant. Grav.* 34.4 (2017), p. 044001. DOI: 10.1088/1361-6382/aa51f4. arXiv: 1607.08697 [astro-ph.IM].

[108] Iosif S. Shklovskii. "Possible causes of the secular increase in pulsar periods." *Sov. Astronom.* 13 (Feb. 1970), p. 562.

[109] Niel Brandt and Philipp Podsiadlowski. "The effects of high-velocity supernova kicks on the orbital properties and sky distributions of neutron-star binaries." *Mon. Not. R. Astron Soc.* 274.2 (May 1995), pp. 461–484. DOI: 10.1093/mnras/274.2.461.

[110] Rebecca G. Martin, Christopher A. Tout, and James E. Pringle. "Supernova kicks and misaligned Be star binaries." *Mon. Not. R. Astron Soc.* 397.3 (Aug. 2009), pp. 1563–1576. DOI: 10.1111/j.1365-2966.2009.15031.x. arXiv: 0905.2362 [astro-ph.SR].

[111] Hans-Thomas Janka et al. "Theory of core-collapse supernovae." *Phys. Rept.* 442 (2007), pp. 38–74. DOI: 10.1016/j.physrep.2007.02.002. arXiv: astro-ph/0612072.

[112] Adam Burrows. "Colloquium: Perspectives on core-collapse supernova theory." *Rev. Mod. Phys.* 85 (1 Feb. 2013), pp. 245–261. DOI: 10.1103/RevModPhys.85.245. URL: https://link.aps.org/doi/10.1103/RevModPhys.85.245.

[113] Francois Foucart et al. "Gravitational waveforms from spectral Einstein code simulations: Neutron star-neutron star and low-mass black hole-neutron star binaries." *Phys. Rev.* D99.4 (2019), p. 044008. DOI: 10.1103/PhysRevD.99.044008. arXiv: 1812.06988 [gr-qc].

[114] *https://www.black-holes.org/code/SpEC.html*. URL: https://www.black-holes.org/code/SpEC.html.

[115] Lawrence E. Kidder et al. "SpECTRE: A task-based discontinuous Galerkin code for relativistic astrophysics." *J. Comput. Phys.* 335 (2017), pp. 84–114. DOI: 10.1016/j.jcp.2016.12.059. arXiv: 1609.00098 [astro-ph.HE].

[116] Dmitrii G. Yakovlev, Kseniya P. Levenfish, and Yurii A. Shibanov. "REVIEWS OF TOPICAL PROBLEMS: Cooling of neutron stars and superfluidity in their cores." *Physics Uspekhi* 42.8 (Aug. 1999), pp. 737–778. DOI: 10.1070/PU1999v042n08ABEH000556. arXiv: astro-ph/9906456 [astro-ph].

[117] Nils Andersson and Greg L. Comer. "On the dynamics of superfluid neutron star cores." *Mon. Not. R. Astron Soc.* 328.4 (Dec. 2001), pp. 1129–1143. DOI: 10.1046/j.1365-8711.2001.04923.x. arXiv: astro-ph/0101193 [astro-ph].

[118] Lee Lindblom and Gregory Mendell. "R modes in superfluid neutron stars." *Phys. Rev. D* 61 (2000), p. 104003. DOI: 10.1103/PhysRevD.61.104003. arXiv: gr-qc/9909084.

[119] Nils Andersson and Kostas D. Kokkotas. "The R mode instability in rotating neutron stars." *Int. J. Mod. Phys.* D10 (2001), pp. 381–442. DOI: 10.1142/S0218271801001062. arXiv: gr-qc/0010102 [gr-qc].

[120] Sizheng Ma, Hang Yu, and Yanbei Chen. "Detecting resonant tidal excitations of Rossby modes in coalescing neutron-star binaries with third-generation gravitational-wave detectors." *Phys. Rev. D* 103.6 (2021), p. 063020. DOI: 10.1103/PhysRevD.103.063020. arXiv: 2010.03066 [gr-qc].

[121] Zack Carson et al. "Equation-of-state insensitive relations after GW170817." *Phys. Rev. D* 99.8 (2019), p. 083016. DOI: 10.1103/PhysRevD.99.083016. arXiv: 1903.03909 [gr-qc].

[122] B. M. Barker and Robert F. O'Connell. "Gravitational two-body problem with arbitrary masses, spins, and quadrupole moments." *Phys. Rev. D* 12.2 (July 1975), pp. 329–335. DOI: 10.1103/PhysRevD.12.329.

[123] Hang Yu et al. "Spin and eccentricity evolution in triple systems: from the Lidov-Kozai interaction to the final merger of the inner binary." *arXiv e-prints*, arXiv:2007.12978 (July 2020), arXiv:2007.12978. arXiv: 2007.12978 [gr-qc].

[124] Karl Wette. "WIGLAL: Python and Octave interfaces to the LALSuite gravitational-wave data analysis libraries." *SoftwareX* 12 (2020), p. 100634. DOI: 10.1016/j.softx.2020.100634.

[125] Mark Hannam et al. "Simple model of complete precessing black-hole-binary gravitational waveforms." *Phys. Rev. Lett.* 113.15, 151101 (Oct. 2014), p. 151101. DOI: 10.1103/PhysRevLett.113.151101. arXiv: 1308.3271 [gr-qc].

[126] Lee Lindblom. "Phase transitions and the mass radius curves of relativistic stars." *Phys. Rev.* D58 (1998), p. 024008. DOI: 10.1103/PhysRevD.58.024008. arXiv: gr-qc/9802072 [gr-qc].

[127] Kip S. Thorne and Alfonso Campolattaro. "Non-radial pulsation of general-relativistic stellar models. I. Analytic analysis for L >= 2." *Astrophys. J.* 149 (Sept. 1967), p. 591. DOI: 10.1086/149288.

[128] James R. Ipser and Richard H. Price. "Nonradial pulsations of stellar models in general relativity." *Phys. Rev. D* 43 (6 Mar. 1991), pp. 1768–1773. DOI: 10.1103/PhysRevD.43.1768. URL: https://link.aps.org/doi/10.1103/PhysRevD.43.1768.

[129] Lee Lindblom, Gregory Mendell, and James R. Ipser. "Relativistic stellar pulsations with near-zone boundary conditions." *Phys. Rev. D* 56 (4 Aug. 1997), pp. 2118–2126. DOI: 10.1103/PhysRevD.56.2118. URL: https://link.aps.org/doi/10.1103/PhysRevD.56.2118.

[130] Tanja Hinderer. "Tidal love numbers of neutron stars." *Astrophys. J.* 677 (2008), pp. 1216–1220. DOI: 10.1086/533487. arXiv: 0711.2420 [astro-ph].

Part III

The initial boundary value problem in numerical relativity

Chapter 7

FULLY RELATIVISTIC 3D CAUCHY-CHARACTERISTIC MATCHING

7.1 Introduction

Since the detection of GW150914 [1], gravitational wave (GW) astronomy has become a flourishing field. Accurate modeling of GW signals is a key ingredient in extracting signals from detector noise and understanding the properties of sources. To date, numerical relativity (NR) remains the only *ab initio* method to simulate the major sources of the GW signals: the coalescence of binary black hole (BBH) systems.

Generally speaking, the formulations of NR can be classified into two groups: Cauchy [2, 3] and characteristic [4–11] formalism, depending on how spacetime is foliated[1]. For the Cauchy approach, a spacelike foliation is adopted, and Einstein's equations are split into evolution and constraint sets. This formalism has successfully led to high-accuracy simulations of BBH systems [3].

On the other hand, in the characteristic case, spacetime is sliced into a sequence of null hypersurfaces that extend to future null infinity. Einstein's equations are formulated in terms of the unambiguous geometric treatment of gravitational radiation in curved spacetimes due to Bondi *et al.* [17] Sachs [18] and Penrose [19]. Meanwhile, future null infinity is rigorously encompassed on the characteristic grid via a compactified coordinate system and treated as a perfect absorbing outer boundary. In this way, one is able to extract faithful GWs with the characteristic formalism at future null infinity without any ambiguity [20–24]. However, the characteristic method cannot evolve the near-field region of BBHs when caustics of null rays are present. Therefore, in practice, one can use the Cauchy evolution to simulate the near-zone of the systems and construct metric data on a timelike worldtube [9–11, 25]. Then the characteristic system propagates the worldtube data nonlinearly to future null infinity, which in turn yields GW information. This procedure of extracting GW is known as *Cauchy-characteristic evolution* (CCE) [4–11, 26]. Studies of characteristic evolution and CCE date back to the 1980s. Isaacson *et al.* [27] and Winicour

[1] The third group adopts hyperboloidal slicing [12–16]. Its discussion is beyond the scope of this chapter.

[28, 29] considered a prototype of CCE by shrinking the worldtube to a timelike geodesic and investigated the GWs emitted by an axially symmetric ideal fluid. More complete and complicated CCE systems were developed later [6, 7, 30–36]. Early applications of the characteristic evolution has been focused on simulating generic 3-dimensional single-black-hole spacetimes [37], Einstein-perfect fluid systems [38–42], Einstein-Klein-Gordon systems [41, 43–46], (nonlinear) perturbation of BHs [47–50], event horizons [51–53], fissioning white holes [54], extreme mass ratio inspirals [55], stellar core collapse [56], as well as linearized systems [57]. By using finite-difference methods, PITT null [6–8] is the first code to implement CCE and characteristic evolution, which led to the first CCE simulation of BBH systems [58–61]. The code was also used to extract GWs emitted by rotating stellar core collapse [62]. On the other hand, a spectral algorithm for CCE was built as a module in SpEC [9, 63–65] and SpECTRE [10, 11], developed by the SXS collaboration [3, 66–69]. Bhagwat *et al.* [70] used SpEC CCE to investigate the start time of BBH ringdown. And SpECTRE CCE has been applied to computing memory effects [71, 72], fixing the Bondi-Metzner-Sachs frame of GWs [73, 74], extracting GWs emitted by black hole-neutron star binaries [75], and computing GW echoes [76].

Although CCE has led to high-accuracy and unambiguous GWs at future null infinity, CCE's data flow is one-way, meaning that the Cauchy evolution does not depend at all on the characteristic evolution. This is inaccurate because for a nonlinear set of equations like general relativity, outgoing radiation at arbitrarily far distances can backscatter off the spacetime curvature and eventually affect the source; the Cauchy evolution (with or without CCE) fails to capture this backscattering. To explain this in more detail, note that to perform a Cauchy simulation, the spatial Cauchy domain is typically truncated at a finite distance from the source, with suitable boundary conditions provided at the artificial outer boundary[2]. Ideally speaking, perfect boundary conditions should make the artificial boundary as transparent as possible so that the numerical solution is identical to one that would be evolved on an infinite domain, and these boundary conditions would ideally include nonlinear backscattering. On the contrary, if poor boundary conditions are prescribed, not only will backscattering be incorrectly implemented, but spurious reflection can also be introduced at the boundary and contaminate the whole simulation. In SpEC [67] and SpECTRE [68, 69], the generalized harmonic (GH) evolution system [77] is adopted, whose boundary conditions can be divided into three subsets: constraint-preserving, physical, and gauge boundary conditions [78]. Effort has

[2]In this chapter we restrict our discussions to the outer boundary.

been made to improve the accuracy of these boundary conditions, such as [79–82]. The boundary conditions on the physical degrees of freedom are expected to encode the information of the back-scattered (incoming) GWs that enter the Cauchy domain. Accurately modeling of the back-scattered radiation is not a trivial task. Although there were some attempts [79, 80] to improve the physical boundary conditions, in most SpEC production runs [3] the incoming GWs at the boundary are treated by freezing the Weyl scalar ψ_0 to zero [78], which effectively eliminates all backscatter from beyond the outer boundary.

It was pointed out that the characteristic evolution is a natural system to compute the value of the back-scattered radiation in an exact and efficient way, e.g., see Ref. [4] and references therein. A matching of the internal Cauchy system and the exterior characteristic system is expected to provide accurate physical boundary conditions for the Cauchy module. In this way, the interface between the two grids is transparent and GWs can pass cleanly off of and onto the Cauchy grid. This algorithm is known as *Cauchy-characteristic matching* (CCM). Historically, the idea of CCM was outlined in Refs. [83] and [84]. Then the algorithm was applied to the evolution of a scalar field on a flat background [85, 86], and around a Schwarzschild BH [87] (with metric being fixed). The CCM simulation of gravitational systems was also visited by a series of papers [88–92] that assumed cylindrical symmetry [88, 89, 92] and axial symmetry [90, 91]. Meanwhile, CCM was used to study an Einstein-perfect fluid system [93] and an Einstein-Klein-Gordon system [94] with spherical symmetry. Going to the 3D regime, Bishop *et al.* investigated a scalar wave [95]. Szilagyi *et al.* [96] performed the matching in linearized harmonic coordinates. An alternative to CCM is Cauchy-perturbative matching [97–99], where the exterior region is not evolved fully nonlinearly with a characteristic code but instead is treated as a linearized Schwarzschild BH. This algorithm led to a simulation of a 3D Teukolsky wave [100] propagating on a flat background [97]. Later, this topic was revisited [101] in 2005 after years of progress in numerical relativity. However, until now, all the existing matching algorithms for the gravitational sector are based on either assumptions (symmetries) or approximations (perturbative matching, linearized equations), a full matching in three spatial dimensions is still missing. Further, the formulation of CCM seems to be ill-posed [102–104].

As a step toward addressing those questions, in this chapter, we report the first successful numerical simulation of fully relativistic 3D CCM for gravitational fields without any approximation. The code is implemented in SpECTRE [68, 69]. Unlike

CCE, the data in CCM flows in both directions, meaning that the Cauchy and characteristic systems need to be evolved simultaneously. The communication from the Cauchy to the characteristic system has been discussed extensively [9–11]. In this chapter, we will be explaining how to feed the information of the characteristic module back to the Cauchy system.

This chapter is organized as follows. In Sec. 7.2, we review the Cauchy evolution and the GH system adopted by SpECTRE, with particular attention given to its physical boundary conditions. Next in Sec. 7.3 we discuss some basic information about the CCE module in SpECTRE. Then a thorough algorithm to complete the matching procedure is introduced in Sec. 7.4. Our code is tested with two types of physical systems in Sec. 7.5. Finally, we summarize the results in Sec. 7.6.

Throughout this chapter we use Latin indices $i, j, k, \ldots$ to denote 3D spatial components; and Greek indices $\mu, \nu, \ldots$ for 4D spacetime components. We generally avoid using abstract indices, denoted by Latin letters from the first part of the alphabet $a, b, \ldots$, to keep the text concise, unless stated otherwise.

7.2 The generalized harmonic system and boundary conditions

The detailed communication (matching) algorithm depends on the formulation of the Cauchy evolution. For instance, the perturbative matching in Ref. [97] was performed through Dirichlet and Sommerfeld boundary conditions. In SpECTRE, the Cauchy data are evolved with the GH formalism. Outer boundary conditions are imposed via the Bjørhus method [78, 105]: the time derivatives of the incoming characteristic fields are replaced on the boundary. In this section, we give a brief introduction to the formulation of the GH system and refer the interested reader to Ref. [77] for more details. In particular, we give more attention to the physical subset of the boundary conditions [78].

Let us consider a spacetime with a metric tensor $g_{\mu'\nu'}$ and its 3 + 1 decomposition

$$\begin{aligned} ds^2 =& g_{\mu'\nu'} dx'^{\mu'} dx'^{\nu'} \\ =& (-\alpha^2 + \beta^{i'}\beta^{i'}\gamma_{i'j'}) dt'^2 + 2\beta^{i'}\gamma_{i'j'} dx'^{j'} dt' + \gamma_{i'j'} dx'^{i'} dx'^{j'}, \end{aligned} \tag{7.1}$$

with α the lapse function, $\beta^{i'}$ the shift function, and $\gamma_{i'j'}$ the spatial metric[3]. We use primes on the coordinates to distinguish them from different coordinate systems

[3] In Ref. [77], the authors used $\psi_{a'b'}$ and $g_{i'j'}$ to refer to the spacetime metric and the spatial metric, respectively.

that will be introduced later; see Fig. 7.1. The GH gauge conditions read

$$\Box' x'^{\mu'} = H^{\mu'}, \tag{7.2}$$

where $x'^{\mu'}$ are the Cauchy coordinates, $\Box' = g^{\tau'\nu'}(\partial_{\tau'}\partial_{\nu'} - \Gamma^{\rho'}{}_{\tau'\nu'}\partial_{\rho'})$, and the gauge source function $H^{\mu'}$ is chosen to be some function of the spacetime metric but not the derivatives of the spacetime metric; for example $H^{\mu'}$ might be chosen according to the damped harmonic gauge [106]. Then the vacuum Einstein equations, $R_{\mu'\nu'} = 0$, can be cast into a first-order symmetric hyperbolic (FOSH) evolution system

$$\partial_{t'} u^{\alpha'} + A^{k'\alpha'}{}_{\beta'}\partial_{k'} u^{\beta'} = F^{\alpha'}, \tag{7.3}$$

where $u^{\alpha'} = \{g_{\mu'\nu'}, \Pi_{\mu'\nu'}, \Phi_{i'\mu'\nu'}\}$ is a collection of dynamical variables, $\Pi_{\mu'\nu'} = \alpha^{-1}(\beta^{i'}\partial_{i'} g_{\mu'\nu'} - \partial_{t'} g_{\mu'\nu'})$ and $\Phi_{i'\mu'\nu'} = \partial_{i'} g_{\mu'\nu'}$ are related to the time and spatial derivatives of the metric.

The FOSH system in Eq. (7.3) is symmetric hyperbolic, and its characteristic fields $u^{\hat{\alpha}'} = e^{\hat{\alpha}'}{}_{\beta'} u^{\beta'}$ play an important role in imposing boundary conditions. Here the left eigenvectors $e^{\hat{\alpha}'}{}_{\beta'}$ are defined by

$$e^{\hat{\alpha}'}{}_{\mu'} s_{k'} A^{k'\mu'}{}_{\beta'} = v_{(\hat{\alpha}')} e^{\hat{\alpha}'}{}_{\beta'}, \tag{7.4}$$

where $s^{k'}$ is the outward-directed unit normal to the boundary of the computational domain:

$$s^{t'} = 0, \qquad s^{k'} = \frac{\gamma^{i'k'}\partial_{i'} r'}{\sqrt{\gamma^{i'j'}\partial_{i'} r' \partial_{j'} r'}}, \tag{7.5}$$

and $v_{(\hat{\alpha}')}$ are the eigenvalues. To impose the Bjørhus boundary conditions [78, 105], we first project the FOSH system in Eq. (7.3) to a characteristic fields $e^{\hat{\alpha}'}{}_{\beta'}$ and obtain

$$d_{t'} u^{\hat{\alpha}'} + v_{(\hat{\alpha}')} d_\perp u^{\hat{\alpha}'} = e^{\hat{\alpha}'}{}_{\beta'}(-A^{i'\beta'}{}_{\alpha'} P^{k'}{}_{i'} \partial_{k'} u^{\alpha'} + F^{\beta'}), \tag{7.6}$$

with

$$d_{t'} u^{\hat{\alpha}'} \equiv e^{\hat{\alpha}'}{}_{\beta'}\partial_{t'} u^{\beta'}, \qquad d_\perp u^{\hat{\alpha}'} \equiv e^{\hat{\alpha}'}{}_{\beta'} s^{k'}\partial_{k'} u^{\beta'}, \tag{7.7}$$

and the projection operator

$$P_{\mu'\nu'} = g_{\mu'\nu'} + n_{\mu'} n_{\nu'} - s_{\mu'} s_{\nu'}, \tag{7.8}$$

as well as the normal vector of the time slice $n_{\mu'}$. At the outer boundary, we replace the normal derivative $d_\perp u^{\hat{\alpha}'}$ by its desired value $d_\perp u^{\hat{\alpha}'}\big|_{\rm BC}$ while leaving the tangential derivative unchanged. A convenient way to achieve the goal is given by [78]

$$d_{t'}u^{\hat{\alpha}'} = D_{t'}u^{\hat{\alpha}'} + v_{(\hat{\alpha}')}\left(d_\perp u^{\hat{\alpha}'} - d_\perp u^{\hat{\alpha}'}\Big|_{\rm BC}\right), \tag{7.9}$$

where

$$D_{t'}u^{\hat{\alpha}'} \equiv e^{\hat{\alpha}'}{}_{\beta'}(-A^{k'\beta'}{}_{\alpha'}\partial_{k'}u^{\alpha'} + F^{\beta'}). \tag{7.10}$$

Note that within the bulk, Eq. (7.9) reduces to

$$d_{t'}u^{\hat{\alpha}'} = D_{t'}u^{\hat{\alpha}'}. \tag{7.11}$$

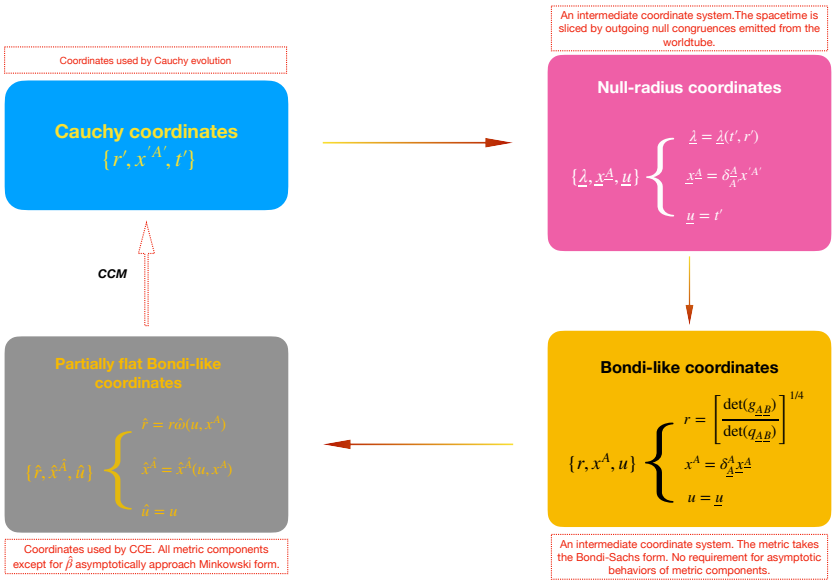

Figure 7.1: Coordinate systems used in the code. The Cauchy coordinates are used by the interior GH evolution, whereas the exterior characteristic system adopts the partially flat Bondi-like coordinates. To achieve their communication, two intermediate coordinate systems (the right column) are introduced.

Boundary conditions must be imposed on each incoming characteristic field $v_{(\hat{\alpha}')} < 0$ [107–109]. In addition, as discussed in Refs. [77, 78], boundary conditions can be divided into three categories: constraint-preserving, physical, and gauge conditions. In this study, we restrict our discussions to the physical subset, where the corresponding characteristic fields read

$$u^{\hat{1}-}_{\mu'\nu'} = \Pi_{\mu'\nu'} - s^{i'}\Phi_{i'\mu'\nu'} - \gamma_2 g_{\mu'\nu'}, \tag{7.12}$$

whose coordinate characteristic speed is given by $-s_{k'}\beta^{k'} - \alpha$. Then the boundary conditions on $u^{\hat{1}-}_{\mu'\nu'}$ can be written as

$$d_{t'}u^{\hat{1}-}_{\mu'\nu'} = P^{\mathrm{P}\rho'\tau'}_{\mu'\nu'}\left[D_{t'}u^{\hat{1}-}_{\rho'\tau'} - (\alpha + s_{j'}\beta^{j'}) \times (w^{-}_{\rho'\tau'} - w^{-}_{\rho'\tau'}\Big|_{\mathrm{BC}} - \gamma_2 s^{i'}c^{3}_{i'\rho'\tau'})\right], \tag{7.13}$$

where the physical projection operator $P^{\mathrm{P}\rho'\tau'}_{\mu'\nu'}$ are given by

$$P^{\mathrm{P}\rho'\tau'}_{\mu'\nu'} \equiv \left(P_{\mu'}{}^{\rho'}P_{\nu'}{}^{\tau'} - \frac{1}{2}P_{\mu'\nu'}P^{\rho'\tau'}\right), \tag{7.14}$$

and the constraint fields $c^{3}_{i'\rho'\tau'}$ read

$$c^{3}_{i'\rho'\tau'} = \partial_{i'}g_{\rho'\tau'} - \Phi_{i'\rho'\tau'}. \tag{7.15}$$

Crucially, $w^{-}_{\rho'\tau'}$ in Eq. (7.13) are the inward propagating components of the Weyl tensor $C_{\mu'\eta'\nu'\alpha'}$,

$$w^{-}_{\rho'\tau'} = P^{\mathrm{P}\mu'\nu'}_{\rho'\tau'}(n^{\eta'} + s^{\eta'})(n^{\alpha'} + s^{\alpha'})C_{\mu'\eta'\nu'\alpha'}, \tag{7.16}$$

and $w^{-}_{\rho'\tau'}\Big|_{\mathrm{BC}}$ are the desired values of $w^{-}_{\rho'\tau'}$ at the outer boundary. The effect of the boundary condition, Eq. (7.13), is to drive $w^{-}_{\rho'\tau'}$ toward $w^{-}_{\rho'\tau'}\Big|_{\mathrm{BC}}$.

The quantity $w^{-}_{\rho'\tau'}$ is related to the Weyl scalar ψ'_0 via

$$w^{-}_{\rho'\tau'} = 2(\psi'_0\bar{m}_{\rho'}\bar{m}_{\tau'} + \bar{\psi}'_0 m_{\rho'}m_{\tau'}), \tag{7.17}$$

where we have used an identity [Eq. (7.8)]

$$P_{\rho'\tau'} = m_{\rho'}\bar{m}_{\tau'} + m_{\tau'}\bar{m}_{\rho'}, \tag{7.18}$$

and the definition of ψ'_0:

$$\psi'_0 = C_{\mu'\nu'\rho'\tau'}l^{\mu'}m^{\nu'}l^{\rho'}m^{\tau'}. \tag{7.19}$$

Here $\{l^{\mu'}, k^{\mu'}, m^{\mu'}\}$ refer to the null tetrad within the Newman-Penrose formalism. The choice of the null vectors $l^{\mu'}$ (outgoing) and $k^{\mu'}$ (ingoing) are determined *uniquely* by Eqs. (7.8) and (7.16) (namely the Cauchy grid):

$$l^{\mu'} = \frac{1}{\sqrt{2}}(n^{\mu'} + s^{\mu'}), \tag{7.20a}$$

$$k^{\mu'} = \frac{1}{\sqrt{2}}(n^{\mu'} - s^{\mu'}). \tag{7.20b}$$

However, the choice of $m^{\mu'}$ is not unique. The requirements on $m^{\mu'}$ read:

$$m^{\mu'} l_{\mu'} = 0, \quad m^{\mu'} k_{\mu'} = 0, \quad m^{\mu'} m_{\mu'} = 1. \tag{7.21}$$

As we shall show later, the only allowed gauge freedom on $m^{\mu'}$ is a rotation: $m^{\mu'} \to m^{\mu'} e^{i\Theta}$, but the values of $w_{\rho'\tau'}$ in Eq. (7.16) do not depend on the gauge variable Θ. Therefore, in our following calculations, we will take advantage of this fact and choose $m^{\mu'}$ as close as possible to that of the characteristic system, in order to simplify calculations.

As mentioned earlier, production SpEC simulations set $w^{-}_{\rho'\tau'}\Big|_{\rm BC}$ to zero. But within the CCM framework, we shall use the characteristic system to determine $w^{-}_{\rho'\tau'}\Big|_{\rm BC}$ from Eq. (7.17), where the ψ'_0 in Eq. (7.17) will be computed from the characteristic evolution and interpolated back to the Cauchy grid. We will explain more details in Sec. 7.4 below.

7.3 The CCE system

In this section we briefly summarize the SpECTRE CCE system as described in Refs. [10, 11]. The procedures for extracting the Cauchy quantities on the worldtube, evolving the characteristic variables in the exterior region, and computing waveform quantities at future null infinity are identical for CCE versus CCM. For more details of the CCE algorithm, see Refs. [10, 11]

The SpECTRE CCE system is based on Bondi-Sachs metric in partially flat Bondi-like coordinates $\{\hat{r}, \hat{x}^{\hat{A}}, \hat{u}\}$ [10, 11]

$$ds^2 = -\left(e^{2\hat{\beta}}\frac{\hat{V}}{\hat{r}} - \hat{r}^2 \hat{h}_{\hat{A}\hat{B}} \hat{U}^{\hat{A}} \hat{U}^{\hat{B}}\right) d\hat{u}^2 - 2e^{2\hat{\beta}} d\hat{u} d\hat{r} - 2\hat{r}^2 \hat{h}_{\hat{A}\hat{B}} \hat{U}^{\hat{B}} d\hat{u} d\hat{x}^{\hat{A}} + \hat{r}^2 \hat{h}_{\hat{A}\hat{B}} d\hat{x}^{\hat{A}} d\hat{x}^{\hat{B}}, \tag{7.22}$$

where $\hat{x}^{\hat{A}}$ stands for the pair of angular coordinates $\{\hat{\theta}, \hat{\phi}\}$. With this coordinate system, a few gauge conditions have been imposed: $g_{\hat{r}\hat{r}} = 0$, $g_{\hat{r}\hat{A}} = 0$, and the determinant of the angular components $\hat{h}_{\hat{A}\hat{B}}$ is set to that of the unit sphere metric $q_{\hat{A}\hat{B}}$

$$\det(\hat{h}_{\hat{A}\hat{B}}) = \det(q_{\hat{A}\hat{B}}) = \sin^2\hat{\theta}. \tag{7.23}$$

Consequently, the system is characterized by 6 degrees of freedom (4 quantities): $\hat{W} = (\hat{V} - \hat{r})/\hat{r}^2$, $\hat{h}_{\hat{A}\hat{B}}$, $\hat{U}^{\hat{B}}$, and $\hat{\beta}$. Near future null infinity, the metric components need to follow falloff rates [10, 11]:

$$\lim_{\hat{r}\to\infty} \hat{W} = O(\hat{r}^{-2}), \tag{7.24a}$$

$$\lim_{\hat{r}\to\infty} \hat{U}^{\hat{A}} = O(\hat{r}^{-2}), \tag{7.24b}$$

$$\lim_{\hat{r}\to\infty} \hat{h}_{\hat{A}\hat{B}} = q_{\hat{A}\hat{B}} + O(\hat{r}^{-1}). \tag{7.24c}$$

Note that the conditions in Eqs. (7.24) are not sufficient for the metric to asymptotically approach the Minkowski metric, as true Bondi-Sachs coordinates do. To bring the partially flat Bondi-like coordinates to a true Bondi-Sachs system (up to BMS transformations), one needs to further impose

$$\lim_{\hat{r}\to\infty} \hat{\beta} = O(\hat{r}^{-1}). \tag{7.25}$$

In practice, it was found that most computations are more straightforward in partially flat Bondi-like coordinates $\{\hat{r}, \hat{x}^{\hat{A}}, \hat{u}\}$ where Eq. (7.25) is not satisfied, or in Bondi-like coordinates $\{r, x^A, u\}$ that do not satisfy Eqs. (7.24); we transform into true Bondi-Sachs coordinates only when necessary for computing waveform quantities at future null infinity [10, 11]. See Fig. 7.1 (and also Table I of [10]) for the various coordinate systems used in CCE and CCM.

Following the algorithm outlined in Refs. [10, 11], the characteristic system needs to take boundary data on a time-like worldtube from the inner Cauchy system. Therefore, one has to perform gauge transformations to convert the Cauchy 3 + 1 metric in Eq. (7.1) to the Bondi-Sachs metric in Eq. (7.22). The procedure involves three steps, and we summarize them in Fig. 7.1. First, the space-like foliation of Eq. (7.1) is converted to null foliation. To achieve the goal, one needs to construct a class of null vectors $\partial_{\underline{\lambda}}$ at the worldtube surface.

$$\left(\partial_{\underline{\lambda}}\right)^{\underline{a}} = \delta^{\underline{a}}_{a'} \frac{n^{a'} + s^{a'}}{\alpha - \gamma_{i'j'}\beta^{i'}s^{j'}}, \tag{7.26}$$

where $\underline{\lambda}$ is an affine parameter, a' and $\underline{a}$ are abstract indices, the unit vector $s^{a'}$ is defined in Eq. (7.5), and $n^{a'}$ still stands for the normal vector of the time slice. A new null coordinate system $\{\underline{u}, \underline{\lambda}, \underline{x^A}\}$ is introduced, and quantities are transformed into this coordinate system.

The second step is to transform the null-radius coordinates to so-called Bondi-like coordinates $\{u, r, x^A\}$ by imposing the gauge condition in Eq. (7.23). At this stage, the metric is brought into Bondi-Sachs form

$$ds^2 = -\left(e^{2\beta}\frac{V}{r} - r^2 h_{AB}U^A U^B\right)du^2 - 2e^{2\beta}dudr - 2r^2 h_{AB}U^B du dx^A + r^2 h_{AB}dx^A dx^B. \tag{7.27}$$

The coordinates still differ from the partially flat Bondi-like coordinates because the falloff rates in Eqs. (7.24) are now relaxed to

$$\lim_{r\to\infty} W = O(r^0), \tag{7.28a}$$

$$\lim_{r\to\infty} U^A = O(r^0), \tag{7.28b}$$

$$\lim_{r\to\infty} h_{AB} = O(r^0). \tag{7.28c}$$

Finally, the Bondi-like coordinates are transformed to the partially-flat Bondi-like coordinates $\{\hat{r}, \hat{x}^{\hat{A}}, \hat{u}\}$ by removing the asymptotic value of U^A at null infinity, $U^{(0)A}$. Here we define $U^{(0)A}$ by

$$U^A = U^{(0)A} + O(r^{-1}). \tag{7.29}$$

Once the worldtube quantities have been computed in partially flat Bondi-like coordinates, these worldtube quantities serve as inner boundary conditions for a set of hierarchichal radial hypersurface equations [7, 63]

$$\hat{\beta}_{,\hat{r}} = S_\beta(\hat{J}), \tag{7.30a}$$

$$(\hat{r}^2\hat{Q})_{,\hat{r}} = S_Q(\hat{J}, \hat{\beta}), \tag{7.30b}$$

$$\hat{U}_{,\hat{r}} = S_U(\hat{J}, \hat{\beta}, \hat{Q}), \tag{7.30c}$$

$$(\hat{r}^2\hat{W})_{,\hat{r}} = S_W(\hat{J}, \hat{\beta}, \hat{Q}, \hat{U}), \tag{7.30d}$$

$$(\hat{r}\hat{H})_{,\hat{r}} + L_H(\hat{J}, \hat{\beta}, \hat{Q}, \hat{U}, \hat{W})\hat{H} + L_{\bar{\hat{H}}}(\hat{J}, \hat{\beta}, \hat{Q}, \hat{U}, \hat{W})\bar{\hat{H}} = S_H(\hat{J}, \hat{\beta}, \hat{Q}, \hat{U}, \hat{W}), \tag{7.30e}$$

that are solved along a surface of constant null coordinate $\hat{u}$ that extends from the worldtube to future null infinity. The expressions for the source functions in Eq. (7.30) can be found in Refs. [7, 63]. Here the quantities determined by Eqs. (7.30) are components of the spacetime metric, which are written as a set of spin-weighted scalars defined by[4]

$$\hat{U} \equiv \hat{U}^{\hat{A}} q_{\hat{A}}, \tag{7.31a}$$

$$\hat{Q} \equiv \hat{r}^2 e^{-2\hat{\beta}} q^{\hat{A}} \hat{h}_{\hat{A}\hat{B}} \partial_{\hat{r}} \hat{U}^{\hat{B}}, \tag{7.31b}$$

$$\hat{J} \equiv \frac{1}{2} q^{\hat{A}} q^{\hat{B}} \hat{h}_{\hat{A}\hat{B}}, \tag{7.31c}$$

$$\hat{K} \equiv \frac{1}{2} q^{\hat{A}} \bar{q}^{\hat{B}} \hat{h}_{\hat{A}\hat{B}} = \sqrt{1 + \hat{J}\bar{\hat{J}}}, \tag{7.31d}$$

[4] We note that there is a typo in Eq. (10e) of Ref. [10]; the correct expression is given in Eq. (7.31d).

$$\hat{H} = \partial_{\hat{u}} \hat{J}, \tag{7.31e}$$

where the complex dyad is defined as

$$q^{\hat{A}} \partial_{\hat{A}} = -\partial_{\hat{\theta}} - \frac{i}{\sin\hat{\theta}} \partial_{\hat{\phi}}, \tag{7.32a}$$

$$q_{\hat{A}} d\hat{x}^{\hat{A}} = -d\hat{\theta} - i \sin\hat{\theta} d\hat{\phi}. \tag{7.32b}$$

The complex dyad obeys the identity

$$q^{\hat{A}} q_{\hat{A}} = 0, \qquad\qquad q^{\hat{A}} \bar{q}_{\hat{A}} = 2, \tag{7.33}$$

and the unit sphere metric $q_{\hat{A}\hat{B}}$ can be written as

$$q_{\hat{A}\hat{B}} = \frac{1}{2}(q_{\hat{A}} \bar{q}_{\hat{B}} + \bar{q}_{\hat{A}} q_{\hat{B}}). \tag{7.34}$$

The final step in the characteristic evolution is to time-evolve the quantity $\hat{J}$ from one null surface $\hat{u}$ to the next null surface $\hat{u} + \delta\hat{u}$. This is accomplished by integrating $\hat{J}$ forward in $\hat{u}$ using Eq. (7.31e); the quantity $\hat{H}$ is known on the entire null hypersurface from the solution of Eq. (7.30e). The time evolution is described in detail in [10, 11] and is identical for CCM versus CCE.

Having determined all the metric components with the CCE algorithm, we can now compute Weyl scalars. For CCM, we need the Weyl scalar ψ_0 in the exterior region, which will be used in the outer-boundary condition for the interior Cauchy system. To assemble ψ_0 from the metric components, we adopt the tetrad provided by Ref. [10]

$$m^{\mu} = -\frac{1}{\sqrt{2}r} \left(\sqrt{\frac{K+1}{2}} q^{\mu} - \frac{J}{\sqrt{2(1+K)}} \bar{q}^{\mu} \right), \tag{7.35a}$$

$$k^{\mu} = \sqrt{2} e^{-2\beta} \left[\delta^{\mu}_{u} - \frac{V}{2r} \delta^{\mu}_{r} + \frac{1}{2} \bar{U} q^{\mu} + \frac{1}{2} U \bar{q}^{\mu} \right], \tag{7.35b}$$

$$l^{\mu} = \frac{1}{\sqrt{2}} \delta^{\mu}_{r}. \tag{7.35c}$$

Note that these tetrad vectors are constructed with the Bondi-like coordinates, of which the partially flat Bondi-like coordinates are subclasses. Therefore, Eqs. (7.35) can be applied directly to the partially flat Bondi-like coordinates as long as all variables are replaced by their partially flat Bondi-like counterparts.

In addition, a full expression of the Bondi-like ψ_0 in terms of Bondi quantities can be written as [10]

$$\psi_0 = \left(\frac{r\partial_r \beta - 1}{4Kr} \right) \left[(1+K)\partial_r J - \frac{J^2 \partial_r \bar{J}}{1+K} \right] + \frac{J(1+K^2)\partial_r J \partial_r \bar{J}}{8K^3}$$

$$+\frac{1}{8K}\left[\frac{J^2\partial_r^2\bar{J}}{1+K}-(1+K)\partial_r^2 J\right]-\frac{J\bar{J}^2(\partial_r J)^2+J^3(\partial_r\bar{J})^2}{16K^3}. \tag{7.36}$$

Similarly, Eq. (7.36) is also applicable to the partially-flat-Bondi-like $\hat{\psi}_0$ when the Bondi quantities are evaluated with the partially flat Bondi-like coordinates.

7.4 Matching characteristic and Cauchy systems

We are now in a position to accomplish Cauchy-characteristic matching. The goal is to use the Weyl scalar ψ_0 obtained with the characteristic system to compute the boundary value $w^-_{\rho'\tau'}\Big|_{\rm BC}$ that goes into the physical boundary condition of the Cauchy system [Eq. (7.13)]. This is done by evaluating $w^-_{\rho'\tau'}\Big|_{\rm BC}$ by inserting CCE's ψ_0 into Eq. (7.17). Notice that the tetrad adopted by the characteristic system in Eqs. (7.35) differs from the one used by Cauchy evolution in Eqs. (7.20), so we need to perform Lorentz transformations to obtain (a) the Cauchy Weyl scalar ψ_0' [defined in Eq. (7.19)] and (b) the null covariant vector $m_{\mu'}$ in Eq. (7.17). Necessary ingredients for the Lorentz transformations involve a set of Jacobian matrices across different coordinate systems. So in Sec. 7.4.1 we first work out the explicit expressions for these Jacobians, and then in Secs. 7.4.2 and 7.4.3 we carry out the transformations. Notice that the evaluation of ψ_0 with the characteristic system [Eq. (7.36)] could be done in either the Bondi-like coordinates or the partially flat Bondi-like coordinates, and different choices lead to different Lorentz transformations. In order to keep our discussions as general as possible, we consider both choices in Secs. 7.4.2 and 7.4.3, respectively. The final step toward finishing the matching is to interpolate the values of ψ_0' and $m_{\mu'}$ from the characteristic grid to the Cauchy grid. This is done in Sec. 7.4.4. Figure 7.2 summarizes the matching procedures.

7.4.1 Jacobians for CCM

As outlined in Sec. 7.3 and summarized in Fig. 7.1, two intermediate coordinate systems are introduced to convert the worldtube data from the Cauchy coordinates to the partially flat Bondi-like coordinates. Below, we provide the definition of these transformations and their Jacobians.

7.4.1.1 *Cauchy and null-radius coordinates*

The null-radius coordinates consist of $\{\underline{u},\underline{\lambda},\underline{x^A}\}$, where $\underline{\lambda}$ is the affine parameter of the null vector in Eq. (7.26). Meanwhile, the time and angular coordinates are the

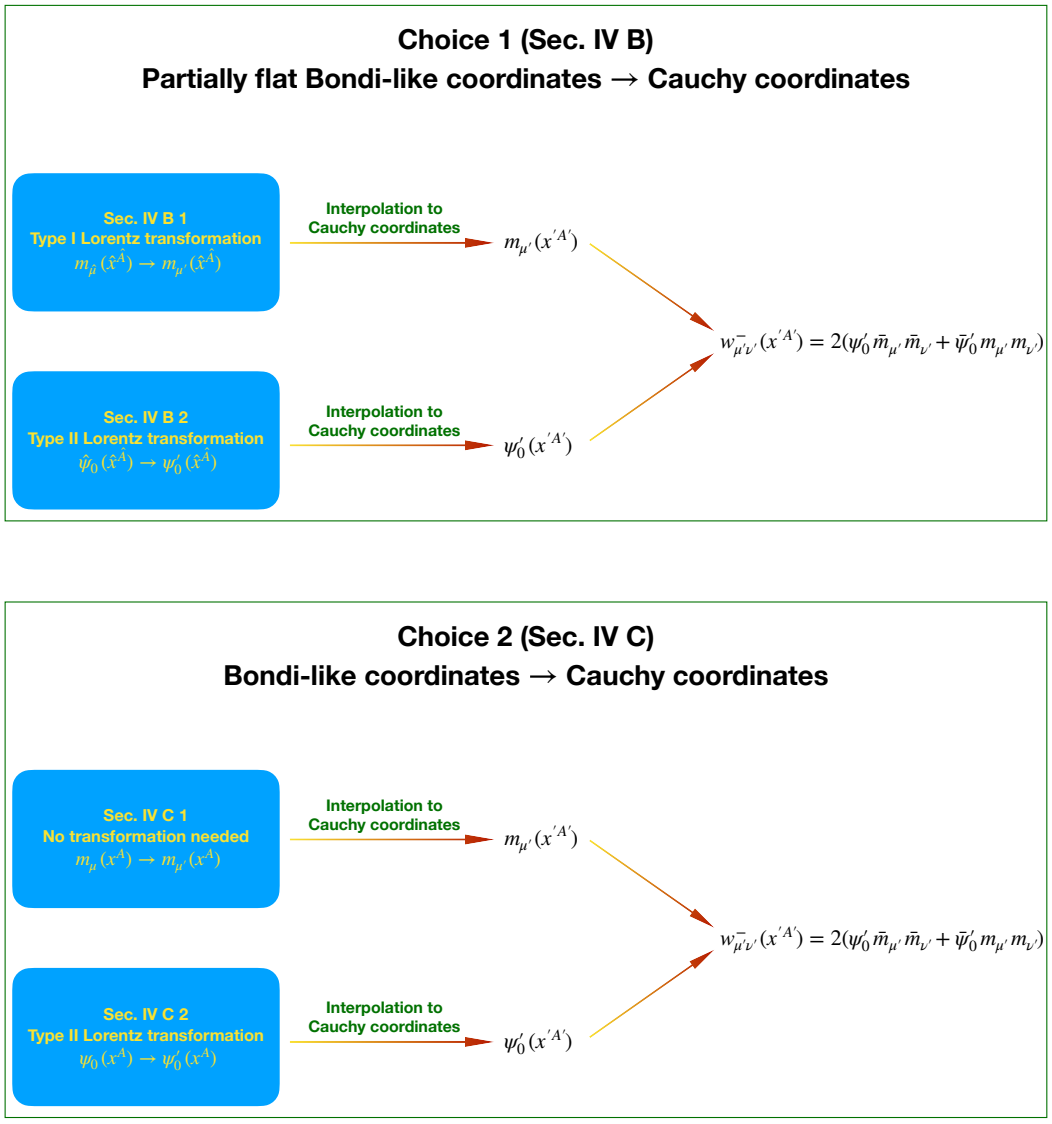

Figure 7.2: Summary of the matching procedures discussed in Sec. 7.4. Since one can compute the relevant characteristic quantities in either the partially flat Bondi-like coordinates $\{\hat{r}, \hat{x}^{\hat{A}}, \hat{u}\}$ (top), or in the Bondi-like coordinates $\{r, x^A, u\}$ (bottom), there are two choices to perform the matching. In practice, Choice 2 is preferred since it is easier to implement.

same as the Cauchy coordinates:

$$\begin{cases} \underline{u} = t', \\ \underline{x}^{\underline{A}} = \delta^{\underline{A}}_{A'} x'^{A'}, \\ \underline{\lambda} = \underline{\lambda}(t', r'). \end{cases} \tag{7.37}$$

Consequently, the metric components in the null-radius coordinates are [10]

$$
\begin{aligned}
&g_{\underline{\lambda u}} = -1, \quad g_{\underline{\lambda\lambda}} = 0, \quad g_{\underline{\lambda A}} = 0, \quad g_{\underline{uu}} = g_{t't'}, \\
&g_{\underline{uA}} = \delta^{A'}_{\underline{A}} g_{t'A'}, \quad g_{\underline{AB}} = \delta^{A'}_{\underline{A}} \delta^{B'}_{\underline{B}} g_{A'B'}.
\end{aligned} \tag{7.38}
$$

Eqs. (7.38) lead to the Jacobian between two coordinate systems:

$$
\frac{\partial(t', r', x'^{A'})}{\partial(\underline{u}, \underline{\lambda}, \underline{x}^{\underline{A}})} = \begin{pmatrix} 1 & \partial_{\underline{\lambda}} t' & 0 \\ 0 & \partial_{\underline{\lambda}} r' & 0 \\ 0 & 0 & \delta^{A'}_{\underline{A}} \end{pmatrix}. \tag{7.39}
$$

7.4.1.2 *Null-radius and Bondi-like coordinates*

To bring the null-radius coordinates to Bondi-like coordinates, one needs to impose the gauge condition in Eq. (7.23) and define the Bondi-like radius:

$$
r = \left[\frac{\det(g_{\underline{AB}})}{\det(q_{\underline{AB}})} \right]^{1/4}. \tag{7.40}
$$

Then the Bondi-like coordinates $\{u, r, x^A\}$ can be written as

$$
\begin{cases} u = \underline{u}, \\ x^A = \delta^A_{\underline{A}} \underline{x}^{\underline{A}}, \\ r = r(\underline{u}, \underline{\lambda}, \underline{x}^{\underline{A}}). \end{cases} \tag{7.41}
$$

Eqs. (7.41) result in the Jocobian

$$
\frac{\partial(u, r, x^A)}{\partial(\underline{u}, \underline{\lambda}, \underline{x}^{\underline{A}})} = \begin{pmatrix} 1 & 0 & 0 \\ \partial_{\underline{u}} r & \partial_{\underline{\lambda}} r & \partial_{\underline{A}} r \\ 0 & 0 & \delta^A_{\underline{A}} \end{pmatrix}, \tag{7.42}
$$

and its inverse

$$
\frac{\partial(\underline{u}, \underline{\lambda}, \underline{x}^{\underline{A}})}{\partial(u, r, x^A)} = \begin{pmatrix} 1 & 0 & 0 \\ -\partial_{\underline{u}} r / \partial_{\underline{\lambda}} r & (\partial_{\underline{\lambda}} r)^{-1} & -\delta^{\underline{A}}_A \partial_{\underline{A}} r / \partial_{\underline{\lambda}} r \\ 0 & 0 & \delta^{\underline{A}}_A \end{pmatrix}. \tag{7.43}
$$

7.4.1.3 *Bondi-like and partially flat Bondi-like coordinates*

One difference between these two coordinate systems is that the quantity U^A is finite at future null infinity, but the quantity $\hat{U}^{\hat{A}}$ vanishes. To remove the asymptotically constant part of U^A, the angular coordinates $\hat{x}^{\hat{A}}$ must satisfy

$$
\partial_u \hat{x}^{\hat{A}} = -\partial_A \hat{x}^{\hat{A}} U^{(0)A}, \tag{7.44}
$$

where $U^{(0)A}$ is defined by Eq. (7.29). The Bondi-like radius r also needs to be adjusted accordingly to meet the gauge condition in Eq. (7.23). Finally, the time coordinate $\hat{u} = u$ remains unchanged. In summary, the transformation is given by

$$\begin{cases} \hat{u} = u, \\ \hat{x}^{\hat{A}} = \hat{x}^{\hat{A}}(u, x^A), \\ \hat{r} = r\hat{\omega}(u, x^A), \end{cases} \tag{7.45}$$

where $\hat{\omega}(u, x^A)$ is a conformal factor

$$\hat{\omega} = \frac{1}{2}\sqrt{\hat{b}\bar{\hat{b}} - \hat{a}\bar{\hat{a}}}, \tag{7.46}$$

and two spin-weighted Jacobian factors $\hat{a}$ and $\hat{b}$ are given by

$$\hat{a} = \hat{q}^{\hat{A}}\partial_{\hat{A}}x^A q_A, \qquad \text{(spin-weight 2)} \tag{7.47}$$

$$\hat{b} = \bar{\hat{q}}^{\hat{A}}\partial_{\hat{A}}x^A q_A. \qquad \text{(spin-weight 0)} \tag{7.48}$$

Since $\{q_A, \bar{q}_A\}$ ($\{\hat{q}_{\hat{A}}, \bar{\hat{q}}_{\hat{A}}\}$) form a complete basis for the angular subspace spanned by $\{x^A\}$ ($\{\hat{x}^{\hat{A}}\}$), we can expand $\partial_{\hat{A}}x^A$ into[5]

$$\partial_{\hat{A}}x^A = \frac{1}{4}\left(\hat{q}_{\hat{A}}, \bar{\hat{q}}_{\hat{A}}\right)\begin{pmatrix} \bar{\hat{a}} & \bar{\hat{b}} \\ \hat{b} & \hat{a} \end{pmatrix}\begin{pmatrix} q^A \\ \bar{q}^A \end{pmatrix}, \tag{7.49}$$

where the expression is written in terms of matrix products. Note that the determinant of the middle 2×2 matrix (together with the factor of $1/4$) is equal to $-\hat{\omega}^2$ [see Eq. (7.46)]. In practice, we find it is also convenient to define spin-weighted factors that are related to the inverse of the Jacobian:

$$a = q^A\partial_A\hat{x}^{\hat{A}}\hat{q}_{\hat{A}}, \qquad \text{(spin-weight 2)} \tag{7.50}$$

$$b = \bar{q}^A\partial_A\hat{x}^{\hat{A}}\hat{q}_{\hat{A}}, \qquad \text{(spin-weight 0)} \tag{7.51}$$

as well as the conformal factor $\omega(\hat{u}, \hat{x}^{\hat{A}})$ associated with them

$$\omega = \frac{1}{2}\sqrt{b\bar{b} - a\bar{a}}. \tag{7.52}$$

Similarly, the counterpart of Eq. (7.49) reads

$$\partial_A\hat{x}^{\hat{A}} = \frac{1}{4}\left(q_A, \bar{q}_A\right)\begin{pmatrix} \bar{a} & \bar{b} \\ b & a \end{pmatrix}\begin{pmatrix} \hat{q}^{\hat{A}} \\ \bar{\hat{q}}^{\hat{A}} \end{pmatrix}. \tag{7.53}$$

[5] To obtain Eq. (7.49), one can exhaust all the possible linear combinations formed by the two bases $\{\hat{q}_{\hat{A}}, \bar{\hat{q}}_{\hat{A}}\}$ and $\{q^A, \bar{q}^A\}$, and then determine the coefficients uniquely via Eqs. (7.33), (7.47) and (7.48).

At the same spacetime point, the identity $\partial_{\hat{A}} x^A \partial_A \hat{x}^{\hat{B}} = \delta^{\hat{B}}_{\hat{A}}$ leads to

$$a = -\frac{\hat{a}}{\hat{\omega}^2}, \qquad\qquad b = \frac{\bar{\hat{b}}}{\hat{\omega}^2}. \tag{7.54}$$

Plugging Eq. (7.54) into Eq. (7.52) we obtain another identity

$$\omega\hat{\omega} = 1. \tag{7.55}$$

We then use Eq. (7.45) to get the Jacobian between the Bondi-like and the partially flat Bondi-like coordinates

$$\frac{\partial(\hat{r}, \hat{x}^{\hat{A}}, \hat{u})}{\partial(r, x^A, u)} = \begin{pmatrix} \hat{\omega} & r\partial_A\hat{\omega} & r\partial_u\hat{\omega} \\ 0 & \partial_A\hat{x}^{\hat{A}} & \partial_u\hat{x}^{\hat{A}} \\ 0 & 0 & 1 \end{pmatrix}. \tag{7.56}$$

Its inverse reads

$$\frac{\partial(r, x^A, u)}{\partial(\hat{r}, \hat{x}^{\hat{A}}, \hat{u})} = \begin{pmatrix} \omega & r\delta^A_{\hat{A}}\partial_A \ln\omega & r\partial_u \ln\omega + rU^{(0)A}\partial_A \ln\omega \\ 0 & \partial_{\hat{A}} x^A & U^{(0)A} \\ 0 & 0 & 1 \end{pmatrix}, \tag{7.57}$$

where we have used Eq. (7.44) to simplify the result.

7.4.2 Choice 1: Transforming $m_{\hat{\mu}}$ and $\hat{\psi}_0$ to the Cauchy tetrad

We first consider Choice 1, as summarized in Fig. 7.2, where the tetrad vector $m_{\hat{\mu}}$ and the Weyl scalar $\hat{\psi}_0$ are evaluated in the partially flat Bondi-like coordinates, using Eqs. (7.35a) and (7.36). Before transforming them into the Cauchy tetrad, we first observe a useful and important fact: The CCE outgoing null tetrad vector $l^{\hat{a}}$ at the worldtube surface, as defined in Eq. (7.35c), is by construction *proportional to* that of the Cauchy system $l^{a'}$, defined in Eq. (7.20a). Again, here $\hat{a}$ and a' stand for abstract indices. To see this, we write

$$l^{\hat{a}} = \frac{1}{\sqrt{2}}(\partial_{\hat{r}})^{\hat{a}} = \frac{1}{\sqrt{2}}\left(\partial_{\underline{\lambda}}\hat{r}\right)^{-1}\delta^{\hat{a}}_{\underline{a}}\left(\partial_{\underline{\lambda}}\right)^{\underline{a}} = \frac{1}{\sqrt{2}}e^{2\hat{\beta}}\delta^{\hat{a}}_{\underline{a}}\left(\partial_{\underline{\lambda}}\right)^{\underline{a}}, \tag{7.58}$$

where the first equality comes from Eq. (7.35c), the second equality is due to the combination of the Jacobian matrices in Eq. (7.43) and (7.57), and the final equality is based on a relationship [see Eqs. (19a) and (33a) of Ref. [10]]

$$\hat{\beta} = -\frac{1}{2}\ln(\partial_{\underline{\lambda}}\hat{r}). \tag{7.59}$$

On the other hand, the null vector $\left(\partial_{\underline{\lambda}}\right)^{\underline{a}}$ in Eq. (7.58) is proportional to the Cauchy outgoing null vector $l^{a'}$ needed by the boundary condition [see Eqs. (7.26) and (7.20a)], but with a different normalization. After combining Eq. (7.58) with (7.26) and (7.20a), we obtain:

$$l^{a'} = (\alpha - \gamma_{i'j'}\beta^{i'}s^{j'})e^{-2\hat{\beta}}l^{\hat{a}}\delta^{a'}_{\hat{a}}. \tag{7.60}$$

Therefore, the statement $l^{a'} \propto l^{\hat{a}}$ is proven. Under this constraint, the allowed Lorentz transformation between the characteristic and Cauchy tetrads can be split into two categories:

- Type I: ($\boldsymbol{l}$ unchanged)

$$\begin{aligned} \boldsymbol{l} &\to \boldsymbol{l}, & \boldsymbol{k} &\to \boldsymbol{k} + \bar{\kappa}\boldsymbol{m} + \kappa\bar{\boldsymbol{m}} + \kappa\bar{\kappa}\boldsymbol{l}, \\ \boldsymbol{m} &\to \boldsymbol{m} + \kappa\boldsymbol{l}, & \bar{\boldsymbol{m}} &\to \bar{\boldsymbol{m}} + \bar{\kappa}\boldsymbol{l}. \end{aligned} \tag{7.61}$$

- Type II: (both $\boldsymbol{l}$ and $\boldsymbol{k}$ changed)

$$\begin{aligned} \boldsymbol{l} &\to A\boldsymbol{l}, & \boldsymbol{k} &\to A^{-1}\boldsymbol{k}, \\ \boldsymbol{m} &\to e^{i\Theta}\boldsymbol{m}, & \bar{\boldsymbol{m}} &\to e^{-i\Theta}\bar{\boldsymbol{m}}, \end{aligned} \tag{7.62}$$

where the complex scalar κ has a spin weight 1, A and Θ are real scalars. The Weyl scalar $\hat{\psi}_0$ transforms correspondingly:

- Type I:

$$\hat{\psi}_0 \to \hat{\psi}_0. \tag{7.63}$$

- Type II:

$$\hat{\psi}_0 \to A^2 e^{2i\Theta}\hat{\psi}_0. \tag{7.64}$$

Notice that $\hat{\psi}_0$ is not mixed with other Weyl scalars. In particular, it remains unchanged within the Type I category. Below we will take advantage of this observation to simplify the calculation.

As summarized in Fig. 7.2, for Choice 1, we need to transform both $m_{\hat{\mu}}$ and $\hat{\psi}_0$ to the Cauchy tetrad in order to evaluate the inward propagating components of the Weyl tensor $w^{-}_{\rho'\tau'}\Big|_{\mathrm{BC}}$ [Eq. (7.17)] in the correct tetrad. We treat the transformation of $m_{\hat{\mu}}$ and $\hat{\psi}_0$ separately in the two following sections.

7.4.2.1 *Type I transformation of* $m_{\hat{\mu}}$

CCE's $m_{\hat{\mu}}$ [Eq. (7.35a)] is not aligned with Cauchy's [Eq. (7.21)]. This is because our choice of the ingoing null vector k^{μ} for the characteristic system [Eq. (7.35b)] is not the same as $k^{\mu'}$ used in the Bjørhus boundary condition, which is defined uniquely by Eq. (7.20b). To transform the characteristic vector $\boldsymbol{m}$ to the corresponding choice in the Cauchy boundary condition, it suffices to add some multiple of the outgoing null vector $\boldsymbol{l}$ to $\boldsymbol{m}$; thus we need to perform a type I transformation. We want to emphasize that the value of $\hat{\psi}_0$ is not impacted by a type I transformation, so when performing such a transformation it is not necessary to keep track of the explicit Lorentz parameter [namely κ in Eq. (7.61)] that was used in the transformation. Accordingly, in some vector expressions below we will simply drop terms that are proportional to the outgoing null vector $\boldsymbol{l}$, when such terms can be removed by making a type I transformation; when this is done we will indicate that such terms have been dropped by a type I transformation by using the symbol $\approx$ instead of $=$.

We first convert the contravariant vector $m^{\hat{\mu}}$ in Eq. (7.35a) to its covariant form

$$m_{\hat{\mu}} = -\frac{\hat{r}}{\sqrt{2}}\left(\sqrt{\frac{\hat{K}+1}{2}}q_{\hat{\mu}} + \frac{\hat{J}}{\sqrt{2(1+\hat{K})}}\bar{q}_{\hat{\mu}}\right), \tag{7.65}$$

where the expression for $q_{\hat{\mu}}$ can be found in Eq. (7.32b). By combining Jacobians in Eqs. (7.39), (7.42) and (7.56), we obtain a relationship

$$d\hat{x}^{\hat{A}} = (\partial_A \hat{x}^{\hat{A}})dx'^{A'}\delta^{A}_{A'} + (\partial_u \hat{x}^{\hat{A}})d\underline{u}. \tag{7.66}$$

Since $-d\underline{u}_{\underline{a}} = g_{\underline{ab}}\left(\partial_{\underline{\lambda}}\right)^{\underline{b}}$ is the covariant form of the outgoing null vector $\left(\partial_{\underline{\lambda}}\right)^{\underline{b}}$ given in Eq. (7.58), the second term in Eq. (7.66) can be removed via a type I Lorentz transformation. We then insert Eqs. (7.66) and (7.53) into Eq. (7.32), which yields

$$q_{\hat{\mu}} \approx \frac{1}{2}a\delta^{\mu'}_{\hat{\mu}}\bar{q}_{\mu'} + \frac{1}{2}b\delta^{\mu'}_{\hat{\mu}}q_{\mu'}, \tag{7.67}$$

where $\approx$ implies that a type I Lorentz transformation has been performed, as described above. Plugging Eq. (7.67) into Eq. (7.65), we obtain

$$\begin{aligned} m_{\hat{\mu}} \approx -\frac{\hat{r}\delta^{\mu'}_{\hat{\mu}}}{\sqrt{2}}\Bigg[&\left(\sqrt{\frac{\hat{K}+1}{2}}\frac{1}{2}a + \frac{\hat{J}}{\sqrt{2(1+\hat{K})}}\frac{1}{2}\bar{b}\right)\bar{q}_{\mu'} \\ &+\left(\sqrt{\frac{\hat{K}+1}{2}}\frac{1}{2}b + \frac{\hat{J}}{\sqrt{2(1+\hat{K})}}\frac{1}{2}\bar{a}\right)q_{\mu'}\Bigg]. \end{aligned} \tag{7.68}$$

Or equivalently

$$m_{\hat{\mu}} \approx \delta^{\mu'}_{\hat{\mu}} m_{\mu'}, \tag{7.69}$$

with $m_{\mu'}$ being the components of a new covariant vector $m_{a'}$

$$m_{a'} = \hat{M}_{\theta'} (d\theta')_{a'} + i\hat{M}_{\phi'} \sin\theta' (d\phi')_{a'}, \tag{7.70}$$

and

$$4/\hat{r}\hat{M}_{\theta'} = (a+b)\sqrt{\hat{K}+1} + (\bar{a}+\bar{b})\frac{\hat{J}}{\sqrt{(1+\hat{K})}}, \tag{7.71}$$

$$4/\hat{r}\hat{M}_{\phi'} = (b-a)\sqrt{\hat{K}+1} + (\bar{\hat{a}}-\hat{b})\frac{\hat{J}}{\sqrt{(1+\hat{K})}}. \tag{7.72}$$

At this stage, we have constructed a Cauchy tetrad vector $m_{a'}$ in Eq. (7.70) that differs from the original characteristic tetrad vector $m_{\hat{a}}$ by only a type I transformation. Meanwhile, we can see $m_{a'}$ has components only within the Cauchy angular subspace $\{\theta', \phi'\}$. Therefore it meets all the requirements in Eq. (7.21), and we can insert $m_{a'}$ into Eq. (7.17) to evaluate $w^{-}_{\rho'\tau'}\Big|_{\mathrm{BC}}$.

Since Cartesian coordinates are used to evolve the Cauchy system, we write down the Cartesian components of two angular bases $(d\theta')_{a'}$ and $(d\phi')_{a'}$ for completeness

$$(d\theta')_{a'} = \frac{1}{R'_{\mathrm{wt}}} (\cos\phi'\cos\theta', \sin\phi'\cos\theta', -\sin\theta'), \tag{7.73}$$

$$\sin\theta' (d\phi')_{a'} = \frac{1}{R'_{\mathrm{wt}}} (-\sin\phi', \cos\phi', 0). \tag{7.74}$$

7.4.2.2 *Type II transformation of* $\hat{\psi}_0$

Eq. (7.60) indicates that two outgoing null vectors $l^{a'}$ and $l^{\hat{a}}$ are related by a Type II transformation [Eq. (7.62)], with the Lorentz parameter $\hat{A}$ given by

$$\hat{A} = (\alpha - \gamma_{i'j'}\beta^{i'}s^{j'})e^{-2\hat{\beta}}, \tag{7.75}$$

which leads to

$$\psi'_0 = \hat{A}^2\hat{\psi}_0. \tag{7.76}$$

On the other hand, there is one more gauge freedom: the rotation of $\boldsymbol{m}$ with a phase factor $e^{i\Theta}$. However, the combination $\psi'_0\bar{m}_{\rho'}\bar{m}_{\tau'}$ that appears in $w^{-}_{\rho'\tau'}$ [Eq. (7.17)] is invariant because ψ'_0 is also transformed accordingly due to Eq. (7.64). Physically speaking, the incoming characteristics $w^{-}_{\rho'\tau'}$ do not depend on the choice of the angular tetrad vector. Therefore, we can neglect this gauge freedom while performing the matching.

7.4.3 Choice 2: Transforming m_μ and ψ_0 to the Cauchy tetrad

Then we consider Choice 2, where the characteristic quantities m_μ and ψ_0 are evaluated in the Bondi-like coordinates. Similar to Sec. 7.4.2, below we treat the transformation of m_μ and ψ_0 separately.

7.4.3.1 *m_μ fulfills the requirements*

The Bondi-like covariant vector m_μ reads[6]

$$m_\mu = -\frac{r}{\sqrt{2}}\left(\sqrt{\frac{K+1}{2}}q_\mu + \frac{J}{\sqrt{2(1+K)}}\bar{q}_\mu\right). \tag{7.77}$$

By combining Jacobians in Eqs. (7.39) and (7.42), we obtain

$$dx^A = \delta^A_{A'}dx'^{A'}, \tag{7.78}$$

which yields

$$m_\mu = \delta^{\mu'}_{\mu} m_{\mu'}, \tag{7.79}$$

with $m_{\mu'}$ being the components of the vector $m_{a'}$

$$m_{a'} = M_{\theta'}\left(d\theta'\right)_{a'} + iM_{\phi'}\sin\theta'\left(d\phi'\right)_{a'}, \tag{7.80}$$

and

$$2/rM_{\theta'} = \sqrt{K+1} + \frac{J}{\sqrt{(1+K)}}, \tag{7.81}$$

$$2/rM_{\phi'} = \sqrt{K+1} - \frac{J}{\sqrt{(1+K)}}. \tag{7.82}$$

We remark that the null vector $m_{\mu'}$, which is identical to m_μ, is already in the Cauchy angular subspace $\{\theta', \phi'\}$, as required by the Cauchy boundary condition in Eq. (7.21), so we do not need to perform any Lorentz transformation.

In practice, the characteristic system is evolved with the partially flat Bondi-like coordinates, as summarized in Fig. 7.1. Therefore, we need to transform the Bondi quantities $\hat{J}$ and $\hat{K}$ [Eq. (7.31)] to the Bondi-like coordinates via [10]

$$J = \frac{\bar{b}^2\hat{J} + a^2\bar{\hat{J}} + 2a\bar{b}\hat{K}}{4\omega^2}, \tag{7.83}$$

$$K = \sqrt{1 + J\bar{J}}, \tag{7.84}$$

and then insert the results into Eq. (7.80) to construct the tetrad vector $m_{\mu'}$ for matching.

[6] Eq. (7.77) is the same as Eq. (7.65) except that all the hatted quantities in Eq. (7.65) are replaced by their unhatted counterparts.

7.4.3.2 *Type II transformation of* ψ_0

In the meantime, after obtaining J and K from Eqs. (7.83) and (7.84), we can evaluate ψ_0 with Eq. (7.36). Similar to the previous discussion, the two outgoing null vectors $l^{\mu'}$ and l^{μ} are related by a Type II transformation, and the corresponding Lorentz parameter A reads

$$A = (\alpha - \gamma_{i'j'}\beta^{i'}s^{j'})e^{-2\beta}. \tag{7.85}$$

Consequently, the desired ψ_0' is given by

$$\psi_0' = A^2\psi_0. \tag{7.86}$$

7.4.4 Interpolating to the Cauchy coordinates

Now we have obtained the desired tetrad vector $m_{\mu'}$ and the Weyl scalar ψ_0'. But they are still evaluated on the partially flat Bondi-like grid for both choices[7]. The final step to complete the matching is to interpolate the results to the Cauchy grid. More specifically, since the matching is performed at a 2D spherical surface, we need to construct a map from the partially flat Bondi-like angular coordinates $\hat{x}^{\hat{A}} = \{\hat{\theta}, \hat{\phi}\}$ to the Cauchy angular coordinates $x'^{A'} = (\theta', \phi')$ for each time step of simulations. Recall from Fig. 7.1 that the Bondi-like angular coordinates x^A are constructed to be the same as $x'^{A'}$, therefore the task is equivalent to constructing the dependence of x^A on $\hat{x}^{\hat{A}}$.

The inverse problem, namely $\hat{x}^{\hat{A}}$ as functions of x^A, has been worked out while we are constructing the worldtube data for the characteristic system [10, 11]—the partially flat Bondi-like angular coordinates $\hat{x}^{\hat{A}}$ are evolved with respect to Bondi-like angular coordinates x^A using Eq. (7.44). In principle, one can invert the dependence numerically to fulfill our purpose, but the process might be numerically expensive. A cheaper way is to evolve x^A as functions of $\hat{x}^{\hat{A}}$ simultaneously. The counterpart of Eq. (7.44) for the evolution of x^A can be read off directly from the Jacobian in Eq. (7.57):

$$\partial_{\hat{u}} x^A = U^{(0)A}. \tag{7.87}$$

In practice, we find it is more convenient to convert x^A to Cartesian coordinates x^i on a unit sphere,

$$x^i = (\sin\theta\cos\phi, \sin\theta\sin\phi, \cos\theta)\,, \tag{7.88}$$

[7] For Choice 2, the Bondi-like J and K obtained from Eqs. (7.83) and (7.84), as well as the Weyl scalar ψ_0 built upon them, are functions of the partially flat Bondi-like coordinates, rather than the Bondi-like coordinates.

since the spin-weight of x^i is 0 and we can make use of the spin-weighted derivatives [110]

$$\eth x^i = q^B D_B x^i, \qquad \bar{\eth} x^i = \bar{q}^B D_B x^i, \tag{7.89}$$

where D_A denotes the covariant derivative associated with the metric $q_{AB} = 1/2(q_A \bar{q}_B + \bar{q}_A q_B)$. Then Eq. (7.87) can be written as

$$\partial_{\hat{u}} x^i = \frac{1}{2}\hat{\mathcal{U}}^{(0)} \bar{\eth} x^i + \frac{1}{2}\bar{\hat{\mathcal{U}}}^{(0)} \eth x^i, \tag{7.90}$$

where we have introduced an auxiliary variable $\mathcal{U}^{(0)\hat{A}}$ such that

$$\mathcal{U}^{(0)\hat{A}} \partial_{\hat{A}} x^B = U^{(0)B}, \tag{7.91}$$

$$\mathcal{U}^{(0)} = \mathcal{U}^{(0)\hat{A}} q_{\hat{A}}. \tag{7.92}$$

The two equations above imply

$$\mathcal{U}^{(0)} = \frac{1}{2\hat{\omega}^2}\left(\hat{\bar{b}} U^{(0)} - \hat{a}\bar{U}^{(0)}\right), \tag{7.93}$$

and its inverse

$$U^{(0)} = \frac{1}{2\omega^2}\left(\bar{b}\mathcal{U}^{(0)} - a\bar{\mathcal{U}}^{(0)}\right). \tag{7.94}$$

For completeness, we also cast Eq. (7.44) into its Cartesian version

$$\partial_u \hat{x}^{\hat{i}} = -\frac{1}{2}U^{(0)} \bar{\eth} \hat{x}^{\hat{i}} - \frac{1}{2}\bar{U}^{(0)} \eth \hat{x}^{\hat{i}}. \tag{7.95}$$

After solving the map $x^A(\hat{u}, \hat{x}^{\hat{A}})$ numerically from Eq. (7.87) and (7.90), we can adopt the spin-weighted Clenshaw algorithm [11] to perform the angular interpolation of $m_{\mu'}$ and ψ_0' to the Cauchy grid; and assemble them into the incoming characteristics $w^-_{\mu'\nu'}$ using Eq. (7.17).

7.5 Numerical tests

In this section, we use two systems to test our CCM algorithm. We first consider a gravitational Teukolsky wave [100] propagating on a flat background nonlinearly in Sec. 7.5.1, where the wave packet is initially on the Cauchy grid. This test demonstrates how CCM improves the accuracy of Cauchy boundary conditions. Next in Sec. 7.5.2, we initialize a GW pulse on the characteristic grid and inject it into the Cauchy domain, whose results illustrate that the interface between the

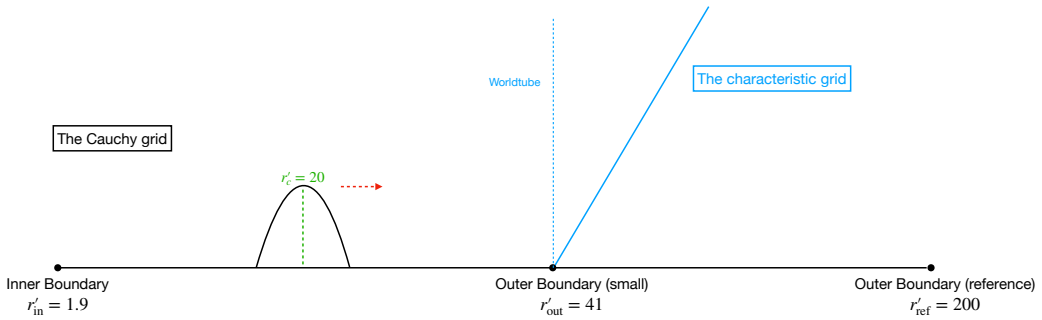

Figure 7.3: The propagation of an outgoing Teukolsky wave on a flat background, and the corresponding numerical setup. The horizontal black line stands for the radial direction of the spatial domain for the Cauchy grid. The initial center of the Teukolsky wave is at $r'_c = 20$, with a width of $\tau = 2$. The radius of the inner boundary $r'_{\rm in}$ is always set to 1.9 to avoid the divergence at $r' = 0$. The outer boundary is placed at $r'_{\rm out} = 41$. We evolve the system with both CCE and CCM. As for the reference solution, we put its outer boundary $r'_{\rm ref}$ at 200 so that it is causally disconnected from the system throughout the entire simulation. The worldtube (vertical blue dashed line) is always at $r'_{\rm wt} = 41$ for wave extraction.

Cauchy and the characteristic systems is transparent to GWs and spurious reflection is reduced.

Throughout the simulations, we focus on the Choice 2 approach provided in Sec. 7.4.3, because it involves only one Lorentz transformation, which makes it easier to implement and for future code development.

7.5.1 A Teukolsky wave propagating on a flat background

Following the tests in Refs. [9, 11], we consider a Teukolsky wave [100] propagating on a flat background. The initial data of the Cauchy system are constructed nonlinearly based on the Extended Conformal Thin Sandwich formulation [111, 112]. Afterward, the system is evolved fully nonlinearly. In the perturbative limit, the metric reads [100]:

$$\begin{aligned} ds^2 = &-dt'^2 + (1 + A f_{r'r'}) dr'^2 + 2B f_{r'\theta'} r' dr' d\theta' \\ &+ 2B f_{r'\phi'} r' \sin\theta' dr' d\phi' + (1 + C f^{(1)}_{\theta'\theta'} + A f^{(2)}_{\theta'\theta'}) r'^2 d\theta'^2 \\ &+ 2(A - 2C) f_{\theta'\phi'} r'^2 \sin\theta' d\theta' d\phi' \\ &+ (1 + C f^{(1)}_{\phi'\phi'} + A f^{(2)}_{\phi'\phi'}) r'^2 \sin^2\theta' d\phi'^2, \end{aligned} \tag{7.96}$$

with

$$A = 3\left[\frac{F^{(2)}}{r'^3} + \frac{3F^{(1)}}{r'^4} + \frac{3F}{r'^5}\right], \tag{7.97a}$$

$$B = -\left[\frac{F^{(3)}}{r'^2} + \frac{3F^{(2)}}{r'^3} + \frac{6F^{(1)}}{r'^4} + \frac{6F}{r'^5}\right], \tag{7.97b}$$

$$C = \frac{1}{4}\left[\frac{F^{(4)}}{r'} + \frac{2F^{(3)}}{r'^2} + \frac{9F^{(2)}}{r'^3} + \frac{21F^{(1)}}{r'^4} + \frac{21F}{r'^5}\right], \tag{7.97c}$$

and

$$\begin{aligned}
&f_{r'r'} = 4\sqrt{\frac{\pi}{5}}Y_{20}(\theta',\phi'), \quad f_{r'\theta'} = 2\sqrt{\frac{\pi}{5}}\partial_{\theta'}Y_{20}(\theta',\phi'),\\
&f_{r'\phi'} = 0, \quad f^{(2)}_{\theta'\theta'} = -1, \quad f_{\theta'\phi'} = 0,\\
&f^{(1)}_{\theta'\theta'} = 2\sqrt{\frac{\pi}{5}}\left(\partial^2_{\theta'} - \cot\theta'\partial_{\theta'} - \frac{\partial^2_{\phi'}}{\sin^2\theta'}\right)Y_{20}(\theta',\phi'),\\
&f^{(1)}_{\phi'\phi'} = -f^{(1)}_{\theta'\theta'}, \quad f^{(2)}_{\phi'\phi'} = 1 - f_{r'r'}.
\end{aligned} \tag{7.98}$$

We are free to specify the form of $F(u')$ in Eq. (7.97). Here we consider an outgoing Gaussian pulse:

$$F(u') = Xe^{-\frac{(u'-r'_c)^2}{\tau^2}}, \tag{7.99}$$

where $u' = t' - r'$ is the retarded time, r'_c is the initial center of the pulse at $t' = 0$, τ is its width, and X is its amplitude. We denote the nth derivative of $F(u')$ as

$$F^{(n)} \equiv \left[\frac{d^n F(u')}{du'^n}\right]_{u'=t'-r'}. \tag{7.100}$$

Our numerical setup is sketched in Fig. 7.3. The Gaussian pulse initially centers at $r'_c = 20$, with a width of $\tau = 2$. We first simulate the system with a small Cauchy domain—its outer grid radius $r'_{\rm out} = 41$ is small enough that the back-scattering of GWs at the outer boundary is not negligible, which consequently makes the improvement due to CCM resolvable by the code. The inner boundary of the Cauchy grid is put at $r'_{\rm in} = 1.9$ to avoid the divergence of the Teukolsky wave at $r' = 0$. We evolve the system with both CCE and CCM, and the time-like worldtube is always placed at $r'_{\rm wt} = 41$, coinciding with the Cauchy boundary $r'_{\rm out} = 41$, to avoid any potential numerical issue.

It is expected that the CCM system provides more accurate boundary conditions at $r'_{\rm out}$ to represent better the true evolution. To see this, we need to design a third reference system whose results are not contaminated by approximations of the numerical simulations (e.g., inaccurate boundary conditions) and can be viewed as the exact solutions. This can be achieved differently under two separate scenarios.

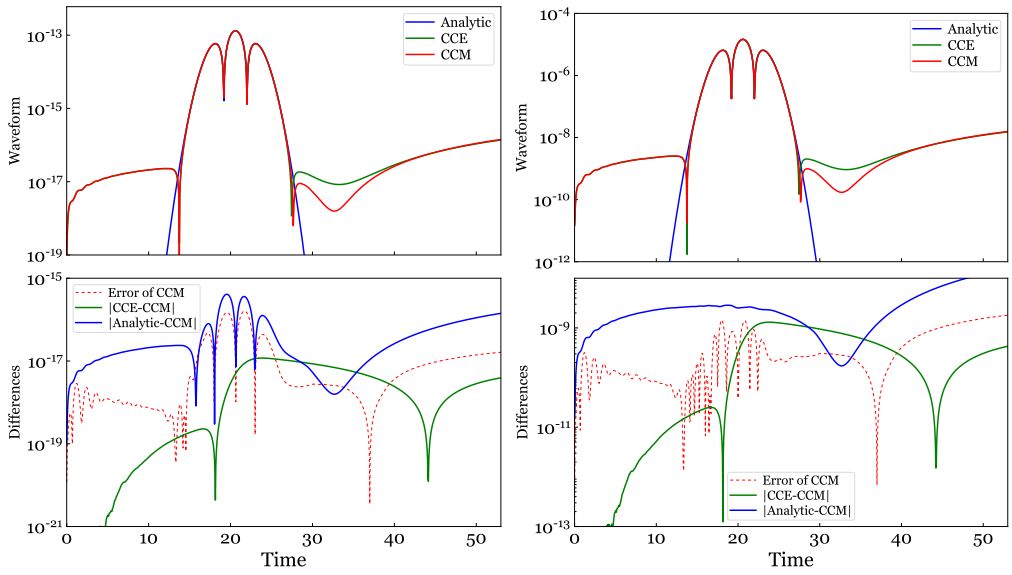

(a) $\psi'_{0,(l=2,m=0)}$ for matching

(b) $r^5\psi_{0,(l=2,m=0)}$ at $\mathscr{I}^+$

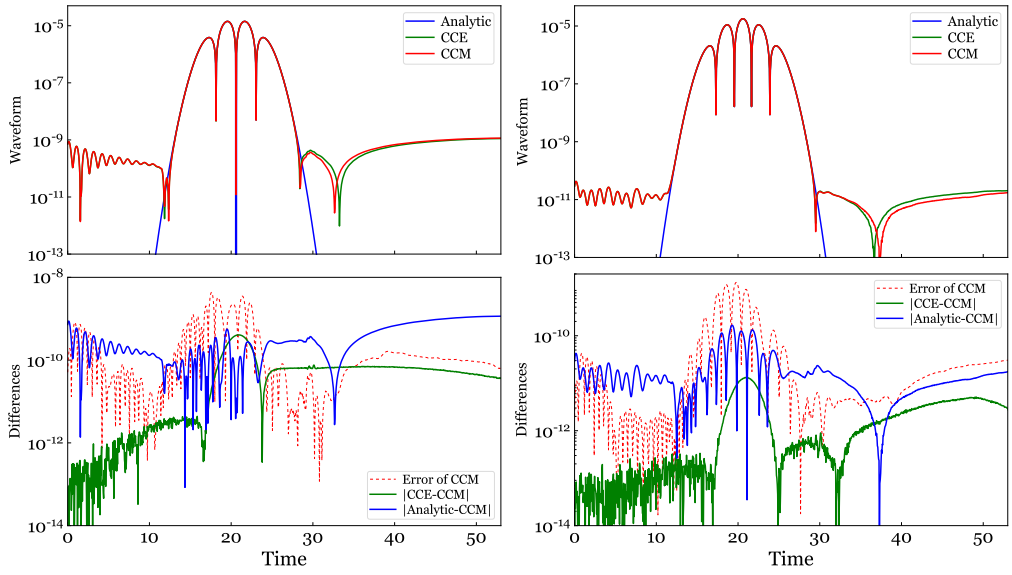

(c) $r^4\psi_{1,(l=2,m=0)}$ at $\mathscr{I}^+$

(d) $r^3\psi_{2,(l=2,m=0)}$ at $\mathscr{I}^+$

Figure 7.4: Various waveform quantities for a Teuskolsky wave, with an amplitude of $X = 10^{-5}$. In the top panel of each subfigure, we plot the analytic results [Eq. (7.102)] in blue, the CCE results in green, and the CCM results in red. In each bottom panel, the difference between the waveforms is provided. The numerical error of the CCM system is computed by taking the difference between two numerical resolutions.

First, when the amplitude of the Teukolsky wave X is small enough, we are in the perturbative regime, and the evolution of the Teukolsky wave is analytically available. Therefore, we can compare the CCE and CCM simulations to the analytic

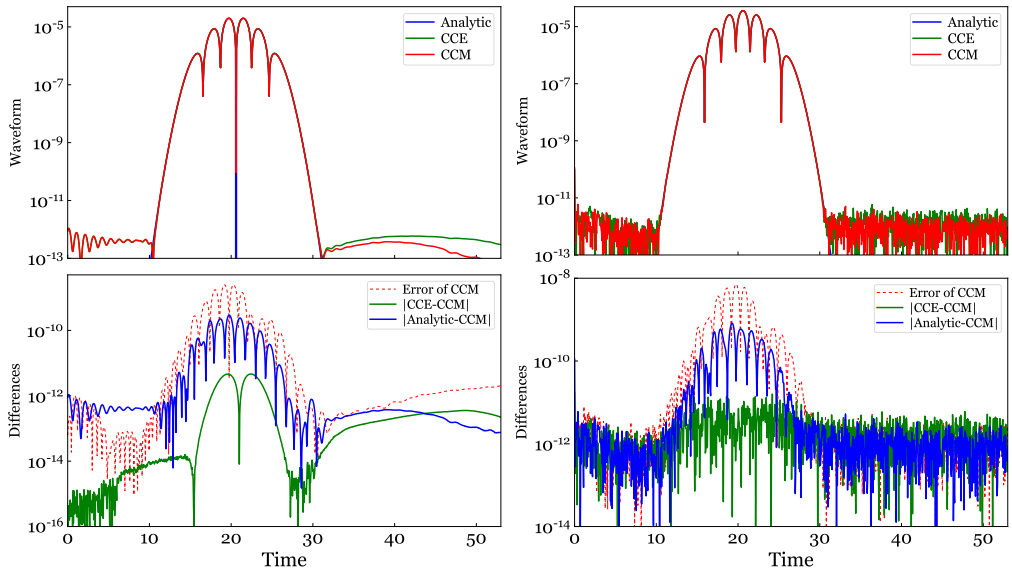

(a) $r^2\psi_{3,(l=2,m=0)}$ at $\mathscr{I}^+$ (b) $r\psi_{4,(l=2,m=0)}$ at $\mathscr{I}^+$

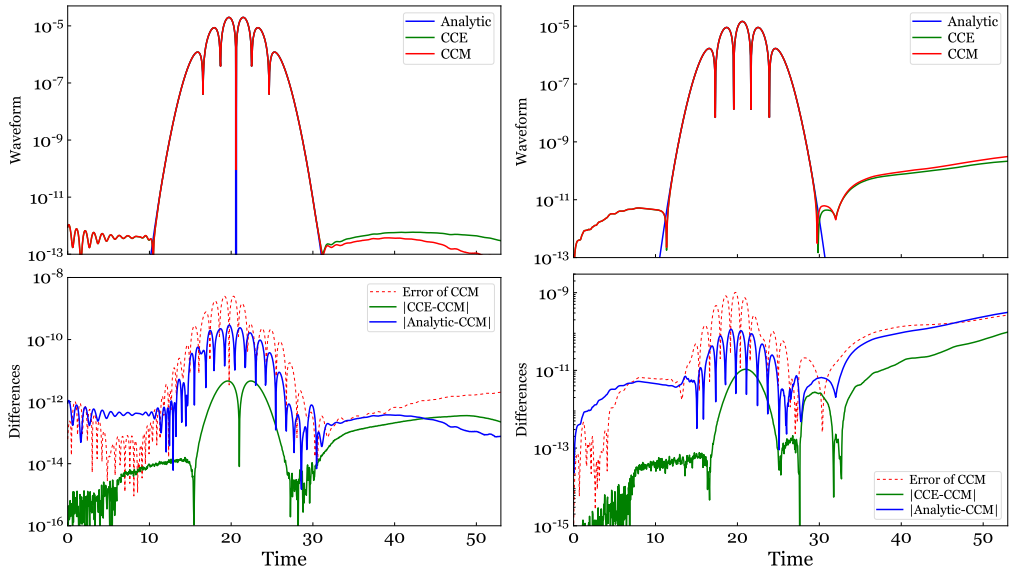

(c) rN_{20} at $\mathscr{I}^+$ (d) rh_{20} at $\mathscr{I}^+$

Figure 7.5: Continuation of Fig. 7.4. More waveforms are provided.

results in Eq. (7.96). Second, when the amplitude X is large and nonlinear effects cannot be neglected, we choose the reference system to be a CCE simulation with a larger Cauchy computational domain such that its outer boundary remains casually disconnected from the system throughout the simulation. In our case, we place its outer boundary at $r'_{\rm ref} = 200$, as displayed in Fig. 7.3. The location of the worldtube for CCE wave extraction is still at $r'_{\rm wt} = 41$, the same as the other two for fair comparisons.

Below, we consider these two scenarios, respectively. We first study the linear-regime case by setting X to 10^{-5} [9, 11]. Then we investigate the nonlinear case with $X = 2$.

7.5.1.1 $X = 10^{-5}$

In Refs. [9, 11], the comparison was for the News function N_{20} only. For our purposes, here we extend their studies to all the waveform quantities including the Weyl scalars $\psi_{0\ldots4}$ and the strain h. Using the Appendix of [100], the metric in Eq. (7.96) leads to analytic expressions for these waveform quantities at the linear order

$$\psi_0 = -\sqrt{\frac{2\pi}{15}}{}_{+2}Y_{20}\left[(6\dddot{C} - 3\ddot{A}) + \frac{1}{2}r(3\ddot{B} + \dddot{A})\right], \tag{7.101a}$$

$$\psi_1 = \frac{1}{2}\sqrt{\frac{2\pi}{15}}{}_{+1}Y_{20}\left[r\dddot{A} + 3\ddot{B}\right], \tag{7.101b}$$

$$\psi_2 = -\sqrt{\frac{\pi}{5}}Y_{20}\ddot{A}, \tag{7.101c}$$

$$\psi_3 = \frac{1}{2}\sqrt{\frac{2\pi}{15}}{}_{-1}Y_{20}\left[r\dddot{A} - 3\ddot{B}\right], \tag{7.101d}$$

$$\psi_4 = \sqrt{\frac{2\pi}{15}}{}_{-2}Y_{20}\left[(3\ddot{A} - 6\dddot{C}) + \frac{1}{2}r(3\ddot{B} + \dddot{A})\right], \tag{7.101e}$$

$$N = -\sqrt{\frac{2\pi}{15}}{}_{-2}Y_{20}\left[(3\dot{A} - 6\ddot{C}) + \frac{1}{2}r(3\ddot{B} + \ddot{A})\right], \tag{7.101f}$$

$$h = -\sqrt{\frac{2\pi}{15}}{}_{-2}Y_{20}\left[(3A - 6C) + \frac{1}{2}r(3\dot{B} + \dot{A})\right]. \tag{7.101g}$$

where (spin-weighted) spherical harmonics are given by

$$\begin{aligned}
{}_{-2}Y_{20} &= {}_{+2}Y_{20} = \frac{1}{4}\sqrt{\frac{15}{2\pi}}\sin^2\theta, \\
{}_{-1}Y_{20} &= {}_{+1}Y_{20} = -\frac{1}{4}\sqrt{\frac{15}{2\pi}}\sin 2\theta, \\
Y_{20} &= \frac{1}{8}\sqrt{\frac{5}{\pi}}(1 + 3\cos 2\theta).
\end{aligned}$$

Eq. (7.101) simplifies at future null infinity $\mathscr{I}^+$ after plugging in Eq. (7.97)

$$rh|_{\mathscr{I}^+} = \sqrt{\frac{6\pi}{5}}F^{(4)} \times {}_{-2}Y_{20}, \tag{7.102a}$$

$$rN|_{\mathscr{I}^+} = \sqrt{\frac{6\pi}{5}}F^{(5)} \times {}_{-2}Y_{20}, \tag{7.102b}$$

$$r\psi_4|_{\mathscr{I}^+} = -\sqrt{\frac{6\pi}{5}}F^{(6)} \times {}_{-2}Y_{20}\,, \tag{7.102c}$$

$$r^2\psi_3|_{\mathscr{I}^+} = \sqrt{\frac{6\pi}{5}}F^{(5)} \times {}_{-1}Y_{20}\,, \tag{7.102d}$$

$$r^3\psi_2|_{\mathscr{I}^+} = -\sqrt{\frac{9\pi}{5}}F^{(4)} \times Y_{20}, \tag{7.102e}$$

$$r^4\psi_1|_{\mathscr{I}^+} = \sqrt{\frac{27\pi}{10}}F^{(3)} \times {}_{+1}Y_{20}\,, \tag{7.102f}$$

$$r^5\psi_0 = -\sqrt{\frac{27\pi}{10}}F^{(2)} \times {}_{+2}Y_{20}\,. \tag{7.102g}$$

In particular, the expression for ψ_0 in Eq. (7.102g) is valid across the entire spacetime. Therefore, we can take advantage of this result to test our calculation of ψ_0' in Eq. (7.17) that is sent to the Cauchy's boundary conditions. On the other hand, we note that ψ_0 scales with distance as r^{-5}; so the back-scattered wave reduces quickly as we move away from the system.

The top panel of Fig. 7.4a displays the evolution of ψ_0' used for matching, evaluated with our CCM code (in red), and the analytic expression in Eq. (7.102g) (in blue). The difference between the CCM and the analytic results is shown as the blue curve in the bottom panel of Fig. 7.4a, which is comparable with the numerical error of CCM (the red dashed curve). This verifies the correctness of our calculation for ψ_0'. Meanwhile, the difference between the CCE and the CCM results (the green curve in the bottom panel of Fig. 7.4a) is also on the same order as the numerical error. This is because the size of ψ_0', namely the back-scattered wave, is $\sim 10^{-13}$, which makes the matching term in the boundary condition [Eq. 7.13] negligible.

Additionally, we provide complete comparisons for $\psi_{0\ldots4}$, N, and h in other panels of Figs. 7.4 and 7.5. All the quantities are evaluated at future null infinity $\mathscr{I}^+$. We see the numerical results agree with analytic expressions in Eq. (7.102). The difference between CCM and CCE is also comparable to numerical error, as expected.

7.5.1.2 $X = 2$

We then switch our attention to nonlinear regime and set the amplitude of the Teukolsky wave X to 2. Figure 7.6a shows ψ_0' used for matching, where we can see its evolution is highly nonlinear because it does not have oscillatory features predicted by the linear analytic expression in Eq. (7.102g). In this scenario, the back-scattered wave ψ_0' leads to a nonnegligible contribution to the Cauchy evolution, and indeed we see the evolution of the CCM ψ_0' is distinguishable from that of CCE.

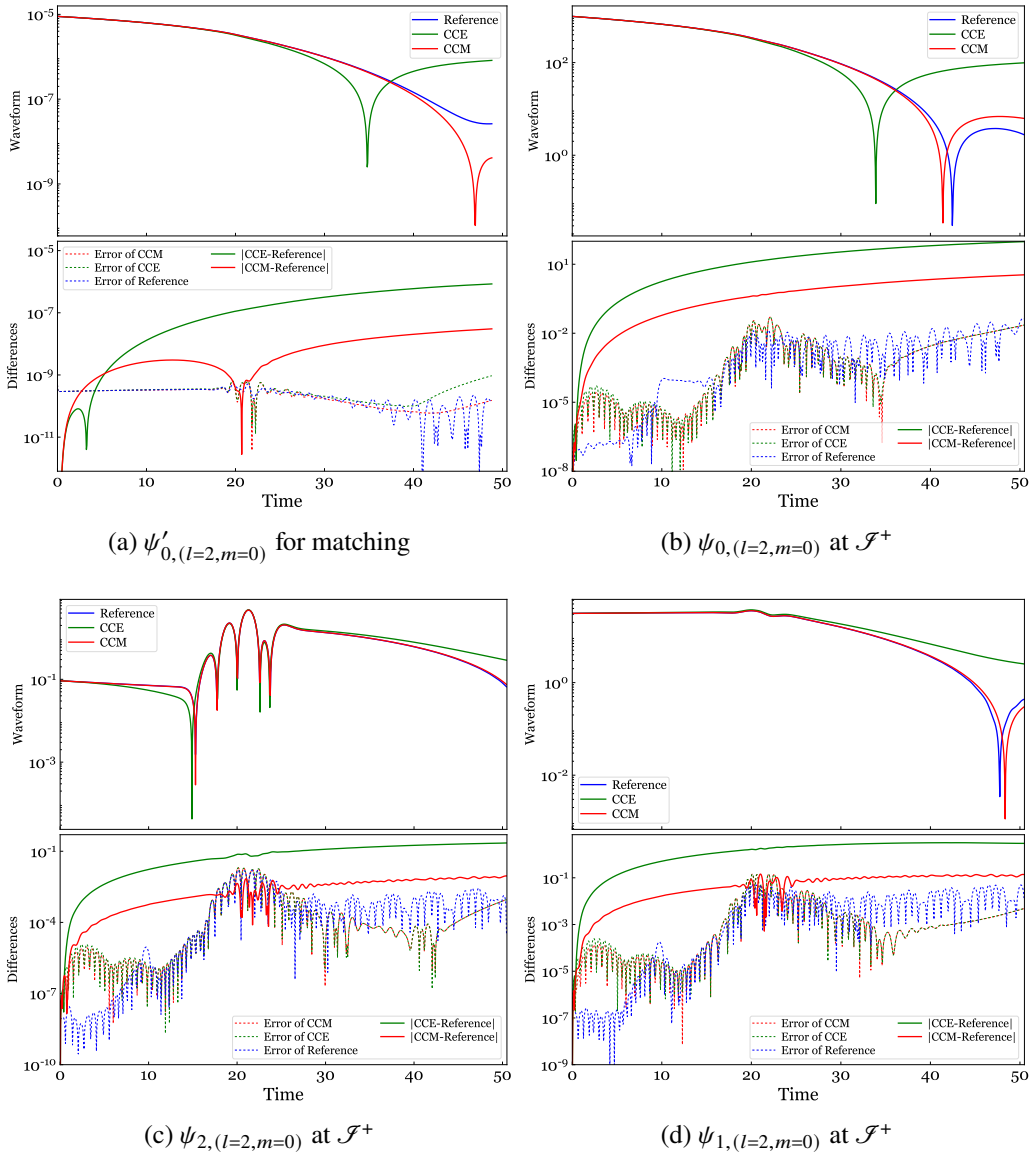

(a) $\psi'_{0,(l=2,m=0)}$ for matching

(b) $\psi_{0,(l=2,m=0)}$ at $\mathscr{I}^+$

(c) $\psi_{2,(l=2,m=0)}$ at $\mathscr{I}^+$

(d) $\psi_{1,(l=2,m=0)}$ at $\mathscr{I}^+$

Figure 7.6: (Similar to Fig. 7.4) Various waveform quantities for a Teuskolsky wave, with an amplitude of $X = 2$. The top panel of each subfigure displays the reference results (blue), the CCE results (green), and the CCM results (red). The bottom panel shows the difference between the waveforms.

Figures 7.6 and 7.7 display all the waveform quantities extracted at future null infinity with CCE (green) and CCM (red). They are compared with the reference results (blue). In the bottom panel of each subfigure, we show their difference as well as the corresponding numerical error. We see for all the results, CCM generally provides systematic improvements by 1-2 orders of magnitude except for ψ_4, since it is the least reflective and least affected by CCM. Finally, we remark that the numerical wiggles in the reference ψ_4 following the main peak are caused by numerical errors.

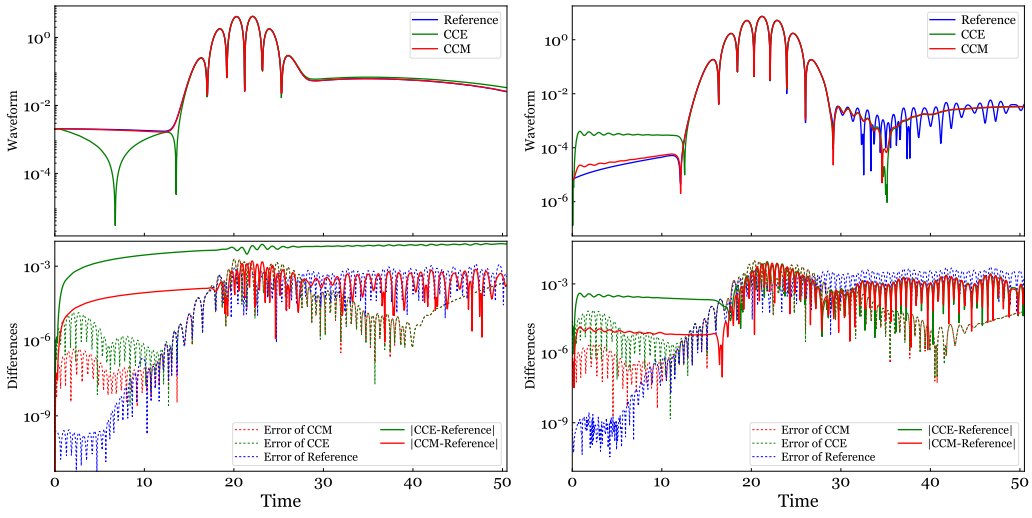

(a) $\psi_{3,(l=2,m=0)}$ at $\mathscr{I}^+$

(b) $\psi_{4,(l=2,m=0)}$ at $\mathscr{I}^+$

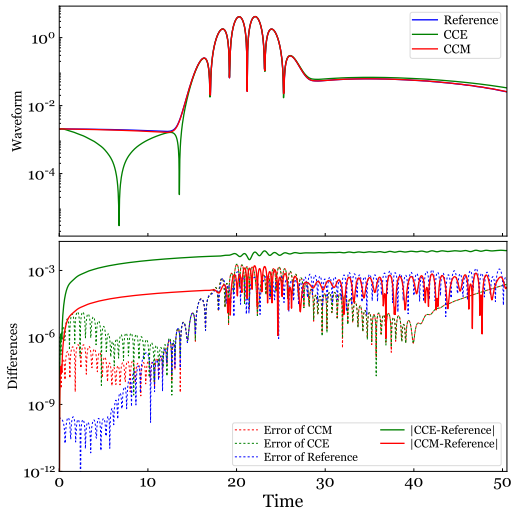

(c) N_{20} at $\mathscr{I}^+$

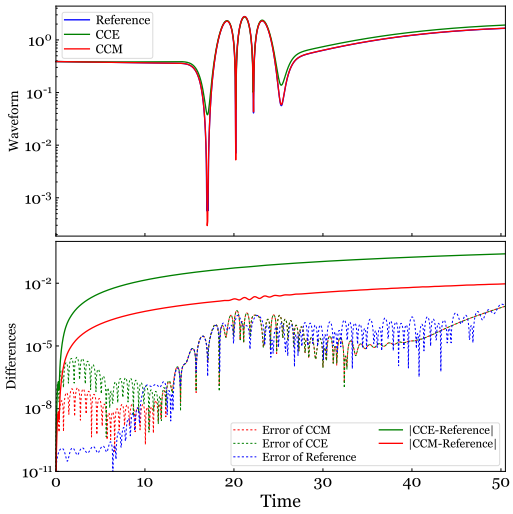

(d) h_{20} at $\mathscr{I}^+$

Figure 7.7: Continuation of Fig. 7.6. More waveforms are provided.

Reducing them with higher resolutions is very computationally expensive. We leave optimization for future work.

7.5.2 Initializing a GW pulse on the characteristic grid

Our second test is to initialize a GW pulse on the characteristic grid and inject it into the Cauchy domain. To do this, we adopt the following initial data for the Bondi variable $\hat{J}$:

$$\hat{J}(\hat{y},\hat{\theta},\hat{\phi}) = \begin{cases} 0, & \hat{y} \leq \hat{y}_{\rm min}, \\ {}_{+2}Y_{20}\,(\hat{\theta},\hat{\phi})\mathcal{J}(\hat{y}), & \hat{y}_{\rm min} \leq \hat{y} \leq \hat{y}_{\rm max}, \\ 0, & \hat{y} \geq \hat{y}_{\rm max}, \end{cases} \tag{7.103}$$

where $\hat{y} = 1 - 2\hat{R}/\hat{r}$, and $\hat{R}$ is the partially flat Bondi-like radius of the worltube. The spin weight of the pulse is set to 2 in order to match with that of ψ_0. The radial profile $\mathcal{J}(y)$ reads

$$\mathcal{J}(\hat{y}) = 4Z\frac{(\hat{y}_{\rm max}-\hat{y})(\hat{y}-\hat{y}_{\rm min})}{(\hat{y}_{\rm max}-\hat{y}_{\rm min})^2}e^{-\frac{(\hat{y}-\hat{y}_c)^2}{\tau^2}}. \tag{7.104}$$

Meanwhile, the inner Cauchy domain is initialized to a flat (Minkowski) spacetime. Figure 7.8 displays our numerical setup. The center of the pulse $\hat{y}_c$ is initially at 0. In addition, we choose $y_{\rm min} = -0.8, y_{\rm max} = 0.8, \tau = 0.15, Z = 10^{-3}$. Here, the amplitude of the pulse Z is small enough to ensure it does not collapse into a BH. Finally, the outer boundary of the Cauchy grid is chosen to be 100, coinciding with the worldtube.

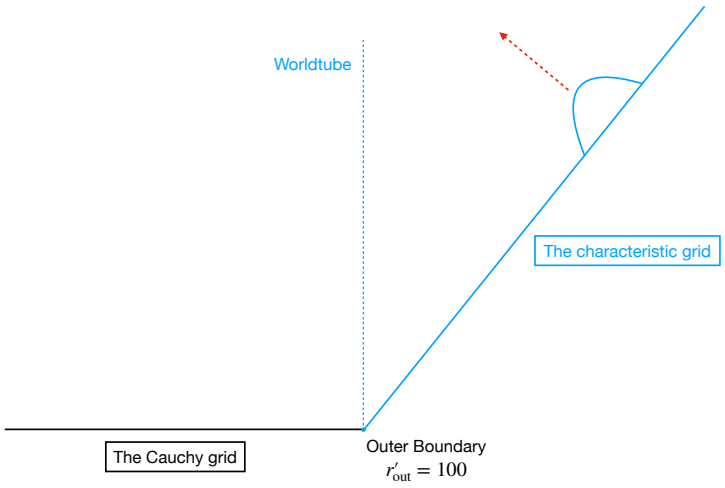

Figure 7.8: Numerical setup of our second test, where a pulse is initialized on the characteristic grid and is injected into the inner Cauchy region. The worldtube locates at the outer boundary of the Cauchy grid ($r'_{\rm out} = 100$).

Since the pulse is imposed on an outgoing null surface, it naturally propagates inwards once we allow the system to evolve. By using the CCM algorithm, the

interface between the Cauchy and the characteristic grid is transparent to this incoming pulse. As a result, the GW is sent to the Cauchy domain by the matching term in the boundary condition [Eq. (7.13)]. Afterward, the pulse falls toward the center and bounces. Finally, it leaves the inner Cauchy region and dispenses to null infinity after the crossing time of the Cauchy domain (namely its diameter). On the contrary, if we turn off the matching term and evolve the system with the standard CCE algorithm, the worldtube at $r'_{\rm wt}$ will become a perfectly reflecting mirror. Consequently, the inner Cauchy system does not see the incoming pulse, and its metric remains the Minkowski one.

In the top panel of Fig. 7.9, we plot the evolution of $\psi'_{0,(l=2,m=0)}$ used for matching, which characterizes the incoming GW seen by the inner Cauchy system. We see both the CCM and the CCE systems result in similar evolution. Below we use the time that $\psi'_{0,(l=2,m=0)}$ reaches its first trough, denoted by t_1, to refer to the moment that the pulse enters into the Cauchy domain. Then the bottom panel of Fig. 7.9 exhibits the evolution of $\psi_{4,(l=2,m=0)}$ at null infinity. In the absence of the matching (CCE), the ingoing pulse is fully reflected by the worldtube—the first peak of the reflected wave takes place at t_1. In contrast, the CCM system has a weaker reflected wave at that moment. After the crossing time of the inner Cauchy domain: $2R$, where R stands for its radius, the pulse leaves the Cauchy grid at $t_2 = t_1 + 2R$ and escapes to null infinity. This result verifies that our CCM algorithm does send the characteristic pulse into the Cauchy system.

Another way to support our conclusion is to look at the evolution of the Bondi mass, as shown in Fig. 7.10. Initially, the two runs evolve identically, but then they start to differ when the pulse comes close to the worldtube ($\sim t_1$). In the CCE case, the entire pulse is reflected by the worldtube, so the Bondi mass reduces sharply when the reflected wave escapes toward null infinity. Oppositely, for CCM, the matching term sends the characteristic pulse into the Cauchy system. Its Bondi mass stays almost constant while the pulse travels across the Cauchy domain. Finally, the Bondi mass decreases to 0 as the pulse leaves the Cauchy grid at t_2.

7.6 Conclusions

In this chapter, we have implemented a fully relativistic 3D CCM algorithm in our numerical relativity code SpECTRE. Core steps towards matching involve (a) evaluating the Weyl scalar ψ_0 and the Newman-Penrose tetrad vector $\boldsymbol{m}$ at Cauchy's outer boundary (b) performing tetrad transformations to the Cauchy tetrad; (c)

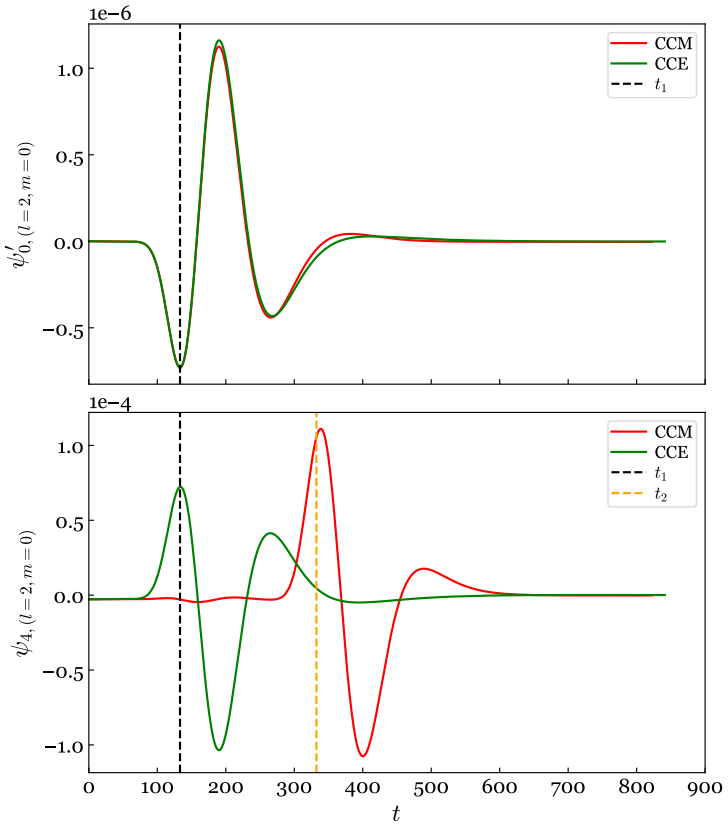

Figure 7.9: The $(l = 2, m = 0)$ harmonic of ψ'_0 using for matching (top), and ψ_4 extracted at null infinity (bottom). The GW pulse is initialized on the characteristic grid; and evolved with CCM (red) and CCE (green). The black dashed line (t_1) is at the first trough of $\psi'_{0,(l=2,m=0)}$, which can be treated as the time that the pulse hits the outer boundary of the Cauchy domain. The yellow dashed line $(t_2 = t_1 + 2R)$ refers to the crossing time of the Cauchy domain after t_1.

interpolating the quantities to the Cauchy grid; (d) completing the physical subset of Cauchy's Bjørhus boundary conditions.

We have designed two systems to test our code. The first case is the propagation of a Teuskolsky wave on a flat background. When its amplitude is small $(X = 10^{-5})$, the evolution of the CCM system is almost identical to that of the CCE system, since the back-scattered wave is negligible. However, after increasing the amplitude to 2, the CCM system displays a better agreement with the reference (exact) solution whose outer boundary is farther out to ensure that the outer boundary is causally disconnected from the system. In this way, we illustrate that the CCM system does improve the accuracy of Cauchy's outer boundary conditions. In the second case, we initialize a pulse on the characteristic grid and send it into the Cauchy system. Without the matching term, the pulse does not pass through the interface between

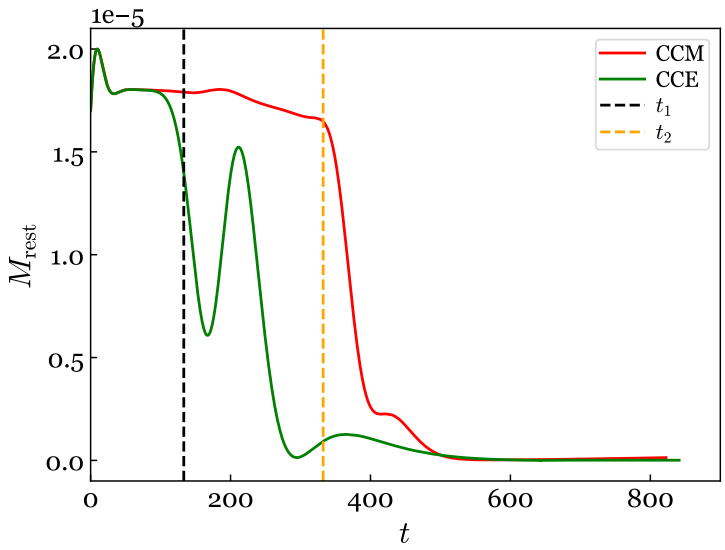

Figure 7.10: The time evolution of the Bondi mass, using the same system as Fig. 7.9. We evolve the system with both CCM (red), and CCE (green). The black dashed line (t_1) stands for the time that the pulse hits the outer boundary of the Cauchy domain, and the yellow dashed line ($t_2 = t_1 + 2R$) represents the crossing time of the Cauchy grid after t_1.

the characteristic and the Cauchy systems, and it is totally reflected while hitting the interface, which in turn leads to a strong prompt reflective wave at null infinity. In addition, the Bondi mass of the system decreases sharply to 0 after the reflection. In contrast, the CCM algorithm sends the pulse to the inner Cauchy system, and the reflective wave is much weaker. After the crossing time of the Cauchy region, the pulse leaves the Cauchy domain and escapes to null infinity. The Bondi-mass of the CCM system remained constant while the pulse propagating on the Cauchy grid.

Although we restrict ourselves to two simple physical systems, the CCM algorithm is generic and should be applicable to any system. Future work could investigate more sophisticated scenarios, such as binary black hole systems. With CCM, we should be able to have a more accurate prediction for the back-scattered GWs, which allows us to adopt a smaller Cauchy domain to improve computational efficiency.

References

[1] Benjamin P. Abbott et al. “Observation of gravitational waves from a binary black hole merger.” *Phys. Rev. Lett.* 116.6 (2016), p. 061102. DOI: 10.1103/PhysRevLett.116.061102. arXiv: 1602.03837 [gr-qc].

[2] Thomas W. Baumgarte and Stuart L. Shapiro. *Numerical relativity: Solving Einstein's equations on the Computer*. Cambridge University Press, 2010. DOI: 10.1017/CBO9781139193344.

[3] SXS Collaboration. *The SXS collaboration catalog of gravitational waveforms*. http://www.black-holes.org/waveforms..

[4] Jeffrey Winicour. "Characteristic evolution and matching." *Living Reviews in Relativity* 15.1 (2012), pp. 1–99. DOI: 10.12942/lrr-2012-2.

[5] Nigel T. Bishop. "Some aspects of the characteristic initial value problem in numerical relativity." *Approaches to Numerical relativity*. Ed. by Ray D'Inverno. Jan. 1992, pp. 20–33.

[6] Nigel T. Bishop et al. "Cauchy-characteristic extraction in numerical relativity." *Phys. Rev.* D54 (1996), pp. 6153–6165. DOI: 10.1103/PhysRevD.54.6153. arXiv: gr-qc/9705033 [gr-qc].

[7] Nigel T. Bishop et al. "High powered gravitational news." *Phys. Rev. D* 56 (1997), pp. 6298–6309. DOI: 10.1103/PhysRevD.56.6298. arXiv: gr-qc/9708065.

[8] Nigel T. Bishop et al. "Cauchy characteristic matching." *Black holes, Gravitational radiation and the Universe: Essays in Honor of C.V. Vishveshwara*. Ed. by Bala R. Iyer and Biblap Bhawal. Jan. 1998, pp. 383–408. DOI: 10.1007/978-94-017-0934-7_24. arXiv: gr-qc/9801070.

[9] Kevin Barkett et al. "Spectral Cauchy-characteristic extraction of the gravitational wave news function." *Phys. Rev. D* 102.2 (2020), p. 024004. DOI: 10.1103/PhysRevD.102.024004. arXiv: 1910.09677 [gr-qc].

[10] Jordan Moxon, Mark A. Scheel, and Saul A. Teukolsky. "Improved Cauchy-characteristic evolution system for high-precision numerical relativity waveforms." *Phys. Rev. D* 102.4 (2020), p. 044052. DOI: 10.1103/PhysRevD.102.044052. arXiv: 2007.01339 [gr-qc].

[11] Jordan Moxon et al. "The SpECTRE Cauchy-characteristic evolution system for rapid, precise waveform extraction." (Oct. 2021). arXiv: 2110.08635 [gr-qc].

[12] Jorg Frauendiener. "Conformal infinity." *Living Rev. Rel.* 3 (2000), p. 4. DOI: https://doi.org/10.12942/lrr-2000-4.

[13] Luisa T. Buchman, Harald P. Pfeiffer, and James M. Bardeen. "Black hole initial data on hyperboloidal slices." *Phys. Rev. D* 80 (2009), p. 084024. DOI: 10.1103/PhysRevD.80.084024. arXiv: 0907.3163 [gr-qc].

[14] Anil Zenginoglu. "Hyperboloidal evolution with the Einstein equations." *Class. Quant. Grav.* 25 (2008), p. 195025. DOI: 10.1088/0264-9381/25/19/195025. arXiv: 0808.0810 [gr-qc].

[15] Alex Vañó-Viñuales, Sascha Husa, and David Hilditch. "Spherical symmetry as a test case for unconstrained hyperboloidal evolution." *Class. Quant. Grav.* 32.17 (2015), p. 175010. DOI: 10.1088/0264-9381/32/17/175010. arXiv: 1412.3827 [gr-qc].

[16] Alex Vañó-Viñuales and Sascha Husa. "Unconstrained hyperboloidal evolution of black holes in spherical symmetry with GBSSN and Z4c." *J. Phys. Conf. Ser.* 600.1 (2015), p. 012061. DOI: 10.1088/1742-6596/600/1/012061. arXiv: 1412.4801 [gr-qc].

[17] Hermann Bondi, M. G. Julian van der Burg, and A. W. Kenneth Metzner. "Gravitational waves in general relativity. VII. Waves from axi-symmetric isolated systems." *Proceedings of the Royal Society of London Series A* 269.1336 (Aug. 1962), pp. 21–52. DOI: 10.1098/rspa.1962.0161.

[18] Rainer K. Sachs. "Gravitational waves in general relativity. 8. Waves in asymptotically flat space-times." *Proc. Roy. Soc. Lond. A* 270 (1962), pp. 103–126. DOI: 10.1098/rspa.1962.0206.

[19] Roger Penrose. "Asymptotic properties of fields and space-times." *Phys. Rev. Lett.* 10 (2 Jan. 1963), pp. 66–68. DOI: 10.1103/PhysRevLett.10.66. URL: https://link.aps.org/doi/10.1103/PhysRevLett.10.66.

[20] Maria Babiuc et al. "Gravitational wave extraction based on Cauchy-characteristic extraction and characteristic evolution." *Class. Quant. Grav.* 22 (2005), pp. 5089–5108. DOI: 10.1088/0264-9381/22/23/011. arXiv: gr-qc/0501008.

[21] Michael Boyle and Abdul H. Mroue. "Extrapolating gravitational-wave data from numerical simulations." *Phys. Rev.* D80 (2009), p. 124045. DOI: 10.1103/PhysRevD.80.124045. arXiv: 0905.3177 [gr-qc].

[22] Tony Chu et al. "On the accuracy and precision of numerical waveforms: Effect of waveform extraction methodology." *Class. Quant. Grav.* 33.16 (2016), p. 165001. DOI: 10.1088/0264-9381/33/16/165001. arXiv: 1512.06800 [gr-qc].

[23] Nicholas W. Taylor et al. "Comparing gravitational waveform extrapolation to Cauchy-characteristic extraction in binary black hole simulations." *Phys. Rev.* D88.12 (2013), p. 124010. DOI: 10.1103/PhysRevD.88.124010. arXiv: 1309.3605 [gr-qc].

[24] Dante A. B. Iozzo et al. "Extending gravitational wave extraction using Weyl characteristic fields." *Phys. Rev. D* 103.2 (2021), p. 024039. DOI: 10.1103/PhysRevD.103.024039. arXiv: 2010.15200 [gr-qc].

[25] Jeffrey Winicour. "Worldtube conservation laws for the null-timelike evolution problem." *Gen. Rel. Grav.* 43 (2011), pp. 3269–3288. DOI: 10.1007/s10714-011-1241-3. arXiv: 1105.3493 [gr-qc].

[26] Bela Szilagyi. "Cauchy characteristic matching in general relativity." Other thesis. June 2000. arXiv: gr-qc/0006091.

[27] Richard A. Isaacson, Joel S. Welling, and Jeffrey Winicour. "Null cone computation of gravitational radiation." *Journal of Mathematical Physics* 24.7 (1983), pp. 1824–1834. DOI: 10.1063/1.525904. URL: https://doi.org/10.1063/1.525904.

[28] J. Winicour. "Newtonian gravity on the null cone." *Journal of Mathematical Physics* 24.5 (Jan. 1983), pp. 1193–1198. DOI: 10.1063/1.525796.

[29] Jeffrey Winicour. "Null infinity from a quasi-Newtonian view." *Journal of Mathematical Physics* 25.8 (1984), pp. 2506–2514. DOI: 10.1063/1.526472. URL: https://doi.org/10.1063/1.526472.

[30] Roberto Gomez, Philippos Papadopoulos, and Jeffrey Winicour. "Null cone evolution of axisymmetric vacuum space–times." *Journal of Mathematical Physics* 35.8 (1994), pp. 4184–4204.

[31] Christian Reisswig, Nigel T. Bishop, and Denis Pollney. "General relativistic null-cone evolutions with a high-order scheme." *Gen. Rel. Grav.* 45 (2013), pp. 1069–1094. DOI: 10.1007/s10714-013-1513-1. arXiv: 1208.3891 [gr-qc].

[32] Roberto Gomez. "Gravitational wave forms with controlled accuracy." *Phys. Rev. D* 64 (2001), p. 024007. DOI: 10.1103/PhysRevD.64.024007. arXiv: gr-qc/0103011.

[33] Nigel T. Bishop and Shrirang S. Deshingkar. "New approach to calculating the news." *Phys. Rev. D* 68 (2003), p. 024031. DOI: 10.1103/PhysRevD.68.024031. arXiv: gr-qc/0303021.

[34] Christian Reisswig et al. "Numerical relativity with characteristic evolution, using six angular patches." *Class. Quant. Grav.* 24 (2007). Ed. by Manuela Campanelli and Luciano Rezzolla, S327–S340. DOI: 10.1088/0264-9381/24/12/S21. arXiv: gr-qc/0610019.

[35] Roberto Gomez, Willians Barreto, and Simonetta Frittelli. "A framework for large-scale relativistic simulations in the characteristic approach." *Phys. Rev. D* 76 (2007), p. 124029. DOI: 10.1103/PhysRevD.76.124029. arXiv: 0711.0564 [gr-qc].

[36] Maria C. Babiuc et al. "Strategies for the characteristic extraction of gravitational waveforms." *Phys. Rev. D* 79 (2009), p. 084011. DOI: 10.1103/PhysRevD.79.084011. arXiv: 0808.0861 [gr-qc].

[37] Roberto Gomez et al. "Stable characteristic evolution of generic three-dimensional single black hole space-times." *Phys. Rev. Lett.* 80 (1998), pp. 3915–3918. DOI: 10.1103/PhysRevLett.80.3915. arXiv: gr-qc/9801069.

[38] Philippos Papadopoulos and Jose A. Font. "Relativistic hydrodynamics on space - like and null surfaces: Formalism and computations of spherically symmetric space-times." *Phys. Rev. D* 61 (2000), p. 024015. DOI: 10.1103/PhysRevD.61.024015. arXiv: gr-qc/9902018.

[39] Nigel T. Bishop et al. "The incorporation of matter into characteristic numerical relativity." *Phys. Rev. D* 60 (1999), p. 024005. DOI: 10.1103/PhysRevD.60.024005. arXiv: gr-qc/9901056.

[40] Florian Siebel et al. "Simulating the dynamics of relativistic stars via a light cone approach." *Phys. Rev. D* 65 (2002), p. 064038. DOI: 10.1103/PhysRevD.65.064038. arXiv: gr-qc/0111093.

[41] Florian Siebel, Jose A. Font, and Philippos Papadopoulos. "Scalar field induced oscillations of neutron stars and gravitational collapse." *Phys. Rev. D* 65 (2002), p. 024021. DOI: 10.1103/PhysRevD.65.024021. arXiv: gr-qc/0108006.

[42] Nigel T. Bishop et al. "On characteristic initial data for a star orbiting a black hole." *Phys. Rev. D* 72 (2005), p. 024002. DOI: 10.1103/PhysRevD.72.024002. arXiv: gr-qc/0412080.

[43] Roberto Gomez, J. Winicour, and Richard Isaacson. "Evolution of scalar fields from characteristic data." *Journal of Computational Physics* 98.1 (Jan. 1992), pp. 11–25. DOI: 10.1016/0021-9991(92)90169-Y.

[44] R. Gómez and J. Winicour. "Asymptotics of gravitational collapse of scalar waves." *Journal of Mathematical Physics* 33.4 (Apr. 1992), pp. 1445–1457. DOI: 10.1063/1.529721.

[45] Willians Barreto et al. "Gravitational instability of a kink." *Phys. Rev. D* 54 (1996), pp. 3834–3839. DOI: 10.1103/PHYSREVD.54.3834. arXiv: gr-qc/0507086.

[46] Willians Barreto et al. "The 3-dimensional Einstein-Klein-Gordon system in characteristic numerical relativity." *Phys. Rev. D* 71 (2005), p. 064028. DOI: 10.1103/PhysRevD.71.064028. arXiv: gr-qc/0412066.

[47] Philippos Papadopoulos. "Nonlinear harmonic generation in finite amplitude black hole oscillations." *Phys. Rev. D* 65 (2002), p. 084016. DOI: 10.1103/PhysRevD.65.084016. arXiv: gr-qc/0104024.

[48] Manuela Campanelli et al. "The close limit from a null point of view: The Advanced solution." *Phys. Rev. D* 63 (2001), p. 124013. DOI: 10.1103/PhysRevD.63.124013. arXiv: gr-qc/0012107.

[49] Sascha Husa et al. "Retarded radiation from colliding black holes in the close limit." *Phys. Rev. D* 65 (2002), p. 084034. DOI: 10.1103/PhysRevD.65.084034. arXiv: gr-qc/0108075.

[50] Yosef Zlochower et al. “Mode coupling in the nonlinear response of black holes.” *Phys. Rev. D* 68 (2003), p. 084014. DOI: 10.1103/PhysRevD.68.084014. arXiv: gr-qc/0306098.

[51] Jeffrey Winicour. “The characteristic treatment of black holes.” *Prog. Theor. Phys. Suppl.* 136 (1999). Ed. by T. Nakamura and H. Kodama, pp. 57–71. DOI: 10.1143/PTPS.136.57. arXiv: gr-qc/9911106.

[52] Sascha Husa and Jeffrey Winicour. “The asymmetric merger of black holes.” *Phys. Rev. D* 60 (1999), p. 084019. DOI: 10.1103/PhysRevD.60.084019. arXiv: gr-qc/9905039.

[53] Roberto Gomez, Sascha Husa, and Jeffrey Winicour. “Complete null data for a black hole collision.” *Phys. Rev. D* 64 (2001), p. 024010. DOI: 10.1103/PhysRevD.64.024010. arXiv: gr-qc/0009092.

[54] Roberto Gomez et al. “Gravitational waves from a fissioning white hole.” *Phys. Rev. D* 66 (2002), p. 064019. DOI: 10.1103/PhysRevD.66.064019. arXiv: gr-qc/0205038.

[55] Nigel T. Bishop et al. “A numerical relativistic model of a massive particle in orbit near a Schwarzschild black hole.” *Phys. Rev. D* 68 (2003), p. 084015. DOI: 10.1103/PhysRevD.68.084015. arXiv: gr-qc/0301060.

[56] Florian Siebel et al. “Axisymmetric core collapse simulations using characteristic numerical relativity.” *Phys. Rev. D* 67 (2003), p. 124018. DOI: 10.1103/PhysRevD.67.124018. arXiv: gr-qc/0301127.

[57] Nigel T Bishop. “Linearized solutions of the Einstein equations within a Bondi–Sachs framework, and implications for boundary conditions in numerical simulations.” *Classical and Quantum Gravity* 22.12 (May 2005), pp. 2393–2406. DOI: 10.1088/0264-9381/22/12/006. URL: https://doi.org/10.1088/0264-9381/22/12/006.

[58] Christian Reisswig et al. “Unambiguous determination of gravitational waveforms from binary black hole mergers.” *Phys. Rev. Lett.* 103 (2009), p. 221101. DOI: 10.1103/PhysRevLett.103.221101. arXiv: 0907.2637 [gr-qc].

[59] Christian Reisswig et al. “Characteristic extraction in numerical relativity: binary black hole merger waveforms at null infinity.” *Class. Quant. Grav.* 27 (2010), p. 075014. DOI: 10.1088/0264-9381/27/7/075014. arXiv: 0912.1285 [gr-qc].

[60] Maria C. Babiuc et al. “A characteristic extraction tool for gravitational waveforms.” *Phys. Rev.* D84 (2011), p. 044057. DOI: 10.1103/PhysRevD.84.044057. arXiv: 1011.4223 [gr-qc].

[61] Maria C. Babiuc, Jeffrey Winicour, and Yosef Zlochower. "Binary black hole waveform extraction at null Infinity." *Class. Quant. Grav.* 28 (2011). Ed. by Luis Lehner, Harald P. Pfeiffer, and E. Poisson, p. 134006. DOI: 10.1088/0264-9381/28/13/134006. arXiv: 1106.4841 [gr-qc].

[62] Christian Reisswig et al. "Gravitational wave extraction in simulations of rotating stellar core collapse." *Phys. Rev. D* 83 (2011), p. 064008. DOI: 10.1103/PhysRevD.83.064008. arXiv: 1012.0595 [gr-qc].

[63] Casey J. Handmer and B. Szilagyi. "Spectral Characteristic evolution: A new algorithm for gravitational wave propagation." *Class. Quant. Grav.* 32.2 (2015), p. 025008. DOI: 10.1088/0264-9381/32/2/025008. arXiv: 1406.7029 [gr-qc].

[64] Casey J. Handmer, Béla Szilágyi, and Jeffrey Winicour. "Gauge invariant spectral Cauchy characteristic extraction." *Class. Quant. Grav.* 32.23 (2015), p. 235018. DOI: 10.1088/0264-9381/32/23/235018. arXiv: 1502.06987 [gr-qc].

[65] Casey J. Handmer, Béla Szilágyi, and Jeffrey Winicour. "Spectral Cauchy characteristic extraction of strain, news and gravitational radiation flux." *Class. Quant. Grav.* 33.22 (2016), p. 225007. DOI: 10.1088/0264-9381/33/22/225007. arXiv: 1605.04332 [gr-qc].

[66] *Simulating eXtreme Spacetimes*. http://www.black-holes.org/..

[67] *The Spectral Einstein Code*. http://www.black-holes.org/SpEC.html.

[68] Lawrence E. Kidder et al. "SpECTRE: A task-based discontinuous Galerkin code for relativistic astrophysics." *J. Comput. Phys.* 335 (2017), pp. 84–114. DOI: 10.1016/j.jcp.2016.12.059. arXiv: 1609.00098 [astro-ph.HE].

[69] Nils Deppe et al. *SpECTRE v2022.06.14*. 10.5281/zenodo.6643787. Version 2022.06.14. June 2022. DOI: 10.5281/zenodo.6643787. URL: https://spectre-code.org.

[70] Swetha Bhagwat et al. "On choosing the start time of binary black hole ringdowns." *Phys. Rev. D* 97.10 (2018), p. 104065. DOI: 10.1103/PhysRevD.97.104065. arXiv: 1711.00926 [gr-qc].

[71] Keefe Mitman et al. "Computation of displacement and spin gravitational memory in numerical relativity." *Phys. Rev. D* 102.10 (2020), p. 104007. DOI: 10.1103/PhysRevD.102.104007. arXiv: 2007.11562 [gr-qc].

[72] Keefe Mitman et al. "Adding gravitational memory to waveform catalogs using BMS balance laws." *Phys. Rev. D* 103.2 (2021), p. 024031. DOI: 10.1103/PhysRevD.103.024031. arXiv: 2011.01309 [gr-qc].

[73] Keefe Mitman et al. "Fixing the BMS frame of numerical relativity waveforms." *Phys. Rev. D* 104.2 (2021), p. 024051. DOI: 10.1103/PhysRevD.104.024051. arXiv: 2105.02300 [gr-qc].

[74] Lorena Magaña Zertuche et al. "High precision ringdown modeling: Multimode fits and BMS frames." *Phys. Rev. D* 105 (2022), p. 104015. DOI: 10.1103/PhysRevD.105.104015. arXiv: 2110.15922 [gr-qc].

[75] Francois Foucart et al. "High-accuracy waveforms for black hole-neutron star systems with spinning black holes." *Phys. Rev. D* 103.6 (2021), p. 064007. DOI: 10.1103/PhysRevD.103.064007. arXiv: 2010.14518 [gr-qc].

[76] Sizheng Ma et al. "Gravitational-wave echoes from numerical-relativity waveforms via spacetime construction near merging compact objects." *Phys. Rev. D* 105.10 (2022), p. 104007. DOI: 10.1103/PhysRevD.105.104007. arXiv: 2203.03174 [gr-qc].

[77] Lee Lindblom et al. "A new generalized harmonic evolution system." *Class. Quant. Grav.* 23 (2006), S447–S462. DOI: 10.1088/0264-9381/23/16/S09. arXiv: gr-qc/0512093 [gr-qc].

[78] Lawrence E. Kidder et al. "Boundary conditions for the Einstein evolution system." *Phys. Rev.* D71 (2005), p. 064020. DOI: 10.1103/PhysRevD.71.064020. arXiv: gr-qc/0412116 [gr-qc].

[79] Luisa T. Buchman and Olivier C. A. Sarbach. "Towards absorbing outer boundaries in general relativity." *Class. Quant. Grav.* 23 (2006), pp. 6709–6744. DOI: 10.1088/0264-9381/23/23/007. arXiv: gr-qc/0608051.

[80] Luisa T. Buchman and Olivier C. A. Sarbach. "Improved outer boundary conditions for Einstein's field equations." *Class. Quant. Grav.* 24 (2007). Ed. by Manuela Campanelli and Luciano Rezzolla, S307–S326. DOI: 10.1088/0264-9381/24/12/S20. arXiv: gr-qc/0703129.

[81] Oliver Rinne, Lee Lindblom, and Mark A. Scheel. "Testing outer boundary treatments for the Einstein equations." *Class. Quant. Grav.* 24 (2007), pp. 4053–4078. DOI: 10.1088/0264-9381/24/16/006. arXiv: 0704.0782 [gr-qc].

[82] Oliver Rinne et al. "Implementation of higher-order absorbing boundary conditions for the Einstein equations." *Class. Quant. Grav.* 26 (2009), p. 075009. DOI: 10.1088/0264-9381/26/7/075009. arXiv: 0811.3593 [gr-qc].

[83] *Approaches to Numerical relativity*. Cambridge University Press, 1992. DOI: 10.1017/CBO9780511524639.

[84] Nigel T Bishop. "Numerical relativity: combining the Cauchy and characteristic initial value problems." *Classical and Quantum Gravity* 10.2 (Feb. 1993), pp. 333–341. DOI: 10.1088/0264-9381/10/2/015. URL: https://doi.org/10.1088/0264-9381/10/2/015.

[85] Chris J. S. Clarke and Ray A. d'Inverno. "Combining Cauchy and characteristic numerical evolutions in curved coordinates." *Classical and Quantum Gravity* 11.6 (June 1994), pp. 1463–1468. DOI: 10.1088/0264-9381/11/6/011.

[86] Nigel T. Bishop et al. "Cauchy-characteristic matching: A new approach to radiation boundary conditions." *Phys. Rev. Lett.* 76 (23 June 1996), pp. 4303–4306. DOI: 10.1103/PhysRevLett.76.4303. URL: https://link.aps.org/doi/10.1103/PhysRevLett.76.4303.

[87] Philippos Papadopoulos and Pablo Laguna. "Cauchy characteristic evolution of Einstein Klein-Gordon systems: The black hole regime." *Phys. Rev. D* 55 (1997), pp. 2038–2043. DOI: 10.1103/PhysRevD.55.2038. arXiv: gr-qc/9610076.

[88] Chris J. S. Clarke, Ray A. d'Inverno, and James A. Vickers. "Combining Cauchy and characteristic codes. I. The vacuum cylindrically symmetric problem." *Phys. Rev. D* 52 (12 Dec. 1995), pp. 6863–6867. DOI: 10.1103/PhysRevD.52.6863. URL: https://link.aps.org/doi/10.1103/PhysRevD.52.6863.

[89] Mark R. Dubal, Ray A. d'Inverno, and Chris J. S. Clarke. "Combining Cauchy and characteristic codes. II. The interface problem for vacuum cylindrical symmetry." *Phys. Rev. D* 52 (12 Dec. 1995), pp. 6868–6881. DOI: 10.1103/PhysRevD.52.6868. URL: https://link.aps.org/doi/10.1103/PhysRevD.52.6868.

[90] Ray A. d'Inverno and James A. Vickers. "Combining Cauchy and characteristic codes. III. The interface problem in axial symmetry." *Phys. Rev. D* 54 (8 Oct. 1996), pp. 4919–4928. DOI: 10.1103/PhysRevD.54.4919. URL: https://link.aps.org/doi/10.1103/PhysRevD.54.4919.

[91] Ray A. d'Inverno and James A. Vickers. "Combining Cauchy and characteristic codes. IV. The characteristic field equations in axial symmetry." *Phys. Rev. D* 56 (2 July 1997), pp. 772–784. DOI: 10.1103/PhysRevD.56.772. URL: https://link.aps.org/doi/10.1103/PhysRevD.56.772.

[92] Ray A. d'Inverno, Mark R. Dubal, and Elizabeth A. Sarkies. "Cauchy characteristic matching for a family of cylindrical vacuum solutions possessing both gravitational degrees of freedom." *Class. Quant. Grav.* 17 (2000), pp. 3157–3170. DOI: 10.1088/0264-9381/17/16/305. arXiv: gr-qc/0002057.

[93] Mark R. Dubal, Ray A. d'Inverno, and James A. Vickers. "Combining Cauchy and characteristic codes. V. Cauchy-characteristic matching for a spherical spacetime containing a perfect fluid." *Phys. Rev. D* 58 (4 July 1998), p. 044019. DOI: 10.1103/PhysRevD.58.044019. URL: https://link.aps.org/doi/10.1103/PhysRevD.58.044019.

[94] Roberto Gomez et al. "Cauchy characteristic evolution of Einstein-Klein-Gordon systems." *Phys. Rev. D* 54 (1996), pp. 4719–4727. DOI: 10.1103/PhysRevD.54.4719. arXiv: gr-qc/9603060.

[95] Nigel T. Bishop et al. "Cauchy characteristic evolution and waveforms." *Journal of Computational Physics* 136.1 (Sept. 1997), pp. 140–167. DOI: 10.1006/jcph.1997.5754.

[96] Bela Szilagyi and Jeffrey Winicour. "Well posed initial boundary evolution in general relativity." *Phys. Rev. D* 68 (2003), p. 041501. DOI: 10.1103/PhysRevD.68.041501. arXiv: gr-qc/0205044.

[97] Andrew M. Abrahams et al. "Gravitational wave extraction and outer boundary conditions by perturbative matching." *Phys. Rev. Lett.* 80 (1998), pp. 1812–1815. DOI: 10.1103/PhysRevLett.80.1812. arXiv: gr-qc/9709082.

[98] Mark E. Rupright, Andrew M. Abrahams, and Luciano Rezzolla. "Cauchy perturbative matching and outer boundary conditions. 1. Methods and tests." *Phys. Rev. D* 58 (1998), p. 044005. DOI: 10.1103/PhysRevD.58.044005. arXiv: gr-qc/9802011.

[99] Luciano Rezzolla et al. "Cauchy perturbative matching and outer boundary conditions: Computational studies." *Phys. Rev. D* 59 (1999), p. 064001. DOI: 10.1103/PhysRevD.59.064001. arXiv: gr-qc/9807047.

[100] Saul A. Teukolsky. "Linearized quadrupole waves in general relativity and the motion of test particles." *Phys. Rev. D* 26 (4 Aug. 1982), pp. 745–750. DOI: 10.1103/PhysRevD.26.745. URL: https://link.aps.org/doi/10.1103/PhysRevD.26.745.

[101] Burkhard Zink et al. "Cauchy-perturbative matching revisited: Tests in spherical symmetry." *Phys. Rev. D* 73 (2006), p. 084011. DOI: 10.1103/PhysRevD.73.084011. arXiv: gr-qc/0511163.

[102] Simonetta Frittelli. "Estimates for the characteristic problem of the first-order reduction of the wave equation." *Journal of Physics A Mathematical General* 37.36 (Sept. 2004), pp. 8639–8655. DOI: 10.1088/0305-4470/37/36/005. arXiv: math-ph/0408007 [math-ph].

[103] Heinz-Otto Kreiss and Jeffrey Winicour. "The well-posedness of the null-timelike boundary problem for quasilinear waves." *Class. Quant. Grav.* 28 (2011), p. 145020. DOI: 10.1088/0264-9381/28/14/145020. arXiv: 1010.1201 [gr-qc].

[104] Thanasis Giannakopoulos, David Hilditch, and Miguel Zilhao. "Hyperbolicity of general relativity in Bondi-like gauges." *Phys. Rev. D* 102.6 (2020), p. 064035. DOI: 10.1103/PhysRevD.102.064035. arXiv: 2007.06419 [gr-qc].

[105] Morten Bjørhus. "The ODE formulation of hyperbolic PDEs discretized by the spectral collocation method". *SIAM Journal on Scientific Computing* 16.3 (1995), pp. 542–557. DOI: 10.1137/0916035. eprint: https://doi.org/10.1137/0916035. URL: https://doi.org/10.1137/0916035.

[106] Bela Szilagyi, Lee Lindblom, and Mark A. Scheel. "Simulations of binary black hole mergers using spectral methods." *Phys. Rev.* D80 (2009), p. 124010. DOI: 10.1103/PhysRevD.80.124010. arXiv: 0909.3557 [gr-qc].

[107] Jeffrey Rauch. "Symmetric positive systems with boundary characteristic of constant multiplicity." *Transactions of the American Mathematical Society* 291.1 (1985), pp. 167–187. ISSN: 00029947. URL: http://www.jstor.org/stable/1999902 (visited on 04/19/2022).

[108] Paolo Secchi. "The initial-boundary value problem for linear symmetric hyperbolic systems with characteristic boundary of constant multiplicity." *Differential and Integral equations* 9.4 (1996), pp. 671–700. DOI: die/1367969881. URL: https://doi.org/.

[109] Paolo Secchi. "Well-posedness of characteristic symmetric hyperbolic systems." *Archive for Rational Mechanics and Analysis* 134.2 (June 1996), pp. 155–197. DOI: 10.1007/BF00379552.

[110] Roberto Gomez et al. "The eth formalism in numerical relativity." *Class. Quant. Grav.* 14 (1997), pp. 977–990. DOI: 10.1088/0264-9381/14/4/013. arXiv: gr-qc/9702002.

[111] James W. York Jr. "Conformal 'thin sandwich' data for the initial-value problem." *Phys. Rev. Lett.* 82 (1999), pp. 1350–1353. DOI: 10.1103/PhysRevLett.82.1350. arXiv: gr-qc/9810051 [gr-qc].

[112] Harald P. Pfeiffer and James W. York Jr. "Extrinsic curvature and the Einstein constraints." *Phys. Rev.* D67 (2003), p. 044022. DOI: 10.1103/PhysRevD.67.044022. arXiv: gr-qc/0207095 [gr-qc].

Chapter 8

EXTENDING SUPERPOSED HARMONIC INITIAL DATA TO HIGHER SPIN

[1] Sizheng Ma et al. "Extending superposed harmonic initial data to higher spin." *Phys. Rev. D* 103.8 (2021), p. 084029. DOI: 10.1103/PhysRevD.103.084029. arXiv: 2102.06618 [gr-qc].

8.1 Introduction

The detection of GW150914 [1] and other binary compact objects [2–6] has opened a new era in astrophysics. With the improvement of detector sensitivity, more and more events are expected to be detected in the near future [7]. Therefore, accurate modeling of coalescing binaries is crucial for data analysis. Numerical relativity (NR) remains the only *ab initio* method to simulate the coalescence of binary black hole (BBH) systems. With NR, one can obtain the entire BBH waveform including inspiral, merger, and ringdown. Moreover, gravitational wave models [8–15] used to analyze detector data are ultimately calibrated against NR.

Numerical simulations of BBHs are based on splitting the Einstein equation into constraint and evolution parts, where the constraint equations provide the initial data to evolve. However, the constructed initial data does not exactly correspond to a quasi-equilibrium state of an inspiral that started at an infinite time in the past. For example, the tidal distortion of a BH is not fully recovered, and the initial data do not usually include gravitational radiation already present. As a result, once the evolution begins, the system relaxes into a quasi-equilibrium state, and gives rise to a pulse of spurious radiation, which is referred to as 'junk radiation.' Several attempts have been made to reduce junk radiation, by introducing PN corrections [16–21], or by using a curved conformal metric [18, 22, 23].

Recently, Varma *et al.* [23] carried out a systematic study of initial data and its effects on junk radiation and computational efficiency of the subsequent time evolution. The simulations studied in Varma *et al.* were performed with an NR code: the Spectral Einstein Code (SpEC) [24], where the construction of initial data is based on the Extended Conformal Thin Sandwich (XCTS) formulation [25, 26]. Within this formalism, several free fields, including the conformal metric, must be provided.

Different choices of the free fields generate different physical initial data; the data still correspond to two black holes with the same desired mass ratio and spins, but the initial tidal distortions and strong-field dynamics differ. Varma *et al.* showed that the junk radiation and efficiency of the subsequent evolution depend on the given free fields. In particular, choosing the initial data based on two superposed black holes in time-independent harmonic coordinates [27] (heretofore called superposed harmonic (SH) data) leads to less junk radiation than superposed Kerr-Schild (SKS) initial data [22], which is typically used in SpEC simulations [28]. Varma *et al.* also found that SH initial data has higher computational efficiency. However, SH initial data works well only for BHs with dimensionless spin $\chi \lesssim 0.7$. For high-spin BHs, the horizons become so highly deformed that it is difficult to construct initial data (cf. Fig. 10 in Ref. [23]).

For both SH and SKS initial data, the conformal spatial metric and the trace of the extrinsic curvature are determined by superposing the analytic solutions for two single Kerr black holes. The difference is that SKS uses the Kerr metric in Kerr-Schild coordinates, and SH uses the Kerr metric in time-independent harmonic coordinates [27]. It may be surprising that making a different coordinate choice—the choice of coordinates for the single-BH analytic solution—leads to a different physical BBH solution. The reason is that the superposition of two single-BH solutions does not solve the Einstein equations for a BBH and is used to compute only *some* of the fields; the remaining fields are computed by solving constraints and by quasi-equilibrium conditions. For a single black hole, following the complete initial data procedure (including solving the constraints numerically) for both SKS and SH would result in the same physical Kerr metric but in different coordinates.

In this chapter, we extend SH to higher spins by using a spatial coordinate map to transform the free data for the single-BH conformal metric, while retaining harmonic time slicing for this single-BH conformal metric. The coordinate transformation defines a class of spatial coordinate systems that are characterized by a continuous parameter α. We refer to these coordinates as the modified harmonic (MH) coordinate system. MH coordinates are purely harmonic with $\alpha = 1$ and correspond to spatial KS when $\alpha = 0$. Similar to the cases of SKS and SH, an initial data for a BBH system can also be constructed by superposing two single Kerr black holes in MH coordinates. We refer to this initial data as superposed modified harmonic (SMH). For the BBH systems with $\chi > 0.7$, a value of $\alpha < 1$ results in less distorted horizons. However, it is desirable to keep α as close to 1 as possible so that SMH

data still shares the desirable properties of SH initial data.

This chapter is organized as follows. In Sec. 8.2, we provide some basic information about how we compute initial data and evolve BBH systems. In Sec. 8.3, we compare the behavior of different single-BH coordinate systems. In particular, in Sec. 8.3.5 we explicitly point out the numerical reason that SH does not work for high-spin BHs. This immediately leads to a class of spatial coordinate transformations, defined in Sec. 8.3.6, that can cure the numerical issues. We then use the MH coordinate system to construct initial data for BBHs (i.e., SMH) with $\chi = 0.8$ and 0.9 and evolve these systems. In Sec. 8.4, we discuss the results of our simulations. Finally in Sec. 8.5, we discuss our results and highlight possible future work.

Throughout this chapter, we use Latin letters to stand for the spatial indices, and use Greek letters to represent spacetime indices.

8.2 BBH initial data and evolution

Following the discussions in Ref. [23], we use the XCTS formulation to construct initial data for a binary black hole system. Within this formalism, one can freely specify the conformal metric $\bar{g}_{ij}$, trace of extrinsic curvature K, and their time derivatives $\partial_t \bar{g}_{ij}$ and $\partial_t K$. To obtain quasi-equilibrium initial data, we choose

$$\partial_t \bar{g}_{ij} = 0, \quad \partial_t K = 0\,. \tag{8.1}$$

The construction of the other free fields, $\bar{g}_{ij}$ and K, is based on the 3-metric g^{β}_{ij} and the trace of extrinsic curvature K^{β} of two single boosted Kerr BHs , where the superscript $\beta = 1, 2$ labels each of the two BHs in the binary system. The conformal metric and the trace of the extrinsic curvature are then given by:

$$\bar{g}_{ij} = f_{ij} + \sum_{\beta=1}^{2} e^{-r_\beta^2/w_\beta^2}(g^{\beta}_{ij} - f_{ij}), \tag{8.2}$$

$$K = \sum_{\beta=1}^{2} e^{-r_\beta^2/w_\beta^2} K^{\beta}\,, \tag{8.3}$$

where f_{ij} is the flat 3-metric, and r_β is the Euclidean coordinate distance from the center of each BH [29]. Note that each metric is weighted by a Gaussian with width

$$w_\beta = 0.6\, d^{L_1}_{\beta}\,, \tag{8.4}$$

where $d^{L_1}_{\beta}$ is the Euclidean distance between the Newtonian L_1 Lagrange point and the center of the black hole labeled by β. Here g^{β}_{ij} and K^{β} correspond to the

Kerr solution expressed either in the KS, harmonic, or MH coordinate systems. BBH initial data constructed from the two Kerr solutions in the aforementioned coordinates are referred to as SKS, SH, and superposed modified harmonic (SMH), respectively.

After specifying the free fields, the initial data are completed by solving a set of coupled elliptic equations that ensure satisfaction of the constraints and an additional quasi-equilibrium condition. Additionally, these elliptic equations require boundary conditions. At the outer boundary (typically chosen to be $10^9\,M$ from the sources), we impose asymptotic flatness [cf. Eq. (11)—(13) in Ref. [23]], and at each inner boundary we enforce an apparent horizon condition [cf. Eq. (15)—(24) in Ref. [23]]. After generating initial data in the XCTS formalism, we also need to specify the initial gauge for time evolution. Here we use the most common choice for SpEC simulations: $\partial_t N = \partial_t N^i = 0$ in a corotating frame, where N is the lapse function and N^i is the shift vector. It was shown that the damped harmonic gauge [30] is the most suitable for mergers, so we do a smooth gauge transformation on a time scale of $\sim 50\,M$ during the early inspiral, to transform from the initial gauge to the better suited damped harmonic gauge.

8.3 Modified harmonic coordinate system

In this section, we aim to investigate the reason that makes the harmonic coordinates problematic for high-spin BHs. We begin with a brief review of KS coordinates in Sec. 8.3.1. Then in Sec. 8.3.2, we outline a method that can be used to study the numerical behavior of Kerr metric in different coordinate systems. It is then applied to KS spatial coordinates with harmonic slicing in Sec. 8.3.3, and to harmonic coordinates in Sec. 8.3.4. Those analyses allow us to explicitly show the numerical problem with using harmonic coordinates for high-spin BHs, as discussed in Sec. 8.3.5. Finally in Sec. 8.3.6, we provide a coordinate map to fix the problem.

8.3.1 Kerr in Kerr-Schild coordinates

For a stationary Kerr BH with mass M and angular momentum χM^2 in the z direction, the metric in KS coordinates $x^\mu_{\rm KS} = (t_{\rm KS}, x_{\rm KS}, y_{\rm KS}, z_{\rm KS})$ is given by [31]

$$ds^2 = g_{\mu\nu} dx^\mu_{\rm KS} dx^\nu_{\rm KS} = (\eta_{\mu\nu} + 2H l_\mu l_\nu) dx^\mu_{\rm KS} dx^\nu_{\rm KS}\,, \tag{8.5}$$

where $\eta_{\mu\nu}$ is the Minkowski metric, H is a scalar function, and l_μ is a null covariant vector. The expressions for H and l_μ are not used here but can be found in Ref. [31].

With KS coordinates, the radial Boyer-Lindquist coordinate r can be written as [31]

$$r^2 = \frac{1}{2}(x_{\rm KS}^2 + y_{\rm KS}^2 + z_{\rm KS}^2 - a^2) + \left[\frac{1}{4}(x_{\rm KS}^2 + y_{\rm KS}^2 + z_{\rm KS}^2 - a^2)^2 + a^2 z_{\rm KS}^2\right]^{1/2} , \quad (8.6)$$

or equivalently

$$\frac{x_{\rm KS}^2 + y_{\rm KS}^2}{r^2 + a^2} + \frac{z_{\rm KS}^2}{r^2} = 1 . \quad (8.7)$$

Here we have used $a = \chi M$ for the sake of conciseness. The outer and inner horizons of the BH are located at

$$r_\pm = M \pm \sqrt{M^2 - a^2} . \quad (8.8)$$

8.3.2 Transforming from KS to a different coordinate system

Now we introduce a new coordinate system $x^\mu = (t, x, y, z)$, which are related to the KS coordinates $x^\mu_{\rm KS}$ through

$$\begin{pmatrix} dt_{\rm KS} \\ dx_{\rm KS} \\ dy_{\rm KS} \\ dz_{\rm KS} \end{pmatrix} = \begin{pmatrix} 1 & \boldsymbol{b} \\ 0 & \boldsymbol{C} \end{pmatrix} \begin{pmatrix} dt \\ dx \\ dy \\ dz \end{pmatrix} , \quad (8.9)$$

where $\boldsymbol{b}$ is a 3D vector, and $\boldsymbol{C}$ is a 3×3 matrix. In Eq. (8.9), we have assumed that the new spatial coordinates are independent of $t_{\rm KS}$[1]. Note that we here keep the forms of $\boldsymbol{b}$ and $\boldsymbol{C}$ generic, so that our present discussion can be applied to different coordinate systems.

With the Jacobian at hand, we could transform the Kerr metric into the new coordinates, and study the numerical features of each metric component, such as the problematic behavior of harmonic coordinates for high-spin black holes, but this usually involves very complicated calculations. However, since $g^{\rm KS}_{\mu\nu}$ can be decomposed into two pieces [Eq. (8.5)], it is simpler to study the transformations of $\eta_{\mu\nu}$[2]. In the new coordinates, we have

$$\eta_{\mu\nu} = \begin{pmatrix} -1 & 0 \\ 0 & \mathbb{I}^3 \end{pmatrix} \to \begin{pmatrix} 1 & \boldsymbol{b} \\ 0 & \boldsymbol{C} \end{pmatrix}^T \begin{pmatrix} -1 & 0 \\ 0 & \mathbb{I}^3 \end{pmatrix} \begin{pmatrix} 1 & \boldsymbol{b} \\ 0 & \boldsymbol{C} \end{pmatrix} = \begin{pmatrix} -1 & -\boldsymbol{b} \\ -\boldsymbol{b}^T & \boldsymbol{C}^T\boldsymbol{C} - \boldsymbol{b}^T\boldsymbol{b} \end{pmatrix} , \quad (8.10)$$

[1] Equivalently, $(x_{\rm KS}, y_{\rm KS}, z_{\rm KS})$ are independent of t.

[2] We have checked that the same problematic terms also occur in the $Hl_\mu l_\nu$ piece of Eq. (8.5).

where $\mathbb{I}^3$ is the three-dimensional identity matrix. Both the 3-metric $(\boldsymbol{C}^T\boldsymbol{C} - \boldsymbol{b}^T\boldsymbol{b})$ and the shift vector $-\boldsymbol{b}$ above are modified by the vector $\boldsymbol{b}$. Any numerically problematic term in $\boldsymbol{b}$ might cause difficulty to resolve the metric in the new coordinates. Below, we focus on the z component of $\boldsymbol{b}$, b^z, at the inner boundary $r = r_+$, and study its numerical behavior for high-spin black holes (especially when $a \to M$) with several coordinates.

8.3.3 Kerr-Schild spatial coordinates with harmonic slicing

We first apply our discussion in Sec. 8.3.2 to a mixed coordinate system: KS *spatial* coordinates together with harmonic *temporal* slicing, then we have

$$\boldsymbol{C}_{\rm KSHS} = \mathbb{I}^3, \tag{8.11a}$$

$$\boldsymbol{b}_{\rm KSHS} = \frac{2M}{r - r_-}\boldsymbol{\nabla} r, \tag{8.11b}$$

where the subscript 'KSHS' stands for Kerr-Schild spatial coordinates with Harmonic Slicing; and r is the radial Boyer-Lindquist coordinate. Note that Eq. (8.11b) is the result of [27]

$$t_{\rm KSHS} = t_{\rm KS} - \int \frac{2M}{r - r_-}\, dr\,. \tag{8.12}$$

We refer the reader to Sec. 8.6 for the detailed expression of $\boldsymbol{\nabla} r$. The z component of $\boldsymbol{b}_{\rm KSHS}$ at the inner boundary $r = r_+$ is given by (as $a \to M$)

$$b^z_{\rm KSHS} = \frac{M^2 z_{\rm KS}}{r_+^4 + (a z_{\rm KS})^2}\,. \tag{8.13}$$

8.3.4 Harmonic coordinates

Let us turn our attention to harmonic coordinates $x^\mu_{\rm H} = (t_{\rm H}, x_{\rm H}, y_{\rm H}, z_{\rm H})$, where the spatial coordinates also become harmonic. For such a coordinate system, we have [27]

$$(r - M)^2 = \frac{1}{2}(x^2_{\rm H} + y^2_{\rm H} + z^2_{\rm H} - a^2) + \left[\frac{1}{4}(x^2_{\rm H} + y^2_{\rm H} + z^2_{\rm H} - a^2)^2 + a^2 z^2_{\rm H}\right]^{1/2}, \tag{8.14}$$

and

$$\frac{x^2_{\rm H} + y^2_{\rm H}}{(r - M)^2 + a^2} + \frac{z^2_{\rm H}}{(r - M)^2} = 1\,, \tag{8.15}$$

where the subscript 'H' stands for harmonic coordinates. The harmonic slicing implies

$$\boldsymbol{b}_{\rm H} = \frac{2M}{r - r_-}\boldsymbol{\nabla} r, \tag{8.16}$$

with z component of $\boldsymbol{b}_{\rm H}$ at $r = r_+$ given by (as $a \to M$)

$$b^z_{\rm H} = \frac{M^2 z_{\rm H}}{(r_+ - M)^4 + (a z_{\rm H})^2}\,. \tag{8.17}$$

Expressions for the 3×3 block matrix, $(C_{\rm H})^i_j = \partial x^i_{\rm KS}/\partial x^j_{\rm H}$, along with additional details, can be found in Sec. 8.6.

8.3.5 Problematic behavior of harmonic coordinates

In SpEC, the Legendre polynomials are used to numerically expand $b^z_{\rm H}$ and $b^z_{\rm KSHS}$ as functions of $\cos\theta$, defined by

$$\cos\theta = \frac{z_{\rm H}}{\sqrt{x^2_{\rm H} + y^2_{\rm H} + z^2_{\rm H}}}\,.$$

Here θ is the polar angle in harmonic coordinates and is not to be confused with the angular Boyer-Lindquist coordinate. As a test, we first represent $b^z_{\rm H}$ [Eq. (8.17)] with twenty Legendre-Gauss collocation points and a BH spin of $a = 0.95\,M$. The results of this test are shown in Fig. 8.1. From Fig. 8.1, we see that the function $b^z_{\rm H}$ is difficult to resolve using Legendre polynomials. This is the primary reason that harmonic coordinates fail to accurately represent high-spin BH initial data. Note that increasing the resolution to $l \gtrsim 60$ (for a single BH) eventually allows us to resolve $b^z_{\rm H}$, but in practice requiring such high resolution is computationally prohibitive; furthermore, the required resolution increases rapidly as the spin increases.

Previous studies have shown success in high-spin BBH simulations with SKS initial data up to spins of $\chi = 0.998$ [32]. A natural question to ask is whether the spatial or the time coordinates are more important in allowing KS coordinates to better resolve highly-spinning black holes. Therefore, we also investigate the behavior of $b^z_{\rm KSHS}$ (see Sec. 8.3.3) in which the time coordinate is harmonic but the spatial coordinates are Kerr-Schild. Again, we represent $b^z_{\rm KSHS}$ with twenty Legendre-Gauss collocation points and a BH spin of $a = 0.95M$, as shown in Fig. 8.1. The representation is much better than the case of harmonic coordinates. And we also confirm that with such mixed coordinates, BBH initial data can be indeed extended to higher spins. However, as we show later, they do not lead to a smaller amount of junk radiation than SKS initial data.

Looking more closely at Fig. 8.1, $b^z_{\rm KSHS}$ has fewer structures than $b^z_{\rm H}$, which makes $b^z_{\rm KSHS}$ easier to represent by Legendre polynomials. More quantitatively, we write

$$b^z_{\rm H} \sim \frac{1}{u^2 + \frac{\epsilon}{1+\epsilon}}, \tag{8.18}$$

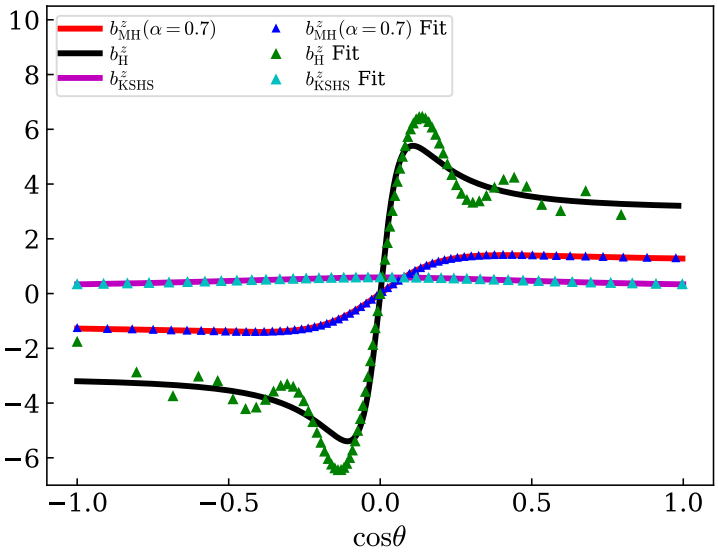

Figure 8.1: The function b^z in KSHS [Eq. (8.13)], harmonic [Eq. (8.17)] and MH [Eq. (8.23)] coordinates with $\alpha = 0.7$. Solid lines represent b^z, whereas triangles represent the Legendre-Gauss collocation approximation to each function b^z using 20 Legendre polynomials. The spin of the BH is $a = 0.95\,M$. b^z is better approximated by a fixed number ($l = 20$) of Legendre polynomials for MH than for harmonic coordinates.

with

$$u = \frac{a}{r_+ - M}\cos\theta, \quad \epsilon = \frac{(r_+ - M)^2}{(r_+ - M)^2 + a^2}. \tag{8.19}$$

In Eq. (8.18), we have omitted unimportant functions of $\cos\theta$ since they are well represented by Legendre polynomials. We see $b^z_{\rm H}$ has two poles $u = \pm i\sqrt{\epsilon/(1+\epsilon)}$. The domain of convergence for Legendre series $P_n(\cos\theta)$ is an elliptic region on the complex plane [33]. If we restrict ourselves to the real axis, we can obtain the radius of convergence as

$$|\cos\theta| \lesssim \sqrt{\frac{1+2\epsilon}{1+\epsilon}}\frac{r_+ - M}{a}. \tag{8.20}$$

The radius becomes less than 1 if $a \gtrsim 0.75M$, thus in that case the Legendre polynomials fail to provide a good representation for the metric. This is the main reason that BBH simulations using SH become difficult when spins are larger than about $a = 0.7M$ [23]. We remark that Chebyshev series have the same domain of convergence as Legendre series; hence we do not expect the situation can be improved by changing basis.

8.3.6 Modified Harmonic coordinates

We have seen that $b^z_{\rm H}$ is sensitive to $\cos\theta$ for high-spin BHs. To reduce such dependence, we define a more general coordinate system

$$\frac{x^2_{\rm MH}+y^2_{\rm MH}}{(r-\alpha M)^2+a^2}+\frac{z^2_{\rm MH}}{(r-\alpha M)^2}=1, \quad t_{\rm MH}=t_{\rm H}\,, \tag{8.21}$$

which leads to

$$\begin{aligned}(r-\alpha M)^2 &= \frac{1}{2}(x^2_{\rm MH}+y^2_{\rm MH}+z^2_{\rm MH}-a^2)\\ &+\left[\frac{1}{4}(x^2_{\rm MH}+y^2_{\rm MH}+z^2_{\rm MH}-a^2)^2+a^2z^2_{\rm MH}\right]^{1/2}.\end{aligned} \tag{8.22}$$

Here we introduce a new constant parameter α. As mentioned earlier, we refer to this new choice of spatial coordinates as the modified harmonic (MH) coordinate system. MH coordinates become harmonic (*spatial*) coordinates when $\alpha=1$ [Eq. (8.15)] and become KS (*spatial*) coordinates when $\alpha=0$ [Eq. (8.7)]. Meanwhile, the time slicing of MH coordinates is the same as in harmonic, regardless of the value of α. With this new coordinate system, the radius of the outer horizon along the spin direction is $(1-\alpha)M+\sqrt{M^2-a^2}$. For $a\to M$, this radius goes to M for KS coordinates ($\alpha=0$) and it goes to zero for harmonic coordinates ($\alpha=1$). Therefore, the horizon with harmonic coordinates is highly compressed in the spin direction. However, if we let α be a number smaller than, but still close to 1, the horizon will be less distorted. On the other hand, since α is close to 1, we can expect that it still shares some similar properties (e.g., less junk radiation) with harmonic coordinates.

As in Sec. 8.3.5, we use the function b^z as an example to see the improvement offered by MH coordinates. In the MH coordinate system, we have

$$b^z_{\rm MH}=\frac{M^2z_{\rm MH}}{(r_+-\alpha M)^4+(az_{\rm MH})^2}\,. \tag{8.23}$$

Now $(r_+-M)^2$ is replaced by $(r_+-\alpha M)^2$. The problematic part of $b^z_{\rm MH}$ takes the same form as Eq. (8.18), except that

$$u=\frac{a}{r_+-\alpha M}\cos\theta, \quad \epsilon=\frac{(r_+-\alpha M)^2}{(r_+-\alpha M)^2+a^2}. \tag{8.24}$$

And the radius of convergence is given by

$$|\cos\theta|\lesssim\sqrt{\frac{1+2\epsilon}{1+\epsilon}}\frac{r_+-\alpha M}{a}. \tag{8.25}$$

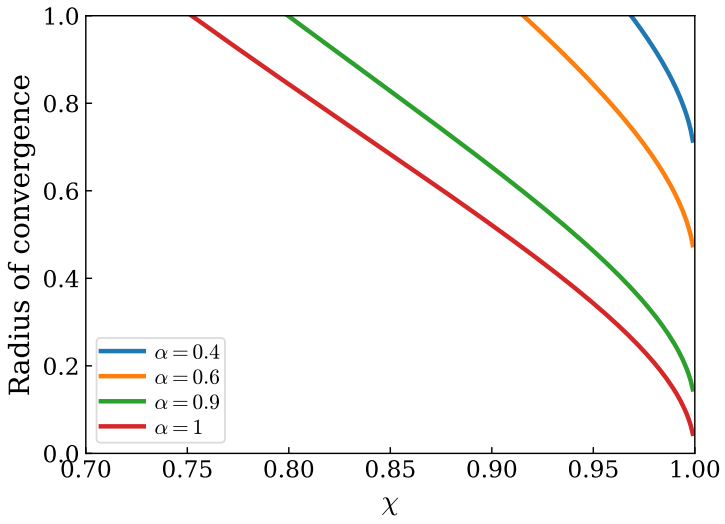

Figure 8.2: The radius of convergence given in Eq. (8.25).

Table 8.1: A summary of parameters (mass ratio q and dimensionless spins $\boldsymbol{\chi}$) for four simulations, where the spins of Case II are chosen randomly. The orbital angular momentum is pointing along $(0, 0, 1)$. In the final column, we show the value of α for MH coordinates.

Simulation label	q	$\boldsymbol{\chi}_1$	$\boldsymbol{\chi}_2$	α
Case I	1	$(0, 0, 0.8)$	$(0, 0, 0.8)$	0.9
Case II	1	$(0.44, 0.44, 0.50)$	$(0.13, 0.64, 0.46)$	0.9
Case III	2	$(0, 0, 0.7)$	$(0, 0, 0.8)$	0.8
Case IV	1	$(0, 0, 0.9)$	$(0, 0, 0.9)$	0.7

In Fig. 8.2, we plot the radius of convergence as a function of $\chi = a/M$ for several values of α. We see the convergent region for a fixed χ is enlarged if α becomes smaller. As a consequence, it should be easier for Legendre polynomials to represent $b^z_{\rm MH}$. To see that this is the case, in Fig. 8.2 we plot $b^z_{\rm MH}$ with $\alpha = 0.7$ and $a = 0.95\,M$, using the same set of angular Legendre-Gauss collocation points as for the other curves in the figure. As expected, the representation in Legendre polynomials of $b^z_{\rm MH}$ shows an enormous improvement over the same representation of $b^z_{\rm H}$.

8.4 Results

In this section we investigate the numerical behavior of BBHs evolved starting with SMH initial data, compared to evolution of SKS data. We pick four cases, as summarized in Table 8.1. To make comparisons, we consider constraint violations, computational efficiency, changes of BH parameters (mass and spin), and junk

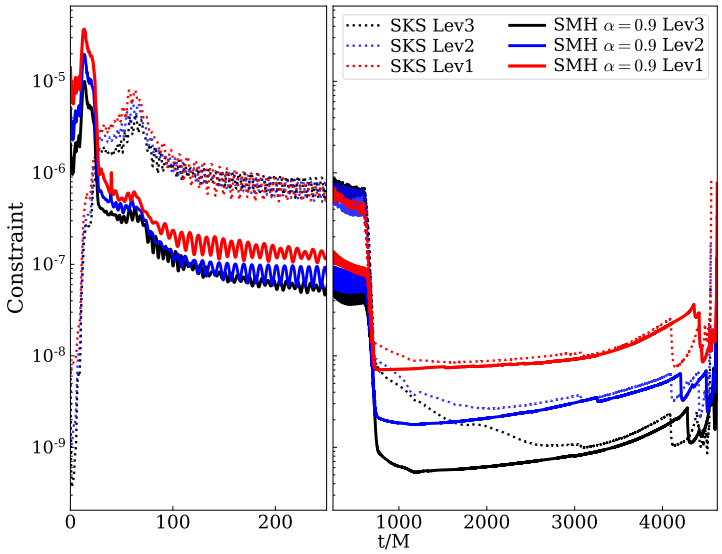

Figure 8.3: The volume-weighted generalized harmonic constraint energy for evolutions of Case I, with both SKS (dotted lines) and SMH (solid lines) initial data. Three resolutions are shown, labeled 'Lev1' (red), 'Lev2' (blue), and 'Lev3' (black) in order of decreasing AMR tolerance (i.e., in order of increasing numerical resolution). At the beginning, BHs of SMH initial data are more distorted on the grid so the constraints are worse. However, as the gauge transition proceeds, the constraints decay quickly. During most of the junk stage ($25M \lesssim t \lesssim 700M$), the constraints of SMH initial data are smaller than SKS by an order of magnitude. They also converge with resolution. After the junk stage, SKS and SMH finally become comparable.

radiation. For the first three factors, we show the general features of SMH by focusing on Case I. For junk radiation, we study all cases. For each simulation, we evolve with three resolutions (labeled Lev 1,2,3 in order of increasing resolution). The resolution is chosen by specifying different numerical error tolerances to the adaptive mesh refinement (AMR) algorithm [34]. The orbital eccentricity is iteratively reduced to below $\sim 10^{-3}$ [35]. The coordinate sizes of the black holes are different for SMH and SKS, so the excision boundaries (which are placed just inside each apparent horizon) are also different for SMH and SKS; this means that the grids are not exactly the same between the two cases, but the grid points are chosen by AMR so that the two cases have the same approximate numerical error.

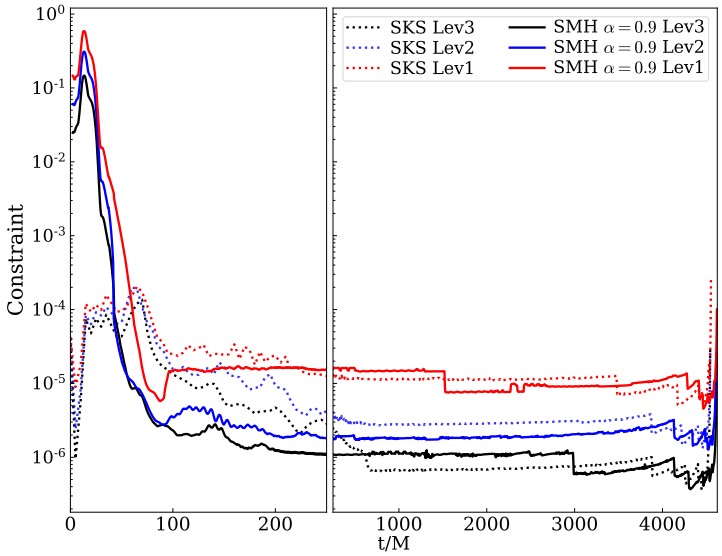

Figure 8.4: Same as Fig. 8.3, except that L^2 norm is used.

8.4.1 Constraint violations and computational efficiency

Figure 8.3 shows the evolution of the volume-weighted generalized harmonic constraint energy $N_{\rm volume}$, which is given by [Eq. (53) of Ref. [36]]

$$N_{\rm volume} = \sqrt{\frac{\int_V F(x)^2 d^3x}{\int_V d^3x}}, \tag{8.26}$$

with $F(x)$ the generalized harmonic constraint energy at x. For the first $\sim 25\,M$ of evolution, the constraints of SMH are much larger than those of SKS. This is because BHs with SMH initial data are more distorted than SKS, and the metric is more difficult to resolve; however, the metric is much easier to resolve for SMH than SH (which is not shown because even constructing the initial data for SH is problematic with a spin of $\chi = 0.8$). Furthermore, at slightly later times, constraints decrease rapidly. During the junk stage ($t \lesssim 700\,M$), the constraints for the evolution of SMH initial data are smaller than those of SKS by an order of magnitude. After the junk leaves the system, the evolution of SMH initial data is still a little bit better than that of SKS initial data, although constraints of SKS and SMH become similar at late times ($t \gtrsim 3000\,M$ for Lev 3 and $t \gtrsim 2000\,M$ for Lev 2).

During the junk stage we make no attempt to resolve the junk oscillations, i.e., the AMR algorithm is intentionally set to change the grid very infrequently (and not at all in the wave zone) during the junk stage of the evolution. We do this because resolving junk is computationally expensive and because the junk is not part of the physical solution we care about. Accordingly, the SKS curves in Figure 8.3 are not

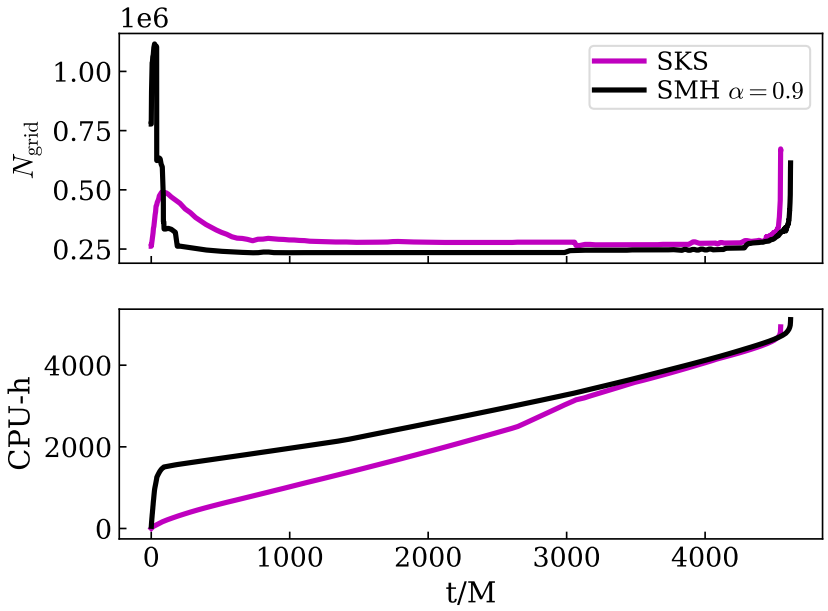

Figure 8.5: Computational efficiency of evolutions of SMH ($\alpha = 0.9$) and SKS initial data for Case I, with the highest resolution. The upper panel is the total number of grid points as a function of time. At the beginning, the SMH initial data requires many more grid points to meet the error tolerance. As the gauge transition to damped harmonic gauge proceeds (on a time scale of $\sim 50\,M$), the BHs become less distorted, so AMR gradually drops points. At the same time, several concentric spherical shells around each of the BHs are dropped, which leads to discontinuous jumps in the number of grid points. In the end, evolutions of SMH initial data has fewer collocation points than for SKS. The lower panel is the accumulated CPU hours versus time. The SMH initial data is extremely slow at the beginning. As the collocation points and subdomains are adjusted, it speeds up. The total CPU hours for evolutions of both initial data sets are similar.

well-resolved during the junk stage and do not show good convergence. However, we notice that the simulations of SMH initial data are better resolved than for SKS, and they converge with resolution even during the junk stage; convergence during the junk stage was also observed for SH with low-spin BHs [23].

The convergence plot looks slightly different when the norm of the constraint energy is determined using a pointwise L^2 norm over grid points rather than an integral over the volume, as given by

$$N_{\rm pointwise} = \sqrt{\frac{\sum_{i=1}^{N} (F_i)^2}{N}}, \tag{8.27}$$

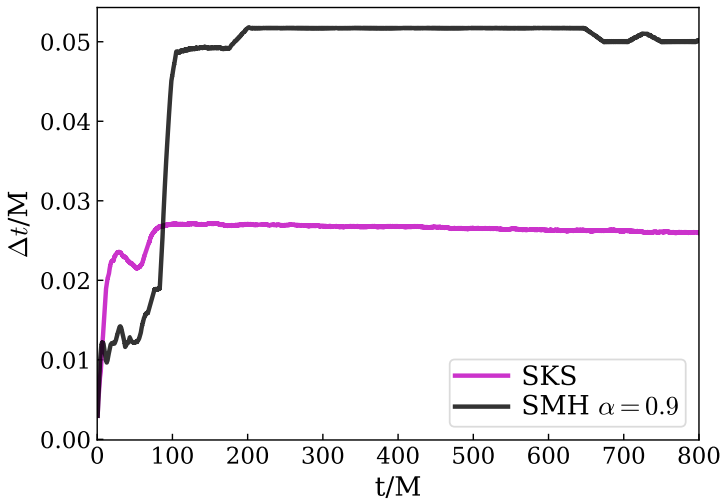

Figure 8.6: The time step as a function of evolution time. The resolution is Lev 3. Initially, the time step for evolutions of SKS initial data is larger than for SMH. However, after several jumps due to the shell-dropping algorithm, SMH eventually has a larger time step than SKS.

where the subscript i stands for the index of a grid point, and N is the total number of grid points. The pointwise norm is shown in Fig.8.4. For the pointwise norm the improvement of convergence of SMH over SKS is not as good as for the volume-weighted norm. This is because the pointwise norm gives larger weight to the interior regions near the BHs where there are more points, whereas the volume norm gives larger weight to the exterior wave zone which covers more volume. The difference beween Figs. 8.3 and 8.4 illustrates that the improvement of the constraints in the case of SMH mainly comes from the outer region, where the high-frequency components in the waveforms are smaller (i.e., less junk radiation). Figure 8.4 also shows that the pointwise norms (L^2 norm) for evolutions of both initial data sets become comparable much earlier than the volume norms ($t \sim 200\,M$). This is because the pointwise norms are monitored by AMR, and therefore their values remain consistent with the numerical error tolerance in AMR during the evolution as AMR makes changes to the grid resolution.

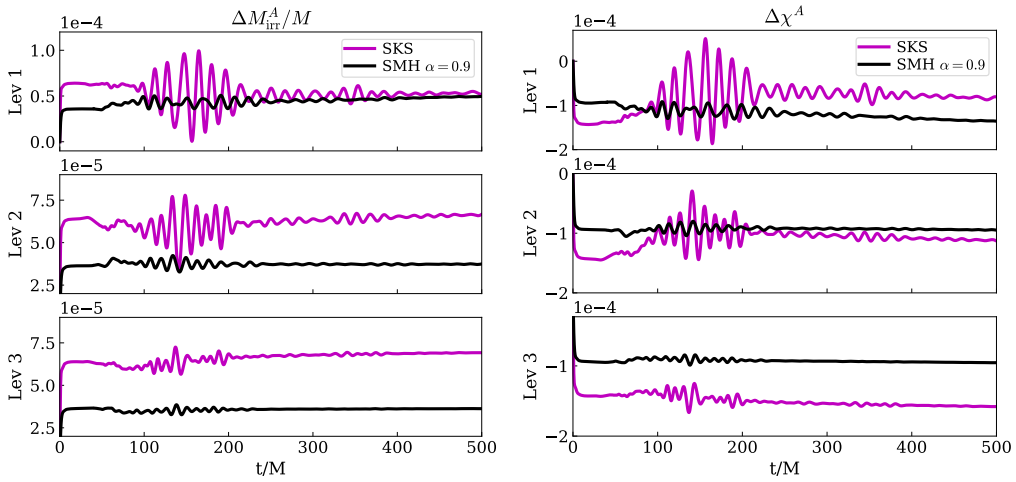

Figure 8.7: The evolution of irreducible mass (left) and dimensionless spin (right) of the first BH for Case I, with three resolutions. The quantities shown are deviations from their values at $t = 0$. Evolutions of SMH initial data have fewer oscillations than SKS. Deviations of three parameters for both initial data sets are on the same order.

To understand how the computational efficiency of the evolution depends on the initial data, in Fig. 8.5 we show the total number of grid points in the computational domain as a function of time. At the beginning, SMH needs many more points than SKS. As the gauge gradually transforms to the damped harmonic gauge, the BHs become less distorted and AMR decides to drop grid points. During the evolution, there are two factors that mainly control the number of grid points. One is AMR,

which adjusts grid points based on the numerical error tolerance. The other one is the domain decomposition [37]. SpEC splits the entire computation region into various subdomains. In particular, there are a series of concentric spherical shells around each BH. The subdomain boundaries are fixed in the "grid frame," the frame in which the BHs do not move, but these boundaries do move in the "inertial frame," the frame in which the BHs orbit and approach each other [38]. As the separation between the BHs decreases, the inertial-frame widths of the subdomains between them decreases as well. During the evolution, the inertial-frame widths of the spherical shells are monitored. Once one of the shells becomes sufficiently squeezed, the algorithm drops one of the shells and redistributes the computational domain. In Ref. [23], the authors pointed out that evolutions of SH initial data are faster than for SKS initial data. However, that statement is not true at very early times, when SH starts with more spherical shells and more grid points, which leads to low speed. The evolution of SH initial data then gradually speeds up after several spherical shells are dropped, and eventually becomes faster than the corresponding evolution of SKS data. Our simulation here is similar. In Fig. 8.5, AMR modifies $N_{\rm grid}$ smoothly, while the discontinuous jump is caused by the shell-dropping algorithm. For each BH, we have six spherical shells initially. However, four of them are dropped during the first $\sim 200\,M$. In the end, the number of grid points for evolutions of SMH is smaller than for evolutions of SKS. This not only improves the computational efficiency of each time step, but also increases the time step Δt allowed by the Courant limit ($\Delta t \sim N_{\rm grid}^{-2}$). As shown in Fig. 8.6, the time step for SMH jumps several times because of the shell-dropping algorithm. In the end, Δt for SMH is larger than the one for SKS. Both $N_{\rm grid}$ and Δt contributes to the high speed of evolutions of SH and SMH initial data. And we have checked that the increase of Δt plays the major role in the speed increase.

The bottom panel of Fig. 8.5 shows the accumulated CPU hours of the simulation. At first, the evolution of SMH is extremely slow. Once several shells are dropped, the simulation gradually speeds up. This suggests that both SH and SMH initial data start with more shells than necessary. Therefore, it might be possible to further improve the computational efficiency solely by reducing the number of shells.

8.4.2 Junk radiation and changes in parameters

Since the BHs in the initial data are not in true quasi-equilibrium, the masses and spins of BHs relax once the evolution begins, resulting in slight deviations from their initial values. In Figure 8.7, we show the change of irreducible mass

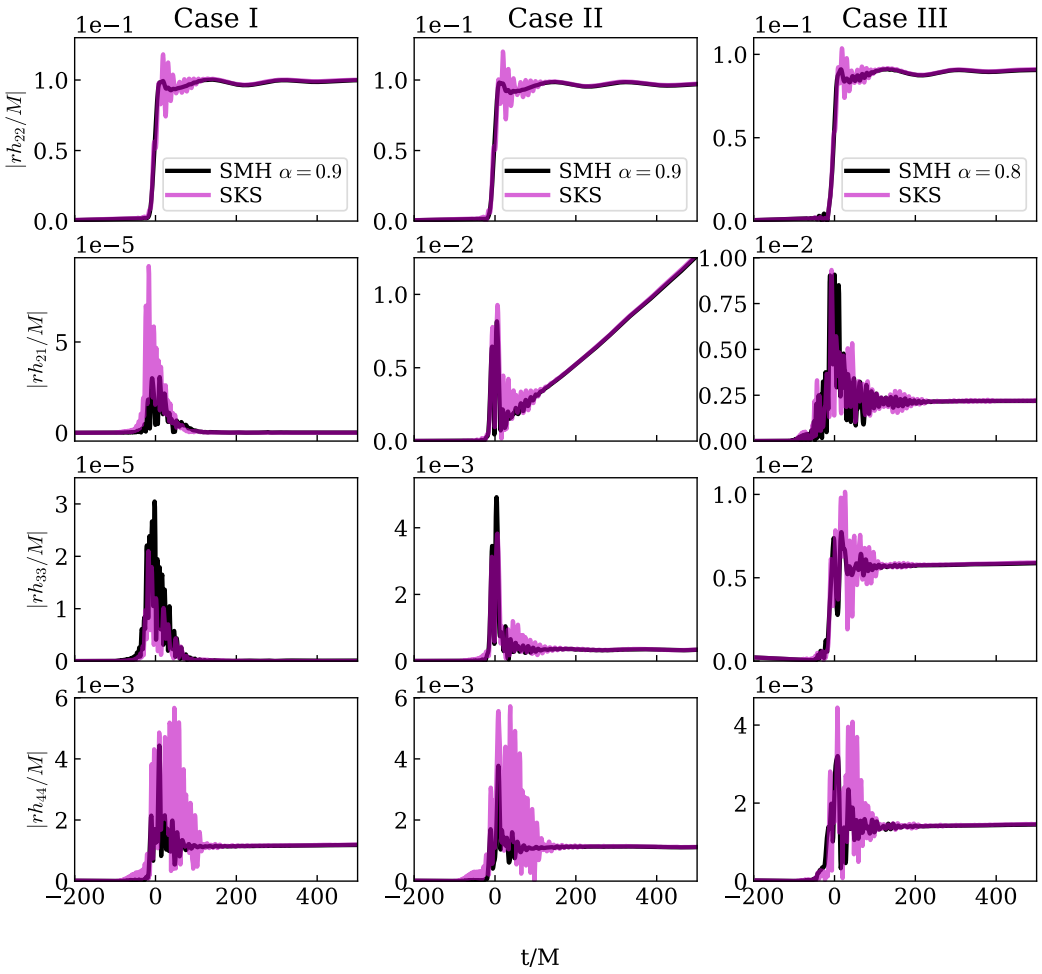

Figure 8.8: Mode amplitudes of waveforms for Case I, II and III with the highest resolution. Columns correspond to three cases, and rows are for different modes. For SMH initial data, we pick $\alpha = 0.9$ for Case I and II, and $\alpha = 0.8$ for Case III. Note that the linear growth of h_{21} for Case II appears because only the initial part of the waveform is shown. Over the entire evolution, the mode is oscillatory. In general, the junk radiation of SMH initial data leaves the system faster. It is also smaller than the junk radiation of SKS for most of the modes. However, there are some modes, such as h_{33}, that have the same peak as SKS.

$\Delta M_{\rm irr}(t) = |M_{\rm irr}(t) - M_{\rm irr}(t=0)|$ and the change of spin $\Delta\chi(t) = |\chi(t) - \chi(t=0)|$ as functions of time, for three resolutions. We can see the variations are on the same order for both SMH and SKS initial data, but SMH has smaller oscillations. With the highest resolution, the deviation of SMH is smaller by a factor of $\sim 1.5 - 2$.

To study the junk radiation in the waveform, in Fig. 8.8 we plot the amplitudes of different spin weighted spherical harmonic modes h_{lm}, for Case I, II and III listed in Table 8.1 (Case IV will be discussed later). Note that the linear growth of h_{21}

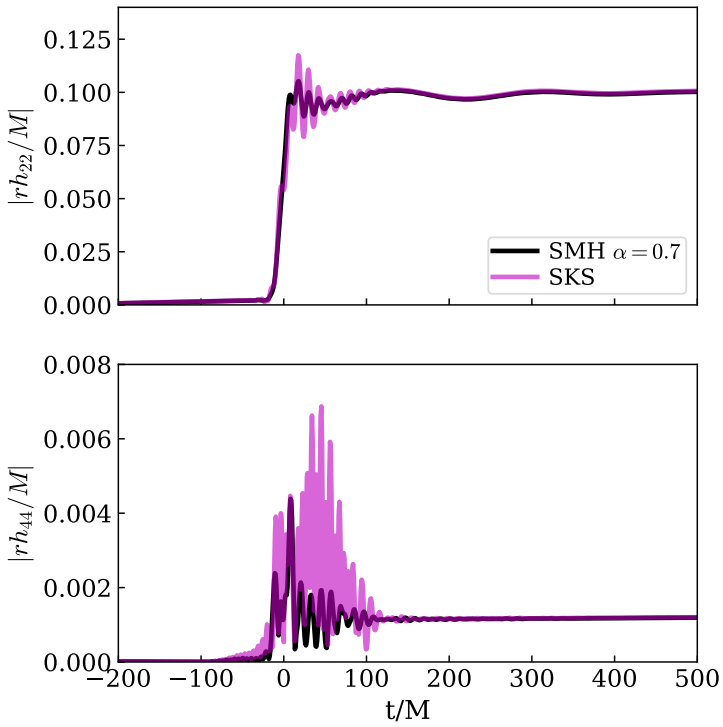

Figure 8.9: The h_{22} and h_{44} modes for the highest resolution of Case IV, an equal-mass BBH system with larger spins. The spins for both BHs are $(0, 0, 0.9)$, which we have not been able to run with SH initial data. We can still see that the junk radiation for SMH is less than SKS.

for Case II appears because only the initial part of the waveform is shown; over the entire evolution, the mode is oscillatory.

We can see that the junk radiation of evolutions of SMH initial data is less than for SKS for most of the modes. In general, the junk radiation leaves the system faster for SMH initial data than for SKS. However, the decrease of junk radiation for SMH is not as significant as SH for low-spin BHs [23]. Some modes of SMH initial data, such as h_{33}, are similar to SKS. Comparing Cases II and III, we note that the junk radiation of $\alpha = 0.8$ SMH is larger than that of $\alpha = 0.9$, presumably because $\alpha = 0.8$ deviates more from SH initial data ($\alpha = 1$). Note that Case II has similar junk radiation as Case III when both cases are evolved from SKS initial data; this suggests that the difference in junk radiation between Cases II and III seen in Figure 8.8 is probably not due to differences in parameters like the mass ratio.

For Case IV, a BBH system with dimensionless spins 0.9, we need to decrease α to 0.7, since for that large of spin $\alpha = 0.8$ requires too high resolution and sometimes the initial data solver doesn't converge. To speed up the evolution, we start the SMH

initial data with fewer spherical shells around each BH than the standard choice made by SpEC. The comparison of the waveform is in Fig. 8.9, where we show only h_{22} and h_{44}. We can see the junk radiation for SMH initial data is still less than for SKS. But the improvement is not as good as other cases. For modes other than h_{22} and h_{44} , we do not see improvements. The main reason appears to be that $\alpha = 0.7$ deviates too much from $\alpha = 1$, so that the benefit of SH initial data is reduced. In addition, in Fig. 8.10 we compare the accumulated CPU hours for evolutions of both initial data sets. We can see the initial computational efficiency for SMH initial data is much lower, but it gradually catches up after several shells are dropped. For evolutions of only a few orbits, the expense of evolving SMH initial data may not be worth the extra computational cost. But for evolutions of many orbits, the extra cost at the beginning of the evolution will be comparatively small.

In most of the evolutions shown here, shortly after the beginning of the simulation several spherical shells around each BH are dropped, leading to a smaller number of grid points, a larger time step, and overall greater computational efficiency. However, for a general evolution, we are not always 'lucky' enough to gain this efficiency, since the current algorithm for dropping spherical shells aims only to avoid narrow shells rather than to speed up the simulation. To improve the computational efficiency for all simulations, we could start with fewer spherical shells at $t = 0$. However, the benefit of this change is limited without changing the shell-dropping algorithm. One workaround is to use smaller α, which speeds up the simulation, but if α deviates too much from $\alpha = 1$, we cannot have less junk radiation. Therefore, we suggest that the algorithm that divides the domain in to subdomains should be modified to account for computational efficiency during the evolution, or a better algorithm should be developed to initialize subdomains. Given such future algorithmic improvements, we could potentially run high-spin BBH evolution with larger α, which can lead to less junk radiation.

8.5 Conclusion

In this chapter, we extended SH initial data [23] to higher-spin BBHs by introducing a class of spatial coordinate systems that represent a time-independent slicing of a single Kerr black hole and are characterized by a continuous parameter α. This coordinate representation of Kerr is used to supply free data for the initial-value problem for BBH systems; we call the resulting initial-value solution SMH initial data. The harmonic ($\alpha = 1$) and KS ($\alpha = 0$) coordinate representations of Kerr are only two special cases of our new representation. The coordinate shape of the

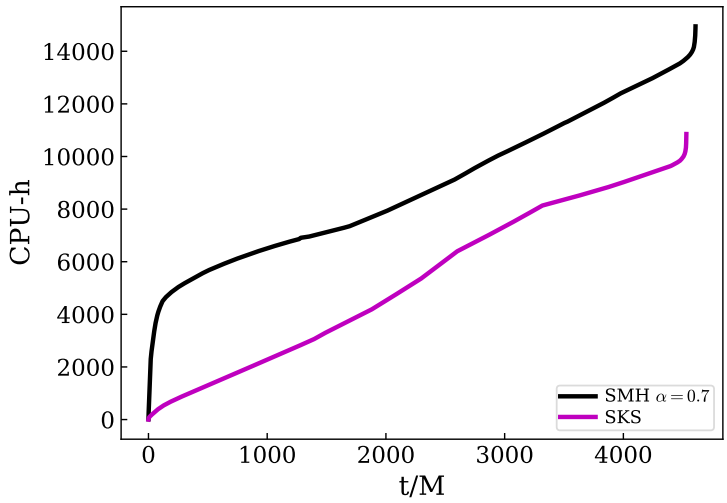

Figure 8.10: The accumulated CPU hours for evolutions of SMH and SKS initial data as functions of time. The BBH system is Case IV, and we plot results for the highest resolution. The initial computational efficiency of SMH initial data is much lower than for SKS, but after a short time both evolutions proceed at the same number of CPU hours per simulation time.

horizon becomes less spherical and more distorted for larger α. Therefore for high-spin BHs, we pick $\alpha < 1$ to decrease the distortion and ease requirements on very high resolution during the BBH simulation. At the same time, α should be close to 1 so that SMH initial data still has the desirable properties of SH initial data as shown in Ref. [23], such as less junk radiation. We have tested that for SMH initial data with $\alpha = 0$, i.e, harmonic time slicing with KS spatial coordinates, there is more junk radiation than for SKS initial data.

We have evolved four BBH systems with dimensionless spins 0.8 or 0.9 starting from SMH initial data with α between 0.7 and 0.9, and we compared with evolutions of the same system starting from SKS initial data. The first three cases, all with dimensionless spins 0.8, represent different situations: a non-precessing system with equal masses, a precessing system with random spin directions, and a non-precessing system with unequal masses. In general, the junk radiation of SMH initial data leaves the system faster than that of SKS. For most gravitational wave modes, the SMH initial data leads to less junk radiation. The exceptions, like the h_{33} mode and the h_{21} mode for Case III, have bursts with amplitudes similar to SKS. Furthermore, $\alpha = 0.8$ SMH has more junk radiation than $\alpha = 0.9$.

Using Case I as an example, we also studied other properties of the evolution, including constraint violations, computational efficiency, and changes in parameters.

We found the values of the volume-weighted constraints for SMH initial data are smaller than those of SKS by factors of 10. Furthermore, the volume-weighted constraints of SMH initial data converge with resolution during the junk stage. However, L^2-norm constraints do not have such convergence. Therefore, the benefit is mainly from the outer regions, where there is less junk radiation.

At the beginning of the evolution for Case I, SMH requires more collocation points than SKS to reach the error tolerance because the horizon is distorted, hence it proceeds more slowly. At later times, SKS and SMH run at approximately the same rate, after both the computational efficiency on each time slice and the size of the time step increase for the SMH case.

For Case IV, which has BHs with dimensionless spin 0.9, we found that we needed to decrease α to 0.7. We simulated an equal-mass BBH system with equal dimensionless spins $\boldsymbol{\chi}_{1,2} = (0, 0, 0.9)$ and compared h_{22} and h_{44} for both SMH and SKS initial data sets. Junk radiation for SMH is still less than for SKS, but the improvement is not as good as the case of lower spin. The comparison of CPU hours for these two cases show that the initial computation efficiency for SMH initial data is much lower. But it gradually becomes the same as SKS after several shells are dropped.

We also found that the algorithm for choosing the number and sizes of subdomains in SpEC could use some improvement, particularly for the initial choice of subdomains and the early stages of the evolution. In most simulations but not all, AMR eventually chooses a subdomain distribution that increases computational efficiency. Some improvements can be gained by simply starting with fewer spherical shells around each BH, but we find that the effects of this change are limited. Therefore, the evolution of SMH initial data for high-spin BBH will benefit from either an algorithm to adjust subdomain sizes based on computational efficiency during the evolution, or a better algorithm to initialize subdomains. Those algorithmic improvements could allow us to run high-spin BBH evolutions with larger α, which can give rise to less junk radiation.

8.6 Appendix: Details of MH coordinates

For a Kerr BH with an arbitrary spin vector $\boldsymbol{a}$, the transformations between KS spatial coordinates and MH spatial coordinates are given by

$$\begin{aligned}\boldsymbol{x}_{\rm KS} =& \frac{a^2 + r(r-\alpha M)}{a^2 + (r-\alpha M)^2}\boldsymbol{x}_{\rm MH} + \frac{\alpha M}{a^2 + (r-\alpha M)^2}(\boldsymbol{x}_{\rm MH} \times \boldsymbol{a}) \\ &+ (\boldsymbol{x}_{\rm MH} \cdot \boldsymbol{a})\boldsymbol{a}\frac{\alpha M}{(r-\alpha M)[a^2 + (r-\alpha M)^2]},\end{aligned} \tag{8.28}$$

where $a^2 = \boldsymbol{a}\cdot\boldsymbol{a}$, and r is the radial Boyer-Lindquist coordinate. For $\alpha = 0$, we have $\boldsymbol{x}_{\rm KS} = \boldsymbol{x}_{\rm MH}$, i.e., the identity transformation. The Jacobian $C^{ij}_{\rm MH} = \partial x^i_{\rm KS}/\partial x^j_{\rm MH}$ between KS and MH coordinates is given by[3]

$$
\begin{aligned}
C^{ij}_{\rm MH} = {} & \frac{a^2 + r(r-\alpha M)}{a^2 + (r-\alpha M)^2}\delta^{ij} + \frac{\alpha M}{a^2 + (r-\alpha M)^2} a_k \epsilon^{ijk} + a^i a^j \frac{\alpha M}{(r-\alpha M)[a^2 + (r-\alpha M)^2]} \\
& + \frac{M\alpha[a^2 - (r - M\alpha)^2]}{[a^2 + (r-M\alpha)^2]^2} x^i_{\rm MH}\partial^j r - \frac{2M\alpha(r-M\alpha)}{(a^2+(r-M\alpha)^2)^2} x^{\rm MH}_m a_k \epsilon^{imk}\partial^j r \\
& - x^m_{\rm MH} a_m a^i \partial^j r \frac{M\alpha[a^2 + 3(r-M\alpha)^2]}{[a^2+(r-M\alpha)^2]^2(r-\alpha M)^2},
\end{aligned}
\tag{8.29}
$$

where ϵ^{ijk} is the Levi-Civita symbol, δ^{ij} is the Kronecker delta, and the Einstein summation convention is used. For $\alpha = 1$, $C^{ij}_{\rm MH}$ becomes C^{ij} defined in Sec. 8.3.4. By differentiating Eq. (8.22), we have

$$
\partial_i r = \frac{x^{\rm MH}_i + (\boldsymbol{a}\cdot\boldsymbol{x}^{\rm MH})a_i/(r-\alpha M)^2}{2(r-\alpha M)\left[1 - \frac{\boldsymbol{x}^{\rm MH}\cdot\boldsymbol{x}^{\rm MH} - a^2}{2(r-\alpha M)^2}\right]}. \tag{8.30}
$$

With MH coordinates, the null covariant vector l in Eq. (8.5) can be written as

$$
\begin{aligned}
l = {} & \left(dt_{\rm MH} + \frac{2M}{r-r_-}dr\right) \\
& + \frac{(r-\alpha M)\boldsymbol{x}_{\rm MH} - \boldsymbol{a}\times\boldsymbol{x}_{\rm MH} + (\boldsymbol{a}\cdot\boldsymbol{x}_{\rm MH})\boldsymbol{a}/(r-\alpha M)}{(r-\alpha M)^2 + a^2}\cdot d\boldsymbol{x}_{\rm MH},
\end{aligned}
\tag{8.31}
$$

where the first bracket corresponds to $dt_{\rm KS}$ [see Eq. (8.12), with $t_{\rm MH} = t_{\rm H}$]. The scalar function H in Eq. (8.5) is given by

$$
H = \frac{Mr(r-\alpha M)^2}{r^2(r-\alpha M)^2 + (\boldsymbol{a}\cdot\boldsymbol{x}_{\rm MH})^2}. \tag{8.32}
$$

In addition, the lapse function N and the shift vector N^i in MH coordinates are given by

$$
N^{-2} = 1 + \frac{2M(r-\alpha M)^2}{r^2(r-\alpha M)^2 + (\boldsymbol{a}\cdot\boldsymbol{x}_{\rm MH})^2}\frac{r^2 + (r+2M)r_+}{r-r_-}, \tag{8.33}
$$

$$
N^i = N^r l^i + N^\phi \frac{a_j x^{\rm MH}_k \epsilon^{jki}}{a}, \tag{8.34}
$$

with

$$
N^r = N^2\frac{2Mr_+}{\rho^2}, \quad N^\phi = -N^2\frac{a}{\rho^2}\frac{2M}{r-r_-}, \tag{8.35}
$$

$$
\rho^2 = r^2 + a^2\cos^2\theta = r^2 + \frac{(\boldsymbol{a}\cdot\boldsymbol{x}_{\rm MH})^2}{(r-\alpha M)^2}, \quad l^i = l_i, \tag{8.36}
$$

where θ is the polar Boyer-Lindquist coordinate, and l_i is the spatial component of the null covariant vector l.

[3] Here we do not distinguish upper and lower indices of a tensor in a Euclidean space.

References

[1] Benjamin P. Abbott et al. "Observation of gravitational waves from a binary black hole merger." *Phys. Rev. Lett.* 116.6 (2016), p. 061102. DOI: 10.1103/PhysRevLett.116.061102. arXiv: 1602.03837 [gr-qc].

[2] Benjamin P. Abbott et al. "GWTC-1: A gravitational-wave transient catalog of compact binary mergers observed by LIGO and Virgo during the first and second observing runs." *Phys. Rev. X* 9.3 (2019), p. 031040. DOI: 10.1103/PhysRevX.9.031040. arXiv: 1811.12907 [astro-ph.HE].

[3] Richard Abbott et al. "GW190521: A binary black hole merger with a total mass of 150 $M_\odot$." *Phys. Rev. Lett.* 125.10 (2020), p. 101102. DOI: 10.1103/PhysRevLett.125.101102. arXiv: 2009.01075 [gr-qc].

[4] https://gracedb.ligo.org/superevents/S190412m/view/.

[5] https://gracedb.ligo.org/superevents/S190425z/view/.

[6] https://gracedb.ligo.org/superevents/S190814bv/view/.

[7] Jacques Abadie et al. "Predictions for the rates of compact binary coalescences observable by ground-based gravitational-wave detectors." *Class. Quant. Grav.* 27 (2010), p. 173001. DOI: 10.1088/0264-9381/27/17/173001. arXiv: 1003.2480 [astro-ph.HE].

[8] Vijay Varma et al. "Surrogate models for precessing binary black hole simulations with unequal masses." *Phys. Rev. Research.* 1 (2019), p. 033015. DOI: 10.1103/PhysRevResearch.1.033015. arXiv: 1905.09300 [gr-qc].

[9] Vijay Varma et al. "Surrogate model of hybridized numerical relativity binary black hole waveforms." *Phys. Rev. D* 99.6 (2019), p. 064045. DOI: 10.1103/PhysRevD.99.064045. arXiv: 1812.07865 [gr-qc].

[10] Serguei Ossokine et al. "Multipolar effective-one-body waveforms for precessing binary black holes: Construction and validation." *Phys. Rev. D* 102.4 (2020), p. 044055. DOI: 10.1103/PhysRevD.102.044055. arXiv: 2004.09442 [gr-qc].

[11] Roberto Cotesta et al. "Enriching the symphony of gravitational waves from binary black holes by tuning higher harmonics." *Phys. Rev.* D98.8 (2018), p. 084028. DOI: 10.1103/PhysRevD.98.084028. arXiv: 1803.10701 [gr-qc].

[12] Alejandro Bohé et al. "Improved effective-one-body model of spinning, nonprecessing binary black holes for the era of gravitational-wave astrophysics with advanced detectors." *Phys. Rev.* D95.4 (2017), p. 044028. DOI: 10.1103/PhysRevD.95.044028. arXiv: 1611.03703 [gr-qc].

[13] Geraint Pratten et al. “Computationally efficient models for the dominant and subdominant harmonic modes of precessing binary black holes.” *Phys. Rev. D* 103.10 (2021), p. 104056. DOI: 10.1103/PhysRevD.103.104056. arXiv: 2004.06503 [gr-qc].

[14] Cecilio García-Quirós et al. “IMRPhenomXHM: A multi-mode frequency-domain model for the gravitational wave signal from non-precessing black-hole binaries.” (Jan. 2020). arXiv: 2001.10914 [gr-qc].

[15] Geraint Pratten et al. “Setting the cornerstone for the IMRPhenomX family of models for gravitational waves from compact binaries: The dominant harmonic for non-precessing quasi-circular black holes.” (Jan. 2020). arXiv: 2001.11412 [gr-qc].

[16] Kashif Alvi. “An Approximate binary black hole metric.” *Phys. Rev. D* 61 (2000), p. 124013. DOI: 10.1103/PhysRevD.61.124013. arXiv: gr-qc/9912113.

[17] Nicolas Yunes and Wolfgang Tichy. “Improved initial data for black hole binaries by asymptotic matching of post-Newtonian and perturbed black hole solutions.” *Phys. Rev. D* 74 (2006), p. 064013. DOI: 10.1103/PhysRevD.74.064013. arXiv: gr-qc/0601046.

[18] Nathan K. Johnson-McDaniel et al. “Conformally curved binary black hole initial data including tidal deformations and outgoing radiation.” *Phys. Rev.* D80 (2009), p. 124039. DOI: 10.1103/PhysRevD.80.124039. arXiv: 0907.0891 [gr-qc].

[19] Bernard J. Kelly et al. “Post-Newtonian initial data with waves: Progress in evolution.” *Class. Quant. Grav.* 27 (2010), p. 114005. DOI: 10.1088/0264-9381/27/11/114005. arXiv: 0912.5311 [gr-qc].

[20] George Reifenberger and Wolfgang Tichy. “Alternatives to standard puncture initial data for binary black hole evolution.” *Phys. Rev. D* 86 (2012), p. 064003. DOI: 10.1103/PhysRevD.86.064003. arXiv: 1205.5502 [gr-qc].

[21] Wolfgang Tichy. “The initial value problem as it relates to numerical relativity.” *Rept. Prog. Phys.* 80.2 (2017), p. 026901. DOI: 10.1088/1361-6633/80/2/026901. arXiv: 1610.03805 [gr-qc].

[22] Geoffrey Lovelace. “Reducing spurious gravitational radiation in binary-black-hole simulations by using conformally curved initial data.” *Class. Quant. Grav.* 26 (2009), p. 114002. DOI: 10.1088/0264-9381/26/11/114002. arXiv: 0812.3132 [gr-qc].

[23] Vijay Varma, Mark A. Scheel, and Harald P. Pfeiffer. “Comparison of binary black hole initial data sets.” *Phys. Rev.* D98.10 (2018), p. 104011. DOI: 10.1103/PhysRevD.98.104011. arXiv: 1808.08228 [gr-qc].

[24] *https://www.black-holes.org/code/SpEC.html*. URL: https://www.black-holes.org/code/SpEC.html.

[25] James W. York Jr. "Conformal 'thin sandwich' data for the initial-value problem." *Phys. Rev. Lett.* 82 (1999), pp. 1350–1353. DOI: 10.1103/PhysRevLett.82.1350. arXiv: gr-qc/9810051 [gr-qc].

[26] Harald P. Pfeiffer and James W. York Jr. "Extrinsic curvature and the Einstein constraints." *Phys. Rev.* D67 (2003), p. 044022. DOI: 10.1103/PhysRevD.67.044022. arXiv: gr-qc/0207095 [gr-qc].

[27] Gregory B. Cook and Mark A. Scheel. "Well-behaved harmonic time slices of a charged, rotating, boosted black hole." *Phys. Rev. D* 56 (8 Oct. 1997), pp. 4775–4781. DOI: 10.1103/PhysRevD.56.4775. URL: https://link.aps.org/doi/10.1103/PhysRevD.56.4775.

[28] Michael Boyle et al. "The SXS collaboration catalog of binary black hole simulations." *Class. Quant. Grav.* 36.19 (2019), p. 195006. DOI: 10.1088/1361-6382/ab34e2. arXiv: 1904.04831 [gr-qc].

[29] Geoffrey Lovelace et al. "Binary-black-hole initial data with nearly-extremal spins." *Phys. Rev.* D78 (2008), p. 084017. DOI: 10.1103/PhysRevD.78.084017. arXiv: 0805.4192 [gr-qc].

[30] Bela Szilagyi, Lee Lindblom, and Mark A. Scheel. "Simulations of binary black hole mergers using spectral methods." *Phys. Rev.* D80 (2009), p. 124010. DOI: 10.1103/PhysRevD.80.124010. arXiv: 0909.3557 [gr-qc].

[31] Roy P. Kerr. "Gravitational field of a spinning mass as an example of algebraically special metrics." *Phys. Rev. Lett.* 11 (1963), pp. 237–238. DOI: 10.1103/PhysRevLett.11.237.

[32] Mark A. Scheel et al. "Improved methods for simulating nearly extremal binary black holes." *Class. Quant. Grav.* 32.10 (2015), p. 105009. DOI: 10.1088/0264-9381/32/10/105009. arXiv: 1412.1803 [gr-qc].

[33] John P Boyd. *Chebyshev and Fourier spectral methods*. Courier Corporation, 2001.

[34] Béla Szilágyi. "Key elements of robustness in binary black hole evolutions using spectral methods." *Int. J. Mod. Phys.* D23.7 (2014), p. 1430014. DOI: 10.1142/S0218271814300146. arXiv: 1405.3693 [gr-qc].

[35] Alessandra Buonanno et al. "Reducing orbital eccentricity of precessing black-hole binaries." *Phys. Rev.* D83 (2011), p. 104034. DOI: 10.1103/PhysRevD.83.104034. arXiv: 1012.1549 [gr-qc].

[36] Lee Lindblom et al. "A new generalized harmonic evolution system." *Class. Quant. Grav.* 23 (2006), S447–S462. DOI: 10.1088/0264-9381/23/16/S09. arXiv: gr-qc/0512093 [gr-qc].

[37] Serguei Ossokine et al. “Improvements to the construction of binary black hole initial data.” *Class. Quant. Grav.* 32 (2015), p. 245010. DOI: 10.1088/0264-9381/32/24/245010. arXiv: 1506.01689 [gr-qc].

[38] Mark A. Scheel et al. “Solving Einstein’s equations with dual coordinate frames.” *Phys. Rev. D* 74 (2006), p. 104006. DOI: 10.1103/PhysRevD.74.104006. arXiv: gr-qc/0607056.

Part IV

Beyond general relativity

Chapter 9

NUMERICAL SIMULATIONS OF BLACK HOLE–NEUTRON STAR MERGERS IN SCALAR-TENSOR GRAVITY

[1] Sizheng Ma, Vijay Varma, Leo C. Stein, Francois Foucart, Matthew D. Duez, Lawrence E. Kidder, Harald P. Pfeiffer, and Mark A. Scheel. "Numerical simulations of black hole-neutron star mergers in scalar-tensor gravity." (Apr. 2023). arXiv: 2304.11836 [gr-qc].

9.1 Introduction

Increasing numbers of gravitational-wave (GW) events [1–4] have allowed us to probe the extreme gravity environment near the coalescence of a compact binary system, which opens up a new chapter for tests of general relativity (GR) [1, 5–25]. To robustly test GR, there is a need for accurate GW predictions both in GR and beyond-GR theories, so that one can use Bayesian model selection to ascertain which theory better agrees with GW observations.

Scalar-tensor (ST) theory [26–29] is the simplest alternative theory of gravity, where the strength of gravity is modulated by scalar field(s). The original formulation of ST theory was due to Jordan [26], Fierz [27], Brans and Dicke [28, 29] (JFBD), and was generalized by Bergmann [30] and Wagoner [31] to capture more general conformal factors, and by Damour and Esposito-Farèse [32] to multiple scalar fields. An important feature of ST theory is scalar radiation, an extra energy dissipation channel in addition to the usual tensor radiation in GR. The leading scalar radiation is dipolar, and thus more important at low frequencies than the quadrupolar waves that control a GR inspiral [5, 32–46]. Under this effect, the evolution of some strong-gravity systems can deviate from the prediction of GR and leave imprints on observables. For instance, binary-pulsar systems have been shown to be a good laboratory [33, 41, 46–58] (see also Refs. [19, 59–65] for reviews) since the celebrated Hulse-Taylor PSR B1913+16 [66]. By measuring the orbital decay rate of the systems, one can examine and constrain ST theory via the parametrized post-Keplerian formalism [53, 54, 65, 67].

The strength of the dipole radiation depends on the scalar charge $\alpha_{\rm NS}$ [32, 51, 68, 69], which characterizes the ability of an object to condense the scalar field. The

scalar charge of a black hole (BH) vanishes as the no-hair theorems have been shown to apply in ST [16, 70–73]. For a binary system, the dipole radiation power is proportional to its charge difference squared [33]: $(\alpha_A - \alpha_B)^2$, where A and B refer to the two objects in the binary system. Typically, neutron stars (NSs) have similar scalar charges so the dipole radiation is suppressed in binary neutron star (BNS) systems. Consequently, the best tests of ST can come from mixed systems, such as BHNS binaries, as only one of the objects carries scalar charge.

While ST theory is strongly constrained in some environments, deviations from GR could also be amplified if a NS undergoes *spontaneous scalarization*[1] in certain conditions [74–83], as pointed out by Damour and Esposito-Farèse [54, 68]. At some critical central density, the equilibrium solutions for NSs' structures bifurcate into several branches, and the GR branch becomes unstable [84, 85]. The most stable solution corresponds to a scalarized NS with a much larger scalar charge [32, 51, 68, 69]. Therefore, the dipole radiation and consequential deviations from GR are significantly amplified in such scalarized BHNS systems, which makes them, if they exist, ideal environments for studying ST theory.

The LIGO-Virgo detectors [86, 87] recently made the landmark observations of the first BHNS binaries via GWs, GW200105 and GW200115 [88]. With the upcoming improvement in GW detector sensitivity [89], including future third-generation detectors [90–93], we can look for effects of gravitational dipole radiation at ever-increasing precision. Therefore, it is timely and vital to give a precise prediction of the evolution of the scalarized BHNS binaries in ST, especially accurate modeling of their dipole GW waveforms. Although there have been significant post-Newtonian (PN) efforts dedicated toward constructing waveforms in ST theory[2] [5, 32–46, 96], PN theory breaks down as one approaches the merger, or for strongly scalarized NSs. To date, numerical relativity (NR) still remains the only *ab initio* method to investigate ST theory near the merger [73–75, 97–103]. For compact binaries, NR has been used to simulate binary black holes (BBHs) [73] and BNSs [74, 75, 98] in ST. A numerical simulation of a scalarized BHNS system is still missing. In this work, we aim to fill this gap by performing fully nonlinear NR simulations of a BHNS merger in ST theory, with a particular focus on how GW emission is impacted by spontaneous scalarization. Motivated by the LIGO-Virgo observations, we consider a GW200115-like system [88].

[1] See Refs. [74–79] for two related phenomena: induced and dynamical scalarization.
[2] See also Refs. [94, 95] for an effective-field-theory approach.

This chapter is organized as follows. In Sec. 9.2 we give a brief introduction to ST theory and our simulation algorithm. Section 9.3 concentrates on our numerical setup and strategy to maximize the effect of spontaneous scalarization. Section 9.4 provides our major simulation results. Next in Sec. 9.5 we investigate distinguishability between waveforms in GR and ST, with a particular focus on to what extent the ST waveform can be mimicked by tidal effects predicted by GR. Finally in Sec. 9.6 we provide some concluding remarks.

Throughout this chapter we use the geometric units with $c = G_* = 1$, where G_* is the bare gravitational constant in the Jordan frame. We use the total Jordan-frame mass to normalize all dimensional quantities (e.g., time and distance). Meanwhile, we use the Latin letters $a, b, c \ldots$ for spacetime indices, and $i, j, k \ldots$ to represent spatial indices.

9.2 Equations of motion and numerical methods

In this work we consider a ST theory with a single massless scalar field ϕ. We first provide some basic features and equations of motion of this theory in Sec. 9.2.1. Then in Sec. 9.2.2 we introduce our numerical algorithm to perform the NR simulation. Finally in Sec. 9.2.3 we provide our method for extrapolating the waveform to future null infinity.

9.2.1 The Jordan and Einstein frames

The ST theory is governed by the action [30, 31]

$$S = \int d^4x \frac{\sqrt{-g}}{16\pi}\left[\phi R - \frac{\omega(\phi)}{\phi}\nabla_c\phi\,\nabla^c\phi\right] + S_M[g_{ab}, \Psi_m], \tag{9.1}$$

where g_{ab} is the metric, g is the metric determinant, R is the Ricci scalar, S_M is the action for all matter fields Ψ_m, and $\omega(\phi)$ is an arbitrary function of ϕ that parameterizes the coupling between the scalar field and metric. The action in Eq. (9.1) is written in the *Jordan frame* in which ϕ is nonminimally coupled with the metric g_{ab}, whereas the matter fields are minimally coupled to the metric and not coupled with the scalar field ϕ, as required by the weak equivalence principle. Therefore, test particles follow the geodesics of the Jordan frame metric. NSs are treated as ideal fluids and are governed by the law of conservation of baryon number and energy-momentum:

$$\nabla_a(\rho_0\, u^a) = 0, \tag{9.2a}$$

$$\nabla_a T^{ab} = 0, \tag{9.2b}$$

where T^{ab} is the stress-energy tensor in the Jordan frame. The stress-energy tensor for an ideal fluid reads

$$T_{ab} = \rho_0 h u_a u_b + P g_{ab}, \tag{9.3}$$

with ρ_0 the rest mass density of the fluid, h the specific enthalpy, P the pressure, and u_a the 4-velocity.

The equations of motion for the metric and the scalar field take complicated forms in the Jordan frame [see Eq. (2.6) of Ref. [22] for example]. In particular, the principal symbols of the PDE system is not diagonal in the (g_{ab}, ϕ) field space, so it is not manifestly symmetric-hyperbolic. Consequently, the Jordan frame is not ideally suited for simulating the metric and scalar fields. A standard approach to get around this issue is to apply a conformal transformation [32]: $\bar{g}_{ab} = \phi\, g_{ab}$. Then the action becomes:

$$S = \int d^4x \sqrt{-\bar{g}} \left[\frac{\bar{R}}{16\pi} - \frac{1}{2} \nabla_c \psi\, \nabla^c \psi \right] + S_M \left[\frac{\bar{g}_{ab}}{\phi}, \Psi_m \right], \tag{9.4}$$

where $\bar{R}$ is the Ricci scalar derived from $\bar{g}_{ab}$, and

$$d\psi = \sqrt{\frac{3 + 2\omega}{16\pi}}\, \frac{d\phi}{\phi}. \tag{9.5}$$

The integration of Eq. (9.5) depends on the form of $\omega(\phi)$, and we will explain more details below in Eqs. (9.17) and (9.18). The transformed metric $\bar{g}_{ab}$ defines a new frame, called the *Einstein frame*; and the scalar field ψ is minimally coupled in the gravitational sector. The corresponding equations of motion become manifestly symmetric-hyperbolic:

$$\bar{G}_{ab} = 8\pi\, (\bar{T}^{\psi}_{ab} + \bar{T}_{ab}), \tag{9.6a}$$

$$\bar{\Box} \psi = \frac{1}{2}\, \frac{d \log \phi}{d\psi}\, \bar{T}. \tag{9.6b}$$

Note that the principal part of the gravitational sector is now identical to its GR counterpart. Here $\bar{G}_{ab}$ is the Einstein tensor obtained from $\bar{g}_{ab}$, $\bar{T}_{ab} = T_{ab}/\phi$ is the matter stress-energy tensor in the Einstein frame, $\bar{T} = \bar{g}^{ab}\, \bar{T}_{ab}$ is its trace, and $\bar{T}^{\psi}_{ab}$ is the stress-energy tensor of the scalar field, given by

$$\bar{T}^{\psi}_{ab} = \nabla_a \psi\, \nabla_b \psi - \frac{1}{2}\, \bar{g}_{ab}\, \nabla_c \psi\, \nabla^c \psi. \tag{9.7}$$

On the other hand, a complication of the Einstein frame is that the hydrodynamic equations gain additional source terms:

$$\bar{\nabla}_a \bar{T}^{ab} = -\frac{1}{2}\, \frac{d \log \phi}{d\psi}\, \bar{T}\, \nabla^b \psi, \tag{9.8a}$$

$$\bar{\nabla}_a(\bar{\rho}_0\,\bar{u}^a) = -\frac{1}{2}\frac{d\log\phi}{d\psi}\,\bar{\rho}_0\,\bar{u}^a\,\nabla_a\psi\,. \tag{9.8b}$$

The scalar field ψ is now directly coupled with the matter fields. Because of the source terms on the RHS, particles do not follow geodesics of $\bar{g}_{ab}$.

9.2.2 Numerical algorithm

The single-scalar-field ST theory has been solved numerically for BBHs [73] and BNSs [74, 75], with the pure Einstein frame [73, 74], and the pure Jordan frame [75]. In our case, we simulate the BHNS system using the Spectral Einstein Code (SpEC) [104], developed by the Simulating eXtreme Spacetimes (SXS) collaboration [105]. SpEC adopts the generalized harmonic formalism [106], where the Einstein equations are cast into a first-order symmetric hyperbolic (FOSH) form. It is ideal to use SpEC to evolve the metric and the scalar field sectors in the Einstein frame [Eqs. (9.6)]. The reason is twofold. (a) The equations of motion in the Einstein frame are manifestly symmetric-hyperbolic, as mentioned in Sec. 9.2.1. Therefore the well-posedness of the Cauchy problem is straightforwardly established. (b) The principal parts of Eqs. (9.6) are identical to that of GR with a Klein-Gordon field. Consequently, we can utilize the existing GR FOSH system [106] and the FOSH system for scalar fields [107, 108] to perform the simulations.

For the hydrodynamics, one could in principle approach the problem in the same Einstein frame by evolving Eqs. (9.8). But this will complicate the problem because the extra source terms in Eqs. (9.8), which depend on the scalar field, need to be added to the existing hydrodynamic code infrastructure in SpEC [109]. Furthermore, any routine in SpEC that assumes the simple form of energy-momentum and Baryon number conservation in Eq. (9.2) will need to be revisited. To save the amount of code changes required, here we propose a simpler algorithm to fulfill the goal.

We adopt a hybrid scheme, illustrated in Fig. 9.1. We evolve the hydrodynamic system in the Jordan frame, where the corresponding equations [Eq. (9.2)] are the same as their GR counterparts due to the weak equivalence principle. This lets us use the entire relativistic hydrodynamics module without modification. Meanwhile, we use the FOSH systems to treat the metric and the scalar field in the Einstein frame. Since the Jordan and Einstein frames are related, a proper data flow needs to be established to evolve them together. An essential step is to pass the Jordan-frame metric g_{ab} and stress-energy tensor T_{ab} back and forth (see App. 9.7 for details): The Einstein-frame metric $\bar{g}_{ab}$ is converted to its Jordan-frame version g_{ab} via $g_{ab} = \bar{g}_{ab}/\phi$, then g_{ab} is sent to the Jordan frame for evolving the hydrodynamics.

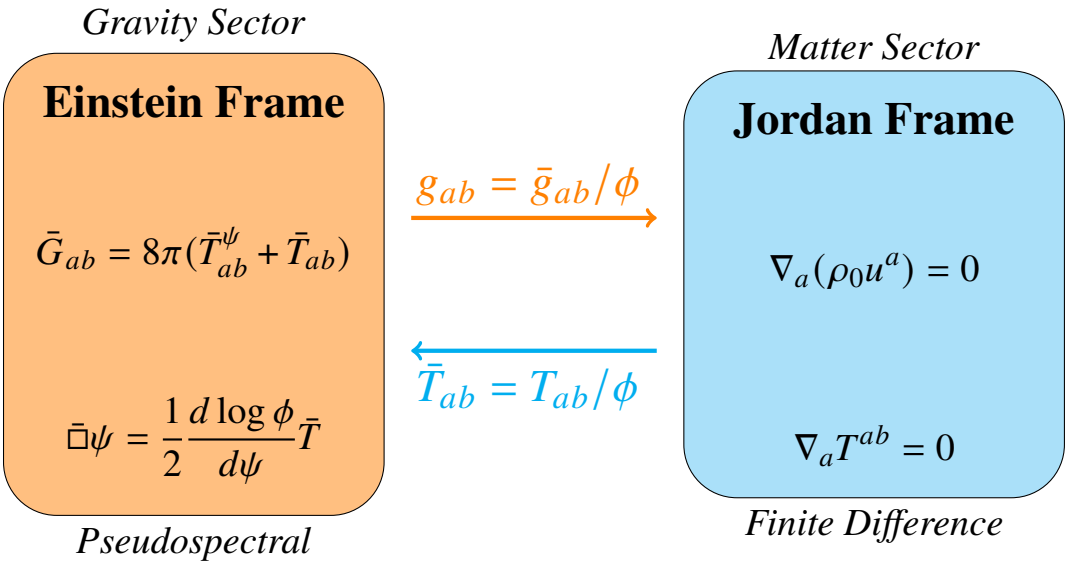

Figure 9.1: The algorithm of our numerical simulations. We use pseudospectral methods to evolve the Einstein-frame metric and scalar field, while we use shock-capturing finite difference to simulate the Jordan-frame matter fields. In practice, we convert the Einstein-frame metric $\bar{g}_{ab}$ to the Jordan-frame one via $g_{ab} = \bar{g}_{ab}/\phi$, and then send g_{ab} to the finite difference domain for hydrodynamics simulations. Similarly, we transfer the Jordan-frame stress-energy tensor T_{ab} from the finite difference grid to the pseudospectral grid, convert it to the Einstein-frame stress-energy tensor through $\bar{T}_{ab} = T_{ab}/\phi$, and then insert $\bar{T}_{ab}$ into the Einstein equations in Eqs. (9.6).

Similarly, the Jordan-frame stress-energy tensor T_{ab} is converted to the Einstein-frame one through $\bar{T}_{ab} = T_{ab}/\phi$, and inserted into the Einstein equations in Eqs. (9.6).

Within SpEC, this communication is made easier by the two-grid method already used in hydrodynamics simulations [109], wherein the metric sector is evolved on a pseudospectral grid, while the hydrodynamic equations are evolved on a finite difference grid that can handle shocks. At each time step, the metric from the pseudospectral grid is already interpolated onto the finite difference grid and is fed to the hydrodynamic equations, and the matter fields are passed by interpolation from the finite difference grid to the pseudospectral grid and are fed to the stress-energy tensor in the Einstein equations. For the ST simulations, the metric and the scalar field are evolved in the Einstein frame [see Eqs. (9.6)] on the pseudospectral grid, but before the metric is interpolated to the finite difference grid, it is first converted to the Jordan frame. Similarly, the hydrodynamics equations [see Eqs. (9.2)] are evolved in the Jordan frame, but before the matter terms are transformed to the Einstein frame, they are first interpolated to the pseudospectral grid.

Table 9.1: Summary of the parameters of the GW200115-like BHNS system we consider. The NS has a baryonic mass $m^{\rm B}$ and a Jordan-frame mass $m^{\rm J}_{\rm NS}$. Its radius in the Jordan frame is $R^{\rm J}_{ST}$. In the absence of the scalar field, its radius is $R_{\rm GR}$, and $C_{\rm GR} = m^{\rm J}_{\rm NS}/R_{\rm GR}$ is its compactness. The tidal Love number of the NS is k_2; Λ_2 is the tidal deformability; $\alpha_{\rm NS}$ is its scalar charge. To maximize the effect of spontaneous scalarization, we choose $(\beta_0, \alpha_0) = (-4.5, -3.5 \times 10^{-3})$. The BH has a Jordan-frame mass $m^{\rm J}_{\rm BH}$. Its dimensionless spin along is denoted by $\boldsymbol{\chi}^{\rm BH}_{init}$ and is anti-aligned with the Newtonian angular momentum direction $\hat{\boldsymbol{L}}_N$. The mass-weighted tidal deformability of the BNHS system is $\tilde{\Lambda}_2$. $R_{\rm bdry}$ indicates the radius of the simulation domain, in the unit of total mass $M = 7.2M_\odot$, and $N_{\rm cycle}$ is the number of orbital cycles before merger. The remnant is a BH with mass m_f and spin χ_f, where m_f is in the unit of M.

$m^{\rm B}/M_\odot$	$m^{\rm J}_{\rm NS}/M_\odot$	$\chi^{\rm NS}_{\rm init}$	$R^{\rm J}_{\rm ST}$/km	$R_{\rm GR}$/km	$C_{\rm GR}$	k_2	Λ_2
1.71	1.5	0.0	10.58	10.55	0.21	0.0803	131.1

$\alpha_{\rm NS}$	$m^{\rm J}_{\rm BH}/M_\odot$	$\boldsymbol{\chi}^{\rm BH}_{\rm init}$	$\tilde{\Lambda}_2$	$R_{\rm bdry}/M$	$N_{\rm cycle}$	m_f/M	χ_f
0.18	5.7	$-0.19\hat{\boldsymbol{L}}_N$	2.95	500	12	0.98	0.38

9.2.3 Waveform extrapolation

One of the most important tasks of our numerical simulations is to compute GWs at future null infinity, where we approximate GW detectors to reside. Methods have been developed, including wave extrapolation [110, 111] and Cauchy-Characteristic Extraction (CCE) [112, 113], to extract the GWs from simulations with finite domains. This chapter adopts the extrapolation method and leaves CCE for future work.

Following the standard treatment in PN theory [36, 37, 39, 43], we define a new conformally transformed metric $\tilde{g}_{ab}$ by

$$\tilde{g}_{ab} = (\phi/\phi_0) g_{ab} = \bar{g}_{ab}/\phi_0, \tag{9.9}$$

which differs from the Einstein frame metric $\bar{g}_{ab}$ by a factor of ϕ_0, the asymptotic value of the scalar field. The factor is introduced so that the metric $\tilde{g}_{ab}$ takes its Minkowski form $\eta_{ab} \equiv \mathrm{diag}(-1, 1, 1, 1)$ far from the system. In our simulations, we find that the value of ϕ_0 is always close to 1, and the difference is negligible, so we will not distinguish $\tilde{g}_{ab}$ from $\bar{g}_{ab}$ below. The gravitational perturbation $\tilde{h}_{ab}$ associated with $\tilde{g}_{ab}$ is given by

$$\tilde{h}^{ab} = \eta^{ab} - \sqrt{-\tilde{g}}\, \tilde{g}^{ab}, \tag{9.10}$$

whose indices are raised and lowered by η^{ab}. Then the Jordan-frame metric can be written as [36]

$$g_{ab} = \eta_{ab} + \tilde{h}_{ab} - \frac{1}{2}\tilde{h}\eta_{ab} - \Psi\eta_{ab} + O\left(\frac{1}{r^2}\right), \tag{9.11}$$

where

$$\Psi = \frac{\phi - \phi_0}{\phi_0}. \tag{9.12}$$

Due to the equation of geodesic deviation [114], the GW measured by a detector corresponds to the components of the Riemann curvature tensor,

$$R_{0i0j} = -\frac{1}{2}\ddot{\tilde{h}}^{\rm TT}_{ij} - \frac{1}{2}\ddot{\Psi}(\hat{N}_i\hat{N}_j - \delta_{ij}), \tag{9.13}$$

where "TT" refers to the transverse-traceless projection of $\tilde{h}_{ij}$, and $\hat{N}_i$ is GW's propagation direction. As a result, the tensor field $\tilde{h}^{\rm TT}_{ij}$ contributes to the + and × polarizations of the GW signal as in GR, while the scalar field Ψ corresponds to a transverse breathing mode.[3]

To extract the three GW polarizations from our numerical simulations, we notice that the gravitational perturbation $\tilde{h}_{ab}$ is associated with the Einstein-frame metric $\bar{g}_{ab}$, so we can restrict ourselves to this frame during the extrapolation. On the scalar sector side, ψ [defined in Eq. (9.5)] is our evolved variable in the Einstein frame. We can convert it to the observable Ψ by integrating Eq. (9.5) and then inserting the result into Eq. (9.12). Note that the integration depends on the form of $\omega(\phi)$ and we will provide more details in Eq. (9.17). In practice, we first measure the values of $\tilde{h}$ and ψ at multiple extraction radii at each timestep, and then extrapolate their values to null infinity $\mathscr{I}^+$. For each radius, we decompose $\tilde{h} = \tilde{h}_+ - i\tilde{h}_\times$ and ψ into a sum over a set of (spin-weighted) spherical harmonics ${}_sY_{lm}(\iota, \varphi)$,

$$r\tilde{h}/M = \sum_{l,m} {}_{-2}Y_{lm}(\iota, \varphi)\tilde{h}_{lm} + O(r^{-1}), \tag{9.14a}$$

$$r\psi/M = \sum_{l,m} Y_{lm}(\iota, \varphi)\psi_{lm} + O(r^{-1}), \tag{9.14b}$$

where we used the fact that $\tilde{h}, \psi \sim 1/r$ in the wave zone. Each field $\tilde{h}_{lm}$ and ψ_{lm} is extrapolated to $\mathscr{I}^+$ following the algorithm outlined in Refs. [111, 115–117], with the `PYTHON` package `scri` [118, 119]. In particular, the null rays are parameterized by an approximate retarded time u, given by

$$u = t_{\rm corr} - r_*, \tag{9.15}$$

[3] Longitudinal and vector polarizations vanish in ST gravity [114].

with

$$r_* = r + 2M^E \log\left(\frac{r}{2M^E} - 1\right), \tag{9.16}$$

where $M^E = m^{\rm E}_{\rm NS} + m^{\rm E}_{\rm BH}$ is the total Einstein-frame mass, and we refer to Refs. [110, 111] for the expression of the corrected time $t_{\rm corr}$. Finally these fields are interpolated to common sets of u and fit in powers of $1/r$, allowing to approximate the $r \to \infty$ limit.

9.3 Binary and scalar parameters

In Sec. 9.3.1, we provide the binary parameters we consider for the BHNS system, which are chosen to be consistent with GW200115 [88]. Then in Sec. 9.3.2, we introduce our strategy for choosing the parameters of the scalar field and the NS. As mentioned in Introduction, a NS can undergo significant scalarization under certain conditions, leading to nonnegligible dipole radiation while the scalarized NS orbits in the binary system. This extra energy dissipation channel accelerates the evolution of the BHNS system and thus makes the emitted GWs distinguishable from their GR counterparts. In our simulations, we want to highlight such distinctions by optimally picking the ST theory parameters and the EOS of the NS.

9.3.1 The binary parameters

We summarize the parameters of the GW200115-like BHNS system [88] we consider in Table 9.1. The binary system consists of a nonrotating NS with a Jordan-frame mass $m^{\rm J}_{NS}$ of $1.5M_\odot$, and a spinning BH with $m^{\rm J}_{\rm BH} = 5.7M_\odot$. The dimensionless spin of the BH $\chi^{\rm BH}_{\rm init}$ is -0.19, i.e., it is anti-aligned with the orbital angular momentum. We set the initial separation between the BH and the NS $D_{\rm init}$ to $11.7M$, where $M \equiv m^{\rm J}_{\rm B}H + m^{\rm J}_{\rm NS} = 7.2M_\odot$ is the total Jordan-frame mass; and place the outer boundary of the system at $R_{\rm bdry} = 500M$. The system undergoes $N_{\rm cycle} \sim 12$ cycles prior to the merger. The orbital eccentricity is reduced iteratively to $e_{\rm orb} \sim 1.6\times10^{-4}$ [120].

Due to our two-grid method described in Fig. 9.1, the NS resides in the Jordan frame while the BH is in the Einstein frame. So in practice one needs to specify the Einstein-frame mass of the BH $m^{\rm E}_{\rm BH}$ instead, which is related to the Jordan-frame mass $m^{\rm J}_{\rm BH}$ through [32]

$$m^{\rm E}_{\rm BH} = \frac{m^{\rm J}_{\rm BH}}{\sqrt{\phi}},$$

where ϕ is evaluated at the position of the BH. We find that $|\phi - 1| \lesssim 5 \times 10^{-5}$ in the vicinity of the BH, during the inspiral stage, therefore the difference between $m^{\rm J}_{\rm BH}$ and $m^{\rm E}_{\rm BH}$ is negligible; thus we simply set $m^{\rm E}_{\rm BH} = 5.7 M_\odot$.

9.3.2 The parameters of the scalar field and the NS

For a given Jordan-frame mass $m^{\rm J}_{\rm NS}$, the strength of spontaneous scalarization for the NS depends on $\omega(\phi)$, as well as the EOS and compactness [69, 121]. To look for the optimal choices to maximize the scalarization in our BHNS simulation, we consider a single Tolman–Oppenheimer–Volkoff (TOV) NS in an isolated gravity environment and investigate the impact of the scalar field on the stellar internal structure.

The function $\omega(\phi)$ characterizes the coupling between the scalar field and gravity. In this work we follow Ref. [122], whose idea was to Taylor expand the coupling function $\ln \phi$ in ψ,

$$\phi = \exp\left[-4\sqrt{\pi}\alpha_0\,(\psi - \psi_0) - 4\pi\,\beta_0\,(\psi - \psi_0)^2\right]. \tag{9.17}$$

Using Eq. (9.5), we obtain

$$\omega = \frac{1}{2}\frac{1}{[\alpha_0 + \sqrt{4\pi}\beta_0(\psi - \psi_0)]^2} - \frac{3}{2}. \tag{9.18}$$

Here ψ_0 is the asymptotic value of ψ that can also be associated with cosmological expansion [123–125]. For simplicity, we follow Ref. [74] and set $\psi_0 = 0$. The other two constants α_0 and β_0 determine the features of the ST theory. In particular, if $\beta_0 = 0$ we get the JFBD theory [26–29], which is parameterized by $\alpha_0 = -(3 + 2\omega_{\rm BD})^{-1/2}$, where $\omega_{\rm BD}$ is the BD parameter. In the low-density solar system environment, its value is severely restricted to $\omega_{\rm BD} > 40000$ by the Cassini mission [19, 126], which corresponds to $|\alpha_0| \lesssim 3.5 \times 10^{-3}$. In addition, current binary pulsar measurements place a constraint $\beta_0 \gtrsim -4.5$, because no spontaneous scalarization has been detected yet [22]. See also Refs. [47–49, 52] for more recent updates.

As pointed out by Damour and Esposito-Farèse [54, 122], even though a scalar-tensor theory with $|\alpha_0| \ll 1$ is indistinguishable from GR within the weak-gravity regime, a negative value of β_0 can lead to significant relativistic deviations in a strong-gravity environment, such as spontaneous scalarization of a NS. The size of the scalarization is characterized by the scalar charge $\alpha_{\rm NS}$ [32, 122]. In this chapter, we adopt the definition of $\alpha_{\rm NS}$ from Refs. [32, 122], which differs from the convention used by the PN community by a minus sign (see App. A of Ref. [37] for translating

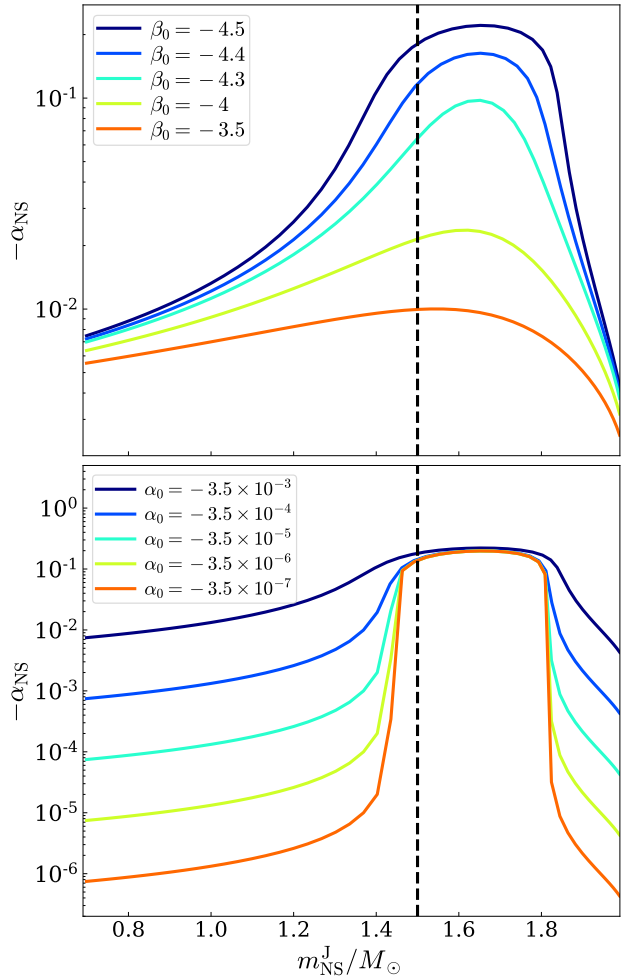

Figure 9.2: The scalar charge of a NS as a function of $m^{\rm J}_{\rm NS}$, with a variety of β_0 (the upper panel) and α_0 (the lower panel) values. Its EOS is summarized in Table 9.1, which has been selected to amplify the scalarization. The vertical dashed lines correspond to the NS in our simulation ($m^{\rm J}_{\rm NS} = 1.5M_\odot$). We choose $\psi_0 = 0$ in both panels.

notation); consequently, we have $\alpha_{\rm NS} < 0$. For a Newtonian star, $\alpha_{\rm NS}$ reduces to α_0; thus is independent of its internal structure (a proof can be found in App. 9.8). For a strongly self-gravitating scalarized star, its structure is governed by the TOV equation with an extra scalar field, see, e.g., Eqs. (7 – 9) of Ref. [122]; we provide a brief review in App. 9.8. We numerically solve the TOV equation, and the choice of the EOS will be discussed shortly. Then we compute the corresponding scalar charge $\alpha_{\rm NS}$ with Eq. (9.48). Figure 9.2 shows $\alpha_{\rm NS}$ as a function of the Jordan-frame mass $m^{\rm J}_{\rm NS}$, using a variety of β_0 (the upper panel) and α_0 (the lower panel) values. Notice that sharp transitions develops at $m^{\rm J}_{\rm NS} \sim 1.4M_\odot$ and $1.8M_\odot$ as $\alpha_0 \to 0$. The NSs between these masses are spontaneously scalarized. In addition, we see the

scalar charge increases with the absolute value of α_0 and β_0 for a fixed $m_{\rm NS}^{\rm J}$ (e.g., the vertical dashed line). Therefore, we chose $(\beta_0, \alpha_0) = (-4.5, -3.5\times10^{-3})$ below to maximize the effect of scalarization.

On the other hand, we can also leverage the freedom of choosing an EOS to magnify the scalarization. Here we restrict ourselves to the spectral EOSs provided in [127], parameterized by the form

$$P(\rho) = \begin{cases} \kappa_0 \rho^{\Gamma_0}, & \rho < \rho_0, \\ P_0 \exp\left[\int_0^x \Gamma(\tilde{x})\, d\tilde{x}\right], & \rho > \rho_0, \end{cases} \tag{9.19}$$

with ρ_0 a reference density, $P_0 = P(\rho_0)$, $\Gamma(x) = \gamma_2 x^2 + \gamma_3 x^3$ and $x = \ln(\rho/\rho_0)$. Among the options, we find the following soft EOS that gives rise to the strongest scalarization effect (obtained from Table III of Ref. [127]):

$$\Gamma_0 = 2, \quad \rho_0 = 8.44019\times10^{-5}, \quad P_0 = 1.20112\times10^{-7}$$
$$\gamma_2 = 0.475296, \quad \gamma_3 = -0.117048.$$

Note that ρ_0 and P_0 are in $G_* = c = M_\odot = 1$ units. For comparison, we also solve a NS with the same Jordan-frame mass in GR, and summarize the corresponding stellar properties in Table 9.1. The compactness of the NS is $C_{\rm GR} \sim 0.22$, with a tidal Love number k_2 of ~ 0.08 [128] and a tidal deformability $\Lambda_2 = \frac{2}{3}\frac{k_2}{C_{\rm GR}^5}$ of ~ 131.1 [129] in the absence of the scalar field.

To end this section, we emphasize that our choices for the EOS and the ST theory parameters are intentionally made to produce a large scalar field: the values of (α_0, β_0) lie on the edge of existing constraints [19, 22, 47–49, 126], even though they may not be preferred in the actual astrophysical environment. The current idealized configuration is to justify our simulation code and to investigate the maximum possible detectability of the dipole radiation emitted by BHNS systems. Future work is being planned to explore more moderate scenarios.

9.4 Numerical results

We present our main simulation results in this section. For comparison, the BHNS system is evolved in both GR and ST theory, and two numerical resolutions are adopted for each case by specifying different numerical error tolerances to the adaptive mesh refinement (AMR) algorithm in SpEC [130]. Below we first give a qualitative panorama view of the GR system in Sec. 9.4.1, and the ST system in Sec. 9.4.2. Then in Sec. 9.4.3 we compare the GR and ST simulations. Finally in

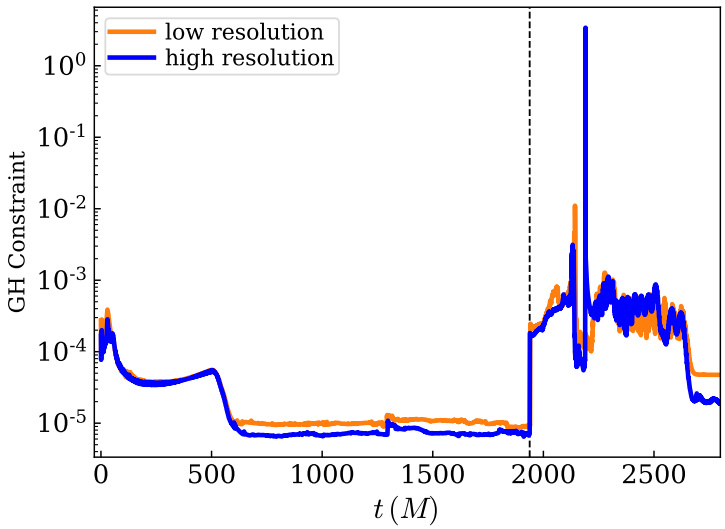

Figure 9.3: The evolution of the volume-weighted constraint energy for the metric, evolved with GR. The orange (blue) curve corresponds to the low (high) resolution. The vertical dashed line indicates the onset of the merger.

Sec. 9.4.4, we conduct more quantitative discussions by comparing our numerical waveforms to existing PN predictions in ST.

9.4.1 The BHNS system in GR

We first evolve the system with GR, whose initial data are built based on the method in Refs. [131, 132]. For the GW200115-like binary parameters we consider (see Table 9.1), the NS is swallowed quickly by the BH during the merger, and there is no tidal disruption. The remnant BH has a mass of $m_f = 0.9785M$, with $M = 7.2M_\odot$ the total Jordan-frame mass defined in Sec. 9.3.1. The remnant dimensionless spin is $\chi_f = 0.38$. As a standard numerical diagnostic, we plot the volume-weighted generalized harmonic constraint energy [see Eq. (53) of Ref. [106]] in Fig. 9.3, where the orange (blue) curve refers to the low (high) resolution run. As expected, the constraint energy decreases with increasing resolution, once the initial transients (known as junk radiation) leave the domain ($t > R_{\rm bdry} = 500M$). Here $R_{\rm bdry}$ is the radius of our simulation domain, as summarized in Table 9.1. In addition, we remark that the constraints jump drastically near $t = 1938M$, when the NS starts to plunge into the BH.

The top panel of Fig. 9.4 shows the dominant $l = m = 2$ harmonic $\tilde{h}_{22}$ emitted by the BHNS system, with low (in orange) and high (in blue) resolution. We see that the two waveforms manifest significant dephasing near the merger. Our current

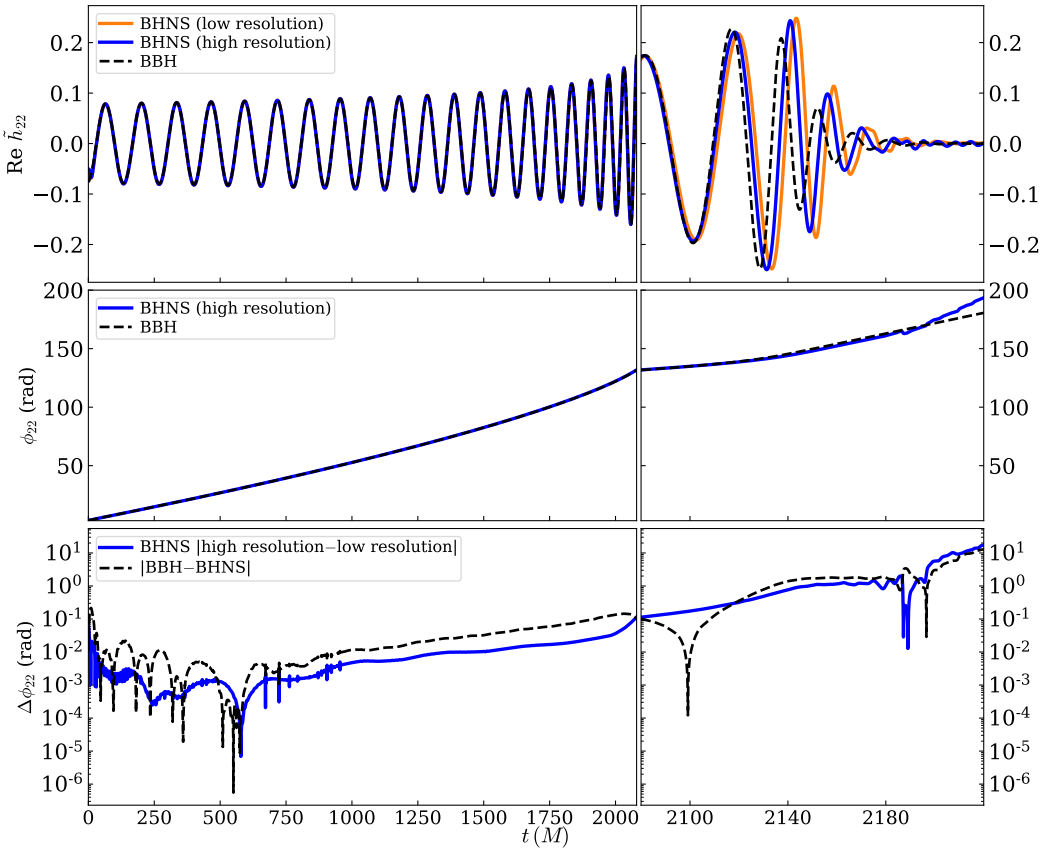

Figure 9.4: GW diagnostics for the GR systems. Upper panels: The GW harmonic $\tilde{h}_{22}$ of the BHNS system evolved with GR, using a low (in orange) and high resolution (in blue). Two BHNS waveforms are compared to that of the BBH system (in black) which has the same mass ratio and spins. We align the three waveforms by minimizing their mismatch over time and phase shifts, with the optimization window chosen to be $[200M, 800M]$. Middle panels: the GW phases of the high-resolution BHNS binary (in blue) and the BBH binary (in black). Lower panels: the GW phase difference between the BBH and the BHNS system (in black). It is compared to the numerical resolution difference of the BHNS waveform (in blue).

waveforms are less accurate than other recent BHNS SpEC simulations [133] even though we use the same criteria to set the numerical error tolerances in AMR. This is mainly because the NS we consider is softer, which has a smaller radius and would require finer grids to resolve its structure. However, as the main purpose of this study is to get a first qualitative understanding of BHNS binaries in ST, we expect the current accuracy to be sufficient (see more details in Sec. 9.4.3).

The leading tidal effect in the GW phase evolution appears at 5PN order [129], and is captured by a mass-weighted tidal parameter $\tilde{\Lambda}_2$ [134]

$$\tilde{\Lambda}_2 = \frac{16}{13}\frac{(M + 11m^{\rm J}_{\rm BH})}{M^5} m^{\rm J\,4}_{\rm NS}\Lambda_2. \tag{9.20}$$

After plugging in the values listed in Table 9.1, we find $\tilde{\Lambda}_2$ is around 2.95, implying that the emitted GWs are almost indistinguishable from that of a BBH system with the same spins and mass ratio. To demonstrate this, we compare the BHNS waveform to that of an equivalent BBH system (black dashed line in the top panel of Fig. 9.4). The data of the BBH binary are obtained from the `NRSur7dq4` surrogate model [135]. We align the two waveforms $\tilde{h}^{\rm BHNS}_{22}$ and $\tilde{h}^{\rm Sur}_{22}$ by minimizing their mismatch $\mathcal{M}$:

$$\mathcal{M} = 1 - \frac{(\tilde{h}^{\rm BHNS}_{22}|\tilde{h}^{\rm Sur}_{22})}{\sqrt{(\tilde{h}^{\rm BHNS}_{22}|\tilde{h}^{\rm BHNS}_{22})(\tilde{h}^{\rm Sur}_{22}|\tilde{h}^{\rm Sur}_{22})}}, \tag{9.21}$$

over time and phase shifts. Here the time-domain inner product between two signals a, b is given by

$$(a|b) = \mathrm{Re}\int_{t_1}^{t_2} a(t)^*\, b(t)\, dt, \tag{9.22}$$

where the star denotes complex conjugation, and we choose the optimization window to be $[t_1, t_2] = [200M, 800M]$. We provide the phase evolution ϕ_{22} of the aligned waveforms:

$$\phi_{22} \equiv \arg \tilde{h}_{22}, \tag{9.23}$$

in the middle panel of Fig. 9.4, as well as the corresponding waveform phase differences $\Delta\phi_{22}$ in the bottom panel. We see the phase difference between the BHNS and BBH (~ 0.4 rad) remains comparable to NR numerical resolution difference up to $\sim 10M$ prior to the waveform peak, which indicates that the tidal effect of this system is negligible.

9.4.2 The BHNS system in ST: Scalar Field

Let us then move on to the ST simulation. For simplicity, we use the same initial data as its GR counterpart to evolve the system, where the scalar field is absent;[4] while this means the initial data do not correctly capture a snapshot of the binary

[4] It is straightforward to check that the GR initial data satisfy the ST constraint equations.

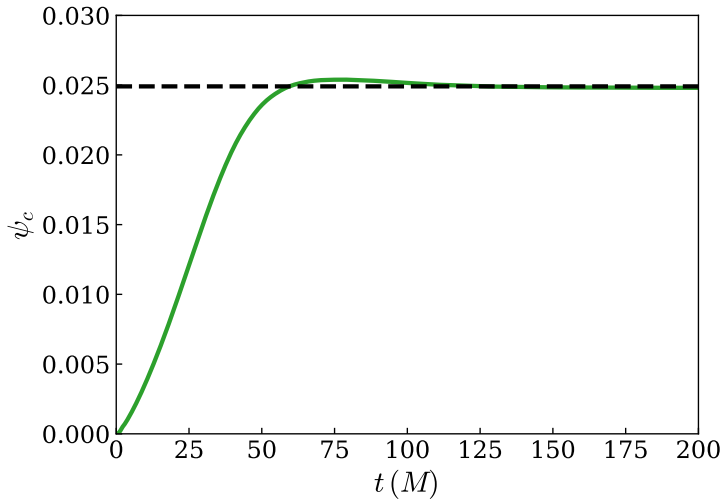

Figure 9.5: The evolution of the scalar field ψ measured at the center of the NS. The plot describes the growth of the scalar field around the NS at the beginning of the simulation. The horizontal dashed line corresponds to the prediction by solving equations of motion for an isolated NS in Sec. 9.3.2.

system in ST gravity that started at an infinite time in the past, this is also true for the GR simulation presented in Sec. 9.4.1, where Fig. 9.3 displays the presence of spurious initial transients during $t < R_{\rm bdry} = 500M$. In our ST simulations, the system undergoes an extra transient regime at the beginning of the evolution, during which a scalar field cloud grows dynamically around the NS. In Fig. 9.5, we plot the scalar field value ψ_c measured at the stellar center as a function of time. During the first $50M$, the value of ψ_c increases and asymptotes to the value predicted by the isolated NS solver (the horizontal dashed line) that we used in Sec. 9.3.2, which serves as a cross-check of our numerical code. Note that the ψ_c growth time scale is much shorter than the aforementioned initial transients ($t \sim 500M$), therefore we expect that our results are not impacted by this additional transition from GR to ST.

We also provide the volume-weighted generalized harmonic constraint energy [see Eq. (53) of Ref. [106]] in the top panel of Fig. 9.6 and find that the additional scalar field does not worsen the constraint violation compared to the GR system (Fig. 9.3): the evolution of the constraint is identical modulo a shift to an earlier time, due to the hastened merger of the ST system. In addition, as for the scalar field's FOSH system [107, 108], we need to introduce an auxiliary dynamical variable $\Phi_i \equiv \partial_i \psi$,

and its associated constraint energy:

$$\mathcal{E}_\psi = \left\| \sqrt{\sum_{i=1}^{3} \left[C_i^{(1)} C_i^{(1)} + C_i^{(2)} C_i^{(2)} \right]} \right\|, \tag{9.24}$$

where $\|\cdot\|$ denotes L^2 norm over the domain. The derivative constraint for ψ, $C_i^{(1)}$, reads

$$C_i^{(1)} = (\partial_i \psi)_{\rm num} - \Phi_i, \tag{9.25}$$

where $(\partial_i \psi)_{\rm num}$ corresponds to the numerical spatial derivative of ψ. The second derivative constraint for ψ, $C_i^{(2)}$, is given by

$$C_i^{(2)} = [ijk]\partial_j \Phi_k \qquad \text{(sum on } j, k\text{)} \tag{9.26}$$

with $[ijk]$ being the Levi-Civita symbol, with $[123] = +1$. We provide the evolution of $\mathcal{E}_\psi$ in the lower panel of Fig. 9.6. As expected, it also decreases with increasing resolution.

Finally, to close this subsection, we give a qualitative description of the scalar field ψ in Fig. 9.7 by taking a snapshot of its distribution at $t = 2062.3M$ across the entire computational domain. In the wave zone, the distribution of the scalar field in the $x - y$ plane (left panel) is singly periodic in φ like $e^{i\varphi}$, where φ is the azimuthal angle defined in Eq. (9.14b); and in the $y - z$ plane (right panel), we see vanishing on the z axis with a single maximum at the equatorial plane ($z = 0$), like $\sin\iota$. These patterns are consistent with the dipolar nature $Y_{11} \sim \sin\iota e^{i\varphi}$ of the scalar field, and we will discuss this in more detail in Sec. 9.4.4.

9.4.3 Comparison between the GR and ST

Figure 9.8 displays the evolution of the coordinate separation between the two compact objects for the GR and the ST systems. We first see that the merger portions of both systems can be aligned perfectly through a time shift, namely, they have a similar $\dot{R} - R$ dependence near the merger and thus a similar plunge dynamic, implying a similar orbital separation (and therefore similar frequency) for the onset of the plunge. This feature is different from the BNS simulations in Ref. [74], where ST binaries were found to merge at significantly larger orbital separation (see their Fig. 1). The difference arises from the size of the gravitational attraction. Recall that the gravitational pull in ST gravity is characterized by the effective gravitational constant $G_{\rm eff} = G_*(1 + \alpha_1\alpha_2)$ [32], which is amplified for BNS systems when

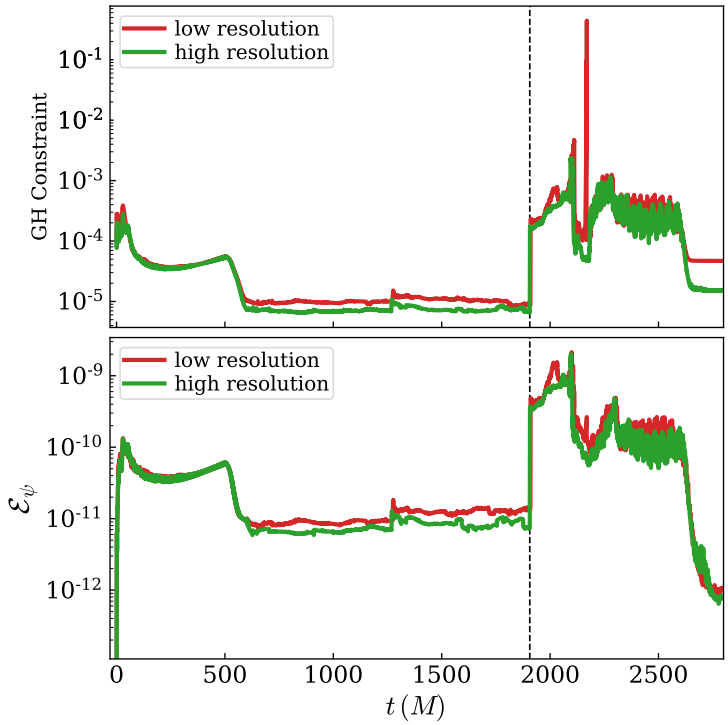

Figure 9.6: The evolution of the volume-weighted constraint energy for the metric (the upper panel) and the scalar field (the lower panel), evolved with ST. The red (green) curve corresponds to the low (high) resolution. The vertical dashed line indicates the onset of the merger.

both the NSs have a nonzero scalar charge. Consequently, their plunges happen at larger orbital separations. By contrast, the gravitational pull in our ST BHNS system is similar to its GR counterpart because the BH's scalar charge vanishes, so the scalar sector has negligible impact on the plunge separation. However, the ST simulation does exhibit a nonnegligible deviation from its GR counterpart over a longer timescale. As shown in Fig. 9.8, the ST simulation has a shorter total duration than the GR case, even though they both start at the same separation. This is because the scalarized NS admits an additional energy dissipation channel via scalar radiation; therefore the system in ST gravity evolves faster during the inspiral.

A direct consequence of the hastened dynamics is a shortening of the GW signal. Figure 9.9 provides the $l = m = 2$ harmonic of the ST waveform for two different resolutions (solid curves). For reference, $\tilde{h}_{22}$ in GR is plotted as the blue dashed curve. Here we still align the waveforms by minimizing the mismatch in Eq. (9.21) over time and phase shifts. The same time window $[t_1, t_2] = [200M, 800M]$ is used. After the peak of the ST waveform, it takes the GR waveform an extra

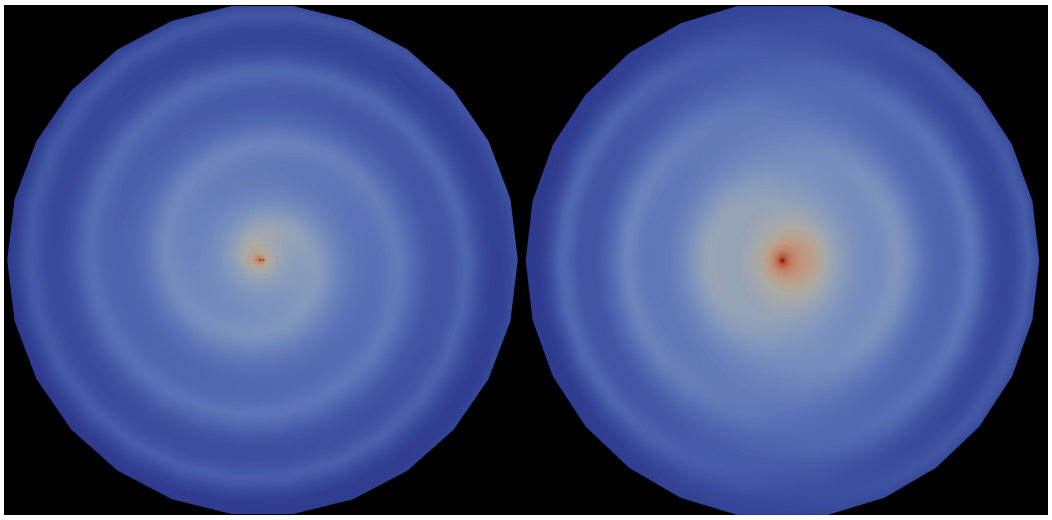

(a) The $x-y$ plane (b) The $y-z$ plane

Figure 9.7: A snapshot of the field $\log|\psi|$ at $t = 2062.3M$ across the entire computational domain, with the outer boundary being at $\sim 500M$. The orbital angular momentum is aligned with the z axis.

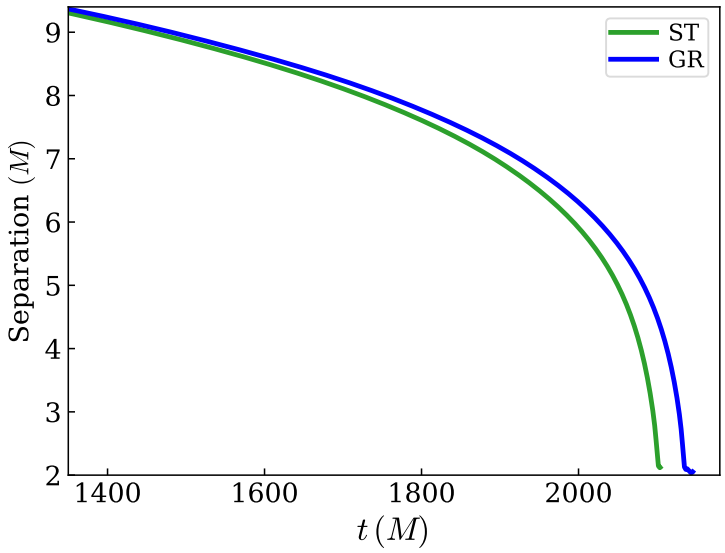

Figure 9.8: The evolution of the orbital separation for the BHNS system, in the ST gravity (green) and GR (blue).

GW cycle, $\Delta\phi_{22} \sim 6.34\,\text{rad}$ [Eq. (9.23)], to reach its peak, smaller than GR's numerical resolution difference at the peak ($\sim 0.6\,\text{rad}$). Therefore our simulations are able to capture the effect of scalar radiation well above the numerical resolution difference, even though our simulations are less accurate than other recent BHNS SpEC simulations [133], as discussed in Sec. 9.4.1.

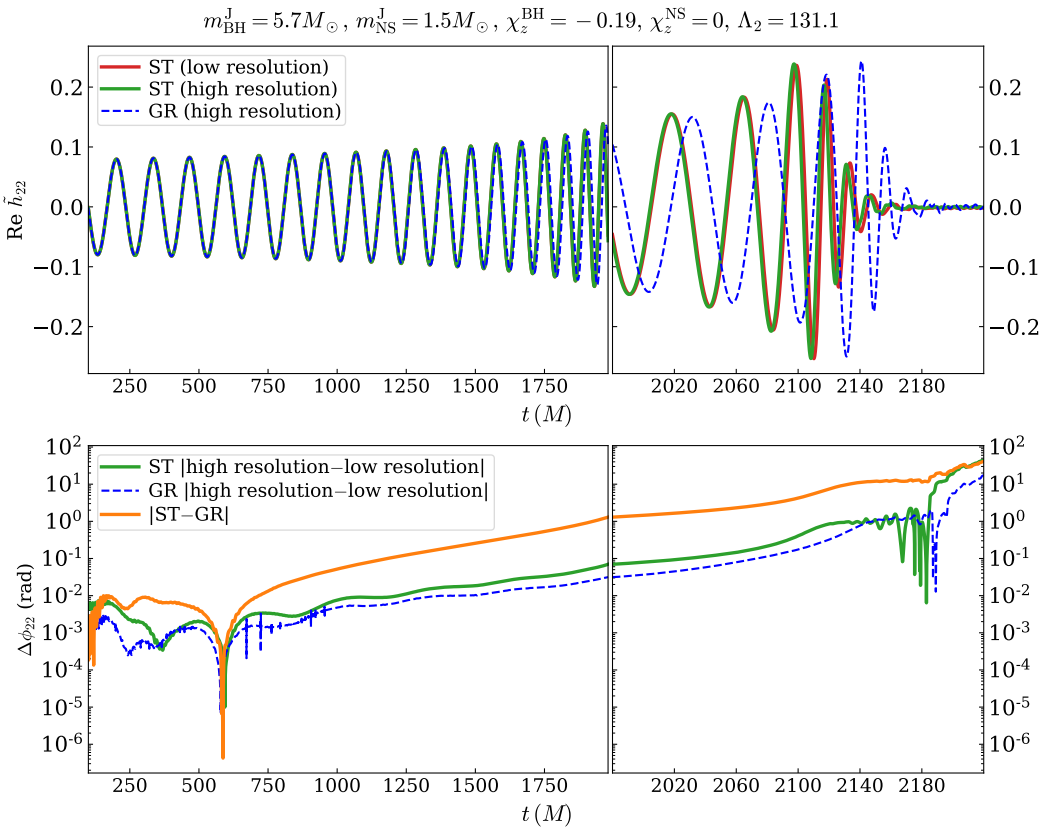

Figure 9.9: GW diagnostics for the ST systems. Upper panel: The ST waveforms with a low (in red) and high (in green) resolution. They are compared to the GR waveform (in blue). Lower panel: the phase difference between the GR and ST waveforms (in orange). For reference, the numerical resolution differences of the GR and the ST waveform are also presented in blue and green, respectively. In addition, we summarize some of the binary parameters in the title.

9.4.4 Comparing to post-Newtonian theory

We now carry out quantitative comparisons between the simulated GW waveforms and existing PN waveform predictions in ST. As pointed out in Refs. [37, 39], the relative size of the leading scalar dipolar radiation and leading tensor quadrupolar radiation is given by

$$\frac{\mathcal{F}_{\rm nd}}{\mathcal{F}_{\rm d}} = \left(\frac{24}{5\zeta \mathcal{S}_-^2}\right) x, \tag{9.27}$$

with $\mathcal{F}$ being energy flux. In our simulation, we find the factor above is greater than 25, i.e., quadrupolar radiation dominates, so we are in the quadrupole-driven regime [37].

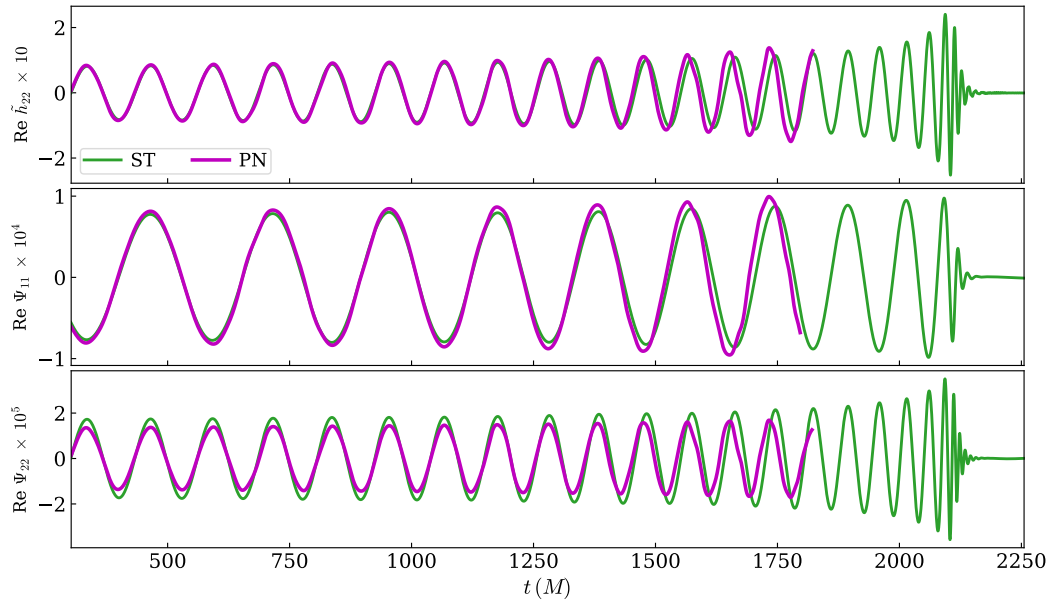

(a) ST

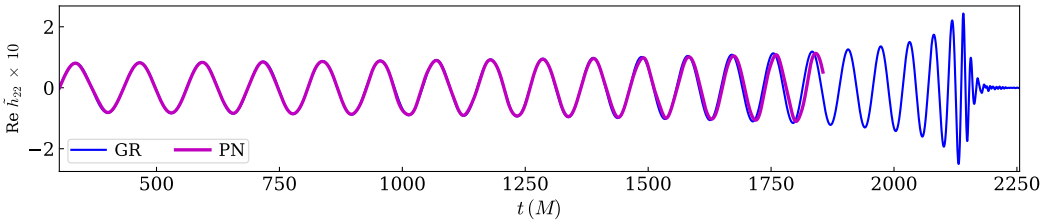

(b) GR

Figure 9.10: Comparing the numerical waveforms (in green and blue) to the PN model (in magenta). Fig. 9.10a shows the ST tensor harmonic $\tilde{h}_{22}$ (top) and the scalar modes Ψ_{11} (middle) and Ψ_{22} (bottom). Note that the modes Ψ_{lm} are defined in Eq. (9.36). Fig. 9.10b provides the GR tensor harmonic $\tilde{h}_{22}$.

We first consider the gravitational modes $\tilde{h}_{lm}$, whose PN expressions read [37]

$$\tilde{h}_{lm} = 2\tilde{G}(1-\zeta)\eta x\sqrt{\frac{16\pi}{5}}\hat{H}_{lm}e^{-im\phi}, \tag{9.28}$$

where $\eta = m^{\rm J}_{\rm BH}m^{\rm J}_{\rm NS}/(m^{\rm J}_{\rm BH}+m^{\rm J}_{\rm NS})^2$ is the symmetric mass ratio, $x = (\tilde{G}M\alpha\Omega_{orb})^{2/3}$ is the PN expansion parameter, $\Omega_{\rm orb}$ is the orbital frequency, and we give ϕ below. We summarize the definition of ST parameters $\tilde{G}, \zeta, \alpha$ in Table 9.2. In Eq. (9.28), comparing with Eq. (65) of Ref. [37], we removed an overall factor M/r which is already divided out in Eq. (9.14a). The expressions for $\hat{H}_{lm}$ are long and they can be found in Eqs. (67) of Ref. [37]. Because the dipolar scalar radiation starts 1PN earlier than the leading quadrupolar gravitational radiation, the inspiral is separated

into two parts: dipolar (D) or non-dipolar (ND). The phase factor ϕ reads

$$\phi = \phi_{\rm nd} + \phi_{\rm d}\,, \tag{9.29a}$$

$$\phi_{\rm nd} = -\frac{x^{-5/2}}{32\eta\xi}\left[1 + \frac{5}{3}\rho_2^{\rm nd}x + \frac{5}{2}\rho_3^{\rm nd}x^{3/2} + 5\rho_4^{\rm nd}x^2 + \frac{5}{2}\rho_3^{\rm spin}x^{3/2} + 5\rho_4^{\rm spin}x^2\right], \tag{9.29b}$$

$$\phi_{\rm d} = \frac{25\mathcal{S}_-^2\zeta x^{-7/2}}{5376\eta\xi^2}\left[1 + \frac{7}{5}\rho_2^{\rm d}x + \frac{7}{4}\rho_3^{\rm d}x^{3/2} + \frac{7}{3}\rho_4^{\rm d}x^2\right], \tag{9.29c}$$

with the coefficients $\rho_i^{\rm nd/d}$'s being listed in Eqs. (B10) of Ref. [37]. The ST parameters ξ and $\mathcal{S}_\pm$ are defined in Table 9.2, and we see that all of them depend on the sensitivity of the NS

$$s_{\rm NS} = \left(\frac{d\ln m_{\rm NS}^{\rm J}}{d\ln\phi}\right)_{\phi_0}. \tag{9.30}$$

The relationship between $s_{\rm NS}$ and the scalar charge $\alpha_{\rm NS}$ reads [37]

$$s_{\rm NS} = \frac{1}{2} - \frac{\alpha_{\rm NS}}{2\alpha_0}\,, \tag{9.31}$$

where α_0 is the ST parameter defined in Eq. (9.18). Equation (9.29b) is controlled by the quadrupolar radiation, while Eq. (9.29c) is controlled by the dipolar radiation starting at -1PN. Spin effects are not considered in Ref. [37]; here we simply add the spin contributions in GR, leading to the second line in Eq. (9.29b), and we leave the relevant ST corrections for future studies. The expressions of $\rho_i^{\rm spin}$'s can be found in Eq. (4.16) of Ref. [136],

$$\rho_3^{\rm spin} = \frac{1}{12}\sum_{i=1,2}\chi_i(\hat{\boldsymbol{L}}_N\cdot\hat{\boldsymbol{s}}_i)\left(113\frac{m_i^2}{M^2} + 75\eta\right), \tag{9.32}$$

$$\rho_4^{\rm spin} = \frac{1}{48}\eta\chi_1\chi_2[247(\hat{\boldsymbol{s}}_1\cdot\hat{\boldsymbol{s}}_2) - 721(\hat{\boldsymbol{L}}_N\cdot\hat{\boldsymbol{s}}_1)(\hat{\boldsymbol{L}}_N\cdot\hat{\boldsymbol{s}}_2)], \tag{9.33}$$

where $\hat{\boldsymbol{L}}_N$ and $\hat{\boldsymbol{s}}_i$ stand for the unit vector along the orbital angular momentum and the individual spin $\boldsymbol{s}_i$. Furthermore, we note that tidal effects are ignored in Eq. (9.29a), which formally enter into the phase evolution at 5PN order [129]. This is reasonable for this study, as the system's mass-weighted tidal deformability $\tilde{\Lambda}_2 \sim 2.95$ is very small and it has little impact on the binary dynamics, as shown in Fig. 9.4. In the top panel of Fig. 9.10a, we compare the ST numerical waveform $\tilde{h}_{22}$ to the PN prediction, finding good agreement until $\sim 500M$ before the merger. For reference, we also plot the GR waveform $\tilde{h}_{22}$ and the corresponding PN prediction in Fig. 9.10b. Additionally, in App. 9.10, we present a more detailed comparison by demonstrating the hierarchical contributions of each PN term.

Table 9.2: Summary of PN parameters used for ST gravity. We have used the fact that a BH's scalar charge vanishes: $\alpha_{\rm BH} = 0$, and thus $s_{\rm BH} = 1/2$ following Eq. (9.31). Note that α is not to be confused with the scalar charge $\alpha_{\rm NS}$.

ω_0	$\tilde{G}$	ζ	α	$\mathcal{S}_-$	$\mathcal{S}_+$	ξ
$\frac{1-3\alpha_0^2}{2\alpha_0^2}$	$\frac{1+\alpha_0^2}{\phi_0}$	$\frac{\alpha_0^2}{1+\alpha_0^2}$	$\frac{1}{1+\alpha_0^2}$	$-\alpha^{1/2} s_{\rm NS}$	$\alpha^{1/2}(1-s_{\rm NS})$	$1+\frac{\zeta \mathcal{S}_+^2}{6}$

We then compare the scalar modes ψ_{lm} extracted from our simulation with predictions from PN. The PN prediction for the (l, m) harmonic of the transverse breathing mode Ψ [see Eq. (9.11)] is given by [39]

$$\Psi_{lm} = 2i\tilde{G}\zeta\sqrt{\alpha}\mathcal{S}_-\eta\sqrt{x}\sqrt{\frac{8\pi}{3}}\hat{\Phi}_{lm}e^{-im\phi}, \tag{9.34}$$

where the expression of $\hat{\Phi}_{lm}$ can be found in Eqs. (6.10) of Ref. [39]; and Ψ_{lm} is defined in parallel with Eq. (9.14b):

$$r\Psi/M = \sum_{l,m} Y_{lm}(\iota, \varphi)\Psi_{lm}. \tag{9.35}$$

Here Ψ_{lm} is related to our numerical extracted scalar mode ψ_{lm} [Eq. (9.14b)] via

$$\Psi_{lm} = -4\sqrt{\pi}\alpha_0\psi_{lm}, \tag{9.36}$$

where Eq. (9.17) has been used. We compare our numerical scalar modes Ψ_{11} and Ψ_{22} to the PN predictions in the middle and bottom rows of Fig. 9.10a, and refer to App. 9.9 for other (subdominant) modes. Similar to $\tilde{h}_{22}$, the PN predictions for the ψ_{lm} phase evolution are accurate until $\sim 500M$ before merger; however, their amplitudes do not match as accurately as their phases.

9.5 Waveform distinguishability

We have discussed features of the BHNSs in GR and ST. Then in this section, we investigate how our numerical simulations can help place constraints on ST theory with GW200115 and future BHNS observations. Specifically, here we focus on whether a ST waveform can be distinguished from a GR waveform. We estimate this by computing the mismatch $\mathcal{M}$ between the two waveforms, defined in Eq. (9.21). Note that in Eq. (9.22), we used a flat noise curve for simplicity, namely assuming an idealized detector.

We first compute the mismatch between the GR and ST waveform $\tilde{h}_{22}$ presented in Fig. 9.9 and find $\mathcal{M} = 0.38$. Since the error in our simulations is larger than other

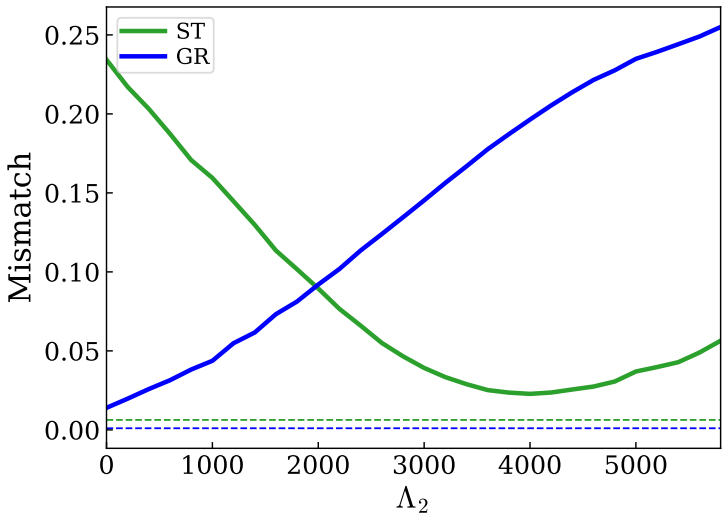

Figure 9.11: The mismatch of the SEOBNRv4T model with the ST waveform (green) and the GR result (blue), as a function of tidal deformability Λ_2. For the sake of comparison, we also compute the mismatch between two resolutions for ST (green dashed line) and GR (blue dashed line).

BHNS SpEC simulations (see discussions around Figs. 9.4 and 9.9), we terminate the integration in Eq. (9.22) at the peak of the ST waveform ($t_2 = 2102M$) to avoid the ringdown region. One criterion for the distinguishability of two waveforms reads [137–141]

$$\mathcal{M} > \frac{D}{2\rho^2}, \tag{9.37}$$

where $D = 5$ is the number of free intrinsic parameters (chirp mass, mass ratio, spin magnitudes on both compact objects, and tidal deformability) of our nonprecessing systems, and ρ is the signal-to-noise ratio (SNR). After inserting the numbers, we find $\rho > 2.56$ is needed to distinguish ST from GR. Such a low SNR threshold is not surprising for this specific case with extreme scalarization and an idealized detector, given the significant dephasing between the two waveforms shown in Fig. 9.9. For more moderate ST parameters and more realistic detectors, the deviation is not expected to be as large, and we leave this exploration for future work.

The subsequent question to consider is the extent to which tidal effects within GR can replicate the ST waveform. To explore this question, we employ an effective-one-body (EOB) model known as SEOBNRv4T [142, 143]. This model includes tidal effects and is characterized by tidal deformability coefficients Λ_l in its tidal sector, with $l = 2$ being the focus in this case. To generate the SEOBNRv4T waveforms with varying Λ_2, we utilize LALSuite [144]. Figure 9.11 showcases the mismatch of

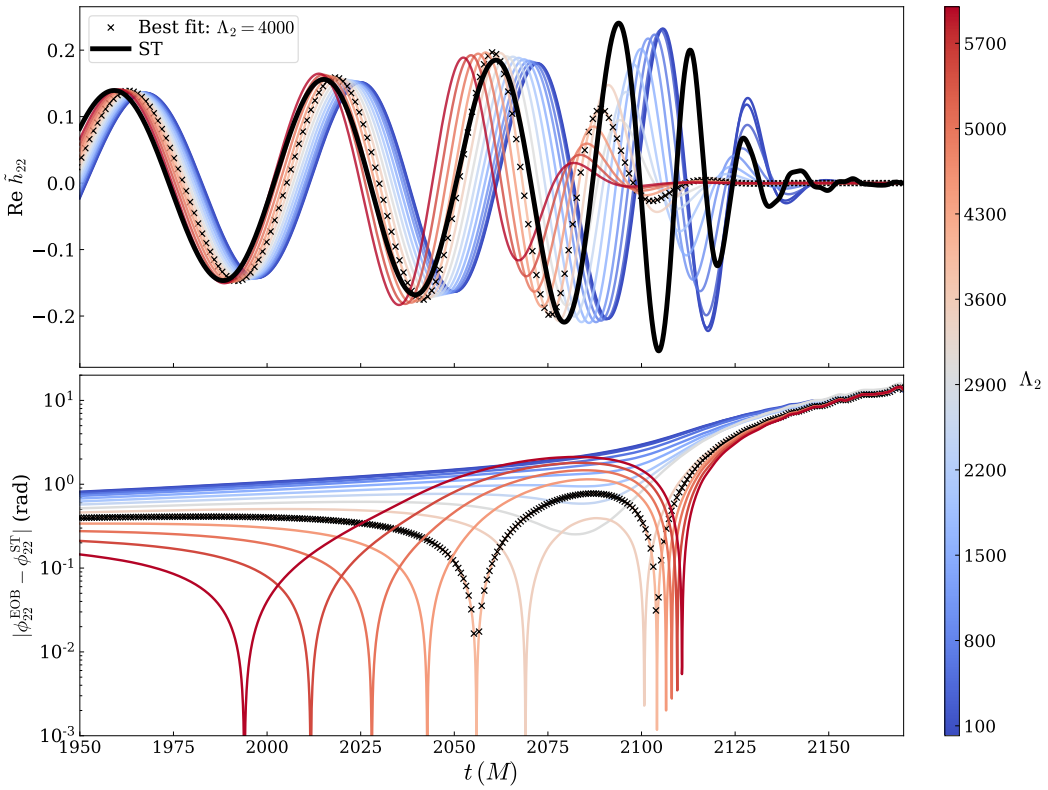

Figure 9.12: Comparing the ST waveform (black) with the SEOBNRv4T model, with a variety of Λ_2, ranging from 0 to 6000. The minimum mismatch $\mathcal{M} \sim 0.023$ happens at $\Lambda_2 \sim 4000$.

these waveforms with the ST waveform $\tilde{h}_{22}$ as a function of Λ_2 while fixing other intrinsic parameters at their NR values. The mismatch first decreases when Λ_2 is small, and the best match $\mathcal{M} \sim 0.023$ happens at $\Lambda_2 \sim 4000$. As a comparison, we repeat the same calculation for the mismatch between the SEOBNRv4T model and the GR waveform. The result is shown as the blue curve in Fig. 9.11, and we can see the mismatch grows monotonically with Λ_2 (recall the tidal effect is negligible in the GR simulation). To better understand the feature, in Fig. 9.12 we provide the SEOBNRv4T waveforms with a variety of Λ_2, ranging from 0 to 6000. In particular, we mark the best-fit waveform ($\Lambda_2 = 4000$) with black crosses. With increasing Λ_2, we see the tidal waveforms gradually shift backward in time, because the tidal effect accelerates the evolution and shortens the length of waveforms. This behavior is similar to the effect of the scalar field and dipole radiation. Notably, as Λ_2 approaches 4000, the last two wave cycles of the SEOBNRv4T waveforms (at $t \sim 2075M$) align more closely with ST's phase evolution, resulting in a smaller mismatch. Further increasing Λ_2 beyond this point causes the tidal waveforms to

deviate again from the ST waveform. Therefore, the mismatch in Fig. 9.11 bounces back.

Our preliminary mismatch comparison shows that both the tidal and scalar sectors could produce similar and potentially degenerate imprints in GWs given the length of our simulations ($\sim$ 12 cycles before the merger). A limitation of our analysis is that the NR waveforms are relatively short and lacked low-frequency components—the dipole radiation appears at -1PN whereas the tidal effect at 5PN. A longer waveform with a broader frequency span may break the degeneracy. A more comprehensive analysis is therefore necessary to fully characterize these features using longer waveforms with a broader frequency span and Bayesian parameter estimation. We leave this exploration to future research.

9.6 Conclusion

In this chapter, we numerically simulate a fully relativistic BHNS binary system in ST theory, chosen to be consistent with GW200115 [88]. To maximize the effect of spontaneous scalarization, we set the ST parameters (β_0, α_0) to be at the boundary of known constraints from other observations [22]: $(-4.5, -3.5 \times 10^{-3})$. In addition, we select a soft EOS for the NS so that it can generate a large scalar charge, as summarized in Table 9.1. Following Refs. [131, 132], we construct the initial data without including the scalar sector. Instead, the scalar field dynamically grows during the first $\sim 50M$, and quickly approaches the desired value predicted by the isolated NS solver.

We evolve the BHNS system with both GR and ST. For the GR binary, we find the soft EOS results in GW emissions that are nearly identical to those of a BBH system with the same spins and mass ratio. In contrast, the ST binary exhibits dominant dipolar radiation due to spontaneous scalarization, with the spatial distribution of the scalar field ψ matching the dipolar emission pattern throughout the computational domain. As a result of this additional dipolar radiation, the ST binary evolves faster than its GR counterpart, and the ST binary reaches its peak amplitude one whole GW cycle earlier than the GR counterpart. We also compare our waveforms, including the tensor mode $\tilde{h}_{22}$ and scalar breathing modes $\Psi_{11,22}$, with existing PN waveform predictions in ST [37, 39, 136], and find reasonable agreement up to $\sim 500M$ before the merger. Finally, we compute the mismatch between our ST waveform and the `SEOBNRv4T` model as a function of tidal deformability Λ_2. We find the ST waveform could be partially mimicked by a GR tidal waveform with a large $\Lambda_2 \sim 4000$, due to

the tidal effect accelerating the evolution of the binary.

Throughout the analysis, we pick optimal choices for the EOS and the ST theory parameters in order to produce a significant scalarization effect, and thus strong dipolar radiation. Under this idealized scenario, we find that the GR and ST waveforms should be distinguishable for SNRs above 2.56. To fully understand observational prospects of constraining ST theory using BHNS systems, future work should explore a wider range of EOSs and more moderate ST parameters. Specifically, the scalar field's ability to alter the properties of NSs, such as compactness and radius, may play a crucial role in determining whether the NSs are disrupted or not [145], potentially leading to rich phenomena in the corresponding GW and even electromagnetic emissions for ST binary systems.

Our mismatch tests using the `SEOBNRv4T` model and the GR waveforms indicate that the ST sector might be partially degenerate with tidal effects during the late inspiral stage (excluding low-frequency regime), which can lead to parameter estimation biases. Here we restrict ourselves to a single degree of freedom: Λ_2, while holding other parameters such as mass ratio and spins constant. A possible avenue for future work is to carry out a more systematic full Bayesian parameter estimation to better account for these degeneracies.

Finally, our waveforms are obtained at null infinity through extrapolation following Refs. [111, 115–117], with the `PYTHON` package `scri` [118, 119]. The method is an approximate approach that relies on the asymptotic behavior of several fields given by the peeling theorem [146]. While this approximate approach captures linear signals, it does not accurately capture nonlinear features such as the memory effect [147–152]. The more correct Cauchy-Characteristic Extraction (CCE) [112, 113] method would be required to fully account for these effects. Therefore, another future avenue could be to evolve the coupled metric-scalar system using a CCE framework adapted to ST, and investigate the memory effect in ST gravity [147–150, 153–155].

9.7 Appendix: The two-grid method and transformations

In the Einstein frame, we adopt the 3+1 decomposition of the metric [156]

$$ds^2 = -\bar{\alpha}^2 dt^2 + \bar{\gamma}_{ij}(dx^i + \bar{\beta}^i dt)(dx^j + \bar{\beta}^j dt), \tag{9.38}$$

where $\bar{\alpha}$, $\bar{\beta}^i$, $\bar{\gamma}_{ij}$ are the lapse, shift, and 3-metric in the Einstein frame. They, their spatial derivatives, and the extrinsic curvature K_{ij} are transformed to the Jordan frame via:

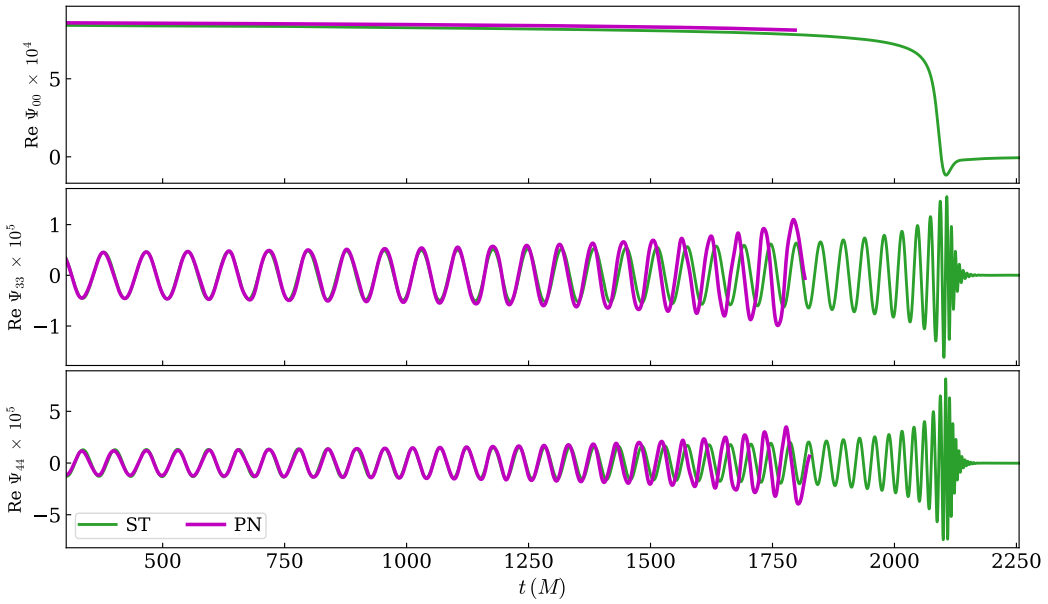

(a) Scalar modes

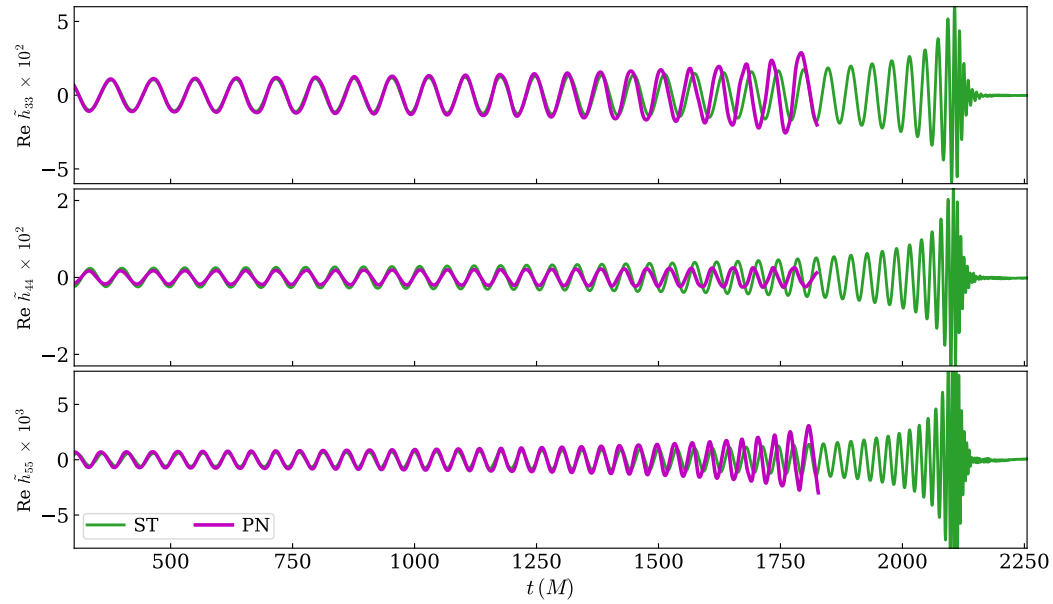

(b) Tensor modes

Figure 9.13: Same as Fig. 9.10, some other scalar and tensor modes. Note that the modes Ψ_{lm} are defined in Eq. (9.36).

$$
\begin{aligned}
&\alpha = \frac{1}{\sqrt{\phi}}\,\bar{\alpha}, \quad \beta^i = \bar{\beta}^i, \quad \gamma_{ij} = \frac{1}{\phi}\,\bar{\gamma}_{ij}, \quad \gamma^{ij} = \phi\,\bar{\gamma}^{ij}, \\
&K_{ij} = \frac{1}{\sqrt{\phi}}\left(\bar{K}_{ij} + \frac{\bar{\gamma}_{ij}}{2}\,\frac{d\log\phi}{d\psi}\,\bar{n}^k\,\partial_k\psi\right), \\
&\partial_k\alpha = \frac{1}{\sqrt{\phi}}\left(\partial_k\bar{\alpha} - \frac{\bar{\alpha}}{2}\,\frac{d\log\phi}{d\psi}\,\partial_k\psi\right), \\
&\partial_k\beta^i = \partial_k\bar{\beta}^i, \\
&\partial_k\gamma^{ij} = \phi\left(\partial_k\bar{\gamma}^{ij} + \bar{\gamma}^{ij}\,\frac{d\log\phi}{d\psi}\,\partial_k\psi\right),
\end{aligned}
\tag{9.39}
$$

where the future-directed unit timelike normal is given by

$$
\bar{n}^a = \bar{\alpha}^{-1}(\partial_t^a - \bar{\beta}^i\partial_i^a). \tag{9.40}
$$

On the other hand, the transformation of the stress-energy tensor $\bar{T}^{ab}$ can be established from its definition

$$
\bar{T}^{ab} = \frac{2}{\sqrt{-\bar{g}}}\frac{\delta S_M}{\delta\bar{g}_{ab}}. \tag{9.41}
$$

After inserting

$$
\begin{aligned}
\bar{g}_{ab} &= \phi g_{ab}, \\
\sqrt{-\bar{g}} &= \phi^2\sqrt{-g},
\end{aligned}
\tag{9.42}
$$

into Eq. (9.41), we obtain

$$
\bar{T}^{ab} = \frac{2}{\sqrt{-\bar{g}}}\frac{\delta S_M}{\delta\bar{g}_{ab}} = \frac{1}{\phi^3}\frac{2}{\sqrt{-g}}\frac{\delta S_M}{\delta g_{ab}} = \frac{1}{\phi^3}T^{ab}, \tag{9.43}
$$

which leads to $\bar{T}_{ab} = T_{ab}/\phi$.

9.8 Appendix: Structure of neutron stars in ST gravity

Following Ref. [122], the Einstein-frame metric of an isolated, nonspinning NS can be written as

$$
d\bar{s}^2 = -e^{\nu(r)}dt^2 + \frac{dr^2}{1-2\mu(r)/r} + r^2(d\theta^2 + \sin^2\theta d\phi^2). \tag{9.44}
$$

Then the equations of motion are given by

$$
\mu' = 4\pi r^2 A^4(\rho_0 h - P) + \frac{1}{2}r(r-2\mu)\varphi^2, \tag{9.45a}
$$

$$
\nu' = 8\pi\frac{r^2A^4P}{r-2\mu} + r\varphi^2 + \frac{2\mu}{r(r-2\mu)}, \tag{9.45b}
$$

$$\psi' = \frac{1}{\sqrt{4\pi}}\varphi, \tag{9.45c}$$

$$\varphi' = 4\pi\frac{rA^4}{r-2\mu}\left[(\alpha_0+\beta_0\sqrt{4\pi}\psi)(\rho_0 h-4P)+r\varphi(\rho_0 h-2P)\right]-\frac{2(r-\mu)}{r(r-2\mu)}\varphi, \tag{9.45d}$$

$$P' = -\rho_0 h\left[\frac{1}{2}\nu'+(\alpha_0+\beta_0\sqrt{4\pi}\psi)\varphi\right], \tag{9.45e}$$

with $A = \phi^{-1/2}$. Note that P, ρ_0, and h are in the Jordan frame. The system of coupled ordinary differential equations can be solved as an initial value problem integrating out from $r = \epsilon > 0$. The asymptotic expansion of the solution near the stellar center $r \to 0$ is

$$\begin{aligned}
\mu(r) &\sim \frac{1}{3!}\mu_3 r^3,\\
\nu(r) &\sim \frac{1}{2!}\nu_2 r^2,\\
\varphi(r) &\sim \varphi_1 r,\\
\psi(r) &\sim \psi_c + \frac{1}{2!}\frac{1}{\sqrt{4\pi}}\varphi_1 r^2,\\
P(r) &\sim P_c + \frac{1}{2!}P_2 r^2,
\end{aligned} \tag{9.46}$$

where

$$\begin{aligned}
\mu_3 &= 8\pi A_c^4(\rho_c h_c - P_c),\\
\nu_2 &= 8\pi A_c^4 P_c + \frac{\mu_3}{3},\\
\varphi_1 &= \frac{4\pi}{3}A_c^4(\alpha_0+\beta_0\sqrt{4\pi}\psi_c)(\rho_c h_c - 4P_c),\\
P_2 &= -\rho_c h_c\left[\frac{1}{2}\nu_2+(\alpha_0+\beta_0\sqrt{4\pi}\psi_c)\varphi_1\right].
\end{aligned} \tag{9.47}$$

We start the integration of Eqs. (9.45) at $\epsilon = 10^{-7}R^{\rm E}_{\rm ST}$ away from the stellar center, and terminate at the stellar surface. From surface values, we obtain the scalar charge of the NS via [122]

$$\alpha_{\rm NS} = \left.\frac{2\varphi}{\nu'}\right|_{\rm surf.}, \tag{9.48}$$

and the Einstein-frame mass

$$m^{\rm E}_{\rm NS} = \exp\left[-\frac{1}{\sqrt{1+\alpha^2_{\rm NS}}}\operatorname{arctanh}\left(\frac{\sqrt{1+\alpha^2_{\rm NS}}}{1+2/(r\nu')}\right)\right]\times\left.\frac{r^2\nu'}{2}\left(1-\frac{2\mu}{r}\right)^{1/2}\right|_{\rm surf.}. \tag{9.49}$$

It is related to the Jordan-frame mass through [32]

$$m^{\rm J}_{\rm NS} = m^{\rm E}_{\rm NS}(1+\alpha_0\alpha_{\rm NS}). \tag{9.50}$$

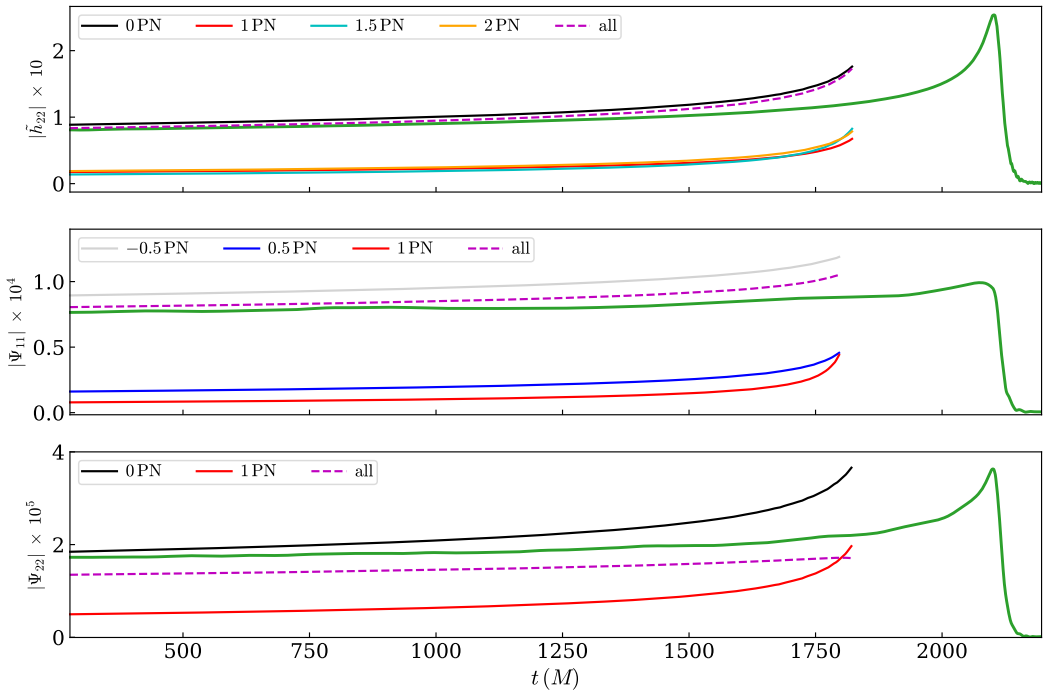

Figure 9.14: Contributions of individual PN orders to the amplitude of $\tilde{h}_{22}$ (top), Ψ_{11} (middle), and Ψ_{22} (bottom). It is important to note that a PN curve only includes contributions from the specific PN order, not lower PN orders. The magenta dashed curves refer to the ones that include all the PN terms.

For a Newtonian star, Eqs. (9.45) reduce to

$$\mu' = 4\pi r^2 A^4(\psi_\infty)\rho_0, \tag{9.51a}$$

$$P' = -\frac{\rho_0 \mu}{r^2}, \tag{9.51b}$$

where the scalar field ψ decouples from the matter and it becomes constant across the star. Here we denote its (background) value as ψ_∞. Next we can compute the baryonic mass m^B and the Einstein-frame mass $m^{\rm E}_{\rm NS}$ of the NS:

$$m^B = A^3(\psi_\infty) \int 4\pi\rho_0 r^2 dr, \tag{9.52a}$$

$$m^{\rm E}_{\rm NS} = A^4(\psi_\infty) \int 4\pi\rho_0 r^2 dr = m^B A(\psi_\infty). \tag{9.52b}$$

As shown in Refs. [32, 122], the scalar charge can be computed alternatively through

$$\alpha_{\rm NS} = \frac{1}{\sqrt{4\pi}} \left(\frac{\partial \ln m^{\rm E}_{\rm NS}}{\partial \psi_\infty} \right)_{m^B}. \tag{9.53}$$

After plugging Eq. (9.52b), we obtain $\alpha_{\rm NS} = \alpha_0$ [see Eq. (9.17)].

Table 9.3: Summary of all the PN orders in the amplitude of $\tilde{h}_{22}$, Ψ_{11}, and Ψ_{22}.

Modes	Available PN orders	References
$\tilde{h}_{22}$	0PN, 1PN, 1.5PN, 2PN	Eqs. (67) of [37]
Ψ_{11}	−0.5PN, 0.5PN, 1PN	Eqs. (6.10b) of [39]
Ψ_{22}	0PN, 1PN	Eqs. (6.10c) of [39]

9.9 Appendix: Some other scalar and tensor modes

Figure 9.13 displays additional scalar and tensor modes of the ST simulation.

9.10 Appendix: Hierarchical contributions from PN terms

In Fig. 9.10, we compared the ST waveforms with the existing PN predictions that include all the PN orders. Exploring the hierarchical contributions of each PN term is also an interesting aspect to investigate. Here we focus on the amplitude of $\tilde{h}_{22}$ [Eq. (9.28)], Ψ_{11} and Ψ_{22} [Eq. (9.34)], which are controlled by $\hat{H}_{lm}$ and $\hat{\Phi}_{lm}$ [37]. Table 9.3 outlines all the relevant PN orders of $\tilde{h}_{22}$, Ψ_{11}, and Ψ_{22}. Our convention considers the leading Newtonian quadrupole approximation in GR, namely $O(1)$ in $\hat{H}_{lm}$, as 0PN. In contrast, the prefactor of Eq. (9.34) is 0.5PN ($x^{1/2}$) lower than that of Eq. (9.28), thus the term $O(1)$ in $\hat{\Phi}_{lm}$ represents −0.5PN.

We depict the size of each PN term as solid lines with different colors in Fig. 9.14. For reference, the dashed lines represent the ones with all the PN contributions. The lowest PN order contributes the most, while higher PN corrections improve consistency. The amplitude of Ψ_{22} is the least accurate. Higher PN terms may be needed to improve the agreement with numerical simulations.

References

[1] Benjamin P. Abbott et al. "Binary black hole mergers in the first advanced LIGO observing run." *Phys. Rev.* X6.4 (2016). [erratum: Phys. Rev.X8,no.3,039903(2018)], p. 041015. DOI: 10.1103/PhysRevX.6.041015,10.1103/PhysRevX.8.039903. arXiv: 1606.04856 [gr-qc].

[2] Benjamin P. Abbott et al. "GWTC-1: A gravitational-wave transient catalog of compact binary mergers observed by LIGO and Virgo during the first and second observing runs." *Phys. Rev. X* 9.3 (2019), p. 031040. DOI: 10.1103/PhysRevX.9.031040. arXiv: 1811.12907 [astro-ph.HE].

[3] Richard Abbott et al. "GWTC-2: Compact binary coalescences observed by LIGO and Virgo during the first half of the third observing run." *Phys. Rev.*

X 11 (2021), p. 021053. DOI: 10.1103/PhysRevX.11.021053. arXiv: 2010.14527 [gr-qc].

[4] Richard Abbott et al. "GWTC-3: Compact binary coalescences observed by LIGO and Virgo during the second part of the third observing run." (Nov. 2021). arXiv: 2111.03606 [gr-qc].

[5] Sizheng Ma and Nicolas Yunes. "Improved Constraints on Modified Gravity with Eccentric gravitational waves." *Phys. Rev. D* 100.12 (2019), p. 124032. DOI: 10.1103/PhysRevD.100.124032. arXiv: 1908.07089 [gr-qc].

[6] Zack Carson, Brian C. Seymour, and Kent Yagi. "Future prospects for probing scalar–tensor theories with gravitational waves from mixed binaries." *Class. Quant. Grav.* 37.6 (2020), p. 065008. DOI: 10.1088/1361-6382/ab6a1f. arXiv: 1907.03897 [gr-qc].

[7] Laura Sampson et al. "Projected Constraints on scalarization with gravitational waves from Neutron star Binaries." *Phys. Rev. D* 90.12 (2014), p. 124091. DOI: 10.1103/PhysRevD.90.124091. arXiv: 1407.7038 [gr-qc].

[8] Paul D. Scharre and Clifford M. Will. "Testing scalar tensor gravity using space gravitational wave interferometers." *Phys. Rev. D* 65 (2002), p. 042002. DOI: 10.1103/PhysRevD.65.042002. arXiv: gr-qc/0109044.

[9] Clifford M. Will and Nicolas Yunes. "Testing alternative theories of gravity using LISA." *Class. Quant. Grav.* 21 (2004), p. 4367. DOI: 10.1088/0264-9381/21/18/006. arXiv: gr-qc/0403100.

[10] Emanuele Berti, Alessandra Buonanno, and Clifford M. Will. "Testing general relativity and probing the merger history of massive black holes with LISA." *Class. Quant. Grav.* 22 (2005). Ed. by B. Mours and F. Marion, S943–S954. DOI: 10.1088/0264-9381/22/18/S08. arXiv: gr-qc/0504017.

[11] Emanuele Berti, Alessandra Buonanno, and Clifford M. Will. "Estimating spinning binary parameters and testing alternative theories of gravity with LISA." *Phys. Rev. D* 71 (2005), p. 084025. DOI: 10.1103/PhysRevD.71.084025. arXiv: gr-qc/0411129.

[12] Kent Yagi and Takahiro Tanaka. "Constraining alternative theories of gravity by gravitational waves from precessing eccentric compact binaries with LISA." *Phys. Rev. D* 81 (2010). [Erratum: Phys.Rev.D 81, 109902 (2010)], p. 064008. DOI: 10.1103/PhysRevD.81.109902. arXiv: 0906.4269 [gr-qc].

[13] Kodanad G. Arun. "Generic bounds on dipolar gravitational radiation from inspiralling compact binaries." *Class. Quant. Grav.* 29 (2012), p. 075011. DOI: 10.1088/0264-9381/29/7/075011. arXiv: 1202.5911 [gr-qc].

[14] Vitor Cardoso et al. “Floating and sinking: The Imprint of massive scalars around rotating black holes.” *Phys. Rev. Lett.* 107 (2011), p. 241101. DOI: 10.1103/PhysRevLett.107.241101. arXiv: 1109.6021 [gr-qc].

[15] Benjamin P. Abbott et al. “Tests of general relativity with GW150914.” *Phys. Rev. Lett.* 116.22 (2016). [Erratum: Phys.Rev.Lett. 121, 129902 (2018)], p. 221101. DOI: 10.1103/PhysRevLett.116.221101. arXiv: 1602.03841 [gr-qc].

[16] Nicolas Yunes, Paolo Pani, and Vitor Cardoso. “Gravitational waves from Quasicircular extreme mass-ratio inspirals as Probes of scalar-tensor theories.” *Phys. Rev. D* 85 (2012), p. 102003. DOI: 10.1103/PhysRevD.85.102003. arXiv: 1112.3351 [gr-qc].

[17] Emanuele Berti et al. “Light scalar field constraints from gravitational-wave observations of compact binaries.” *Phys. Rev. D* 85 (2012), p. 122005. DOI: 10.1103/PhysRevD.85.122005. arXiv: 1204.4340 [gr-qc].

[18] Semih Tuna, Kivanç İ. Ünlütürk, and Fethi M. Ramazanoğlu. “Constraining scalar-tensor theories using neutron star mass and radius measurements.” *Phys. Rev. D* 105.12 (2022), p. 124070. DOI: 10.1103/PhysRevD.105.124070. arXiv: 2204.02138 [gr-qc].

[19] Clifford M. Will. “The Confrontation between General relativity and Experiment.” *Living Rev. Rel.* 17 (2014), p. 4. DOI: 10.12942/lrr-2014-4. arXiv: 1403.7377 [gr-qc].

[20] Nicolás Yunes and Xavier Siemens. “Gravitational-wave tests of general relativity with ground-based detectors and pulsar timing-arrays.” *Living Rev. Rel.* 16 (2013), p. 9. DOI: 10.12942/lrr-2013-9. arXiv: 1304.3473 [gr-qc].

[21] Nicolas Yunes, Kent Yagi, and Frans Pretorius. “Theoretical physics implications of the binary black-hole mergers GW150914 and GW151226.” *Phys. Rev. D* 94.8 (2016), p. 084002. DOI: 10.1103/PhysRevD.94.084002. arXiv: 1603.08955 [gr-qc].

[22] Emanuele Berti et al. “Testing general relativity with present and future astrophysical observations.” *Class. Quant. Grav.* 32 (2015), p. 243001. DOI: 10.1088/0264-9381/32/24/243001. arXiv: 1501.07274 [gr-qc].

[23] Benjamin P. Abbott et al. “Tests of general relativity with GW170817.” *Phys. Rev. Lett.* 123.1 (2019), p. 011102. DOI: 10.1103/PhysRevLett.123.011102. arXiv: 1811.00364 [gr-qc].

[24] Andrzej Krolak, Kostas D. Kokkotas, and Gerhard Schaefer. “On estimation of the postNewtonian parameters in the gravitational wave emission of a coalescing binary.” *Phys. Rev. D* 52 (1995), pp. 2089–2111. DOI: 10.1103/PhysRevD.52.2089. arXiv: gr-qc/9503013.

[25] Kent Yagi and Takahiro Tanaka. "DECIGO/BBO as a probe to constrain alternative theories of gravity." *Prog. Theor. Phys.* 123 (2010), pp. 1069–1078. DOI: 10.1143/PTP.123.1069. arXiv: 0908.3283 [gr-qc].

[26] Pascual Jordan. "Schwerkraft und Weltall: Grundlagen der theoretischen Kosmologie." *Die Wissenschaft* (1955).

[27] Markus Fierz. "On the physical interpretation of P. Jordan's extended theory of gravitation." *Helv. Phys. Acta* 29 (1956), pp. 128–134.

[28] Carl Brans and Robert H. Dicke. "Mach's principle and a relativistic theory of gravitation." *Phys. Rev.* 124 (3 Nov. 1961), pp. 925–935. DOI: 10.1103/PhysRev.124.925. URL: https://link.aps.org/doi/10.1103/PhysRev.124.925.

[29] Carl H. Brans. "Scalar-tensor theories of gravity: Some personal history." *Gravitation and Cosmology*. Ed. by Alfredo Herrera-Aguilar et al. Vol. 1083. American Institute of Physics Conference Series. Dec. 2008, pp. 34–46. DOI: 10.1063/1.3058577.

[30] Peter G Bergmann. "Comments on the scalar-tensor theory." *International Journal of Theoretical Physics* 1.1 (1968), pp. 25–36.

[31] Robert V. Wagoner. "Scalar tensor theory and gravitational waves." *Phys. Rev. D* 1 (1970), pp. 3209–3216. DOI: 10.1103/PhysRevD.1.3209.

[32] Thibault Damour and Gilles Esposito-Farese. "Tensor multiscalar theories of gravitation." *Class. Quant. Grav.* 9 (1992), pp. 2093–2176. DOI: 10.1088/0264-9381/9/9/015.

[33] Clifford M. Will and Helmut W. Zaglauer. "Gravitational radiation, close binary systems, and the Brans-Dicke theory of gravity." *Astrophys. J.* 346 (Nov. 1989), p. 366. DOI: 10.1086/168016.

[34] Maura Brunetti et al. "Gravitational wave radiation from compact binary systems in the Jordan-Brans-Dicke theory." *Phys. Rev. D* 59 (1999), p. 044027. DOI: 10.1103/PhysRevD.59.044027. arXiv: gr-qc/9805056.

[35] Clifford M. Will. "Testing scalar - tensor gravity with gravitational wave observations of inspiraling compact binaries." *Phys. Rev. D* 50 (1994), pp. 6058–6067. DOI: 10.1103/PhysRevD.50.6058. arXiv: gr-qc/9406022.

[36] Ryan N. Lang. "Compact binary systems in scalar-tensor gravity. II. Tensor gravitational waves to second post-Newtonian order." *Phys. Rev. D* 89.8 (2014), p. 084014. DOI: 10.1103/PhysRevD.89.084014. arXiv: 1310.3320 [gr-qc].

[37] Noah Sennett, Sylvain Marsat, and Alessandra Buonanno. "Gravitational waveforms in scalar-tensor gravity at 2PN relative order." *Phys. Rev. D* 94.8 (2016), p. 084003. DOI: 10.1103/PhysRevD.94.084003. arXiv: 1607.01420 [gr-qc].

[38] Ryan N. Lang. "Compact binary systems in scalar-tensor gravity. III. Scalar waves and energy flux." *Phys. Rev. D* 91.8 (2015), p. 084027. DOI: 10.1103/PhysRevD.91.084027. arXiv: 1411.3073 [gr-qc].

[39] Laura Bernard, Luc Blanchet, and David Trestini. "Gravitational waves in scalar-tensor theory to one-and-a-half post-Newtonian order." *JCAP* 08.08 (2022), p. 008. DOI: 10.1088/1475-7516/2022/08/008. arXiv: 2201.10924 [gr-qc].

[40] Motoyuki Saijo, Hisa-aki Shinkai, and Kei-ichi Maeda. "Gravitational waves in Brans-Dicke theory : Analysis by test particles around a Kerr black hole." *Phys. Rev. D* 56 (1997), pp. 785–797. DOI: 10.1103/PhysRevD.56.785. arXiv: gr-qc/9701001.

[41] Douglas M. Eardley. "Observable effects of a scalar gravitational field in a binary pulsar." *Astrophys. J. Lett.* 196 (Mar. 1975), pp. L59–L62. DOI: 10.1086/181744.

[42] Thibault Damour and Gilles Esposito-Farese. "Testing gravity to second postNewtonian order: A field theory approach." *Phys. Rev. D* 53 (1996), pp. 5541–5578. DOI: 10.1103/PhysRevD.53.5541. arXiv: gr-qc/9506063.

[43] Saeed Mirshekari and Clifford M. Will. "Compact binary systems in scalar-tensor gravity: Equations of motion to 2.5 post-Newtonian order." *Phys. Rev. D* 87.8 (2013), p. 084070. DOI: 10.1103/PhysRevD.87.084070. arXiv: 1301.4680 [gr-qc].

[44] Laura Bernard. "Dynamics of compact binary systems in scalar-tensor theories: Equations of motion to the third post-Newtonian order." *Phys. Rev. D* 98.4 (2018), p. 044004. DOI: 10.1103/PhysRevD.98.044004. arXiv: 1802.10201 [gr-qc].

[45] Laura Bernard. "Dynamics of compact binary systems in scalar-tensor theories: II. Center-of-mass and conserved quantities to 3PN order." *Phys. Rev. D* 99.4 (2019), p. 044047. DOI: 10.1103/PhysRevD.99.044047. arXiv: 1812.04169 [gr-qc].

[46] Clifford M. Will. "Gravitational radiation from binary systems in alternative metric theories of gravity: dipole radiation and the binary pulsar." *Astrophys. J.* 214 (June 1977), pp. 826–839. DOI: 10.1086/155313.

[47] Lijing Shao et al. "Constraining nonperturbative strong-field effects in scalar-tensor gravity by combining pulsar timing and laser-interferometer gravitational-wave detectors." *Phys. Rev. X* 7.4 (2017), p. 041025. DOI: 10.1103/PhysRevX.7.041025. arXiv: 1704.07561 [gr-qc].

[48] David Anderson, Paulo Freire, and Nicolás Yunes. "Binary pulsar constraints on massless scalar–tensor theories using Bayesian statistics." *Class. Quant. Grav.* 36.22 (2019), p. 225009. DOI: 10.1088/1361-6382/ab3a1c. arXiv: 1901.00938 [gr-qc].

[49] Anne M. Archibald et al. "Universality of free fall from the orbital motion of a pulsar in a stellar triple system." *Nature* 559.7712 (2018), pp. 73–76. DOI: 10.1038/s41586-018-0265-1. arXiv: 1807.02059 [astro-ph.HE].

[50] John Antoniadis et al. "A massive pulsar in a compact relativistic binary." *Science* 340 (2013), p. 6131. DOI: 10.1126/science.1233232. arXiv: 1304.6875 [astro-ph.HE].

[51] Junjie Zhao et al. "Reduced-order surrogate models for scalar-tensor gravity in the strong field regime and applications to binary pulsars and GW170817." *Phys. Rev. D* 100.6 (2019), p. 064034. DOI: 10.1103/PhysRevD.100.064034. arXiv: 1907.00780 [gr-qc].

[52] Junjie Zhao et al. "Closing a spontaneous-scalarization window with binary pulsars." *Class. Quant. Grav.* 39.11 (2022), 11LT01. DOI: 10.1088/1361-6382/ac69a3. arXiv: 2201.03771 [astro-ph.HE].

[53] Thibault Damour and J. H. Taylor. "Strong-field tests of relativistic gravity and binary pulsars." *Phys. Rev. D* 45 (6 Mar. 1992), pp. 1840–1868. DOI: 10.1103/PhysRevD.45.1840. URL: https://link.aps.org/doi/10.1103/PhysRevD.45.1840.

[54] Thibault Damour and Gilles Esposito-Farese. "Tensor - scalar gravity and binary pulsar experiments." *Phys. Rev. D* 54 (1996), pp. 1474–1491. DOI: 10.1103/PhysRevD.54.1474. arXiv: gr-qc/9602056.

[55] Thibault Damour and Gilles Esposito-Farese. "Gravitational wave versus binary - pulsar tests of strong field gravity." *Phys. Rev. D* 58 (1998), p. 042001. DOI: 10.1103/PhysRevD.58.042001. arXiv: gr-qc/9803031.

[56] Joseph H. Taylor et al. "Experimental constraints on strong field relativistic gravity." *Nature* (Oct. 1991). DOI: 10.1038/355132a0.

[57] Dimitrios Psaltis. "Constraining Brans-Dicke gravity with millisecond pulsars in ultracompact binaries." (Jan. 2005). arXiv: astro-ph/0501234.

[58] Paulo C. C. Freire et al. "The relativistic pulsar-white dwarf binary PSR J1738+0333 II. The most stringent test of scalar-tensor gravity." *Mon. Not. Roy. Astron. Soc.* 423 (2012), p. 3328. DOI: 10.1111/j.1365-2966.2012.21253.x. arXiv: 1205.1450 [astro-ph.GA].

[59] Ingrid H. Stairs. "Testing general relativity with pulsar timing." *Living Rev. Rel.* 6 (2003), p. 5. DOI: 10.12942/lrr-2003-5. arXiv: astro-ph/0307536.

[60] Lijing Shao and Norbert Wex. "Tests of gravitational symmetries with radio pulsars." *Sci. China Phys. Mech. Astron.* 59.9 (2016), p. 699501. DOI: 10.1007/s11433-016-0087-6. arXiv: 1604.03662 [gr-qc].

[61] Michael Kramer. "Pulsars as probes of gravity and fundamental physics." *Int. J. Mod. Phys. D* 25.14 (2016), p. 1630029. DOI: 10.1142/S0218271816300299. arXiv: 1606.03843 [astro-ph.HE].

[62] Norbert Wex. "Testing relativistic gravity with radio pulsars." (Feb. 2014). arXiv: 1402.5594 [gr-qc].

[63] Gilles Esposito-Farese. "Binary pulsar tests of strong field gravity and gravitational radiation damping." *10th Marcel Grossmann Meeting on Recent Developments in Theoretical and Experimental General relativity, Gravitation and relativistic Field Theories (MG X MMIII)*. Feb. 2004, pp. 647–666. DOI: 10.1142/9789812704030_0039. arXiv: gr-qc/0402007.

[64] Michael Kramer and Norbert Wex. "The double pulsar system: A unique laboratory for gravity." *Class. Quant. Grav.* 26 (2009), p. 073001. DOI: 10.1088/0264-9381/26/7/073001.

[65] Thibault Damour. "Binary systems as test-beds of gravity theories." *6th SIGRAV Graduate School in Contemporary Relativity and Gravitational Physics: A Century from Einstein Relativity: Probing Gravity Theories in binary Systems*. Apr. 2007. arXiv: 0704.0749 [gr-qc].

[66] Russell Alan Hulse and Joseph Hooton Taylor. "Discovery of a pulsar in a binary system." *Astrophys. J. Lett.* 195 (Jan. 1975), pp. L51–L53. DOI: 10.1086/181708.

[67] Michael W. Horbatsch and Cliff P. Burgess. "Model-independent comparisons of pulsar timings to scalar-tensor gravity." *Class. Quant. Grav.* 29 (2012), p. 245004. DOI: 10.1088/0264-9381/29/24/245004. arXiv: 1107.3585 [gr-qc].

[68] Thibault Damour and Gilles Esposito-Farese. "Nonperturbative strong field effects in tensor - scalar theories of gravitation." *Phys. Rev. Lett.* 70 (1993), pp. 2220–2223. DOI: 10.1103/PhysRevLett.70.2220.

[69] David Anderson and Nicolás Yunes. "Scalar charges and scaling relations in massless scalar–tensor theories." *Class. Quant. Grav.* 36.16 (2019), p. 165003. DOI: 10.1088/1361-6382/ab2eda. arXiv: 1901.00937 [gr-qc].

[70] Kip S. Thorne and John J. Dykla. "Black holes in the Dicke-Brans Theory of gravity." *Astrophys. J. Lett.* 166 (June 1971), p. L35. DOI: 10.1086/180734.

[71] Thomas P. Sotiriou and Valerio Faraoni. "Black holes in scalar-tensor gravity." *Phys. Rev. Lett.* 108 (2012), p. 081103. DOI: 10.1103/PhysRevLett.108.081103. arXiv: 1109.6324 [gr-qc].

[72] Stephen W. Hawking. "Black holes in the Brans-Dicke theory of gravitation." *Commun. Math. Phys.* 25 (1972), pp. 167–171. DOI: 10.1007/BF01877518.

[73] James Healy et al. "Late inspiral and merger of binary black holes in scalar-tensor theories of gravity." *Class. Quant. Grav.* 29 (2012), p. 232002. DOI: 10.1088/0264-9381/29/23/232002. arXiv: 1112.3928 [gr-qc].

[74] Enrico Barausse et al. "Neutron-star mergers in scalar-tensor theories of gravity." *Phys. Rev. D* 87 (2013), p. 081506. DOI: 10.1103/PhysRevD.87.081506. arXiv: 1212.5053 [gr-qc].

[75] Masaru Shibata et al. "Coalescence of binary neutron stars in a scalar-tensor theory of gravity." *Phys. Rev. D* 89.8 (2014), p. 084005. DOI: 10.1103/PhysRevD.89.084005. arXiv: 1310.0627 [gr-qc].

[76] Keisuke Taniguchi, Masaru Shibata, and Alessandra Buonanno. "Quasiequilibrium sequences of binary neutron stars undergoing dynamical scalarization." *Phys. Rev. D* 91.2 (2015), p. 024033. DOI: 10.1103/PhysRevD.91.024033. arXiv: 1410.0738 [gr-qc].

[77] Carlos Palenzuela et al. "Dynamical scalarization of neutron stars in scalar-tensor gravity theories." *Phys. Rev. D* 89.4 (2014), p. 044024. DOI: 10.1103/PhysRevD.89.044024. arXiv: 1310.4481 [gr-qc].

[78] Noah Sennett and Alessandra Buonanno. "Modeling dynamical scalarization with a resummed post-Newtonian expansion." *Phys. Rev. D* 93.12 (2016), p. 124004. DOI: 10.1103/PhysRevD.93.124004. arXiv: 1603.03300 [gr-qc].

[79] Noah Sennett, Lijing Shao, and Jan Steinhoff. "Effective action model of dynamically scalarizing binary neutron stars." *Phys. Rev. D* 96.8 (2017), p. 084019. DOI: 10.1103/PhysRevD.96.084019. arXiv: 1708.08285 [gr-qc].

[80] Hajime Sotani. "Slowly rotating relativistic stars in scalar-tensor gravity." *Phys. Rev. D* 86 (2012), p. 124036. DOI: 10.1103/PhysRevD.86.124036. arXiv: 1211.6986 [astro-ph.HE].

[81] Daniela D. Doneva et al. "Scalarization." (Nov. 2022). arXiv: 2211.01766 [gr-qc].

[82] Fethi M. Ramazanoğlu and Frans Pretorius. "Spontaneous scalarization with massive fields." *Phys. Rev. D* 93.6 (2016), p. 064005. DOI: 10.1103/PhysRevD.93.064005. arXiv: 1601.07475 [gr-qc].

[83] Roxana Rosca-Mead et al. "Core collapse in massive scalar-tensor gravity." *Phys. Rev. D* 102.4 (2020), p. 044010. DOI: 10.1103/PhysRevD.102.044010. arXiv: 2005.09728 [gr-qc].

[84] Tomohiro Harada. "Stability analysis of spherically symmetric star in scalar - tensor theories of gravity." *Prog. Theor. Phys.* 98 (1997), pp. 359–379. DOI: 10.1143/PTP.98.359. arXiv: gr-qc/9706014.

[85] Tomohiro Harada. "Neutron stars in scalar tensor theories of gravity and catastrophe theory." *Phys. Rev. D* 57 (1998), pp. 4802–4811. DOI: 10.1103/PhysRevD.57.4802. arXiv: gr-qc/9801049.

[86] J. Aasi et al. "Advanced LIGO." *Class. Quant. Grav.* 32 (2015), p. 074001. DOI: 10.1088/0264-9381/32/7/074001. arXiv: 1411.4547 [gr-qc].

[87] Fausto Acernese et al. "Advanced Virgo: a second-generation interferometric gravitational wave detector." *Class. Quant. Grav.* 32.2 (2015), p. 024001. DOI: 10.1088/0264-9381/32/2/024001. arXiv: 1408.3978 [gr-qc].

[88] Richard Abbott et al. "Observation of gravitational waves from two neutron star–black hole coalescences." *Astrophys. J. Lett.* 915.1 (2021), p. L5. DOI: 10.3847/2041-8213/ac082e. arXiv: 2106.15163 [astro-ph.HE].

[89] Benjamin P. Abbott et al. "Prospects for observing and localizing gravitational-wave transients with advanced LIGO, Advanced Virgo and KAGRA." *Living Rev. Rel.* 21.1 (2018), p. 3. DOI: 10.1007/s41114-018-0012-9,10.1007/lrr-2016-1. arXiv: 1304.0670 [gr-qc].

[90] Michele Punturo et al. "The Einstein Telescope: A third-generation gravitational wave observatory." *Class. Quant. Grav.* 27 (2010), p. 194002. DOI: 10.1088/0264-9381/27/19/194002.

[91] Stefan Hild et al. "Sensitivity studies for third-generation gravitational wave observatories." *Class. Quant. Grav.* 28 (2011), p. 094013. DOI: 10.1088/0264-9381/28/9/094013. arXiv: 1012.0908 [gr-qc].

[92] Benjamin P Abbott et al. "Exploring the sensitivity of next generation gravitational wave detectors." *Class. Quant. Grav.* 34.4 (2017), p. 044001. DOI: 10.1088/1361-6382/aa51f4. arXiv: 1607.08697 [astro-ph.IM].

[93] David Reitze et al. "Cosmic Explorer: The U.S. contribution to gravitational-wave astronomy beyond LIGO." *Bull. Am. Astron. Soc.* 51 (July 2019), p. 035. arXiv: 1907.04833 [astro-ph.IM].

[94] Mohammed Khalil et al. "Theory-agnostic framework for dynamical scalarization of compact binaries." *Phys. Rev. D* 100.12 (2019), p. 124013. DOI: 10.1103/PhysRevD.100.124013. arXiv: 1906.08161 [gr-qc].

[95] Mohammed Khalil et al. "Effective-action model for dynamical scalarization beyond the adiabatic approximation." *Phys. Rev. D* 106.10 (2022), p. 104016. DOI: 10.1103/PhysRevD.106.104016. arXiv: 2206.13233 [gr-qc].

[96] Laura Bernard. "Dipolar tidal effects in scalar-tensor theories." *Phys. Rev. D* 101.2 (2020), p. 021501. DOI: 10.1103/PhysRevD.101.021501. arXiv: 1906.10735 [gr-qc].

[97] Tomohiro Harada et al. "Scalar gravitational wave from Oppenheimer-Snyder collapse in scalar - tensor theories of gravity." *Phys. Rev. D* 55 (1997), pp. 2024–2037. DOI: 10.1103/PhysRevD.55.2024. arXiv: gr-qc/9611031.

[98] Miguel Bezares et al. "No evidence of kinetic screening in simulations of merging binary neutron stars beyond general relativity." *Phys. Rev. Lett.* 128.9 (2022), p. 091103. DOI: 10.1103/PhysRevLett.128.091103. arXiv: 2107.05648 [gr-qc].

[99] Mark A. Scheel, Stuart L. Shapiro, and Saul A. Teukolsky. "Collapse to black holes in Brans-Dicke theory. 2. Comparison with general relativity." *Phys. Rev. D* 51 (1995), pp. 4236–4249. DOI: 10.1103/PhysRevD.51.4236. arXiv: gr-qc/9411026.

[100] Mark A. Scheel, Stuart L. Shapiro, and Saul A. Teukolsky. "Collapse to black holes in Brans-Dicke theory. 1. Horizon boundary conditions for dynamical space-times." *Phys. Rev. D* 51 (1995), pp. 4208–4235. DOI: 10.1103/PhysRevD.51.4208. arXiv: gr-qc/9411025.

[101] Masaru Shibata, Ken-ichi Nakao, and Takashi Nakamura. "Scalar type gravitational wave emission from gravitational collapse in Brans-Dicke theory: Detectability by a laser interferometer." *Phys. Rev. D* 50 (1994), pp. 7304–7317. DOI: 10.1103/PhysRevD.50.7304.

[102] Takuya Matsuda and Hidekazu Nariai. "Hydrodynamic calculations of spherical gravitational collapse in the scalar-tensor theory of gravity." *Progress of Theoretical Physics* 49.4 (Apr. 1973), pp. 1195–1204. ISSN: 0033-068X. DOI: 10.1143/PTP.49.1195. eprint: https://academic.oup.com/ptp/article-pdf/49/4/1195/5444774/49-4-1195.pdf. URL: https://doi.org/10.1143/PTP.49.1195.

[103] Jerome Novak. "Spherical neutron star collapse in tensor - scalar theory of gravity." *Phys. Rev. D* 57 (1998), pp. 4789–4801. DOI: 10.1103/PhysRevD.57.4789. arXiv: gr-qc/9707041.

[104] *The Spectral Einstein Code*. http://www.black-holes.org/SpEC.html.

[105] *Simulating eXtreme Spacetimes*. http://www.black-holes.org/..

[106] Lee Lindblom et al. "A new generalized harmonic evolution system." *Class. Quant. Grav.* 23 (2006), S447–S462. DOI: 10.1088/0264-9381/23/16/S09. arXiv: gr-qc/0512093 [gr-qc].

[107] Michael Holst et al. "Optimal constraint projection for hyperbolic evolution systems." *Phys. Rev. D* 70 (2004), p. 084017. DOI: 10.1103/PhysRevD.70.084017. arXiv: gr-qc/0407011.

[108] Mark A. Scheel et al. "3-D simulations of linearized scalar fields in Kerr space-time." *Phys. Rev. D* 69 (2004), p. 104006. DOI: 10.1103/PhysRevD.69.104006. arXiv: gr-qc/0305027.

[109] Matthew D. Duez et al. "Evolving black hole-neutron star binaries in general relativity using pseudospectral and finite difference methods." *Phys. Rev. D* 78 (2008), p. 104015. DOI: 10.1103/PhysRevD.78.104015. arXiv: 0809.0002 [gr-qc].

[110] Michael Boyle and Abdul H. Mroue. "Extrapolating gravitational-wave data from numerical simulations." *Phys. Rev.* D80 (2009), p. 124045. DOI: 10.1103/PhysRevD.80.124045. arXiv: 0905.3177 [gr-qc].

[111] Dante A. B. Iozzo et al. "Extending gravitational wave extraction using Weyl characteristic fields." *Phys. Rev. D* 103.2 (2021), p. 024039. DOI: 10.1103/PhysRevD.103.024039. arXiv: 2010.15200 [gr-qc].

[112] Jordan Moxon, Mark A. Scheel, and Saul A. Teukolsky. "Improved Cauchy-characteristic evolution system for high-precision numerical relativity waveforms." *Phys. Rev. D* 102.4 (2020), p. 044052. DOI: 10.1103/PhysRevD.102.044052. arXiv: 2007.01339 [gr-qc].

[113] Jordan Moxon et al. "The SpECTRE Cauchy-characteristic evolution system for rapid, precise waveform extraction." (Oct. 2021). arXiv: 2110.08635 [gr-qc].

[114] Eric Poisson and Clifford M Will. *Gravity: Newtonian, post-newtonian, relativistic*. Cambridge University Press, 2014.

[115] Michael Boyle. "Angular velocity of gravitational radiation from precessing binaries and the corotating frame." *Phys. Rev.* D87.10 (2013), p. 104006. DOI: 10.1103/PhysRevD.87.104006. arXiv: 1302.2919 [gr-qc].

[116] Michael Boyle et al. "Gravitational-wave modes from precessing black-hole binaries." (Sept. 2014). arXiv: 1409.4431 [gr-qc].

[117] Michael Boyle. "Transformations of asymptotic gravitational-wave data." *Phys. Rev.* D93.8 (2016), p. 084031. DOI: 10.1103/PhysRevD.93.084031. arXiv: 1509.00862 [gr-qc].

[118] Michael Boyle. *Scri*. https://github.com/moble/scri.

[119] Mike Boyle, Dante Iozzo, and Leo C. Stein. *moble/scri: v1.2*. Version v1.2. Sept. 2020. DOI: 10.5281/zenodo.4041972. URL: https://doi.org/10.5281/zenodo.4041972.

[120] Alessandra Buonanno et al. "Reducing orbital eccentricity of precessing black-hole binaries." *Phys. Rev.* D83 (2011), p. 104034. DOI: 10.1103/PhysRevD.83.104034. arXiv: 1012.1549 [gr-qc].

[121] Kent Yagi and Michael Stepniczka. "Neutron stars in scalar-tensor theories: Analytic scalar charges and universal relations." *Phys. Rev. D* 104.4 (2021), p. 044017. DOI: 10.1103/PhysRevD.104.044017. arXiv: 2105.01614 [gr-qc].

[122] Thibault Damour and Gilles Esposito-Farèse. "Nonperturbative strong-field effects in tensor-scalar theories of gravitation." *Phys. Rev. Lett.* 70 (15 Apr. 1993), pp. 2220–2223. DOI: 10.1103/PhysRevLett.70.2220. URL: https://link.aps.org/doi/10.1103/PhysRevLett.70.2220.

[123] David Anderson, Nicolas Yunes, and Enrico Barausse. "Effect of cosmological evolution on solar system constraints and on the scalarization of neutron stars in massless scalar-tensor theories." *Phys. Rev. D* 94.10 (2016), p. 104064. DOI: 10.1103/PhysRevD.94.104064. arXiv: 1607.08888 [gr-qc].

[124] Paul J. Steinhardt and Clifford M. Will. "High frequency oscillations of Newton's constant induced by inflation." *Phys. Rev. D* 52 (1995), pp. 628–639. DOI: 10.1103/PhysRevD.52.628. arXiv: astro-ph/9409041.

[125] Bruno Boisseau et al. "Reconstruction of a scalar tensor theory of gravity in an accelerating universe." *Phys. Rev. Lett.* 85 (2000), p. 2236. DOI: 10.1103/PhysRevLett.85.2236. arXiv: gr-qc/0001066.

[126] Bruno Bertotti, Luciano Iess, and Paolo Tortora. "A test of general relativity using radio links with the Cassini spacecraft." *Nature* 425 (2003), pp. 374–376. DOI: 10.1038/nature01997.

[127] Francois Foucart et al. "Smooth equations of state for high-accuracy simulations of neutron star binaries." *Phys. Rev. D* 100.10 (2019), p. 104048. DOI: 10.1103/PhysRevD.100.104048. arXiv: 1908.05277 [gr-qc].

[128] Tanja Hinderer. "Tidal love numbers of neutron stars." *Astrophys. J.* 677 (2008), pp. 1216–1220. DOI: 10.1086/533487. arXiv: 0711.2420 [astro-ph].

[129] Eanna E. Flanagan and Tanja Hinderer. "Constraining neutron star tidal Love numbers with gravitational wave detectors." *Phys. Rev. D* 77 (2008), p. 021502. DOI: 10.1103/PhysRevD.77.021502. arXiv: 0709.1915 [astro-ph].

[130] Béla Szilágyi. "Key elements of robustness in binary black hole evolutions using spectral methods." *Int. J. Mod. Phys.* D23.7 (2014), p. 1430014. DOI: 10.1142/S0218271814300146. arXiv: 1405.3693 [gr-qc].

[131] Francois Foucart et al. "Initial data for black hole-neutron star binaries: A flexible, high-accuracy spectral method." *Phys. Rev. D* 77 (2008), p. 124051. DOI: 10.1103/PhysRevD.77.124051. arXiv: 0804.3787 [gr-qc].

[132] Nick Tacik et al. "Initial data for black hole–neutron star binaries, with rotating stars." *Class. Quant. Grav.* 33.22 (2016), p. 225012. DOI: 10.1088/0264-9381/33/22/225012. arXiv: 1607.07962 [gr-qc].

[133] Francois Foucart et al. "High-accuracy waveforms for black hole-neutron star systems with spinning black holes." *Phys. Rev. D* 103.6 (2021), p. 064007. DOI: 10.1103/PhysRevD.103.064007. arXiv: 2010.14518 [gr-qc].

[134] Leslie Wade et al. "Systematic and statistical errors in a bayesian approach to the estimation of the neutron-star equation of state using advanced gravitational wave detectors." *Phys. Rev. D* 89.10 (2014), p. 103012. DOI: 10.1103/PhysRevD.89.103012. arXiv: 1402.5156 [gr-qc].

[135] Vijay Varma et al. "Surrogate models for precessing binary black hole simulations with unequal masses." *Phys. Rev. Research.* 1 (2019), p. 033015. DOI: 10.1103/PhysRevResearch.1.033015. arXiv: 1905.09300 [gr-qc].

[136] Lawrence E. Kidder. "Coalescing binary systems of compact objects to post-Newtonian 5/2 order. 5. Spin effects." *Phys. Rev. D* 52 (1995), pp. 821–847. DOI: 10.1103/PhysRevD.52.821. arXiv: gr-qc/9506022.

[137] Eanna E. Flanagan and Scott A. Hughes. "Measuring gravitational waves from binary black hole coalescences: 2. The Waves' information and its extraction, with and without templates." *Phys. Rev.* D57 (1998), pp. 4566–4587. DOI: 10.1103/PhysRevD.57.4566. arXiv: gr-qc/9710129 [gr-qc].

[138] Lee Lindblom, Benjamin J. Owen, and Duncan A. Brown. "Model Waveform Accuracy Standards for gravitational wave Data Analysis." *Phys. Rev.* D78 (2008), p. 124020. DOI: 10.1103/PhysRevD.78.124020. arXiv: 0809.3844 [gr-qc].

[139] Sean T. McWilliams, Bernard J. Kelly, and John G. Baker. "Observing mergers of non-spinning black-hole binaries." *Phys. Rev.* D82 (2010), p. 024014. DOI: 10.1103/PhysRevD.82.024014. arXiv: 1004.0961 [gr-qc].

[140] Katerina Chatziioannou et al. "Constructing gravitational waves from Generic Spin-precessing compact binary inspirals." *Phys. Rev.* D95.10 (2017), p. 104004. DOI: 10.1103/PhysRevD.95.104004. arXiv: 1703.03967 [gr-qc].

[141] Michael Boyle et al. "The SXS collaboration catalog of binary black hole simulations." *Class. Quant. Grav.* 36.19 (2019), p. 195006. DOI: 10.1088/1361-6382/ab34e2. arXiv: 1904.04831 [gr-qc].

[142] Tanja Hinderer et al. "Effects of neutron-star dynamic tides on gravitational waveforms within the effective-one-body approach." *Phys. Rev. Lett.* 116.18 (2016), p. 181101. DOI: 10.1103/PhysRevLett.116.181101. arXiv: 1602.00599 [gr-qc].

[143] Jan Steinhoff et al. "Dynamical tides in general relativity: Effective action and effective-one-body hamiltonian." *Phys. Rev.* D94.10 (2016), p. 104028. DOI: 10.1103/PhysRevD.94.104028. arXiv: 1608.01907 [gr-qc].

[144] Karl Wette. "WIGLAL: Python and Octave interfaces to the LALSuite gravitational-wave data analysis libraries." *SoftwareX* 12 (2020), p. 100634. DOI: 10.1016/j.softx.2020.100634.

[145] Francois Foucart, Tanja Hinderer, and Samaya Nissanke. "Remnant baryon mass in neutron star-black hole mergers: Predictions for binary neutron star mimickers and rapidly spinning black holes." *Phys. Rev. D* 98.8 (2018), p. 081501. DOI: 10.1103/PhysRevD.98.081501. arXiv: 1807.00011 [astro-ph.HE].

[146] Ezra Newman and Roger Penrose. "An approach to gravitational radiation by a method of spin coefficients." *J. Math. Phys.* 3 (1962), pp. 566–578. DOI: 10.1063/1.1724257.

[147] Song Ming Du and Atsushi Nishizawa. "Gravitational wave memory: A new approach to study modified gravity." *Phys. Rev. D* 94.10 (2016), p. 104063. DOI: 10.1103/PhysRevD.94.104063. arXiv: 1609.09825 [gr-qc].

[148] Kazuya Koyama. "Testing Brans-Dicke gravity with screening by scalar gravitational wave memory." *Phys. Rev. D* 102.2 (2020), p. 021502. DOI: 10.1103/PhysRevD.102.021502. arXiv: 2006.15914 [gr-qc].

[149] Shaoqi Hou and Zong-Hong Zhu. "Gravitational memory effects and Bondi-Metzner-Sachs symmetries in scalar-tensor theories." *JHEP* 01 (2021), p. 083. DOI: 10.1007/JHEP01(2021)083. arXiv: 2005.01310 [gr-qc].

[150] Ali Seraj. "Gravitational breathing memory and dual symmetries." *JHEP* 05 (2021), p. 283. DOI: 10.1007/JHEP05(2021)283. arXiv: 2103.12185 [hep-th].

[151] Keefe Mitman et al. "Computation of displacement and spin gravitational memory in numerical relativity." *Phys. Rev. D* 102.10 (2020), p. 104007. DOI: 10.1103/PhysRevD.102.104007. arXiv: 2007.11562 [gr-qc].

[152] Keefe Mitman et al. "Adding gravitational memory to waveform catalogs using BMS balance laws." *Phys. Rev. D* 103.2 (2021), p. 024031. DOI: 10.1103/PhysRevD.103.024031. arXiv: 2011.01309 [gr-qc].

[153] Shammi Tahura et al. "Brans-Dicke theory in Bondi-Sachs form: Asymptotically flat solutions, asymptotic symmetries and gravitational-wave memory effects." *Phys. Rev. D* 103.10 (2021), p. 104026. DOI: 10.1103/PhysRevD.103.104026. arXiv: 2007.13799 [gr-qc].

[154] Shammi Tahura, David A. Nichols, and Kent Yagi. "Gravitational-wave memory effects in Brans-Dicke theory: Waveforms and effects in the post-Newtonian approximation." *Phys. Rev. D* 104.10 (2021), p. 104010. DOI: 10.1103/PhysRevD.104.104010. arXiv: 2107.02208 [gr-qc].

[155] Lavinia Heisenberg, Nicolás Yunes, and Jann Zosso. "Gravitational wave memory beyond general relativity." (Mar. 2023). arXiv: 2303.02021 [gr-qc].

[156] Thomas W. Baumgarte and Stuart L. Shapiro. *Numerical relativity: Solving Einstein's equations on the Computer*. Cambridge University Press, 2010. DOI: 10.1017/CBO9781139193344.

Chapter 10

GRAVITATIONAL-WAVE ECHOES FROM NUMERICAL-RELATIVITY WAVEFORMS VIA SPACE-TIME CONSTRUCTION NEAR MERGING COMPACT OBJECTS

[1] Sizheng Ma et al. "Gravitational-wave echoes from numerical-relativity waveforms via spacetime construction near merging compact objects." *Phys. Rev. D* 105.10 (2022), p. 104007. DOI: 10.1103/PhysRevD.105.104007. arXiv: 2203.03174 [gr-qc].

10.1 Introduction

Delayed and repeating gravitational wave echoes emitted by compact-binary mergers [1–3], following the main gravitational waves (GWs), can be signatures of (i) deviations of laws of gravity from general relativity [4, 5], (ii) near-horizon quantum structures surrounding black holes (BHs) [6–15], and (iii) the absence of event horizon, namely the existence of horizonless Exotic Compact Objects (ECOs) [16–20]. We must emphasize that strong arguments (within the context of general relativity and standard model of matter) exist against the existence of echoes and ECOs, including: (i) the ergoregion instability [21–24], (ii) the formation of a trapped surface due to the pileup of energy near the stable photon orbit [25–28], (iii) the collapse of ECO due to the gravity of incident GWs [29, 30], and (iv) other nonlinear effects [31]. Nevertheless, if GW echoes do exist, their detection will serve as an important tool for studying the physics of BHs or ECOs. A lot of efforts have been made to search for echoes in observed data (see Ref. [32] for a thorough review). As a result, constructing accurate waveform models for GW echoes is necessary and timely [33, 34].

If we restrict deviation from general relativity (GR) to be localized near the would-be horizon, then due to Birkhoff's theorem, the region outside a spherically symmetric ECO can still be described by a Schwarzschild geometry. Consequently, studies of echoes from non-spinning ECOs were mostly based on the black hole perturbation (BHP) theory and the Zerilli-Regge-Wheeler equations [35, 36]. For instance, Cardoso *et al.* [1, 2] showed that the initial ringdown signal of different ECO models has a universal feature, and is identical to that of a Schwarzschild BH, even

though the quasinormal mode (QNM) spectra of ECOs are completely different from the ones of the Schwarzschild BH. This implies that the initial pulse of the ringdown is more related to space-time geometry near the light ring, rather than the formal spectra of QNMs. The following echoes do depend on the structure of the QNM spectra [37], which is characterized by modes trapped between the ECO surface and the peak of BH potential barrier [38]. Mark *et al.* [39] developed a framework to systematically compute scalar echoes from non-spinning ECOs, in terms of GWs propagating toward the would-be horizon, and transfer functions that convert this horizon-going wave into echoes toward infinity. Testa *et al.* [40] used a Poschl-Teller potential to approximate the BH potential for perturbations, and derived an analytical echo template. Meanwhile, Ref. [41] estimated the contribution of GW echoes to stochastic background. In terms of the membrane diagram, Maggio *et al.* [42] and Chakraborty *et al.* [14] treated the ECO surface as a dissipative fluid, and related the reflectivity to the bulk and the shear viscosity. Cardoso *et al.* [43] studied resonant excitation of the modes of non-spinning ECOs during an extreme-mass-ratio inspiral. More recently, the echoes of fuzzballs [44, 45] were computed numerically in Ref. [46], and the GW echo from a three-body system was studied in Ref. [47].

In astrophysical situations, merger remnants usually have non-negligible spins [48], hence it is of great practical interest to model echoes from spinning ECOs. Even if GR is valid away from ECOs, the space-time geometry there can deviate significantly from Kerr, having a general multipole structure [49, 50]. Nevertheless, we shall restrict ourselves to Kerr geometry, whose linear perturbation is described by the Teukolsky equation [51, 52]. An early attempt towards constructing echo waveforms studied scalar perturbations around a Kerr-like wormhole [53]. Working on a sourceless system, Nakano *et al.* [54] imposed a complete reflecting boundary condition at a constant Boyer-Lindquist radius. Later, the effect of source terms was investigated [55–60]. Sago *et al.* [55] and Maggio *et al.* [56] studied main GWs and echoes generated by a particle that plunges into a Kerr black hole. The case of a particle (with scalar charge) spiraling into a Kerr black hole was studied in Ref. [57]. Refs. [58–60] further introduced the back-reaction of GW emissions on the orbital motion.

Recently, Chen *et al.* [61] proposed a more physically-motivated boundary condition, by considering the tidal fields experienced by fiducial observers with zero angular momentum orbiting just above the ECO surface. This model established a relation

between the ingoing component of the Weyl scalar ψ_0 and the outgoing piece of the Weyl scalar ψ_4. Using this new boundary condition, Xin *et al.* [59] calculated GW echoes by computing explicitly the ψ_4 falling down the ECO surface, and converting it to ψ_0 via the Teukolsky-Starobinsky (TS) identity [62, 63]. They found weaker echoes than those obtained from other approaches [11, 64]. A flaw in their calculation is that the TS identity is only applicable in the absence of source terms. A direct computation of ψ_0 propagating toward the ECO surface was later carried out by Srivastava *et al.* [60].

As we move away from extreme mass ratio inspirals, several approaches have been adopted to model echoes from comparable-mass binary black-hole (BBH) mergers. These include the *inside/outside* formulations, which do not involve modeling the merger dynamics; the adaptation of the Effective One-Body (EOB) [65, 66]; and the Close-Limit Approximation (CLA) approaches [67–70], which have played important roles in modeling BBH ringdown waveforms in GR.

In the *outside prescription* [71, 72], the main GR GW emitted by a BBH merger was modeled as having been generated by the reflection of an initial pulse originated from null infinity (see Fig. 1 in Ref. [71]). The rest of this pulse travels through the light-ring potential, bounces back and forth between the surface of ECO and the peak of the potential. As a result, a sequence of echoes follows the main GR GW at null infinity. In the *inside prescription* [11, 64], the main GR GW was modeled instead as the transmitted wave of an initial wave emerging from the past horizon (see Fig. 1 in Ref. [11]). Wang *et al.* [11] computed this initial wave by matching the main GW to that of a BBH merger event, whereas Maggio *et al.* [64] treated the main pulse as a superposition of QNMs, which led to analytical echo templates. Both the inside and outside prescriptions make direct connections between the main BBH GW and the ensuing echoes; they do not require detailed modeling of the merger dynamics.

In contrast, the approach based on the EOB formulation does rely on the orbital dynamics. Following the same spirit as the EOB method, Micchi *et al.* [58] considered the back-reaction on the orbital evolution due to GW emissions. With more accurate orbital dynamics, they were able to obtain a complete inspiral-merger-ringdown waveform and the subsequent echoes. Xin *et al.* [59] calibrated the dissipative force to a surrogate model [73, 74] so that the GW at infinity matches the prediction of numerical relativity (NR).

Recently, the CLA approach was applied to the computation of echoes from a head-on collision of two equal-mass ECOs [75], where the Brill-Lindquist initial data [76] for two BHs was ported into a linear perturbation of a single Schwarzschild space-time, with a modified boundary condition on a surface right above the horizon.

In addition to the EOB and CLA approaches, a so-called *hybrid approach* [77, 78] has also been proposed to jointly use Post-Newtonian (PN) and Black-Hole Perturbation (BHP) theories to model comparable-mass BBH mergers. To illustrate this method, a Penrose diagram of a BBH merger space-time is shown in Fig. 10.1. The space-time is split by a time-like world tube $\Sigma_{\rm Shell}$ (which asymptotes toward a null tube in its upper-left section) into an inner PN region III and an outer BHP region (I+II). The hybrid approach offers a way to construct space-time geometries in both regions—including GWs at null infinity; it was able to accurately predict the GW waveform and kick velocity of a head-on collision [77, 78].

In this chapter, we shall take a similar point of view as the hybrid approach—by dividing the space-time into a linear BHP region (I and II in Fig. 10.1) and a region (III) in which the space-time is not a linear perturbation of the remnant BH. We shall not attempt to *approximately solve for* the entire space-time geometry in all regions, but instead use gravitational waveform at the null infinity $\mathscr{I}^+$ already obtained from NR, and reconstruct the space-time geometry in the BHP region—including GWs propagating toward the future horizon $\mathscr{H}^+$. In particular, we find the location of the worldtube $\Sigma_{\rm Shell}$ at $\mathscr{H}^+$can be determined by looking for when the linearly quasi-normal ringing of horizon GW starts. Equipped with this information, together with the recent physically-motivated boundary condition near the would-be future horizon [61], we can construct gravitational echoes at $\mathscr{I}^+$.

As a first step toward demonstrating our space-time reconstruction approach, in this chapter, we restrict ourselves to inspiraling BBHs whose remnants are non-rotating[1,2]. Specifically, we shall use a NR technique *Cauchy-characteristic extraction* (CCE) [79–84] to extract the Weyl scalars ψ_4 and ψ_0 of the BBH events in question, and use them to reconstruct space-time geometry in the linear BH regions I and II.

This chapter is organized as follows. In Sec. 10.2 we explain more details about space-time reconstruction using Fig. 10.1 and outline the basic ideas of the hybrid method. We then describe our NR techniques and simulations in Sec. 10.3. Taking

[1] The initial parameters of BBHs are fine-tuned so that the remnants are Schwarzschild BHs

[2] Our method will also be applicable to head-on collisions.

these NR simulations we explicitly carry out space-time reconstruction in Sec. 10.4, in particular obtaining gravitational waves propagating toward the future horizon $\mathscr{H}^+$. With these horizon waveforms, we construct gravitational-wave echoes at $\mathscr{I}^+$ in Sec. 10.5. Section 10.6 focuses on the detectability of GW echo and parameter estimation, using the Fisher information matrix formalism. Finally in Sec. 10.7 we summarize our results.

Throughout this chapter we use geometric units with $G = c = 1$. Unless stated otherwise, we use the remnant mass M_f to normalize all dimensional quantities[3] (e.g., time, length, and Weyl scalars). Note that this choice is different from the typical convention adopted by the NR community, where the initial total mass of the system $M_{\rm tot}$ is used.

10.2 Space-time reconstruction from gravitational waves at future null infinity: theory

In this section, we shall describe our theoretical strategy for space-time reconstruction based on BBH GWs at the future null infinity $\mathscr{I}^+$. We shall divide the entire space-time into two regions, the black-hole perturbation region (I+II in Fig. 10.1), and the strong-field region (III in Fig. 10.1), as proposed during the construction of the hybrid model for BBH coalescence [77, 78]. In Sec. 10.2.1, we shall review the hybrid method, focusing on how space-time geometry in the bulk of the BHP region depends on boundary values. In Sec. 10.2.2, we discuss in particular how the bulk geometry can be expressed in terms of waves at $\mathscr{I}^+$. In Sec. 10.2.3, we focus on GWs that propagate toward the future horizon $\mathscr{H}^+$, in particular propose a way to determine the boundary between the BHP region II and the strong field region III. In Sec. 10.2.4, we comment on how our approach is connected to previous works.

10.2.1 From the hybrid method to space-time reconstruction

In the Penrose diagram of a coalescing BBH space-time (Fig. 10.1), the red curve represents the dynamical horizon, which is well-known to be inside the event horizon [85]. Nichols and Chen [77] proposed using a 3-dimensional time-like tube $\Sigma_{\rm Shell}$, shown as the blue curve, to divide the space-time into two regions. The exterior regions (I+II) can be treated as a linearly perturbed Schwarzschild spacetime. Interior to the tube $\Sigma_{\rm Shell}$, is a strong field region (III), which Nichols and Chen modeled using post-Newtonian theory; this PN metric is matched to the exterior perturbed Schwarzschild metric on the $\Sigma_{\rm Shell}$. Note that the PN expansion for the

[3] Namely $M_f = 1$.

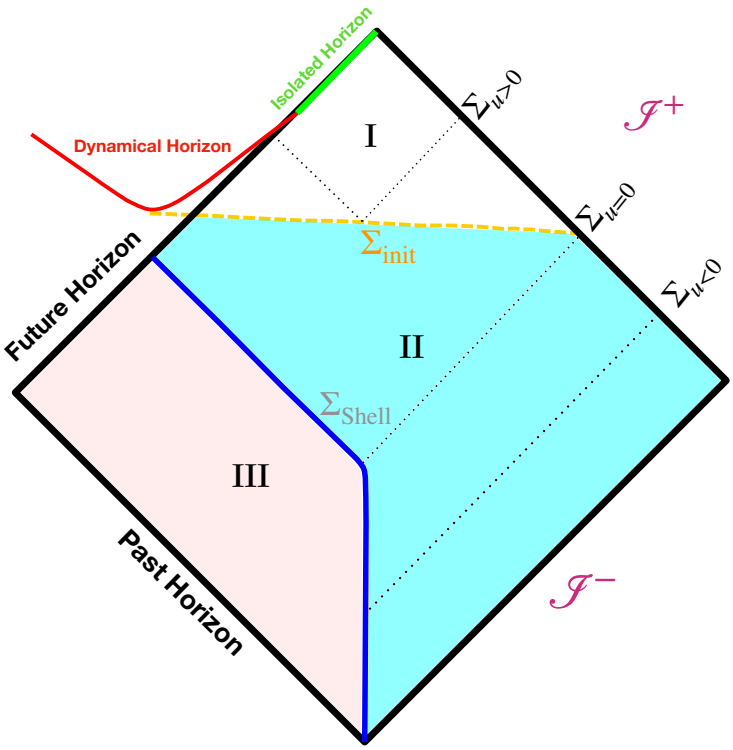

Figure 10.1: The space-time of a BBH merger event. The hybrid method divides space-time into an inner PN region (III) and an outer BHP region (I+II). The two regions communicate via boundary conditions at the worldtube $\Sigma_{\rm Shell}$ (the blue curve), which was assumed to track the motion of the BH. The dynamical horizon (the red curve) lies inside the future horizon, and it eventually settles down to the isolated horizon. The common horizon forms at the time slice $\Sigma_{\rm init}$ (the horizontal dashed line). The time slice $\Sigma_{\rm init}$ is not unique and is determined by gauge conditions. The CLA focuses exclusively on the region I, where the system is treated as a Cauchy problem—an initial data needs to be provided on $\Sigma_{\rm init}$, whereas the hybrid method gives attention to both region I and II and handles the system as a boundary value problem.

interior space-time may break down toward the late stage of evolution, but the shell does fall rapidly to the horizon so the errors might stay within the BH potential and not propagate toward infinity.

For a head-on collision, the tube $\Sigma_{\rm Shell}$ passes through the centers of the two BHs, and follows plunge geodesic of the remnant BH (i.e., the BH on which regions I and II are based). A more sophisticated framework was developed later [78] to determine the motion of $\Sigma_{\rm Shell}$ for an inspiralling BBH system. This framework added a radiation-reaction force to account for the dissipative effect of GW emission. In the end, this PN-BHP system, accompanied by the no-incoming-wave condition at $\mathscr{I}^-$, forms a complete set of evolution equations, which leads to an approximated,

ab initio waveform model. This method was able to predict a reasonable waveform for a BBH system merging in quasi-circular orbits.

In this chapter, we focus mainly on the region I+II, where the space-time is treated as a linear perturbation to a Schwarzschild BH. Let us first examine this linear perturbation using the Sasaki-Nakamura (SN) formalism [86], in which the SN variable ${}_s\Psi^{\rm SN}_{lm}$ satisfies the Regge-Wheeler (RW) equation [35]

$$\left(\frac{\partial^2}{\partial u \partial v} + \frac{V^l_{\rm RW}}{4}\right) {}_s\Psi^{\rm SN}_{lm} = 0, \tag{10.1}$$

where $u = t - r_*$ and $v = t + r_*$ are the retarded and advanced time, respectively, with the tortoise coordinate $r_* = r + 2\ln\left(\frac{r}{2} - 1\right)$. The RW potential reads [87]

$$V^l_{\rm RW} = \frac{\Delta}{r^5}[(l^2 + l)r - 2(s^2 - 1)]. \tag{10.2}$$

Here s corresponds to the spin weight of ${}_s\Psi^{\rm SN}_{lm}$ and $\Delta = r^2 - 2r$. In the hybrid approach, no-incoming wave condition was imposed on $\mathscr{I}^-$, while PN data was imposed on $\Sigma_{\rm shell}$. One way to obtain ${}_s\Psi^{\rm SN}_{lm}$ throughout regions I+II from these boundary conditions is to use the characteristic method, as we discuss in Sec. 10.9.

In this chapter, while keeping the no-incoming condition on $\mathscr{I}^-$, we shall revert the rest of the reconstruction process by imposing outgoing waves obtained from NR on $\mathscr{I}^+$(e.g., with the CCE method). In particular, we will obtain perturbative fields near $\mathscr{H}^+$, which will inform us of the gravitational waveform going down the horizon, and serve as a foundation for obtaining GW echoes.

10.2.2 Space-time reconstruction using homogeneous Teukolsky solutions

As we reconstruct space-time geometry, instead of SN variables, we will directly consider both ψ_0 and ψ_4, because they both have explicit physical meanings, as explained in Ref. [61]. Since the new boundary $\mathscr{I}^+ \cup \mathscr{I}^-$for space-time reconstruction has a regular shape (unlike $\Sigma_{\rm shell}$), we can carry out space-time reconstruction by superimposing homogeneous solutions to the Teukolsky equation that already satisfy no-ingoing boundary condition—traditionally referred to as the *up solutions*.

Let us first write general homogeneous solutions for ψ_0 and ψ_4 in mode expansions:

$$\psi_4(t, r, \theta, \phi) = \frac{1}{r^4}\sum_{lm}\int d\omega\, {}_{-2}R_{lm\omega}(r)\, {}_{-2}Y_{lm}(\theta, \phi)e^{-i\omega t}, \tag{10.3a}$$

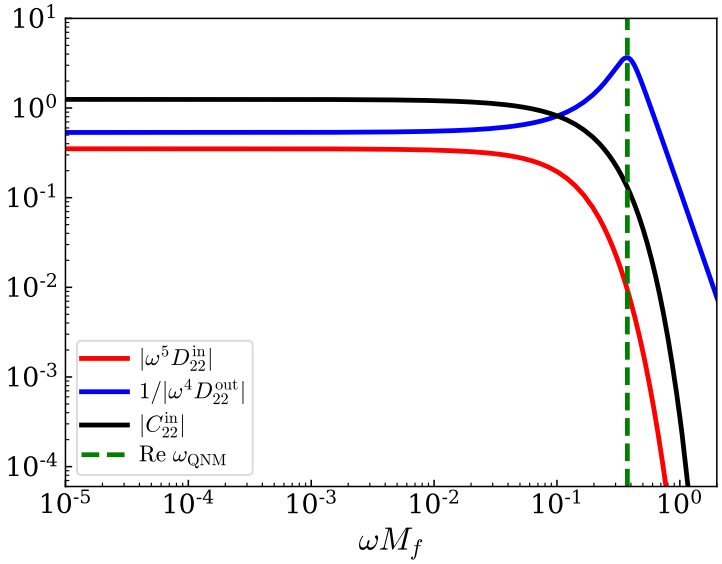

Figure 10.2: The coefficients $C^{\rm in}_{lm\omega}$ and $D^{\rm in/out}_{lm\omega}$ predicted by the Teukolsky equation, assuming a Schwarzschild BH. The vertical dashed line represents the real part of the fundamental QNM $(0.374 - 0.0890i)$. Data are obtained from the Black Hole Perturbation Toolkit [88].

$$\psi_0(t, r, \theta, \phi) = \sum_{lm} \int d\omega \, {}_{+2}R_{lm\omega}(r) \, {}_{+2}Y_{lm}(\theta, \phi) e^{-i\omega t}. \tag{10.3b}$$

Here ${}_sY_{lm}$ are spin-weighted spherical harmonics. The radial functions ${}_sR_{lm\omega}(r)$ satisfy the radial Teukolsky equation [52]

$$\Delta^{-s} \frac{d}{dr} \left(\Delta^{s+1} \frac{d}{dr} {}_sR_{lm\omega} \right) + V \, {}_sR_{lm\omega} = 0, \tag{10.4}$$

with

$$V = 4is\omega r - l(l+1) + \frac{r^4\omega^2 - 2is(r-M)r^2\omega}{\Delta}.$$

The up solutions, with their conventional normalization (with unity outgoing wave amplitude at infinity), have the following asymptotic forms near infinity and horizon

$${}_{-2}R^{\rm up}_{lm\omega} \sim \begin{cases} r^3 e^{i\omega r_*}, & r_* \to +\infty, \\ D^{\rm out}_{lm\omega} e^{i\omega r_*} + \Delta^2 D^{\rm in}_{lm\omega} e^{-i\omega r_*}, & r_* \to -\infty, \end{cases} \tag{10.5a}$$

$${}_{+2}R^{\rm up}_{lm\omega} \sim \begin{cases} r^{-5} e^{i\omega r_*}, & r_* \to +\infty, \\ C^{\rm out}_{lm\omega} e^{i\omega r_*} + \Delta^{-2} C^{\rm in}_{lm\omega} e^{-i\omega r_*}, & r_* \to -\infty. \end{cases} \tag{10.5b}$$

Numerical values of the coefficients $C^{\rm in/out}_{lm\omega}$ and $D^{\rm in/out}_{lm\omega}$ are available from the Black-Hole Perturbation Toolkit [88].

In a BBH coalescence space-time, the ψ_0 and ψ_4 in the I+II region have the following asymptotic forms:

$$ {}_{-2}R^{\rm BBH}_{lm\omega} \sim \begin{cases} r^3 Z^{\infty}_{lm\omega} e^{i\omega r_*}, & r_* \to +\infty, \\ Z^{\rm H\ out}_{lm\omega} e^{i\omega r_*} + \Delta^2 Z^{\rm H\,in}_{lm\omega} e^{-i\omega r_*}, & r_* \to -\infty, \end{cases} \tag{10.6a} $$

$$ {}_{+2}R^{\rm BBH}_{lm\omega} \sim \begin{cases} r^{-5} Y^{\infty}_{lm\omega} e^{i\omega r_*}, & r_* \to +\infty, \\ Y^{\rm H\ out}_{lm\omega} e^{i\omega r_*} + \Delta^{-2} Y^{\rm H\,in}_{lm\omega} e^{-i\omega r_*}, & r_* \to -\infty. \end{cases} \tag{10.6b} $$

Here the amplitudes at infinity, $Z^{\infty}_{lm\omega}$ and $Y^{\infty}_{lm\omega}$ in Eq. (10.6), can be directly obtained from NR simulations. For completeness, the strain h^{∞}_{lm} observed at $\mathscr{I}^+$ is related to $Z^{\infty}_{lm\omega}$ via

$$ h^{\infty}_{lm}(\omega) = \frac{1}{\omega^2} Z^{\infty}_{lm\omega}. \tag{10.7} $$

Note that h^{∞}_{lm} is defined later in Eq. (10.15b). By comparing Eqs. (10.6) with the standard up solutions in Eqs. (10.5), we can obtain amplitudes near the horizon:

$$ Z^{\rm H\ out}_{lm\omega} = D^{\rm out}_{lm\omega} Z^{\infty}_{lm\omega}, \quad Z^{\rm H\ in}_{lm\omega} = D^{\rm in}_{lm\omega} Z^{\infty}_{lm\omega}, \tag{10.8a} $$

$$ Y^{\rm H\ out}_{lm\omega} = C^{\rm out}_{lm\omega} Y^{\infty}_{lm\omega}, \quad Y^{\rm H\ in}_{lm\omega} = C^{\rm in}_{lm\omega} Y^{\infty}_{lm\omega}. \tag{10.8b} $$

In this way, from waves escaping at infinity, $Z^{\infty}_{lm\omega}$ and $Y^{\infty}_{lm\omega}$, the coefficients $D^{\rm in}_{lm\omega}$ and $C^{\rm in}_{lm\omega}$ will allow us to reconstruct ingoing waves $Z^{\rm in}_{lm\omega}$ and $Y^{\rm in}_{lm\omega}$ toward $\mathscr{H}^+$. We plot $D^{\rm in}_{22\omega}$ and $C^{\rm in}_{22\omega}$ in Fig. 10.2.

We note that for the same linear perturbative spacetime of Schwarzschild governed by the vacuum Teukolsky equation, the ψ_0 and ψ_4 can be related by the Teukolsky-Starobinsky (TS) relations, which state [62, 63]:

$$ \frac{4\omega^4}{C^*} Y^{\infty}_{lm\omega} = Z^{\infty}_{lm\omega}, \tag{10.9a} $$

$$ Y^{\rm H\,in}_{lm\omega} = \frac{D}{C} Z^{\rm H\,in}_{lm\omega} \tag{10.9b} $$

with

$$ C = (l-1)l(l+1)(l+2) + 12i\omega \tag{10.10a} $$

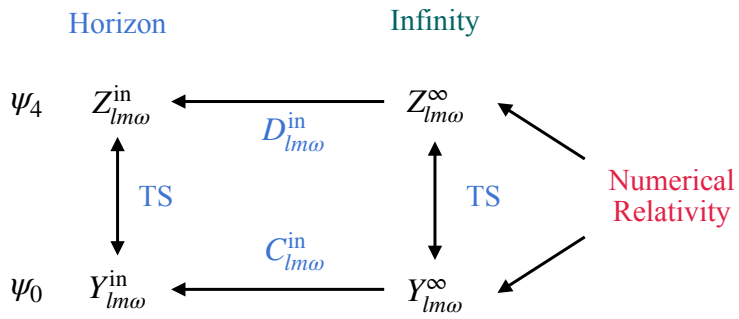

Figure 10.3: A diagram summarizing relations between BHP quantities on the horizon, $Z^{\rm in}_{lm\omega}$ and $Y^{\rm in}_{lm\omega}$, and those at infinity, $Z^{\infty}_{lm\omega}$ and $Y^{\infty}_{lm\omega}$.

$$D = 64i\omega\left(128\omega^2+8\right)(1-2i\omega)\,. \tag{10.10b}$$

These relations are consistent with coefficients in Eqs. (10.8). For example, because[4]

$$\frac{|C|^2}{4\omega^4}C^{\rm in}_{lm} = DD^{\rm in}_{lm}, \tag{10.11}$$

one can obtain $Y^{\rm H\,in}$ from Z^{∞} either by: (i) using the TS relation at infinity to obtain Y^{∞}, followed by Eq. (10.8b), or (ii) using Eq. (10.8a) to obtain $Z^{\rm H\,in}$, and then use the TS relation near the horizon [i.e., Eq. (10.9b)]. Relations between the BHP quantities have been summarized in Fig. 10.3. We will check the TS relations directly in Sec. 10.4.1.

We would like to caution here that while it has been established [62, 63] that the TS transformation maps between solutions of ψ_0 and ψ_4, these work alone did not explicitly establish the one-to-one relations in Eqs. (10.9) between $Z_{lm\omega}$ and $Y_{lm\omega}$ for the same GW. Further work by Wald [89] explicitly related both ψ_0 and ψ_4 to the Hertz potential, while more recent work by Loutrel *et al.* [90] provided a new way to reconstruct metric (hence ψ_0) from ψ_4. From Ref. [90], for the same, generic GW, the one-to-one relation is in between $(Z_{l,m,\omega}, Z_{l,-m,-\omega})$ and $(Y_{l,m,\omega}, Y_{l,-m,-\omega})$, rather than simply between $Z_{lm\omega}$ and $Y_{lm\omega}$. Nevertheless, as will be seen later in this chapter (see Sec. 10.4.1), our numerical results for ψ_0 and ψ_4 do agree with Eqs. (10.9). This might be due to the fact that we have non-precessing systems which satisfy [91]

$$Z_{l,m,\omega} = (-1)^l Z^*_{l,-m,-\omega}\,, \quad Y_{l,m,\omega} = (-1)^l Y^*_{l,-m,-\omega}\,. \tag{10.12}$$

However, for more generic, e.g., precessing binaries, the naive TS relation Eq. (10.9) may not hold.

[4] We have checked that Eq. (10.11) holds up to numerical accuracy, which is at the order of 10^{-13} for the Black Hole Perturbation Toolkit.

10.2.3 Connection to the inside prescription and determining the location of $\Sigma_{\rm Shell}$

To understand the physical meaning of $Z^{\rm H\,out}_{lm\omega}$ and $Y^{\rm H\,out}_{lm\omega}$, which mathematically appears to be emitted from the past horizon $\mathscr{H}^-$, we have to go to Fig. 10.4 and remind ourselves that region I+II does not contain the past horizon of the background BH. Anything below the red curve (the Shell) in Fig. 10.4 are *linear extrapolations*. Nevertheless, this extrapolation asserts that waveforms at infinity can be thought of as generated by "image waves" with $Z^{\rm H\,out}$ and $Y^{\rm H\,out}$ that rise from the past horizon. This follows the same reasoning as the inside prescription [11, 64].

Since the image wave encounters the BH potential barrier (from the inside), it is partially transmitted toward $\mathscr{I}^+$, while partially reflected toward $\mathscr{H}^+$. We can rewrite

$$Z^{\infty}_{lm\omega} = \frac{1}{D^{\rm out}_{lm\omega}} Z^{\rm H\ out}_{lm\omega}, \quad Z^{\rm H\ in}_{lm\omega} = \frac{D^{\rm in}_{lm\omega}}{D^{\rm out}_{lm\omega}} Z^{\rm H\ out}_{lm\omega} \tag{10.13a}$$

$$Y^{\infty}_{lm\omega} = \frac{1}{C^{\rm out}_{lm\omega}} Y^{\rm H\ out}_{lm\omega}, \quad Y^{\rm H\ in}_{lm\omega} = \frac{C^{\rm in}_{lm\omega}}{C^{\rm out}_{lm\omega}} Y^{\rm H\ out}_{lm\omega} \tag{10.13b}$$

Here $1/D^{\rm out}_{lm\omega}$ and $1/C^{\rm out}_{lm\omega}$ are the transmissivities from $\mathscr{H}^-$to $\mathscr{I}^+$, across the potential barrier, while $D^{\rm in}_{lm\omega}/D^{\rm out}_{lm\omega}$ and $C^{\rm in}_{lm\omega}/C^{\rm out}_{lm\omega}$ are reflectivities at the potential barrier that direct the wave toward $\mathscr{H}^+$. (The dependence of $1/D^{\rm out}_{22\omega}$ on ω is plotted in Fig. 10.2.)

In this way, we have shown that the inside prescription and the hybrid method correspond to the same reconstruction of space-time geometry in the regime where the linear BHP applies. However, we want to emphasize that the two methods adopt different ways when choosing the linear BHP region. In the hybrid method, it is given by the exterior region of $\Sigma_{\rm Shell}$. In particular, in order to compute echoes, we will need to terminate the linear perturbation region at the intersection of the shell $\Sigma_{\rm shell}$ and the future horizon, which is denoted by the advanced time $v = v^{\rm (H)}_{\Sigma}$ in Fig. 10.4. One natural way to determine the intersection is to first evaluate the time-domain waveform

$$Y^{\rm H\ in}_{lm}(v) = \int d\omega Y^{\rm H\ in}_{lm\omega} e^{-i\omega v} \tag{10.14}$$

and then define $v^{\rm (H)}_{\Sigma}$ as the starting time after which $Y^{\rm H\ in}_{lm}(v)$ can be decomposed as a sum of QNM overtones. We shall provide more details when we carry out this decomposition in Sec. 10.4.2.

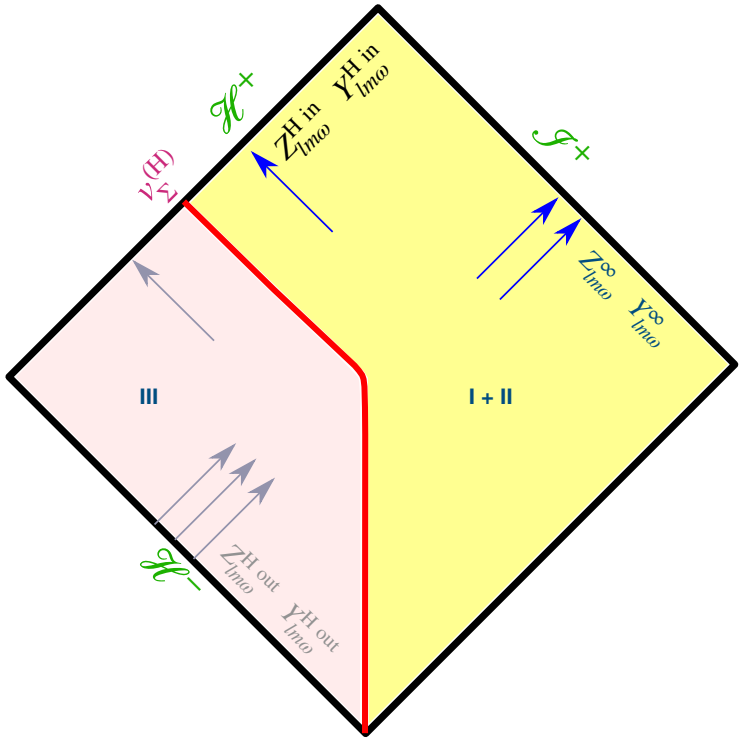

Figure 10.4: The space-time diagram illustrating the BHP region I+II and their linear extrapolation into region III. Outside the matching shell, curvature perturbations are linear combinations of the up-mode solutions to the homogeneous Teukolsky equation. At the infinity $\mathscr{I}^+$, the value of $Z^{\infty}_{lm\omega}$ and $Y^{\infty}_{lm\omega}$ are chosen to be consistent with the predictions of CCE. The past horizon exists in the strong gravity region III, where $Z^{\rm H\,out}_{lm\omega}$ and $Y^{\rm H\,out}_{lm\omega}$ represent the image wave that give rise to waves in the region I+II. They serve the same role as the initial wavepacket within the inside prescription [11, 64]. The future horizon lies partially outside the matching shell, only the outside portion ($v > v^{(\rm H)}_\Sigma$) of $Z^{\rm H\,in}_{lm}$ and $Y^{\rm H\,in}_{lm}$ corresponds to the actual wave that falls down the horizon. One natural way to self-consistently determine the location of $\Sigma_{\rm shell}$ is to evaluate the starting time after which $Y^{\rm H\,in}_{lm}(v)$ can be decomposed as a sum of QNM overtones. More details can be found in Sec. 10.4.2.

On the contrary, the inside prescription uses only the late-time evolution as the linear region. We shall give more discussions regarding this comparison in the next subsection (Sec. 10.2.4).

10.2.4 Further comparisons with the inside prescription and the close limit approximation

To fit the inside prescription into our framework, in Fig. 10.1, we choose a time slice $\Sigma_{\rm init}$ after which the space-time (i.e., the region I) is consistent with that of a single, perturbed BH. The time slice is usually not unique and is determined by a

gauge condition. An appropriate choice is to let $\Sigma_{\rm init}$ represent a moment when the common horizon just forms, following the close limit approximation [92–99]. Then the inside prescription corresponds to only taking the region I, and treating it as the linear BHP area. Consequently, one needs to take the ringdown of the main GWs at the null infinity as input, which is equivalent to imposing a filter at $\mathscr{I}^+$ [64], and use that information to calculate echoes. In fact, since region II is not included, the indeterminate condition at past null infinity leaves room for the outside prescription [71, 72].

Similarly, the CLA corresponds to region I as well. This is an approach to studying space-time based on the fact that the gravitational field in the region I can be modeled as the one of a single perturbed BH. The system in region I is then treated as a Cauchy problem (i.e., an initial value problem) as long as initial data is provided on $\Sigma_{\rm init}$. Previous studies have investigated the Misner initial data [100], the Brill-Lindquist initial data [76], the Bowen-York initial data [101] as well as numerically generated initial data [102, 103]. Once the gravitational field in the region I is solved, one can read off the value of $Z^{\rm H\ in}_{lm\omega}$ and $Y^{\rm H\ in}_{lm\omega}$ at future horizon and compute echo waveforms [75].

The hybrid method, however, is a boundary value problem. It divides the space-time into two regions via the time-like shell $\Sigma_{\rm Shell}$, as opposed to the space-like hypersurface $\Sigma_{\rm init}$ adopted by the CLA. In addition, both region I and II are regarded as BHP areas.

10.3 Numerical relativity simulations

In this section, we adopt two BBH merger simulations performed using the Spectral Einstein Code (SpEC) [104], developed by the Simulating eXtreme Spacetimes (SXS) collaboration [105]. These binaries have their initial parameters fine-tuned, such that the remnant black holes are nearly non-spinning. Gravitational waveforms (at infinity) of these simulations are publicly available through the SXS catalog [105], with the identifier SXS:BBH:0207 and SXS:BBH:1936.

We summarize the properties of these binaries in Table 10.1, where we adopt the standard convention in SpEC, namely labeling the heavier hole with '1' and the lighter one with '2', and assuming the $z-$axis to be aligned with the initial orbital angular momentum. Our two systems have mass ratios $q = m_2/m_1 = 7, 4$, respectively; they undergo $N_{\rm cycle} = 36, 16.5$ orbit cycles before the merger, with the initial orbital eccentricity already reduced to $\sim 10^{-4}$. Both systems are non-

Table 10.1: A summary of NR simulations used in this chapter. The first column is the identifier in the SXS catalog [105]. The second column $q = m_2/m_1 > 1$ shows the mass ratio. The third column is the number of orbit cycles that a system undergoes before the merger. The fourth and fifth columns give the initial individual dimensionless spins. They have only the $z-$component, where the $z-$axis is chosen to be aligned with the orbital angular momentum. The sixth and seventh columns exhibit the remnant mass (in the unit of initial total mass $M_{\rm tot}$) and remnant spin. The final column corresponds to the radius of the extraction worldtube for CCE.

ID SXS:BBH:	q	$N_{\rm cycle}$	χ_1^z	χ_2^z	$\frac{M_f}{M_{\rm tot}}$	χ_f	Extraction Radius($M_{\rm tot}$)
0207	7.0	36	-0.6	10^{-6}	0.991	-0.077	300
1936	4.0	16.5	-0.8	-0.8	0.985	0.022	273

precessing, with initial spins anti-aligned with the orbital angular momentum (or vanishing), as indicated by the negative signs of the dimensionless spin components, χ_1^z and χ_2^z. The remnant BHs have small spins at the $\chi_f \sim 10^{-2}$ level, with the remnant mass M_f slightly less than the initial total mass of the system $M_{\rm tot} = m_1+m_2$.

We extract gravitational waveforms at the null infinity $\mathscr{I}^+$ using the Cauchy Characteristic Extraction (CCE) method [83, 84], implemented in the new NR code SpECTRE [106, 107]. The CCE system evolves the Einstein field equations on a foliation of null hypersurfaces, where the metric is written in the Bondi-Sachs coordinates [108]. This method is most efficient in evolving the space-time far from the BBH system, and is reliable enough to produce all Weyl scalars $\psi_{0,1,2,3,4}$ with high accuracy [83, 84]. In practice, CCE first reads off boundary data on a worldtube covered by the inner Cauchy evolution, and then evolves a hierarchical system from the worldtube towards future null infinity. The radii of the extraction worldtubes for SXS:BBH:0207 and SXS:BBH:1936 are summarized in Table 10.1. Same as the standard treatment in NR, CCE decomposes each of the Weyl scalars $\psi_{0,1,2,3,4}$, and the strain h, into sums over a set of spin-weighted spherical harmonics ${}_sY_{lm}(\theta,\phi)$. Using the notation defined in Eqs. (10.6), the decomposition reads

$$[rM_f\psi_4]_{\mathscr{I}^+} = \sum_{l,m} {}_{-2}Y_{lm}(\theta,\phi) Z^{\infty}_{lm}, \tag{10.15a}$$

$$[rh/M_f]_{\mathscr{I}^+} = \sum_{l,m} {}_{-2}Y_{lm}(\theta,\phi) h^{\infty}_{lm}, \tag{10.15b}$$

$$[r^5 M_f^{-3}\psi_0]_{\mathscr{I}^+} = \sum_{l,m} {}_{+2}Y_{lm}(\theta,\phi) Y^{\infty}_{lm}, \tag{10.15c}$$

where θ and ϕ are the polar and azimuthal angles, respectively, on the sky in the source frame. Note that in Eqs. (10.15) the asymptotic r-dependences of ψ_4, h and ψ_0, as $r \to \infty$, are consistent with the peeling theorem [109]. Furthermore, these fields are normalized by the appropriate powers of M_f so that Z^{∞}_{lm}, Y^{∞}_{lm} and h^{∞}_{lm} are dimensionless. We want to emphasize again that as opposed to the usual NR convention, where the initial total mass of the system $M_{\rm tot}$ is used as the unit for time and length, in this chapter, we use the remnant mass M_f to normalize all dimensional quantities, because we mainly deal with perturbations of the remnant (approximately) Schwarzschild BH.

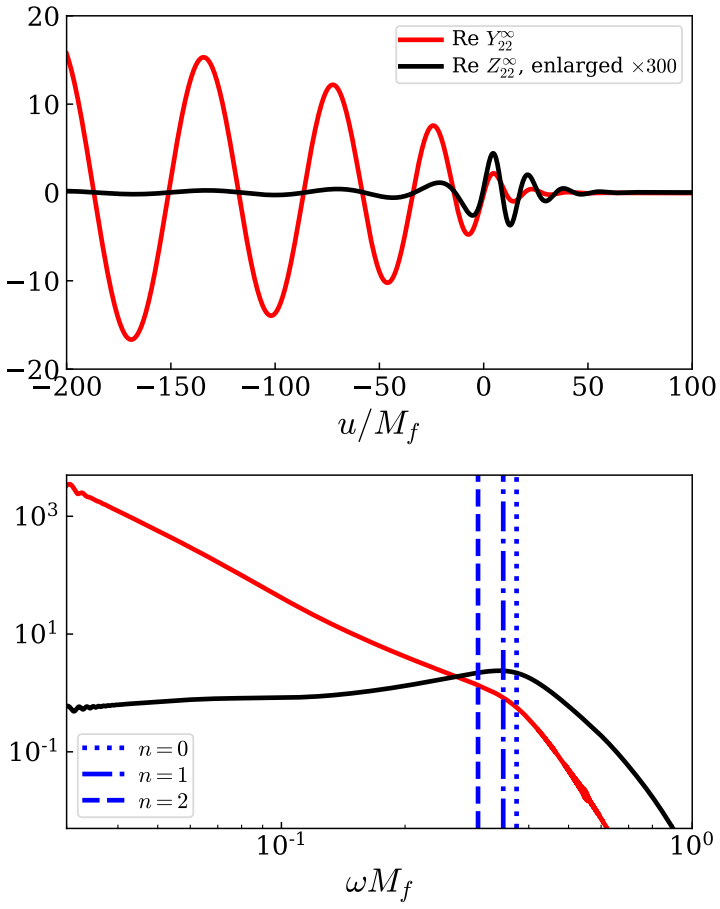

Figure 10.5: The spherical modes Y^{∞}_{22} and Z^{∞}_{22} of SXS:BBH:0207, in the time domain (the upper panel), and in the frequency domain (the lower panel). The vertical lines in the lower panel stand for QNM frequencies of a Schwarzschild BH, labeled by the overtone index n. The absolute value of Z^{∞}_{22} is amplified by a factor of 300 for ease of reading.

Furthermore, we shift all temporal coordinates such that $u = 0$ corresponds to the peak of total rms strain amplitude:

$$\left.\sqrt{\sum_{lm} |h_{lm}(u)|^2}\right|_{u=0} = \text{peak}. \tag{10.16}$$

10.4 Numerical implementations of the hybrid method

In this section, we apply the space-time reconstruction procedure of Sec. 10.2 to SXS:BBH:0207 and SXS:BBH:1936. In Sec. 10.4.1, we first investigate the validity of TS identities at future null infinity $\mathscr{I}^+$ [see Eq. (10.9a)], given that the future null infinity lies completely in the BHP region. We also provide the horizon-ψ_0 at future horizon $\mathscr{H}^+$. Then in Sec. 10.4.2, we use the horizon-ψ_0 to determine the location of the matching tube Σ_{Shell} by looking for when its linearly quasi-normal ringing starts.

10.4.1 At null infinity and future horizon: The Weyl scalars and the Teukolsky-Starobinsky identities

For SXS:BBH:0207, we plot its $Z^{\infty}_{l=2,m=2}$ and $Y^{\infty}_{l=2,m=2}$ in Fig. 10.5, in both time domain (upper panel) and frequency domain (lower panel). In the frequency domain, Z^{∞}_{22} (black curve) peaks at the fundamental (2,2) quasi-normal mode frequency (the vertical dotted line). On the other hand, Y^{∞}_{22} rises sharply in low frequencies, where its magnitude is much greater than that of Z^{∞}_{22}. This feature in the frequency domain is consistent with the TS identity at infinity [see Eq. (10.9a)]. To be concrete, we test the validity of Eq. (10.9a) in Fig. 10.6. The actual Z^{∞}_{22} (in black) is compared to $\frac{4\omega^4}{C^*}Y^{\infty}_{22}$ (in red), in the time domain (the left two panels) and frequency domain (the right panel). We see the TS identity holds throughout the entire region. The comparison for SXS:BBH:1936 is similar and can be found in Sec. 10.10.

At the future horizon, $Y^{\text{H in}}_{lm}$ [Eq. (10.6)] is essential for us to compute echoes (see Sec. 10.5.1 for more details). In Fig. 10.7, we plot $Y^{\text{H in}}_{22}$ of SXS:BBH:0207 in the time domain (blue curve), where the advanced time v is used as the time coordinate. Similar to Y^{∞}_{22} [see Fig. 10.5], $Y^{\text{H in}}_{22}$ has a dominated low-frequency content. At an early stage, $Y^{\text{H in}}_{22}$ is inside the strong gravity region III and should be excised—as we shall discuss in Secs. 10.4.2 and 10.5.3. For comparison, we also plot Y^{∞}_{22} in the same figure (red curve)—using u as the time coordinate. We caution that this comparison only has a qualitative meaning, because the two waveforms are emitted in different directions. Showing the v dependence of $Y^{\text{H in}}_{22}$ and the u dependence of Y^{∞}_{22} in the same plot effectively traces both of these waves back to the same time

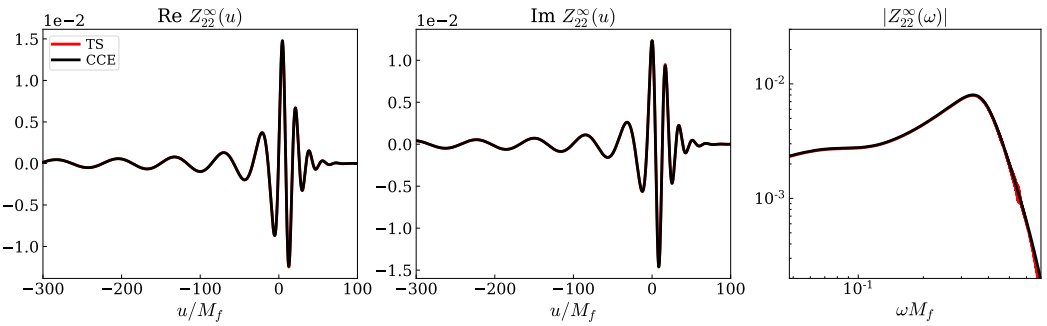

Figure 10.6: The validity of the TS identity at infinity [Eq. (10.9a)], using SXS:BBH:0207. The predicted form $\frac{4\omega^4}{C^*}Y^{\infty}_{22}$ (in red) is compared to the actual Z^{∞}_{22} (in black), in the time domain (the left two panels), and in the frequency domain (the right panel). The comparison for SXS:BBH:1936 is in Fig. 10.20.

t at $r_* = 0$. This is qualitatively meaningful because the ringdown wave can be thought of as having originated from the light ring at $r = 3M$, where $r_* \approx 0$. From this comparison, we can see $Y^{\mathrm{H\,in}}_{22}$ decreases faster and undergoes fewer cycles of oscillation at the late phase than Y^{∞}_{22}.

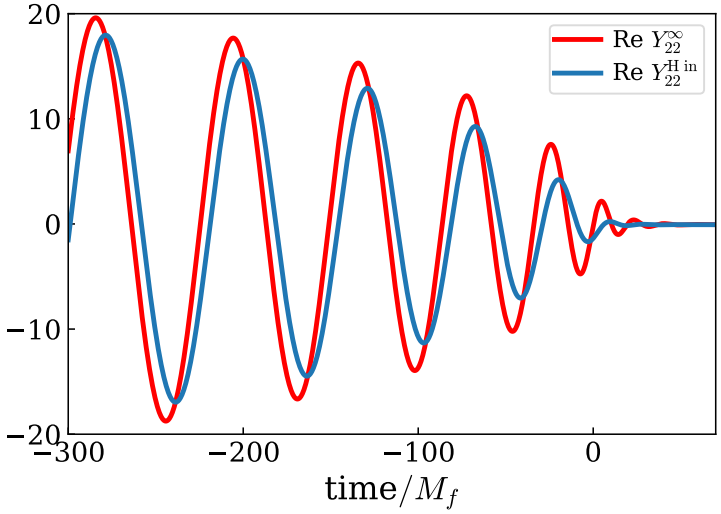

Figure 10.7: The real part of $Y^{\mathrm{H\,in}}_{22}$ [Eq. (10.6)] and Y^{∞}_{22} in the time domain, using SXS:BBH:0207. The temporal coordinate for $Y^{\mathrm{H\,in}}_{22}$ is v, while is u for Y^{∞}_{22}. Both coordinates are in the unit of final mass.

10.4.2 Determining the location of Σ_{Shell}

As mentioned in Sec. 10.2, the region outside the matching tube Σ_{Shell} is consistent with a sourceless, linearly perturbed Schwarzschild space-time. Accordingly, the part of $Y^{\mathrm{H\,in}}_{lm}$ that is in region I+II can be decomposed into a sum of QNMs (in the

time domain). Conversely, we can use this fact to determine the location of $\Sigma_{\rm Shell}$. Indeed, this method has been used not only to determine the start time of a BBH ringdown at the future infinity[5] [110], but also to investigate the dynamics of a final apparent horizon in a BBH system approaching to equilibrium [111]. More specifically, we write [112],

$$h_{22}^{\infty}(u > u^{(h)}) = \sum_{n=0}^{n_{\rm max}} [\mathcal{A}_n^{(h)} e^{-i\omega_n u} + \mathcal{B}_n^{(h)} e^{i\omega_n^* u}], \tag{10.17a}$$

$$Y_{22}^{\infty}(u > u^{(\infty)}) = \sum_{n=0}^{n_{\rm max}} [\mathcal{A}_n^{(\infty)} e^{-i\omega_n u} + \mathcal{B}_n^{(\infty)} e^{i\omega_n^* u}], \tag{10.17b}$$

$$Y_{22}^{\rm H\,in}(v > v_{\Sigma}^{(\rm H)}) = \sum_{n=0}^{n_{\rm max}} [\mathcal{A}_n^{(\rm H)} e^{-i\omega_n v} + \mathcal{B}_n^{(\rm H)} e^{i\omega_n^* v}], \tag{10.17c}$$

where ω_n is the QNM frequency of a Schwarzchild BH, and n refers to the overtone index (we have restricted to $l = 2$). Note that for a Schwarzchild BH, the QNM frequency is independent of its spin weight and azimuthal quantum number. Unlike Ref. [110], we include both prograde modes $\mathcal{A}_n$ and retrograde modes $\mathcal{B}_n$ for generality [113]. In Eq. (10.17) we use $u^{(\infty/h)}$ and $v_{\Sigma}^{(\rm H)}$ to indicate the time at which ringdown begins, and we emphasize again that the retarded time u is used for h_{22}^{∞} and Y_{22}^{∞} at the null infinity, whereas the advanced time v is used for $Y_{22}^{\rm H\,in}$ at the future horizon.

In making the decomposition, we follow the procedure of Ref. [110], namely we use the mismatch $\mathcal{M}$ between the quasi-normal mode ringdown waveform model (e.g., $h_{22}^{\rm Ringdown}$) and the NR result (e.g., $h_{22}^{\rm NR}$) as a loss function

$$\mathcal{M} = 1 - \frac{(h_{22}^{\rm NR}, h_{22}^{\rm Ringdown})}{\sqrt{(h_{22}^{\rm Ringdown}, h_{22}^{\rm Ringdown})(h_{22}^{\rm NR}, h_{22}^{\rm NR})}}, \tag{10.18}$$

with

$$(h_{22}^{\rm NR}, h_{22}^{\rm Ringdown}) = {\rm Re} \int_{u_{\Sigma}^{(h)}}^{T} h_{22}^{\rm NR} h_{22}^{\rm Ringdown\ *} dt, \tag{10.19}$$

where the upper limit of the integral T is taken to be $90M_f$ after the peak of total rms strain amplitude. In addition, we use unweighted linear least squares to fit the mode amplitudes and use nonlinear least squares to fit the final spin and mass. The mode frequency ω_n is obtained from a Python package qnm [114]. During the fit,

[5] The linear perturbation regime was found to be valid as early as the peak of strain if seven overtones are included.

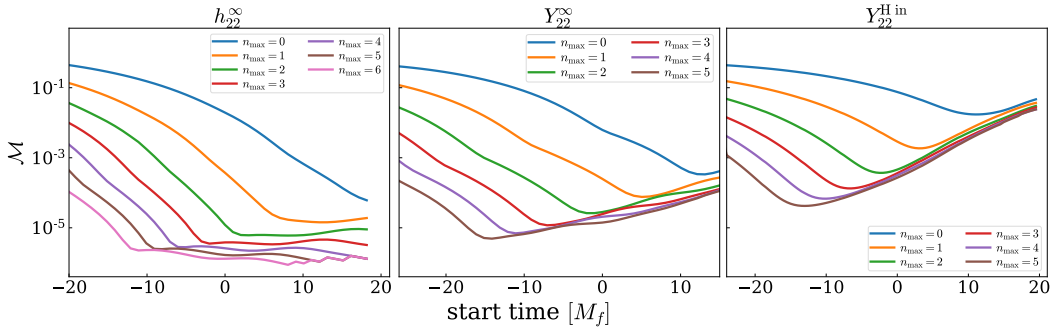

(a) SXS:BBH:0207

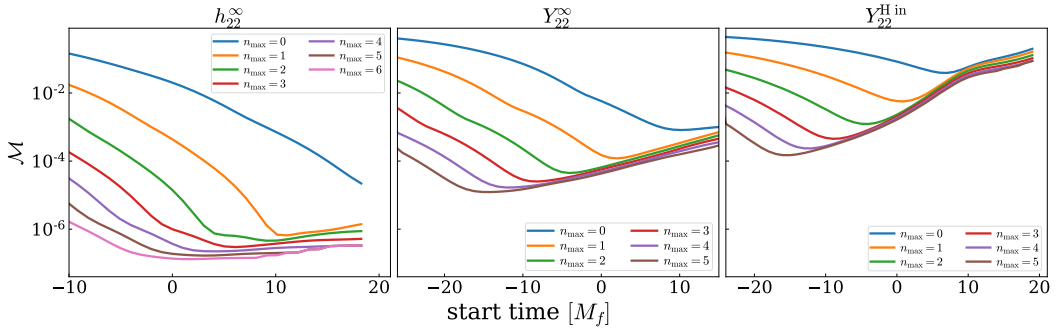

(b) SXS:BBH:1936

Figure 10.8: Mismatch as a function of the start time (in the unit of remnant mass) for different models [Eq. (10.17)]. Each model includes up to $n_{\max}$ overtones. The left panel corresponds to the strain h_{22}^{∞} at infinity, the middle one Y_{22}^{∞}, and the right panel $Y_{22}^{\mathrm{H\,in}}$ [see Eqs. (10.6) and (10.15b)]. The upper row refers to SXS:BBH:0207, whereas the lower one SXS:BBH:1936. All waveforms are aligned such that $t = 0$ occurs at the peak of $\sqrt{\sum_{lm} |h_{lm}(t)|^2}$.

we find that the numerical accuracy of Y_{22}^{∞} and $Y_{22}^{\mathrm{H\,in}}$ is much worse than that of h_{22}^{∞}, which makes the remnant mass and spin more difficult to recover.

In Fig. 10.8, we plot the mismatch $\mathcal{M}$ for h_{22}^{∞} (the left panel), Y_{22}^{∞} (the middle panel), and $Y_{22}^{\mathrm{H\,in}}$ (the right panel), for SXS:BBH:0207 (the upper panel) and SXS:BBH:1936 (the lower panel). We see the strain h_{22}^{∞} can be decomposed into a sum of the fundamental mode and six overtones[6]. For SXS:BBH:0207, the linear regime can be extended to $16M_f$ before the peak of h_{22}^{∞}, whereas for SXS:BBH:1936, the linear quasinormal ringing regime starts from $2.0M_f$, similar to the case of GW150914 [110] and superkick systems [115].

On the other hand, since the numerical accuracy of Y_{22}^{∞} and $Y_{22}^{\mathrm{H\,in}}$ from CCE is not as high as h_{22}^{∞}, only five overtones can be resolved. In particular, the late-

[6]Including more overtones no longer improves the match.

Table 10.2: A summary for the QNM decomposition of h^{∞}_{22}, Y^{∞}_{22} and $Y^{\mathrm{H\,in}}_{22}$. The second row refers to the maximum number of overtones we include in Eq. (10.17). The third and fourth rows correspond to the time from which the waveform is consistent with a linear quasinormal ringing. The values are from the minimum of the corresponding curves in Fig. 10.8.

		h^{∞}_{22}	Y^{∞}_{22}	$Y^{\mathrm{H\,in}}_{22}$
$n_{\max}$		6	5	5
$u^{(\infty/h)}$ or $v^{(\mathrm{H})}_{\Sigma}$	SXS:BBH:0207	−11.1	−14.1	−13
	SXS:BBH:1936	2.0	−14.2	−15

time portion is dominated by numerical noise, therefore the mismatch $\mathcal{M}$ tends to increase significantly. The start times of the linear regime for h^{∞}_{22}, Y^{∞}_{22}, and $Y^{\mathrm{H\,in}}_{22}$ are summarized in Table 10.2. Below, we will use the start time of $Y^{\mathrm{H\,in}}_{22}$, denoted by $v^{(\mathrm{H})}_{\Sigma}$, as the advanced time of the matching tube Σ_{Shell} (Figs. 10.1 and 10.4), and utilize the exterior portion of the GW to approximate the actual wave falling down the future horizon.

Apart from searching for the start time of the quasinormal ringing regime of $Y^{\mathrm{H\,in}}_{22}$, it is also interesting to investigate their QNM amplitudes [115, 116]. This topic is beyond the scope of our study and we only provide a brief discussion in Sec. 10.8.

10.5 Constructing echoes

Now we utilize the horizon-going GW obtained above to construct GW echoes at infinity. In Sec. 10.5.1, we first introduce physical boundary conditions near an ECO surface [61], and obtain formulas that relate horizon waves to echoes at infinity. Then in Sec. 10.5.2, we focus on the Boltzmann reflectivity and discuss QNM structures of the ECO. Next in Sec. 10.5.3, we compute echo waveforms numerically and investigate the impact of prescriptions made at the matching shell Σ_{Shell} (see Fig. 10.1), taking SXS:BBH:0207 for example. Finally, we compare the hybrid method with the inside prescription in Sec. 10.5.4.

10.5.1 Constructing echoes using the physical boundary condition near an ECO surface

Chen *et al.* [61] recently proposed imposing boundary conditions near the ECO surface using the Membrane Paradigm, in which a family of zero-angular-momentum fiducial observers (FIDOs) are considered. Within their own rest frame, the FIDOs experience a tidal tensor field [117]

$$\mathcal{E}_{ij} = h^a_i h^c_j C_{abcd} U^b U^d, \tag{10.20}$$

where C_{abcd} is the Weyl tensor, U^b is the four-velocity of the FIDOs, and $h_i^a = \delta_i^a + U^a U_i$ is the projection operator. The transverse component of $\mathcal{E}_{ij}$ is of particular interest [61]

$$\mathcal{E}_{\text{transverse}} \sim -\frac{\Delta}{4r^2}\psi_0 - \frac{r^2}{\Delta}\psi_4^*, \tag{10.21}$$

since it represents the stretching and squeezing effect due to GW. In analogous to the tidal response of a neutron star, the response of the ECO was proposed to be linear in $\mathcal{E}_{\text{transverse}}$, namely [61]

$$\left[-\frac{r^2}{\Delta}\psi_4^*\right]_{\text{surface}} = \left[\frac{\mathcal{R}^{\text{ECO}}}{\mathcal{R}^{\text{ECO}}-1}\mathcal{E}_{\text{transverse}}\right]_{\text{surface}}. \tag{10.22}$$

The reflectivity $\mathcal{R}^{\text{ECO}}$ depends on the (non-GR) property of ECO as we shall discuss in Sec. 10.5.2.

Near the ECO surface, ψ_0 is dominated by the incident wave (toward the horizon), whereas ψ_4 by the reflected wave (by the ECO), i.e.,

$${}_{+2}R_{lm}^{\text{ECO}}(u,v) \sim \int \frac{d\omega}{\Delta^2} Y_{lm\omega}^{\text{H in ECO}} e^{-i\omega v}, \tag{10.23a}$$

$${}_{-2}R_{lm\omega}^{\text{ECO}}(u,v) \sim \int d\omega Z_{lm\omega}^{\text{H out ECO}} e^{-i\omega u}, \tag{10.23b}$$

with ${}_{\pm 2}R_{lm}^{\text{ECO}}(u,v)$ the radial Teukolsky function for the ECO. Here we use the same notation as Eq. (10.6), and we emphasize that $Y_{lm\omega}^{\text{H in ECO}}$ stands for the *actual* ψ_0-wave that falls down the future horizon.

After simplification, the boundary condition in Eq. (10.22) becomes

$$Z_{lm\omega}^{\text{H out ECO}} = \frac{(-1)^{l+m+1}}{4}\mathcal{R}^{\text{ECO}} Y_{lm\omega}^{\text{H in ECO}}, \tag{10.24}$$

where we have used the symmetry of a nonprecessing BBH system under reflection across the orbital plane [91]

$$[Y_{l,-m,-\omega}^{\text{H in ECO}}]^* = (-1)^l Y_{lm\omega}^{\text{H in ECO}}. \tag{10.25}$$

Subsequently, the echo waveform at null infinity reads [59]

$$Z_{lm\omega}^{\infty\ \text{echo}} = \mathcal{K}(\omega) Y_{lm\omega}^{\text{H in ECO}}, \tag{10.26}$$

with the transfer function $\mathcal{K}(\omega)$

$$\mathcal{K}(\omega) = \frac{(-1)^{l+m+1}\mathcal{R}^{\text{ECO}}}{1-\mathcal{R}^{\text{ECO}}\mathcal{R}^{\text{BH T}}}\frac{1}{4D_{lm}^{\text{out}}} = \frac{C}{DD_{lm}^{\text{in}}}\sum_{n=1}\left(\mathcal{R}^{\text{ECO}}\mathcal{R}^{\text{BH T}}\right)^n, \tag{10.27}$$

and

$$\mathcal{R}^{\rm BH\,T} = (-1)^{l+m+1}\frac{D^{\rm in}_{lm}}{D^{\rm out}_{lm}}\frac{D}{4C}. \tag{10.28}$$

In Eq. (10.27), we have written the total echo signal as a sum of individual echoes.

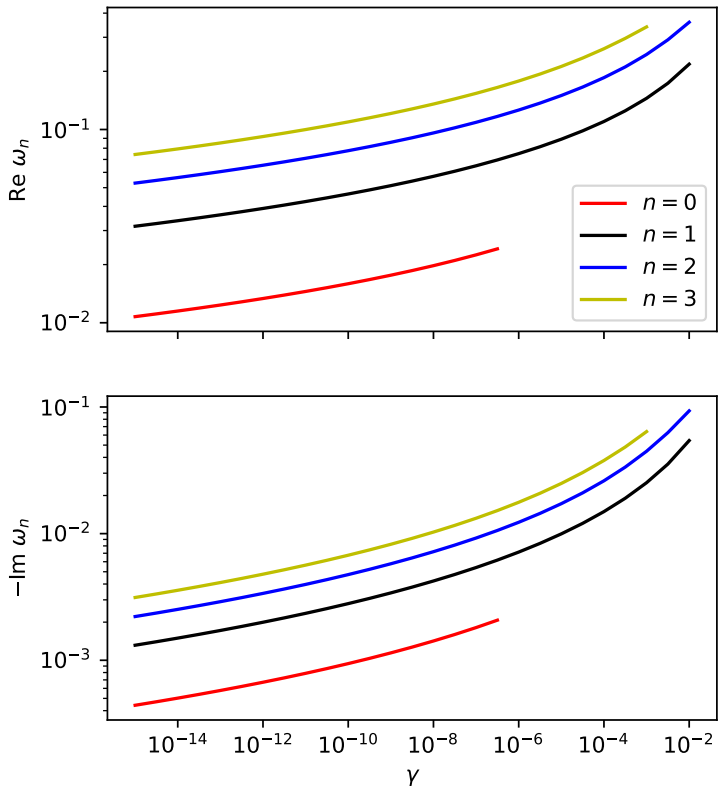

Figure 10.9: The real and imaginary parts of QNMs for an irrotational ECO, as functions of γ. They are the solutions to Eq. (10.31). The Boltzmann reflectivity is used, assuming $T_{\rm QH} = T_H$. Each mode is labeled by the overtone index n. The imaginary part of QNMs is negative, meaning that the mode is stable.

10.5.2 The Boltzmann reflectivity

To model quantum effects around the horizon, Oshita *et al.* [12] and Wang *et al.* [11] proposed that GWs around the horizon interact with a quantum thermal bath. Specifically, these waves are subject to a position-dependent dissipation $\Omega(r_*)/E_{\rm Pl}$, and driven by a position-dependent stochastic source $\xi(r_*)$—levels of the driving and the dissipation are related by the fluctuation-dissipation theorem [118]. Then the BHP equation is modified to [11, 12]

$$\left[-i\gamma\frac{\Omega(r_*)}{E_{\rm Pl}}\frac{d^2}{dr_*^2}+\frac{d^2}{dr_*^2}+\omega^2-V^l_{\rm RWZ}\right]{}_s\Psi^{\rm SN}_{lm}(r_*)=\xi(r_*), \tag{10.29}$$

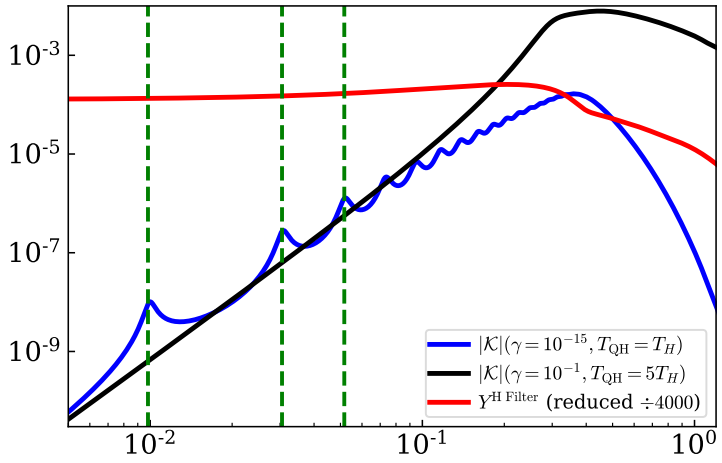

Figure 10.10: The transfer function $\mathcal{K}$ of the ECO using $(\gamma = 10^{-15}, T_{\rm QH} = T_H)$ (the blue curve), and $(\gamma = 10^{-1}, T_{\rm QH} = 5T_H)$ (the black curve). The QNM resonances are visible in the former case, where the location of first three resonances are labeled by the dashed vertical lines, based on the estimation in Eq. (10.33). By comparison, the red curve corresponds to the absolute value of the filtered horizon wave $Y^{\rm H\ Filter}$ for SXS:BBH:0207, assuming $v_\Sigma^{\rm H} = -13$ and $\Delta v = 2/\kappa$ [see Eq. (10.36)]. Its value is decreased by a factor of 4000 for ease of read.

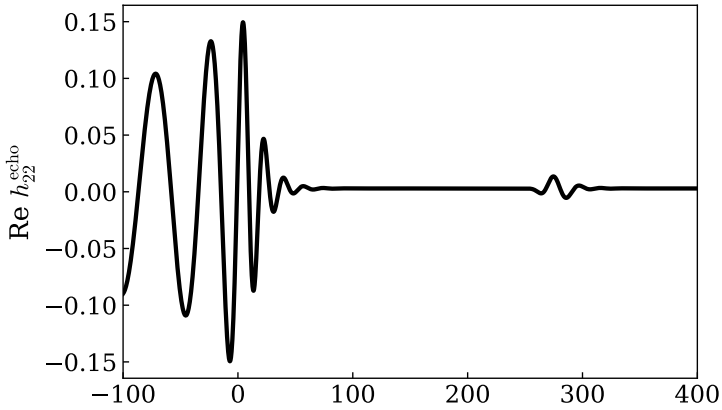

Figure 10.11: The echo emitted by SXS:BBH:0207, following the main GW. Here we set $v_\Sigma^{\rm (H)} = -13, \Delta v = 2/\kappa = 8, \gamma = 10^{-15}$, and $T_{\rm QH} = T_H$.

where $\Omega(r_*) = |\omega|/\sqrt{|g_{00}(r_*)|}$ is the proper frequency measured in the frame of the Schwarzschild observers, $E_{\rm Pl}$ is the Planck energy, and γ is a dimensionless dissipation parameter that controls how the damping ramps up as the wave gets close to the horizon. Note that Eq. (10.29) reduces to the classical Zerilli-RW equation in the limit of $\gamma \to 0$ (vanishing of the dissipative effect) and $\xi \to 0$ (vanishing of the fluctuation source). Consequently, the modified equation leads to

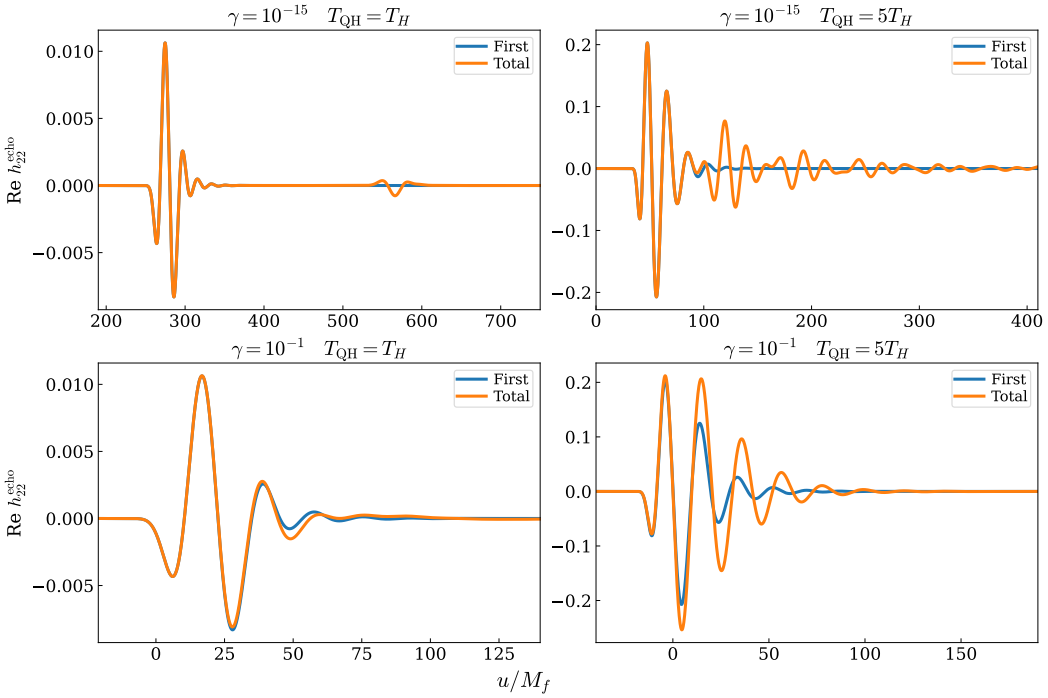

Figure 10.12: The echoes emitted by SXS:BBH:0207, with a variety of $T_{\rm QH}$ and γ. The width of filer Δv is equal to $2/\kappa$. The total echoes (orange curves) are compared with the first echoes (blue curves). In the upper left panel, the values of $T_{\rm QH}$ and γ are small enough that the spacing between echoes is greater than the echo duration, hence the individual pulses are well separated, whereas in the other three panels, different pulses overlap and interfere with each other.

the Boltzmann reflectivity [11, 12]:

$$\mathcal{R}^{\rm ECO} = \exp\left[-i\frac{\omega}{\pi T_{\rm QH}}\ln(\gamma|\omega|)\right]\exp\left(-\frac{|\omega|}{2T_{\rm QH}}\right), \tag{10.30}$$

where the quantity $T_{\rm QH}$ is the effective horizon temperature. The first term on the right hand side of Eq. (10.30) implies that as $\gamma \ll 1$, the region between $r_* \sim \frac{\ln\gamma}{2\pi T_{\rm QH}}$ and the peak of the BH potential forms a cavity. In this way, the ECO's QNM frequencies, ω_n, are determined as poles of the transfer function $\mathcal{K}(\omega)$ [see Eq. (10.27)]

$$\mathcal{R}^{\rm ECO}(\omega_n)\mathcal{R}^{\rm BH\,T}(\omega_n) = 1. \tag{10.31}$$

We solve Eq. (10.31) numerically and plot the value of ω_n as a function of γ in Fig. 10.9, where the quantum horizon temperature $T_{\rm QH}$ is set to be the Hawking temperature T_H:

$$T_H := \frac{\kappa}{2\pi} = \frac{1}{8\pi}, \tag{10.32}$$

with $\kappa = 1/4$ the surface gravity. We can see that the absolute value of the real and imaginary parts of ω_n increases with γ and n. In particular, the negative sign of Im ω_n ensures the stability of the QNMs. For the fundamental mode $n = 0$, its decay rate is less than 10^{-3}, hence it is long-lived.

The feature of ECO's QNMs is also visible in the transfer function $\mathcal{K}$ (Fig. 10.10). The blue curve corresponds to the case with $(\gamma = 10^{-15}, T_{\rm QH} = T_H)$. There are a number of local maxima whose locations are close to the real part of the corresponding QNMs. With $\gamma \ll 1$, the peak frequency $\omega^{(n)}_{\rm peak}$ is given by

$$\omega^{(n)}_{\rm peak} = \omega^{(n)}_{\rm FSR} - \frac{\omega^{(n)}_{\rm FSR}}{(2n+1)\pi} \mathrm{Im} \ln \left[\mathcal{R}^{\rm BH\,T}(\omega^{(n)}_{\rm FSR}) \right], \tag{10.33}$$

where the free spectral range (SFR) of the cavity writes

$$\omega^{(n)}_{\rm FSR} = (2n+1)\frac{T_{\rm QH}\pi^2}{|\ln\gamma|}\left\{1 - \frac{1}{\ln\gamma}\ln\left[(2n+1)\frac{T_{\rm QH}\pi^2}{|\ln\gamma|}\right]\right\} + O\left[(\ln\gamma)^{-2}\right], \quad n = 0, 1\ldots \tag{10.34}$$

In Fig. 10.10 we label the location of $\omega^{(n)}_{\rm peak}$ for $n = 0, 1, 2$ using the dashed vertical lines. Additionally, $\mathcal{K}$ has a global maximum at the fundamental QNM of a Schwarzschild BH $(0.374 - 0.0890i)$, contributed by the factor $1/D^{\rm out}_{22}$ (see the blue curve in Fig. 10.2). Within the frequency band $\omega < 0.374$, $\mathcal{K}$ is dominated by $1/D^{\rm out}_{22}$, hence its asymptotic behavior is $\sim \omega^4$ as $\omega \to 0$. Whereas for the band $\omega > 0.374$, $\mathcal{K}$ decays exponentially due to the second term on the right hand side of Eq. (10.30).

On the other hand, when γ is comparable to 1, GWs cannot be effectively trapped near the ECO surface, and the ECO QNMs do not exist. This fact is clearly manifested in the transfer function of the case with $(\gamma = 10^{-1}, T_{\rm QH} = 5T_H)$, as shown in the black curve in Fig. 10.10. Moreover, since the value of $T_{\rm QH}$ is greater than the previous one, more high-frequency contents can be reflected by the ECO surface hence emerge at infinity.

10.5.3 Numerical computation of echo waveforms

In order to use Eq. (10.26) to compute echo waveforms, we first need to estimate the actual wave $Y^{\rm H\,in\ \ ECO}_{lm\omega}$ [see Eq. (10.23)] that falls down the future horizon. In the context of hybrid method, the future horizon exists partially in region I+II, only the late-time portion of $Y^{\rm H\,in}_{lm}$ [see Eq. (10.14)] can represent $Y^{\rm H\,in\,ECO}_{lm}$, namely

$$Y^{\rm H\,in\,ECO}_{lm}(v) = Y^{\rm H\,in}_{lm}(v), \qquad \text{when } v > v^{(\rm H)}_{\Sigma}. \tag{10.35}$$

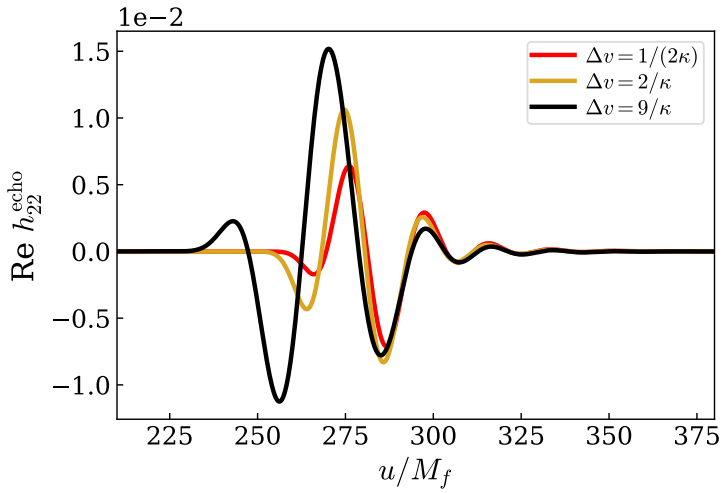

Figure 10.13: The influence of the filter parameter Δv on echo waveforms. Each curve corresponds to the real part of the first echo (with different Δv), using SXS:BBH:0207 and the Boltzmann reflectivity ($\gamma = 10^{-15}$ and $T_{\rm QH} = T_H$) . The filter is applied at the future horizon with $v_\Sigma^{(\rm H)} = -13$.

Note again that the condition is in the time domain. The value of $v_\Sigma^{(\rm H)}$ was determined by searching for the starting time after which $Y_{lm}^{\rm H\,in}(v)$ can be decomposed as a sum of QNM overtones, as discussed in Sec. 10.4.2. In practice, we impose the condition in Eq. (10.35) via a filter:

$$\begin{aligned} Y_{lm}^{\rm H\ in\ ECO}(v) &\to Y_{lm}^{\rm H\ Filter}(v), \\ &= Y_{lm}^{\rm H\,in}(v)\mathcal{F}(v) + \text{Const.} \times [1 - \mathcal{F}(v)], \end{aligned} \tag{10.36}$$

where the Planck-taper filter $\mathcal{F}(v)$ is given by [119]

$$\mathcal{F}(v; v_\Sigma^{(\rm H)}, \Delta v) = \begin{cases} 0, & v < v_\Sigma^{(\rm H)} - \Delta v, \\ \frac{1}{\exp z + 1}, & v_\Sigma^{(\rm H)} - \Delta v < v < v_\Sigma^{(\rm H)}, \\ 1, & v > v_\Sigma^{(\rm H)}. \end{cases} \tag{10.37}$$

and $z = \frac{\Delta v}{v - v_\Sigma^{(\rm H)}} + \frac{\Delta v}{v - v_\Sigma^{(\rm H)} + \Delta v}$. The Planck-taper filter $\mathcal{F}(v)$ is a function that gradually ramps up from 0 to 1 within the time interval $[v_\Sigma^{(\rm H)} - \Delta v, v_\Sigma^{(\rm H)}]$. Therefore, $Y_{lm}^{\rm H\ Filter}(v)$ in Eq. (10.36) represents a quantity that switches from a constant value to $Y_{lm}^{\rm H\,in}(v)$ that is predicted by the hybrid method. The value of the constant does not affect the echo waveform since this zero-frequency content cannot penetrate the BH potential (see the value of $D_{22}^{\rm out}$ in Fig. 10.2). In our case, we set the constant to 0.

With the transfer function at hand, we are able to compute echo waveforms. Figure 10.11 shows an echo signal following the main GW, emitted by the sys-

tem SXS:BBH:0207, assuming $v_\Sigma^{(H)} = -13$, as summarized in Table 10.2, and $(\Delta v = 2/\kappa = 8, \gamma = 10^{-15}, T_{\rm QH} = T_H)$. To further investigate how the echo signal is impacted by the parameters $(\gamma, T_{\rm QH})$, we vary their values and exhibit the results in Fig. 10.12. The echo waveform of SXS:BBH:1936 looks similar to that of SXS:BBH:0207, and it can be found in Sec. 10.10. The total echo waveform is compared with the first echo. In the case of $(\gamma = 10^{-15}, T_{\rm QH} = T_H)$ (shown in the upper left panel), distinct echo pulses are separated by an equal time interval of

$$\Delta u^{\rm echo} \sim |\ln\gamma|/(\pi T_{\rm QH}), \tag{10.38}$$

which is long compared with the duration of BBH ringdown. These well-separated echoes do result mathematically from a collective excitation of ECO's multiple QNMs displayed in Fig. 10.10—even though each individual QNM bears little resemblance to the echo pulse. On the other hand, for greater values of $T_{\rm QH}$ and γ ($\gamma = 10^{-1}, T_{\rm QH} = 5T_H$, shown in the lower right panel), the spacing between nearby pulses becomes comparable to the pulse duration, distinct echo pulses interfere with each other, and we cannot resolve any single pulse. In addition, since the ECO with greater $T_{\rm QH}$ reflects a broader frequency band, the final echo is stronger.

We then investigate the impact of the filter parameter Δv in Eq. (10.37). As shown in Fig. 10.13, we compute the first echo emitted by SXS:BBH:0207, using $(\gamma = 10^{-15}, T_{\rm QH} = T_H)$ and $v_\Sigma^{(\rm H)} = -13$—for a variety of Δv. We can see that the waveforms have different amplitude evolution within the first two cycles, but the distinction is suppressed shortly afterward.

10.5.4 Comparison with the inside prescription

The horizon filter is absent in the framework of inside prescription [11, 64]. Taking $v_\Sigma^{(\rm H)} \to -\infty$, Eq. (10.35) reduces to

$$Y^{\rm H\ in\ ECO}_{lm\omega} = C^{\rm in}_{lm}(\omega) Y^{\infty}_{lm\omega}, \tag{10.39}$$

and Eq. (10.26) becomes

$$Z^{\infty\ echo}_{lm\omega} = \sum_{n=1}^{\infty} \left(\mathscr{R}^{\rm ECO}\mathcal{R}^{\rm BH\ T}\right)^n Z^{\infty}_{lm\omega}, \tag{10.40}$$

where we have used the TS identities in Eqs. (10.9). Direct usage of Eq. (10.40) will lead to undesired low-frequency contents, contributed by the inspiral stage. A workaround would be taking only the ringdown portion of $Z^{\infty}_{lm}(u)$, following Ref. [64]. We compare the hybrid method [Eq. (10.26)] with the inside formula

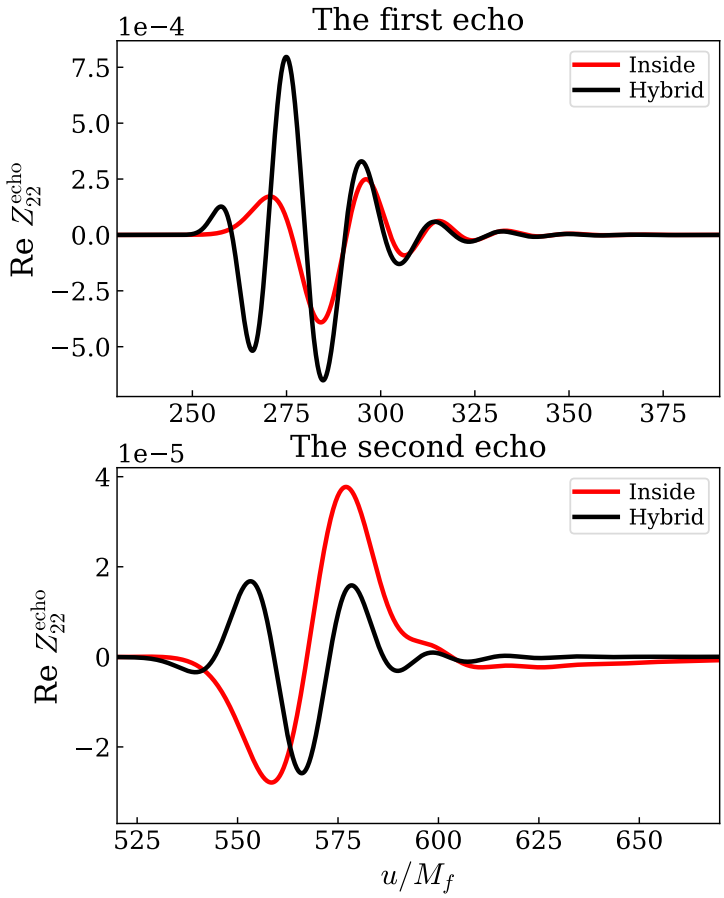

Figure 10.14: A comparison between the hybrid approach and the inside prescription, using SXS:BBH:0207. We choose the Boltzmann reflectivity with $(\gamma = 10^{-15}, T_{\rm QH} = T_H)$. The upper panel shows the first echo, whereas the bottom panel is the second echo. The filter is applied at null infinity (labeled by "Inside," in red), and at future horizon (labeled by "Hybrid," in black). The width of both filters Δv is $2/\kappa$.

[Eq. (10.40)] in Fig. 10.14, assuming SXS:BBH:0207. Here we choose $\Delta v = 2/\kappa$ and $(\gamma = 10^{-15}, T_{\rm QH} = T_H)$. We see for the first echo, the hybrid method leads to a stronger signal, but the inside prescription has a stronger second echo. Meanwhile, for the initial part of the first echo, the hybrid method gives rise to one more cycle, but the evolution is almost identical afterward.

10.6 Detectability and parameter estimation

In this section, we focus on the detectability of the echoes computed in this chapter by current and future detectors. We first give a brief summary of detector response, signal-to-noise ratio (SNR) and Fisher matrix calculations in Sec. 10.6.1. Then we study the detectability of echoes by calculating SNR in Sec. 10.6.2, and discuss

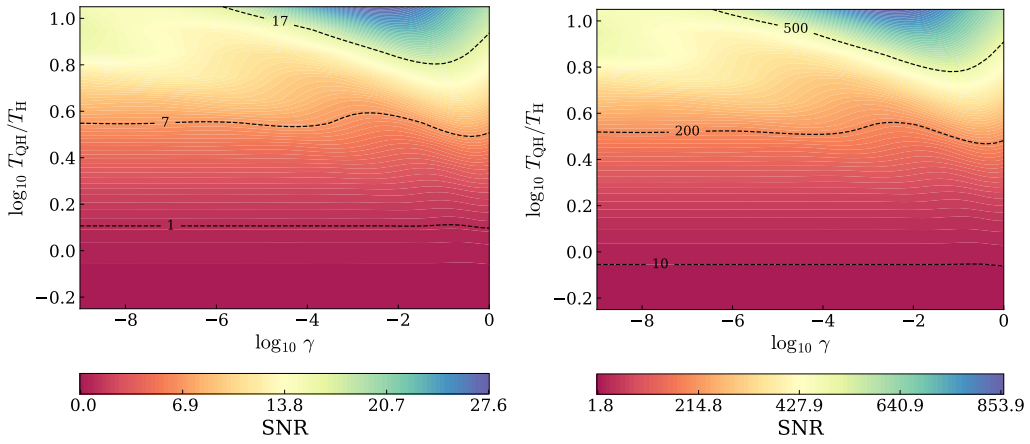

(a) aLIGO, SXS:BBH:0207

(b) CE, SXS:BBH:0207

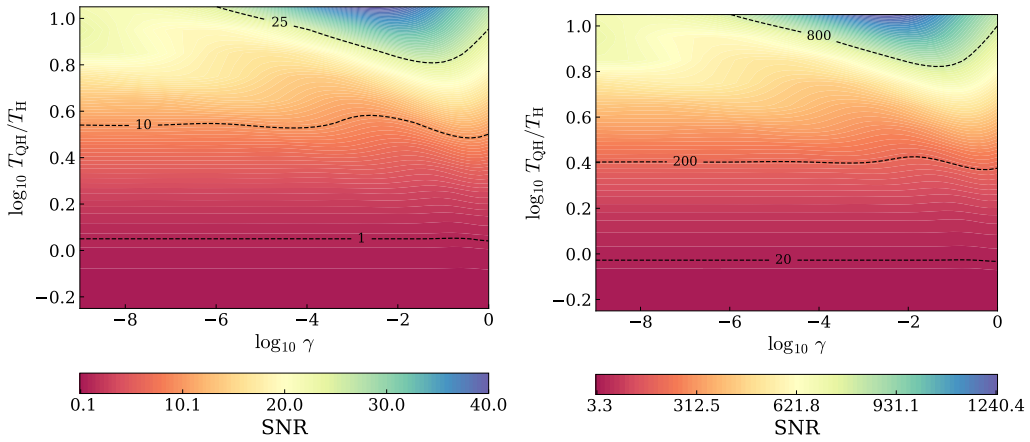

(c) aLIGO, SXS:BBH:1936

(d) CE, SXS:BBH:1936

Figure 10.15: The sky-averaged echo SNR across the $T_{\rm QH} - \gamma$ space, using SXS:BBH:0207 (the upper panel) and SXS:BBH:1936 (the lower panel), as well as aLIGO (the left column) and CE (the right column). The binary system is 100Mpc away from the detector, with a total mass of $60M_{\odot}$. We set Δv to $2/\kappa$ and the values of $v_{\Sigma}^{(\rm H)}$ are listed in Table 10.2.

parameter estimation by adopting the Fisher matrix in Sec. 10.6.3.

10.6.1 The signal-to-noise ratio and Fisher-matrix formalism

We first construct two polarizations of an echo $h^{\rm echo}_{+,\times}$ by assembling $h^{\rm echo}_{lm}$:

$$h^{\rm echo}_{+} - i h^{\rm echo}_{\times} = \sum_{m=\pm 2} {}_{-2}Y_{l=2,m}(\theta,\phi) h^{\rm echo}_{l=2,m}, \tag{10.41}$$

where we are using the leading contributions $h^{\rm echo}_{2,\pm 2}$, who satisfy the condition $h^{\rm echo}_{2,-2} = (h^{\rm echo}_{2,2})^*$. The echo strain $h^{\rm echo}$ detected by a detector is given by

$$h^{\rm echo} = F_+(\theta_S,\phi_L,\psi_L) h^{\rm echo}_{+} + F_\times(\theta_S,\phi_L,\psi_L) h^{\rm echo}_{\times}, \tag{10.42}$$

with (θ_S,ϕ_L) the sky location of a source with respect to the detector, and ψ_L the polarization angle. The SNR of a given GW signal h is written as $\sqrt{(h|h)}$, where the inner product between two waveforms $(h|g)$ reads

$$(h|g) = 4{\rm Re}\int \frac{h^*(f)g(f)}{S_n(f)} df. \tag{10.43}$$

Here $S_n(f)$ is the spectral density of the noise when detecting GWs. The averaged SNR over angular parameters $(\theta_S,\phi_L,\psi_L,\theta,\phi)$ is given by [120]

$$\left\langle \rho^2 \right\rangle = \frac{16}{25}\int \frac{|h_+|^2(\theta=0)}{S_n(f)} df. \tag{10.44}$$

We shall adopt the sky-averaged SNR throughout this chapter.

On the other hand, the Fisher matrix for a given gravitational waveform $h(\lambda^i)$ can be written as

$$\Gamma_{ij} = \left(\frac{\partial h}{\partial \lambda^i} \middle| \frac{\partial h}{\partial \lambda^j} \right), \tag{10.45}$$

where λ^i are parameters to be estimated. In this chapter, we restrict ourselves to $(\gamma, T_{\rm QH})$ that determine the Boltzmann reflectivity [Eq. (10.30)]. By inverting Γ_{ij}, we obtain parameter estimation accuracies for λ^i as

$$\Delta\lambda^i = \sqrt{(\Gamma^{-1})_{ii}}. \tag{10.46}$$

10.6.2 Detectability of echoes

To study how the SNR is impacted by the reflectivity parameters $(\gamma, T_{\rm QH})$, we adopt a aLIGO-like detector [121] and a Cosmic Explorer (CE)-like detector [122], for both SXS:BBH:0207 and SXS:BBH:1936. We assume the binaries to have a total mass of $60M_\odot$, and to be located 100Mpc from the detector.

In the baseline case with $T_{\rm QH} = T_H$, $\gamma = 10^{-1}$, $\Delta v = 2/\kappa$ and using values of $v_\Sigma^{(\rm H)}$ in Table 10.2, we obtain (sky-averaged) echo SNR of ~ 0.45 for aLIGO, and ~ 15 for CE. Echo SNRs of SXS:BBH:1936 are greater than SXS:BBH:0207 by a factor of ~ 1.5 in both detectors. In order to compare with Ref. [58], we also estimate the ratios between echo SNR and ringdown SNR. To first obtain the ringdown SNR, we choose the lower limit of integration in Eq. (10.44) to be the frequency of h_{22}^{∞} evaluated at $u^{(h)}$ [see Eq. (10.17a) and Table 10.2]. For aLIGO, the ringdown SNR for SXS:BBH:0207 is around 7.0, and the ratio $\rm SNR_{echo}/SNR_{ringdown} = 6.5\%$, close to the blue curve in the bottom left panel of Fig. 9 in Ref. [58].

In Figure 10.15, we explore how the echo SNR depends on values of γ and $T_{\rm QH}$, for both detectors and both binaries, respectively, assuming $\Delta v = 2/\kappa$ and the values of $v_\Sigma^{(\rm H)}$ being listed in Table 10.2. The SNR increases with $T_{\rm QH}$ since a larger $T_{\rm QH}$ corresponds to a broader reflection frequency band, and more incident waves are reflected. The γ dependence of SNR is more complex. For small values of $T_{\rm QH}$ (i.e., around unity, as originally proposed by Ref. [11]), the SNR barely depends on γ, because in this case the echoes are weak and mainly dominated by the first pulse, where γ only controls the separation between the echoes in time, then it does not affect the SNR. By contrast, for $T_{\rm QH} \gtrsim 5T_H$, the echoes may overlap with each other, and (constructively) interfere, elevating the SNR.

Next, we investigate the impact of filters on the horizon, namely the advanced time $v_\Sigma^{(\rm H)}$ at which the shell Σ crosses the horizon, and the thickness Δv of the transition region in which we cut off reflection. Taking SXS:BBH:0207 and CE for example, we plot, in Fig. 10.16, the sky-averaged echo SNR as a function of two filter parameters $v_\Sigma^{(\rm H)}$ and Δv [see Eq. (10.37)], where we choose $\gamma = 10^{-15}$ and $T_{\rm QH} = T_H$. As expected, the SNR decreases as either $v_\Sigma^{(\rm H)}$ increases or Δv decreases. The global pattern suggests that the dependence on $v_\Sigma^{(\rm H)}$ and Δv is linearly correlated.

10.6.3 Parameter estimation

We now use the Fisher-matrix formalism to study parameter estimation. Here we restrict ourselves to reflectivity parameters $(\gamma, T_{\rm QH})$, resulting in 2-D Fisher Matrices. This will result in an under-estimate of measurement errors. As shown in Fig. 10.17, we compute the fractional errors of $T_{\rm QH}$ and γ, using SXS:BBH:0207. We still assume that the system has a total mass of $60M_\odot$, and is located 100Mpc from the detector. Two filter parameters $v_\Sigma^{(\rm H)}$ and Δv are still set to -13 and $2/\kappa$, respectively. We vary the value of $T_{\rm QH}$ from 0.4 to 10 while fixing the value of γ to

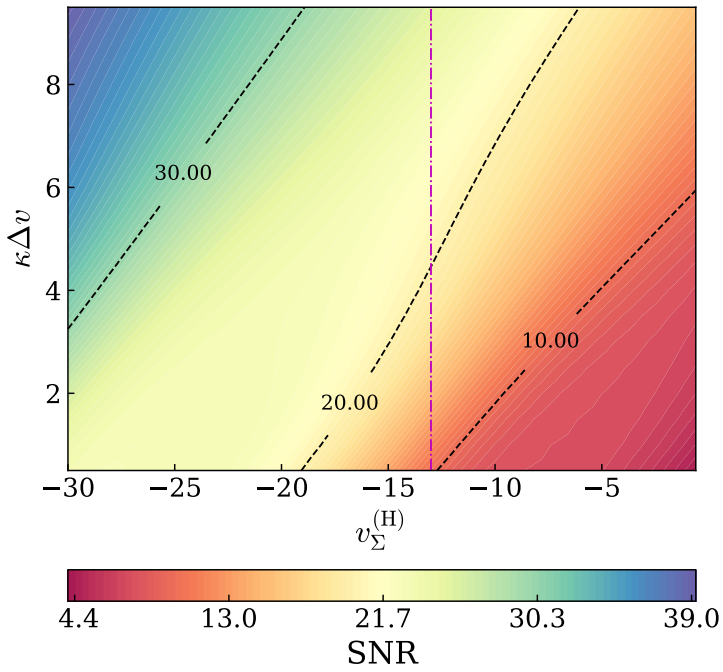

Figure 10.16: The sky-averaged echo SNR as a function of filter parameters $v_\Sigma^{(\mathrm{H})}$ and Δv [see Eq. (10.37)], using CE. The binary system is SXS:BBH:0207 and has the same total mass and distance as Fig. 10.15. We use the Boltzmann reflectivity with $\gamma = 10^{-15}$ and $T_{\mathrm{QH}} = T_H$. The vertical dot-dashed line stands for the value of $v_\Sigma^{(\mathrm{H})}$ in Table 10.2.

10^{-15}. We see the fractional error decreases as T_{QH} increases, since the echo signal is stronger. The constraint on T_{QH} is greater than γ since it has a bigger impact on the echo's profile and SNR. Choosing $T_{\mathrm{QH}} = T_H$, the aLIGO can constrain γ and T_{QH} to the level of 366.7% and 10.2%, respectively. These two constraints lead to 20.9% measurement uncertainty in the time interval Δu^{echo} between individual echoes, based on Eq. (10.38). For CE, the fractional errors of γ, T_{QH}, and Δu^{echo} are 11.4% and 0.3%, and 0.65%, respectively.

10.7 Conclusion

In this chapter, we made use of the hybrid method [77, 78] to establish an echo waveform model for comparable-mass merging binaries whose remnants do not rotate. The hybrid method was proposed originally to predict GWs emitted by BBH coalescences—it separates the space-time of a BBH event into an inner PN region and an outer BHP region (see Fig. 10.1). The two regions communicate via boundary conditions on a worldtube Σ. To build the echo model, we first took the Weyl scalars of the BBH systems from CCE [83] at the future null infinity. Then we

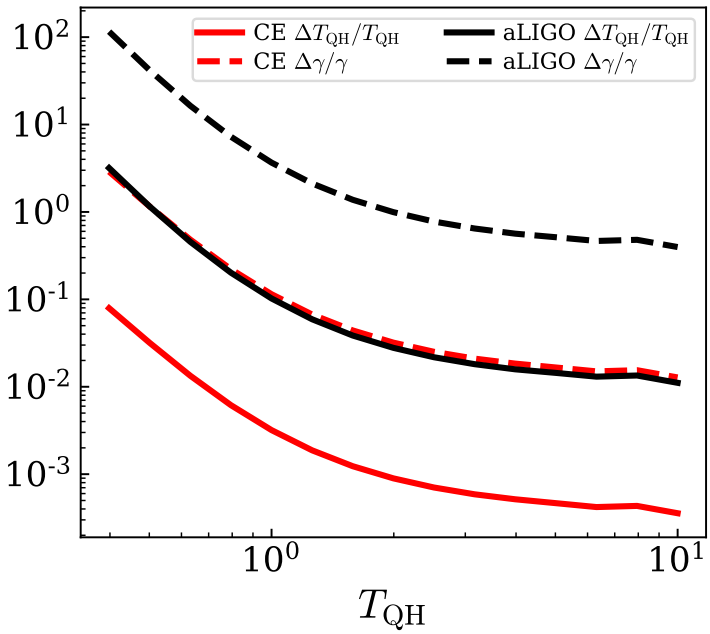

Figure 10.17: The fractional error of $T_{\rm QH}$ (solid curves) and γ (dashed curves) as functions of $T_{\rm QH}$, using aLIGO (in black) and CE (in red). The binary system is SXS:BBH:0207, who has a total mass of $60M_\odot$, and is located 100Mpc from the detector. Two filter parameters $v_\Sigma^{(\rm H)}$ and Δv are still set to -13 and $2/\kappa$, respectively. We vary the value of $T_{\rm QH}$ from 0.4 to 10 while fixing the value of γ to 10^{-15}.

reversed the process of the hybrid method by evolving Weyl scalars back into the bulk, and the solution in the BHP region is proportional to the up-mode solution to the homogeneous Teukolsky equation, as required by the uniqueness of solutions. With the solution at hand, we were able to compute the GW that falls down the future horizon.

Since the BHP theory is not valid inside the matching shell Σ, only the portion of GW that lies outside the worldtube $\Sigma_{\rm Shell}$ is physical. Consequently, the usefulness of our method is limited to the ringdown phase. We determined the location of Σ, namely the advanced time $v_\Sigma^{(\rm H)}$ at which it crosses the future horizon, by looking for the quasi-normal ringing regime of the horizon–ψ_0—we fitted $Y_{lm}^{\rm H\,in}$ to a superposition of five overtones [Eq. (10.17)]. We then removed the earlier piece of ψ_0 (with $v < v_\Sigma^{(H)}$) by applying a Planck-taper filter, whose width Δv (a free parameter in our model) can be viewed as the effective thickness of the matching shell.

Next, by utilizing the physical boundary condition near ECO surfaces [61] and the Boltzmann reflectivity [11], we computed the QNMs of irrotational ECOs, as well as echo signals of two systems: SXS:BBH:0207 and SXS:BBH:1936. We picked

these two runs because their remnant spins vanish, in which the prediction of the hybrid method for ringdown signals has proved to be accurate [77]. Finally, we studied the detectability and parameter estimation of echoes.

We summarize our main conclusions as follows:

(i) The hybrid method is similar to the inside prescription of Refs. [11, 64] in the sense that both of them treat the main GW as a transmitted wave of an initial pulse emerging from the past horizon (see Fig. 10.4). Furthermore, filters are involved in both treatments, which, however, have different physical interpretations. The inside prescription (also the CLA) handles the system as an initial value problem (the Cauchy problem), where the whole process is split into two stages. Only the late time portion lies in the BHP region. Therefore, the filter needs to be applied at the future null infinity. Oppositely, in our case, the exterior system is described by a boundary value problem—a spatial volume is separated at every moment. Accordingly, the filter is imposed at the future horizon to remove the unrealistic portion of the incoming GW. We took SXS:BBH:0207 as an example and compared the hybrid method with the inside prescription. We found that the inside prescription leads to fewer cycles than the hybrid method for the initial part of the echo. Meanwhile, the first echo predicted by the inside prescription is weaker than the result by the hybrid method.

(ii) The Weyl scalars $\psi_{0,4}$ from CCE are consistent with the TS identities throughout the entire frequency band in question. This supports the treatment of the hybrid method that uses the BHP theory to describe the exterior region, at least when the remnant object does not rotate.

(iii) Similar to the studies of Refs. [110, 115], using six overtones, the ringdown of the strain for SXS:BBH:1936 starts at $2M_f$ after the peak. However, the time for SXS:BBH:0207 can be extended to $\sim 11M_f$ before the peak. For the horizon and infinity ψ_0: $Y_{22}^{\mathrm{H}/\infty}$, the prediction of CCE is less accurate, and we were only able to resolve five overtones. The linearly quasi-normal ringing regime of $Y_{22}^{\mathrm{H}\ in}$ for SXS:BBH:0207 and SXS:BBH:1936 are similar and they start at $\sim 13-15M_f$ before the peak.

We have restricted ourselves to inspiralling compact binaries whose remnants are Schwarzschild-like ECOs. Future work could extend the hybrid method to Kerr-like ECOs and utilize it to compute echoes emitted by more general comparable-mass coalescence systems. It is worth pointing out that throughout the process, the Kerr-

like background should have an adiabatically evolving mass and angular momentum due to GW emission. It will be a limitation for the hybrid method if one fails to capture this feature. Another possible avenue for future work is to apply our calculations to head-on collisions and compare the echo waveform with the results in Ref. [75].

10.8 Appendix: The QNM amplitudes of SXS:BBH:0207 and 1936

Figure 10.18 shows the absolute value and phase of $\mathcal{A}_n^{(h/\infty/\mathrm{H})}$ and $\mathcal{B}_n^{(h/\infty/\mathrm{H})}$ [see Eq. (10.17)]. For SXS:BBH:1936, $\mathcal{A}_n^{(h)}$ peaks at $n = 5$, consistent with previous studies [110, 115, 116]. However, in this case the absolute value of the retrograde mode $\mathcal{B}_n^{(h)}$ is comparable with that of $\mathcal{A}_n^{(h)}$, thus it is not negligible. For SXS:BBH:0207, the contribution of the retrograde mode $\mathcal{B}_n^{(h)}$ is considerable as well, and $\mathcal{A}_n^{(h)}$ peaks at $n = 2$ and $\mathcal{B}_n^{(h)}$ at $n = 3$.

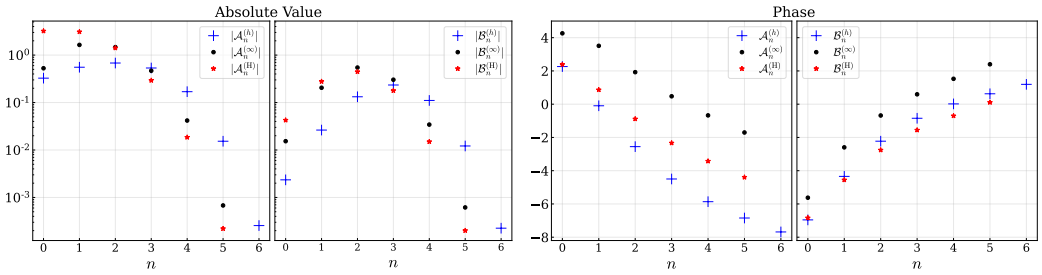

(a) SXS:BBH:0207

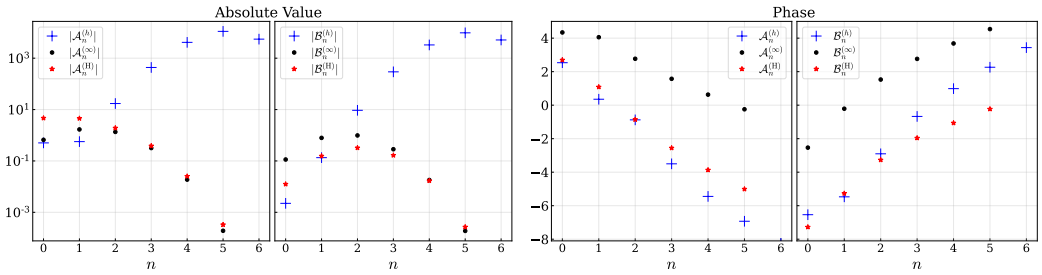

(b) SXS:BBH:1936

Figure 10.18: The absolute value (the left two panels) and phase (the right two panels) of the prograde mode $\mathcal{A}_n$ and the retrograde mode $\mathcal{B}_n$, assuming SXS:BBH:0207 (the upper row) and SXS:BBH:1936 (the lower row). We fit Eqs. (10.17) to the data of h_{22}^{∞} (blue), Y_{22}^{∞} (black) as well as $Y_{22}^{\mathrm{H}\ in}$ (red) obtained from CCE.

10.9 Appendix: The characteristic approach for solving the RW equation

Eq. (10.1) can be solved numerically via a second-order-accurate, characteristic method, proposed by Gundlach *et al.* [123]. As shown in Fig. 10.19, Gundlach *et*

al. [123] picked four points on a discretized (u, v) grid:

$$
\begin{aligned}
{}_s\Psi^{\rm N}_{lm} &= {}_s\Psi^{\rm SN}_{lm}(u+h, v+h), & {}_s\Psi^{\rm E}_{lm} &= {}_s\Psi^{\rm SN}_{lm}(u, v+h),\\
{}_s\Psi^{\rm W}_{lm} &= {}_s\Psi^{\rm SN}_{lm}(u+h, v), & {}_s\Psi^{\rm S}_{lm} &= {}_s\Psi^{\rm SN}_{lm}(u, v),
\end{aligned}
\tag{10.47}
$$

with h the step size. The value on left corner ${}_s\Psi^{\rm W}_{lm}$ can be obtained through

$$
\begin{aligned}
{}_s\Psi^{\rm W}_{lm} =& {}_s\Psi^{\rm N}_{lm} + {}_s\Psi^{\rm S}_{lm} - {}_s\Psi^{\rm E}_{lm}\\
&+ \frac{h^2}{8} V^l_{\rm RW}(r_c)({}_s\Psi^{\rm N}_{lm} + {}_s\Psi^{\rm S}_{lm}) + \mathcal{O}(h^3),
\end{aligned}
\tag{10.48}
$$

where $V^l_{\rm RW}(r_c)$ is the value of the RW potential at the center $r_c = (u + h/2, v + h/2)$. We note that Eq. (10.48) is different from the one used in Refs. [77, 78], where ${}_s\Psi^{\rm N}_{lm}$ was calculated based on the other three. This is because we evolve the system back into the bulk (from $\mathscr{I}^+$ to past horizon).

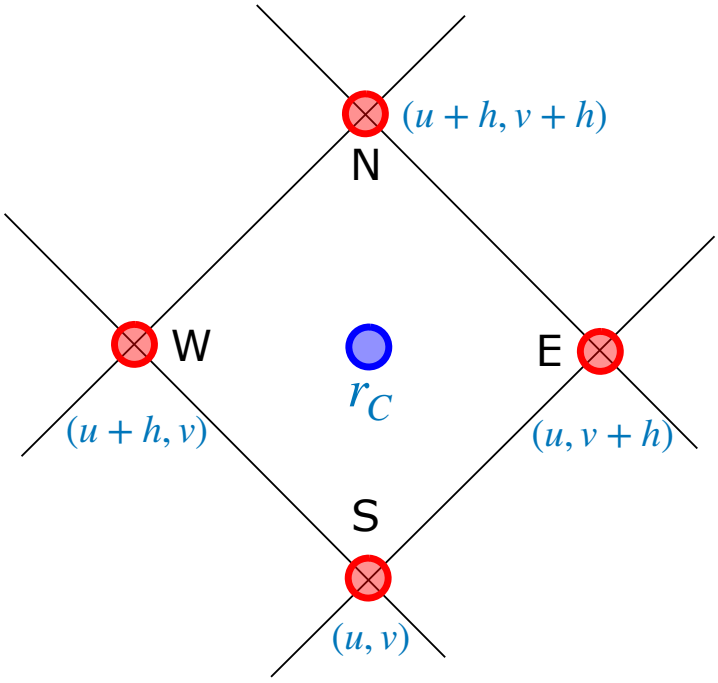

Figure 10.19: The (u, v) grid cell in characteristic evolution scheme for the RW equation.

10.10 Appendix: SXS:BBH:1936

Using SXS:BBH:1936, we test the validity of the TS identity at the null infinity [see Eq. (10.9a)] in Fig. 10.20. Conventions are the same as Fig. 10.6.

In Fig. 10.21, we present the total echo and the first echo with a variety of $(\gamma, T_{\rm QH})$. The location of the filter is listed in Table 10.2, and the width of the filter is set to $2/\kappa$.

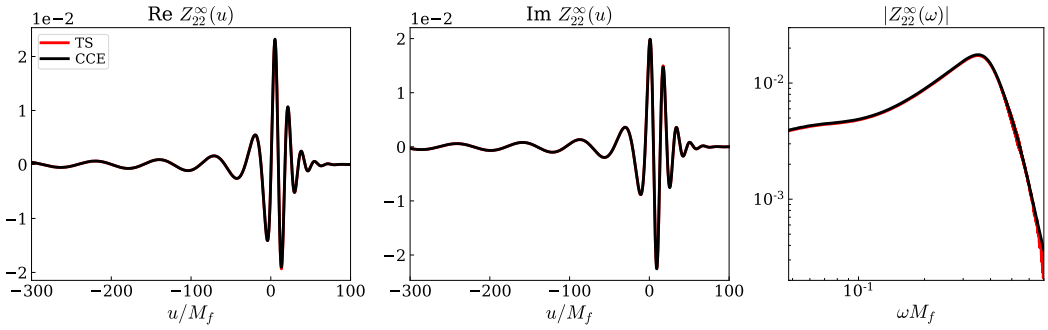

Figure 10.20: Same as Fig. 10.6, using SXS:BBH:1936.

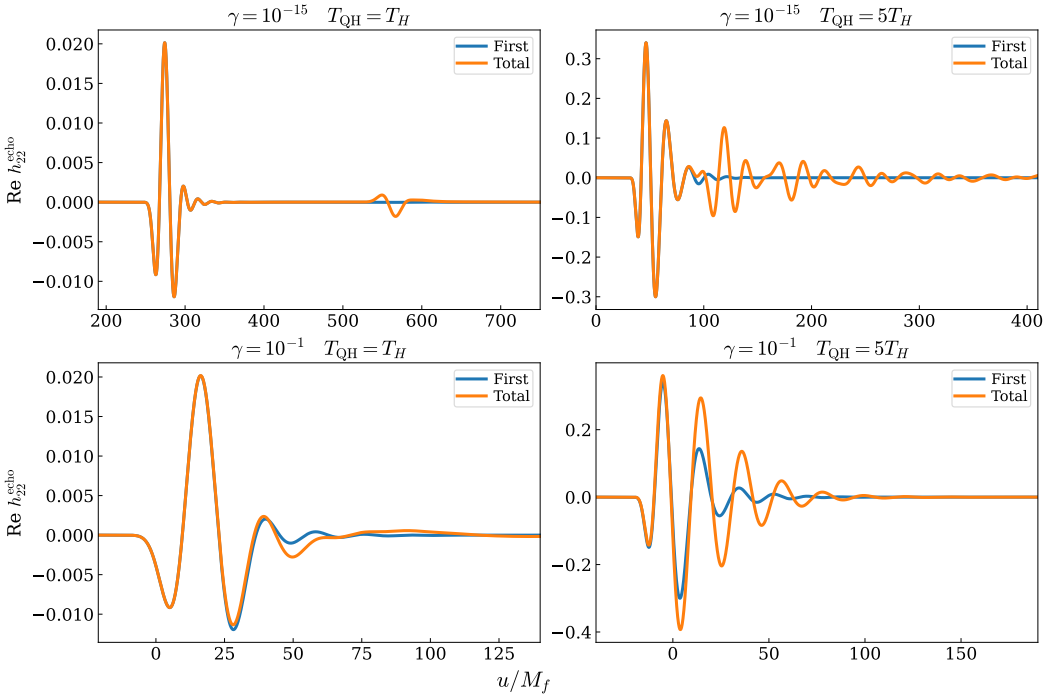

Figure 10.21: Same as Fig. 10.12, using SXS:BBH:1936.

References

[1] Vitor Cardoso, Edgardo Franzin, and Paolo Pani. "Is the gravitational-wave ringdown a probe of the event horizon?" *Phys. Rev. Lett.* 116.17 (2016). [Erratum: Phys.Rev.Lett. 117, 089902 (2016)], p. 171101. DOI: 10.1103/PhysRevLett.116.171101. arXiv: 1602.07309 [gr-qc].

[2] Vitor Cardoso et al. “Gravitational-wave signatures of exotic compact objects and of quantum corrections at the horizon scale.” *Phys. Rev. D* 94.8 (2016), p. 084031. DOI: 10.1103/PhysRevD.94.084031. arXiv: 1608.08637 [gr-qc].

[3] Vitor Cardoso and Paolo Pani. “Tests for the existence of black holes through gravitational wave echoes.” *Nature Astron.* 1.9 (2017), pp. 586–591. DOI: 10.1038/s41550-017-0225-y. arXiv: 1709.01525 [gr-qc].

[4] Jun Zhang and Shuang-Yong Zhou. “Can the graviton have a large mass near black holes?” *Phys. Rev. D* 97.8 (2018), p. 081501. DOI: 10.1103/PhysRevD.97.081501. arXiv: 1709.07503 [gr-qc].

[5] Ruifeng Dong and Dejan Stojkovic. “Gravitational wave echoes from black holes in massive gravity.” *Phys. Rev. D* 103.2 (2021), p. 024058. DOI: 10.1103/PhysRevD.103.024058. arXiv: 2011.04032 [gr-qc].

[6] Ahmed Almheiri et al. “Black holes: Complementarity or firewalls?” *JHEP* 02 (2013), p. 062. DOI: 10.1007/JHEP02(2013)062. arXiv: 1207.3123 [hep-th].

[7] Kabir Chakravarti, Rajes Ghosh, and Sudipta Sarkar. “Signature of nonuniform area quantization on black hole echoes.” *Phys. Rev. D* 105.4 (2022), p. 044046. DOI: 10.1103/PhysRevD.105.044046. arXiv: 2112.10109 [gr-qc].

[8] Steven B. Giddings. “Gravitational wave tests of quantum modifications to black hole structure – with post-GW150914 update.” *Class. Quant. Grav.* 33.23 (2016), p. 235010. DOI: 10.1088/0264-9381/33/23/235010. arXiv: 1602.03622 [gr-qc].

[9] Naritaka Oshita and Niayesh Afshordi. “Probing microstructure of black hole spacetimes with gravitational wave echoes.” *Phys. Rev. D* 99.4 (2019), p. 044002. DOI: 10.1103/PhysRevD.99.044002. arXiv: 1807.10287 [gr-qc].

[10] Vitor Cardoso, Valentino F. Foit, and Matthew Kleban. “Gravitational wave echoes from black hole area quantization.” *JCAP* 08 (2019), p. 006. DOI: 10.1088/1475-7516/2019/08/006. arXiv: 1902.10164 [hep-th].

[11] Qingwen Wang, Naritaka Oshita, and Niayesh Afshordi. “Echoes from quantum black holes.” *Phys. Rev. D* 101.2 (2020), p. 024031. DOI: 10.1103/PhysRevD.101.024031. arXiv: 1905.00446 [gr-qc].

[12] Naritaka Oshita, Qingwen Wang, and Niayesh Afshordi. “On reflectivity of quantum black hole horizons.” *JCAP* 04 (2020), p. 016. DOI: 10.1088/1475-7516/2020/04/016. arXiv: 1905.00464 [hep-th].

[13] Jahed Abedi, Luis Felipe Longo Micchi, and Niayesh Afshordi. “GW190521: First measurement of stimulated Hawking radiation from black holes.” (Dec. 2021). arXiv: 2201.00047 [gr-qc].

[14] Sumanta Chakraborty et al. “Implications of the quantum nature of the black hole horizon on the gravitational-wave ringdown.” (Feb. 2022). arXiv: 2202.09111 [gr-qc].

[15] Kabir Chakravarti, Rajes Ghosh, and Sudipta Sarkar. “Signature of nonuniform area quantization on gravitational waves.” *Phys. Rev. D* 104.8 (2021), p. 084049. DOI: 10.1103/PhysRevD.104.084049. arXiv: 2108.02444 [gr-qc].

[16] Pawel O. Mazur and Emil Mottola. “Gravitational vacuum condensate stars.” *Proc. Nat. Acad. Sci.* 101 (2004), pp. 9545–9550. DOI: 10.1073/pnas.0402717101. arXiv: gr-qc/0407075.

[17] Matt Visser and David L. Wiltshire. “Stable gravastars: An alternative to black holes?” *Class. Quant. Grav.* 21 (2004), pp. 1135–1152. DOI: 10.1088/0264-9381/21/4/027. arXiv: gr-qc/0310107.

[18] Thibault Damour and Sergey N. Solodukhin. “Wormholes as black hole foils.” *Phys. Rev. D* 76 (2007), p. 024016. DOI: 10.1103/PhysRevD.76.024016. arXiv: 0704.2667 [gr-qc].

[19] Bob Holdom and Jing Ren. “Not quite a black hole.” *Phys. Rev. D* 95.8 (2017), p. 084034. DOI: 10.1103/PhysRevD.95.084034. arXiv: 1612.04889 [gr-qc].

[20] Samir D. Mathur. “The fuzzball proposal for black holes: An elementary review.” *Fortsch. Phys.* 53 (2005). Ed. by E. Kiritsis, pp. 793–827. DOI: 10.1002/prop.200410203. arXiv: hep-th/0502050.

[21] Vitor Cardoso et al. “Ergoregion instability of ultracompact astrophysical objects.” *Phys. Rev. D* 77 (2008), p. 124044. DOI: 10.1103/PhysRevD.77.124044. arXiv: 0709.0532 [gr-qc].

[22] Rodrigo Vicente, Vitor Cardoso, and Jorge C. Lopes. “Penrose process, superradiance, and ergoregion instabilities.” *Phys. Rev. D* 97.8 (2018), p. 084032. DOI: 10.1103/PhysRevD.97.084032. arXiv: 1803.08060 [gr-qc].

[23] Elisa Maggio, Paolo Pani, and Valeria Ferrari. “Exotic compact objects and how to quench their ergoregion instability.” *Phys. Rev. D* 96.10 (2017), p. 104047. DOI: 10.1103/PhysRevD.96.104047. arXiv: 1703.03696 [gr-qc].

[24] Elisa Maggio et al. “Ergoregion instability of exotic compact objects: Electromagnetic and gravitational perturbations and the role of absorption.” *Phys. Rev. D* 99.6 (2019), p. 064007. DOI: 10.1103/PhysRevD.99.064007. arXiv: 1807.08840 [gr-qc].

[25] Pedro V. P. Cunha, Emanuele Berti, and Carlos A. R. Herdeiro. “Light-ring stability for ultracompact objects.” *Phys. Rev. Lett.* 119.25 (2017), p. 251102. DOI: 10.1103/PhysRevLett.119.251102. arXiv: 1708.04211 [gr-qc].

[26] Joe Keir. "Slowly decaying waves on spherically symmetric spacetimes and ultracompact neutron stars." *Class. Quant. Grav.* 33.13 (2016), p. 135009. DOI: 10.1088/0264-9381/33/13/135009. arXiv: 1404.7036 [gr-qc].

[27] Vitor Cardoso et al. "Light rings as observational evidence for event horizons: long-lived modes, ergoregions and nonlinear instabilities of ultracompact objects." *Phys. Rev. D* 90.4 (2014), p. 044069. DOI: 10.1103/PhysRevD.90.044069. arXiv: 1406.5510 [gr-qc].

[28] Rajes Ghosh and Sudipta Sarkar. "Light rings of stationary spacetimes." *Phys. Rev. D* 104.4 (2021), p. 044019. DOI: 10.1103/PhysRevD.104.044019. arXiv: 2107.07370 [gr-qc].

[29] Baoyi Chen et al. "Instability of exotic compact objects and its implications for gravitational-wave echoes." (Feb. 2019). arXiv: 1902.08180 [gr-qc].

[30] Andrea Addazi, Antonino Marcianò, and Nicolás Yunes. "Gravitational instability of exotic compact objects." *Eur. Phys. J. C* 80.1 (2020), p. 36. DOI: 10.1140/epjc/s10052-019-7575-9. arXiv: 1905.08734 [gr-qc].

[31] Vitor Cardoso and Paolo Pani. "Testing the nature of dark compact objects: a status report." *Living Rev. Rel.* 22.1 (2019), p. 4. DOI: 10.1007/s41114-019-0020-4. arXiv: 1904.05363 [gr-qc].

[32] Jahed Abedi et al. "Quantum black holes in the sky." *Universe* 6.3 (2020), p. 43. DOI: 10.3390/universe6030043. arXiv: 2001.09553 [gr-qc].

[33] Randy S. Conklin and Niayesh Afshordi. "Boltzmann meets Lorentz: A surrogate model for black hole echoes." (Dec. 2021). arXiv: 2201.00027 [gr-qc].

[34] Samanwaya Mukherjee et al. "Towards establishing the presence or absence of horizons in coalescing binaries of compact objects by using their gravitational wave signals." (Feb. 2022). arXiv: 2202.08661 [gr-qc].

[35] Tullio Regge and John A. Wheeler. "Stability of a Schwarzschild singularity." *Phys. Rev.* 108 (1957), pp. 1063–1069. DOI: 10.1103/PhysRev.108.1063.

[36] Frank J. Zerilli. "The gravitational field of a particle Falling in a Schwarzschild geometry analyzed in tensor harmonics." PhD thesis. PRINCETON UNIVERSITY., Jan. 1969.

[37] Lam Hui, Daniel Kabat, and Sam S. C. Wong. "Quasinormal modes, echoes and the causal structure of the Green's function." *JCAP* 12 (2019), p. 020. DOI: 10.1088/1475-7516/2019/12/020. arXiv: 1909.10382 [gr-qc].

[38] Mark Ho-Yeuk Cheung et al. "The elephant and the flea: Destabilizing the fundamental mode of black holes." (Nov. 2021). arXiv: 2111.05415 [gr-qc].

[39] Zachary Mark et al. "A recipe for echoes from exotic compact objects." *Phys. Rev. D* 96.8 (2017), p. 084002. DOI: 10.1103/PhysRevD.96.084002. arXiv: 1706.06155 [gr-qc].

[40] Adriano Testa and Paolo Pani. "Analytical template for gravitational-wave echoes: signal characterization and prospects of detection with current and future interferometers." *Phys. Rev. D* 98.4 (2018), p. 044018. DOI: 10.1103/PhysRevD.98.044018. arXiv: 1806.04253 [gr-qc].

[41] Song Ming Du and Yanbei Chen. "Searching for near-horizon quantum structures in the binary black-hole stochastic gravitational-wave background." *Phys. Rev. Lett.* 121.5 (2018), p. 051105. DOI: 10.1103/PhysRevLett.121.051105. arXiv: 1803.10947 [gr-qc].

[42] Elisa Maggio et al. "How does a dark compact object ringdown?" *Phys. Rev. D* 102.6 (2020), p. 064053. DOI: 10.1103/PhysRevD.102.064053. arXiv: 2006.14628 [gr-qc].

[43] Vitor Cardoso, Adrian del Rio, and Masashi Kimura. "Distinguishing black holes from horizonless objects through the excitation of resonances during inspiral." *Phys. Rev. D* 100 (2019). [Erratum: Phys.Rev.D 101, 069902 (2020)], p. 084046. DOI: 10.1103/PhysRevD.100.084046. arXiv: 1907.01561 [gr-qc].

[44] Massimo Bianchi et al. "Distinguishing fuzzballs from black holes through their multipolar structure." *Phys. Rev. Lett.* 125 (22 Nov. 2020), p. 221601. DOI: 10.1103/PhysRevLett.125.221601. URL: https://link.aps.org/doi/10.1103/PhysRevLett.125.221601.

[45] Iosif Bena and Daniel R. Mayerson. "Multipole ratios: A new window into black holes." *Phys. Rev. Lett.* 125 (22 Nov. 2020), p. 221602. DOI: 10.1103/PhysRevLett.125.221602. URL: https://link.aps.org/doi/10.1103/PhysRevLett.125.221602.

[46] Taishi Ikeda et al. "Black-hole microstate spectroscopy: Ringdown, quasinormal modes, and echoes." *Phys. Rev. D* 104.6 (2021), p. 066021. DOI: 10.1103/PhysRevD.104.066021. arXiv: 2103.10960 [gr-qc].

[47] Yun Fang, Rong-Zhen Guo, and Qing-Guo Huang. "Tests for the existence of horizon through gravitational waves from a small binary in the vicinity of a massive object." *Phys. Lett. B* 822 (2021), p. 136654. DOI: 10.1016/j.physletb.2021.136654. arXiv: 2108.04511 [astro-ph.CO].

[48] Richard Abbott et al. "GWTC-2: Compact binary coalescences observed by LIGO and Virgo during the first half of the third observing run." *Phys. Rev. X* 11 (2021), p. 021053. DOI: 10.1103/PhysRevX.11.021053. arXiv: 2010.14527 [gr-qc].

[49] Robert P. Geroch. "Multipole moments. II. Curved space." *J. Math. Phys.* 11 (1970), pp. 2580–2588. DOI: 10.1063/1.1665427.

[50] Richard O. Hansen. "Multipole moments of stationary space-times." *J. Math. Phys.* 15 (1974), pp. 46–52. DOI: 10.1063/1.1666501.

[51] Saul A. Teukolsky. "Rotating black holes - separable wave equations for gravitational and electromagnetic perturbations." *Phys. Rev. Lett.* 29 (1972), pp. 1114–1118. DOI: 10.1103/PhysRevLett.29.1114.

[52] Saul A. Teukolsky. "Perturbations of a rotating black hole. I. Fundamental equations for gravitational, electromagnetic, and neutrino-field perturbations." *Astrophysical Journal* 185 (Oct. 1973), pp. 635–648. DOI: 10.1086/152444.

[53] Pablo Bueno et al. "Echoes of Kerr-like wormholes." *Phys. Rev. D* 97.2 (2018), p. 024040. DOI: 10.1103/PhysRevD.97.024040. arXiv: 1711.00391 [gr-qc].

[54] Hiroyuki Nakano et al. "Black hole ringdown echoes and howls." *PTEP* 2017.7 (2017), 071E01. DOI: 10.1093/ptep/ptx093. arXiv: 1704.07175 [gr-qc].

[55] Norichika Sago and Takahiro Tanaka. "Gravitational wave echoes induced by a point mass plunging into a black hole." *PTEP* 2020.12 (2020), 123E01. DOI: 10.1093/ptep/ptaa149. arXiv: 2009.08086 [gr-qc].

[56] Elisa Maggio, Maarten van de Meent, and Paolo Pani. "Extreme mass-ratio inspirals around a spinning horizonless compact object." (June 2021). arXiv: 2106.07195 [gr-qc].

[57] Luis Felipe Longo Micchi and Cecilia Chirenti. "Spicing up the recipe for echoes from exotic compact objects: Orbital differences and corrections in rotating backgrounds." *Phys. Rev. D* 101 (8 Apr. 2020), p. 084010. DOI: 10.1103/PhysRevD.101.084010. URL: https://link.aps.org/doi/10.1103/PhysRevD.101.084010.

[58] Luis Felipe Longo Micchi, Niayesh Afshordi, and Cecilia Chirenti. "How loud are echoes from exotic compact objects?" *Phys. Rev. D* 103.4 (2021), p. 044028. DOI: 10.1103/PhysRevD.103.044028. arXiv: 2010.14578 [gr-qc].

[59] Shuo Xin et al. "Gravitational-wave echoes from spinning exotic compact objects: Numerical waveforms from the Teukolsky equation." *Phys. Rev. D* 104.10 (2021), p. 104005. DOI: 10.1103/PhysRevD.104.104005. arXiv: 2105.12313 [gr-qc].

[60] Manu Srivastava and Yanbei Chen. "Gravitational radiation close to a black hole horizon: Waveform regularization and the out-going echo." (Aug. 2021). arXiv: 2108.01329 [gr-qc].

[61] Baoyi Chen, Qingwen Wang, and Yanbei Chen. "Tidal response and near-horizon boundary conditions for spinning exotic compact objects." *Phys. Rev. D* 103.10 (2021), p. 104054. DOI: 10.1103/PhysRevD.103.104054. arXiv: 2012.10842 [gr-qc].

[62] Alexei A. Starobinsky. "Amplification of waves reflected from a rotating "black hole."" *Sov. Phys. JETP* 37.1 (1973), pp. 28–32.

[63] Saul A. Teukolsky and William H. Press. "Perturbations of a rotating black hole. III - Interaction of the hole with gravitational and electromagnetic radiation." *Astrophys. J.* 193 (1974), pp. 443–461. DOI: 10.1086/153180.

[64] Elisa Maggio et al. "Analytical model for gravitational-wave echoes from spinning remnants." *Phys. Rev. D* 100.6 (2019), p. 064056. DOI: 10.1103/PhysRevD.100.064056. arXiv: 1907.03091 [gr-qc].

[65] Alessandra Buonanno and Thibault Damour. "Effective one-body approach to general relativistic two-body dynamics." *Phys. Rev.* D59 (1999), p. 084006. DOI: 10.1103/PhysRevD.59.084006. arXiv: gr-qc/9811091 [gr-qc].

[66] Wen-Biao Han. "Gravitational waves from extreme-mass-ratio inspirals in equatorially eccentric orbits." *International Journal of Modern Physics D* 23.7, 1450064 (June 2014), p. 1450064. DOI: 10.1142/S0218271814500643.

[67] Richard H. Price and Jorge Pullin. "Colliding black holes: The close limit." *Phys. Rev. Lett.* 72 (21 May 1994), pp. 3297–3300. DOI: 10.1103/PhysRevLett.72.3297. URL: https://link.aps.org/doi/10.1103/PhysRevLett.72.3297.

[68] Reinaldo J. Gleiser et al. "Colliding black holes: How far can the close approximation go?" *Phys. Rev. Lett.* 77 (22 Nov. 1996), pp. 4483–4486. DOI: 10.1103/PhysRevLett.77.4483. URL: https://link.aps.org/doi/10.1103/PhysRevLett.77.4483.

[69] Zeferino Andrade and Richard H. Price. "Head-on collisions of unequal mass black holes: Close-limit predictions." *Phys. Rev. D* 56 (10 Nov. 1997), pp. 6336–6350. DOI: 10.1103/PhysRevD.56.6336. URL: https://link.aps.org/doi/10.1103/PhysRevD.56.6336.

[70] Gaurav Khanna et al. "Inspiraling black holes: The close Limit." *Phys. Rev. Lett.* 83 (18 Nov. 1999), pp. 3581–3584. DOI: 10.1103/PhysRevLett.83.3581. URL: https://link.aps.org/doi/10.1103/PhysRevLett.83.3581.

[71] Qingwen Wang and Niayesh Afshordi. "Black hole echology: The observer's manual." *Phys. Rev. D* 97.12 (2018), p. 124044. DOI: 10.1103/PhysRevD.97.124044. arXiv: 1803.02845 [gr-qc].

[72] Randy S. Conklin and Bob Holdom. "Gravitational wave echo spectra." *Phys. Rev. D* 100.12 (2019), p. 124030. DOI: 10.1103/PhysRevD.100.124030. arXiv: 1905.09370 [gr-qc].

[73] Scott E. Field et al. "Fast prediction and evaluation of gravitational waveforms using surrogate models." *Phys. Rev. X* 4.3, 031006 (July 2014), p. 031006. DOI: 10.1103/PhysRevX.4.031006. arXiv: 1308.3565 [gr-qc].

[74] Vijay Varma et al. "Surrogate models for precessing binary black hole simulations with unequal masses." *Phys. Rev. Research.* 1 (2019), p. 033015. DOI: 10.1103/PhysRevResearch.1.033015. arXiv: 1905.09300 [gr-qc].

[75] Lorenzo Annulli, Vitor Cardoso, and Leonardo Gualtieri. "Generalizing the close limit approximation of binary black holes." (Apr. 2021). arXiv: 2104.11236 [gr-qc].

[76] Dieter R. Brill and Richard W. Lindquist. "Interaction energy in Geometrostatics." *Phys. Rev.* 131 (1 July 1963), pp. 471–476. DOI: 10.1103/PhysRev.131.471. URL: https://link.aps.org/doi/10.1103/PhysRev.131.471.

[77] David A. Nichols and Yanbei Chen. "A hybrid method for understanding black-hole mergers: Head-on case." *Phys. Rev. D* 82 (2010), p. 104020. DOI: 10.1103/PhysRevD.82.104020. arXiv: 1007.2024 [gr-qc].

[78] David A. Nichols and Yanbei Chen. "Hybrid method for understanding black-hole mergers: Inspiralling case." *Phys. Rev. D* 85 (2012), p. 044035. DOI: 10.1103/PhysRevD.85.044035. arXiv: 1109.0081 [gr-qc].

[79] Nigel T. Bishop et al. "Cauchy-characteristic extraction in numerical relativity." *Phys. Rev. D* 54 (10 Nov. 1996), pp. 6153–6165. DOI: 10.1103/PhysRevD.54.6153. URL: https://link.aps.org/doi/10.1103/PhysRevD.54.6153.

[80] Nigel T. Bishop et al. "High-powered gravitational news." *Phys. Rev. D* 56 (10 Nov. 1997), pp. 6298–6309. DOI: 10.1103/PhysRevD.56.6298. URL: https://link.aps.org/doi/10.1103/PhysRevD.56.6298.

[81] Jeffrey Winicour. "Characteristic evolution and matching." *Living Rev. Rel.* 12 (2009), p. 3. DOI: 10.12942/lrr-2009-3. arXiv: 0810.1903 [gr-qc].

[82] Christian Reisswig et al. "Unambiguous determination of gravitational waveforms from binary black hole mergers." *Phys. Rev. Lett.* 103 (22 Nov. 2009), p. 221101. DOI: 10.1103/PhysRevLett.103.221101. URL: https://link.aps.org/doi/10.1103/PhysRevLett.103.221101.

[83] Jordan Moxon, Mark A. Scheel, and Saul A. Teukolsky. "Improved Cauchy-characteristic evolution system for high-precision numerical relativity waveforms." *Phys. Rev. D* 102.4 (2020), p. 044052. DOI: 10.1103/PhysRevD.102.044052. arXiv: 2007.01339 [gr-qc].

[84] Jordan Moxon et al. "The SpECTRE Cauchy-characteristic evolution system for rapid, precise waveform extraction." (Oct. 2021). arXiv: 2110.08635 [gr-qc].

[85] Stephen W Hawking and George Francis Rayner Ellis. *The large scale structure of space-time*. Vol. 1. Cambridge university press, 1973.

[86] Misao Sasaki and Hideyuki Tagoshi. "Analytic black hole perturbation approach to gravitational radiation." *Living Rev. Rel.* 6 (2003), p. 6. DOI: 10.12942/lrr-2003-6. arXiv: gr-qc/0306120.

[87] E. W. Leaver. "An analytic representation for the quasi normal modes of Kerr black holes." *Proc. Roy. Soc. Lond. A* 402 (1985), pp. 285–298. DOI: 10.1098/rspa.1985.0119.

[88] *Black hole Perturbation Toolkit*. (bhptoolkit.org).

[89] Robert M. Wald. "Construction of solutions of gravitational, electromagnetic, or other perturbation equations from solutions of decoupled equations." *Phys. Rev. Lett.* 41 (4 July 1978), pp. 203–206. DOI: 10.1103/PhysRevLett.41.203. URL: https://link.aps.org/doi/10.1103/PhysRevLett.41.203.

[90] Nicholas Loutrel et al. "Second order perturbations of Kerr black holes: Reconstruction of the metric." *Phys. Rev. D* 103.10 (2021), p. 104017. DOI: 10.1103/PhysRevD.103.104017. arXiv: 2008.11770 [gr-qc].

[91] Michael Boyle et al. "Gravitational-wave modes from precessing black-hole binaries." (Sept. 2014). arXiv: 1409.4431 [gr-qc].

[92] Richard H. Price and Jorge Pullin. "Colliding black holes: The close limit." *Phys. Rev. Lett.* 72 (1994), pp. 3297–3300. DOI: 10.1103/PhysRevLett.72.3297. arXiv: gr-qc/9402039.

[93] Andrew M. Abrahams and Richard H. Price. "Black hole collisions from Brill-Lindquist initial data: Predictions of perturbation theory." *Phys. Rev. D* 53 (1996), pp. 1972–1976. DOI: 10.1103/PhysRevD.53.1972. arXiv: gr-qc/9509020.

[94] Zeferino Andrade and Richard H. Price. "Headon collisions of unequal mass black holes: Close limit predictions." *Phys. Rev. D* 56 (1997), pp. 6336–6350. DOI: 10.1103/PhysRevD.56.6336. arXiv: gr-qc/9611022.

[95] Gaurav Khanna et al. "Inspiralling black holes: The close limit." *Phys. Rev. Lett.* 83 (1999), pp. 3581–3584. DOI: 10.1103/PhysRevLett.83.3581. arXiv: gr-qc/9905081.

[96] Carlos F. Sopuerta, Nicolas Yunes, and Pablo Laguna. "Gravitational recoil from binary black hole mergers: The close-limit approximation." *Phys. Rev. D* 74 (2006). [Erratum: Phys.Rev.D 75, 069903 (2007), Erratum: Phys.Rev.D 78, 049901 (2008)], p. 124010. DOI: 10.1103/PhysRevD.78.049901. arXiv: astro-ph/0608600.

[97] Carlos F. Sopuerta, Nicolas Yunes, and Pablo Laguna. "Gravitational recoil velocities from eccentric binary black hole mergers." *Astrophys. J. Lett.* 656 (2007), pp. L9–L12. DOI: 10.1086/512067. arXiv: astro-ph/0611110.

[98] Alexandre Le Tiec and Luc Blanchet. "The close-limit approximation for black hole binaries with post-Newtonian initial conditions." *Class. Quant. Grav.* 27 (2010), p. 045008. DOI: 10.1088/0264-9381/27/4/045008. arXiv: 0910.4593 [gr-qc].

[99] Nathan K. Johnson-McDaniel et al. "Conformally curved binary black hole initial data including tidal deformations and outgoing radiation." *Phys. Rev. D* 80 (2009), p. 124039. DOI: 10.1103/PhysRevD.80.124039. arXiv: 0907.0891 [gr-qc].

[100] Charles W. Misner. "Wormhole initial conditions." *Phys. Rev.* 118 (1960), pp. 1110–1111. DOI: 10.1103/PhysRev.118.1110.

[101] Jeffrey M. Bowen and James W. York. "Time-asymmetric initial data for black holes and black-hole collisions". *Phys. Rev. D* 21 (8 Apr. 1980), pp. 2047–2056. DOI: 10.1103/PhysRevD.21.2047. URL: https://link.aps.org/doi/10.1103/PhysRevD.21.2047.

[102] John G. Baker, Manuela Campanelli, and Carlos O. Lousto. "The Lazarus project: A Pragmatic approach to binary black hole evolutions." *Phys. Rev. D* 65 (2002), p. 044001. DOI: 10.1103/PhysRevD.65.044001. arXiv: gr-qc/0104063.

[103] Manuela Campanelli, Bernard J. Kelly, and Carlos O. Lousto. "The Lazarus project. II. Space-like extraction with the quasi-Kinnersley tetrad." *Phys. Rev. D* 73 (2006), p. 064005. DOI: 10.1103/PhysRevD.73.064005. arXiv: gr-qc/0510122.

[104] *https://www.black-holes.org/code/SpEC.html*. URL: https://www.black-holes.org/code/SpEC.html.

[105] Michael Boyle et al. "The SXS collaboration catalog of binary black hole simulations." *Class. Quant. Grav.* 36.19 (2019), p. 195006. DOI: 10.1088/1361-6382/ab34e2. arXiv: 1904.04831 [gr-qc].

[106] Lawrence E. Kidder et al. "SpECTRE: A task-based discontinuous Galerkin code for relativistic astrophysics." *J. Comput. Phys.* 335 (2017), pp. 84–114. DOI: 10.1016/j.jcp.2016.12.059. arXiv: 1609.00098 [astro-ph.HE].

[107] Nils Deppe et al. *SpECTRE v2022.06.14*. 10.5281/zenodo.6643787. Version 2022.06.14. June 2022. DOI: 10.5281/zenodo.6643787. URL: https://spectre-code.org.

[108] Thomas Mädler and Jeffrey Winicour. "Bondi-Sachs Formalism." *Scholarpedia* 11 (2016), p. 33528. DOI: 10.4249/scholarpedia.33528. arXiv: 1609.01731 [gr-qc].

[109] Roger Penrose and Wolfgang Rindler. *Spinors and space-time: Volume 2, Spinor and twistor methods in space-time geometry*. Vol. 2. Cambridge University Press, 1984.

[110] Matthew Giesler et al. "Black hole ringdown: The importance of overtones." *Phys. Rev.* X9.4 (2019), p. 041060. DOI: 10.1103/PhysRevX.9.041060. arXiv: 1903.08284 [gr-qc].

[111] Pierre Mourier et al. "Quasinormal modes and their overtones at the common horizon in a binary black hole merger." *Phys. Rev. D* 103.4 (2021), p. 044054. DOI: 10.1103/PhysRevD.103.044054. arXiv: 2010.15186 [gr-qc].

[112] Halston Lim et al. "Exciting black hole modes via misaligned coalescences: II. The mode content of late-time coalescence waveforms." *Phys. Rev. D* 100.8 (2019), p. 084032. DOI: 10.1103/PhysRevD.100.084032. arXiv: 1901.05902 [gr-qc].

[113] Arnab Dhani. "Importance of mirror modes in binary black hole ringdown waveform." *Phys. Rev. D* 103.10 (2021), p. 104048. DOI: 10.1103/PhysRevD.103.104048. arXiv: 2010.08602 [gr-qc].

[114] Leo C. Stein. "qnm: A Python package for calculating Kerr quasinormal modes, separation constants, and spherical-spheroidal mixing coefficients." *J. Open Source Softw.* 4.42 (2019), p. 1683. DOI: 10.21105/joss.01683. arXiv: 1908.10377 [gr-qc].

[115] Sizheng Ma et al. "Universal features of gravitational waves emitted by superkick binary black hole systems." *Phys. Rev. D* 104.8 (2021), p. 084003. DOI: 10.1103/PhysRevD.104.084003. arXiv: 2107.04890 [gr-qc].

[116] Naritaka Oshita. "Ease of excitation of black hole ringing: Quantifying the importance of overtones by the excitation factors." *Phys. Rev. D* 104.12 (2021), p. 124032. DOI: 10.1103/PhysRevD.104.124032. arXiv: 2109.09757 [gr-qc].

[117] Fan Zhang et al. "Visualizing spacetime curvature via frame-drag vortexes and tidal tendexes II. Stationary black holes." *Phys. Rev. D* 86 (2012), p. 084049. DOI: 10.1103/PhysRevD.86.084049. arXiv: 1208.3034 [gr-qc].

[118] Ryogo Kubo. "The fluctuation-dissipation theorem." *Reports on Progress in Physics* 29.1 (Jan. 1966), pp. 255–284. DOI: 10.1088/0034-4885/29/1/306. URL: https://doi.org/10.1088/0034-4885/29/1/306.

[119] David J. A. McKechan, Craig Robinson, and Bangalore S. Sathyaprakash. "A tapering window for time-domain templates and simulated signals in the detection of gravitational waves from coalescing compact binaries." *Class. Quant. Grav.* 27 (2010), p. 084020. DOI: 10.1088/0264-9381/27/8/084020. arXiv: 1003.2939 [gr-qc].

[120] Lee Samuel Finn and David F. Chernoff. "Observing binary inspiral in gravitational radiation: One interferometer." *Phys. Rev. D* 47 (1993), pp. 2198–2219. DOI: 10.1103/PhysRevD.47.2198. arXiv: gr-qc/9301003.

[121] J. Aasi et al. “Characterization of the LIGO detectors during their sixth science run.” *Class. Quant. Grav.* 32.11 (2015), p. 115012. DOI: 10.1088/0264-9381/32/11/115012. arXiv: 1410.7764 [gr-qc].

[122] Benjamin P Abbott et al. “Exploring the sensitivity of next generation gravitational wave detectors.” *Class. Quant. Grav.* 34.4 (2017), p. 044001. DOI: 10.1088/1361-6382/aa51f4. arXiv: 1607.08697 [astro-ph.IM].

[123] Carsten Gundlach, Richard H. Price, and Jorge Pullin. “Late time behavior of stellar collapse and explosions: 1. Linearized perturbations.” *Phys. Rev. D* 49 (1994), pp. 883–889. DOI: 10.1103/PhysRevD.49.883. arXiv: gr-qc/9307009.